Topics in Current Chemistry 352

David Beljonne
Jerome Cornil *Editors*

Multiscale Modelling of Organic and Hybrid Photovoltaics

Springer

352
Topics in Current Chemistry

Aims and Scope

The series Topics in Current Chemistry presents critical reviews of the present and future trends in modern chemical research. The scope of coverage includes all areas of chemical science including the interfaces with related disciplines such as biology, medicine and materials science.

The goal of each thematic volume is to give the non-specialist reader, whether at the university or in industry, a comprehensive overview of an area where new insights are emerging that are of interest to larger scientific audience.

Thus each review within the volume critically surveys one aspect of that topic and places it within the context of the volume as a whole. The most significant developments of the last 5 to 10 years should be presented. A description of the laboratory procedures involved is often useful to the reader. The coverage should not be exhaustive in data, but should rather be conceptual, concentrating on the methodological thinking that will allow the non-specialist reader to understand the information presented.

Discussion of possible future research directions in the area is welcome.

Review articles for the individual volumes are invited by the volume editors.

Readership: research chemists at universities or in industry, graduate students.

More information about this series at
http://www.springer.com/series/128

David Beljonne • Jerome Cornil
Editors

Multiscale Modelling of Organic and Hybrid Photovoltaics

With contributions by

F. De Angelis · R. Berardi · J. Bisquert · J.-L. Brédas · G. D'Avino · N.C. Greenham · C. Groves · E. Hontz · T. Kirchartz · R.A. Marcus· D.P. McMahon · L. Muccioli · J. Nelson · S. Orlandi · M. Pastore · A. Pizzirusso · M. Ricci · C. Risko · O.M. Roscioni · T. Van Voorhis · A.B. Walker · S.R. Yost · C. Zannoni

Springer

Editors
David Beljonne
Centre d'Innovation et de Recherche
en Matériaux Polymères
Université de Mons - UMONS Chimie
des Matériaux Nouveaux
Mons
Belgium

Jerome Cornil
Université de Mons
Mons
Belgium

ISSN 0340-1022 ISSN 1436-5049 (electronic)
ISBN 978-3-662-43873-2 ISBN 978-3-662-43874-9 (eBook)
DOI 10.1007/978-3-662-43874-9
Springer Heidelberg New York Dordrecht London

Library of Congress Control Number: 2014945968

Printed on acid-free paper

Springer is part of Springer Science+Business Media (www.springer.com)

Preface

The massive exploitation of fossil fuels as an energy source has enabled the development of the industrial era that we have witnessed over the last 80 years. Yet oil resources are limited and the use of alternative techniques, such as extraction of unconventional hydrocarbons or deep sea, extreme offshore drilling, brings along its cortege of problems (poor energy efficiency, pollution, etc.). We therefore need a new paradigm. Besides relying on perennial sources, the new standard for energy production will need to reduce carbon dioxide dumping in the atmosphere and be efficient. Among the various options (which will likely have to be combined to replace fossil energy), solar energy appears as one of the most promising. The amount of solar energy technologically, economically, and ecologically exploitable today (about 22 TW) could indeed cover a large fraction of current energy needs.

If the photovoltaic market is currently dominated by first-generation silicon-based modules, second-generation devices based on thin film technologies have emerged over the last decade as an attractive, low-cost, flexible, lightweight alternative (while we are en route towards cells able to break the Schockley–Queisser limit of around 34%). This volume focuses on two technologies which have developed in parallel and rely on the use of organic conjugated molecules and/or polymers to harvest solar light, namely organic bulk heterojunction photovoltaics (OPV) and dye sensitized solar cells (DSSC). Remarkable developments in terms of device efficiency, now approaching or even surpassing that of thin-film silicon solar cells which is around 12%, and long-term stability have been achieved recently. These breakthroughs were driven by the body of knowledge which has accumulated on the working devices using experimental investigation techniques combined with modeling studies.

Over the years, theoretical modeling has turned out to be a valuable tool in understanding the key electronic processes taking place in organic-based solar cells, such as light absorption, light conversion into electrical charges, and charge transport, and this has subsequently led to the emergence of improved material and device architectures. Multiple computational techniques and theoretical models have been developed and applied to OPV and DSSC, which have allowed the assessing of structural, electronic and optical processes spanning multiple time

and length scales. At one extreme, quantum-mechanical methods explicitly take into account all atomistic details in the calculation of geometric and electronic structures but are limited to a few hundred atoms. At the other extreme, continuum models and classical equations predict the response properties at the device scale. In between, mesoscopic models have been developed where progressive coarse graining of the atomistic degrees of freedom provides a natural link between the molecular and macroscopic views.

This volume of *Topics in Current Chemistry* addresses the latest developments in the modeling of organic and dye sensitized solar cells and provides an overview of the main processes going on in such devices. In the chapter "Small Optical Gap Molecules and Polymers: Using Theory to Design More Efficient Materials for Organic Photovoltaics", *Risko* and *Brédas* review some recent quantum-chemical investigations of donor–acceptor copolymers, systems that have found wide use as the primary absorbing and hole-transport materials in bulk-heterojunction solar cells. As often with organics, structure defines function. In the chapter "Supramolecular Organization of Functional Organic Materials in the Bulk and at Organic/Organic Interfaces: A Modeling and Computer Simulation Approach", *Muccioli* et al. address the molecular organization of functional organic materials on the basis of force-field calculations, with special attention to applications in organic photovoltaics. Electronic processes at organic/organic interfaces are discussed in the chapter "Electronic and Optical Properties at Organic/Organic Interfaces in Organic Solar Cells" by *Van Voorhis* and co-workers on the basis of quantum-chemical calculations; in particular, the possible mechanisms allowing charges at donor-acceptor interfaces to escape from their Coulomb attractive potential are addressed. The chapter "Modeling Materials and Processes in Dye-Sensitized Solar Cells: Understanding the Mechanism, Improving the Efficiency" by *Pastore* and *De Angelis* provides molecular insights at the quantum-chemical level into electronic and optical processes which are relevant to DSSC. The following two chapters, "Monte Carlo Studies of Electronic Processes in Dye-Sensitized Solar Cells" by *Walker* and "Monte Carlo Simulations of Organic Photovoltaics" by *Groves and Greenham*), deal with mesoscopic studies of charge transport and dissociation in OPV and DSSC based on Monte–Carlo methods and aim at establishing structure-property relationships. The final two chapters, "Device Modelling of Organic Bulk Heterojunction Solar Cells" by *Kirchartz* and *Nelson* and "Device Modeling of Dye-Sensitized Solar Cells" by *Bisquert* and *Marcus*, introduce the state-of-the-art methods for the modeling of electrical device characteristics.

These different contributions lay the ground for future developments aiming at the optimization of these tools and their integration into a single modeling framework linking the different scales in a self-consistent way (with, e.g., electric fields predicted from macroscopic models injected into molecular electronic structure calculations). We foresee that multiscale modeling will continue to improve in the near future and move from its current status of an instrument-fostering fundamental assets to become a truly predictive tool.

Mons, Belgium David Beljonne and Jérôme Cornil

Contents

Top Curr Chem (2014) 352: 1–38
DOI: 10.1007/128_2013_459

Published online: 8 May 2014

Small Optical Gap Molecules and Polymers: Using Theory to Design More Efficient Materials for Organic Photovoltaics

Chad Risko and Jean-Luc Brédas

Abstract Recent improvements in the power conversion efficiencies of organic solar cells have been derived through a combination of new materials, processing, and device designs. A key factor has also been quantum-chemical studies that have led to a better understanding not only of the intrinsic electronic and optical properties of the materials but also of the physical processes that take place during the photovoltaic effect. In this chapter we review some recent quantum-chemical investigations of donor–acceptor copolymers, systems that have found wide use as the primary absorbing and hole-transport materials in bulk-heterojunction solar cells. We underline a number of current limitations with regard to available electronic structure methods and in terms of the understanding of the processes involved in solar cell operation. We conclude with a brief outlook that discusses the need to develop multiscale simulation methods that combine quantum-chemical techniques with large-scale classically-based simulations to provide a more complete picture.

Keywords Donor-acceptor copolymers · Electronic structure methods · Organic solar cells

Contents

C. Risko
School of Chemistry and Biochemistry and Center for Organic Photonics and Electronics, Georgia Institute of Technology, Atlanta, GA 30332-0400, USA

J.-L. Brédas (✉)
School of Chemistry and Biochemistry and Center for Organic Photonics and Electronics, Georgia Institute of Technology, Atlanta, GA 30332-0400, USA

Department of Chemistry, King Abdulaziz University, Jeddah 21589, Saudi Arabia
e-mail: jean-luc.bredas@chemistry.gatech.edu

1 Introduction

Building on the legacy of the first demonstration of the conversion of light into electricity by Becquerel in 1839 [1], over the past several decades academic and industry researchers alike have sought materials and device architectures to convert solar radiation efficiently into electrical power through the photovoltaic effect with the hope of providing clean, sustainable, and widespread energy generation. Organic photovoltaics (OPVs), pioneered by Tang nearly three decades ago [2], has been of particular recent interest due to the promise of solar energy harvesting technologies that can be flexible, lightweight, of large area, and produced by low-cost printing techniques. The most efficient (lab-scale) single-junction OPV cells to date are based on active layers comprised of polymer-fullerene blends that take advantage of the bulk-heterojunction (BHJ) thin-film architecture [3–5]; their efficiencies have progressed from 5% to beyond 9% over the course of a few years [6–20, 21]. OPV cells where the active layers are based solely on small molecule donors and acceptors have demonstrated considerable improvement as well [22–24], with power conversion efficiencies for (solution-processed) single-junction devices reaching almost 7% [25] and (vacuum-deposited) tandem devices surpassing 12% [26].

The active layer in a solar cell needs to absorb light efficiently, create free charge carriers, and transport the carriers to the electrodes for charge collection. Tang's pivotal work [2] showed that the active layer in an OPV should be composed of two distinct materials: (1) an electron-donating, hole-transport material (HTM) with a small ionization potential (easily oxidized) and (2) an electron-accepting, electron-transport material (ETM) with a large electron affinity (easily reduced).[1] Much of the recent improvement in OPV device efficiency has been a consequence of the capabilities that synthetic chemistry provides to adapt readily and rapidly the chemical structure of π-conjugated molecules and polymers to tune both the electronic and optical properties and structural organization of the active layer [27, 28]. In particular, recent advances in the design of polymers [7, 8, 10–19,

[1] We are using here the HTM and ETM notations to denote the two components of the active layer, instead of the more conventional donor and acceptor (D/A) notations, in order to prevent any confusion with the donor/acceptor character of the copolymers used in the BHJ solar cells.

29–94] and molecules [22, 95–99] that combine electron-rich donor (D) and electron-deficient acceptor (A) moieties in the chemical structure and are used as the primary absorber and HTM (in combination with a fullerene-based ETM) have been at the forefront of these improvements.

The use of quantum-chemical (electronic-structure) methods has proved to be a powerful complement for designing new molecular/polymer-based materials and for understanding their performance in OPVs [100]. Our goal in this contribution will be to discuss the application of these techniques to study the intrinsic electronic and optical materials properties and the broader processes involved in OPV operation. We will first outline the current understanding of the complex processes involved in OPV operation. We will then consider how these processes dictate the materials design process and why the donor–acceptor (DA) architecture, with a particular emphasis on DA copolymers used as HTMs, is an appealing way to meet the materials needs. This will be followed by an overview of how electronic-structure methods can be employed in the study of these materials. We will conclude with an outlook for future investigations.

2 Processes Involved in OPV Operation

Multiple processes need to be optimized for efficient OPV operation [22, 100–106]. The initial process involves the absorption of solar radiation (photoexcitation) and the subsequent formation of excitons, Coulombically-bound electron-hole pairs with no net charge. At this stage, we note that exciton binding energies in π-conjugated systems can be of the order of several hundreds of millielectronvolts (meV) [107], a condition in stark contrast to the few meV binding energies of inorganic semiconductors that allow for the creation of free charge carriers upon photon absorption at room temperature. As the generation of photocurrent requires that the excitons fully dissociate into separated charges prior to decaying back to the ground state, the second step involves exciton migration through sequential energy-transfer processes to the HTM–ETM interface [108]. Remember that as the exciton is charge neutral, the diffusion process is not influenced by the presence of an electric field.

Once at the HTM–ETM interface, the exciton must dissociate into separated, charged (positive and negative) polarons in the respective HTM and ETM components. The Coulombic potential holding the hole in the HTM close to the electron in the ETM has to be overcome to form the fully charge-separated state (largely defined by the [adiabatic] ionization potential of the HTM and electron affinity of the ETM) [109]. We note that the mechanism by which excitons dissociate and separate into fully separated polarons still remains unclear and that substantial experimental and theoretical effort is ongoing to determine whether differences in the chemical potentials of the HTM and ETM components, the involvement of higher-energy (“hot”) charge-transfer states, or some other processes play the key role in this dissociation process. Once separated, and neglecting non-geminate (bimolecular) recombination processes, the hole and electron migrate via drift and diffusion through the HTM and ETM phases to the anode and cathode, respectively, where the charges are finally collected.

3 Rationale Behind DA Polymers and Molecules

The processes discussed above suggest a number of design principles for HTMs (that generally act as the primary absorbing material when used in combination with fullerene ETMs) regarding both their electronic and structural properties [27, 100, 110, 111]. To generate a large photocurrent, a broad portion of the solar spectrum needs to be absorbed, in particular down to the near-infrared region. Hence, materials with low-energy first-excited states – on the order of 1.2–1.9 eV (≈1,000 to 650 nm) – are necessary; materials with such attributes are often referred to as having small, low, or narrow optical gaps. The molecules and polymers, critically, need to be designed such that they present large transition dipole moments to translate into films with large absorption coefficients to promote efficient photon capture.

In addition to the optical properties, the ionization potentials and electron affinities (often related to the quantum-mechanically-derived highest-occupied (HOMO) and lowest-unoccupied (LUMO) molecular orbital energies, respectively) need to be addressed in order to ensure efficient charge transfer and charge separation at the organic/organic (HTM/ETM) interface and charge collection at the electrodes. Lastly, to facilitate sufficiently large charge-carrier mobilities in the active layer, planar conjugated backbones are sought so as to lead to close-packed, parallel stacking arrangements (often referred to as π–π stacking) amongst neighboring molecules/polymers. A more planar structure can lead to strong intramolecular electronic coupling along the backbone (in the case of polymers) and small reorganization energies for the sequential redox processes (i.e., geometry relaxation energies on going from the neutral state to the charged state and vice versa) that occur during charge-carrier transport (assuming a charge-hopping picture), while the close-packed configurations can lead to strong intermolecular electronic couplings [110, 112, 113].

The donor–acceptor (DA) copolymer construct (Fig. 1) is well suited to meet a number of these requirements; a number of recent research accounts and reviews provide an overview of the development and applications of such copolymers [20, 33, 45, 84, 101–106, 108, 110, 111, 114–127]. Havinga and co-workers first proposed the concept of combining an electron-rich donor and an electron-deficient acceptor to form the monomer repeat unit as a means to design materials with transparency in the visible spectral region and/or large intrinsic conductivities [29, 30]. Combining the donor which has a small ionization potential (i.e., an energetically destabilized HOMO) and acceptor which has a large electron affinity (i.e., energetically stabilized LUMO) leads to a set of hybridized molecular orbitals with a smaller HOMO–LUMO energy gap (often denoted E_g) than either constituent (Fig. 1). By adjusting the relative strength of the donor and acceptor components, the electronic coupling amongst the components, and the geometric structure (e.g., twisting between the components), one can readily tune to a large degree such factors as the ionization potential, electron affinity, and optical gap and transition dipole moments [128].

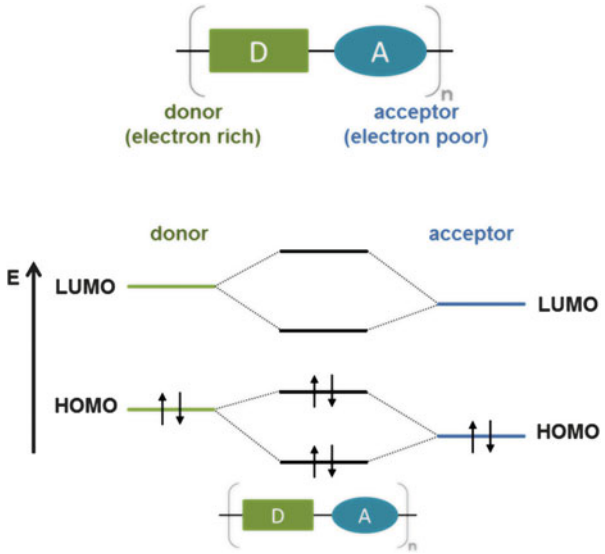

Fig. 1 *Top*: Donor–acceptor monomer construct. *Bottom*: Molecular orbital energy correlation diagram showing the hybridization that generally takes place between the donor and acceptor molecular orbitals

We also note that the introduction of quinoidal character, for instance via the presence of a single conjugated carbon between arylene rings or the use of fused structures [110, 129–133], is another means to construct small optical gap polymers. The quinoidal structure reduces the energetic gap between the HOMO and LUMO by lessening the aromatic stabilization energy of the molecular building blocks [130]. In theoretical structures, the quinoidal character can be enforced within an oligomer by placing, for instance, terminal methylene ($=CH_2$) units at the oligomer ends and examining the differences in the degree of bond-length alternation (BLA) vs capping the oligomer with hydrogen atoms [134, 135]; the relative stability of the quinoid vs aromatic structures is then evaluated as a function of oligomer length by comparing the energy per repeat unit [136, 137]. A second route is to place a single methylene unit between each aromatic ring, which forces every other ring to turn quinoidal [131–133]. While such strategies can be of use for the design of low-energy absorbing materials for OPV applications, most recent developments in the design of small optical-gap copolymers have mainly considered the DA-copolymer strategy.

4 Application of Quantum–Chemical Methods for DA Copolymers

Studies of model oligomers via quantum–chemical (electronic structure) methods can serve as a means to rationalize the intrinsic electronic and optical properties of a particular conjugated structure and determine the nature and strength of

intermolecular interactions found in the solid state; they can also be a valuable tool in the pre-synthesis screening of candidate systems [100]. Theoretical studies of the interplay between structural and chemical modifications and the resulting influence on the electronic structure and optical properties – through the application of wave-function theories (i.e., Hartree–Fock [HF] methods, post-HF methods that include electron correlation, and semiempirical HF methods), density functional theory, or combinations thereof – have been widely used to provide fundamental insight into materials of interest for numerous organic-based electronics applications, including OPVs.

A key condition to describe accurately the electronic and optical properties of polymers is that relatively long oligomers need to be studied to ensure that the conjugation path length is sufficient to describe the polymer system [138]. To meet this requirement, semiempirical HF-based methods have found wide use [90, 139–147] as they formally scale as N^3, where N is the number of basis functions in the system; these semiempirical methods include the Modified Neglect of Differential Overlap (MNDO) [148], Austin Model 1 (AM1) [149], and Parameterized Method 3 (PM3) [150, 151] Hamiltonians. Due to the need for parameterization against experimental results (which can include solvent polarizability dependence), the use of small basis sets, and the explicit lack of a description of electron correlation (though there is an implicit accounting of electron correlation through the parameterization), semiempirical methods can suffer severe limitations that affect the descriptions of the geometric and electronic structures, oxidation and reduction properties, and electronic excitations.

As an aside, an important feature of HF theory is the capacity to improve systematically the methodology through the inclusion of electron correlation. HF theory, on average, captures 99% of the total energy of a system; unfortunately, the remaining 1% is critical to the description of many chemically relevant features and processes. There are, in general, three routes used to include the effects of electron correlation: configuration interaction (CI), many-body perturbation theory (MBPT), and coupled–cluster (CC) theory [152]. While these post-HF methods quickly become computationally expensive, even for systems of moderate size, they hold particular value as benchmark calculations to evaluate the effects of electron correlation on the electronic structure and optical properties of conjugated molecules.

A complete CI calculation (with an infinite basis set) taking into account all possible electron populations is not feasible, though full CI calculations in a finite basis are achievable for very small systems. Hence, truncated CI methods (which include some segment of single, double, triple, etc., excitations within a defined active space) are often used, though with increasing computational cost as the number of electrons included and size of the active space increase. As we will see below, however, such methods paired with semiempirical Hamiltonians are widely used in the evaluation of the excited-state properties of large, conjugated organic systems.

For approximately the same computational cost as the truncated CI methods using the HF Hamiltonian, considerable improvements have been made with MBPT and CC methods and subsequently applied to model conjugated organics. Building

on the second-order perturbation theory of Møller and Plesset (MP2) [153], Grimme introduced the spin-component-scaled (SCS) method to treat separately the electron correlation effects of electron pairs with the same and opposite spins [154]. The SCS approach, coupled with both truncated CI and CC methods, has been used to examine the low-lying excited states of organic dyes, including the effects of aggregation [155–159]. In a second approach, both restricted and unrestricted spin–orbital formalisms of the algebraic diagrammatic construction scheme of second order (ADC(2)) have recently been employed in the study of the electronic, ionization, and optical properties of small-to-medium conjugated molecules and their radical ions [160–165].

Variations on the GW method, a perturbation-based approach that determines the self-energy from the direct product of the one-particle Green's function (G) and the dynamically screened Coulomb interaction (W) [166, 167], have found use in evaluating the electronic and optical properties of isolated molecules and organic solids as well as electronic-level alignment at heterogeneous interfaces [168–186]. Of particular importance are theoretical applications where the electronic eigenenergies computed through the GW formalism are coupled with the Bethe–Salpeter equation (BSE) to evaluate excitonic effects [168–174, 181]. The non-self-consistent G_0W_0 approach is finding use in the description of the electronic properties of molecules, though the lack of self-consistency means that the results are highly dependent on the parameters derived from lower-level calculations [177, 178, 180, 181, 185, 186]. While this overview of post-HF methods is not exhaustive, our aim is to show that considerable work is ongoing to provide more reliable, accurate extensions of HF theory – work that will continue to gain in importance as computational power increases and the theoretical understanding progresses.

The main focus of the review will center on density functional theory (DFT) methods, which have also been extensively applied to the theoretical characterization and design of DA oligomers [8, 38, 50, 68, 69, 71, 81, 85, 87, 92, 100, 128, 135, 141, 187–209]. While DFT methods generally provide a good balance between chemical accuracy and computational cost, limitations in size do arise as DFT methods scale as N^4. Efforts to reduce this scaling through linear scaling techniques [210–214] do allow DFT to be applied to considerably larger systems ($\approx 10^6$ atoms). DFT calculations that take into account periodic boundary conditions have also been employed to determine the electronic band structure of polymeric materials [38, 48, 199, 215, 216] and evaluate interfacial interactions with metal electrodes [217].

Of concern with traditional DFT methods, including the widely used standard hybrid functionals (e.g., the B3LYP [218–220] functional that combines Becke's three-parameter exchange functional [221] and the Lee–Yang–Parr correlation functional [218, 222]), are (1) electron self-interaction errors that generally lead to an over-delocalized description of the wave function and (2) artifacts due to the approximations needed to describe the exchange functional. Advances in the development and application of density functionals that include long-range corrections to the exchange functional [223–230], and in particular functionals

where the range-separation is tuned (optimized) for the system under study [231–237], do offer the possibility to correct for these limitations. Recent results with these functionals will be highlighted below, in particular with regard to the examination of the low-lying excited states of DA copolymers [238].

5 Geometric and Electronic Structures and Their Impact on Redox Properties

We now turn to the application of quantum-mechanical methods to describe the interplay of the geometric and electronic structures and the subsequent impact on the redox properties. The geometric structure of a π-conjugated system impacts the electronic properties of the system primarily through the degree of BLA along the backbone, aromatic stabilization of the individual building blocks, inductive or mesomeric effects due to substitutions along the backbone, relative coplanarity along the backbone, and degree of intermolecular coupling in the solid state [118]. To evaluate these effects in some detail, let us consider two donor architectures where a central five-membered ring is fused on both sides by either thiophene rings (structure denoted as CPDT, cyclopentadithiophene) or benzene rings (CPDP, cyclopentadiphenylene); see Fig. 2 [128]. These donors constitute some of the most widely used electron-rich fragments in small optical gap DA copolymers for bulk-heterojunction OPVs; the chemical structure is often further varied through substitution of the carbon at the 9-position by either nitrogen or silicon atoms (denoted X in Fig. 2) [7, 8, 46, 54, 239–243]. To pair with these donor sets, commonly used acceptors are coupled in one of two configurations, either directly or via bis-thiophene linkages (denoted Y and T-Y-T in Fig. 2). In the case of Fig. 2, combining these donor and acceptor segments leads to 144 different DA monomer configurations, which provides a broad study platform [128]. The data evaluated below are those determined for tetramers at the B3LYP/6-31G(d,p) level of theory.

The ground-state geometries of these DA oligomers are very much influenced by the choice of donor and acceptor fragments, and present varying degrees of linearity along the long molecular axis and of deviations from coplanarity. The X/CPDP-Y oligomers tend to deviate more from a coplanar architecture compared to X/CPDT-Y oligomers, a result of steric interactions between the hydrogen atoms in the 1-, 3-, 5-, and 7-positions of X/CPDP (vs the 3- and 7-positions of X/CPDT) and the nearest-neighbor atoms of the acceptor fragment. These deviations are the largest for oligomers with the TQ, QX, and PP acceptors due to the increased bulkiness of these acceptor heterocycles. The additional increase in torsion angle in systems with the TQ acceptor is a result of the increased bulkiness from the extension of the heterocycle and the steric hindrance from the two hydrogen atoms in the 6- and 8-positions. These large deviations from planarity, importantly, can impact the electronic structure through reduction of the wave-function delocalization.

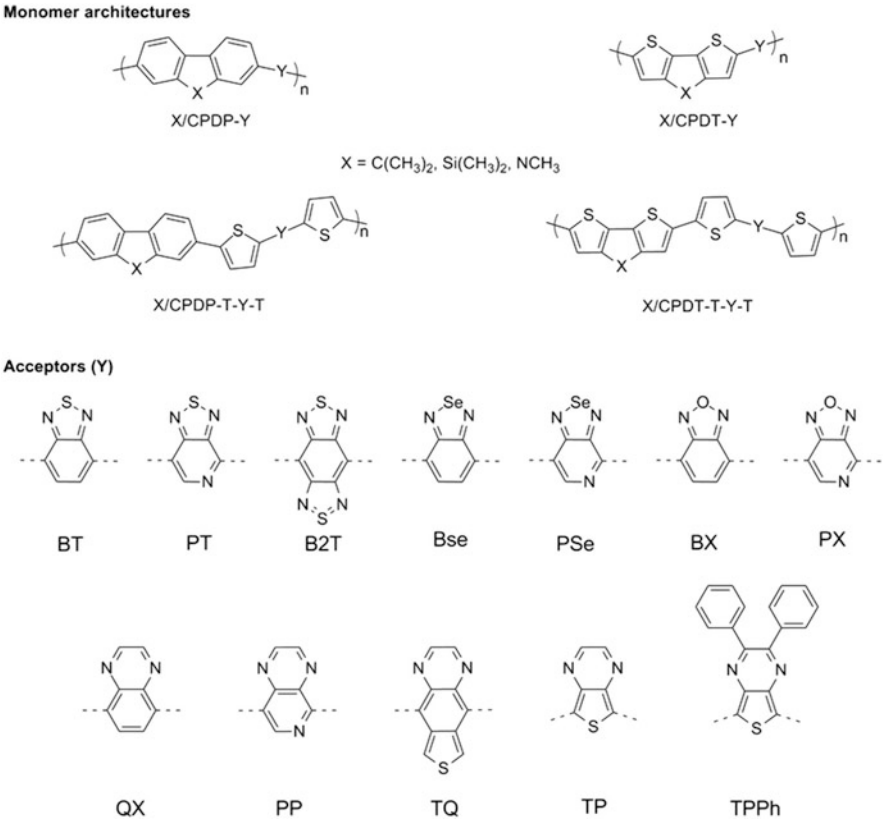

Fig. 2 *Top*: Monomer architectures with the various donors denoted in the chemical structure. *Bottom*: Chemical structures of 12 commonly used acceptors

The goal behind the introduction of thiophene rings between the donors and acceptors has been, in general, to reduce these torsion angles [125], which it usually does. These smaller twists arise from limiting the steric interactions between neighbor donor/acceptor segments. This is especially true for interactions with the neighboring six-membered rings in the X/CPDP-Y fragment, while coupling the bis-thiophene-substituted acceptors to the X/CPDT-based donors has a lesser impact on the degree of twisting. We note that there can be a wide range of energy cost, from some 2–60 kcal/mol (or, in the context of thermal energy, from some 1,200 to 30,000 K), required to coplanarize the DA oligomers that present torsion angles $\geq 25^\circ$ [128].

Turning to the electronic structure, the HOMOs in the DA oligomers are generally delocalized over both donor and acceptor fragments. These wave functions in most cases correspond to the out-of-phase combination of the donor and acceptor fragment HOMOs. The LUMOs of most systems, on the other hand, are predominantly composed of the acceptor LUMO and have contributions mainly

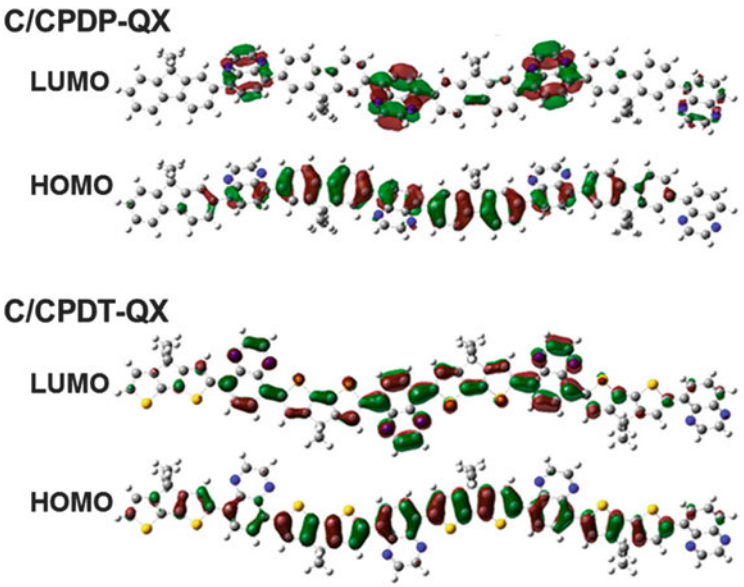

Fig. 3 Illustrations of the HOMO and LUMO for C/CPDP-QX and C/CPDT-QX as determined at the B3LYP/6-31G(d,p) level

over the acceptor. Obviously, the level of mixing and localization/delocalization of the HOMO and LUMO in the DA oligomers is also a function of the torsion angles along the donor and acceptor conjugation bridge. Inspection of Fig. 3 highlights the roles of energetic alignment and (departure from) coplanarity. For C/CPDP-QX, while the LUMO is delocalized over the oligomer, it is mainly found on the acceptor fragments due to the combination of a large mismatch between the LUMO energies and large torsion angles among the D and A components. With slightly better matching of the LUMO energies and substantial decrease in torsion angles (we note that the C/ and N/ torsion angles are comparable), the LUMO in C/CPDT-QX is delocalized over both the donor and acceptor components.

Overall, the X/CPDP-Y tetramers have energetically-stabilized HOMOs compared to the X/CPDT-Y family, a trend consistent with those of the isolated donor fragments [128]. The X/CPDP-T-Y-T HOMO energies are significantly destabilized (by 0.11–0.43 eV) when compared to X/CPDP-Y oligomers, a result of a more coplanar configuration across the backbone and increased delocalization of the HOMO (it should be borne in mind that the extent of localization/delocalization discussed here is a simple qualitative description based on inspection of the MOs). The effect of the various X-substituents on the DA tetramer HOMO energy is smaller (0.04–0.16 eV) than in the isolated donors. Although small, such differences can play a role on the open-circuit voltage of the solar cell [242, 244]. The fundamental gap of the DA tetramers is a function of the HOMO and LUMO energy trends discussed above, with X/CPDP-based tetramers presenting a

larger fundamental gap compared to X/CPDT-based tetramers. The X/CPDP-T-Y-T tetramers have substantially reduced fundamental gaps compared to the X/CPDP-Y tetramers while the effect of adding the bridge thiophene rings is much smaller in the X/CPDT-based tetramers.

In general, there is good agreement among the trends in the molecular orbital eigenvalues/estimated ionization energies and available empirical data. An important note, however, is that experimental estimates of the ionization energies derived from electrochemical measurements can be misleading. Electrochemical measurements (e.g., cyclic voltammetry or differential pulse voltammetry) of oxidation and reduction potentials are at best estimates of the bulk ionization energies, since the dielectric environment of the polymer in solution can differ considerably from that of the polymer in the solid state. It is also important to keep in mind that the redox potentials determined for π-conjugated polymers are not solely governed by the chemical structure of the repeat units. This is highlighted by a study of DA copolymers containing electron-rich segments with CPDT and a varying number of unsubstituted thiophenes coupled to BT acceptors [114]. While the estimated ionization potentials and electron affinities determined for similarly-sized oligomers across the polymer series at the B3LYP/6-31G(d,p) level of theory were comparable, polymers with the same conjugated backbone structure that varied in terms of the degree of order/crystallinity of the polymer packing in the solid state (which is a function of the molecular-weight distribution), side-chain concentration, and side-chain structure presented very different solid-state ionization potentials [114]. This underlines the need not only to be able to evaluate the intrinsic electronic structure and redox properties of "isolated" single (macro) molecules via electronic-structure methods, but also to be able to use multiscale approaches to determine the molecular/polymer packing configurations present in the solid state that influence the electronic properties of these larger systems.

6 Excited-State Properties

Electronic-structure methods are also of value to describe the processes involved during photoexcitation and exciton formation as a function of chemical and geometric structure. The most widely used methods for evaluating the (singlet) excited-state properties of DA oligomers are based on semiempirical HF [36, 92, 139, 140, 142, 143, 145, 146, 187, 188, 193, 200] and (time-dependent) density functional theory [68, 69, 71, 87, 141, 187–197, 201, 245]. The intermediate neglect of differential overlap (INDO) Hamiltonian coupled with a CI scheme that allows for excitations of single electrons (CIS) is amongst the most widely used semiempirical HF methods for such calculations. An important consideration in the use of these methods, therefore, involves the proper choice of the CI active space, which for π-conjugated systems is one in general that allows for all π–π* transitions within the system to be considered. Of note concerning the use of semiempirical Hamiltonians is a recent benchmark study that reveals (1) a general underestimation

of vertical excitation energies and (2) limitations concerning the evaluation of oscillator strengths (transition dipole moments); orthogonalization-corrected approaches (e.g., OM1, OM2, and OM3) were suggested as good candidates for the evaluation of vertical excitation processes of organic molecules [246].

Time-dependent DFT (TDDFT), an extension of DFT whose foundations lie in the rigorous proof of correspondence between a time-dependent external potential and the time-dependent one-particle density [247, 248], is also widely exploited as it offers accurate results for well-behaved systems with reasonable computational costs [249]. As an example, we return to the tetramers derived for the DA components shown in Fig. 2, where TDDFT calculations at the B3LYP/6-31G(d,p) level were used to gain insight into the vertical singlet ($S_0 \rightarrow S_n$) electronic transitions [128]. As is the case for most DA copolymers examined in the literature, the $S_0 \rightarrow S_1$ transitions for these tetramers can be principally described as HOMO $\rightarrow$ LUMO one-electron excitations. The magnitude and trends of the optical gaps are similar to those of the fundamental gaps.

It is of interest to evaluate how well the calculated transition energies for oligomers compare with respect to the optical excitation energies measured for the full polymers, a topic that has been reviewed recently [250]. A variety of procedures, from simple linear and polynomial fits to extrapolation procedures derived empirically [138, 251] and theoretically [250, 252], have been applied to extract vertical transition energies at the (infinite) polymer limit [68, 69, 71, 87, 92, 142, 145, 187–191, 193, 245, 253]. Two main regions – a linear regime where the vertical transition energy decreases with increasing oligomer size, and a saturation regime where continued increase of the oligomer length no longer influences the transition energy – generally arise from these analyses, with the turnover point described as the "effective conjugation length" [251] or the "maximum conducive chain length" [250]. We suggest that such extrapolation procedures should be used with care, however, as the errors associated with the assumptions employed in the chosen computational methodology can outweigh the improvement in predicted value at the polymer limit [250]. In addition, the appropriate choice of extrapolation procedure can change considerably depending on the particular characteristic being analyzed for convergence behavior [253].

Beyond the description of the $S_0 \rightarrow S_1$ transitions, more extensive TDDFT calculations can be used to span the entire near-infrared–visible–ultraviolet spectrum. To illustrate this, we turn to an investigation of a series of DA copolymers that have been used in a number of high-performing OPV cells (Fig. 4) [6–8, 10–16, 18, 70, 100, 147]. Building on the themes of previous studies, it is of interest to determine whether these copolymers present any intrinsic properties that make them stand out against other less successful DA constructs.

Simulated absorption spectra (Fig. 5) for tetramers in the series were derived through Gaussian-function convolution (fwhm = 0.3 eV) of the vertical transition energies and oscillator strengths (see below) computed with TDDFT at the B3LYP/6-31G(d,p) level of theory [100]. There is generally good agreement between the overall shape of the simulated spectra for the tetramers and the literature-reported polymer (both solution and thin-film) absorption spectra [6–8, 10–16, 18, 70, 100,

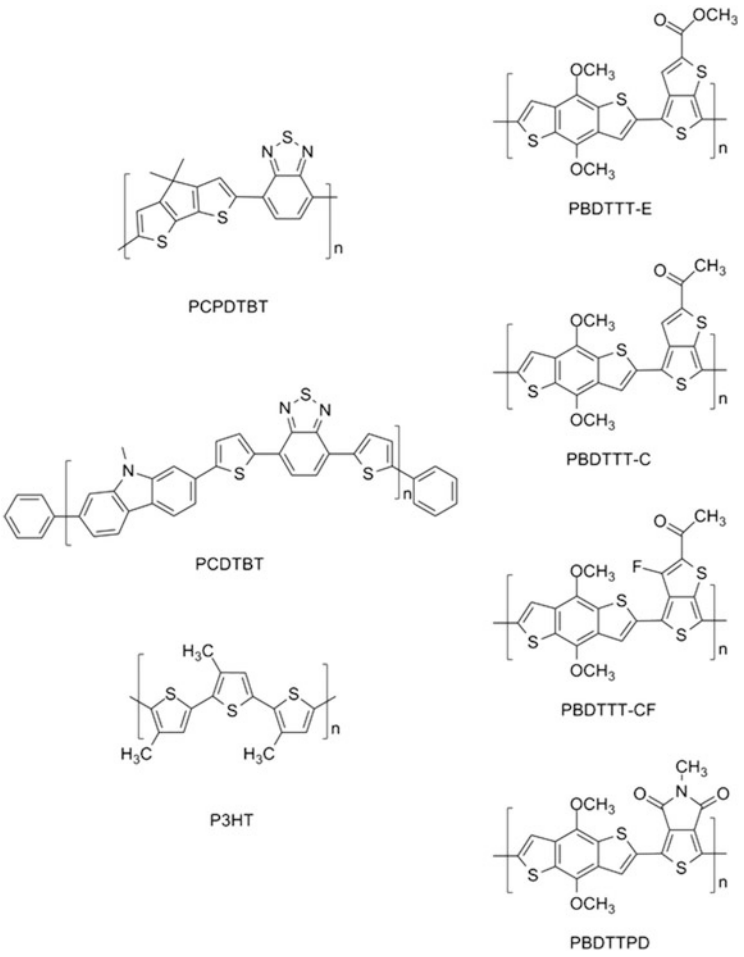

Fig. 4 Monomer structures for a series of DA copolymers used as the HTMs in combination with fullerene-based ETMs in high-performance BHJ organic solar cells. The structure of a trimer of P3HT is provided for reference. All alkyl chains have been truncated to methyl groups

147]. However, it is worth noting that there is no single observation arising from the study indicative as to why these materials behave so well in OPV cells vs other DA copolymers.

The spectra, in general, are characterized by one dominant, low-energy transition with large oscillator strength followed by a second, high-energy transition (or series of transitions) with smaller oscillator strengths. We note two items of interest evident for the benzodithiophene (BDT)-containing polymers (PBDTTT series and PBDTTPD). First, the substitution of the thienothiophene (TT) acceptor by thieno [3,4-*c*]pyrrole-4,6-dione (TPD) leads to a blue shift of the low-energy optical absorption maximum, a consistent result when comparing reported spectra for the

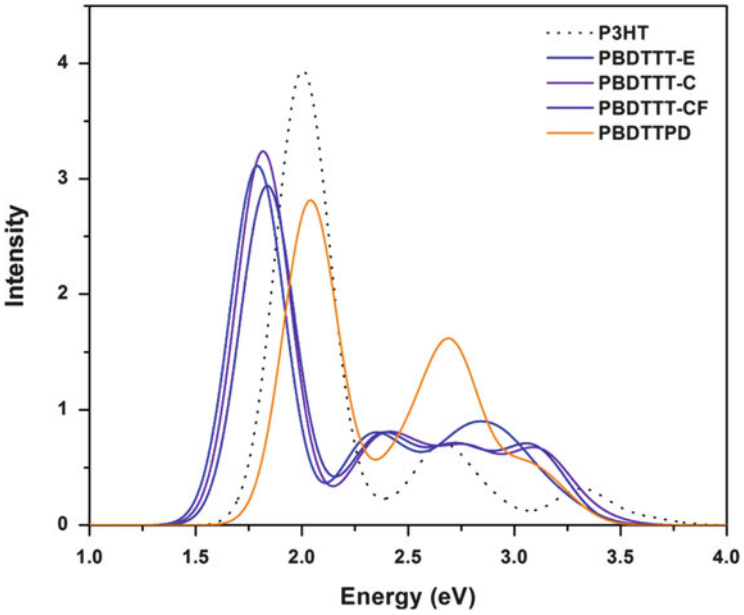

Fig. 5 Simulated absorption spectra for the tetramers of the PBDTTT family, PBDTTTPD, and P3HT as determined with TDDFT at the B3LYP/6-31G(d,p) level of theory. The absorption spectra were simulated through convolution of the vertical transition energies and oscillator strengths with Gaussian functions characterized by a full width at half-maximum (fwhm) of 0.3 eV

copolymers containing the two acceptor units [13, 15, 59, 88]. Second, the low-energy band seen in the experimental absorption spectra [11, 13, 15, 16, 18, 88, 93] is comprised of two peaks with an energetic splitting on the order of 0.15–0.20 eV (~1,210 to 1,615 cm^{-1}), while the TDDFT results reveal the presence of only one, dominant low-energy transition. This is consistent with the presence in the experimental data of a vibronic progression typical of the coupling of the electronic excitation with C–C stretching modes (such electron-vibration couplings have not been considered in the calculations discussed here).

In addition to excitation energies and spectral line shapes, information pertaining to the nature of the excited state [254] – including the electronic configuration, transition dipole moment (oscillator strength), distribution of the correlated electron-hole pair, transition density, and charge-density difference with the ground state – can be obtained and provide key insight into how the DA moieties along the backbone interact in the excited state. Chemists often use molecular orbitals to describe the nature of low-lying electronic transitions in conjugated materials, as most systems involve transitions among the frontier π orbitals (for instance HOMO → LUMO as noted above). Further scrutiny of the ground- and excited-state wave functions involved in the electronic transitions, however, can provide for even deeper understanding vs what can be gained from simple molecular orbital analyses. For example, correlated electron-hole distributions have been used to visualize how

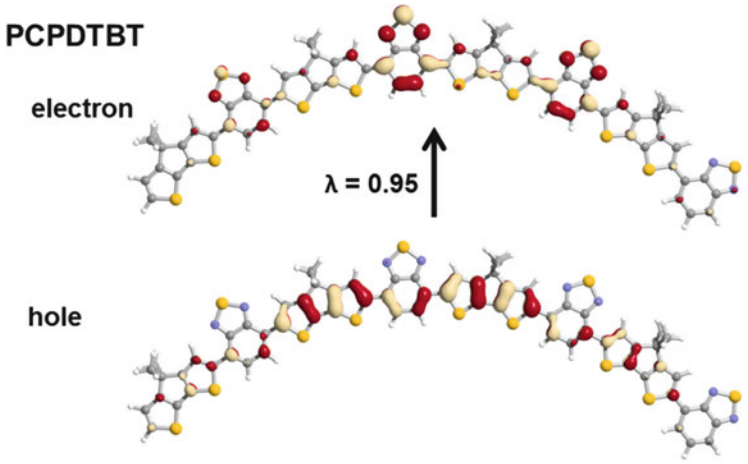

Fig. 6 Illustrations of the natural transition orbitals (NTO) describing the PCPDTBT $S_0 \rightarrow S_1$ transition as determined with TDDFT at the B3LYP/6-31G** level of theory. λ is the fraction of the hole-particle contribution to the excitation

the electron and hole in the excited state (de)localize across the conjugated backbone [36, 139, 195, 255], while the transition density and charge-difference density give access to the areas of the conjugated system directly involved in the transition and the change in electron density on excitation, respectively [36, 195, 254].

Natural transition orbitals (NTOs) [256], derived through analysis of the transition density matrix, provide a means to reduce the often complex descriptions of the mixed electronic configurations (i.e., linear combinations of multiple electronic excitations) that frequently describe an excited-state transition into a single hole-particle excitation; the eigenvalue λ denotes the fraction of the hole (in the occupied space) – particle (promoted into the unoccupied space) pair contribution for the given electronic transition [254, 256]. Figures 6 and 7 show illustrations of the NTOs for the PCPDTBT and PCDTBT $S_0 \rightarrow S_1$ transitions as determined at the B3LYP/6-31G(d,p) level of theory [100]. As the $S_0 \rightarrow S_1$ transitions are primarily HOMO → LUMO, the corresponding NTOs have similar character to the molecular orbital distributions [100]. For PCPDTBT (and the benzodithiophene-containing polymers), both the hole and electron are fairly well delocalized over the entire conjugated backbone. We note here that, while these transitions are often referred to as being charge-transfer (CT) transitions, a strict interpretation of such a description can be misleading. As is seen for PCPDTBT, the NTOs reveal what might best be termed "partial charge-transfer-like character" to the excitation, where the hole NTO is delocalized (through the acceptors) across the donor components and the electron NTO is mainly on the acceptor.

The situation differs somewhat for PCDTBT (Fig. 7), where two sets of NTOs are needed to describe the transition, a function of the $S_0 \rightarrow S_1$ transition being a linear combination of mainly four single-electron excitations. For the leading

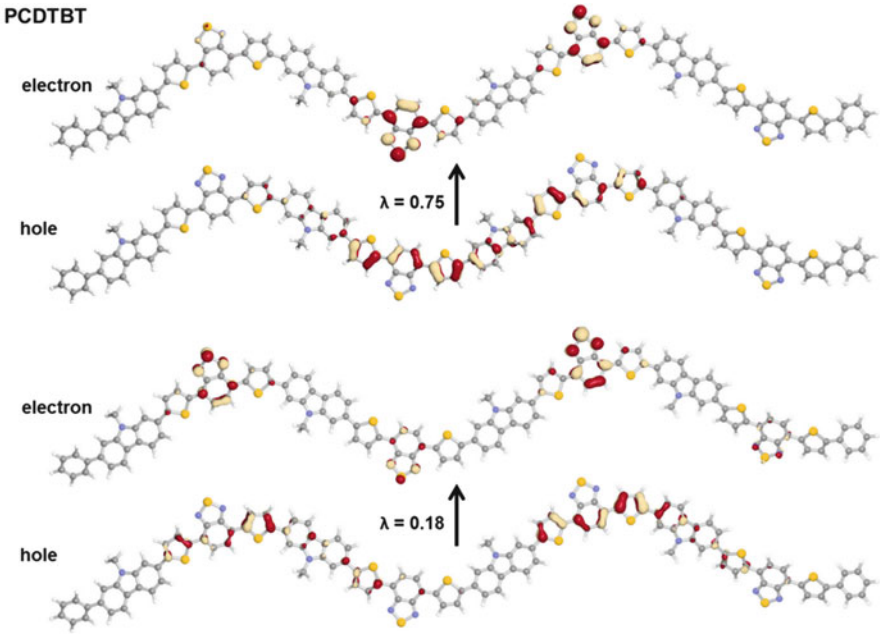

Fig. 7 Illustrations of the natural transition orbitals (NTO) for the PCDTBT $S_0 \rightarrow S_1$ transition as determined with TDDFT at the B3LYP/6-31G** level of theory. λ is the fraction of the hole-particle contribution to the excitation

hole-electron couple, the hole has again a fairly delocalized (continuous) nature (as observed for PCPDTBT), while the electron is highly localized on the benzothiadiazole acceptors (though it is "delocalized" on the latter across the entire oligomer). As the hole and electron reside within the same spatial extent of the oligomer, there remains a rather large spatial overlap between the hole and electron NTOs and the dominant hole-particle couple remains as a partial charge-transfer-like transition. The similar delocalization of the electron and hole, though the electron tends towards the benzodithiazole acceptors, is consistent with the negligible solvatochromism reported for PCDTBT [204]. These NTOs are reminiscent of the molecular orbitals discussed earlier for the CPDT-QX DA combination (Fig. 3) and reveal how the electronic structure in turn affects the nature of the low-lying excited state. The minor participant to the excited state is mostly localized on the *p*-dithiophenebenzothiadiazole subunits.

The NTO analysis can also be applied to the examination of the high-energy transitions [100, 257, 258]. This is of interest as it is often stated in the DA copolymer literature that the secondary, high-energy band corresponds to a donor-localized π–π* transition. The NTOs for these transitions reveal, in fact, that the high-energy transitions in the DA chains possess a substantial contribution of partial charge-transfer-like character and are not donor localized [100]. For both PCPDTBT and PCDTBT, the hole in the main high-energy excitation is again delocalized; however,

the electron is also well delocalized over both the donor and acceptor, with the wave function on the benzothiadiazole unit confined to the thiadiazole. A secondary excitation for PCPDTBT is more reminiscent of the partial-charge-transfer transition observed for the $S_0 \rightarrow S_1$ excitation, while in PCDTBT the secondary transition is (again) *p*-dithiophenebenzothiadiazole localized [100].

While this analysis is highly beneficial, there are still concerns regarding the use of the appropriate level of theory, in particular with the optical transitions containing such charge-transfer-like character. As noted above, the effects of the electron self-interaction error in the general DFT formalism can tend to lead to over-delocalization of the excited-state wave function, and hence a red shift in the calculated vertical transition energies vs experiment; this is a consistent feature of the B3LYP-calculated transition energies of the high-performance polymers [100]. The degree of the shift is largely dependent on the choice of functional, with improvements observed in general for hybrid functionals that include some quantity of HF exchange. Modern long-range corrected (LRC) functionals where the range-separation parameter is tuned specifically for the system under study show promise for overcoming these difficulties. In a follow-up study of these high-performance copolymers [238], tuning the range-separation parameter of the ωB97 functional [229] of Chai and Head-Gordon provides for a very good agreement with experimental absorption spectra, especially when compared to the red-shifted spectra provided by the B3LYP functional. This improvement can be related to better balance in the description of the local and charge-transfer excitations provided by the optimization of the range-separation parameter.

In addition, there appears to be a difference regarding the NTOs derived from the TDDFT calculations employing the tuned ωB97 functional for the PCDTBT $S_0 \rightarrow S_1$ excitation. Three hole-electron pairs, where each hole is localized within a specific thiophene–benzene (belonging to a benzothiadiazole segment) – thiophene segment and the electron localized within the benzothiadiazole unit, are found to play a key role. This alternative picture suggests that the decreased absorption energy and increased oscillator strength in PCDTBT with increasing chain length arises not solely from the delocalized partial charge-transfer-like excitations but rather from the coupling of the dithienylbenzothiadiazole-localized excitations along the chain. Though the NTO description of the excitation differs with respect to that at the B3LYP level, the hole and electron remain delocalized to a similar extent over the same spatial area of the oligomer, a result that is again consistent with the negligible solvatochromism of PCDTBT [204]. Similar differences between the B3LYP and tuned ωB97 functionals are noted for the other oligomer systems as well [238]. The LRC functionals offer the possibility for improved descriptions of the intrinsic electronic and optical properties, though a substantial benchmarking effort remains to understand fully the benefits and limitations of these functionals.

For a material to act as an efficient solar energy absorber, it not only has to absorb over a broad spectral (energy) range, it also has to absorb the photons effectively. Hence, the electronic transition dipole moment is a parameter of importance as it translates into both the molar extinction coefficient (solution)

and absorption coefficient (thin film) and, therefore, provides direct information on empirically measured absorption strengths. For an electronic excitation, the probability that a transition will occur between two states is given by the electronic transition dipole moment:

$$\langle \mu \rangle = \int \psi_e^*(\vec{r}) \hat{\mu} \psi_g(\vec{r}) d\vec{r} \tag{1}$$

where $\psi_e^*(\vec{r})$ and $\psi_g(\vec{r})$ are the excited-state and ground-state wave functions, and $\hat{\mu}$ is the dipole moment operator; (1) is the basis of the orbital selection rules for electronic transitions.[2] In addition to the transition dipole moment, the oscillator strength – a unitless parameter directly determined by the square of the transition dipole moment – is often reported.

Returning to the oligomer study discussed at the outset of the review, we again see an important interplay between the geometric structure of the oligomer and the resulting optical properties (in this case) as the oscillator strengths of the X/CPDT-based oligomers, in general, are larger than those for the X/CPDP tetramers, a result that relates to the more coplanar nature of the geometric structure. Notably, the DA oligomers that have the bisthiophene substitution about the acceptors have considerably larger oscillator strengths. This enlargement, again, arises from the increased coplanarity (especially for the X/CPDP-based oligomers) that in turn leads to extended conjugated paths along the backbone and improvements in the spatial overlap of the ground- and excited-state wave functions. There is effectively no change in oscillator strength as a function of the X-substituent in the X/CPDP-based oligomers. However, for the X/CPDT-based oligomers there occurs some increase in oscillator strength (up to 8% and 12% for the X/CPDT-Y and X/CPDT-T-Y-T oligomers, respectively) when X changes from $Si(CH_3)_2$ to $C(CH_3)_2$. This is possibly a contribution from a decrease in the backbone curvature, or reduced distortion of the cyclopentadithiophene unit (due to the smaller atomic size of carbon vs silicon) as described by Scharber et al. [90].

Both wave-function and DFT methods can be used to determine excited-state geometries and as a result the degree of relaxation and (de)localization of the exciton. This is of particular relevance with regard to describing intramolecular and intermolecular exciton diffusion within the bulk. HF/CIS has been the principal method employed to date to determine the nature of the geometry in the first excited state [187–191, 245]; recent developments with regards to TDDFT [259], however, have allowed for these methods to be increasingly considered. Using the first-excited state geometries in combination with the methods described above, additionally, allows for the evaluation of fluorescence spectra.

Finally, the nature and energies of the low-lying triplet states can also be evaluated with similar computational methodologies. This is particularly useful as the

[2] Note that both vibrational (i.e., Franck–Condon factor) and spin selection rules also play an important role in the probability of a transition.

experimental determination of triplet-state properties is often difficult [196, 260]. Both vertical and adiabatic energy differences with respect to the ground state, geometric consequences of triplet-state formation (e.g., localization of the triplet state), and singlet–triplet exchange energies [139, 140, 142, 145, 196, 261] are accessible. For organic solar cells, the characterization of the low-lying triplet states is important as they can serve as pivotal energy-loss pathways [260, 262, 263].

7 Exciton Migration

As the above section indicates, the use of electronic-structure methods readily allows for reasonable descriptions of the geometric and energetic characteristics of low-lying singlet- and triplet-excited states. The ability to describe accurately the migration (diffusion) of these excitons in organic thin films, on the other hand, remains an elusive problem [103, 264]. Though the use of the customary point-dipole model is inappropriate for energy transfer between nearby chromophores, long-range Förster resonant energy transfer (FRET) theory is often applied to describe singlet exciton diffusion [264, 265]. Conversely, triplet exciton diffusion has been described through short-range Dexter mechanisms. Important for the description of energy transfer is the determination of electronic coupling between interacting sites [139, 266]. Electronic coupling has been determined on the basis of atomic transition densities to deal with the limitations of the point-dipole model in FRET [267, 268]. Complicating the picture further is recent work on oligoacene single crystals that reveals substantial contributions from charge-transfer configurations (where the hole and the electron are found on adjacent molecules) in the description of the lowest singlet exciton, a result that will have significant implications for the proper theoretical description of exciton diffusion [269].

8 Exciton Dissociation and Charge Separation

The description of exciton dissociation at the HTM–ETM interface also remains ambiguous. This is a function of the fact that a number of aspects – including the nature of the ground state (e.g., molecular orientation, degree of charge transfer) at the heterojunction interface, polarization effects and the formation of heterojunction interface dipoles, the nature of the exciton (singlet or triplet) state that reaches the interface, and the coupling between the exciton state and the charge-transfer (CT) states at the interface – complicate the description [103, 270–273]. Recent work on isolated HTM and ETM molecular pairs has been performed to develop and test methods to probe the rates of charge-transfer, charge-separation, and charge-recombination processes at the interface [270, 272, 274–276].

While work is ongoing to examine these rates for DA oligomers with fullerenes, a recent combined experimental and theoretical study of a series of polythiophenes [277] (Fig. 8) was performed to evaluate the impact of synthetically-induced

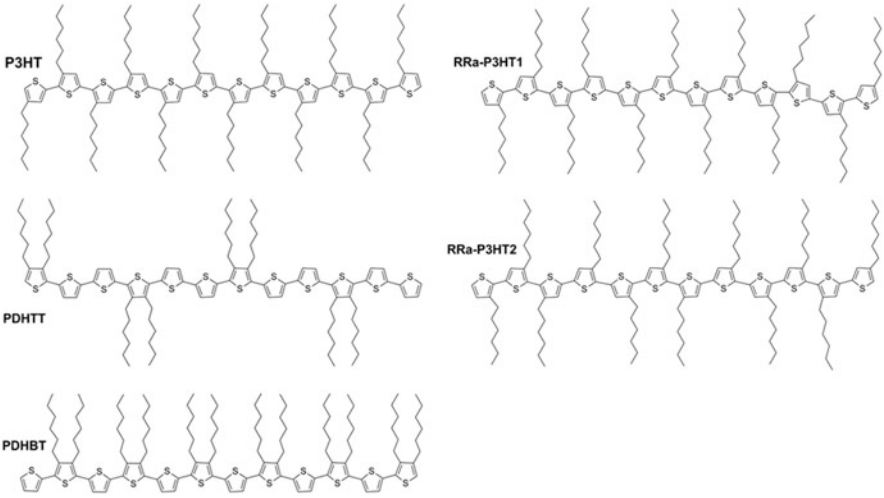

Fig. 8 Oligothiophene chemical structures considered for the DFT investigations

backbone twisting on the electronic coupling and charge-transfer state energies between the polymers and fullerenes at the heterojunction interface. It has been suggested that reducing the electronic coupling between the HTM and ETM materials at their interface through increased steric interactions could subsequently increase the open-circuit voltage (V_{oc}) by limiting the dark current and radiative recombination losses [278–280]. A linear correlation was observed experimentally across the polymer series between the energy of the charge-transfer state, the V_{oc} value, and the polymer ionization potential [277], with the consistent difference (0.57 V) between V_{oc} and E_{CT}/q (the charge-transfer state energy divided by the elementary charge) suggesting that radiative losses and intermolecular electronic couplings at the heterojunction (assuming nonradiative losses to be similar) were of the same order for all the polymers.

To examine these effects computationally, complexes between oligothiophene donors and a fullerene acceptor were derived by placing the pentagonal face of C_{60} (used as a model for the substituted fullerene) parallel to the plane of the central unsubstituted thiophene unit in PDHTT and PDHBT or hexyl-substituted thiophene unit in P3HT. Here, Grimme's dispersion-corrected B97D functional [281] and a 6-31G(d,p) basis set were used to determine the binding energy of the complex as the oligomer-C_{60} distance was varied from 2.8 to 4.4 Å; the largest binding-energy configuration was then used to evaluate both the charge-transfer state energy and effective electronic coupling between the oligomer and C_{60}.

As expected, the largest binding energy for a given complex was determined to shift to larger oligomer-fullerene distances with increased twist within the conjugated backbones. Across the series, the oligomer-fullerene distances ranged from 3.15 to 3.25 Å [277]. These complex geometries were then used to evaluate the energy of the charge-transfer state through the constrained DFT formalism [282] at

the B3LYP/6-31G(d,p) level coupled with the continuum solvation conductor-like screening model [283]. The DFT-derived charge-transfer state energies followed well the trend of the experimental data determined by measurements of the external quantum efficiency, though the DFT-based absolute values overestimated the experimental results by some 0.3–0.5 eV (a discrepancy that could arise from a variety of sources, including the simplicity of taking into account only a two-molecule complex) [277].

A fragment orbital approach [284] was then used to evaluate the effective electronic couplings between the oligothiophene HOMO and the triply-degenerate C_{60} LUMO at the B3LYP/6-31G(d,p) level. Importantly, the theoretical evaluation of the electronic couplings corroborated the experimental results. As expected, the increased distance between the oligomer and C_{60} as a function of the degree of backbone twisting led to a reduced electronic coupling between the oligomer and fullerene. Though the computed couplings correlate fairly well with the increased open-circuit voltage with increased backbone twisting, the variation in the electronic coupling is quite small and results in estimates for the increased open-circuit voltages that are roughly one order of magnitude smaller than the experimental data. These evaluations, in total, suggest that multi-step theoretical determinations of the charge-transfer state energies and electronic couplings can provide valuable insight into the exciton dissociation process at the interface, though considerable improvements in the methodology and general understanding are still necessary.

Finally, the energy of the fully charge-separated state is defined as the energy difference between the (adiabatic) ionization potential of the HTM and the (adiabatic) electron affinity of the ETM. To determine such energies theoretically, the radical-cation and radical-anion states need to be evaluated in the solid state. Both wave-function and DFT methods have been widely used to examine these states for isolated DA oligomers [69, 187–191, 194, 197, 245]. Accurate evaluations of the polarization energies appearing in condensed phases, however, remain a challenging task [271, 285–299]. Hence, there remains a significant challenge to describe the conceptually simple charge-separated state from current theoretical methods.

9 Charge-Carrier Transport

Charge-carrier transport is generally discussed in terms of semiclassical Marcus theory [112, 113, 300–303]. The charge-carrier mobility (in the weak coupling limit) is related to the rate of electron transfer, k_{ij}, between two adjacent molecules/polymer chain segments:

$$k_{ij} = \frac{2\pi}{\hbar} |H_{ij}|^2 \sqrt{\frac{1}{4\pi k_B T \lambda}} \exp\left[-\frac{(\lambda + \Delta G^\circ)^2}{4\lambda k_B T} \right] \tag{2}$$

where k_B and $\hbar$ represent the Boltzmann and reduced Planck constants, respectively, T the temperature, ΔG° is the Gibbs' free energy change during electron transfer, H_{ij} denotes the electronic coupling (transfer integral) between initial state i and final state j, and λ is the reorganization energy, which consists of two components – the outer-sphere (λ_o) and inner-sphere (or intramolecular, λ_i) reorganization energies. Quantum-chemical evaluations of the electronic coupling and intramolecular reorganization energy are common and have been applied to the study of DA oligomers [69, 143, 193, 194]; reviews on the evaluation of charge-carrier transport through organic crystals and thin films have been published elsewhere [112, 113]. We note that atomistic molecular dynamics simulations coupled with electronic structure evaluations of the electronic coupling and intramolecular reorganization energies have proved to be useful for the evaluation of charge-carrier transport in polymers [304–308], though considerable work remains to derive the appropriate theoretical understanding of these processes in both ordered (including both short- and medium-range order) and disordered organic media.

10 Charge Collection

The investigation of charge collection at the electrodes is a difficult task as one has to consider the complexity of the organic–metal/organic–conducting–oxide interface, including how molecular orientation, chemical substitution, or charge-density redistributions influence the energy-level alignment between the frontier molecular orbitals of the organic layer and the Fermi energy of the electrode [309–321]. Such investigations, importantly, provide valuable physical insight into the empirical results obtained from photoelectron spectroscopy experiments. Limited studies currently exist concerning polymer–electrode interfaces, though a recent examination of the oligothiophene–gold interface details the importance of oligomer/polymer orientation at these contacts [217].

11 Outlook

In this overview, we have discussed the application and results of oligomer-based quantum-chemical characterizations of DA copolymers to illustrate useful concepts concerning the intrinsic and materials-scale properties of systems of interest for OPVs. Details concerning the interplay of the chemical structure and geometric, electronic, and optical properties were provided, and methodologies that result in improved agreement with experiment were considered. We have also highlighted a number of areas where continued work to gain better insight into the physical processes involved in OPV operation is necessary so as to derive appropriate theoretical models.

Notably, theoretical efforts are emerging that employ the quantum-chemical approaches discussed here to perform extensive calculations pre-synthesis to offer potential targets for synthetic and materials chemists to consider [322, 323]. We need to keep in mind, however, that while such studies are valuable, they constitute only a first component in the much broader multiscale modeling and experimental efforts that need to be performed to push further both materials design and a more complete understanding of the underlying photochemistry and device physics. Major challenges remain to understand how the intrinsic properties of each component change as a function of bulk and interface effects in the solid state and how key intermolecular interactions are influenced by molecular packing arrangements. These topics will be considered in more detail in later chapters by Zannoni and Van Voorhis. This issue is underlined by the fact that there now exist a number of molecules and polymers in the literature that seemingly have appropriate ionization energies and optical absorption profiles to work well as the HTM and primary absorber in concert with fullerene acceptors, yet the performance of devices employing these materials can range from very good to nil. Therefore, it will be important to develop integrated multiscale theoretical approaches that, when combined with experimental efforts regarding the determination of structure/morphology at the nano- and mesoscales, will develop the broader understanding required for directed materials design.

Acknowledgements This work was funded by the Office of Naval Research (Award No. N00014-11-1-0211) and by the Deanship of Scientific Research (DSR) of King Abdulaziz University (Award No. 23-3-1432/HiCi), which the authors acknowledge for technical and financial support. We are also greatly indebted to our many colleagues that have contributed to the work in organic photovoltaics reviewed herein, including Zhenan Bao, Pierre M. Beaujuge, David Beljonne, Jérôme Cornil, Veaceslav Coropceanu, Bernard Kippelen, Hong Li, Seth R. Marder, Michael D. McGehee, Joseph E. Norton, Laxman Pandey, John R. Reynolds, Alberto Salleo, John S. Sears, and Yuanping Yi.

References

1. Becquerel E (1839) Mémoire sur les effets électroniques produits sous l'influence des rayons solaires. C R Acad Sci 9:561
2. Tang CW (1986) Two-layer organic photovoltaic cell. Appl Phys Lett 48:183
3. Halls JJM, Walsh CA, Greenham NC, Marseglia EA, Friend RH, Moratti SC, Holmes AB (1995) Efficient photodiodes from interpenetrating polymer networks. Nature 376:498
4. Yu G, Gao J, Hummelen JC, Wudl F, Heeger AJ (1995) Polymer photovoltaic cells: enhanced efficiencies via a network of internal donor–acceptor heterojunctions. Science 270:1789
5. Yu G, Heeger AJ (1995) Charge separation and photovoltaic conversion in polymer composites with internal donor/acceptor heterojunctions. J Appl Phys 78:4510
6. Peet J, Kim JY, Coates NE, Ma WL, Moses D, Heeger AJ, Bazan GC (2007) Efficiency enhancement in low-bandgap polymer solar cells by processing with alkane dithiols. Nature Mater 6:497
7. Blouin N, Michaud A, Leclerc M (2007) A low-bandgap poly(2,7-carbazole) derivative for use in high-performance solar cells. Adv Mater 19:2295

8. Blouin N, Michaud A, Gendron D, Wakim S, Blair E, Neagu-Plesu R, Belletete M, Durocher G, Tao Y, Leclerc M (2008) Toward a rational design of poly(2,7-carbazole) derivatives for solar cells. J Am Chem Soc 130:732
9. Park SH, Roy A, Beaupre S, Cho S, Coates N, Moon JS, Moses D, Leclerc M, Lee K, Heeger AJ (2009) Bulk heterojunction solar cells with internal quantum efficiency approaching 100%. Nature Photon 3:297
10. Beaupre S, Boudreault P-LT, Leclerc M (2010) Solar-energy production and energy-efficient lighting: photovoltaic devices and white-light-emitting diodes using poly(2,7-fluorene), poly (2,7-carbazole), and poly(2,7-dibenzosilole) derivatives. Adv Mater 22:E6
11. Zou Y, Najari A, Berrouard P, Beaupre S, Reda Aich B, Tao Y, Leclerc M (2010) A thieno [3,4-c]pyrrole-4,6-dione-based copolymer for efficient solar cells. J Am Chem Soc 132:5330
12. Liang Y, Xiao S, Feng D, Yu L (2008) Control in energy levels of conjugated polymers for photovoltaic application. J Phys Chem C 112:7866
13. Chen H-Y, Hou J, Zhang S, Liang Y, Yang G, Yang Y, Yu L, Wu Y, Li G (2009) Polymer solar cells with enhanced open-circuit voltage and efficiency. Nature Photon 3:649
14. Liang Y, Feng D, Guo J, Szarko JM, Ray C, Chen LX, Yu L (2009) Regioregular oligomer and polymer containing thieno[3,4-b]thiophene moiety for efficient organic solar cells. Macromolecules 42:1091
15. Liang Y, Feng D, Wu Y, Tsai S-T, Li G, Ray C, Yu L (2009) Highly efficient solar cell polymers developed via fine-tuning of structural and electronic properties. J Am Chem Soc 131:7792
16. Liang Y, Wu Y, Feng D, Tsai S-T, Son H-J, Li G, Yu L (2009) Development of new semiconducting polymers for high performance solar cells. J Am Chem Soc 131:56
17. Guo J, Liang Y, Szarko J, Lee B, Son HJ, Son HJ, Rolczynski BS, Yu L, Chen LX (2010) Structure, dynamics, and power conversion efficiency correlations in a new low bandgap polymer: PCBM solar cell. J Phys Chem B 114:742
18. Liang Y, Xu Z, Xia J, Tsai S-T, Wu Y, Li G, Ray C, Yu L (2010) For the bright future-bulk heterojunction polymer solar cells with power conversion efficiency of 7.4%. Adv Mater 22:E135
19. Muhlbacher D, Scharber M, Morana M, Zhu ZG, Waller D, Gaudiana R, Brabec C (2006) High photovoltaic performance of a low-bandgap polymer. Adv Mater 18:2884
20. Liang Y, Yu L (2010) A new class of semiconducting polymers for bulk heterojunction solar cells with exceptionally high performance. Acc Chem Res 43:1227
21. Press release (2012) Solarmer energy, Incorporated. August 21, 2012
22. Hains AW, Liang Z, Woodhouse MA, Gregg BA (2010) Molecular semiconductors in organic photovoltaic cells. Chem Rev 110:6689
23. Zhang Y, Dang X-D, Kim C, Nguyen T-Q (2011) Effect of charge recombination on the fill factor of small molecule bulk heterojunction solar cells. Adv Energy Mater 1:610
24. Wei G, Lunt RR, Sun K, Wang S, Thompson ME, Forrest SR (2010) Efficient, ordered bulk heterojunction nanocrystalline solar cells by annealing of ultrathin squaraine thin films. Nano Lett 10:3555
25. Sun Y, Welch GC, Leong WL, Takacs CJ, Bazan GC, Heeger AJ (2012) Solution-processed small-molecule solar cells with 6.7% efficiency. Nature Mater 11:44
26. Press release (2013) Heliatek GmbH. January 16, 2013
27. Beaujuge PM, Frechet JMJ (2011) Molecular design and ordering effects in pi-functional materials for transistor and solar cell applications. J Am Chem Soc 133:20009
28. Henson ZB, Mullen K, Bazan GC (2012) Design strategies for organic semiconductors beyond the molecular formula. Nature Chem 4:699
29. Havinga EE, Hoeve W, Wynberg H (1992) A new class of small band gap organic polymer conductors. Polym Bull 29:119
30. Havinga EE, Tenhoeve W, Wynberg H (1993) Alternate donor–acceptor small-band-gap semiconducting polymers – polysquaraines and polycroconaines. Synth Met 55:299

31. Dhanabalan A, van Dongen JLJ, van Duren JKJ, Janssen HM, van Hal PA, Janssen RAJ (2001) Synthesis, characterization, and electrooptical properties of a new alternating N-dodecylpyrrole-benzothiadiazole copolymer. Macromolecules 34:2495
32. Dhanabalan A, van Duren JKJ, van Hal PA, van Dongen JLJ, Janssen RAJ (2001) Synthesis and characterization of a low bandgap conjugated polymer for bulk heterojunction photovoltaic cells. Adv Funct Mater 11:255
33. van Mullekom HAM, Vekemans J, Havinga EE, Meijer EW (2001) Developments in the chemistry and band gap engineering of donor–acceptor substituted conjugated polymers. Mat Sci Eng R 32:1
34. Jenekhe SA, Lu L, Alam MM (2001) New conjugated polymers with donor–acceptor architectures: synthesis and photophysics of carbazole–quinoline and phenothiazine–quinoline copolymers and oligomers exhibiting large intramolecular charge transfer. Macromolecules 34:7315
35. Brabec CJ, Winder C, Sariciftci NS, Hummelen JC, Dhanabalan A, Van Hal PA, Janssen RAJ (2002) A low-bandgap semiconducting polymer for photovoltaic devices and infrared emitting diodes. Adv Funct Mater 12:709
36. Persson N-K, Sun M, Kjellberg P, Pullerits T, Inganäs O (2005) Optical properties of low band gap alternating copolyfluorenes for photovoltaic devices. J Chem Phys 123:204718
37. Thompson BC, Kim Y-G, McCarley TD, Reynolds JR (2006) Soluble narrow band gap and blue propylenedioxythiophene-cyanovinylene polymers as multifunctional materials for photovoltaic and electrochromic applications. J Am Chem Soc 128:12714
38. Cheng KF, Liu CL, Chen WC (2007) Small band gap conjugated polymers based on thiophene-thienopyrazine copolymers. J Polym Sci A Polym Chem 45:5872
39. Colladet K, Fourier S, Cleij TJ, Lutsen L, Gelan J, Vanderzande D, Nguyen LH, Neugebauer H, Sariciftci S, Aguirre A, Janssen G, Goovaerts E (2007) Low band gap donor–acceptor conjugated polymers toward organic solar cells applications. Macromolecules 40:65
40. Gadisa A, Mammo W, Andersson LM, Admassie S, Zhang F, Andersson MR, Inganaes O (2007) A new donor–acceptor–donor polyfluorene copolymer with balanced electron and hole mobility. Adv Funct Mater 17:3836
41. Tang W, Ke L, Tan L, Lin T, Kietzke T, Chen Z-K (2007) Conjugated copolymers based on fluorene-thieno[3,2-b]thiophene for light-emitting diodes and photovoltaic cells. Macromolecules 40:6164
42. Wong HMP, Wang P, Abrusci A, Svensson M, Andersson MR, Greenham NC (2007) Donor and acceptor behavior in a polyfluorene for photovoltaics. J Phys Chem C 111:5244
43. Zhang M, Yang C, Mishra AK, Pisula W, Zhou G, Schmaltz B, Baumgarten M, Mullen K (2007) Conjugated alternating copolymers containing both donor and acceptor moieties in the main chain. Chem Commun 1704
44. Zhu Z, Waller D, Gaudiana R, Morana M, Muhlbacher D, Scharber M, Brabec C (2007) Panchromatic conjugated polymers containing alternating donor/acceptor units for photovoltaic applications. Macromolecules 40:1981
45. Blouin N, Leclerc M (2008) Poly(2,7-carbazole)s: structure–property relationships. Acc Chem Res 41:1110
46. Hou J, Chen H-Y, Zhang S, Li G, Yang Y (2008) Synthesis, characterization, and photovoltaic properties of a low band gap polymer based on silole-containing polythiophenes and 2,1,3-benzothiadiazole. J Am Chem Soc 130:16144
47. Hou J, Park M-H, Zhang S, Yao Y, Chen L-M, Li J-H, Yang Y (2008) Bandgap and molecular energy level control of conjugated polymer photovoltaic materials based on benzo[1,2-b:4,5-b']dithiophene. Macromolecules 41:6012
48. Kumar A, Bokria JG, Buyukmumcu Z, Dey T, Sotzing GA (2008) Poly(thieno[3,4-b]furan), a new low band gap polymer: experiment and theory. Macromolecules 41:7098
49. Moule AJ, Tsami A, Buennagel TW, Forster M, Kronenberg NM, Scharber M, Koppe M, Morana M, Brabec CJ, Meerholz K, Scherf U (2008) Two novel cyclopentadithiophene-based alternating copolymers as potential donor components for high-efficiency bulk-heterojunction-type solar cells. Chem Mater 20:4045

50. Peng Q, Park K, Lin T, Durstock M, Dai L (2008) Donor-pi-acceptor conjugated copolymers for photovoltaic applications: tuning the open-circuit voltage by adjusting the donor/acceptor ratio. J Phys Chem B 112:2801
51. Walker W, Veldman B, Chiechi R, Patil S, Bendikov M, Wudl F (2008) Visible and near-infrared absorbing, low band gap conjugated oligomers based on cyclopentadieneones. Macromolecules 41:7278
52. Zhang F, Bijleveld J, Perzon E, Tvingstedt K, Barrau S, Inganaes O, Andersson MR (2008) High photovoltage achieved in low band gap polymer solar cells by adjusting energy levels of a polymer with the LUMOs of fullerene derivatives. J Mater Chem 18:5468
53. Ahmed E, Kim FS, Xin H, Jenekhe SA (2009) Benzobisthiazole-thiophene copolymer semiconductors: synthesis, enhanced stability, field-effect transistors, and efficient solar cells. Macromolecules 42:8615
54. Beaujuge PM, Pisula W, Tsao HN, Ellinger S, Mullen K, Reynolds JR (2009) Tailoring structure-property relationships in dithienosilole-benzothiadiazole donor–acceptor copolymers. J Am Chem Soc 131:7514
55. Bijleveld JC, Shahid M, Gilot J, Wienk MM, Janssen RAJ (2009) Copolymers of cyclopentadithiophene and electron-deficient aromatic units designed for photovoltaic applications. Adv Funct Mater 19:3262
56. Bijleveld JC, Zoombelt AP, Mathijssen SGJ, Wienk MM, Turbiez M, de Leeuw DM, Janssen RAJ (2009) Poly(diketopyrrolopyrrole-terthiophene) for ambipolar logic and photovoltaics. J Am Chem Soc 131:16616
57. Gedefaw D, Zhou Y, Hellstroem S, Lindgren L, Andersson LM, Zhang F, Mammo W, Inganaes O, Andersson MR (2009) Alternating copolymers of fluorene and donor–acceptor–donor segments designed for miscibility in bulk heterojunction photovoltaics. J Mater Chem 19:5359
58. Hellstroem S, Zhang F, Inganaes O, Andersson MR (2009) Structure–property relationships of small bandgap conjugated polymers for solar cells. Dalton Trans 10032
59. Hou J, Chen H-Y, Zhang S, Chen RI, Yang Y, Wu Y, Li G (2009) Synthesis of a low band gap polymer and its application in highly efficient polymer solar cells. J Am Chem Soc 131:15586
60. Hou J, Chen H-Y, Zhang S, Yang Y (2009) Synthesis and photovoltaic properties of two benzo[1,2-b:3,4-b']dithiophene-based conjugated polymers. J Phys Chem C 113:21202
61. Hou J, Chen TL, Zhang S, Chen H-Y, Yang Y (2009) Poly[4,4-bis(2-ethylhexyl)cyclopenta [2,1-b;3,4-b']dithiophene-2,6-diyl-alt-2,1,3- benzoselenadiazole-4,7-diyl], a new low band gap polymer in polymer solar cells. J Phys Chem C 113:1601
62. Huo L, Chen H-Y, Hou J, Chen TL, Yang Y (2009) Low band gap dithieno[3,2-b:2',3'-d] silole-containing polymers, synthesis, characterization and photovoltaic application. Chem Commun 5570
63. Huo L, Hou J, Chen H-Y, Zhang S, Jiang Y, Chen TL, Yang Y (2009) Bandgap and molecular level control of the low-bandgap polymers based on 3,6-dithiophen-2-yl-2,5-dihydropyrrolo [3,4-c]pyrrole-1,4-dione toward highly efficient polymer solar cells. Macromolecules 42:6564
64. Inganas O, Zhang F, Andersson MR (2009) Alternating polyfluorenes collect solar light in polymer photovoltaics. Acc Chem Res 42:1731
65. Lee SK, Cho NS, Cho S, Moon S-J, Lee JK, Bazan GC (2009) Synthesis and characterization of low-bandgap cyclopentadithiophene-biselenophene copolymer and its use in field-effect transistor and polymer solar cells. J Polym Sci A Polym Chem 47:6873
66. Lindgren LJ, Zhang F, Andersson M, Barrau S, Hellstroem S, Mammo W, Perzon E, Inganaes O, Andersson MR (2009) Synthesis, characterization, and devices of a series of alternating copolymers for solar cells. Chem Mater 21:3491
67. Mei JG, Heston NC, Vasilyeva SV, Reynolds JR (2009) A facile approach to defect-free vinylene-linked benzothiadiazole-thiophene low-bandgap conjugated polymers for organic electronics. Macromolecules 42:1482

68. Mondal R, Ko S, Norton JE, Miyaki N, Becerril HA, Verploegen E, Toney MF, Brédas JL, McGehee MD, Bao ZN (2009) Molecular design for improved photovoltaic efficiency: band gap and absorption coefficient engineering. J Mater Chem 19:7195
69. Mondal R, Miyaki N, Becerril HA, Norton JE, Parmer J, Mayer AC, Tang ML, Brédas J-L, McGehee MD, Bao Z (2009) Synthesis of acenaphthyl and phenanthrene based fused-aromatic thienopyrazine co-polymers for photovoltaic and thin film transistor applications. Chem Mater 21:3618
70. Park SH, Roy A, Beaupre S, Cho S, Coates N, Moon JS, Moses D, Leclerc M, Lee K, Heeger AJ (2009) Bulk heterojunction solar cells with internal quantum efficiency approaching 100%. Nat Photonics 3:297
71. Steckler TT, Zhang X, Hwang J, Honeyager R, Ohira S, Zhang XH, Grant A, Ellinger S, Odom SA, Sweat D, Tanner DB, Rinzler AG, Barlow S, Brédas JL, Kippelen B, Marder SR, Reynolds JR (2009) A spray-processable, low bandgap, and ambipolar donor–acceptor conjugated polymer. J Am Chem Soc 131:2824
72. Xin H, Guo X, Kim FS, Ren G, Watson MD, Jenekhe SA (2009) Efficient solar cells based on a new phthalimide-based donor–acceptor copolymer semiconductor: morphology, charge-transport, and photovoltaic properties. J Mater Chem 19:5303
73. Zhang S, Guo Y, Fan H, Liu Y, Chen H-Y, Yang G, Zhan X, Liu Y, Li Y, Yang Y (2009) Low bandgap pi-conjugated copolymers based on fused thiophenes and benzothiadiazole: synthesis and structure-property relationship study. J Polym Sci A Polym Chem 47:5498
74. Zoombelt AP, Fonrodona M, Turbiez MGR, Wienk MM, Janssen RAJ (2009) Synthesis and photovoltaic performance of a series of small band gap polymers. J Mater Chem 19:5336
75. Zoombelt AP, Fonrodona M, Wienk MM, Sieval AB, Hummelen JC, Janssen RAJ (2009) Photovoltaic performance of an ultrasmall band gap polymer. Org Lett 11:903
76. Zoombelt AP, Gilot J, Wienk MM, Janssen RAJ (2009) Effect of extended thiophene segments in small band gap polymers with thienopyrazine. Chem Mater 21:1663
77. Zoombelt AP, Leenen MAM, Fonrodona M, Nicolas Y, Wienk MM, Janssen RAJ (2009) The influence of side chains on solubility and photovoltaic performance of dithiophene-thienopyrazine small band gap copolymers. Polymer 50:4564
78. Baran D, Balan A, Celebi S, Meana Esteban B, Neugebauer H, Sariciftci NS, Toppare L (2010) Processable multipurpose conjugated polymer for electrochromic and photovoltaic applications. Chem Mater 22:2978
79. Beaujuge PM, Subbiah J, Choudhury KR, Ellinger S, McCarley TD, So F, Reynolds JR (2010) Green dioxythiophene-benzothiadiazole donor–acceptor copolymers for photovoltaic device applications. Chem Mater 22:2093
80. Chen C-H, Hsieh C-H, Dubosc M, Cheng Y-J, Hsu C-S (2010) Synthesis and characterization of bridged bithiophene-based conjugated polymers for photovoltaic applications: acceptor strength and ternary blends. Macromolecules 43:697
81. Chen H-Y, Hou J, Hayden AE, Yang H, Houk KN, Yang Y (2010) Silicon atom substitution enhances interchain packing in a thiophene-based polymer system. Adv Mater 22:371
82. Huo L, Hou J, Zhang S, Chen H-Y, Yang Y (2010) A polybenzo[1,2-b:4,5-b']dithiophene derivative with deep HOMO level and its application in high-performance polymer solar cells. Angew Chem Int Edit 49:1500
83. Kim B-S, Ma B, Donuru VR, Liu H, Frechet JMJ (2010) Bodipy-backboned polymers as electron donor in bulk heterojunction solar cells. Chem Commun 46:4148
84. Li J, Grimsdale AC (2010) Carbazole-based polymers for organic photovoltaic devices. Chem Soc Rev 39:2399
85. Liu B, Najari A, Pan C, Leclerc M, Xiao D, Zou Y (2010) New low bandgap dithienylbenzothiadiazole vinylene based copolymers: synthesis and photovoltaic properties. Macromol Rapid Commun 31:391
86. Marchiori CFN, Koehler M (2010) Dipole assisted exciton dissociation at conjugated polymer/fullerene photovoltaic interfaces: a molecular study using density functional theory calculations. Synth Met 160:643

87. Mondal R, Becerril HA, Verploegen E, Kim D, Norton JE, Ko S, Miyaki N, Lee S, Toney MF, Brédas J-L, McGehee MD, Bao Z (2010) Thiophene-rich fused-aromatic thienopyrazine acceptor for donor–acceptor low band-gap polymers for OTFT and polymer solar cell applications. J Mater Chem 20:5823
88. Piliego C, Holcombe TW, Douglas JD, Woo CH, Beaujuge PM, Frechet JMJ (2010) Synthetic control of structural order in *N*-alkylthieno[3,4-c]pyrrole-4,6-dione-based polymers for efficient solar cells. J Am Chem Soc 132:7595
89. Qian G, Wang ZY (2010) Design, synthesis, and properties of benzobisthiadiazole-based donor-pi-acceptor-pi-donor type of low-band-gap chromophores and polymers. Can J Chem 88:192
90. Scharber MC, Koppe M, Gao J, Cordella F, Loi MA, Denk P, Morana M, Egelhaaf HJ, Forberich K, Dennler G, Gaudiana R, Waller D, Zhu ZG, Shi XB, Brabec CJ (2010) Influence of the bridging atom on the performance of a low-bandgap bulk heterojunction solar cell. Adv Mater 22:367
91. Wu J-S, Cheng Y-J, Dubosc M, Hsieh C-H, Chang C-Y, Hsu C-S (2010) Donor–acceptor polymers based on multi-fused heptacyclic structures: synthesis, characterization and photovoltaic applications. Chem Commun 46:3259
92. Zhang X, Steckler TT, Dasari RR, Ohira S, Potscavage WJ Jr, Tiwari SP, Coppee S, Ellinger S, Barlow S, Brédas J-L, Kippelen B, Reynolds JR, Marder SR (2010) Dithienopyrrole-based donor–acceptor copolymers: low band-gap materials for charge transport, photovoltaics and electrochromism. J Mater Chem 20:123
93. Zhang Y, Hau SK, Yip H-L, Sun Y, Acton O, Jen AK-Y (2010) Efficient polymer solar cells based on the copolymers of benzodithiophene and thienopyrroledione. Chem Mater 22:2696
94. Zoombelt AP, Mathijssen SGJ, Turbiez MGR, Wienk MM, Janssen RAJ (2010) Small band gap polymers based on diketopyrrolopyrrole. J Mater Chem 20:2240
95. Walker B, Kim C, Nguyen T-Q (2010) Small molecule solution-processed bulk heterojunction solar cells†. Chem Mater 23:470
96. Zhang F, Wu D, Xu Y, Feng X (2011) Thiophene-based conjugated oligomers for organic solar cells. J Mater Chem 21:17590
97. Mishra A, Bäuerle P (2012) Small molecule organic semiconductors on the move: promises for future solar energy technology. Angew Chem Int Edit 51:2020
98. Liu X, Sun Y, Perez LA, Wen W, Toney MF, Heeger AJ, Bazan GC (2012) Narrow-band-gap conjugated chromophores with extended molecular lengths. J Am Chem Soc 134:20609
99. Henson ZB, Welch GC, van der Poll T, Bazan GC (2012) Pyridalthiadiazole-based narrow band gap chromophores. J Am Chem Soc 134:3766
100. Risko C, McGehee MD, Brédas JL (2011) A quantum-chemical perspective into low optical-gap polymers for highly-efficient organic solar cells. Chem Sci 2:1200
101. Blom PWM, Mihailetchi VD, Koster LJA, Markov DE (2007) Device physics of polymer: fullerene bulk heterojunction solar cells. Adv Mater 19:1551
102. Thompson BC, Fréchet JMJ (2008) Polymer-fullerene composite solar cells. Angew Chem Int Edit 47:58
103. Brédas JL, Norton JE, Cornil J, Coropceanu V (2009) Molecular understanding of organic solar cells: the challenges. Acc Chem Res 42:1691
104. Kippelen B, Brédas JL (2009) Organic photovoltaics. Energ Environ Sci 2:251
105. Clarke TM, Durrant JR (2010) Charge photogeneration in organic solar cells. Chem Rev 110:6736
106. Venkataraman D, Yurt S, Venkatraman BH, Gavvalapalli N (2010) Role of molecular architecture in organic photovoltaic cells. J Phys Chem Lett 1:947
107. Knupfer M (2003) Exciton binding energies in organic semiconductors. Appl Phys A 77:623
108. Heremans P, Cheyns D, Rand BP (2009) Strategies for increasing the efficiency of heterojunction organic solar cells: material selection and device architecture. Acc Chem Res 42:1740

109. Morteani AC, Sreearunothai P, Herz LM, Friend RH, Silva C (2004) Exciton regeneration at polymeric semiconductor heterojunctions. Phys Rev Lett 92:247402
110. Cheng YJ, Yang SH, Hsu CS (2009) Synthesis of conjugated polymers for organic solar cell applications. Chem Rev 109:5868
111. Guenes S, Neugebauer H, Sariciftci NS (2007) Conjugated polymer-based organic solar cells. Chem Rev 107:1324
112. Brédas JL, Beljonne D, Coropceanu V, Cornil J (2004) Charge-transfer and energy-transfer processes in pi-conjugated oligomers and polymers: a molecular picture. Chem Rev 104:4971
113. Coropceanu V, Cornil J, da Silva DA, Olivier Y, Silbey R, Brédas JL (2007) Charge transport in organic semiconductors. Chem Rev 107:926
114. Beaujuge PM, Tsao HN, Hansen MR, Amb CM, Risko C, Subbiah J, Choudhury KR, Mavrinskiy A, Pisula W, Brédas JL, So F, Mullen K, Reynolds JR (2012) Synthetic principles directing charge transport in low-band-gap dithienosilole-benzothiadiazole copolymers. J Am Chem Soc 134:8944
115. Ajayaghosh A (2003) Donor–acceptor type low band gap polymers: polysquaraines and related systems. Chem Soc Rev 32:181
116. Coakley KM, McGehee MD (2004) Conjugated polymer photovoltaic cells. Chem Mater 16:4533
117. Hoppe H, Sariciftci NS (2004) Organic solar cells: an overview. J Mater Res 19:1924
118. Roncali J (1997) Synthetic principles for bandgap control in linear pi-conjugated systems. Chem Rev 97:173
119. Benanti TL, Venkataraman D (2006) Organic solar cells: an overview focusing on active layer morphology. Photosynth Res 87:73
120. Bundgaard E, Krebs FC (2007) Low band gap polymers for organic photovoltaics. Sol Energy Mater Sol Cells 91:954
121. Kroon R, Lenes M, Hummelen JC, Blom PWM, De Boer B (2008) Small bandgap polymers for organic solar cells (polymer material development in the last 5 years). Polym Rev 48:531
122. Roncali J (2007) Molecular engineering of the band gap of pi-conjugated systems: facing technological applications. Macromol Rapid Commun 28:1761
123. Scharber MC, Wuhlbacher D, Koppe M, Denk P, Waldauf C, Heeger AJ, Brabec CL (2006) Design rules for donors in bulk-heterojunction solar cells – towards 10% energy-conversion efficiency. Adv Mater 18:789
124. Spanggaard H, Krebs FC (2004) A brief history of the development of organic and polymeric photovoltaics. Sol Energy Mater Sol Cells 83:125
125. Boudreault P-L, Najari A, Leclerc M (2011) Processable low-bandgap polymers for photovoltaic applications. Chem Mater 23:456
126. Brabec CJ, Gowrisanker S, Halls JJM, Laird D, Jia S, Williams SP (2010) Polymer–fullerene bulk-heterojunction solar cells. Adv Mater 22:3839
127. Peet J, Heeger AJ, Bazan GC (2009) "Plastic" solar cells: self-assembly of bulk heterojunction nanomaterials by spontaneous phase separation. Acc Chem Res 42:1700
128. Pandey L, Risko C, Norton JE, Brédas JL (2012) Donor–acceptor copolymers of relevance for organic photovoltaics: a theoretical investigation of the impact of chemical structure modifications on the electronic and optical properties. Macromolecules 45:6405
129. Wudl F, Kobayashi M, Heeger AJ (1984) Poly(Isothianaphthene). J Org Chem 49:3382
130. Brédas JL (1985) Relationship between band-gap and bond length alternation in organic conjugated polymers. J Chem Phys 82:3808
131. Brédas JL, Heeger AJ, Wudl F (1986) Towards organic polymers with very small intrinsic band-gaps.1. Electronic-structure of polyisothianaphthene and derivatives. J Chem Phys 85:4673
132. Jira R, Braunling H (1987) Synthesis of polyarenemethines, a new class of conducting polymers. Synth Met 17:691
133. Braunling H, Jira R (1987) Synthesis of polyphenylenemethines – a reinvestigation. Synth Met 20:375

134. Hoogmartens I, Adriaensens P, Vanderzande D, Gelan J, Quattrocchi C, Lazzaroni R, Brédas JL (1992) Low-bandgap conjugated polymers – a joint experimental and theoretical-study of the structure of polyisothianaphthene. Macromolecules 25:7347
135. Salzner U, Karalti O, Durdagi S (2006) Does the donor–acceptor concept work for designing synthetic metals? III. Theoretical investigation of copolymers between quinoid acceptors and aromatic donors. J Mol Model 12:687
136. Cui CX, Kertesz M, Jiang Y (1990) Extraction of polymer properties from oligomer calculations. J Phys Chem 94:5172
137. Karpfen A, Kertesz M (1991) Energetics and geometry of conducting polymers from oligomers. J Phys Chem 95:7680
138. Rissler J (2004) Effective conjugation length of pi-conjugated systems. Chem Phys Lett 395:92
139. Cornil J, Gueli I, Dkhissi A, Sancho-Garcia JC, Hennebicq E, Calbert JP, Lemaur V, Beljonne D, Brédas JL (2003) Electronic and optical properties of polyfluorene and fluorene-based copolymers: a quantum-chemical characterization. J Chem Phys 118:6615
140. Sancho-Garcia JC, Foden CL, Grizzi I, Greczynski G, de Jong MP, Salaneck WR, Brédas JL, Cornil J (2004) Joint theoretical and experimental characterization of the structural and electronic properties of poly(dioctylfluorene-alt-*N*-butylphenyl diphenylamine). J Phys Chem B 108:5594
141. Ozen AS, Atilgan C, Sonmez G (2007) Noncovalent intramolecular interactions in the monomers and oligomers of the acceptor and donor type of low band gap conducting polymers. J Phys Chem C 111:16362
142. Karsten BP, Viani L, Gierschner J, Cornil J, Janssen RAJ (2008) An oligomer study on small band gap polymers. J Phys Chem A 112:10764
143. Van Vooren A, Kim J-S, Cornil J (2008) Intrachain versus interchain electron transport in poly(fluorene-alt-benzothiadiazole): a quantum-chemical insight. Chemphyschem 9:989
144. Zhang L, Zhang QY, Ren H, Yan HL, Zhang JP, Zhang HP, Gu JW (2008) Calculation of band gap in long alkyl-substituted heterocyclic-thiophene-conjugated polymers with electron donor–acceptor fragment. Sol Energy Mater Sol Cells 92:581
145. Karsten BP, Viani L, Gierschner J, Cornil J, Janssen RAJ (2009) On the origin of small band gaps in alternating thiophene–thienopyrazine oligomers. J Phys Chem A 113:10343
146. Winfield JM, Van Vooren A, Park M-J, Hwang D-H, Cornil J, Kim J-S, Friend RH (2009) Charge-transfer character of excitons in poly[2,7-(9,9-di-*n*-octylfluorene)(1-x)-co-4,7-(2,1, 3-benzothiadiazole)(x)]. J Chem Phys 131:035104
147. Szarko JM, Rolczynski BS, Guo J, Liang Y, He F, Mara MW, Yu L, Chen LX (2010) Electronic processes in conjugated diblock oligomers mimicking low band-gap polymers: experimental and theoretical spectral analysis. J Phys Chem B 114:14505
148. Dewar MJS, Thiel W (1977) J Am Chem Soc 99:4899
149. Dewar MJS, Zoebisch EG, Healy EF, Stewart JJP (1985) J Am Chem Soc 107:3902
150. Stewart JJP (1989) Optimization of parameters for semiempirical methods. 1. Method. J Comput Chem 10:209
151. Stewart JJP (1989) Optimization of parameters for semiempirical methods. 2. Applications. J Comput Chem 10:221
152. Pople JA, Krishnan R, Schlegel HB, Binkley JS (1978) Electron correlation theories and their application to the study of simple reaction potential surfaces. Int J Quantum Chem 14:545
153. Møller C, Plesset MS (1934) Note on an approximation treatment for many-electron systems. Phys Rev 46:618
154. Grimme S (2003) Improved second-order Møller–Plesset perturbation theory by separate scaling of parallel- and antiparallel-spin pair correlation energies. J Chem Phys 118:9095
155. Head-Gordon M, Rico RJ, Oumi M, Lee TJ (1994) A doubles correction to electronic excited states from configuration interaction in the space of single substitutions. Chem Phys Lett 219:21

156. Grimme S, Izgorodina EI (2004) Calculation of 0–0 excitation energies of organic molecules by CIS(D) quantum chemical methods. Chem Phys 305:223
157. Rhee YM, Head-Gordon M (2007) Scaled second-order perturbation corrections to configuration interaction singles: efficient and reliable excitation energy methods. J Phys Chem A 111:5314
158. Goerigk L, Grimme S (2010) Assessment of TD-DFT methods and of various spin scaled CIS (D) and CC2 versions for the treatment of low-lying valence excitations of large organic dyes. J Chem Phys 132:184103
159. Settels V, Liu W, Pflaum J, Fink RF, Engels B (2012) Comparison of the electronic structure of different perylene-based dye-aggregates. J Comput Chem 33:1544
160. Hättig C (2005) Structure optimizations for excited states with correlated second-order methods: CC2 and ADC(2). In: Jensen HJÅ (ed) Advances in quantum chemistry, vol 50. Academic, San Diego, p 37
161. Starcke JH, Wormit M, Schirmer J, Dreuw A (2006) How much double excitation character do the lowest excited states of linear polyenes have? Chem Phys 329:39
162. Starcke JH, Wormit M, Dreuw A (2009) Nature of the lowest excited states of neutral polyenyl radicals and polyene radical cations. J Chem Phys 131:144311
163. Starcke JH, Wormit M, Dreuw A (2009) Unrestricted algebraic diagrammatic construction scheme of second order for the calculation of excited states of medium-sized and large molecules. J Chem Phys 130:024104
164. Knippenberg S, Starcke JH, Wormit M, Dreuw A (2010) The low-lying excited states of neutral polyacenes and their radical cations: a quantum chemical study employing the algebraic diagrammatic construction scheme of second order. Mol Phys 108:2801
165. Knippenberg S, Eisenbrandt P, Sistik L, Slavicek P, Dreuw A (2011) Simulation of photoelectron spectra using the reflection principle in combination with unrestricted excitation ADC(2) to assess the accuracy of excited-state calculations. Chemphyschem 12:3180
166. Hedin L (1965) New method for calculating the one-particle Green's function with application to the electron–gas problem. Phys Rev 139:A796
167. Hybertsen MS, Louie SG (1986) Electron correlation in semiconductors and insulators: band gaps and quasiparticle energies. Phys Rev B 34:5390
168. Ethridge EC, Fry JL, Zaider M (1996) Quasiparticle spectra of *trans*-polyacetylene. Phys Rev B 53:3662
169. van der Horst JW, Bobbert PA, Michels MAJ, Brocks G, Kelly PJ (1999) Ab initio calculation of the electronic and optical excitations in polythiophene: effects of intra- and interchain screening. Phys Rev Lett 83:4413
170. Rohlfing M, Louie SG (1999) Optical excitations in conjugated polymers. Phys Rev Lett 82:1959
171. Grossman JC, Rohlfing M, Mitas L, Louie SG, Cohen ML (2001) High accuracy many-body calculational approaches for excitations in molecules. Phys Rev Lett 86:472
172. Tiago ML, Northrup JE, Louie SG (2003) Ab initio calculation of the electronic and optical properties of solid pentacene. Phys Rev B 67:115212
173. Tiago ML, Rohlfing M, Louie SG (2004) Bound excitons and optical properties of bulk trans-polyacetylene. Phys Rev B 70:193204
174. Tiago ML, Chelikowsky JR (2005) First-principles GW–BSE excitations in organic molecules. Solid State Commun 136:333
175. Neaton JB, Hybertsen MS, Louie SG (2006) Renormalization of molecular electronic levels at metal–molecule interfaces. Phys Rev Lett 97:216405
176. Dori N, Menon M, Kilian L, Sokolowski M, Kronik L, Umbach E (2006) Valence electronic structure of gas-phase 3,4,9,10-perylene tetracarboxylic acid dianhydride: experiment and theory. Phys Rev B 73:195208
177. Rostgaard C, Jacobsen KW, Thygesen KS (2010) Fully self-consistent GW calculations for molecules. Phys Rev B 81:085103

178. Umari P, Stenuit G, Baroni S (2010) GW quasiparticle spectra from occupied states only. Phys Rev B 81:115104
179. Tamblyn I, Darancet P, Quek SY, Bonev SA, Neaton JB (2011) Electronic energy level alignment at metal–molecule interfaces with a GW approach. Phys Rev B 84:201402
180. Blase X, Attaccalite C, Olevano V (2011) First-principles GW calculations for fullerenes, porphyrins, phthalocyanine, and other molecules of interest for organic photovoltaic applications. Phys Rev B 83:115103
181. Faber C, Attaccalite C, Olevano V, Runge E, Blase X (2011) First-principles GW calculations for DNA and RNA nucleobases. Phys Rev B 83:115123
182. Faber C, Duchemin I, Deutsch T, Attaccalite C, Olevano V, Blase X (2012) Electron–phonon coupling and charge-transfer excitations in organic systems from many-body perturbation theory. J Mater Sci 47:7472
183. Sharifzadeh S, Biller A, Kronik L, Neaton JB (2012) Quasiparticle and optical spectroscopy of the organic semiconductors pentacene and PTCDA from first principles. Phys Rev B 85:125307
184. Refaely-Abramson S, Sharifzadeh S, Govind N, Autschbach J, Neaton JB, Baer R, Kronik L (2012) Quasiparticle spectra from a nonempirical optimally tuned range-separated hybrid density functional. Phys Rev Lett 109:226405
185. Sharifzadeh S, Tamblyn I, Doak P, Darancet PT, Neaton JB (2012) Quantitative molecular orbital energies within a G(0)W(0) approximation. Eur Phys J B 85:323
186. Körzdörfer T, Marom N (2012) Strategy for finding a reliable starting point for G(0)W(0) demonstrated for molecules. Phys Rev B 86:041110
187. Wang J-F, Feng J-K, Ren A-M, Liu X-D, Ma Y-G, Lu P, Zhang H-X (2004) Theoretical studies of the absorption and emission properties of the fluorene-based conjugated polymers. Macromolecules 37:3451
188. Yang L, Feng J-K, Liao Y, Ren A-M (2005) A theoretical investigation on the electronic and optical properties of pi-conjugated copolymers with an efficient electron-accepting unit bithieno[3,2-b:2'3'-e]pyridine. Polymer 46:9955
189. Yang L, Feng J-K, Ren A-M (2005) Theoretical studies on the electronic and optical properties of two new alternating fluorene/carbazole copolymers. J Comput Chem 26:969
190. Yang L, Feng J-K, Ren A-M (2005) Theoretical study on electronic structure and optical properties of phenothiazine-containing conjugated oligomers and polymers. J Org Chem 70:5987
191. Yang L, Liao Y, Feng J-K, Ren A-M (2005) Theoretical studies of the modulation of polymer electronic and optical properties through the introduction of the electron-donating 3,4-ethylenedioxythiophene or electron-accepting pyridine and 1,3,4-oxadiazole moieties. J Phys Chem A 109:7764
192. Pai C-L, Liu C-L, Chen W-C, Jenekhe SA (2006) Electronic structure and properties of alternating donor–acceptor conjugated copolymers: 3,4-ethylenedioxythiophene (EDOT) copolymers and model compounds. Polymer 47:699
193. Medina BM, Van Vooren A, Brocorens P, Gierschner J, Shkunov M, Heeney M, McCulloch I, Lazzaroni R, Cornil J (2007) Electronic structure and charge-transport properties of polythiophene chains containing thienothiophene units: a joint experimental and theoretical study. Chem Mater 19:4949
194. Yang L, Feng J-K, Ren A-M (2007) Theoretical study on electronic structure and optical properties of novel donor–acceptor conjugated copolymers derived from benzothiadiazole and benzoselenadiazole. THEOCHEM 816:161
195. Ding Y, Zhao JF, Wang XS, Liu SS, Ma FC (2009) Optical properties of neutral and charged low band gap alternating copolyfluorenes: TD-DFT investigation. Chinese J Chem Phys 22:389
196. Karsten BP, Bijleveld JC, Viani L, Cornil J, Gierschner J, Janssen RAJ (2009) Electronic structure of small band gap oligomers based on cyclopentadithiophenes and acceptor units. J Mater Chem 19:5343

197. Liang DD, Tang SS, Liu JB, Liu JH, Kang LJ (2009) First principles calculations of optical and electronical properties for 2,7-carbazole derivatives as solar cells materials. THEOCHEM 908:102
198. Peng Q, Xu J, Zheng W (2009) Low band gap copolymers based on thiophene and quinoxaline: their electronic energy levels and photovoltaic application. J Polym Sci A Polym Chem 47:3399
199. Tian YH, Kertesz M (2009) Ladder-type polyenazine based on intramolecular S ... N interactions: a theoretical study of a small-bandgap polymer. Macromolecules 42:6123
200. Kang JG, Kim HJ, Jeong YK, Nah MK, Park C, Bae YJ, Lee SW, Kim IT (2010) Optical and conformational studies on benzobisthiazole derivatives. J Phys Chem B 114:3791
201. Ko S, Mondal R, Risko C, Lee JK, Hong S, McGehee MD, Brédas J-L, Bao Z (2010) Tuning the optoelectronic properties of vinylene-linked donor–acceptor copolymers for organic photovoltaics. Macromolecules 43:6685
202. Steyrleuthner R, Schubert M, Howard I, Klaumunzer B, Schilling K, Chen ZH, Saalfrank P, Laquai F, Facchetti A, Neher D (2012) Aggregation in a high-mobility n-type low-bandgap copolymer with implications on semicrystalline morphology. J Am Chem Soc 134:18303
203. Sumpter BG, Meunier V (2012) Can computational approaches aid in untangling the inherent complexity of practical organic photovoltaic systems? J Polym Sci B Polym Phys 50:1071
204. Banerji N, Gagnon E, Morgantin PY, Valouch S, Mohebbi AR, Seo JH, Leclerc M, Heeger AJ (2012) Breaking down the problem: optical transitions, electronic structure, and photoconductivity in conjugated polymer PCDTBT and in its separate building blocks. J Phys Chem C 116:11456
205. Schroeder BC, Huang ZG, Ashraf RS, Smith J, D'Angelo P, Watkins SE, Anthopoulos TD, Durrant JR, McCulloch I (2012) Silaindacenodithiophene-based low band gap polymers – the effect of fluorine substitution on device performances and film morphologies. Adv Funct Mater 22:1663
206. Rolczynski BS, Szarko JM, Son HJ, Liang YY, Yu LP, Chen LX (2012) Ultrafast intramolecular exciton splitting dynamics in isolated low-band-gap polymers and their implication in photovoltaic materials design. J Am Chem Soc 134:4142
207. Longo L, Carbonera C, Pellegrino A, Perin N, Schimperna G, Tacca A, Po R (2012) Comparison between theoretical and experimental electronic properties of some popular donor polymers for bulk-heterojunction solar cells. Sol Energy Mater Sol Cells 97:139
208. Fazzi D, Grancini G, Maiuri M, Brida D, Cerullo G, Lanzani G (2012) Ultrafast internal conversion in a low band gap polymer for photovoltaics: experimental and theoretical study. Phys Chem Chem Phys 14:6367
209. Ozen AS (2011) Peripheral and structural effects on the band gap of acceptor–donor type conducting polymers containing pendant bisfulleroid groups. J Phys Chem C 115:25007
210. White CA, Johnson BG, Gill PMW, Headgordon M (1994) The continuous fast multipole method. Chem Phys Lett 230:8
211. White CA, Johnson BG, Gill PMW, HeadGordon M (1996) Linear scaling density functional calculations via the continuous fast multipole method. Chem Phys Lett 253:268
212. Scuseria GE (1999) Linear scaling density functional calculations with Gaussian orbitals. J Phys Chem A 103:4782
213. Zhou BJ, Ligneres VL, Carter EA (2005) Improving the orbital-free density functional theory description of covalent materials. J Chem Phys 122:044103
214. Bowler DR, Miyazaki T (2010) Calculations for millions of atoms with density functional theory: linear scaling shows its potential. J Phys Condens Matter 22:074207
215. Northrup JE (2007) Atomic and electronic structure of polymer organic semiconductors: P3HT, PQT, and PBTTT. Phys Rev B 76:245202
216. Cho E, Risko C, Kim D, Gysel R, Cates Miller N, Breiby DW, McGehee MD, Toney MF, Kline RJ, Brédas J-L (2012) Three-dimensional packing structure and electronic properties of biaxially oriented poly(2,5-bis(3-alkylthiophene-2-yl)thieno[3,2-b]thiophene) films. J Am Chem Soc 134:6177

217. Heimel G, Salzmann I, Duhm S, Rabe JP, Koch N (2009) Intrinsic surface dipoles control the energy levels of conjugated polymers. Adv Funct Mater 19:3874
218. Lee C, Yang W, Parr RG (1988) Development of the Colle–Salvetti correlation-energy formula into a functional of the electron density. Phys Rev B 37:785
219. Vosko SH, Wilk L, Nusair M (1980) Accurate spin-dependent electron liquid correlation energies for local spin density calculations: a critical analysis. Can J Phys 58:1200
220. Stephens PJ, Devlin FJ, Chabalowski CF, Frisch MJ (1994) Ab initio calculation of vibrational absorption and circular dichroism spectra using density functional force fields. J Phys Chem 98:11623
221. Becke AD (1993) Density-functional thermochemistry. III. The role of exact exchange. J Chem Phys 98:5648
222. Miehlich B, Savin A, Stoll H, Preuss H (1989) Results obtained with the correlation energy density functionals of Becke and Lee, Yang and Parr. Chem Phys Lett 157:200
223. Savin A, Flad H-J (1995) Density functionals for the Yukawa electron–electron interaction. Int J Quantum Chem 56:327
224. Tawada Y, Tsuneda T, Yanagisawa S, Yanai T, Hirao K (2004) A long-range-corrected time-dependent density functional theory. J Chem Phys 120:8425
225. Yanai T, Tew DP, Handy NC (2004) A new hybrid exchange-correlation functional using the Coulomb-attenuating method (CAM-B3LYP). Chem Phys Lett 393:51
226. Vydrov OA, Heyd J, Krukau AV, Scuseria GE (2006) Importance of short-range versus long-range Hartree–Fock exchange for the performance of hybrid density functionals. J Chem Phys 125:074106
227. Vydrov OA, Scuseria GE (2006) Assessment of a long-range corrected hybrid functional. J Chem Phys 125:234109
228. Krukau AV, Scuseria GE, Perdew JP, Savin A (2008) Hybrid functionals with local range separation. J Chem Phys 129:124103
229. Chai JD, Head-Gordon M (2008) Systematic optimization of long-range corrected hybrid density functionals. J Chem Phys 128:084106
230. Chai JD, Head-Gordon M (2008) Long-range corrected hybrid density functionals with damped atom–atom dispersion corrections. Phys Chem Chem Phys 10:6615
231. Stein T, Kronik L, Baer R (2009) Prediction of charge-transfer excitations in coumarin-based dyes using a range-separated functional tuned from first principles. J Chem Phys 131:244119
232. Baer R, Livshits E, Salzner U (2010) Tuned range-separated hybrids in density functional theory. Annu Rev Phys Chem 61:85
233. Stein T, Eisenberg H, Kronik L, Baer R (2010) Fundamental gaps in finite systems from eigenvalues of a generalized Kohn–Sham method. Phys Rev Lett 105:266802
234. Korzdorfer T, Sears JS, Sutton C, Brédas JL (2011) Long-range corrected hybrid functionals for pi-conjugated systems: dependence of the range-separation parameter on conjugation length. J Chem Phys 135:204107
235. Karolewski A, Stein T, Baer R, Kummel S (2011) Communication: tailoring the optical gap in light-harvesting molecules. J Chem Phys 134:151101
236. Kuritz N, Stein T, Baer R, Kronik L (2011) Charge-transfer-like $\pi \rightarrow \pi^*$ excitations in time-dependent density functional theory: a conundrum and its solution. J Chem Theory Comput 7:2408
237. Refaely-Abramson S, Baer R, Kronik L (2011) Fundamental and excitation gaps in molecules of relevance for organic photovoltaics from an optimally tuned range-separated hybrid functional. Phys Rev B 84:075144
238. Pandey L, Doiron C, Sears JS, Brédas JL (2012) Lowest excited states and optical absorption spectra of donor–acceptor copolymers for organic photovoltaics: a new picture emerging from tuned long-range corrected density functionals. Phys Chem Chem Phys 14:14243
239. Herguth P, Jiang X, Liu MS, Jen AKY (2002) Highly efficient fluorene- and benzothiadiazole-based conjugated copolymers for polymer light-emitting diodes. Macromolecules 35:6094

240. Svensson M, Zhang F, Veenstra SC, Verhees WJH, Hummelen JC, Kroon JM, Inganäs O, Andersson MR (2003) High-performance polymer solar cells of an alternating polyfluorene copolymer and a fullerene derivative. Adv Mater 15:988
241. Kim JY, Lee K, Coates NE, Moses D, Nguyen T-Q, Dante M, Heeger AJ (2007) Efficient tandem polymer solar cells fabricated by all-solution processing. Science 317:222
242. Wang E, Wang L, Lan L, Luo C, Zhuang W, Peng J, Cao Y (2008) High-performance polymer heterojunction solar cells of a polysilafluorene derivative. Appl Phys Lett 92:033307
243. Liao L, Dai L, Smith A, Durstock M, Lu J, Ding J, Tao Y (2007) Photovoltaic-active dithienosilole-containing polymers. Macromolecules 40:9406
244. Ashraf RS, Chen Z, Leem DS, Bronstein H, Zhang W, Schroeder B, Geerts Y, Smith J, Watkins S, Anthopoulos TD, Sirringhaus H, de Mello JC, Heeney M, McCulloch I (2010) Silaindacenodithiophene semiconducting polymers for efficient solar cells and high-mobility ambipolar transistors†. Chem Mater 23:768
245. Yang L, Feng J-K, Ren A-M, Sun J-Z (2006) The electronic structure and optical properties of carbazole-based conjugated oligomers and polymers: a theoretical investigation. Polymer 47:1397
246. Silva-Junior MR, Thiel W (2010) Benchmark of electronically excited states for semiempirical methods: MNDO, AM1, PM3, OM1, OM2, OM3, INDO/S, and INDO/S2. J Chem Theory Comput 6:1546
247. Runge E, Gross EKU (1984) Density-functional theory for time-dependent systems. Phys Rev Lett 52:997
248. Gross EKU, Kohn W (1985) Local density-functional theory of frequency-dependent linear response. Phys Rev Lett 55:2850
249. Tao J, Tretiak S, Zhu J-X (2009) Prediction of excitation energies for conjugated polymers using time-dependent density functional theory. Phys Rev B 80:235110
250. Gierschner J, Cornil J, Egelhaaf H-J (2007) Optical bandgaps of pi-conjugated organic materials at the polymer limit: experiment and theory. Adv Mater 19:173
251. Meier H, Stalmach U, Kolshorn H (1997) Effective conjugation length and UV/vis spectra of oligomers. Acta Polym 48:379
252. Kuhn W (1948) Helv Chim Acta 31:1780
253. Zade SS, Zamoshchik N, Bendikov M (2011) From short conjugted oligomers to conjugated polymers. lessons from studies on long conjugated oligomers. Acc Chem Res 44:14
254. Dreuw A, Head-Gordon M (2005) Single-reference ab initio methods for the calculation of excited states of large molecules. Chem Rev 105:4009
255. Kohler A, dos Santos DA, Beljonne D, Shuai Z, Brédas JL, Holmes AB, Kraus A, Mullen K, Friend RH (1998) Charge separation in localized and delocalized electronic states in polymeric semiconductors. Nature 392:903
256. Martin RL (2003) Natural transition orbitals. J Chem Phys 118:4775
257. Wiebeler C, Tautz R, Feldmann J, von Hauff E, Da Como E, Schumacher S (2013) Spectral signatures of polarons in conjugated co-polymers. J Phys Chem B ASAP 117: 4454–4460
258. Tautz R, Da Como E, Wiebeler C, Soavi G, Dumsch I, Fröhlich N, Grancini G, Allard S, Scherf U, Cerullo G, Schumacher S, Feldmann J (2013) Charge photogeneration in donor–acceptor conjugated materials: influence of excess excitation energy and chain length. J Am Chem Soc 135:4282
259. Furche F, Ahlrichs R (2002) Adiabatic time-dependent density functional methods for excited state properties. J Chem Phys 117:7433
260. Kohler A, Bassler H (2009) Triplet states in organic semiconductors. Mat Sci Eng R 66:71
261. Kohler A, Beljonne D (2004) The singlet–triplet exchange energy in conjugated polymers. Adv Funct Mater 14:11
262. Veldman D, Meskers SCJ, Janssen RAJ (2009) The energy of charge-transfer states in electron donor–acceptor blends: insight into the energy losses in organic solar cells. Adv Funct Mater 19:1939

263. Schueppel R, Schmidt K, Uhrich C, Schulze K, Wynands D, Brédas JL, Brier E, Reinold E, Bu HB, Baeuerle P, Maennig B, Pfeiffer M, Leo K (2008) Optimizing organic photovoltaics using tailored heterojunctions: a photoinduced absorption study of oligothiophenes with low band gaps. Phys Rev B 77:085311
264. Beljonne D, Curutchet C, Scholes GD, Silbey RJ (2009) Beyond förster resonance energy transfer in biological and nanoscale systems. J Phys Chem B 113:6583
265. Wiesenhofer H, Beljonne D, Scholes GD, Hennebicq E, Brédas JL, Zojer E (2005) Limitations of the Forster description of singlet exciton migration: the illustrative example of energy transfer to ketonic defects in ladder-type poly(para-phenylenes). Adv Funct Mater 15:155
266. Neuteboom EE, Meskers SCJ, Van Hal PA, Van Duren JKJ, Meijer EW, Janssen RAJ, Dupin H, Pourtois G, Cornil J, Lazzaroni R, Brédas J-L, Beljonne D (2003) Alternating oligo(p-phenylene vinylene)-perylene bisimide copolymers: synthesis, photophysics, and photovoltaic properties of a new class of donor–acceptor materials. J Am Chem Soc 125:8625
267. Krueger BP, Scholes GD, Fleming GR (1998) Calculation of couplings and energy-transfer pathways between the pigments of LH2 by the ab initio transition density cube method. J Phys Chem B 102:5378
268. Marguet S, Markovitsi D, Millie P, Sigal H, Kumar S (1998) Influence of disorder on electronic excited states: an experimental and numerical study of alkylthiotriphenylene columnar phases. J Phys Chem B 102:4697
269. Yamagata H, Norton JE, Hontz E, Olivier Y, Beljonne D, Brédas JL, Silbey RJ, Spano FC (2011) The nature of sinlget excitons in oligoacene molecular crystals. J Chem Phys 134:204703
270. Kawatsu T, Coropceanu V, Ye AJ, Brédas JL (2008) Quantum-chemical approach to electronic coupling: application to charge separation and charge recombination pathways in a model molecular donor–acceptor system for organic solar cells. J Phys Chem C 112:3429
271. Linares M, Beljonne D, Cornil J, Lancaster K, Brédas JL, Verlaak S, Mityashin A, Heremans P, Fuchs A, Lennartz C, Ide J, Mereau R, Aurel P, Ducasse L, Castet F (2010) On the interface dipole at the pentacene–fullerene heterojunction: a theoretical study. J Phys Chem C 114:3215
272. Lee J, Vandewal K, Yost SR, Bahlke ME, Goris L, Baldo MA, Manca JV, Voorhis TV (2010) Charge transfer state versus hot exciton dissociation in polymer–fullerene blended solar cells. J Am Chem Soc 132:11878
273. Bakulin AA, Rao A, Pavelyev VG, van Loosdrecht PHM, Pshenichnikov MS, Niedzialek D, Cornil J, Beljonne D, Friend RH (2012) The role of driving energy and delocalized states for charge separation in organic semiconductors. Science 335:1340
274. Yi YP, Coropceanu V, Brédas JL (2009) Exciton-dissociation and charge-recombination processes in pentacene/C-60 solar cells: theoretical insight into the impact of interface geometry. J Am Chem Soc 131:15777
275. Yi Y, Coropceanu V, Brédas J-L (2011) A comparative theoretical study of exciton-dissociation and charge-recombination processes in oligothiophene/fullerene and oligothiophene/perylenediimide complexes for organic solar cells. J Mater Chem 21:1479
276. Rand BP, Cheyns D, Vasseur K, Giebink NC, Mothy S, Yi Y, Coropceanu V, Beljonne D, Cornil J, Brédas J-L, Genoe J (2012) The impact of molecular orientation on the photovoltaic properties of a phthalocyanine/fullerene heterojunction. Adv Funct Mater 22:2987
277. Ko S, Hoke ET, Pandey L, Hong S, Mondal R, Risko C, Yi Y, Noriega R, McGehee MD, Brédas J-L, Salleo A, Bao Z (2012) Controlled conjugated backbone twisting for an increased open-circuit voltage while having a high short-circuit current in poly(hexylthiophene) derivatives. J Am Chem Soc 134:5222
278. Perez MD, Borek C, Forrest SR, Thompson ME (2009) Molecular and morphological influences on the open circuit voltages of organic photovoltaic devices. J Am Chem Soc 131:9281

279. Vandewal K, Tvingstedt K, Gadisa A, Inganas O, Manca JV (2010) Relating the open-circuit voltage to interface molecular properties of donor:acceptor bulk heterojunction solar cells. Phys Rev B 81:125204
280. Vandewal K, Tvingstedt K, Gadisa A, Inganas O, Manca JV (2009) On the origin of the open-circuit voltage of polymer–fullerene solar cells. Nature Mater 8:904
281. Pauck T, Bassler H, Grimme J, Scherf U, Mullen K (1996) A comparative site-selective fluorescence study of ladder-type para-phenylene oligomers and oligo-phenylenevinylenes. Chem Phys 210:219
282. Wu Q, Van Voorhis T (2005) Direct optimization method to study constrained systems within density-functional theory. Phys Rev A 72:024502
283. Klamt A, Schuurmann G (1993) COSMO: a new approach to dielectric screening in solvents with explicit expressions for the screening energy and its gradient. J Chem Soc Perkin Trans 2:799
284. Valeev EF, Coropceanu V, da Silva Filho DA, Salman S, Brédas J-L (2006) Effect of electronic polarization on charge-transport parameters in molecular organic semiconductors. J Am Chem Soc 128:9882
285. Bounds PJ, Munn RW (1979) Polarization energy of a localized charge in a molecular-crystal. Chem Phys 44:103
286. Bounds PJ, Munn RW (1981) Polarization energy of a localized charge in a molecular-crystal. 2. Charge-quadrupole energy. Chem Phys 59:41
287. Bounds PJ, Munn RW (1981) Polarization energy of a localized charge in a molecular-crystal. 3. Sub-molecule treatment. Chem Phys 59:47
288. Eisenstein I, Munn RW, Bounds PJ (1983) Polarization energy of a localized charge in a molecular-crystal. 4. Effect of polarizability changes. Chem Phys 74:307
289. Eisenstein I, Munn RW (1983) Polarization energy of a localized charge in a molecular-crystal. 6. Effect of excitons. Chem Phys 79:189
290. Eisenstein I, Munn RW (1983) Polarization energy of a localized charge in a molecular-crystal. 5. Effect of vacancies. Chem Phys 77:47
291. Soos ZG, Tsiper EV, Pascal RA (2001) Charge redistribution and electronic polarization in organic molecular crystals. Chem Phys Lett 342:652
292. Tsiper EV, Soos ZG (2001) Charge redistribution and polarization energy of organic molecular crystals. Phys Rev B 64:195124
293. Tsiper EV, Soos ZG, Gao W, Kahn A (2002) Electronic polarization at surfaces and thin films of organic molecular crystals: PTCDA. Chem Phys Lett 360:47
294. Tsiper EV, Soos ZG (2003) Electronic polarization in pentacene crystals and thin films. Phys Rev B 68:085301
295. Verlaak S, Heremans P (2007) Molecular microelectrostatic view on electronic states near pentacene grain boundaries. Phys Rev B 75:115127
296. Norton JE, Brédas JL (2008) Polarization energies in oligoacene semiconductor crystals. J Am Chem Soc 130:12377
297. Castet F, Aurel P, Fritsch A, Ducasse L, Liotard D, Linares M, Cornil J, Beljonne D (2008) Electronic polarization effects on charge carriers in anthracene: a valence bond study. Phys Rev B 77:115210
298. Verlaak S, Beljonne D, Cheyns D, Rolin C, Linares M, Castet F, Cornil J, Heremans P (2009) Electronic structure and geminate pair energetics at organic–organic interfaces: the case of pentacene/C-60 heterojunctions. Adv Funct Mater 19:3809
299. Beljonne D, Cornil J, Muccioli L, Zannoni C, Brédas J-L, Castet F (2011) Electronic processes at organic–organic interfaces: insight from modeling and implications for opto-electronic devices. Chem Mater 23:591
300. Marcus RA (1956) On the theory of oxidation–reduction reactions involving electron transfer. J Chem Phys 24:966
301. Marcus RA (1956) Electrostatic free energy and other properties of states having nonequilibrium polarization. J Chem Phys 24:979

302. Marcus RA, Sutin N (1985) Electron transfers in chemistry and biology. Biochim Biophys Acta 811:265
303. Marcus RA (1993) Electron–transfer reactions in chemistry – theory and experiment. Rev Mod Phys 65:599
304. Nelson J, Kwiatkowski JJ, Kirkpatrick J, Frost JM (2009) Modeling charge transport in organic photovoltaic materials. Acc Chem Res 42:1768
305. Cheung DL, McMahon DP, Troisi A (2009) Computational study of the structure and charge-transfer parameters in low-molecular-mass P3HT. J Phys Chem B 113:9393
306. Cheung DL, McMahon DP, Troisi A (2009) A realistic description of the charge carrier wave function in microcrystalline polymer semiconductors. J Am Chem Soc 131:11179
307. McMahon DP, Cheung DL, Goris L, Dacuña J, Salleo A, Troisi A (2011) Relation between microstructure and charge transport in polymers of different regioregularity. J Phys Chem C 115:19386
308. Poelking C, Cho E, Malafeev A, Ivanov V, Kremer K, Risko C, Brédas J-L, Andrienko D (2013) Characterization of charge-carrier transport in semicrystalline polymers: electronic couplings, site energies, and charge-carrier dynamics in poly(bithiophene-alt-thienothiophene) [PBTTT]. J Phys Chem C 117:1633
309. Heimel G, Romaner L, Brédas JL, Zojer E (2006) Phys Rev Lett 96:196806
310. Heimel G, Romaner L, Brédas JL, Zojer E (2006) Surf Sci 600:4548
311. Rusu PC, Brocks G (2006) Surface dipoles and work functions of alkylthiolates and fluorinated alkylthiolates on Au(111). J Phys Chem B 110:22628
312. Rusu PC, Brocks G (2006) Work functions of self-assembled monolayers on metal surfaces by first-principles calculations. Phys Rev B 74:073414
313. Segev L, Salomon A, Natan A, Cahen D, Kronik L, Amy F, Chan CK, Kahn A (2006) Electronic structure of Si(111)-bound alkyl monolayers: theory and experiment. Phys Rev B 74:165323
314. Heimel G, Romaner L, Brédas JL, Zojer E (2007) Nano Lett 7:932
315. Natan A, Kronik L, Haick H, Tung RT (2007) Electrostatic properties of ideal and non-ideal polar organic monolayers: implications for electronic devices. Adv Mater 19:4103
316. Paramonov PB, Paniagua SA, Hotchkiss PJ, Jones SC, Armstrong NR, Marder SR, Brédas JL (2008) Theoretical characterization of the indium tin oxide surface and of its binding sites for adsorption of phosphonic acid monolayers. Chem Mater 20:5131
317. Hotchkiss PJ, Li H, Paramonov PB, Paniagua SA, Jones SC, Armstrong NR, Brédas JL, Marder SR (2009) Modification of the surface properties of indium tin oxide with benzylphosphonic acids: a joint experimental and theoretical study. Adv Mater 21:4496
318. Li H, Duan YQ, Paramonov P, Coropceanu V, Brédas JL (2009) Electronic structure of self-assembled (fluoro)methylthiol monolayers on the Au(111) surface: impact of fluorination and coverage density. J Electron Spectrosc 174:70
319. Rusu PC, Giovannetti G, Weijtens C, Coehoorn R, Brocks G (2009) Work function pinning at metal–organic interfaces. J Phys Chem C 113:9974
320. Li H, Paramonov P, Brédas JL (2010) Theoretical study of the surface modification of indium tin oxide with trifluorophenyl phosphonic acid molecules: impact of coverage density and binding geometry. J Mater Chem 20:2630
321. Rusu PC, Giovannetti G, Weijtens C, Coehoorn R, Brocks G (2010) First-principles study of the dipole layer formation at metal–organic interfaces. Phys Rev B 81:125403
322. O'Boyle NM, Campbell CM, Hutchison GR (2011) Computational design and selection of optimal organic photovoltaic materials. J Phys Chem C 115:16200
323. Hachmann J, Olivares-Amaya R, Atahan-Evrenk S, Amador-Bedolla C, Sánchez-Carrera RS, Gold-Parker A, Vogt L, Brockway AM, Aspuru-Guzik A (2011) The Harvard clean energy project: large-scale computational screening and design of organic photovoltaics on the world community grid. J Phys Chem Lett 2:2241

Top Curr Chem (2014) 352: 39–102
DOI: 10.1007/128_2013_470

Published online: 10 December 2013

Supramolecular Organization of Functional Organic Materials in the Bulk and at Organic/Organic Interfaces: A Modeling and Computer Simulation Approach

Luca Muccioli, Gabriele D'Avino, Roberto Berardi, Silvia Orlandi, Antonio Pizzirusso, Matteo Ricci, Otello Maria Roscioni, and Claudio Zannoni

Abstract The molecular organization of functional organic materials is one of the research areas where the combination of theoretical modeling and experimental determinations is most fruitful. Here we present a brief summary of the simulation approaches used to investigate the inner structure of organic materials with semiconducting behavior, paying special attention to applications in organic photovoltaics and clarifying the often obscure jargon hindering the access of newcomers to the literature of the field. Special attention is paid to the choice of the computational "engine" (Monte Carlo or Molecular Dynamics) used to generate equilibrium configurations of the molecular system under investigation and, more importantly, to the choice of the chemical details in describing the molecular interactions. Recent literature dealing with the simulation of organic semiconductors is critically reviewed in order of increasing complexity of the system studied, from low molecular weight molecules to semiflexible polymers, including the challenging problem of determining the morphology of heterojunctions between two different materials.

Keywords Atomistic · Coarse-graining · Organic semiconductors · Molecular dynamics · Monte · Carlo · Molecular mechanics · Force field · Gay–Berne · Liquid crystals · Timescales · Polymers

L. Muccioli, G. D'Avino, R. Berardi, S. Orlandi, A. Pizzirusso, M. Ricci, O.M. Roscioni and C. Zannoni (✉)
Department of Industrial Chemistry "Toso Montanari", University of Bologna, viale del Risorgimento 4, Bologna IT-40136, Italy
e-mail: claudio.zannoni@unibo.it

Contents

Abbreviations

1D	One-dimensional
2D	Two-dimensional
3D	Three-dimensional
Alq_3	Tris(8-hydroxyquinolinato) aluminum
BI	Boltzmann inversion (method)
CF	Correlation function
CG	Coarse-grained
CPU	Central processing unit
DPD	Dissipative particle dynamics
FF	Force field
GB	Gay–Berne (potential)
GPU	Graphics processing unit
KMC	Kinetic Monte Carlo (method)
LC	Liquid crystal
LJ	Lennard–Jones (potential)
MC	Monte Carlo (method)
MD	Molecular dynamics
ODF	Orientational distribution function
OLED	Organic light emitting diode
MEH-PPV	Poly[2-methoxy-5-(2-ethylhexyloxy)-1,4-phenylene vinylene
P3HT	Poly(3-hexylthiophene-2,5-diyl)
PBTTT	Poly[2,5-bis(3-alkylthiophen-2-yl)thieno[3,2-*b*]thiophene]
PCBM	[6,6]-Phenyl C61 butyric acid methyl ester
PPV	Poly[phenylene vinylene]
QM	Quantum mechanics
RDF	Radial distribution function
RM	Reverse mapping

SCP	Semi conducting polymers
T6	α-Sexithiophene
UA	United atom (force field)

1 Introduction

The functioning and performance of many organic electronic devices, including organic solar cells, depends on the molecular organization of functional organic materials such as donors and acceptors, both in the bulk and at interfaces. Thus it would clearly be desirable to rationalize fully, and eventually to predict, these supramolecular arrangements from just a knowledge of the molecular structure. Actually this seemingly simple and well defined task turns out to be surprisingly difficult even for small molecules. To quote the mythical Nature editor Sir J. R. Maddox "one of the continuing scandals in the physical sciences is that it remains in general impossible to predict the structure of even the simplest crystalline solids from a knowledge of their chemical composition" [1]. After 25 years this issue, although far from being solved, has been extensively investigated and considerable progress has been made, thanks to computer modeling and simulations and, of course, the huge progress in hardware power. To give an idea of the improvement in potentialities, a super computer of 1988, like the Cray Y-MP, had eight cores with a total performance of some 2.3 Gflops, and a current one like the Blue Gene Q at Lawrence Livermore National Laboratory (US) has 1,572,864 cores with a total peak performance of 20,132.7 Tflops, an increase of about 7 orders of magnitude.

This progress, associated with the improvement, more difficult to quantify, in computer codes, has led to an impressive enhancement in the predictive power of simulations, now starting to give, e.g., transition temperatures within a few degrees from experiment, and physical observables like densities, birefringence, and other orientational order-related tensor properties, and mobilities comparable to experiment [2].

As further boosts in computing power are expected, e.g., for the increased availability of graphics processing units, and simulation programs start to be widely accessible, either commercially or on an open source basis, it is important to avoid these being used as black boxes without knowing the methods behind the various packages that, despite the variations available in the scientific community, reduce basically to two families of methods connecting molecular properties to observables: Monte Carlo (MC) and Molecular Dynamics (MD).

Here we aim to review briefly these basic approaches and list some of their differences and limitations. We shall also review the major ways of providing input to the simulations, i.e., of representing real molecules with models of various spatial resolution and detail, ranging from atomistic models more akin to the chemist's view of a molecule, to coarse grain models where even an entire molecule is replaced by a simple spherical or anisotropic object. We shall only discuss

off-lattice models, where molecular positions can change during the simulation, instead of being fixed on a lattice, even though this class of model can be used for studying less local scales that we intend here, for instance in simulating optical defects [3] or, in a context close to that of this volume [4, 5], in modeling bulk heterojunction morphologies to perform kinetic Monte Carlo simulations of charge and energy transport at the device scale [6]. To keep the discussion practical, we shall present a number of recent applications to organic semiconductors. Moreover we include a list of the major current packages available to users with some comments on their features and typical applications.

2 Levels of Modeling

Molecules and their mutual interactions can be described at very different levels of modeling, starting from the most rigorous quantum mechanical picture, down to empirical lattice models. Nevertheless, not all the available theoretical instruments are suitable for targeting the supramolecular organization of organic semiconductors. For instance, first principle Car–Parrinello MD [7], by describing the motion of nuclei in the potential of electronic clouds, is a very computationally expensive method, which is limited to a few molecules for a few picoseconds, i.e., well below the time and length scales of our interest.

Molecular modeling at the classic level consists in describing a chemical object, here a semiconducting molecule or a polymer, with a mathematical function containing tunable parameters. This mapping process is not unique and several options are left to the chemical and physical intuition of computational materials scientists. The choice of the level of modeling is the first and maybe most important step of any simulation study and thus should always be primarily dictated by the scientific problems or questions that motivate the research. In choosing the level of modeling one should also take into account practical issues, such as the feasibility of the simulation in terms of computing power requests, the availability of suitable codes, or the time and skill required to develop new ones.

In this section, three levels of modeling which have proved to be useful in organic electronics are described in decreasing order of chemical detail (Fig. 1). In general, simpler models grant access to longer simulation times and to larger system sizes, at the expense of partially or totally losing track of the chemical nature of the investigated material. *Atomistic* models provide the highest resolution picture, in virtue of the 1:1 mapping existing between atoms and simulated objects. When carefully parameterized, these models give a very accurate description of a specific material, and quantitatively reproduce or predict its physical properties.

Though any model less detailed than atomistic can, broadly speaking, be called *coarse-grained* (CG), a more precise distinction in two categories is established according to the model purpose and the scheme used to parameterize it. Specific CG models are aimed at describing a given chemical system, though at a lower computational cost than atomistic ones. They are demanding to derive and are used

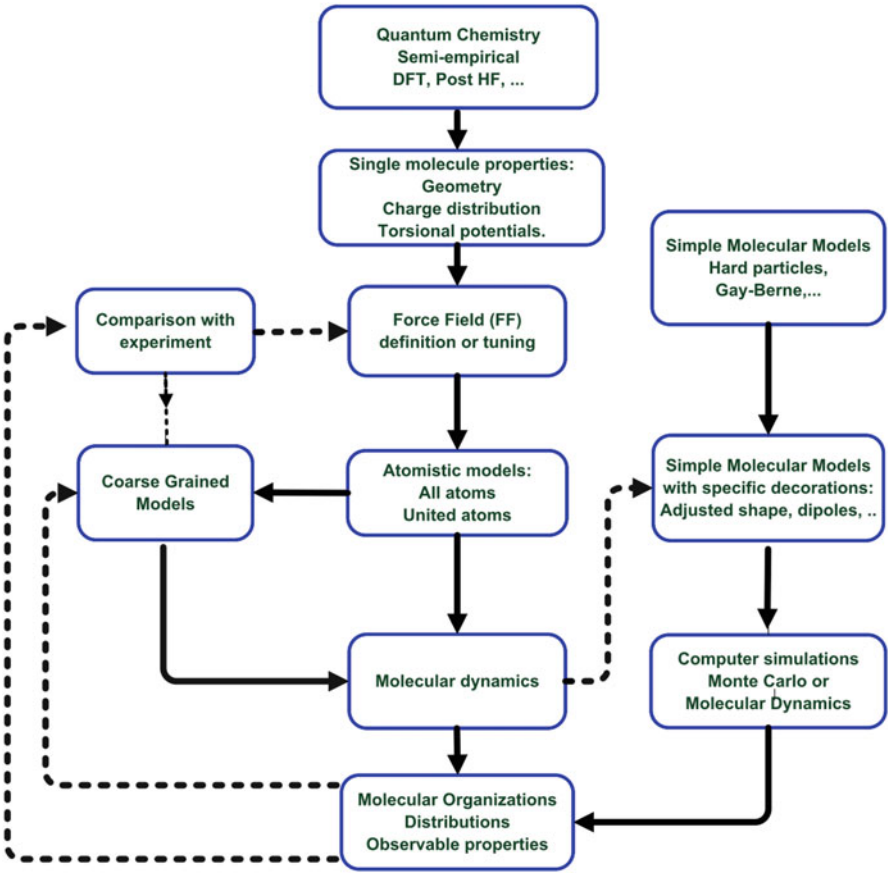

Fig. 1 A sketch of the main modeling approaches used in computer simulations and of their interrelations, when they exist. *Dotted lines* indicated possible steps for feedback loops and model improvements

when equilibration timescales become prohibitive for atomistic simulations, as is the case for DNA, proteins and, more generally, polymers in solution and bulk phase.

An alternative approach is to start from the onset with a low resolution model, which is set up essentially by physical intuition, where a whole molecule or monomer is replaced by one or few beads. The typical aim of those *simple empirical* models is to examine the minimum set of molecular features needed to obtain a given molecular organization, for instance a certain anisotropy of shape or the presence of electric multipole moments, and the qualitative relation between variations in the microscopic model and macroscopic properties. This type of modeling does not necessitate a preliminary well-defined and known chemical structure, but is more akin to a reverse molecular engineering process, where one guesses what key features are needed to achieve the desired macroscopic behavior before actually trying to write down and possibly synthesize a certain molecule.

2.1 Atomistic Models

The internal energy of a system of molecules, e.g., an organic material in the condensed phase, is a complex function of the positions and momenta of all nuclei and electrons. If one is interested in studying the morphology and dynamics at the molecular scale, an effective way of tackling this difficult task is to describe atoms as charged classical particles and completely neglect electrons. Without any approximation, the potential energy of the system can be expanded into a series of many-body interaction terms [8]:

$$U = \sum_i U_i + \sum_{i<j} U_{ij} + \sum_{i<j<k} U_{ijk} + \sum_{i<j<k<l} U_{ijkl} + \ldots \tag{1}$$

where the terms represent the self-energy of the atoms, the pairwise interaction between two atoms, and so on. The assumption of fixed connectivity between the atoms allows for dividing them between those belonging to the same molecule, giving rise to a set of intramolecular interactions, typically approximated with up to four-body terms, and those belonging to different molecules, responsible of intermolecular interactions. In order to limit the number of interactions to be computed, the intermolecular expansion is usually truncated at the two-body term, although three-body contributions are not negligible [8]. This choice determines the computational cost to grow proportionally to the number of pair interactions, so roughly to the square of the number of particles; this is still extremely demanding for long-range interactions and is often limited with the introduction, when possible, of a cutoff radius. To compensate for neglecting higher terms, some adjustable parameters (e.g., the atomic size and the interaction strength when representing the atoms) are normally fitted to reproduce basic thermodynamic properties, giving rise to effective pairwise potentials rather than exact ones.

The set of mathematical functions and parameters used to express the internal energy is referred to as *force field* (FF). In the simplest category of FF, so-called "Class I," the interactions between atoms have a direct physical meaning: for example, the total energy of the system is divided into bonded (bonds, angles, and torsions) and non-bonded (dispersion and electrostatic) interactions:

$$U_{\text{total}} = U_{\text{bonded}} + U_{\text{non-bonded}} \tag{2}$$

Among the most used force fields of this kind we cite AMBER-GAFF [9, 10], OPLS [11], and CHARMM [12], all relying on intramolecular potential energy functions like the following:

$$\begin{aligned} U_{\text{bonded}} = & \sum_{\text{bonds}} K_r (r - r_{\text{eq}})^2 + \sum_{\text{angles}} K_\omega (\omega - \omega_{\text{eq}})^2 \\ & + \sum_{\text{dihedrals}} \sum_n V_n [1 + \cos(n\phi - \gamma_n)], \end{aligned} \tag{3}$$

where the three contributions represent bond stretching, bending, and internal rotations or torsions. The first two terms are described with simple harmonic potentials, characterized by the equilibrium bond distances r_{eq} and angles ω_{eq}, with force constants K_r and K_ω. The third is a cosine expansion, with coefficients V_n and phases γ_n, of the torsional potential for each internal rotation angle ϕ. Note that the three functions involve respectively two-, three-, and four-body (intramolecular) interactions, referring to the expansion in (1).

Non-bonded atom–atom interactions are instead assumed to be pairwise additive and include the sum of 12–6 Lennard–Jones terms, allowing for steric repulsion A_{ij}/r_{ij}^{12}, dispersive van der Waals attraction B_{ij}/r_{ij}^{6}, and unscreened electrostatic Coulomb terms between the partial charges q_i, q_j of the two atoms at distance r_{ij}:

$$U_{\text{non-bonded}} = \sum_{i<j} \left[\frac{A_{ij}}{r_{ij}^{12}} - \frac{B_{ij}}{r_{ij}^{6}} + \frac{q_i q_j}{r_{ij}} \right] \tag{4}$$

These charges reflect local differences in electronegativity and chemical environment. In practice, partial charges are obtained, often together with the geometrical parameters in (3), from preliminary quantum chemistry calculations on isolated molecules. Non-bonded interactions are normally excluded for directly bonded atoms (also labeled as 1–2 interactions) and for atoms sharing a common bonded atom (1–3), while for atoms which are 1–4 connected they are often reduced, with respect to 1–5 or other intramolecular or intermolecular ones, by a factor which depends on the adopted force field.

In general, atomistic FFs can offer an adequate description or, in the most favorable cases, prediction of the properties of complex molecular systems at equilibrium. However, it should not be overlooked that parameterization and validation of FFs is carried out on certain classes of compounds (e.g., proteins) and that their transferability to other categories (e.g., organic functional materials) should not be taken for granted, not even in the case of more complicated functional forms with respect to those detailed in (3) and (4). When exploiting the FF for modeling a compound not present in the original training set, its performance should be thoroughly cross-checked against experimental data for the target system, such as transition temperatures, density, crystal structures, which depend on the correct description of both intra and intermolecular terms, and parameters should be modified accordingly to improve the agreement with the experiment.

The most common customization scheme includes the computation of atomic charges, small adjustment of equilibrium values for bond lengths and angles, and fitting of torsional potentials to ab initio calculation results [13–15]. The reparameterization of torsional terms is very important for reproducing correctly the molecular shape, in particular when several interconnected aromatic units are present in the systems, for instance in a semiconducting oligomer or a polymer [2, 13, 16]. Atomic charges can easily be computed with one of the several electrostatic potential fitting methods which are implemented in modern quantum mechanics (QM) computer

programs. We recall here that well established population analysis methods, such as Mulliken's or Löwdin's, fail to give a reliable charge distribution in many cases [17]. A better option is to obtain atomic charges which reproduce the molecular electrostatic potential calculated from the ground-state electron density [10, 18, 19]. This choice ensures that the electrostatic interactions between molecules are correctly approximated with a simple Coulomb potential acting between point charges [20].

A higher degree of sophistication is reached by incorporating polarization effects in molecular systems, enabling a dynamic response of molecular charge densities to changes in dielectric environment. Several groups attempted to introduce polarizability into the molecular mechanics model, either as induced point-multipoles or classical Drude oscillators, or even fluctuating charges [21]. We refer the reader to recent reviews [21, 22] for details about the cited models and their current states of implementation.

The increasing number of publications appearing and the fact that most polarizable approaches are now implemented in high performance MD codes such as NAMD [23], CHARMM [24], and AMBER [25] (see the Appendix), together with the good results obtained so far in improving the accuracy of intermolecular interaction energy for aminoacids [25, 26] and in reproducing experimental dielectric constants of pure alkanes [27] and aromatic compounds [28], suggest that polarizable FFs, although rarely used so far, will soon also become a very useful tool for studying organic electronic materials. In terms of computing performance, a recent implementation of the Drude scheme has been shown to scale efficiently on supercomputing platforms, with a computational cost only less than doubled, compared to non-polarizable FFs [23]. Further computational savings can be gained by treating as polarizable only the non-hydrogen atoms [28], exploiting the fact that polarizability is roughly proportional to atomic volume and then almost negligible for hydrogen atoms. This small contribution can be added to the closest "heavy" atoms such as carbon, oxygen, nitrogen, and sulfur.

This concept was previously introduced in static FFs, leading to the so-called "united atom" (UA, also called "extended atom") approximation. In this case, hydrogen atoms are combined with the heavier atoms they are bonded to (in particular carbon) to form single interacting bodies. This was the original scheme adopted by many FF developers in the 1980s, and several sets of updated parameters exist [29–31]. The research in the field is still very active, in particular for organic solvents with the "transferable potentials for phase equilibria" series of publications [32]. It is generally found that UA FFs can be just as accurate as full atom FFs in terms of phase organization and static physical properties [29, 33, 34], also in combination with full atom FFs [35]. The computational saving achieved by adopting a UA FF can be rather rewarding: just considering the reduction of the number of interacting centers to about one half (see Fig. 2), a factor of four can easily be gained. For instance, the P3HT monomer has the chemical formula $C_{10}H_{14}S$, with 11 "heavy" atoms and 14 hydrogens; removing the hydrogens, the computational cost will be reduced by a factor of $[(11+14)/(11)]^2 \approx 5$, while for pentacene ($C_{22}H_{14}$) we obtain about 3. Other advantages, in analogy

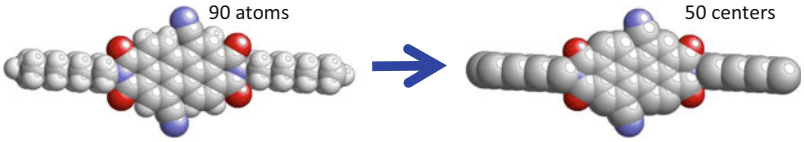

Fig. 2 The UA approximation allows one to reduce to about one half the number of interacting sites per molecule, with only a small loss of detail in the description of molecular shape: in this example, the n-type semiconductor *N, N′*-bis(*n*-octyl)-dicyanoperylene-3,4:9,10-bid(dicarboximide) (PDI8CN2) is shown

with coarse-grained models, are offered when using these FFs in MD simulations. First, completely removing hydrogens – the lightest particles – from the simulation system also allows for an increase of the MD integration timestep from ~1 fs, typical of full atom FFs, to ~2 fs. Besides, the system dynamics may become up to an order of magnitude faster [29, 36], enhancing the space sampling and reducing equilibration times. For these reasons we believe that united atom models, together with the coarse-grained ones discussed in the following section, are likely to find extensive application in computational photovoltaics.

2.2 *Coarse Graining*

When looking at molecular and supramolecular organization at the length scale of the order of the micrometers and for time windows of the order of microseconds, atomistic simulations are not affordable, even with the most recent and powerful parallel computers, particularly in view of the many state points needed to characterize the changes in molecular organization with temperature, pressure, or chemical composition. Moreover, the huge amount of detail brought by a hypothetical atomistic simulation might appear superfluous for many practical purposes. Luckily, nature is organized in a hierarchical way, and phenomena occurring on larger scales typically do not depend on atomic detail but rather on a smaller number of mesoscopic degrees of freedom, derived in principle from a proper average over microscopic features [37]. Natural and synthetic materials offer many examples of crucial properties which can be satisfactorily described on a (much) coarser level of detail with respect to the atomistic one. Among them, it is worth mentioning the self-organization of molecules in mesophases, mainly governed by the molecular shape or the mechanical properties of polymers, resulting from the interaction and entanglement of macromolecular chains.

Specific coarse graining is more ambitious than the simple empirical molecular-scale models treated in the next section, since it aims at quantitatively reproducing selected physical properties of a given system and, in principle, it allows a reverse mapping of morphologies to atomistic resolution. In practice, mapping an atomistic structure onto a CG model consists in defining a reduced number of particles (superatoms or beads) and deriving the potential for the interaction between

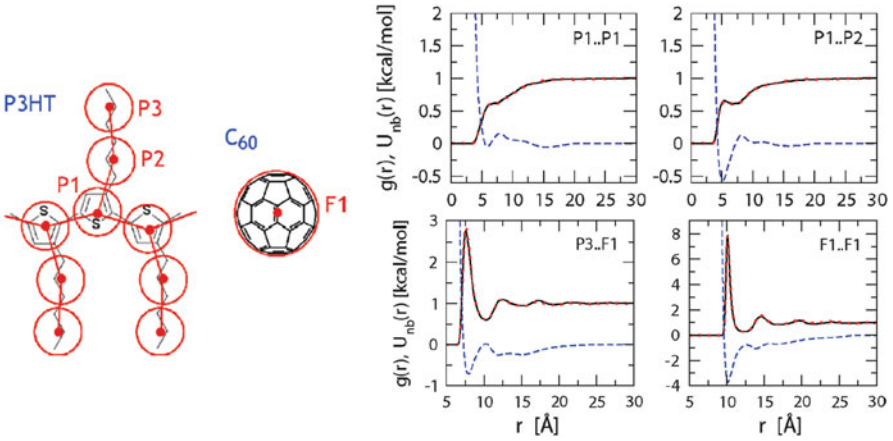

Fig. 3 Chemical structure of P3 HT and C_{60} with definition of CG beads (*left*). *Right panels* show selected CG nonbonded potentials between CG sites (*dashed line*), obtained through iterative Boltzmann inversion. The atomistic target radial distribution functions (*solid line*) and its CG analogous (*dotted line*) are indistinguishable on the figure scale. Reprinted with permission from [38]. Copyright 2010 American Chemical Society

them. As an illustrative example, Fig. 3 shows the CG model for P3HT and C_{60} proposed by Huang et al. [38]. The adoption of a CG model implies approximations and arbitrary choices, such as defining which atoms are incorporated in a given bead. An optimal atom-to-bead mapping is expected to reduce the number of degrees of freedom without losing the essential features of the chemical structure.

As a matter of fact, the CG model is physically different from the reference atomistic one and cannot describe all of its features; instead, systematic procedures to derive CG potentials are actually based on the reproduction of selected target properties (e.g., structure, thermodynamic data, or inter-molecular potential and forces) obtained from a reference atomistic model or, less frequently, from experimental data.

Approximating intermolecular potentials with a reduced number of pair interaction sites is a viable opportunity also explored for small molecules. For instance, for copper phthalocyanines a 13-site representation has been proposed and has proved to be successful in reproducing the main features of the full atomistic potential [39]. A somewhat similar approach was also applied to polycyclic aromatic hydrocarbons from benzene to hexabenzocoronene, for which a model with one interaction site per benzene ring was derived by fitting the DFT face-to-face intermolecular interaction curves [30]. For the highly symmetric C_{60} fullerene, a single site potential was proposed by Girifalco [40]. This intermolecular potential was derived by averaging the atomistic potential, expressed in terms of 6–12 Lennard–Jones centers for each carbon, over molecular orientations, supported by the fact that above 250 K C_{60} undergoes a transition to a plastic crystal phase in which buckyballs rotate rather freely. The Girifalco potential accurately reproduces

the main features of the original atomistic potential, with the considerable advantage of reducing the number of interaction sites from 60 to just 1! It is worth pointing out that the Girifalco potential can also be very accurately approximated by the Gay–Berne potential [41] described in the next section. The same approach, which assumes a continuum of Lennard–Jones interaction sites uniformly distributed over the molecular surface, has been applied to model interactions between other allotropic forms of carbon, such as fullerenes, nanotubes, and graphene [42, 43].

More general procedures to derive CG potentials have been developed, mainly in the context of thermoplastic polymers [44–48] and biological systems [49–51] research. CG models for polymers are mainly to be credited to the group of Polymer Theory of the Max Planck Institute in Mainz (Kremer, Müller-Plate, and co-workers). These models, which require a reference atomistic simulation for the derivation of the CG potential, can be classified in terms of the properties of the reference model they aim to reproduce. Conversely, *Force-based* approaches parameterize the CG potential by reproducing the instantaneous forces, sampled along simulation trajectories, between CG beads from atomistic models [52].

A different family of methods involves the use of structural data, such as pair distributions from atomistic simulation or experiments, to derive the potential between beads. Among them, Boltzmann Inversion (BI) is the simplest and provides an intuitive framework to introduce more sophisticated structure-based methods. An atomistic simulation is performed to compute the probability distribution, $P_{\mathrm{AT}}(q)$, along a given coordinate, q, of the CG model (lengths and angles). The relevant potential of mean force is then obtained by reversing the distribution, i.e., $U_{\mathrm{CG}}(q) = -k_B T \log P_{\mathrm{AT}}(q)$. This approach relies on the assumption of statistical independence between coordinates, which should be verified in each specific case. Actually, being the potential of mean force a free energy potential, simple BI works properly for only energy-dominated and weakly interdependent interactions, such as stretchings and, in some cases, bendings. For softer interactions, such as torsions and nonbonded terms, where the entropic contribution to free energy can be more important, simple BI can be used as a starting guess for other methods, such as iterative BI [53] and inverse Monte Carlo [54]. Through these methods, a genuine energy CG potential capable of exactly reproducing the targeted atomistic properties is derived by means of a self consistent iterative procedure. Such potentials can be expressed, and introduced in simulation engines, either through (possibly piecewise) analytical expressions or with numerical (tabulated) values, the latter option being the most accurate. As shown in Fig. 3 for P3HT/C_{60} mixture [38], simulations adopting a numerical CG potential obtained through iterative BI reproduce with high accuracy the reference atomistic radial distribution functions. An alternative approach is adopted by the MARTINI force field, originally developed for application to biomolecules [51], but recently extended to fullerene [55] and polystyrene [56]. The MARTINI approach resorts to analytic potentials (stretching, bending, Lennard–Jones, and screened Coulomb interactions are considered) and is parameterized only against experimental data. Originally developed for lipid membranes, the target properties mainly encompass thermodynamic data

related to phase equilibria between polar and apolar molecules. However, in a more recent application to polymers [56], a hybrid approach has been preferred, where FF parameters have been optimized to reproduce structural and thermodynamic properties from both experiment and atomistic simulations, such as pair distributions for bonded interactions, and density and radius of gyration for non-bonded terms.

System-specific CG promises the possibility of reintroducing the atomistic detail from the CG model by means of reverse mapping (RM) techniques [45, 57–59]. RM has a great potential for applications where long equilibration times and atomistic information are both required, though it should be kept in mind that RM has no unique solution, since every CG bead represents an ensemble-averaged structure for a group of atoms. A typical RM strategy is a three-step process, including (1) reintroduction of atoms on the basis of geometrical criteria, (2) minimization to avoid too close interatomic contacts, and (3) short atomistic molecular dynamics simulation to sample microscopic configurations. In general, these procedures are pretty straightforward for rigid systems and become increasingly problematic for flexible chemical structures.

The obvious advantage of CG MD simulations is that accessible time and length scales are far larger than those achievable with atomistic models. This speedup is the result of three different factors: (1) the smaller number of particles enormously reduces the computational cost of evaluation of pair interactions, characterized by the well known N^2 scaling with the number of particles N; (2) the smoother and softer CG potentials allow longer time-steps to be used in the numerical integration of the equations of motion; (3) the dynamics of CG models is intrinsically faster than in atomistic ones (see below), allowing for a reduction of equilibration times.

Of course the advantages come with some limitations and issues. First, CG force fields are derived for a specific thermodynamic state and hence are strictly temperature-dependent. While small temperature variations (about 10–20%) are considered tolerable, these models cannot describe systems across phase transitions, where significant changes of molecular organization can occur in relatively narrow temperature intervals. A second fundamental limitation is the already mentioned accelerated dynamics [44, 60]. This general feature originates from the fact that CG potentials, in reducing molecular details, also lead to a reduction in friction with the environment. In single-component systems, the bridging between atomistic and GC timescales can be achieved by scaling dynamic quantities calculated at the two different levels. For instance, a linear time scaling has been found to relate the mean square displacement of polymer chain beads calculated at different levels, as shown for polystyrene in Fig. 4 [60]. It is, however, well acknowledged that the dynamics of different phenomena, especially in multi component systems, is affected by coarse graining in different ways and bridging the timescales of models with different levels of resolution remains a critical open problem [44, 60].

Besides these fundamental issues, other practical limitations hamper the applications of CG models. One is that the development of a CG potential relies on a proper atomistic FF, whose derivation is itself not a straightforward task

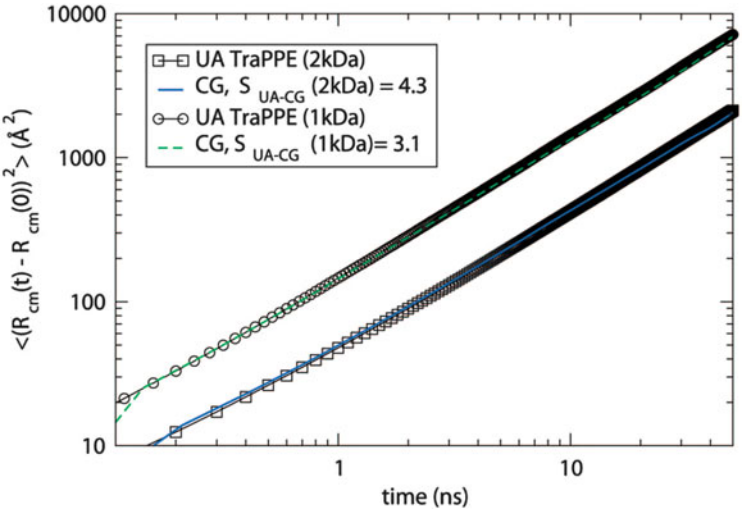

Fig. 4 Scaling of dynamics between atomistic (united atom) and CG model for melt polystyrene ($T = 463$ K): time dependence of the mean squared displacement for chains of different molecular weight (see inset). Quantitative agreement with atomistic data requires a linear scaling factor, $S_{\mathrm{UA-CG}}$. Different factors are necessary for chains of different length. Reprinted with permission from [61]. Copyright 2009 American Chemical Society

(see Sect. 2.1). For instance, in a recent paper on liquid crystal modeling [62] the CG model was shown to reproduce well the atomistic results, but these in turn were not adherent to the real phase sequence (the experimentally observed nematic was not obtained). Moreover, the intellectual and computational effort required to develop CG models limits their applicability to most popular systems.

Coarse graining promises to be a powerful technique in the context of the multiscale modeling of materials for organic electronics and photovoltaics, although only a few studies in this field have appeared in the literature. Key phenomena such as phase separation in bulk heterojunction [38, 63] or the formation of polymeric or molecular organic films from solvent casting are nowadays accessible only at the CG level. Moreover, the systematic application of coarse and fine graining would allow the spanning of extended size and timescales without precluding the possibility of reintroducing the atomistic structure for ensuing quantum chemistry calculations.

2.3 Simple Empirical Models

In this section we focus on simple molecular-scale empirical models which aim at describing the properties of classes of systems characterized by some common physical features. These models target the qualitative prediction of general trends

as a result of changes made to the constituent molecules such as the effect of modifying molecular elongation, or adding dipoles, on phase behavior. Two different families of models will be presented, the first tailored for anisotropic molecules and the second suitable for describing polymers.

The Gay–Berne (GB) potential is the most extensively studied interaction model for soft anisotropic particles, described as rigid bodies of ellipsoidal shape, and represents the reference model for simulating thermotropic mesogens. Originally developed [64] to fit a linear arrangement of four Lennard–Jones (LJ) [65] sites, the model can be considered as a generalization of the LJ 12–6 potential, where shape and interaction anisotropies have been introduced. The GB interaction potential between particles i and j therefore depends on their orientations, defined by the unit vectors $\hat{\mathbf{u}}_i$, $\hat{\mathbf{u}}_j$, and by their distance vector, $\mathbf{r}_{ij}$:

$$U(\hat{\mathbf{u}}_i,\, \hat{\mathbf{u}}_j,\, \hat{\mathbf{r}}_{ij}) = 4\varepsilon_0 \varepsilon(\hat{\mathbf{u}}_i,\, \hat{\mathbf{u}}_j,\, \hat{\mathbf{r}}_{ij}) \times \left[\left(\frac{\sigma_0}{r_{ij} - \sigma(\hat{\mathbf{u}}_i,\, \hat{\mathbf{u}}_j,\, \hat{\mathbf{r}}_{ij}) + \sigma_0} \right)^{12} - \left(\frac{\sigma_0}{r_{ij} - \sigma(\hat{\mathbf{u}}_i,\, \hat{\mathbf{u}}_j,\, \hat{\mathbf{r}}_{ij}) + \sigma_0} \right)^{6} \right], \tag{5}$$

where σ_0 and ε_0 fix the scales of length and energy, while $\sigma(\hat{\mathbf{u}}_i,\, \hat{\mathbf{u}}_j,\, \hat{\mathbf{r}}_{ij})$ and $\varepsilon(\hat{\mathbf{u}}_i,\, \hat{\mathbf{u}}_j,\, \hat{\mathbf{r}}_{ij})$ are the anisotropic contact distance and potential well depth, respectively. The contact distance reads

$$\sigma(\hat{\mathbf{u}}_i,\, \hat{\mathbf{u}}_j,\, \hat{\mathbf{r}}) = \sigma_0 \left\{ 1 - \frac{\chi}{2} \left[\frac{(\hat{\mathbf{u}}_i \cdot \hat{\mathbf{r}} + \hat{\mathbf{u}}_j \cdot \hat{\mathbf{r}})^2}{1 + \chi(\hat{\mathbf{u}}_i \cdot \hat{\mathbf{u}}_j)} + \frac{(\hat{\mathbf{u}}_i \cdot \hat{\mathbf{r}} - \hat{\mathbf{u}}_j \cdot \hat{\mathbf{r}})^2}{1 - \chi(\hat{\mathbf{u}}_i \cdot \hat{\mathbf{u}}_j)} \right] \right\}^{-1/2}, \tag{6}$$

where

$$\chi = \frac{k^2 - 1}{k^2 + 1} \tag{7}$$

is the shape anisotropy parameter, defined by the length-to-breadth ratio, k. The well depth is determined by two functions:

$$\varepsilon(\hat{\mathbf{u}}_i, \hat{\mathbf{u}}_j, \hat{\mathbf{r}}) = \left[\varepsilon_1(\hat{\mathbf{u}}_i, \hat{\mathbf{u}}_j, \hat{\mathbf{r}}) \right]^{\mu} \left[\varepsilon_2(\hat{\mathbf{u}}_i, \hat{\mathbf{u}}_j) \right]^{\nu}, \tag{8}$$

where

$$\varepsilon_1(\hat{\mathbf{u}}_i, \hat{\mathbf{u}}_j, \hat{\mathbf{r}}) = 1 - \frac{\chi'}{2} \left[\frac{(\hat{\mathbf{u}}_i \cdot \hat{\mathbf{r}} + \hat{\mathbf{u}}_j \cdot \hat{\mathbf{r}})^2}{1 + \chi'(\hat{\mathbf{u}}_i \cdot \hat{\mathbf{u}}_j)} + \frac{(\hat{\mathbf{u}}_i \cdot \hat{\mathbf{r}} + \hat{\mathbf{u}}_j \cdot \hat{\mathbf{r}})^2}{1 - \chi'(\hat{\mathbf{u}}_i \cdot \hat{\mathbf{u}}_j)} \right] \tag{9}$$

$$\varepsilon_2(\hat{\mathbf{u}}_i, \hat{\mathbf{u}}_j) = \left[1 - \chi^2 (\hat{\mathbf{u}}_i, \hat{\mathbf{u}}_j)^2 \right]^{-1/2}. \tag{10}$$

while the parameter

$$\chi' = \frac{(k')^{1/\mu} - 1}{(k')^{1/\mu} + 1} \tag{11}$$

is defined in terms of the well depth anisotropy k', i.e., the ratio between well depths for the side-by-side and end-to-end interactions, respectively. The exact form of the GB potential is determined by the four parameters μ, ν, k, k', with the exponents μ, ν tuning the orientational dependence of the energy. The original formulation, with parameters $k = 3$, $k' = 5$, $\mu = 2$, $\nu = 1$, gives rise to stable nematic and smectic LC phases. A similar parameterization with $\mu = 1$, $\nu = 3$, exhibiting stronger side–side interaction (Fig. 5), gives a wider nematic range and has often been used [66]. Indeed, a powerful feature of the GB model is that it can be tuned to represent the interaction between a wide range of different shapes simply by adjusting μ and ν and by changing the relative well depths. Therefore the model is not limited to rod-like molecules (prolate ellipsoids), but for k and k' values smaller than unity it describes disk-like mesogens (oblate ellipsoids), and their discotic and columnar mesophases [67, 68].

The original form of the GB potential applies to systems consisting of identical uniaxial particles. Some extensions of the Gay–Berne model have been proposed to overcome this limitation by generalizing the potential to dissimilar biaxial molecules [69, 70]. Moreover, the GB model can easily be combined with other potentials to add a few chemical details and establish a closer link with the structure of real molecules [71]. The effects of adding electric multipoles to the GB potential have been studied and important modifications have been observed in the overall molecular organization [68, 72].

GB particles are quite realistic models for small molecules, but once linked together with specific bonded interactions similar to those in (3), they can also be used as building blocks of more complex systems, such as polymers [73–77], LC dendrimers [78], and elastomers [79], as well as covalently bonded fullerene-mesogen systems [41, 80] or end-capped oligomers [81]. Among these studies, a few attempts have also been made to use the GB potential as a basis for CG-like parameterization, using atomistic simulations as the reference potential [68, 76, 81].

Multi-site GB models can provide valuable insights into the organization of molecules in complex systems but, both for historical reasons (the GB model is probably seen as specific for LCs) and because sometimes the anisotropy of the shape is either neglected or not important in determining the phase organization, even simpler models can be adopted. One of them is the so-called *bead and spring* polymer model, where interactions between monomers are evaluated with the computationally cheaper LJ potential or other expressions for excluded volume interaction. These models made an important contribution to rationalizing generic features of polymer melts, mostly depending on chains topology and entanglement rather than on chemical detail, such as scaling relationships (with the chain length) or rheological properties [82, 83].

A computationally more efficient approach to the modeling of polymer systems is the Dissipative Particle Dynamics (DPD) method, introduced by Hoogerbrugge and Koelman [84] to describe the dynamics and rheological properties of complex fluids,

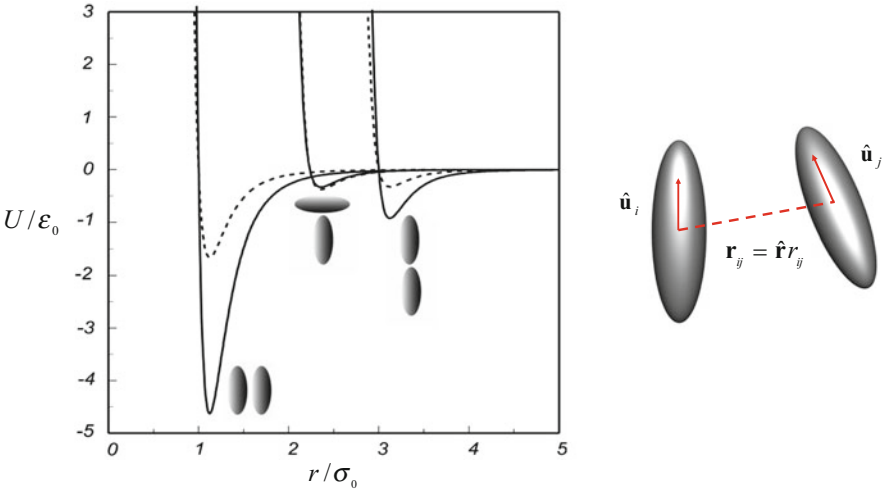

Fig. 5 The GB potential as a function of dimensionless intermolecular distance for $k = 3, k' = 5$ in side-by-side, T-shaped, and end-to-end configurations (*left panel*). Energy parameters are $\mu = 2$, $\nu = 1$ (*dashed line*) and $\mu = 1$, $\nu = 3$ (*continuous line*). Adapted and reproduced from [66] with permission from The Royal Society of Chemistry. The sketch in the *right panel* defines $\hat{\mathbf{u}}_i$, $\hat{\mathbf{u}}_j$, and $\mathbf{r}_{ij}$ for a pair of GB molecules

which has been applied to several systems, ranging from immiscible polymer blends [85] to linear [85, 86] and branched copolymer melts [87] to polymer brushes [88]. The polymer model is a simple extension of the basic DPD fluid model, where the system is considered as a collection of point DPD particles, each particle containing a large number of molecules [89]. DPD particles interact with each other via a pairwise, short-ranged force, $\mathbf{F}_{ij}^{\mathrm{DPD}}$, which is written as the sum of a conservative, dissipative, and a random term [84, 90, 91]:

$$\mathbf{F}_{ij}^{\mathrm{DPD}} = \mathbf{F}_{ij}^{C}(\hat{\mathbf{r}}_{ij}) + \mathbf{F}_{ij}^{D}(\hat{\mathbf{r}}_{ij}, \hat{\mathbf{v}}_{ij}) + \mathbf{F}_{ij}^{R}(\hat{\mathbf{r}}_{ij}), \tag{12}$$

with $\mathbf{r}_{ij}$ being the interparticle vector, and $\mathbf{v}_{ij} = \mathbf{v}_j - \mathbf{v}_i$ the difference in the velocities. The conservative repulsive term reads

$$\mathbf{F}_{ij}^{C}(\hat{\mathbf{r}}_{ij}) = \begin{cases} a_{ij}(1 - r_{ij})\hat{\mathbf{r}}_{ij} & r_{ij} < r_c \\ 0 & r_{ij} \geq r_c \end{cases}, \tag{13}$$

where r_c is the cutoff distance and a_{ij} is the finite maximum value (soft-core potential), which allows for particle overlap (repulsion parameter). The appealing characteristics of the DPD model is its versatility and flexibility to simulate different classes of complex fluids, simply adding specific features (e.g., harmonic bonding terms) by modifying the conservative forces. In addition, by suitably tuning the a_{ij},

and even the cutoff radius r_c which can be transformed in an effective contact distance r_c^{ij}, different DPD beads can be created and some chemical detail introduced.

The dissipative and random forces are written as

$$\mathbf{F}_{ij}^{D}(\hat{\mathbf{r}}_{ij}, \hat{\mathbf{v}}_{ij}) = -\gamma\omega^{D}(r_{ij})(\hat{\mathbf{r}}_{ij} \cdot \mathbf{v}_{ij})\hat{\mathbf{r}}_{ij} \tag{14}$$

$$\mathbf{F}_{ij}^{R}(\hat{\mathbf{r}}_{ij}) = -\sigma\omega^{R}(r_{ij})\theta_{ij}\hat{\mathbf{r}}_{ij}, \tag{15}$$

where the damping constant γ and the noise strength σ give the relative strength of different interactions and are related respectively to viscosity and temperature of the system; $\omega^{D}(r_{ij})$ and $\omega^{R}(r_{ij})$ are r-dependent arbitrary weighting functions (assuming finite values for $r_{ij} < r_c$ and vanishing for $r_{ij} \geq r_c$) and θ_{ij} is a Gaussian random variable with zero mean and unit variance.

Espanol and Warren [90] showed that, unlike the conservative force, the dissipative and stochastic forces cannot be independent and must be coupled together through a fluctuation–dissipation relation:

$$\omega^{D}(r_{ij}) = \left[\omega^{R}(r_{ij})\right]^2, \quad \sigma^2 = 2\gamma k_B T \tag{16}$$

These conditions are necessary to reach the thermodynamic equilibrium and keep the system in the NVE or NVT ensemble. For simplicity, the weight functions are selected to be similar in form to the conservative force, that is:

$$\omega^{D}(r_{ij}) = \left[\omega^{R}(r_{ij})\right]^2 = \begin{cases} (1 - r_{ij})^2 & r_{ij} < r_c \\ 0 & r_{ij} \geq r_c. \end{cases} \tag{17}$$

i.e., $\omega^{R}(r_{ij})$ is the same function as in the conservative force.

Within this framework, polymers are constructed in DPD by linking dissipative particles (soft core beads) through harmonic springs or other kinds of bonded interactions [92–94], following exactly the same philosophy used for multi site Gay–Berne or atomistic models (3). The system of course can contain different species of DPD particles and, in analogy to CG models (see Fig. 3, left), each of them can be used to model a chemical unit or different monomers in a block copolymer. For instance, in [93] Cheung and Troisi used different types of DPD parameters for modeling the backbone and the side chains of semiconducting polymers: their microsegregation can easily be induced by using higher a_{ij} values for the mixed backbone-chain interaction with respect to those for the respective self-interactions. We point out that, as in this example, to achieve a meaningful description of a conjugated system in the bulk phase, any molecular (CG or simple empirical) model should include to some extent the different chemical nature and anisotropy of the monomers or segments, namely the distinction between aliphatic and π-stacking aromatic moieties.

3 Simulation Techniques and Observables

3.1 Simulation Techniques

In a nutshell, computer simulations are virtual experiments allowing the computation of macroscopic properties of a system of model particles with known microscopic interactions [95]. Monte Carlo (MC) simulations perform a statistical sampling of the configuration space, while Molecular Dynamics (MD) simulations compute the classical mechanics trajectory in phase space. The raw output of computer simulations is actually a large number of configurations, namely tables of all particle coordinates (e.g., positions, orientations, and for MD also linear and angular momenta) which completely describe the state of the simulated sample and in turn, are used to compute the macroscopic observables. Besides particle coordinates, a configuration also specifies the geometry and boundaries of the sample, which are usually periodic in 3D for bulk systems or with one (or more) non-periodic boundaries when studying surface or confinement effects. The reader should be aware that the basic MC and MD algorithms described below have practical limits in the size and time ranges which can be effectively explored. Moreover, the sampling of the density of states and the computation of entropy and free energy with these techniques are fairly difficult and demanding tasks [95, 96]. As a consequence of these issues the current research effort concerning methodologies has mainly focused on two challenges: overcoming the sampling limitations [97, 98] and devising flexible and reliable algorithms for computing free energy and entropy [99, 100].

The MC and MD simulation approaches have become viable only after the introduction of fast computers. Starting from the pioneering works of Metropolis et al. [101] and Alder and Wainwright [102], the basic algorithms on which computer simulations are based were developed in the ensuing 20–30 years. They are now well established and described in standard textbooks [95, 96], and able to provide a useful link between experiment and theory. Nowadays MC simulations are typically used for lattice and simple off-lattice models, while MD models are largely employed for atomistic systems (which are tricky to sample with MC) but also for coarse-grained models.

3.1.1 Monte Carlo

MC simulations rely on a massive usage of pseudo-random numbers [103] to sample configuration space (Fig. 6). The standard MC algorithm considers the canonical ensemble (*NVT*) of statistical mechanics with a constant number of particles N, volume V, and temperature T. Collective properties are governed by the statistical distribution of configurations $\mathbf{X} \equiv \{\mathbf{x}_i\}$, where $\mathbf{x}_i$ is a shorthand for the position and orientation of the ith particle. The equilibrium values of thermodynamic observables are statistical mechanics averages over the configuration space:

$$\langle A \rangle = \int \mathrm{d}\mathbf{X} f(\mathbf{X}) A(\mathbf{X}), \tag{18}$$

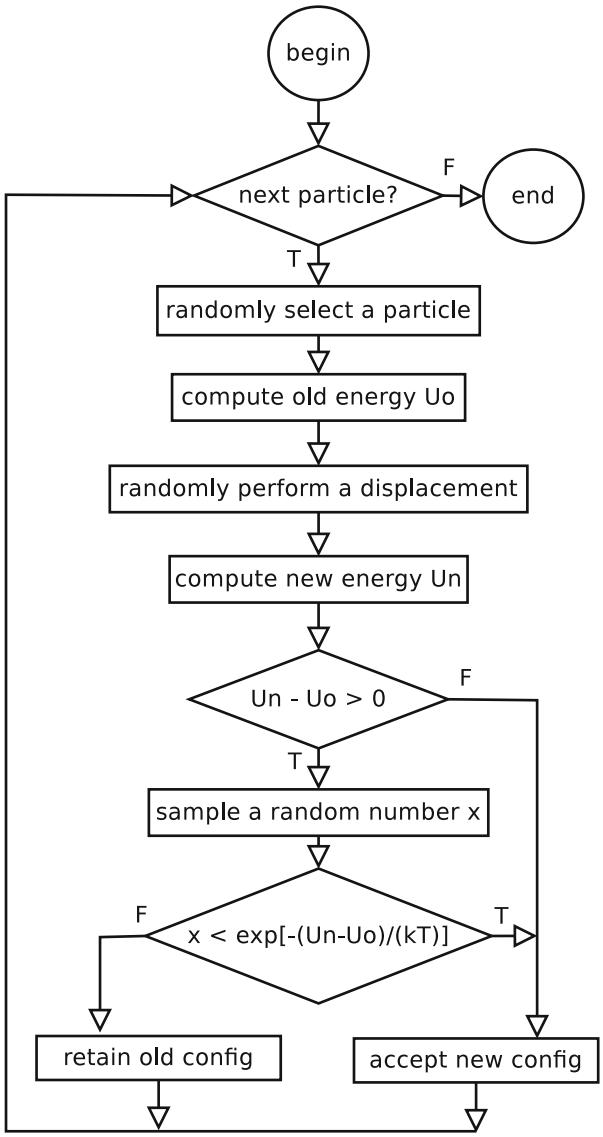

Fig. 6 A flow chart of the Metropolis algorithm

where the statistical weight of each configuration is given by the Boltzmann distribution:

$$f(\mathbf{X}) = \frac{1}{Z_0} \exp[-U(\mathbf{X})/(k_B T)], \tag{19}$$

with $U(\mathbf{X}) = \sum_{i \neq j} U_{ij}(\mathbf{x}_i, \mathbf{x}_j)$ the total (pair) potential energy discussed before, and $Z_0 = \int \mathrm{d}\mathbf{X} f(\mathbf{X})$ is the configuration integral – or partition function – enforcing the normalization constraint. In practice, Z_0 cannot be computed with a finite length simulation, and a straightforward numerical integration of (18) is not possible due to the large number of variables contained in $\mathbf{X}$. To overcome these difficulties the MC algorithm estimates the average thermodynamic properties of a system performing the so-called importance sampling of the configuration space. This sampling is obtained by running a Markov process [104] generating a large number of configurations randomly sampled from the Boltzmann distribution itself. In practice, in a typical MC run a new configuration (with total energy U_n) is generated from a previous one (with total energy U_o) by randomly selecting a particle and attempting a random displacement of its position and orientation. This new configuration is accepted or rejected according to the Metropolis criterion [101]:

$$p_{\mathrm{acc}}(o \rightarrow n) = \begin{cases} 1, & \text{if } (U_n - U_o) \leq 0 \\ \exp[-(U_n - U_o)/(k_B T)], & \text{if } (U_n - U_o) > 0. \end{cases} \tag{20}$$

which ensures the detailed balance condition. Since the frequency according to which each configuration is generated is proportional to the Boltzmann distribution, the canonical (weighted) averages of (18) are eventually estimated as

$$\langle A \rangle \approx \frac{1}{M} \sum_{m=1}^{M} A(m), \tag{21}$$

where M is a sufficiently large (typically $> 10^5$–10^6) number of configurations. Further generalizations of the Metropolis method allow one to sample other thermodynamic ensembles besides the standard NVT (notably isobaric-isothermal NpT, constant stress, grand canonical μVT with constant chemical potential μ), and also two phases in equilibrium with the so-called Gibbs MC method [96]. Attempts have also been made to improve the phase space sampling with respect to the standard Metropolis algorithm. One family of approaches avoids being trapped in metastable states by violating in a purposeful and controlled way the detailed balance condition and compensating for the added biases when performing the final averaging process [96]. Alternatively it is possible to enhance the sampling efficiency by exchanging configurations between independent simulation runs at similar but different temperatures (e.g., parallel tempering, overlapping histograms).

A last increasingly popular family of MC simulations, not to be confused with the Metropolis method, exploits sampling from non-Boltzmann distributions to simulate kinetic events which are extremely rare compared to the typical molecular timescales, e.g., as is the case of charge transfer (dynamic or Kinetic MC [105], KMC) or reactive events (Gillespie's stochastic simulation algorithm [106]).

3.1.2 Molecular Dynamics

A standard MD computer simulation consists in the computation of the trajectory in the phase space of a system of N interacting bodies. The time evolution is determined by solving Newton's equations of motion of classical mechanics with finite difference methods. Such a model system corresponds to the microcanonical ensemble (*NVE*) of statistical mechanics with a constant number of particles N, volume V, and total energy E. In MD simulations the collective properties are then determined from the trajectory of all particles, i.e., from the time evolution of positions $\mathbf{r} \equiv \{\mathbf{r}_i\}$ and momenta $\mathbf{p} \equiv \{\mathbf{p}_i\}$. The method relies on the assumption that stationary values of every average observable A can be defined as time integrals over the trajectory in the phase space:

$$\langle A \rangle = \lim_{\tau \to \infty} \frac{1}{\tau} \int_0^\tau \mathrm{d}t\, A[\mathbf{r}(t), \mathbf{p}(t)]. \tag{22}$$

In more detail, an MD simulation performs a finite difference integration of the equations of motion usually cast into the Hamilton's form

$$\dot{\mathbf{r}}_i = \frac{\partial H}{\partial \mathbf{p}_i} = \frac{\mathbf{p}_i}{m_i}, \quad \dot{\mathbf{p}}_i = \frac{-\partial H}{\partial \mathbf{r}_i} = \mathbf{f}_i = -\nabla_i U, \tag{23}$$

where H is the Hamiltonian of the system and U the total potential energy. In practice, the classical mechanics trajectory is computed at discrete times $t = 0$, $t = \Delta t$, ..., $t = N_t \Delta t$. The discrete time step Δt determines the time resolution of the trajectory and has to be sufficiently small to ensure proper integration of the equations of motion. For instance, the popular velocity–Verlet integrator (see Fig. 7) is a three step algorithm solving the 6 N first order Hamilton's equations.

1. The momenta at half time step $t + \Delta t/2$ are computed from those at time t and the forces at time t:

$$\mathbf{p}_i(t + \Delta t/2) = \mathbf{p}_i(t) + \frac{\Delta t}{2} \mathbf{f}_i(t), \tag{24}$$

2. The new coordinates at time $t + \Delta t$ are computed from those at time t and the momenta at half time step $t + \Delta t/2$:

$$\mathbf{r}_i(t + \Delta t) = \mathbf{r}_i(t) + \frac{\Delta t}{m} \mathbf{p}_i(t + \Delta t/2), \tag{25}$$

3. The new momenta at time $t + \Delta t$ are computed from those at half time step $t + \Delta t/2$ and the forces at time $t + \Delta t$:

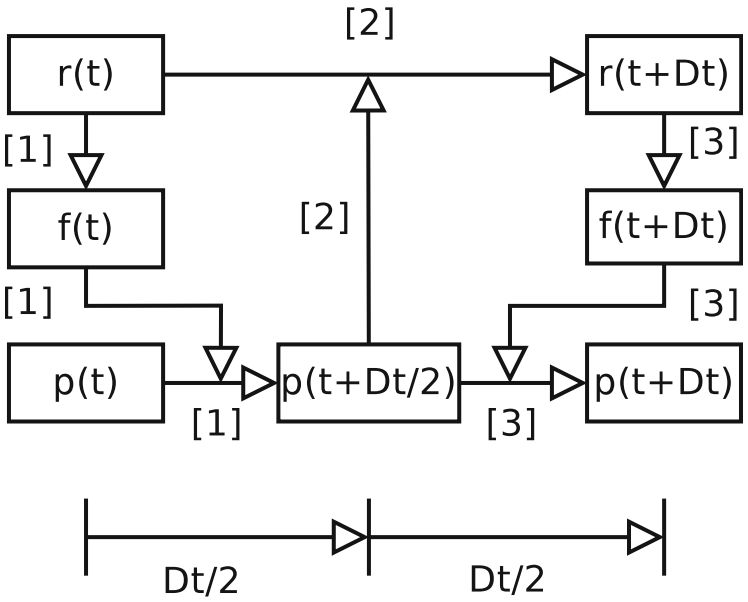

Fig. 7 A flowchart of the velocity–Verlet algorithm for the evolution of position **r** and linear momentum **p**

$$\mathbf{p}_i(t + \Delta t) = \mathbf{p}_i(t + \Delta t/2) + \frac{\Delta t}{2}\mathbf{f}_i(t + \Delta t). \tag{26}$$

Similar schemes allow the integration of the equations of rotational motion for nonspherical particles [95, 107], even though in that case care must be taken to avoid singularities, and this is frequently accomplished by using quaternionic formulations [108, 109] to describe orientations.

In analogy with the MC method (21), the instantaneous values of a certain physical observable $A(t)$ can be computed from the configurations to estimate the corresponding time average, in practice replacing the integral in (22) with a discrete summation:

$$\langle A \rangle \approx \frac{1}{N_t} \sum_{n=1}^{N_t} A(n\Delta t). \tag{27}$$

Since momenta are available in MD configurations, dynamical observables (e.g., diffusion coefficient, viscosity) can be also computed, and in this respect MD can be considered more versatile than the MC method. The basic microcanonical MD technique has been readily extended to perform simulations at constant temperature and pressure, and a considerable number of thermostats [110] and barostats [96] are currently available.

3.2 Computation of Physical Observables

The atomic or particle positions produced by MD and MC simulations are the starting point for the calculation of a variety of physical properties, e.g., electronic properties such as the couplings which govern charge carrier and exciton diffusion [81, 111], as discussed in other chapters of this book. Here, instead, we review briefly the main structural observables employed in analyzing simulation trajectories.

More specifically, a basic and yet fundamental fingerprint of any condensed phase that allows one to inspect its local positional order and structuring is the radial distribution function (RDF). The RDF gives the probability of finding a couple of particles i and j at distance r from one another, relative to the probability expected from a completely random distribution. It is defined as [95]

$$g(r) = \frac{V}{4\pi r^2 N} \left\langle \delta(r - r_{ij}) \right\rangle_{ij}, \tag{28}$$

where r_{ij} is the distance between the two particles, N is the number of particles in the system, V is the volume, and δ is the Dirac delta. In practice, the delta function in (28) is replaced by another that is equal to one when the separation is in the range $[r - \Delta r/2, r + \Delta r/2]$ and equal to zero otherwise; RDF is thus computed piecewise as a histogram with bin width Δr. The RDF for a liquid or an LC is zero in the excluded volume region, where there are no neighbor particles, and one where the pair correlation is lost. At short distances it shows peaks in correspondence to coordination shells. For an atomistic model it is possible to define the RDF either in terms of the molecular center-of-mass or for each possible combination of atom types; these quantities are directly related, through a Fourier transform, to the structure factor which can be measured from X-ray or neutron scattering experiments. For systems with long range positional order, it becomes possible to assign the position of selected RDF peaks to a specific (hkl) direction in the reciprocal space and compare the corresponding distances d_{hkl} with the experimental reflections. To quantify the degree of crystallinity, a viable solution applied to polymers [112] is to focus on a meaningful peak of the RDF (e.g., the interlamellar distance) and calculate its normalized standard deviation during the simulation, so as to estimate a paracrystallinity parameter that quantifies the degree of positional order along the chosen direction:

$$g_{hkl} = \left[\frac{\left\langle d_{hkl}^2 \right\rangle - \left\langle d_{hkl} \right\rangle^2}{\left\langle d_{hkl} \right\rangle^2} \right]^{1/2} \tag{29}$$

The parameter also takes into account the broadening effect of temperature, and is limited to between 0 (no peak at all) and 1 (the peak is a delta function).

For anisotropic systems (LCs, crystals, interfaces) it is also common to calculate the components of the correlation functions parallel, $g_{\parallel}(r)$, and perpendicular, $g_{\perp}(r)$,

to a reference direction $\hat{z}$ (the normal to a given surface or interface) or a phase director $\hat{n}$. The function $g_{\parallel}(r)$ is useful for identifying smectic phases since the layer structure is revealed by periodic fluctuations [2, 33, 36], while $g_{\perp}(r)$ helps to detect in-plane positional order, for instance in columnar phases [111, 113, 114]. In the case of layered systems such as smectic LCs, the probability density along the layer normal can be expanded in terms of positional order parameters – also called smectic order parameters:

$$f(z) = \frac{1}{d} + \frac{2}{d} \sum_{n=1}^{\infty} \tau_n \cos(2\pi n z/d) \tag{30}$$

where f is the normalized distribution function, d is the layer spacing, and τ_n is the nth positional order parameter, defined as

$$\tau_n = \int_0^d f(z) \cos(2\pi n z/d)\, dz = \langle \cos(2\pi n z/d) \rangle,\ n \geq 1 \tag{31}$$

The option is also viable for crystals, but many terms are needed to describe correctly the distribution function, while for smectics the term with $n = 1$ is often sufficient. Similar to other order parameters, the τ_n range from zero (no positional order) to 1 (perfect order along the z direction), and are then useful to track disorder–order phase transitions, e.g., isotropic-smectic, or nematic–smectic.

Another fundamental physical observable characterizing an anisotropic bulk phase or film is the orientational distribution function (ODF)[115]. For the special case of a system with uniaxial symmetry, or when one is interested only in probing the order along a specific direction, the ODF reduces to $f(\beta)$, the probability of finding one molecule with a particular orientation β with respect to it. When this direction is not dictated by the geometry of the simulation box, it is customary to use that of maximum alignment direction $\hat{n}$, also called the phase director. Its calculation requires one to set up an ordering matrix, $\mathbf{Q}$ [115], summing over all N molecules of the sample:

$$\mathbf{Q} = \sum_{i=1}^{N} [3\hat{\mathbf{u}}_i \otimes \hat{\mathbf{u}}_i - \mathbf{I}]/2N, \tag{32}$$

where $\hat{\mathbf{u}}_i$ is the chosen molecular reference axis and $\mathbf{I}$ is the identity matrix. The director is then obtained as the eigenvector of $\mathbf{Q}$ corresponding to the maximum eigenvalue.

The ODF can be expanded in a series of Legendre polynomials P_L (cos β):

$$f(\beta) = \sum_{L=0}^{\infty} \frac{2L+1}{2} \langle P_L \rangle P_L(\cos\beta), \tag{33}$$

with the first terms of the series being

$$P_0(\cos\beta) = 1 \tag{34}$$

$$P_1(\cos\beta) = \cos\beta \tag{35}$$

$$P_2(\cos\beta) = \frac{3}{2}\cos^2\beta - \frac{1}{2}, \tag{36}$$

and with the distribution $f(\beta)$ normalized so that $\int_0^\pi f(\beta)\sin\beta\, d\beta = 1$. Of course if the symmetry of the phase requires it, a more general expression of the ODF can be written, considering all three Euler angles α, β, γ, and expanding the ODF in terms of Wigner matrix elements [115]. Limiting ourselves to the simplest uniaxial case, the average order parameter $\langle P_1 \rangle$ is relevant in the case of polar order, for example for polar molecules in contact with a surface, and ranges from -1 (antiparallel) to 1 (parallel orientation). The second rank order parameter $\langle P_2 \rangle$ is instead commonly used to characterize the average degree of alignment of a liquid crystal phase and the transition from a disordered to an orientationally ordered phase, such as the isotropic–nematic one. This order parameter assumes again a value of 1 for perfectly parallel molecules, 0 for an isotropic distribution of orientations, and -0.5 for molecules perpendicular to the phase director. The special orientation in which P_2 is equal to zero but the system is still ordered is called "magic angle" (about 54.74°). Just to give an example of its usefulness, in Fig. 8 we report the order parameter $\langle P_2 \rangle$ computed for thin films of the 5-cyanobiphenyl LC supported on different inorganic substrates, revealing that the morphology of the substrates affects the degree of ordering of the organic phase, which is then transmitted across the entire sample [116, 117].

It is also possible to couple the information given by the RDF with the knowledge of the local intermolecular orientation, by computing the orientational correlation functions (CF):

$$G_1(r) = \left\langle \delta(r - r_{ij})(\hat{\mathbf{u}}_i \cdot \hat{\mathbf{u}}_j) \right\rangle_{ij} / \left\langle \delta(r - r_{ij}) \right\rangle_{ij} \tag{37}$$

$$G_2(r) = \left\langle \delta(r - r_{ij}) \left[\frac{3}{2}(\hat{\mathbf{u}}_i \cdot \hat{\mathbf{u}}_j)^2 - \frac{1}{2} \right] \right\rangle_{ij} / \left\langle \delta(r - r_{ij}) \right\rangle_{ij}, \tag{38}$$

where $\hat{\mathbf{u}}_i$ and $\hat{\mathbf{u}}_j$ are again convenient unit vectors in molecules i and j, while r is the distance between the reference centers. In an atomistic simulation, the choice of the reference centers and of the unit vectors is not univocal, and thus in some cases it is convenient to introduce more than one, to achieve a more in-depth description of the system. For instance, if we take the charges as reference centers and the electric moments as unit vectors, $G_1(r)$ gives information on the local polar ordering, and $G_2(r)$ on the overall quadrupolar ordering.

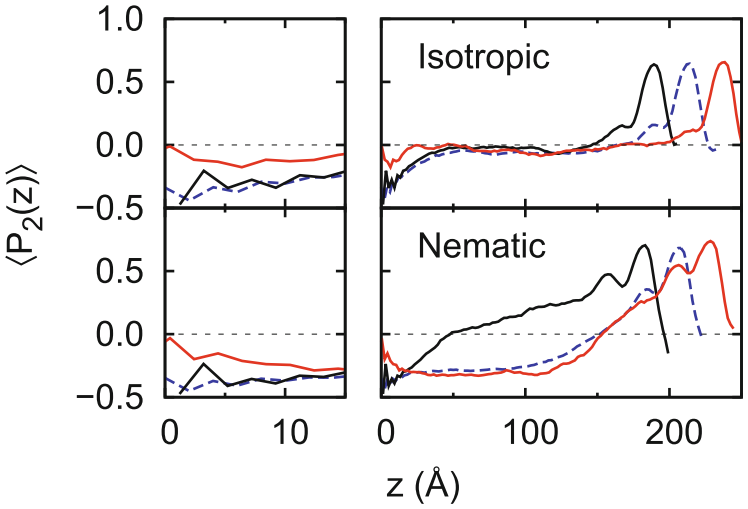

Fig. 8 Order parameter $\langle P_2 \rangle$ of 5CB LC films supported on various substrates, computed with respect to the normal to the surface. A solid substrate is placed at $z = 0$ [Si:H (*blue dashed*), cristobalite (*black*), amorphous silica (*red*)], while the film is interfaced to vacuum for $z > 200$ Å. Adapted from [116, 117]

The dynamic properties of systems are usually characterized in terms of time CF, and as already mentioned they can be evaluated only from MD simulation trajectories. Given two real time-dependent observables, $A(t)$ and $B(t)$, their CF is defined as

$$C_{AB}(t) = \frac{\langle A(0)B(t)\rangle - \langle A\rangle\langle B\rangle}{\langle AB\rangle - \langle A\rangle\langle B\rangle}, \tag{39}$$

normalized here so that it starts from 1 at the time origin, and decays to 0 as the asymptotic $t \to \infty$ limit is reached. When A and B are vector quantities, the simple product becomes a dot product, while the CF of an observable with itself, $C_{AA}(t)$, is called time autoCF. The pivotal importance of equilibrium time CF is due to their link with the response to small external perturbations provided by linear response theory and the fluctuation–dissipation theorem [118], which allow for the calculation of out-of-equilibrium physical properties from equilibrium properties, such as, for instance, transport coefficients (through velocity autoCF, see below) and optical absorption spectra (Fourier transform of dipole autoCF). The dynamics of molecules as a whole can often be described in terms of stochastic processes, such as translational and rotational diffusion. Molecular mobility is quantified through the diffusion coefficient:

$$D = \frac{1}{3}\int_0^\infty \langle \mathbf{v}(0)\cdot\mathbf{v}(t)\rangle \, \mathrm{d}t \tag{40}$$

$$= \lim_{t\to\infty} \frac{\left\langle |\mathbf{r}(0)-\mathbf{r}(t)|^2 \right\rangle}{6t} \tag{41}$$

expressed in the first equality with respect to the particle velocity autoCF, and in the second through the formally equivalent Einstein relation. Molecular rotations are instead quantified by the autoCF of a given molecular axis, $\hat{\mathbf{u}}$.

If the molecular model has a submolecular resolution, the conformational dynamics is accessible through the autoCF of internal coordinates (bond length and angles) or by some specific intramolecular coordinates (distances or angles defined by given atoms), such as, for example, the molecular head-to-tail vector. To overcome the issue related to the $[-\pi{:}\pi]$ definition of a dihedral angle ϕ, the torsional dynamics is given by the autoCF:

$$C_{\mathrm{dih}} = \langle \cos[\phi(t)-\phi(0)]\rangle = \langle \cos[\phi(0)]\cos[\phi(t)]\rangle + \langle \sin[\phi(0)]\sin[\phi(t)]\rangle \tag{42}$$

though often only one of the two terms on the right-hand-side is evaluated.

3.3 Timescales of Different Phenomena

Here we attempt to relate the dynamic processes, measured by time correlation functions, to their characteristic timescales in the temperature range 300–600 K, relevant to organic electronic devices operation and fabrication. It is worth mentioning that in such applications, beyond the structural dynamics treated here, the timescales associated with charge or exciton dynamics are also very important, in particular for assessing the coupling between electron and nuclear dynamics.

In the most common case where the target is the equilibrium dynamics, the analysis has to be carried out on samples at thermal equilibrium. Albeit trivial, the above observation is not always respected in MD studies. Even in some recent papers we may find that equilibration runs limited to a few hundreds of picoseconds are often employed, although it is known that, e.g., molecular rotations relax over much longer timescales [34, 119]. A possible definition of the timescale associated with a process modulating a given dynamic property, $A(t)$, is its correlation (or relaxation) time:

$$\tau_A = \int_0^\infty C_{AA}(t)\,\mathrm{d}t, \tag{43}$$

where $C_{AA}(t)$ is the time CF of $A(t)$, as defined in (39). Dynamic phenomena often follow an activated Arrhenius behavior, with a marked dependence of the activation energy E_A of the process on the state of matter:

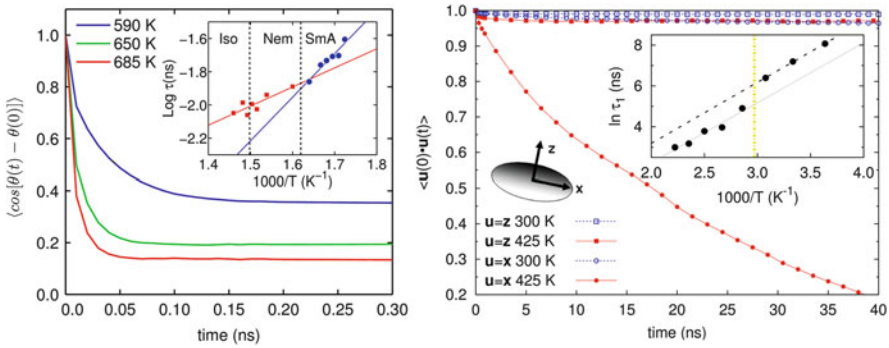

Fig. 9 *Left panel*: time autoCF of the central torsion of T6 in the smectic (590 K), nematic (650 K) and isotropic (685 K) phase; *inset* shows the Arrhenius plot of the torsional correlation time, with different regimes observed in the smectic (*circles*) and nematic-isotropic (*squares*) phases [2]. *Right panel*: time autoCF of molecular axes for alkoxy-substituted phthalocyanines in the rectangular (300 K) and hexagonal (425 K) columnar phase; *inset* shows an Arrhenius plot of the correlation times for the in-plane rotation, revealing the phase transition at about 330 K. Reprinted with permission from [34]. Copyright 2009 American Chemical Society

$$\langle A(T) \rangle = A_0 \exp[-E_A/k_B T], \tag{44}$$

where $\langle A(T) \rangle$ can be also a correlation time. Phase changes can then be detected by plotting $\ln \langle A(T) \rangle$ vs $1/T$ and determining where the slope varies [33, 34] (see insets of Fig. 9). The exponential dependence on temperature and the change of activation energy from phase to phase, and from material to material, imply that it is not possible to define an exact timescale for a given phenomenon, but only rely on experience and results found in the literature.

Systems composed of small molecules in the solid state may take a few nanoseconds of simulation to reach thermal equilibrium upon starting from the experimental crystal structure, but in other cases equilibration can be 1–2 orders of magnitude slower depending on the phase (solid, LC, liquid) and the temperature. Such timescales make these systems treatable at the atomistic level. In contrast, energy equilibration in polymers is out of the reach of atomistic simulations, since kinetic barriers arising from entangled chains are practically impossible to be crossed in the accessible timescales. Consequently the equilibration of melt or solvated polymers is directly accessible, although with some limitations, only with coarse grained models or by simulating oligomers and extrapolating results for longer chains through scaling relationships.

Intramolecular degrees of freedom, such as bond stretching and angle bending, are typically fast, with timescales in the range 10–100 fs. They represent the highest frequency motions in a simulated system, setting the value of the MD timestep used in the integration of the equations of motions to 1 and 2 fs in full- and united-atom models, respectively. In classical simulations, stretching and bending are weakly coupled to softer intramolecular degrees of freedom and even less to the supramolecular organization. Conversely, low-frequency or soft intramolecular modes, such as torsions, librations, or other manifestations of molecular flexibility are

intrinsically entangled with the supramolecular structure, especially in liquid phases. Soft torsions are found on the main chain of conjugated polymers and oligomers, such as thiophene–thiophene, phenyl–phenyl, or phenyl–vinyl rigid rotations. These systems feature a torsional potential characterized by two local and nearly degenerate minima separated by energy barriers of at most a few kcal/mol, which makes both conformations accessible at the temperatures of interest. The torsional dynamics is characterized by relatively fast oscillations around the local minima [33, 120] and a occasional flipping between different conformations. Small oscillations, governed by the curvature of the torsional potential, are characterized by timescales in the sub-picosecond range, similar to other intramolecular modes. Conformer interconversion is instead strongly affected by the environment: it is essentially inhibited by the tight molecular packing in the crystalline state, and shows an Arrhenius behavior in liquids, as well as a marked dependence on chemical features such as bulky groups or side chains. For instance in non-substituted oligomers, such as sexithiophene or *p*-quinquiphenyl, the characteristic time of inter-ring torsion flipping is of the order of 10 ps at 600 K [2] (see Fig. 9), while at the same temperature in indenofluorene trimers, the bulkier monomer and the presence of octyl chains yield values which are more than five times larger, as extrapolated from data in [33]. Other very common torsions in organic semiconductors are those involving alkyl chains. For the hexyl chain of P3HT at 300 K we found that the torsional correlation time decreases along the chain from 4 ns for the hexyl-thiophene bond to 20 ps for the last torsion [121].

In the solid state the translational motion of rigid molecules is limited to small oscillations around equilibrium positions with typical frequencies of acoustic lattice phonons (below 100 cm^{-1}). Conversely, self-diffusion is instead possible in the liquid phases and for small molecules in a solid matrix, as is the case for dopants in polymers. Diffusion coefficients of molecules are most often evaluated in MD simulations by the Einstein relation (41), which assumes a linear asymptotic behavior of the mean square displacement of the molecular center of mass with time. The attainment of this linear regime must be explicitly checked in each case and may require simulation lengths of 1–10 ns, depending on the system under investigation. The alternative Green–Kubo formulation, where the diffusion coefficient is obtained as integral of the velocity time correlation function (40), also requires similar timescales to be spanned with simulations. In the case of two-dimensional diffusion of organic molecules adsorbed on flat organic substrates, the random walk limit is typically reached within 1 ns [122, 123]; this should be considered as a lower limit only, because again the dynamics can depend on several factors and in particular on the surface roughness. It is worth adding that the dynamics of molecules of a liquid at the interface (wetting layer) with a solid can also be different (typically slower) than in the bulk, as recently shown by some of us for nematic and isotropic 4-*n*-pentyl-4-cyano biphenyl on crystalline silicon [116]. Rotational dynamics is a major feature of phases of interest for organic electronic applications, such as plastic crystalline fullerenes and columnar liquid crystals. In the nearly spherical C_{60}, rotation is isotropic with $\tau \sim 15$ ns at 300 K [119], but buckyball rotation is considerably slowed down when solubilizing

substituents are present, e.g., in PCBM ($\tau \sim 300$ ns at 300 K [121]). Discotic liquid crystal phases feature anisotropic rotations often limited to being around the column axis. For instance, in tetra alkoxy-substituted phthalocyanine the rotation correlation time for this motion was found to be very sensitive to the mesophase organization (see left panel of Fig. 9), with $\tau \sim 20$ ns at 425 K in the hexagonal lattice, and rotation almost hindered in the rectangular phase at 300 K [34].

To recap, in this short overview we have enumerated the main dynamics phenomena driving the molecular motion and shown that their characteristic timescales can differ by several orders of magnitude depending on chemical and physical factors, preventing the definition of simple rules of thumb.

Therefore the timescales of the phenomena of interest must be estimated on a case-by-case basis, and carefully considered in the choice of appropriate simulation techniques, models, and times, in order to avoid meaningless investigations or biased conclusions.

4 Applications to Bulk Systems and Interfaces

4.1 Small Molecules

Low molecular mass semiconductors are particularly appealing for computational scientists because the timescales of their rearrangements are relatively fast and often accessible to atomistic simulations. It is then becoming possible to reproduce both the equilibrium structure and the self-assembly process of crystalline, liquid crystalline, and amorphous organic semiconductors. Among those, thermotropic LCs are certainly the most fascinating and challenging materials from the structural point of view because of the variety of different phases (nematic, smectic, columnar, and many more [124]) they exhibit in relatively small temperature windows.

In the solid state weak intermolecular interactions between flexible and anisotropic molecules lead to very complex free energy landscapes, often characterized by multiple minima corresponding to different (meta)stable polymorphs, possibly coexisting at the same temperature. Nevertheless, molecular solids offer less stimuli to simulation studies in terms of structural variety, as MD or MC are only able to explore the free energy landscape close to the initial structure, usually the experimental one when this is known. On the other hand, the limitations of standard simulation techniques prompted fundamental research on methods capable of performing a thorough sampling of the phase space [97], and the prediction of organic crystal structures from molecular information is still an open fundamental problem and one of the most vital fields in terms of development of methods and of force fields [125, 126]. MD simulations are in general preferred to MC for studying small molecules, since MD produces the time evolution of the system, providing a link between structural and charge or exciton dynamics. Given that electronic properties are calculated with QM methods using the MD simulation trajectories as an input, it is not surprising that atomistic models dominate the literature:

mapping from the classical to the quantum model is straightforward if the interplay between electron and nuclear dynamics can be neglected.

4.1.1 Solid State

The simulation of molecular crystals can be addressed with atomistic MD, fully accounting for finite temperature and anharmonic effects. Here, a typical simulation is set up by considering a sample built as an $l \times m \times n$ replica of the unit cell (supercell) with 3D periodic boundary conditions applied. The dynamics below the melting point is in most cases limited to intramolecular vibrations, and oscillations of molecular positions and orientations around their equilibrium values. From the point of view of the supramolecular organization these simulations may not add further information to that of the equilibrium crystal structure, but they can be very useful for other purposes. The simulation of crystal supercells in the *NpT* ensemble, in which the simulation box is free to rearrange under the effect of molecular forces, can be used to benchmark the FF employed [2, 119, 127]. The explicit verification that the FF is able to maintain (within a tolerance of a few percent) the crystal cell parameters measured at the same temperature and pressure than in experiments is a necessary test of the accuracy of the model potential.

Supercell simulations have been extensively applied in recent years to study the effects of temperature on charge transport in single crystals. Because of the soft nature of organic materials, thermal molecular and lattice vibrations have a major influence on key microscopic parameters governing the charge transport, i.e., charge transfer integrals and site energies. The evaluation of those quantities by means of electronic structure calculations at the geometries extracted along atomistic MD trajectories provides their ensemble averages as well as their time evolution, and grants full access to the temperature dependence of charge mobility. With this methodology, Troisi and Orlandi characterized the temperature dependence of transfer integrals in anthracene and pentacene [128], the latter also being the subject of subsequent studies by other authors [129, 130]. Further remarkable results based on MD simulations are the quantitative evaluation of charge mobility of rubrene [131] and the investigations by Martinelli et al. on anthracene [132] and perfluoropentacene [133]. Other studies sharing a similar methodology focused on the structure–property relationship, investigating the effect of core twisting due to chlorination in the bay region of perylene bisimide derivatives [134], the role of polar groups on the mobility of dicyanovinyl-substituted oligothiophenes [135], and the influence of connectivity and dimensionality of the supramolecular network on charge transport in different molecular crystals (rubrene, indolocarbazole, and benzothiophene derivatives with and without side chains) [136, 137].

More interesting are the simulations of fullerene derivatives, which, in virtue of their nearly spherical shape, can enjoy rotational freedom in the solid state. The occurrence of an orientational order–disorder phase transition in C_{60} at 260 K has been described with different simulation methods. MC simulations based on an atomistic model, complemented with additional interaction sites placed at the

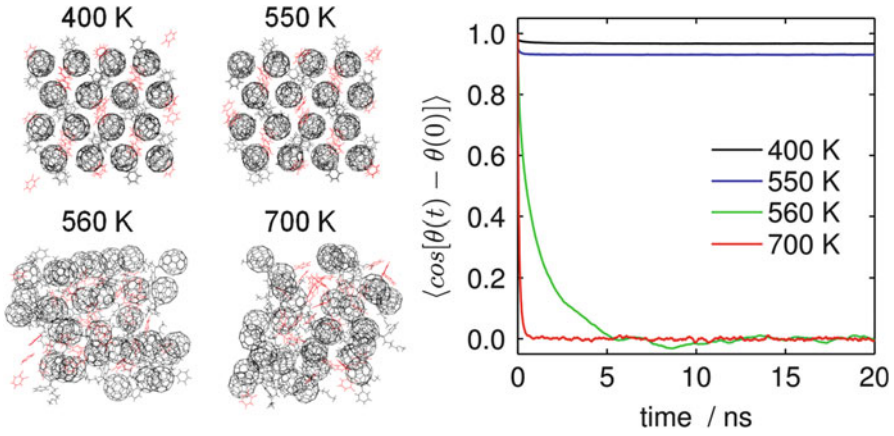

Fig. 10 Snapshots of MD simulation of PCBM: *ortho*-dichlorobenzene co-crystal below (400 and 550 K) and above (560 and 700 K) the melting point. The *right panel* shows time autoCF of a molecular axis of PCBM, quantifying the frozen molecular orientation in the crystal and the rotational freedom in the liquid [140]

centers of short (shared by hexagons) bonds, quantitatively reproduced the transition temperature and free energy [138], while some of us characterized the onset of molecular rotations by calculating molecular axis time correlation functions [119]. Other simulation works focused on the fullerene derivative PCBM [139, 140], for which only structures where it co-crystallizes with solvent molecules have been reported. These studies showed that PCBM co-crystals do not undergo notable structural modifications up to the melting point, as shown in Fig. 10. Specifically, molecular orientations remain fixed in the tight crystalline packing, and rotational freedom is attained only in the liquid, with characteristic timescales of thousands and hundreds of picoseconds at 560 and 700 K, respectively [140] (see Fig. 10). Remarkably, molecular rotations can instead take place down to room temperature in amorphous PCBM (in absence of the co-crystallizing solvent), although on much longer timescales with respect to the liquid phase ($\tau \sim 300$ ns at 300 K) [121].

Besides PCBM, several other amorphous organic semiconducting materials have been studied, mainly at the atomistic level and in combination with QM/CT simulations. The most popular material is Alq_3, one of the first n-type semiconductors to be identified, together with other compounds employed in OLEDs emitting layers [141], where organic crystals are less popular in mainstream applications due to their poor performances as emitters. Actually Alq_3 is a tricky system to model: it contains a metal atom, rather hard to parameterize efficiently with purely classical FFs; it presents two coordination isomers and several polymorphs that complicate the comparison with experimental samples, and the strong molecular dipole moment may affect CT mobility in multiple ways. It is then not surprising that no quantitative agreement with experimental mobilities has been obtained so far, despite the fact that, after a few rather unsuccessful attempts to reproduce the experimental density [142, 143], a reliable force field is now

available [144]. Overall it emerges that amorphous organic materials, similarly to liquids but more markedly so, possess a local positional order dictated by the molecular shape, which shows itself in the presence of at least two peaks in the center of mass RDF [121, 141, 143, 144]. From the methodological point of view it has been found that, for these glassy systems, MC-based simulated annealing schemes for generating the morphology are unable to pack the molecules efficiently [142], while a simple and working strategy is to start from a liquid sample at very high temperature and quench it at room temperature [81, 143, 145]. It is also interesting that the volumetric method, commonly employed to determine the glass transition temperature (T_g) of polymers, and consisting in plotting the volume vs the temperature and finding two (almost) linear regimes with lower (higher) slope below (above) the T_g, has been shown to work in simulated systems and can be used to compare with the experimental values of T_g [141, 144].

4.1.2 Liquid Crystal Phases

Among the classes of materials discussed so far, liquid-crystalline semiconductors are probably those where phase organization simulation studies have seen the greatest advancements in the last decade. Nowadays it is possible either to sketch complete pressure or volume vs temperature phase diagrams using simple empirical models or to determine quantitatively transition temperatures with atomistic simulations in heating or cooling scans, starting from either a crystalline or an isotropic liquid phase. This is particularly true for rodlike semiconducting materials, typically oligomers containing π-conjugated aromatic units in the main chain, such as oligophenyls or oligothiophenes. These molecules can form smectic (layered) and nematic phases that are fluid enough to allow proper equilibration with atomistic MD simulations and the temperature-dependent phase behavior has been reproduced for some of them [2, 146]. One application that has emerged for LC semiconductors, in fact, is the use of atomistic simulations to complement experimental techniques in the characterization of newly synthesized materials [147–150]. For instance, in mesophases presenting positional order, whereas X-ray measurements provide only the lattice parameters, simulations can also grant information over molecular orientations and positions, which in turn can be employed as input for charge transport calculations, to compare with the experimental measurements of mobility. For rodlike molecules smectic phases prevail over nematic, though for many semiconductors these phases occur well above room temperature and are thus difficult to characterize experimentally. A paradigmatic example is that of sexithiophene (T6), whose high temperature LC phases, suggested by experiments in the 1990s, were only recently confirmed with atomistic simulations [2] by Pizzirusso et al. They showed in silico that T6 exhibits both a smectic and a nematic phase (Fig. 11), and obtained them by progressively heating a crystalline sample, with excellent agreement with experimental data in terms of transition temperatures and enthalpies. Interestingly, all the phase transitions of T6 are assisted by an increase of conformational disorder in the thiophene–thiophene dihedrals, which

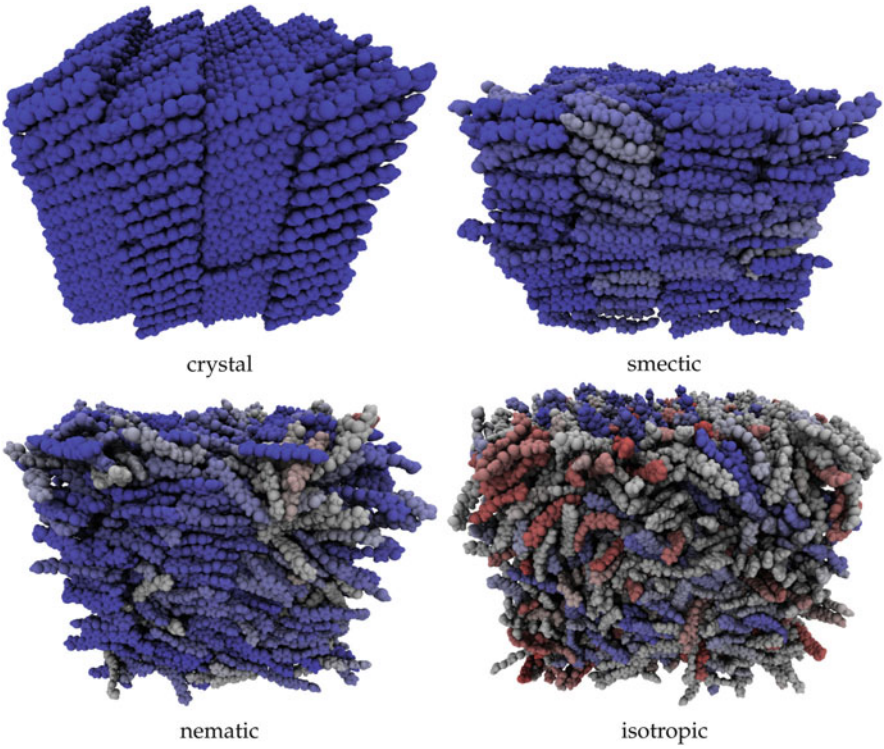

Fig. 11 Sequence of phases obtained by heating sexithiophene: crystalline (570 K), smectic (580 K), nematic (650 K), and isotropic (685 K) [2]. The color of each molecule codes its orientation with respect to the phase director, from perfect parallel (*blue*, $P_2 = 1$) to perpendicular (*red*, $P_2 = -1/2$)

in turn results in bent molecular shapes in the LC phases, a feature probably shared with other all-aromatic LCs.

Smectic phases are also intriguing in terms of electronic properties, because it is not yet well known whether and to which extent their 1D positional order affects the anisotropy of charge and energy transport, and whether this transport is more efficient than in other phases. To this end, Papadopoulos and coworkers simulated the smectic to isotropic transition of dioctyl-indenofluorene trimers, together with the associated temperature dependent energy transport [33]. They found that energy transport is slightly anisotropic in the smectic phase, but, surprisingly enough, its average rate is rather insensitive to temperature variations and is not affected by the phase change. Schrader et al. instead studied amorphous and smectic morphologies of α, ω dicyanovinyl-T6 and simulated the charge transport for a system of more than 4,000 molecules. Also in this case the results were quite unexpected, with a predicted charge mobility higher in the amorphous phase than in the smectic one. This finding, rationalized in terms of the higher connectivity of the supramolecular

network provided by electronic couplings in the amorphous, contradicts the common belief that mobility necessarily increases with structural order.

In comparison with nematics and smectics, columnar phases formed by high molecular weight discotic semiconductors are more similar to plastic crystals than to isotropic liquids. In fact both experiments and atomistic simulations [34, 151, 152] have shown that the nematic order parameter, $<P_2>$, of columnar phases is often higher than 0.8 (with a value of 1 indicating perfect order), with the translational degrees of freedom reduced to one direction (the column axis) and rotations typically either frozen (in rectangular phases) or only possible about the column axis (in hexagonal phases).

Atomistic simulations of discotics share similarities with those of crystal supercells previously discussed, with the difference that the timescales spanned are much longer (of the order of 10–100 ns) in order to average, at least partially, the slow rotational motion of molecules. Particularly delicate is the choice of the initial sample configuration, which typically consists in preformed columns of molecules: the self organization of discotic molecules from the isotropic into a columnar phase has not been demonstrated so far with atomistic simulations, while it is possible to obtain a hexagonal phase (Fig. 11) by heating a rectangular or herringbone one [151], or vice versa [34]. Besides the prototypical family of triphenylene-based compounds [113], hexabenzocoronenes [114, 151] and even larger polyaromatic cores [152], phthalocyanines [34], and perylenes [148, 150, 153] have been studied, always obtaining a good match between the available X-ray peak positions for the inter- and intra-column distances and those calculated from the simulations. A recurring feature in many studies is the presence of helicoidal arrangement of molecules within the columns, though its origin has not yet been clarified and could be simply a reminiscence of the chosen initial configuration or an effect imposed by periodic boundary conditions and the small simulation box. In many investigations the simulated morphologies were employed to estimate charge carrier mobilities along the columns [34, 111, 148, 150, 153]. As expected for a 1D semiconductor, the charge mobility turned out to be very sensitive to the way it is averaged over the nuclear dynamics. Two opposite approaches, corresponding to charges much faster and much slower than molecular motion, are possible [34]. In the first, different mobility calculations are performed for instantaneous charge transfer rates, and then mobilities obtained at different snapshots are averaged. In the second approach, a single mobility KMC simulation is run with rates averaged over many different configurations. The first approach gives mobility values that are typically one to two order of magnitude lower than those given by the second, with the experimental values lying in between these two extremes. This is an indication that charge transport and molecular dynamics are to some extent coupled in columnar LCs (Fig. 12), and there is room for future theoretical improvement on dealing with this fundamental issue.

With atomistic simulations still being unsuccessful in obtaining spontaneous supramolecular organization for discotic mesogens, the approaches based on the simpler GB potential lead instead to interesting results. Examples of the application of the GB potential to discotic LC are the studies on triphenylene-based discotics by Orlandi

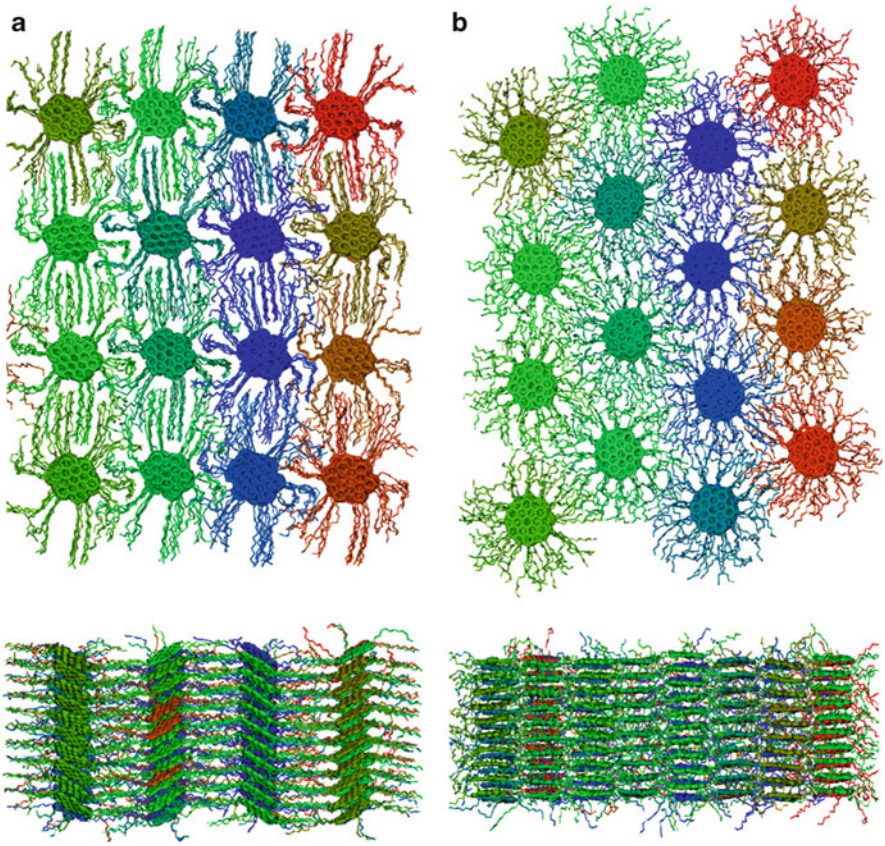

Fig. 12 Configurations of a hexabenzocoronene dodecyl derivative in the columnar herringbone phase at 300 K (**a**) and the hexagonal one at 400 K (**b**). Reprinted with permission from [151]. Copyright 2008, American Institute of Physics

et al., where the set of model parameters ($k = 0.1948$, $k' = 0.15$, $\mu = 1$, $\nu = 0$) have been derived by fitting the LJ interaction energy obtained from atomistic simulations of hexa-thio-octyl-triphenylene [68]. MC simulations showed that the GB potential qualitatively reproduced the phase diagram and morphology of triphenylene discotic semiconductors and clarified the role of electrostatic interactions on the phase organization of two different compounds (hexa-thio triphenylene and hexa-thio azatriphenylene). By describing the molecular charge distributions with a minimal set of point charges approximating the ab initio charge density [20], it was shown that electrostatic interactions stabilize the columnar structure in triphenylene systems, while they favor the nematic phase for azatriphenylenes. More recently, the morphologies obtained from MC simulations have been employed to study the temperature dependence of charge mobility in triphenylene-based discotics and in particular across crystal-columnar and columnar-isotropic transitions [154]. Mobility calculations based on Miller–Abrahams charge hopping rates qualitatively reproduced

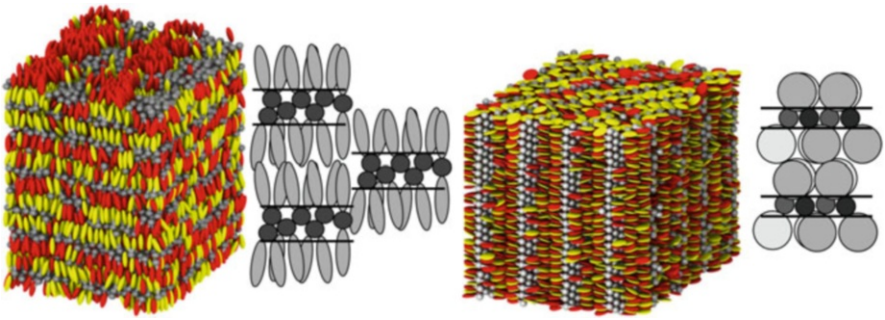

Fig. 13 Snapshots and schematization of supramolecular assemblies formed by a central fullerene with two mesogenic units laterally attached: rod-like (*left*) and disk-like (*right*). Adapted and reproduced from [80] with permission from The Royal Society of Chemistry

the temperature dependence of the mobility, mainly governed by the modulation of the average transfer integral in the different phases.

The predictive power of the GB model has also been demonstrated for more complex molecular and phase architectures. In [80] MC simulations were carried out to study the supramolecular organization of covalently bonded mesogen-fullerene-mesogen systems. Here, both the mesogenic units, either rod- or disk-shaped, and the central C_{60} have been described with a generalized GB potential and connected with flexible spacers. These systems showed a striking tendency to self-organize in nanosegregated structures, where, especially for the case of discotic mesogens, fullerenes form monolayers of closely packed buckyballs ("walls"). The predicted structural features and the derived molecular design rules shown in Fig. 13 seem very promising for application in organic electronics and photovoltaics, where well-defined domains of microsegregated donor and acceptor moieties are sought.

4.2 Polymers

The simulation of polymeric materials is more demanding than that of low molecular mass semiconductors, because of two main additional difficulties arising from (1) the slow dynamics, with diffusion coefficients decreasing as a power law with the number of monomers per chain [155] (see also the inset of Fig. 4), and (2) the requirement of a simulation box large enough to contain the entire polymeric chain even in its extended conformation. Owing to these physical and technical constraints, the computer simulation study of bulk semiconducting polymers (SCP) represents one of the major challenges of computational chemistry, also because these systems are rapidly growing in chemical variety and applications.

The modeling of SCP is somehow more complex than that of their flexible (coil) thermoplastic analogues because of the presence of rigid aromatic units (rod) which, besides granting the semiconducting behavior, also confer a rich range of

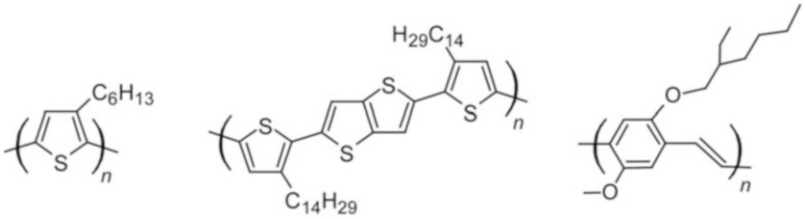

Fig. 14 The three most studied semiconducting polymers: from the *left* to the *right*, poly (3-hexylthiophene-2,5-diyl) (P3HT), poly[2,5-bis(3-alkylthiophen-2-yl)thieno[3,2-*b*]thiophene] (PBTTT, tetradecyl C14 version is drawn), poly[2-methoxy-5-(2-ethylhexyloxy)-1,4-phenylene-vinylene] (MEH-PPV)

morphologies, characterized by the presence of ordered domains even above the glass transition temperature. On the other hand, if compared to semiconducting molecular crystals, SCP systems can be considered only semi-crystalline (and consequently more disordered), also in the solid state. The morphological inhomogeneities can be considered static on the timescale of the charge conduction [156].

In the most typical case, the functional rod-like segments constitute a linear backbone while the coiled flexible chains are grafted laterally to confer to the SCP higher solubility and, more generally, ease of processability. In polymer physics terminology these structures fall into the category of semi-flexible polymers, where flexibility is introduced by the presence of soft aromatic–aromatic rotational degrees of freedom along the backbone (see, e.g., the chemical structure of the three most studied SCP in Fig. 14). Other chemical combinations are possible and in particular the alternation of rod and coil segments along the main chain (the so-called multiblock or rod-coil block copolymers) is a subject of intense research [157, 158]. Although in principle multiblock polymers may confer additional morphological control over different length scales [159], along with the possibility of including in the same macromolecule both the p- and the n-semiconducting functions [157, 158], semiflexible and rod-coil polymers form very similar structures and present identical challenges from the modeling point of view.

The chemical origin of the phase behavior of SCP is threefold, emerging from: (1) the chain connectivity topological constraints; (2) the different chemical nature of rod and coil segments: rods are relatively rigid, and interacting via aromatic π-stacking and quadrupole–quadrupole interactions, while coils are flexible and more weakly interacting via London forces, (3) steric repulsion, related to the shape of segments, with rods being linear and more anisotropic than coils. Thermodynamically speaking, the factors in play are: (1) the conformational entropy, higher for coils than for rods, (2) the relative interaction energies (rod–rod, coil–coil, and rod–coil), and (3) the mixing entropy [159]. As a matter of fact, for the majority of SCP at room temperature internal energy prevails to some extent over entropy, and microsegregation between coils and rods takes place,

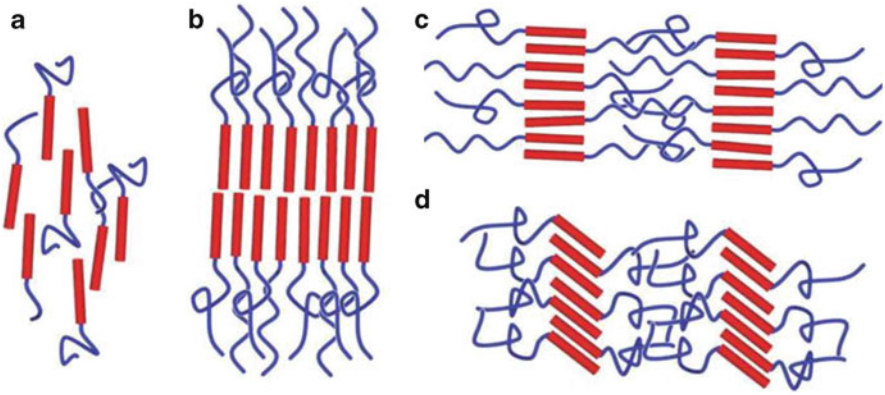

Fig. 15 Illustrations of some typical phases exhibited by semiflexible polymers and liquid crystals. (**a**) Nematic. (**b**) Bilayer smectic A/lamellae. (**c**) Monolayer smectic A/lamellae. (**d**) Monolayer smectic C/tilted lamellae. *Red sticks* represent π-stacked rod rigid sections, *blue lines* flexible coil sections. Adapted and reproduced with permission from [157]. Copyright 2011 Wiley Periodicals, Inc

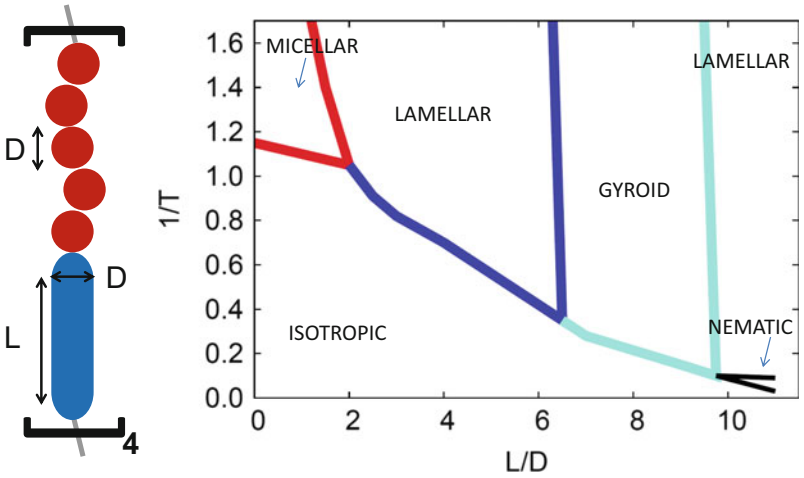

Fig. 16 Model of a rod–coil copolymer and phase behavior as a function of the rod aspect ratio L/D and inverse temperature 1/T (a.u.) [94]

accompanied by partial crystallization either of the rod segments, or even of the whole system. The interplay between segregation and crystallization gives rise to a rich number of possible arrangements, depending again on the chemical nature of the polymer, ranging from the common lamellar and honeycomb phases to different kinds of liquid crystalline phases, as schematized in Figs. 15 and 16. These phases are inevitably present and intermixed with amorphous domains in SCP thin films

constituting a real device; at the micrometric length scale, SCP may also form mesoscale structures, such as spherulites, fibers, dendrites, fractals, and rings [160].

4.2.1 Mesoscale Models

At present, approaching the mesoscale phase behavior of SCP with off-lattice models is possible only with the low-resolution and rather generic potentials discussed in Sect. 2.3. Still, these models can be useful in attempting to capture the qualitative effects of possible chemical changes to the polymer structure. Particularly effective are repulsive softcore potentials, where spherical beads representing either chemical groups or oligomers are connected together with harmonic springs. The number and dimensions of these particles can be changed to imitate different chemical structures, and the repulsion parameters between different species of beads can be tuned to enhance/disfavor microsegregation, the volume being varied to mimic the presence of a fraction of (bad) solvent in NVT simulations. Excellent examples of the rich information that can be gained from this genre of studies have been published for semiflexible "hairy" rods [93] and rod–coil block copolymers [94]. In the former publication, spherical dissipative particle dynamics (DPD) beads of two species A and B, representing the aromatic backbone and the side chains respectively, were used to build repeating units of different composition but fixed main chain length of 20 backbone A units. It was found that this simple model is capable both of reproducing the transition from isotropic to ordered phases by decreasing temperature and of showing the passage from a lamellar phase to a cylindrical honeycomb phase by decreasing the length of the B side chains with respect to the main chain A from A1B2 to A2B1 [93]. In another successful study, Lintuvuori and Wilson [94] assessed the liquid crystalline behavior of linear rod–coil block copolymers by devising a soft-core attractive–repulsive potential for the rods, while using spherical DPD beads for the coils (Fig. 16). With several simulations at different temperature and lengths of the rod segments, they were able to sketch a phase diagram encompassing micelles, lamellar, nematic, and gyroid phases by cooling from an isotropic melt. They also showed that having longer rod segments increases the order–disorder transition temperature, eventually stabilizing the formation of a nematic phase.

With respect to DPD-like models, an additional level of realism is reached when using the more complex and tunable Gay–Berne potential that has already been applied to liquid crystalline main chain polymers [74, 161, 162]. However, parameterizing the GB ellipsoids for a specific semiconducting polymer was pursued only recently by Lee et al. [76, 77], who obtained a coarse-grained GB-based force field for poly[2-methoxy-5-(2′-ethylhexyloxy)-1,4-phenylene-vinylene] (MEH-PPV). By mapping segments of ten monomers to a single GB ellipsoid, the authors were able to reduce the computation time by a factor of 10^5 with respect to the atomistic model, while keeping good agreement with the atomistic model in NVT simulations of a bulk sample of 200 ellipsoids. Despite the promising results, neither was this MEH-PPV model further employed for

simulating larger bulk systems, nor have other attempts of customizing the GB model for coarse graining SCP been reported so far. We believe that there is still room for this category of investigations, in particular to take into account the biaxiality and the dual chemical nature of the SCP structure for properly describing microsegregation and to exploit soft-core potentials to reduce equilibration times and improve phase space sampling [94, 163]. It is also worth noting that, at least for these simple models, it was demonstrated that in situ polymerization is feasible during the simulation, possibly leading to different structures with respect to a preformed polymer, and adding a touch of realism as this option explicitly includes the polydispersity of the system [74, 161, 164].

4.2.2 Atomistic Models

At the opposite extreme of complexity of the potential energy function stand the atomistic models introduced in Sect. 2.1. Besides their chemical specificity, they take advantage of previous research in the simulations of liquids and complex systems which produced a number of high performance simulations codes (cf. the Appendix) and well tested force fields. Focusing on the FF parameters, the transferability of the soft torsional potentials is very limited, because many "exotic" dihedrals exist in SCP, e.g., between aromatic rings including heteroatoms like nitrogen, silicon, sulfur, or selenium. It is then becoming common knowledge and practice to reparameterize the backbone torsional terms before attempting a simulation [165–168], also because the correct description of the chain conformation is fundamental for the reproduction of the physical and electronic properties of these materials. Another very important prescription is to test the FF predictions vs any available experimental data, such as thermodynamic properties, NMR couplings, IR-Raman spectra, second harmonic generation order parameters, electron, X-ray, and neutron scattering diffraction data. In principle, neutron scattering should be the method of choice for investigating polymers because it also provides rich structural and dynamical information for amorphous systems [169]. However, X-ray diffraction studies are much more frequent, due to the wider instrumentation availability and lower cost [170] (particularly as these measurements do not require extensive deuteration as neutron scattering normally does). The knowledge of the unit cell dimensions of a polymer is certainly an advantageous starting point for an atomistic simulation, although the usual poor quality of X-ray diffraction data, caused by the semicrystalline nature of SCP and by the possible existence of domains and polymorphs, does not allow for an exact determination of atomic coordinates and point group symmetry. As a consequence, it often occurs that atomistic force fields are used to refine and rationalize the X-ray analysis through molecular mechanics energy minimizations rather than the opposite. These reverse Monte Carlo-like investigations are based on (1) selecting several minimum energy guesses for the atomic coordinates, (2) computing X-ray (powder or 2D) spectra from the guess models, by adding an arbitrary amount of disorder/noise, and (3) selecting the best guess or refining it by comparing the experimental and calculated patterns. This method has been rather successful in the last few years,

having been applied, for instance, to poly(3-butylthiophene) [165], PBTTT [171, 172], diphenyl-PPV [173], and to a cyclopentadithiophene-benzothiadiazole copolymer [167]. Overall, useful pseudo-crystallographic molecular structures and force field refinements have been produced and interesting information as well, such as the dominance of alkyl chain orientation and conformation in determining the packing and consequently the position of the X-ray peaks.

If the structures generated by the above procedure represent a limiting case, i.e., that of a highly ordered picture of SCP, simulations of amorphous samples and melts can provide the opposite limiting situation, that of a perfectly disordered system, with physical reality likely lying in between the two. In the case of a bulk melt simulation and of polymer chain lengths shorter than the box dimension, the starting configuration may be a random, non-overlapping disposition at very low density, which is subsequently compressed, annealed, and thermalized [174, 175]. Even in the case where final box size turns out to be shorter than the polymer chain length in its extended conformation, the simulation could be affected by the system size bias with the consequence of overestimating the chain bending (or other folded conformations) and underestimating the experimental density [176]. Therefore, multiple starting configurations [177], or even better, large system sizes and relatively short chains, are recommended to avoid such pitfalls, as shown in [178], where Linares and coworkers studied different boxes of unsubstituted PPV tetra- and hexamers containing several thousands of monomers each, demonstrating the current possibilities of large scale MD simulations. In other interesting work, Do et al. compared the packing of P3HT and C12-PBTTT in their respective melt, simulating 60 chains of 12 monomers each at different high temperatures [179]. Even in the melt they found evidence of closer packing of the aromatic backbone for PBTTT with respect to P3HT, which may be a possible explanation for the higher hole mobility shown by the first polymer. The authors also realized that the absence of alkyl chains in the thienothiophene group makes its rotation in the melt, and maybe also in the crystal phase, possible. This rotation on one hand could enhance the inter-chain packing, and on the other reduce the intra-chain charge transport. As this structural design is shared by many modern SCP, in particular donor–acceptor ones, further focus on the role of this backbone degree of freedom is welcome for the future.

Several authors also attempted the more ambitious investigation of crystalline SCP by simulating supercells of the available or guessed crystal structure, consisting of a bundle of initially perfectly parallel and regioregular polymeric chains. Thermostatting the initial system at room temperature typically injects conformational disorder to backbone and side groups, and often also some strain and tilt to the backbone (see Fig. 17). The origin of this strain can be either physical, or more simply it can be due again to the limited MD sample size, the constant volume or cell shape constraint, and to the shortcomings of the employed force field. Disregarding its origin, it is very likely that any injection of disorder will lead to a more realistic situation with respect to the ideal unitary cells comprising a few monomers. In possibly the first of these attempts, Beljonne and coworkers investigated the relationship between the conformational disorder and the excited state electronic structure of

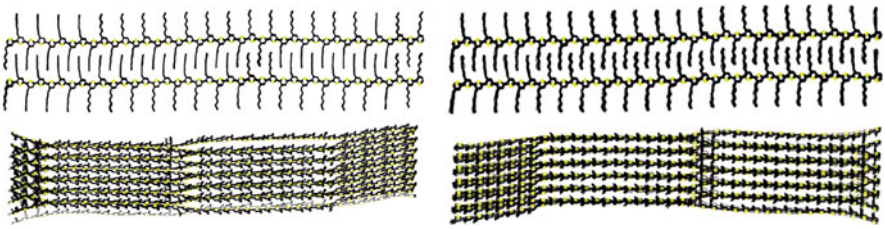

Fig. 17 MD simulation snapshots of P3HT at $T = 100$ K (*left*), where the crystalline structure of alkyl chains is apparent and at 300 K (*right*), where chains present a more liquidlike motion. Snapshots consist of 10 superimposed simulation configurations (separated by 10 ps), and for clarity, hydrogen atoms have been omitted. Reprinted with permission from [16]. Copyright (2009) American Chemical Society

MEH-PPV, either isolated or in bulk-like phase consisting of three parallel and close packed decamers [120]. They found both a planarization effect in the bulk, and an increase of the correlation time for backbone phenyl group rotation from a few picoseconds for isolated chains to 100 ps for interacting chains. Other successful studies dealt with more exotic SCP, such as carbazole macrocycle rings forming columnar phases [180] and thiophene–peptide diblock oligomers forming nanofibers [181]. One dimensional systems like these are somehow simpler to study because the removal of 3D packing constraint allows for an easier guess of the possible starting structure. The self-assembly in low dimensional structures has also been studied for P3HT by Melis et al. [182]. It turned out that π–π interaction is the driving force for stacking isolated P3HT chains, and that the tilted orientation of the thiophene aromatic rings with respect to alkyl chains, typical of the bulk crystal, is already present in those stacks. The aggregation of these 2D stacks leads in turn to a crystal structure with a zig-zag alternation of the core tilt angles in adjacent lamellae. Conversely, if planarity of cores and chains is forced by a surface, the final 3D crystal retains the tilt angle but without zig-zag alternations, with all the lamellae presenting parallel tilts. In a similar study, Dag and Wang found only the tilted parallel structure for the 3D crystal [183], and conjectured that its origin resides in the alkyl–alkyl side chain interactions.

P3HT is by far the polymer most studied through simulations, and probably the best available FF for oligo- and polythiophene has been derived by Raos and coworkers through a series of MD investigations of their crystal structures [165, 166, 184]. In particular, in [166] they derived three variants of the OPLS-AA force field with modified atomic charges and torsional potentials, which were benchmarked against experimental crystal structures. They also carried out room-temperature MD simulations of poly(3-methylbutylthiophene) and poly (3-butylthiophene) 144 monomers-supercells, showing that a certain degree of side-chain disorder is present also in the crystalline domains of alkylthiophene-based polymers. The most comprehensive theoretical study of P3HT and its interface with PCBM, ranging from electronic to structural properties, was carried out by Troisi, Cheung, and coworkers. Limiting ourselves to morphological aspects, in

[16] they studied the thermal evolution of a periodic box containing 12 chains, each comprising 40 monomers forming one lamella, finding that, upon heating, a conformational order–disorder change in the side chains takes place below room temperature, as shown in Fig. 17. They attributed to this conformational transition the experimental variation in optical properties of P3HT, and the corresponding decrease of the conjugation length. Surprisingly, the loss of the alkyl chain crystalline packing corresponds to a variation of only 2° in the average values of backbone dihedrals. Similarly to other polymers and oligomers in the bulk phase [33, 120], the time evolution of torsion angles shows both dynamic fluctuations of a few degrees around their equilibrium value and on average no change of conformational structure during the simulation. Further evidence of transition from a more liquid-like to a glassy or semi-crystalline state at room temperature was produced by Alexiadis and Mavrantzas by cooling amorphous P3HT samples previously annealed at very high temperatures [185]. A similar temperature-induced transition between crystalline and disordered alkyl chains was indentified with simulations for PBTTT tetramers by Poelking et al. [112], in this case at about 375 K (compared to 300 K for P3HT). Indeed, the higher transition temperature measured is a confirmation of the higher rigidity of PBTTT with respect to P3HT, as reported in [179].

In a follow-up article of [16], Troisi and coworkers [186] investigated the rarely addressed effect of regioregularity on P3HT structure, by adding 8, 23, and 46% of head-to-head defects to samples formed by 24 chains of 40 monomers each. It was found that head-to-head defects have a remarkably low disrupting effect on backbone planarity and on side chain orientations, and consequently on the electronic states of P3HT. However, these defects affect to some extent the linearity of the polymer chains. Finally, a united atom level force field for P3HT was recently obtained in Bologna by tuning the AMBER UA force field [29] in order to reproduce the crystal cells parameters; in this study [121] the relaxation times for conformational changes on the polymer backbone and side chains were estimated in the bulk, and a surprisingly high occurrence of *cis* defects in the first dihedral of the hexyl side chains was found at room temperature.

4.2.3 Coarse-Grained Models

In the effort of increasing the size of the systems studied, coarse-graining schemes were derived for the three "best seller" SCP shown in Fig. 14. For PPV polymers, several CG models have been used to investigate chain conformations and gyration radii in solution, which are known to be affected not only by the nature of the solvent but also by the density and the distribution of saturated defects along the polymeric chain, granting a fraction of flexible coil character to the otherwise rigid backbone. Lee, Hua, and Chen were the first to tackle this problem, adopting a representation in which each monomer is described by a CG bead [187]. They studied single and aggregated chains of 100–500 monomers in solutions of chloroform and toluene, comparing atomistic and GC descriptions, and obtained very similar results in terms of radius of gyration and a speedup of about 100 times in

favor of the CG model. Later in [188] they refined their model to account explicitly for saturated defects, this time using three CG beads per monomer and adding chlorobenzene to the solvent list. Despite the improvements, their CG FF has been blamed for the inconsistency by Huang and coworkers [189], which then derived a novel three-beads-per-monomer FF with specific parameters for saturated and unsaturated monomers. With this tool, the authors were able to study chains up to 1,000 monomer-long (very close to the experimental degree of polymerization) in implicit solvent, and found that the number of saturated defects enhances the folding of 300-monomer chains, while it has no significant impact for longer chains. Using a similar methodology, Andrienko and coworkers obtained a three-monomers-per-bead CG FF for diphenyl-PPV with decyl side chains [190]. This model is however able to describe only qualitatively the experimental behavior of short polymers in solution, probably because the saturated monomers were again neglected in the model. The authors also hinted at the difficulties of choosing the correct approximations in a CG FF when the available experimental data are scarce and scattered: certainly at the moment this problem is more general and relevant for all the SCP polymers, P3HT excluded.

For this polymer, two CG FFs have been derived, both with the purpose of studying its heterojunction with fullerenes: the first by Lee and Pao [191], the second by Huang et al. [38]. This latter FF must be considered a priori superior because it includes a refinement of the thiophene–thiophene torsion parameters and uses three beads per monomer instead of one. Lee and Pao also derived the only existing CG model of PBTTT, using one bead for each two monomers, and compared PBTTT/PCBM and P3HT/PCBM blends [192]. It must be noted that such low resolution approximations including one or more monomers per bead, although very cost-effective, are unlikely to be very accurate because they miss the anisotropic character of the monomer–monomer interactions, caused by the different chemical nature of the aromatic core and the alkyl chains; therefore they are unlikely to produce the quantitatively correct morphology when used for modeling SCP bulk phases.

4.3 Interfaces

Organic solar cells are interfacial devices with the organic–organic interface in practice encompassing the whole light harvesting section, which is typically hundreds of nanometers thick, and composed by an n-type and p-type semiconductor opportunely intermixed. This interface is certainly the most important part of an organic solar cell and its structure has major implications on the optical and electronic phenomena at the basis of its functioning and efficiency, such as light absorption, exciton diffusion, and charge separation. As a consequence, accurately modeling such interfaces would offer a unique possibility for assessing structure–electronic properties relationships and aiding materials and device design.

Nevertheless, the accurate modeling of organic–organic interfaces stands at the top of a hypothetical scale of increasing complexity of photovoltaic-related systems. In fact, besides inheriting the difficulties of a proper description of two semiconducting materials, either polymeric or molecular, their mixed interactions should also be properly addressed and, more importantly, the interface morphology is not uniquely defined by its composition. Also within the two main categories of cell architecture, i.e., bilayer and bulk heterojunction, different interface morphologies have been reported depending on preparation and post-processing conditions. This poses an additional challenge to the modeling: as the nature of the interface morphology arises in general from the interplay of thermodynamic parameters and kinetic factors specific to the preparation protocol, the simulation study should to some extent reproduce the experimental conditions [193]. For instance, the degree of crystallinity of a spin coated polymer can vary depending on the chosen temperature and solvent. The commensurism and the facets in contact in a planar interface between two organic crystals may also depend on the sequence used in the vapor deposition of the two components. The specificity of the interface morphology and its intimate connection with device functioning has caused most of the studies carried out so far to be experimentally driven and based on an extensive use of chemically specific atomistic or coarse-grained models. The technical problems arising from the necessity of treating relatively large system sizes at atomic resolution, and the plethora of possible preparation techniques and samples to compare with, has led to rather scattered literature, where a comprehensive understanding of solid–solid interfacial phenomena is only starting to emerge. Here we attempt a rationalization of the most recent work in terms of the increasing degrees of positional and orientational order of the system studied.

4.3.1 Bulk Heterojunctions

Probably the simplest way of manufacturing a bulk heterojunction solar cell is by preparing a polymer/polymer mixture (or blend) or a polymer/small molecule globally amorphous mixture of donor and acceptor materials, obtained by drop casting and evaporation of the solvent. This type of approach is also possible in principle with computer simulations, and it should be preferred because it does not rely on any a priori assumption on the structure of the polymers; however it is computationally very demanding, both because of the large amount of solvent molecules to be included, and of the long simulation times required to follow their evaporation. Thus it can be accomplished only by resorting to massively parallel computational resources, and it actually has been demonstrated by Tsige and Grest [194] for generic LJ bead and spring models of block copolymers, relative to systems containing hundreds of thousands of monomer and solvent molecules. In their setup, periodic boundary conditions are used in the x- and y-directions, while in the z-direction an empty space is left above the polymer solution to allow for solvent evaporation; solvent molecules are then dynamically removed from the box when their z-coordinate exceeds a threshold value, within a

grand canonical MC scheme. They found that although the diffusion of the solvent is almost independent on the polymer concentration, the rate of solvent evaporation decreases exponentially with time. This peculiar observation is determined by the increase of polymer density at the film–vapor interface as the solvent evaporates: this density gradient acts as a barrier "trapping" the solvent far away from the surface. The increase of density and positional order at the surface is probably a general phenomenon of organic–vacuum interfaces, as it has also been observed for amorphous free-standing films of P3HT – together with an increase of the orientational order [195] - and for LC phases [116, 117]. An alternative, simpler approach for simulating blends is to start from a high temperature, disordered, and fully homogeneous mixture and to cool it down progressively. With this method we can expect to observe the self-organization and/or phase segregation phenomena, if the model potential is simple enough to prevent phenomena such as glassification, or more broadly speaking if the cooling rate is not faster than the reorganization process itself. For instance, mixtures of fullerene and polymers, described as chains or isolated LJ spheres, were investigated by Marsh et al. by varying the polymer fraction and flexibility [196]. This study showed that the relative interaction strengths between the components is a key parameter for the final morphology, which can range from amorphous to liquid crystalline and crystalline, and be either phase-separated or arranged in alternate layers, very similar to the structures found by some of us in a system where monomers and fullerenes were covalently linked [80].

Despite the usefulness of generic models for discriminating the effect of one parameter, like the interaction strength in the previous example, it is difficult to relate them quantitatively to the chemical structure of real systems. For reaching chemical accuracy while keeping the fast dynamics of simple models, CG potentials are the best choice and indeed they have been applied to a few selected systems. As already mentioned, Huang et al. derived a CG force field for both P3HT and C_{60}, parameterizing their mixed interaction, and studied device-scale bulk heterojunctions with MD simulations [38, 63]. The process of phase separation upon annealing was followed for mixtures of different compositions starting from arbitrary random configurations, and monitored by tracking the number of aggregated fullerenes vs time. In the simulated time window (20–140 ns), the aggregation was not observed for mixtures of composition P3HT:C_{60} 1.85:1 (w/w), but only for P3HT:C_{60} = 1.27:1, with the process rate found as expected to be dependent on the P3HT degree of polymerization. The aggregation of this mixture, shown in Fig. 18, occurred in about 100 ns (Fig. 18), somehow defining a lower limit for observing this process in MD simulation studies, taking into account the accelerated dynamics granted by the CG models, and the relatively short chain length used for P3HT (12 monomers). In two similar but more device-oriented studies, Lee et al. again used CG MD simulations for characterizing P3HT:PCBM and PBTTT:PCBM solid mixtures [191, 192], with the aim of measuring the extent of segregation of the two components. They were able to show that the blending ratio which maximizes percolation, defined as the possibility of reaching one side of the box from the opposite side by "hopping" on neighboring molecules of the same

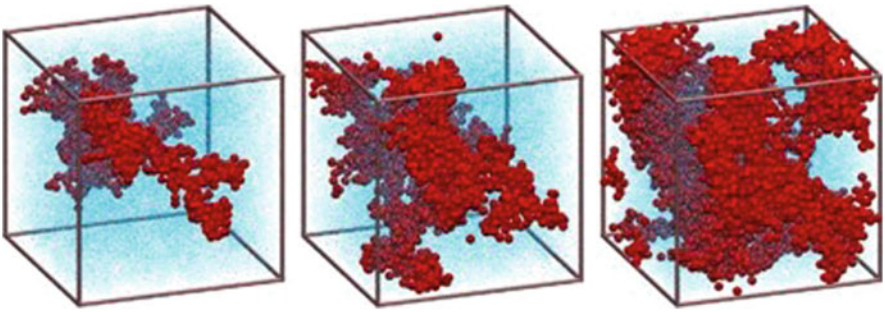

Fig. 18 Snapshots of the simulation configuration of the system with P3HT:C_{60} = 1.27:1 (w/w) at $t = 0$ ns (*left*), $t = 30$ ns (*center*), and $t = 135$ ns (*right*). The C_{60} molecules in the largest cluster are highlighted in *red* and all other particles in the system shown as *light blue dots*. Adapted and reprinted from [63] with permission from Elsevier

material, depends on the chemical nature of the polymer. PCBM is insoluble in P3HT and as a consequence the mixing ratio which maximizes percolation is 1:1, while PBTTT solubilizes part of PCBM and the optimal ratio becomes close to 1:3. In addition, the authors showed that both annealing and high polymer fraction increase the orientational order and the crystallinity of the polymer itself, and that PBTTT tends to be more crystalline than P3HT, although at the optimal blending ratio with PCBM both materials are rather disordered.

Overall, the simulations of bulk heterojunctions are very useful for relating the performance of polymer solar cells to their structure; therefore we shall expect a lot of effort on this area in the next few years.

4.3.2 Planar Interfaces

An alternate approach to simulate an amorphous and disordered blend of donor and acceptor materials is to focus on a single, well defined interface between the two species, which may be representative either of a nanosized domain inside a bulk heterojunction or of a macroscopically planar heterojunction. In the simplest case, such a junction can be generated by putting into contact two specific crystal faces of the two components, optimizing their relative orientation and position. Although this approach does not provide insights on the interface morphology, at least as long as the two crystals are treated as rigid bodies, it is useful for characterizing the energy landscape for charge carriers, critically depending on the relative orientation of the molecules at the interface and on the electric field they generate [197]. However, relaxing the intermolecular degrees of freedom can lead to very important, and sometimes counterintuitive, surface effects. For example, Gee and coworkers found that P3HT tends to assume a very regular structure on irregular and disordered self-assembled monolayers, while its crystalline packing is disrupted by a more ordered surface [198]. Simulations are also useful when one of the two components is amorphous or of unknown crystal structure: in that case, it is good

practice to equilibrate first a bulk sample, then create a free surface by removing periodic boundary conditions, and finally allowing for surface reconstruction before adding the second material (see, e.g., [127] for pentacene on polymer dielectrics). In general, the equilibration times for materials are shorter if the starting configuration is close to their bulk structure. In that case a time window of about 10 ns is typically sufficient to allow the structure to relax to the closest local minimum and introduce a certain amount of thermal and interfacial disorder.

Until now, studies of polymeric systems have been mainly limited to the prototypical P3HT/PCBM interface, for which a good amount of information has been gained for model systems in which P3HT chains extend face-on and parallel to the PCBM surface [121, 200, 201]. One of the most important results is that PCBM introduces a consistent amount of torsional distortion on the P3HT backbone (0.1–0.15 eV in energy): this disorder, also reported for free surfaces of tetrathiophene [202], in turn favors the localization of positive charges on few monomers at the interface, and pushes them towards the bulk where they can better delocalize and diffuse. P3HT then forms a relatively soft interface, in particular in the alkyl chain region, where PCBM can penetrate for a few Ångstroms [121]; nevertheless, it confers some positional order to the first layer of PCBM molecules, whose centers of mass preferentially lie at about 10 Å from P3HT chains. The results for the P3HT–PCBM interface can, in our opinion, be generalized to all systems where a crystalline and an amorphous solid material are put in contact: partial disorder is induced in the ordered material and, mutually, partial order in the disordered material.

While the investigation of polymer planar interfaces has focused primarily on P3HT/PCBM, several authors studied planar heterojunctions formed by low molar mass donor–acceptor (D/A) molecular crystals placed one on top of another. Wenzel and coworkers attempted a rationalization of the degree of disorder present at the pentacene–PTCDA interface for several orientations of the two crystals [199]. They found that at room temperature the interface stabilizes after about 1 ns of MD simulation, and that its final structure arises from two factors: the energy cost for disrupting the bulk crystal structure and the mixed interaction between the two components. In this case pentacene, due to its small molecular volume and apolar nature, has the smallest lattice energy per molecule and consequently it undergoes the largest interfacial deformation with respect to the bulkier PTDCA (Fig. 19). With the same methodology, Yost et al. investigated an interface between a metal-free phthalocyanine (001) and a substituted perylene (010) [203]. Here, the two molecules are of similar size and interaction strength, and, not unexpectedly, the interface-induced deformations were found to induce shifts of the electronic energies up to +0.2 eV on both sides of the interface; in addition, thermal fluctuation effects were estimated to produce fluctuations of up to 0.1 eV to orbital energies. Reddy and Kuppa investigated instead the interface between crystalline C_{60} and an amorphous thin layer of quaterthiophene (T4) [204, 205]. The structure of the latter was analyzed as a function of temperature in the range 275–375 K without registering any significant changes: this is typical for organic semiconductors that are solid up to very high temperatures. Nevertheless, the interaction with the regular and flat C_{60} surface was

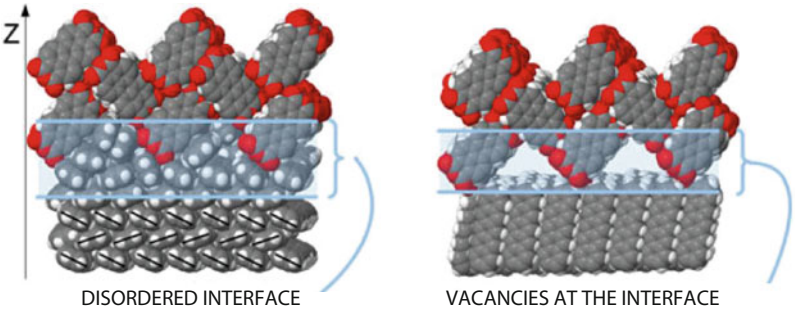

Fig. 19 Pentacene and PTCDA crystalline interfaces. On the *left*, PTCDA (212) on pentacene (100): pentacene molecules relax to close the gaps between the two crystal structures. On the *right*, PTCDA (212) on pentacene (001): both materials keep their crystal structure and vacancies remain. Adapted and reprinted from [199]

found to influence the otherwise disordered T4 structure, inducing both orientational and positional order in its proximity (<1 nm): in practice, T4 forms a few overlayers of flat-lying molecules at the interface with C_{60}. Despite this induced local order, the authors verified that the overall alignment between thiophene units is decreased by the presence of the interface, and conjectured that this effect could be detrimental for charge transport [205]. Mou et al., with a similar approach, studied instead wetting monolayers of rubrene and tetracene on C_{60} (111), finding the same tendency of the molecular aromatic planes to align flat on the surface [206, 207]. Compared with the previous cases of T4 and tetracene, charge transport in rubrene seems not to be affected by the planarization at the interface, thanks to the "bridging" role of side phenyl groups.

We conclude this section by discussing the study of Brédas et al. [208] on C_{60}/pentacene heterojunctions, because on one hand it introduces some themes typical of crystal growth, and on the other it confirms the trend regarding ordering and disordering effects induced by interfacing two solid materials. In this case, we are dealing with two crystal phases, and, similarly to [197, 199], two different combinations of surfaces, C_{60} (*111*)/pentacene (*001*) and C_{60} (*111*)/pentacene (*010*) were investigated starting from perfectly regular structures. In both cases the final simulated structures were found to be more disordered than in the bulk crystal, but while for the low energy pentacene (*001*) facet only a local distortion of the lattice occurs, for the high energy (*010*) facet a true intermixing takes place in the first few nanometers across the junction. The same phenomenon happens to a lesser extent when terraces, and hence portions of high energy surfaces, are present in the sample. Generalizing the outcome of this study, we can argue that, for heterojunctions formed by two molecular crystals, the presence of high energy surfaces may generate important deviations from the geometry of their bulk phases. It should also be kept in mind that during the process of crystal growth the area of those high energy surfaces is usually minimized, and that they are likely to occur only at terrace steps.

4.3.3 Organic Crystal Growth

For interfaces composed of molecular crystals it would be desirable not only to simulate the rearrangements between two preformed phases, but to mimic the growth of one crystal phase on top of another. Unfortunately, the timescales for growth are in the microsecond range or longer, and hence almost prohibitive even for classical simulations, with the additional complication that nucleation is a rare event, at least in solution. Therefore, simulating crystal growth with brute force MD simulations is still deemed as almost impossible [126], and indeed, to overcome these technical difficulties, accelerated approaches such as Kinetic Monte Carlo (KMC) are finding useful application in the study of this topic [209]. For the time being, computational materials scientists have focused their attention on single aspects of crystal growth from vapor, mainly regarding the prototypical cases of pentacene and fullerene, because of the abundance of experimental data, the relative simplicity of their structure, and their p/n-type character. Several studies have provided insights on the elementary steps of the growth process, such as adsorption at different surface sites, diffusion, and insertion, while simulating their dynamics and measuring their energetics.

In one of the first investigations, Verlaak et al. [210] modeled with molecular mechanics the energetics of four possible ways of adding a vertical pentacene molecule to an ideal preformed monolayer: at a terrace edge or at a kink, between two kinks, and between two parallel edges. They found that most of the defective structures that may form in these positions easily relax to the ideal crystal structure, with the exception of the molecules between two terraces, an ideal model for a grain boundary. In that case, in fact, the minimum of the internal energy does not correspond to a crystal lattice site, and point defects or dislocations may form, ultimately affecting charge transport. An analogous study was carried out for C_{60} on graphite [211]: here, in addition, the frequency and the temperature dependence of "jump" events (C_{60} moving from a lattice site to another) were evaluated with MD, and their activation energies by an Arrhenius fit (see (44)). It was found that, due to the large cohesive energy between C_{60} molecules, only those with less than two neighbors can be considered mobile. In a clever multiscale approach, jump rates were used as parameters in a KMC simulation on a 2D lattice, able to reproduce the real shape of the growing islands. This method was then extended to 3D by Cantrell et al. to study the deposition of layers of C_{60} on pentacene [212]: however, the need to consider several matching geometries between the two crystal lattices introduces technical complications, suggesting that an off-lattice approach would be more accurate, although more resource-demanding. For some of the most common organic semiconductors, like oligoacenes, Clancy and coworkers also measured with molecular mechanics the Ehrlich-Schwöbel barrier, i.e., the extra energy required for a molecule to descend a terrace step edge in addition to that for the surface diffusion. These energies are highly molecule-specific and estimated to be of the order of 2–10 kcal/mol; nevertheless they are roughly correlated to the crystal cohesive energy and to the binding energy to the terrace surface [213]. The same

research group also investigated several dynamic processes relevant to vapor phase deposition. In [214, 215], the effect of the kinetic energy and of the incident angle on the final position of a colliding pentacene molecule on a preformed crystalline and incomplete (001) bilayer was determined. As expected, very high energies (5 eV or greater) lead to unsuccessful events such as immediate desorption (a sort of elastic collision, or rebounding), but also two-layers-deep penetration is possible. Interestingly, the kinetic energy is not very relevant as long as the incident angle is roughly parallel to the layer normal; besides, at terrace edges the deposition attempt is in practice always successful for angles lower than 45°. The diffusion of C_{60} interfaced to crystalline surfaces of pentacene, either standing or flat lying, was inspected respectively in [122] and [123], again by MD simulations. In this case, an isolated C_{60} molecule diffuses rather freely on the very smooth pentacene (001) surface, with activation energy of about 0.1 eV; the diffusion is nevertheless anisotropic and faster along the $[1\bar{1}0]$ directions. The addition of more C_{60} molecules causes immediate aggregation and a fourfold drop of the diffusion coefficient, suggesting the tendency of C_{60} to grow in a 3D fashion due to its high cohesive energy. Conversely, on a high energy recumbent pentacene surface, similar to the $(01\bar{1})$ [197], C_{60} can form nanowires if the pentacene plane is perpendicular to the surface. These nanowires may form either on top or between pentacene rows, depending on the mismatch between C_{60} and pentacene lattices in the simulation cell.

The first simulation prediction on the phenomenon of nucleation and growth of organic semiconductors was carried out in Bologna by some of us [119] to mimic the essential features of the experiment on vapor deposition of pentacene on C_{60}. This work stands out as it couples the application of non-equilibrium MD simulations (such as those performed in [215]) to the consecutive insertion of many molecules in the system one after another, similar to what happens in KMC simulations of crystal growth. In this way, the structure of one side of the planar heterojunction can be predicted from scratch, depending on the growth conditions, such as temperature and deposition rate, albeit this latter parameter must, for practical reasons, be much higher than the experimental ones. In this fortunate case, the high deposition rate did not prevent the formation of a crystalline pentacene aggregate. The pentacene crystal structure obtained with the deposition technique is similar but more tilted than the bulk pentacene structure, and the relative orientation between the C_{60} and pentacene lattice is not random, but templated by the channels along the C_{60} $[1\bar{1}0]$ directions, and by the C_{60} surface roughness, inducing positional disorder to the first pentacene monolayer. It was also found that the growth proceeds in two coverage-dependent regimes: in the first, pentacene molecules lie flat and orientationally disordered on the C_{60} surface while forming amorphous aggregates; in the second, starting at ~2 molecules/nm^2, they reorient perpendicular to the surface and self assemble in a crystalline partial monolayer (Fig. 20). Going from the first to the second monolayer, the mechanism is qualitatively the same but the lower energy of the pentacene (001) surface with respect to the C_{60} (001) determines that the collective reorientation from recumbent

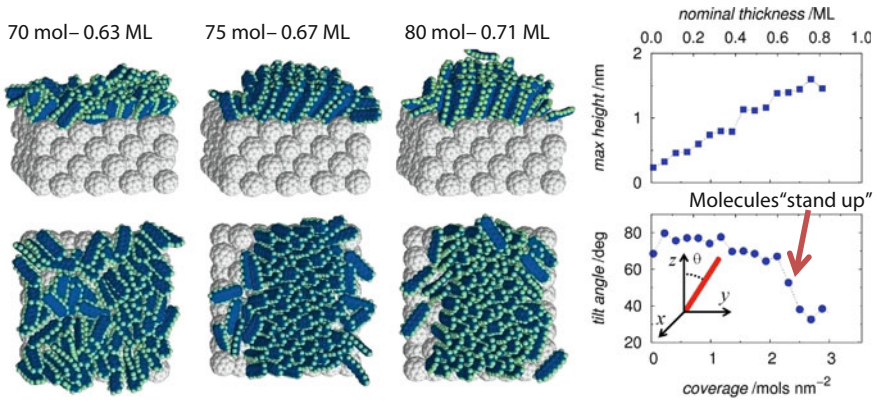

Fig. 20 *Left*: side and top view snapshots showing the aggregation and onset of herringbone packing during the nucleation of pentacene on C_{60} (001). *Right*: evolution of film height and tilt angle as the coverage increases upon deposition of one pentacene molecule every 250 ps [119]

to vertical takes place earlier. It is likely that this two-step mechanism could be general for the deposition of elongated π-conjugated molecules forming thin films of standing molecules. Future studies of organic crystal growth will surely address this issue and the fascinating concept of surface-induced phases (or polymorphs), also formed by more than one component. In this respect, we believe that a combination of off-lattice KMC to displace cleverly the molecules, alternated with MD to reach the closest free energy minimum, would ideally suit the task, and also allow extending of the length and timescales spanned, in order to be able to simulate the formation of grain boundaries, that are considered important in determining device performances. The simulation studies conducted so far on organic–organic interfaces reveal a picture of organic semiconductors being soft rather than hard materials, also in their crystal phase, and hence able to adapt and deform their structure in the interfacial region. This adaptability, driven by the balance between the gain of interfacial free energy and the loss of bulk cohesive energy, seems on one hand to decrease positional, orientational, and conformational order if the material is crystalline and on the other to increase the order if the material is amorphous. In the case of an interface between two crystals, weak forms of epitaxy are also possible, but again coupled with a general disordering, whose amount decreases with the cohesive energy of the bulk phase.

5 Conclusions

In the last few years intense activity has taken place in the field of structural simulation of organic semiconductors, resulting in several specific advances in the understanding of their structure–property relationships. Much work has been done in terms of developing and adapting computational tools and theoretical

models to this class of materials and in designing simulation strategies to approach as closely as possible the experimental conditions.

It should be apparent from this overview that the field is vigorously expanding and that it will likely continue to do so, pushed by the relevance of the problems to be solved and interests at stake, and technically supported by the predictable increase of available computational resources, exploitable through the use of parallelism of CPUs and GPUs. Further scientific development can be expected as the field stands on the solid ground of decades of research on complex systems and thermoplastic polymers. Although the transfer of knowledge from the condensed matter to the organic electronic communities has been slow at the beginning, it is now becoming smoother as witnessed, for instance, by the machinery of coarse-grained modeling now being applied to polymeric semiconductors.

Many challenges still await computational material scientists working on organic electronics and hopefully some of them will be tackled in the next few years. For *low molecular mass systems*, simulations should possibly prove to be predictive instruments for helping the design of materials, rather than just reproducing the experimental properties. In *polymeric systems*, the capability of predicting crystalline structures with atomistic models, and phase behaviors with simpler ones, still has to be fully demonstrated, leaving a lot of room for the application of coarse-grained and soft-core empirical models. *Organic interfacial systems* are the most challenging to study, mainly for technical reasons, since the systems sizes and timescales are still prohibitive. A consistent picture of the phenomena taking place at the interface and of their relationship with electronic properties, a general understanding of the interplay between the structure of the interface and the electrostatic landscape it generates, in particular for bulk heterojunction systems, must be gained to prompt the improvement of existing devices.

Regarding the *computer simulation protocols*, we stress again the necessity of imitating experimental preparation techniques to be able to compare with the corresponding experiments. One of the major open issues still awaiting a methodological solution is probably the lack of a robust and widely available *multiscale* simulation platform, where the well defined quantum mechanical and classical simulations methodologies could be connected to the device scale and thus permit the design and optimization of solar cells, transistors, or other emerging applications of functional organic materials. This integration will be one of the main areas of future scientific and technological developments.

Appendix: Simulation Packages

This Appendix is intended to serve as an overview of the more common computer simulation packages suitable for molecular simulation studies of organic materials. Actually the landscape of available packages is essentially dominated by MD-based codes. In fact, MC and KMC codes are commonly developed in-house by researchers

to handle specific problems requiring ad hoc sampling algorithms, and hence have a much less wide user base than MD ones. In contrast, many computer codes are available to the end-user willing to carry out MD simulations. Some of them come with an extensive support including manuals, tutorials, and online discussion boards such as forums and mailing lists. Here we report a selection of packages which are suitable for simulating large systems of organic molecules and which are used by a large community of users. This is of course not a measure of the quality of the program, but rather it ensures that a large body of published works are available as reference, therefore constituting a valuable starting point for those approaching the field of MD for the first time. Moreover, the more popular codes are continuously maintained and updated, an important aspect to take into account as machine architectures change very often. It is worth noting that while the standard packages provide MD trajectories (as sequences of instantaneous configurations), the calculation of many observables of interest have to be specifically added by the end-user and suitable algorithms often have to be devised. The available MD packages are characterized by various factors:

1. Features and capabilities, e.g., multiple-timestep integration algorithms [96, 216], physical representation of simulated objects (coarse-grained or all-atoms), constrained dynamics (e.g., SHAKE [217]) with many codes allowing for multiple options.
2. License and cost, i.e., free-academic, open source, commercial.
3. Portability, i.e., the code can easily be compiled and run on many platforms, from common (e.g., computer desktops) to specialized hardware (e.g., IBM's BlueGene).
4. Performance and parallelization, i.e., the ability to run faster and simulate bigger systems by splitting work among multiple processors. Nowadays support of GPU boards is widely available and allows the deployment of graphics cards alongside traditional CPUs.
5. Extensibility of the code in order to tailor specific problems or to implement new force-fields/simulation algorithms/computation of observables, which were not available in the original code.

The choice of a particular MD package depends on the first instance on the system being studied, particularly on the model used to describe the interactions between the particles and on its scalability (i.e., the computational efficiency as the number of processing units increases), which can be a limiting factor when the system size exceed tens or even hundreds of thousands of particles. A necessarily partial list of computer programs to carry out MD simulations is reported in Table 1.

Two well-established computer programs for MD simulations are CHARMM [24] and AMBER [219], which implement a similar functional form of the atomistic force field and include a large number of tools for setting up the files required to run an MD simulation.

NAMD [227] is a more recent program which works with AMBER and CHARMM potential functions, parameters, and file formats, and it is specifically designed for high-performance simulation of large systems. The current version (*2.9*) is able to run on heterogeneous architectures made up of multiple CPUs and GPUs.

Table 1 Partial list of MD simulation packages

Name	Website	License	References
ACEMD	http://multiscalelab.org/acemd	Commercial	[218]
AMBER	http://ambermd.org/	Free/Commercial	[219]
CHARMM	http://www.charmm.org/	Commercial	[24]
Desmond	http://www.deshawresearch.com/resources_desmond.html	Free academic	[220]
DL_POLY	http://www.ccp5.ac.uk/DL_POLY/	Free academic	[221]
ESPResSo	http://espressomd.org/	Free	[222]
GROMACS	http://www.gromacs.org/	Free	[223]
HOOMD	http://codeblue.umich.edu/hoomd-blue/	Free	[224]
LAMMPS	http://lammps.sandia.gov/	Free	[225]
Material Studio	http://accelrys.com/products/materials-studio/	Commercial	[226]
NAMD	http://www.ks.uiuc.edu/Research/namd/	Free	[227]
OCTA	http://octa.jp/	Free	
OpenMM	https://simtk.org/home/openmm	Free	[228]
ProtoMol	http://protomol.sourceforge.net/	Free	[229]
TINKER	http://dasher.wustl.edu/ffe/	Free	
VOTCA	http://www.votca.org/	Free	[230]

LAMMPS [225] is a classical MD program implementing potentials for soft materials (biomolecules, polymers), solid-state materials (metals, semiconductors), and coarse-grained or mesoscopic systems. The code is designed to be easy to modify or extend with new functionalities. The comprehensive manual compensates for the somewhat clumsy input script syntax. Most of its model potentials have been parallelized and run on systems with multiple CPUs and GPUs, granting very good speedups, especially for the most complicated pair potential styles, like the Gay–Berne and other CG potentials.

GROMACS [231] is conceived to carry out simulations with millions of particles. The syntax of input files is user-friendly and a major advantage is that the program comes with a large selection of tools for trajectory analysis. In version *4.5* only single GPU support is present, but from version *4.6* multiple GPUs will also be enabled.

The output of an MD simulation typically includes a trajectory file containing the position of every particle, saved with a given time increment. Trajectory files can be visualized with specific programs such as VMD [232–234], which also offers basic tools for data analysis, Jmol [235], a powerful and highly portable program written in Java, Mercury [236], and GDIS [237], two programs particularly well suited to visualize and manipulate crystal structures, and Avogadro [238, 239], which offers advanced molecular modeling tools. Among the other visualizers available, we mention OVITO [240, 241], PyMOL [242], Molekel [243], V_Sim (http://www-drfmc.cea.fr/L_Sim/V_Sim/index.en.html), Ras-Mol [(http://rasmol.org/), 244], FOX [245, 246], QMGA [247, 248], UCSF Chimera [249, 250], and BALLView [251, 252].

The vast choice of available packages might be a bit intimidating at first, so here are listed some of our (objectionable) views on the key issues. Given the high quality of many open source packages, they are probably to be preferred over commercial ones with closed sources, both for their plentiful features (as everybody can contribute to further development) and because the sources can be directly inspected to check how algorithms are implemented and can be customized to suit particular needs. As many algorithms work well only under specific conditions and many compromises are usually made, this is in some cases the most reliable way to check the validity of the simulation results.

As long as small samples and/or short timescales are needed and the package provides the required features, it really does not matter which code is used, and the one easier to run is to be preferred. If instead the problem at hand requires what can be accomplished currently to be pushed to the limits, a well optimized code becomes the only choice. Given the typical speedups of GPU systems, codes able to run on heterogeneous architectures (mixed CPU/GPU) environments are the best performers. Note: most of the codes running today on GPU use CUDA (http://www.nvidia.com/object/cuda_home_new.html) instead of OpenCL (http://www.khronos.org/opencl), which means they will run only on NVidia cards.

References

1. Maddox J (1988) Nature 335:201
2. Pizzirusso A, Savini M, Muccioli L, Zannoni C (2011) J Mater Chem 21:125
3. Pasini P, Zannoni C (2000) Advances in the computer simulations of liquid crystals. NATO ASI Series, kluwer, Dordrecht
4. Groves C, Greenham NC (2013) Monte Carlo simulations of organic photovoltaics. Top Curr Chem. doi:10.1007/128_2013_467.
5. Walker A (2013) Monte Carlo studies of electronic processes in dye-sensitized solar cells. Top Curr Chem. doi:10.1007/128_2013_472.
6. Athanasopoulos S, Emelianova EV, Walker AB, Beljonne D (2009) Phys Rev B 80:195209
7. Car R, Parrinello M (1985) Phys Rev Lett 55:2471
8. Stone AJ (1996) The theory of intermolecular forces, international series of monographs on chemistry, vol 32. Oxford University Press, Oxford
9. Cornell WD, Cieplak P, Bayly CI, Gould IR, Merz KM, Ferguson DM, Spellmeyer DC, Fox T, Caldwell JW, Kollman PA (1995) J Am Chem Soc 117:5179
10. Wang J, Wolf RM, Caldwell JW, Kollman PA, Case DA (2004) J Comput Chem 25:1157
11. Jorgensen WL, Maxwell DS, Tirado-Rives J (1996) J Am Chem Soc 118:11225
12. Mackerell AD, Bashford D, Bellott M, Dunbrack RL, Evanseck JD, Field MJ, Fischer S, Gao J, Guo H, Ha S, Joseph-McCarthy D, Kuchnir L, Kuczera K, Lau FTK, Mattos C, Michnick S, Ngo T, Nguyen DT, Prodhom B, Reiher WE, Roux B, Schlenkrich M, Smith JC, Stote R, Straub J, Watanabe M, Wiorkiewicz-Kuczera J, Yin D, Karplus M (1998) J Phys Chem B 102:3586
13. Marcon V, van der Vegt N, Wegner G, Raos G (2006) J Phys Chem B 110:5253
14. Sancho-García J, Karpfen A (2009) Chem Phys Lett 473:49
15. Bhatta RS, Yimer YY, Tsige M, Perry DS (2012) Comput Theor Chem 995:36
16. Cheung DL, McMahon DP, Troisi A (2009) J Phys Chem B 113:9393
17. Rigby J, Izgorodina EI (2013) Phys Chem Chem Phys 15:1632

18. Kramer C, Gedeck P, Meuwly M (2012) J Comput Chem 33:1673
19. Wang B, Truhlar DG (2012) J Chem Theory Comput 8:1989
20. Berardi R, Muccioli L, Orlandi S, Ricci M, Zannoni C (2004) Chem Phys Lett 389:373
21. Lopes P, Roux B, MacKerell AD Jr (2009) Theor Chem Acc 124:11
22. Cieplak P, Dupradeau FY, Duan Y, Wang J (2009) J Phys Condens Matter 21:333102
23. Jiang W, Hardy DJ, Phillips JC, Mackerell AD, Schulten K, Roux B (2011) J Phys Chem Lett 2:87
24. Brooks BR, Brooks CL III, Mackerell AD, Nilsson L, Petrella RJ, Roux B, Won Y, Archontis G, Bartels C, Boresch S, Caflisch A, Caves L, Cui Q, Dinner AR, Feig M, Fischer S, Gao J, Hodoscek M, Im W, Kuczera K, Lazaridis T, Ma J, Ovchinnikov V, Paci E, Pastor RW, Post CB, Pu JZ, Schaefer M, Tidor B, Venable RM, Woodcock HL, Wu X, Yang W, York DM, Karplus M (2009) J Comput Chem 30:1545
25. Ponder JW, Wu C, Ren P, Pande VS, Chodera JD, Schnieders MJ, Haque I, Mobley DL, Lambrecht DS, DiStasio RA, Head-Gordon M, Clark GNI, Johnson ME, Head-Gordon T (2010) J Phys Chem B 114:2549
26. Wang J, Cieplak P, Li J, Wang J, Cai Q, Hsieh M, Lei H, Luo R, Duan Y (2011) J Phys Chem B 115:3100
27. Vorobyov IV, Anisimov VM, Mackerell AD (2005) J Phys Chem B 109:18988
28. Lopes PEM, Lamoureux G, Roux B, Mackerell AD (2007) J Phys Chem B 111:2873
29. Yang L, Tan C, Hsieh MJ, Wang J, Duan Y, Cieplak P, Caldwell J, Kollman PA, Luo R (2006) J Phys Chem B 110:13166
30. von Lilienfeld OA, Andrienko D (2006) J Chem Phys 124:054307
31. Scott WRP, Hünenberger PH, Tironi IG, Mark AE, Billeter SR, Fennen J, Torda AE, Huber T, Krüger P, van Gunsteren WF (1999) J Phys Chem A 103:3596
32. Keasler SJ, Charan SM, Wick CD, Economou IG, Siepmann JI (2012) J Phys Chem B 116:11234
33. Papadopoulos TA, Muccioli L, Athanasopoulos S, Walker AB, Zannoni C, Beljonne D (2011) Chem Sci 2:1025
34. Olivier Y, Muccioli L, Lemaur V, Geerts YH, Zannoni C, Cornil J (2009) J Phys Chem B 113:14102
35. Sapay N, Tieleman DP (2011) J Comput Chem 32:1400
36. Palermo MF, Pizzirusso A, Muccioli L, Zannoni C (2013) J Chem Phys 138:204901
37. Theodorou DN (2007) Chem Eng Sci 62:5697
38. Huang DM, Faller R, Do K, Moule AJ (2010) J Chem Theory Comput 6:526
39. Liu DJ, Selinger RLB, Weeks JD (1996) J Chem Phys 105:4751
40. Girifalco LA (1992) J Phys Chem 96:858
41. Sazonovas A, Orlandi S, Ricci M, Zannoni C, Gorecka E (2006) Chem Phys Lett 430:297
42. Kniaz K, Girifalco LA, Fischer JE (1995) J Phys Chem 99:16804
43. Girifalco LA, Hodak M, Lee RS (2000) Phys Rev B 62:13104
44. Peter C, Kremer K (2010) Faraday Discuss 144:9
45. Peter C, Kremer K (2009) Soft Matter 5:4357
46. Karimi-Varzaneh HA, Müller-Plathe F (2012) In: Kirchner B, Vrabec J (eds) Multiscale molecular methods in applied chemistry, Topics in current chemistry, vol 307. Springer, Berlin, pp. 295–321
47. Karimi-Varzaneh HA, van der Vegt NFA, Müller-Plathe F, Carbone P (2012) Chemphyschem 13:3428
48. Müller-Plathe F (2002) Chemphyschem 3:754
49. Takada S (2012) Curr Opin Struct Biol 22:130
50. Ayton GS, Lyman E, Voth GA (2010) Faraday Discuss 144:347
51. Marrink SJ, Risselada HJ, Yefimov S, Tieleman DP, de Vries AH (2007) J Phys Chem B 111:7812
52. Rudzinski JF, Noid WG (2011) J Chem Phys 135:214101
53. Reith D, Pütz M, Müller-Plathe F (2003) J Comput Chem 24:1624
54. Lyubartsev AP, Laaksonen A (1995) Phys Rev E 52:3730

55. Wong-Ekkabut J, Baoukina S, Triampo W, Tang IM, Tieleman DP, Monticelli L (2008) Nat Nanotechnol 3:363
56. Rossi G, Monticelli L, Puisto SR, Vattulainen I, Ala-Nissila T (2011) Soft Matter 7:698
57. Tschöp W, Kremer K, Hahn O, Batoulis J, Bürger T (1998) Acta Polymerica 49:75
58. Marcon V, Fritz D, van der Vegt NFA (2012) Soft Matter 8:5585
59. Fritz D, Herbers CR, Kremer K, van der Vegt NFA (2009) Soft Matter 5:4556
60. Fritz D, Koschke K, Harmandaris VA, van der Vegt NFA, Kremer K (2011) Phys Chem Chem Phys 13:10412
61. Harmandaris VA, Kremer K (2009) Macromolecules 42(3):791
62. Mukherjee B, Delle Site L, Kremer K, Peter C (2012) J Phys Chem B 116:8474
63. Huang DM, Moule AJ, Faller R (2011) Fluid Phase Equilibria 302:21
64. Gay J, Berne B (1981) J Chem Phys 74:3316
65. Lennard-Jones J (1924) Proc R Soc London Ser A 106:463
66. Zannoni C (2001) J Mater Chem 11:2637
67. Emerson A, Luckhurst G, Whatling S (1994) Mol Phys 82:113
68. Orlandi S, Muccioli L, Ricci M, Berardi R, Zannoni C (2007) Chem Cent J 1:15
69. Cleaver D, Care C, Allen M, Neal M (1996) Phys Rev E 54:559
70. Berardi R, Fava C, Zannoni C (1998) Chem Phys Lett 297:8
71. Fejer SN, Chakrabarti D, Wales DJ (2011) Soft Matter 7:3553
72. Berardi R, Orlandi S, Zannoni C (1996) Chem Phys Lett 261:357
73. Wilson M (1997) J Chem Phys 107:8654
74. Berardi R, Micheletti D, Muccioli L, Ricci M, Zannoni C (2004) J Chem Phys 121:9123
75. Stimson L, Wilson M (2005) J Chem Phys 123:034908
76. Lee CK, Hua CC, Chen SA (2010) J Chem Phys 133:064902
77. Lee CK, Hua CC, Chen SA (2012) J Chem Phys 136:084901
78. Wilson M, Stimson L, Ilnytskyi J (2006) Liq Cryst 33:1167
79. Skacej G, Zannoni C (2012) PNAS 109:10193
80. Orlandi S, Muccioli L, Ricci M, Zannoni C (2009) Soft Matter 5:4484
81. Bacchiocchi C, Hennebicq E, Orlandi S, Muccioli L, Beljonne D, Zannoni C (2008) J Phys Chem B 112:1752
82. Kremer K, Grest GS (1990) J Chem Phys 92:5057
83. Everaers R, Sukumaran SK, Grest GS, Svaneborg C, Sivasubramanian A, Kremer K (2004) Science 303:823
84. Hoogerbrugge P, Koelman J (1992) Europhys Lett 19:155
85. Groot RD, Madden TJ, Tildesley DJ (1999) J Chem Phys 110:9739
86. Martinez-Veracoechea FJ, Escobedo FA (2006) J Chem Phys 125:104907/1
87. Huang HK, Lin CH (2008) Phys Rev E 77:031804/1
88. Pal S, Seidel C (2006) Macromol Theor Simul 15:668
89. Espanol P (1995) Phys Rev E 52:1734
90. Espanol P, Warren P (1995) Europhys Lett 30:191
91. Groot R, Warren P (1997) J Chem Phys 107:4423
92. Chen S, Phan-Thien N, Fan XJ, Khoo B (2004) J Nonnewton Fluid Mech 118:65
93. Cheung DL, Troisi A (2009) Phys Chem Chem Phys 11:2105
94. Lintuvuori JS, Wilson MR (2009) Phys Chem Chem Phys 11:2116
95. Allen MP, Tildesley DJ (1989) Computer simulation of liquids. Oxford University Press, Oxford
96. Frenkel D, Smit B (2001) Understanding molecular simulations, 2nd edn. Academic, San Diego
97. Voter AF, Montalenti F, Germann TC (2002) Annu Rev Mater Res 32:321
98. Theodorou DN (2010) Ind Eng Chem Res 49:3047
99. Chipot C, Pohorille A (2007) Free energy calculations: theory and applications in chemistry and biology, Springer series in chemical physics. Springer–Verlag, Berlin Heidelberg
100. Christ CD, Mark AE, van Gunsteren WF (2010) J Comput Chem 31:1569
101. Metropolis N, Rosenbluth AW, Rosenbluth MN, Teller AH, Teller E (1953) J Chem Phys 21:1087

102. Alder BJ, Wainwright TE (1959) J Chem Phys 31:459
103. Knuth D (1998) Seminumerical algorithms. Addison–Wesley
104. Van Kampen N (1992) Stochastic processes in physics and chemistry. North-Holland Personal Library, Elsevier Science, Amsterdam
105. Chatterjee A, Vlachos DG (2007) J Comp Mater Design 14:253
106. Gillespie DT (2007) Ann Rev Phys Chem 58:35
107. Kamberaj H, Low RJ, Neal MP (2005) J Chem Phys 122:224114
108. Altmann SL (2005) Rotations, quaternions, and double groups. Dover, New York
109. Berardi R, Muccioli L, Zannoni C (2008) J Chem Phys 128:024905
110. Hünenberger PH (2005) In: Holm C, Kremer K (eds) Advanced computer simulation approaches for soft matter sciences I—series: advances in polymer science, vol 173. Springer, chap. 2, pp 105–149. http://link.springer.com/chapter/10.1007/b99427
111. Kirkpatrick J, Marcon V, Kremer K, Nelson J, Andrienko D (2008) J Chem Phys 129:094506
112. Poelking C, Cho E, Malafeev A, Ivanov V, Kremer K, Risko C, Brédas JL, Andrienko D (2013) J Chem Phys C 117:1633
113. Cinacchi G, Colle R, Tani A (2004) J Phys Chem B 108:7969
114. Andrienko D, Marcon V, Kremer K (2006) J Chem Phys 125:124902
115. Zannoni C (1994) In: Luckhurst G, Veracini C (eds) The molecular dynamics of liquid crystals. Kluwer, Dordrecht, Chap. 2, pp 11–36
116. Pizzirusso A, Berardi R, Muccioli L, Ricci M, Zannoni C (2012) Chem Sci 3:573
117. Roscioni OM, Muccioli L, Della Valle RG, Pizzirusso A, Ricci M, Zannoni C (2013) Langmuir 23:8950
118. Marconi UMB, Puglisi A, Rondoni L, Vulpiani A (2008) Phys Rep 461:111
119. Muccioli L, D'Avino G, Zannoni C (2011) Adv Mat 23:4532
120. De Leener C, Hennebicq E, Sancho-Garcia JC, Beljonne D (2009) J Phys Chem B 113:1311
121. D'Avino G, Mothy S, Muccioli L, Zannoni C, Wang L, Cornil J, Beljonne D, Castet F (2013) J Phys Chem C 117:12981
122. Cantrell R, Clancy P (2008) Surf Sci 602:3499
123. Cantrell RA, James C, Clancy P (2011) Langmuir 27:9944
124. O'Neill M, Kelly SM (2011) Adv Mater 23:566
125. Bardwell DA, Adjiman CS, Arnautova YA, Bartashevich E, Boerrigter SXM, Braun DE, Cruz-Cabeza AJ, Day GM, Della Valle RG, Desiraju GR, van Eijck BP, Facelli JC, Ferraro MB, Grillo D, Habgood M, Hofmann DWM, Hofmann F, Jose KVJ, Karamertzanis PG, Kazantsev AV, Kendrick J, Kuleshova LN, Leusen FJJ, Maleev AV, Misquitta AJ, Mohamed S, Needs RJ, Neumann MA, Nikylov D, Orendt AM, Pal R, Pantelides CC, Pickard CJ, Price LS, Price SL, Scheraga HA, van de Streek J, Thakur TS, Tiwari S, Venuti E, Zhitkov IK (2011) Acta Crystallogr B 67:535
126. Anwar J, Zahn D (2011) Angew Chem Int Ed 50:1996
127. Martinelli NG, Savini M, Muccioli L, Olivier Y, Castet F, Zannoni C, Beljonne D, Cornil J (2009) Adv Funct Mater 19:3254
128. Troisi A, Orlandi G (2006) J Phys Chem A 110:4065
129. Motta SD, Donato ED, Negri F, Orlandi G, Fazzi D, Castiglioni C (2009) JACS 131:6591
130. Wang L, Li Q, Shuai Z, Chen L, Shi Q (2010) Phys Chem Chem Phys 12:3309
131. Troisi A (2007) Adv Mater 19:2000
132. Martinelli NG, Ide J, Sanchez-Carrera RS, Coropceanu V, Bredas JL, Ducasse L, Castet F, Cornil J, Beljonne D (2010) J Phys Chem C 114:20678
133. Martinelli NG, Olivier Y, Athanasopoulos S, Delgado MCR, Pigg KR, da Silva Filho DA, Sanchez-Carrera RS, Venuti E, Valle RGD, Bredas JL, Beljonne D, Cornil J (2009) Chemphyschem 10:2265
134. Motta SD, Siracusa M, Negri F (2011) J Phys Chem C 115:20754
135. Schrader M, Fitzner R, Hein M, Elschner C, Baumeier B, Leo K, Riede M, Bäuerle P, Andrienko D (2012) J Am Chem Soc 134:6052
136. Vehoff T, Chung YS, Johnston K, Troisi A, Yoon DY, Andrienko D (2010) J Phys Chem C 114:10592
137. Vehoff T, Baumeier B, Troisi A, Andrienko D (2010) J Am Chem Soc 132:11702

138. Chang J, Sandler SI (2006) J Chem Phys 125:054705
139. Cheung DL, Troisi A (2010) J Phys Chem C 114:20479
140. Frigerio F, Casalegno M, Carbonera C, Nicolini T, Meille SV, Raos G (2012) J Mater Chem 22:5434
141. May F, Al-Helwi M, Baumeier B, Kowalsky W, Fuchs E, Lennartz C, Andrienko D (2012) J Am Chem Soc 134:13818
142. Kwiatkowski JJ, Nelson J, Li H, Bredas JL, Wenzel W, Lennartz C (2008) Phys Chem Chem Phys 10:1852
143. Nagata Y, Lennartz C (2008) J Chem Phys 129:034709
144. Lukyanov A, Lennartz C, Andrienko D (2009) Phys Status Solidi A 206:2737
145. Schrader M, Körner C, Elschner C, Andrienko D (2012) J Mater Chem 22:22258
146. Tiberio G, Muccioli L, Berardi R, Zannoni C (2009) Chem Phys Chem 10:125
147. Tant J, Geerts YH, Lehmann M, De Cupere V, Zucchi G, Laursen BW, Bjornholm T, Lemaur V, Marcq V, Burquel A, Hennebicq E, Gardebien F, Viville P, Beljonne D, Lazzaroni R, Cornil J (2005) J Phys Chem B 109:20315
148. Marcon V, Breiby DW, Pisula W, Dahl J, Kirkpatrick J, Patwardhan S, Grozema F, Andrienko D (2009) J Am Chem Soc 131:11426
149. Lemaur V, Bouzakraoui S, Olivier Y, Brocorens P, Burhin C, El Beghdadi J, Martin-Hoyas A, Jonas AM, Serban DA, Vlad A, Boucher N, Leroy J, Sferrazza M, Mouthuy PO, Melinte S, Sergeev S, Geerts Y, Lazzaroni R, Cornil J, Nysten B (2010) J Phys Chem C 114:4617
150. May F, Marcon V, Hansen MR, Grozema F, Andrienko D (2011) J Mater Chem 21:9538
151. Marcon V, Vehoff T, Kirkpatrick J, Jeong C, Yoon DY, Kremer K, Andrienko D (2008) J Chem Phys 129:094505
152. Feng X, Marcon V, Pisula W, Hansen MR, Kirkpatrick J, Grozema F, Andrienko D, Kremer K, Müllen K (2009) Nat Mater 8:1476
153. Idé J, Mereau R, Ducasse L, Castet F, Olivier Y, Martinelli N, Cornil J, Beljonne D (2011) J Phys Chem B 115:5593
154. Lamarra M, Muccioli L, Orlandi S, Zannoni C (2012) Phys Chem Chem Phys 14:5368
155. Doi M, Edwards S (1988) The theory of polymer dynamics. Oxford science publications. Oxford University Press
156. McMahon DP, Troisi A (2010) Chemphyschem 11:2067
157. Topham PD, Parnell AJ, Hiorns RC (2011) J Polym Sci Part B Polym Phys 49:1131
158. Yassar A, Miozzo L, Gironda R, Horowitz G (2013) Prog Polym Sci 38:791
159. Bates FS, Hillmyer MA, Lodge TP, Bates CM, Delaney KT, Fredrickson GH (2012) Science 336:434
160. Ramanathan M, Darling SB (2011) Prog Polym Sci 36:793
161. Micheletti D, Muccioli L, Berardi R, Ricci M, Zannoni C (2005) J Chem Phys 123:224705
162. Yung KL, He L, Xu Y, Shen YW (2005) Polymer 46:11881
163. Berardi R, Lintuvuori JS, Wilson MR, Zannoni C (2011) J Chem Phys 135:134119
164. Makke A, Lame O, Perez M, Barrat JL (2012) Macromolecules 45:8445
165. Arosio P, Moreno M, Famulari A, Raos G, Catellani M, Meille SV (2009) Chem Mater 21:78
166. Moreno M, Casalegno M, Raos G, Meille SV, Po R (2010) J Phys Chem B 114:1591
167. Niedzialek D, Lemaur V, Dudenko D, Shu J, Hansen MR, Andreasen JW, Pisula W, Müllen K, Cornil J, Beljonne D (2013) Adv Mater 25:1939
168. DuBay KH, Hall ML, Hughes TF, Wu C, Reichman DR, Friesner RA (2012) J Chem Theory Comput 8:4556
169. Arbe A, Alvarez F, Colmenero J (2012) Soft Matter 8:8257
170. Rivnay J, Mannsfeld SCB, Miller CE, Salleo A, Toney MF (2012) Chem Rev 112:5488
171. Brocorens P, Van Vooren A, Chabinyc ML, Toney MF, Shkunov M, Heeney M, McCulloch I, Cornil J, Lazzaroni R (2009) Adv Mat 21:1193
172. Cho E, Risko C, Kim D, Gysel R, Cates Miller N, Breiby DW, McGehee MD, Toney MF, Kline RJ, Bredas JL (2012) J Am Chem Soc 134:6177
173. Ren XK, Wu YC, Wang SJ, Jiang SD, Zheng JF, Yang S, Chen EQ, Wang CL, Hsu CS (2013) Macromolecules 46:155
174. Fonner JM, Schmidt CE, Ren P (2010) Polymer 51:4985

175. Granadino-Roldan J, Vukmirovic N, Fernandez-Gomez M, Wang LW (2011) Phys Chem Chem Phys 13:14501
176. Curcó D, Alemán C (2007) J Comput Chem 28:1743
177. Kilina S, Batista ER, Yang P, Tretiak S, Saxena A, Martin RL, Smith DL (2008) ACS Nano 2:1381
178. Jakobsson M, Linares M, Stafstrom S (2012) J Chem Phys 137:114901
179. Do K, Huang DM, Faller R, Moule AJ (2010) Phys Chem Chem Phys 12:14735
180. Vehoff T, Baumeier B, Andrienko D (2010) J Chem Phys 133:134901
181. Shaytan AK, Schillinger EK, Khalatur PG, Mena-Osteritz E, Hentschel J, Börner HG, Bäuerle P, Khokhlov AR (2011) ACS Nano 5:6894
182. Melis C, Colombo L, Mattoni A (2011) J Chem Phys C 115:576
183. Dag S, Wang LW (2010) J Phys Chem B 114:5997
184. Buono A, Son NH, Raos G, Gila L, Cominetti A, Catellani M, Meille SV (2010) Macromolecules 43:6772
185. Alexiadis O, Mavrantzas VG (2013) Macromolecules 46:2450
186. McMahon DP, Cheung DL, Goris L, na Javier D, Salleo A, Troisi A (2011) J Chem Phys C 115:19386
187. Lee CK, Hua CC, Chen SA (2008) J Phys Chem B 112:11479
188. Lee CK, Hua CC, Chen SA (2011) Macromolecules 44:320
189. Chiu M, Kee TW, Huang DM (2012) Aust J Chem 65:463
190. Lukyanov A, Malafeev A, Ivanov V, Chen HL, Kremer K, Andrienko D (2010) J Mater Chem 20:10475
191. Lee CK, Pao CW, Chu CW (2011) Energy Environ Sci 4:4124
192. Lee CK, Pao CW (2012) J Chem Phys C 116:12455
193. Beljonne D, Cornil J, Muccioli L, Zannoni C, Brédas JL, Castet F (2011) Chem Mater 23:591
194. Tsige M, Grest GS (2005) J Phys Condens Matter 17:S4119
195. Yimer YY, Dhinojwala A, Tsige M (2012) J Chem Phys 137:044703
196. Marsh HS, Jayaraman A (2013) J Polym Sci Part B Polym Phys 51:64
197. Verlaak S, Beljonne D, Cheyns D, Rolin C, Linares M, Castet F, Cornil J, Heremans P (2009) Adv Funct Mater 19:3809
198. Meredig B, Salleo A, Gee R (2009) ACS Nano 3:2881
199. Poschlad A, Meded V, Maul R, Wenzel W (2012) Nanoscale Res Lett 7:1
200. Liu T, Cheung DL, Troisi A (2011) Phys Chem Chem Phys 13:21461
201. McMahon DP, Cheung DL, Troisi A (2011) J Phys Chem Lett 2:2737
202. Marcon V, Raos G (2006) J Am Chem Soc 128:1408
203. Yost SR, Wang LP, Van Voorhis T (2011) J Chem Phys C 115:14431
204. Reddy SY, Kuppa VK (2012) J Chem Phys C 116:14873
205. Reddy SY, Kuppa VK (2012) Synth Met 162:2117
206. Mou W, Ohmura S, Hattori S, Nomura K, Shimojo F, Nakano A (2012) J Chem Phys 136:184705
207. Hattori S, Mou W, Rajak P, Shimojo F, Nakano A (2013) Appl Phys Lett 102:093302
208. Fu YT, Risko C, Brédas JL (2013) Adv Mater 25:878
209. Clancy P (2011) Chem Mater 23:522
210. Verlaak S, Rolin C, Heremans P (2007) J Phys Chem B 111:139
211. Liu H, Lin Z, Zhigilei LV, Reinke P (2008) J Chem Phys C 112:4687
212. Cantrell RA, Clancy P (2012) J Chem Theory Comput 8:1048
213. Goose JE, First EL, Clancy P (2010) Phys Rev B 81:205310
214. Goose JE, Clancy P (2007) J Chem Phys C 111:15653
215. Goose JE, Killampalli A, Clancy P, Engstrom JR (2009) J Phys Chem C 113:6068
216. Tuckerman M, Berne BJ, Martyna GJ (1992) J Chem Phys 97:1990
217. Ryckaert J, Ciccotti G, Berendsen HJC (1977) J Comput Phys 23:327
218. Harvey M, Frabritiis GD (2009) J Chem Theory Comput 5:2371
219. Case D, Darden T, Cheatham T III, Simmerling C, Wang J, Duke R, Luo R, Walker R, Zhang W, Merz K, Roberts B, Hayik S, Roitberg A, Seabra G, Swails J, Goetz A, Kolossvry I, Wong K, Paesani F, Vanicek J, Wolf R, Liu J, Wu X, Brozell S, Steinbrecher T, Gohlke H,

Cai Q, Ye X, Wang J, Hsieh MJ, Cui G, Roe D, Mathews D, Seetin M, Salomon-Ferrer R, Sagui C, Babin V, Luchko T, Gusarov S, Kovalenko A, Kollman P. Amber 12. http://ambermd.org. University of California, San Francisco
220. Bowers KJ, Chow E, Xu H, Dror RO, Eastwood MP, Gregersen BA, Klepeis JL, Kolossvary I, Moraes MA, Sacerdoti FD, Salmon JK, Shan Y, Shaw DE (2006) In: Proceedings of the 2006 ACM/IEEE conference on Supercomputing, SC'06. ACM, New York
221. Smith Y (2002) Mol Sim 28:385
222. Limbach H, Arnold A, Mann B, Holm C (2006) Comput Phys Comm 174:704
223. Berendsen HJC, van der Spoel D, van Drunen R (1995) Comput Phys Commun 91:43
224. Morozov I, Kazennov A, Bystryi R, Norman G, Pisarev V, Stegailov V (2011) Comput Phys Commun 182:1974
225. Plimpton S (1995) J Comput Phys 117:1
226. Accelrys Software Inc. (2013) Material studio, release 6.1. Accelrys Software Inc., San Diego
227. Phillips J, Braun R, Wang W, Gumbart J, Tajkhorshid E, Villa E, Chipot C, Skeel R, Kale L, Schulten K (2005) J Comput Chem 26:1781
228. Eastman P, Friedrichs MS, Chodera JD, Radmer RJ, Bruns CM, Ku JP, Beauchamp KA, Lane TJ, Wang LP, Shukla D, Tye T, Houston M, Stich T, Klein C, Shirts MR, Pande VS (2013) J Chem Theory Comput 9:461
229. Matthey T, Cickovski T, Hampton SS, Ko A, Ma Q, Nyerges M, Raeder T, Slabach T, Izaguirre JA (2004) ACM Trans Math Softw 30:237
230. Rühle V, Junghans C, Lukyanov A, Kremer K, Andrienko D (2009) J Chem Theory Comput 5:3211
231. Hess B, Kutzner C, van der Spoel D, Lindahl E (2008) J Chem Theory Comput 4:435
232. Vmd – visual molecular dynamics. www.ks.uiuc.edu/Research/vmd
233. Humphrey W, Dalke A, Schulten K (1996) J Mol Graphics 14:33
234. Eargle J, Wright D, Luthey-Schulten Z (2006) Bioinformatics 22:504
235. Jmol: an open-source Java viewer for chemical structures in 3D. http://www.jmol.org
236. Mercury-crystal structure visualisation, exploration and analysis made easy. http://www.ccdc.cam.ac.uk/products/mercury/
237. GDIS, a program for the display and manipulation of isolated molecules and periodic systems. http://gdis.sourceforge.net/
238. Avogadro: an open-source molecular builder and visualization tool. http://avogadro.openmolecules.net
239. Hanwell MD, Curtis DE, Lonie DC, Vandermeersch T, Zurek E, Hutchison GR (2012) J Chem Inf 4:17
240. OVITO – the open visualization tool. http://www.ovito.org
241. Stukowski A (2010) Model Simul Mater Sci Eng 18:015012
242. Schrödinger LLC (2013) The PyMOL molecular graphics system, version 1.5.0.4. http://pymol.org/
243. Varetto U Molekel molecular visualization. http://molekel.cscs.ch. Swiss National Supercomputing Centre, Lugano
244. Sayle R, Milner-White EJ (1995) Trends Biochem Sci 20:374
245. Fox wiki. http://vincefn.net/Fox/
246. Favre-Nicolin V, Cerny R (2007) Z Kristallogr 222:105
247. QMGA: Qt-based molecular graphics application. www.qmga.sourceforge.net
248. Gabriel AT, Meyer T, Germano G (2008) J Chem Theory Comput 4:468
249. UCSF Chimera package. http://www.cgl.ucsf.edu/chimera
250. Pettersen E, Goddard T, Huang C, Couch G, Greenblatt D, Meng E, Ferrin T (2004) J Comput Chem 25:1605
251. BALLView – the BALL website. www.ballview.org/
252. Moll A, Hildebrandt A, Lenhof H, Kohlbacher O (2006) Bioinformatics 22:365

Top Curr Chem (2014) 352: 103–150
DOI: 10.1007/128_2013_462

Published online: 7 July 2013

Electronic and Optical Properties at Organic/Organic Interfaces in Organic Solar Cells

Shane R. Yost, Eric Hontz, David P. McMahon, and Troy Van Voorhis

Abstract In organic photovoltaic (OPV) devices the formation of free charges from a singlet excited state is the key step in converting light to electrical energy. However, questions still remain as to why the process is so fast and efficient in some OPV devices while not in others. Currently, it is not understood how the binding energy of the charge transfer state formed at an organic/organic interface, ~40 kT, is overcome in order to create free charge carriers. Given the difficulty of experimentally probing the electronic processes occurring at the organic/organic interface, it falls to theoretical and computational studies to provide essential insights into the processes occurring on the microscopic level. In this review we will cover the contributions made by theoretical studies to improve our understanding of the organic/organic interface. We will address the advantages and disadvantages of different theoretical approaches to studying the numerous interesting effects observed, such as shifts in the HOMO and LUMO levels due to the electrostatic environment, increased localization due to disorder, and the general impact of molecular orientation on different molecular properties. Further, we will discuss the currently proposed mechanisms of charge separation at the organic/organic interface and the implications that these mechanisms have on the choice of materials for use in OPV devices.

Keywords Band bending · Charge separation · Localization · Organic solar cell · Organic/organic interface

S.R. Yost, E. Hontz, D.P. McMahon, and T. Van Voorhis (✉)
Department of Chemistry, Massachusetts Institute of Technology, Cambridge, MA 02139-4307, USA
e-mail: tvan@mit.edu

Contents

1 Introduction

The role of photovoltaic (PV) materials in today's energy market is continually increasing, with the main challenge of efficiently and affordably harnessing the energy produced by the sun [1, 2]. A wide range of PV materials have emerged over the years including inorganic- [3–5], organic/organic- [2, 6, 7], and hybrid inorganic/organic-based PVs [8, 9]. In any photovoltaic device, the major step in creating electrical work from solar energy is the creation of free charges from an excited electronic state. In plants and bacteria, this is achieved via a chemical reaction in the reaction center of a protein [10]. For inorganic semiconductors, the absorbed photon immediately creates an electron and hole pair with a binding energy on the order of kT [11]. On the other hand, in organic semiconductor (OSC) materials, instead of the direct generation of free charge carriers upon absorption of solar energy, a coulombically-bound electron-hole pair (known as an exciton) is formed [12–15]. Excitons are the result of a small dielectric screening between the electron and hole, which leads to a large exciton binding energy. In organic photovoltaics (OPVs), this binding energy is overcome at an interface of two OSC materials, where there is an energy offset that drives the electron and hole apart [16, 17].

OPVs have the advantage of utilizing cheap, abundant materials which require less-demanding processing techniques than their inorganic counterparts, but their efficiency is currently limited to 12% [18]. In a functioning OPV device: (1) sunlight is absorbed and forms a singlet excited state, called an exciton; (2) the exciton diffuses to an interface; (3) at the interface the exciton forms a charge transfer

(CT) state, where now the electron and hole are on two different molecules; (4) the electron and hole separate and diffuse to the cathode and anode, respectively [16]. Schockley and Queisser [19] derived a fundamental thermodynamic limit for single-junction solar cells. Assuming that the PV has unity quantum efficiency above its band gap, the maximum efficiency is 33% and represents the limit for single junction inorganic and organic PVs [20]. To reach the Schockley–Queisser limit, each of the four processes needs to be optimized, which requires a fundamental understanding of each process, followed by intelligent engineering.

The blueprint for designing new and improved OSCs has not evolved much over the years, partly because some properties, such as absorption, were previously well known, so a good set of design principles already existed. Other properties, such as insufficient exciton and charge diffusion, can be partly addressed by minimizing the distance they have to travel (e.g., bulk-hetero-junction OPVs [21–24]) and optimizing contacts at the electrodes [25]. One process that does not yet have a good set of design principles, however, is the splitting of the exciton into free charges. Experimentally, it has been shown that the charge separation process at the organic/organic interface can be very efficient [7, 26, 27], but the processes governing this fast breakup of the exciton are not fully understood. Various experiments ascribe the efficiency to thermal storage of excess energy [28, 29] as vibrational energy (resulting in what are known as hot charge transfer states), which then provides the energy necessary to overcome the binding energy between the electron and hole of the charge transfer state. Other experiments appear instead to indicate that efficient charge separation occurs even from relaxed charge transfer states [30, 31]. Theory is therefore essential in filling in the gaps in our understanding and helping rationalize the disparity between different experimental results.

The key to rational design of fast and efficient exciton break-up at the organic/organic interface is understanding the interplay between molecular properties and device performance. At an organic/organic interface, the crucial properties are the highest occupied molecular orbital (HOMO) and lowest unoccupied molecular orbital (LUMO) levels of each material, the offset between the LUMOs (ΔL) and HOMOs (ΔH), and the difference between the acceptor LUMO and donor HOMO (E_{gap}), all of which are represented in Fig. 1. The energy gap, E_{gap}, is the maximum limit to the open-circuit voltage V_{OC}, and is reduced by the relative efficiency of charge separation vs recombination [32].

We should note that here we are using the terms HOMO and LUMO to describe the ionization potential (IP) and electron affinity (EA) of the materials. These terms are often used interchangeably in the literature, because, in the case of inorganic crystals, the HOMO and LUMO are the same thing as the IP and EA, respectively. For OPVs, however, the HOMO and LUMO are not equivalent to the IP and EA, and in fact, the HOMO and LUMO are very poor estimates of the IP and EA for most calculations. While many computational papers use the terms HOMO and LUMO, they are actually computing the IP and EA by $E_{\text{IP}} = E_{\text{cation}} - E_{\text{ground}}$ and $E_{\text{EA}} = E_{\text{ground}} - E_{\text{anion}}$, respectively, to obtain the more correct and accurate values. These values more closely resemble what is measured in experiments.

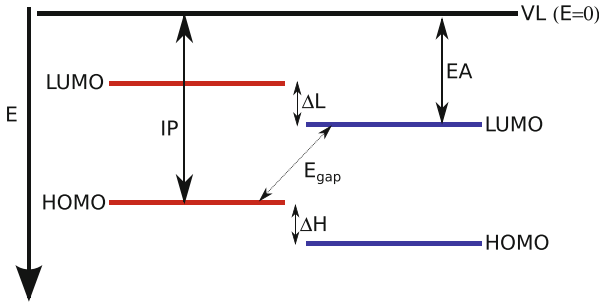

Fig. 1 General band diagram for an OPV device with the donor (*red*) and acceptor (*blue*) HOMO/IP and LUMO/EA levels. All of the energies are relative to the vacuum level (VL). The energy difference ΔL between the LUMO of the donor and acceptor provides the driving force for charge formation from an exciton on the donor, and E_{gap} is the maximum possible open-circuit voltage from an organic photovoltaic device

To model the kinetics of charge separation and recombination, the well known Marcus Theory approximation is often applied [33]:

$$k_{da} = \frac{2\pi}{\hbar} |V_{da}|^2 \sqrt{\frac{1}{4\pi k_B T \lambda}} \exp\left[-\frac{(\Delta G^\circ + \lambda)^2}{4\lambda k_B T} \right] \quad (1)$$

Here, the three important molecular parameters are the coupling between the donor and acceptor states V_{da}, the free energy change ΔG°, and the reorganization energy λ. Assuming the exciton is on the donor, then the free energy change for the formation of an interface charge transfer state is ΔL plus the change in the coulombic binding energy between the electron and hole, and the free energy change for charge recombination of the charge transfer state is E_{gap} minus the charge transfer binding energy. Thus, in order to create new design principles for molecules and device structures, we need to understand how the molecular parameters in (1) are dependent on the relative locations and orientations of the molecules and their environment.

With the key properties of charge separation and recombination in an OPV laid out, it is important to discuss the impact of the molecular packing and the structure found at the organic/organic interface on these properties. The molecular packing in OPVs is typically disordered due to the weak van der Waals intermolecular interactions holding the molecules together [12] and the processing techniques used to make the devices, such as spin-casting [34, 35]. The interplay between structural disorder, molecular distance and orientation significantly affect the electronic properties at the interface, which in turn affects the nature and mechanism by which free charge carriers can be generated. Without the inclusion of these considerations, any computational study will be incapable of accurately describing the performance of OPV materials. The geometry, electronic structure, and energetics of an isolated molecule/anion/cation are defined by its gas-phase Hamiltonian, but the

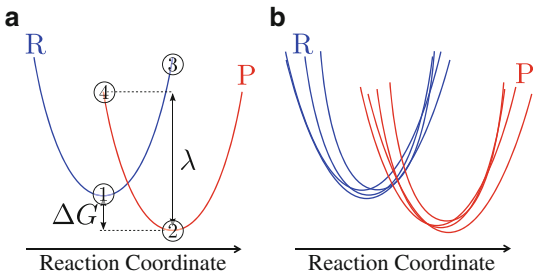

Fig. 2 Marcus free energies describing a transition from reactant (R) to product (P) states. (**a**) *Circles* indicate calculations for four-point determination of λ, ΔG. (**b**) Static disorder creates a distribution of reactant and product energy landscapes. Reprinted with permission from [36] Copyright 2010 American Chemical Society

surrounding molecules in an OPV cause perturbations through electrostatic and polarization interactions. Thus, the singlet, HOMO, and LUMO energies can be highly dependent upon the configuration of the surrounding molecules or, more importantly, the proximity to the interface. Disorder also affects intermolecular couplings and charge transfer state energies, because they are highly dependent upon the distance between and the relative orientation of the molecules involved. In effect, charge separation and recombination rates can vary substantially from location to location along an interface. This leads to a picture like Fig. 2, where the simple Marcus curves are replaced by many Marcus curves, all yielding their own unique rate that must be averaged to get experimentally relevant rates. Through careful study of the effect of the interface geometry and the impact of structural disorder on the electronic structure, general design rules for the interface can be created.

To show how computation can help with understanding the electronic and optical properties at organic/organics interfaces in OPVs, we outline the rest of this chapter as follows. First, we discuss a variety of computational methods useful for interface studies. We then look at some of the important physical effects learnt from computations, highlighting results from a variety of studies. Finally, we discuss the possible mechanisms for efficient charge separation at the organic/organic interface based on what we have learned from the computations, and conclude with future work and directions for this field.

2 Computational Methods

As discussed in the Introduction, the most relevant properties at the interface of an OPV are the singlet excited state energy, the HOMO/IP, the LUMO/EA, the charge transfer-state energy, and electronic coupling values that enter into the Marcus rate expression Eq. (1). In this section we discuss a variety of computational methods useful in calculating these properties.

Accurate calculations of OPV properties can be difficult. A major hurdle for applying computations to OPV interfaces arises due to the disordered nature

of the interface and surrounding layers. Gas-phase calculations are insufficient, and efficient periodic-type calculations, like those used for inorganic semiconductors [37, 38], are only applicable to systems with highly regular arrangements. In addition, experimental quantities of interest are actually ensemble averages over the disordered system. Thus, an ideal method not only needs sufficient accuracy for computing the desired property, but also has to be cheap enough to be used on a potentially large number of molecules and repeated many times over – not an easy feat. As a good first approximation one can assume that the relevant quantum states are localized on only one or two molecules because of the weak intermolecular interactions in the material giving rise to lots of disorder, which localizes the quantum states [12, 39].

Due to the demanding task of modeling the interfacial structure and the limits of modern-day computing, a range of computational methods have been applied and even combined to facilitate learning about these properties. In this section, we introduce a variety of these techniques, discuss some of their advantages and disadvantages, and highlight some of their common applications in the scope of interface studies. We first discuss single-scale methods, where only one level of theory is used, and then move to multi-scale methods, where multiple levels of theory are combined in order to concentrate accuracy where it is most needed, while still accounting for auxiliary effects. A common theme will arise: accuracy is often sacrificed for affordability, but recognizing where accuracy is important and where it isn't can lead to methods that are sufficient in obtaining the targeted properties.

2.1 Single-Scale Methods

The most widely used method in the study of interfaces and OPVs in general is ab initio quantum mechanics (QM). While there are a variety of QM flavors, they all involve solving for approximate solutions to the Schrödinger equation and require a self-consistent solution. The biggest differentiator between the various flavors is the way in which they incorporate approximations to electron–electron interactions.

One of the original approximate methods is the wavefunction-theory-based Hartree–Fock (HF) method [40]. The HF method is a single determinant method that does not include any correlation interactions between the electrons, and as such has limited accuracy [41, 42]. Higher level wavefunction-based methods such as coupled cluster [43–45], configuration interaction [40, 46, 47], and complete active space [48–50] methods include multiple determinants to incorporate some of the electron–electron correlation. Methods based on perturbation theory, such as second order Møller–Plesset perturbation theory [51], go beyond the HF method by perturbatively adding electron correlation. These correlated wavefunction-based methods have well-defined ways in which they approach the exact solution to the Schrödinger equation and thus have the potential to be extremely accurate, but this accuracy comes at a price [52].

Another very common approximate method is the electron-density-based Kohn–Sham density functional theory (DFT) [53–56]. Here the electron exchange

and correlation interactions are lumped into what is known as an exchange-correlation functional (simply referred to as a functional), of which many variations exist [57–61]. The different approximate functionals include pure functionals, such as LDA [53] and PBE [62], which only use properties of the electron density itself. Hybrid functionals, such as PBE0 [63] and B3LYP [64], incorporate some amount (specific to the functional) of HF exchange. Additionally, a recent class of functionals, known as long-range-corrected (LRC) functionals, smoothly separate electron interactions into short-range and long-range components and treat the short-range component using a typical functional and the long-range component using only HF exchange [65–68]. In most cases, it is more expensive for a wavefunction-based correlation method to achieve similar or greater accuracy than DFT [69]. In other words, DFT has the best cost-to-accuracy ratio and is, therefore, the most widely used QM method.

Since QM methods explicitly consider electrons, they are the most accurate methods available for interface studies. Their ab initio nature requires only an input geometry specifying the locations of the nuclei; there is no parameterization required, although the user should be aware of the limitations of the particular method and its approximations. Unfortunately, the accuracy of QM methods comes at a relatively high computational cost, limiting their applicability to only a few hundred heavy (non-hydrogen) atoms. Thus, the typical system size is limited to a small cluster of OSC molecules or less than 20 monomers, in the case of polymer systems. The effects of surrounding molecules need to be incorporated by combining QM calculations with more approximate methods, which will be discussed later when we visit multi-scale methods.

The most important use of QM in studying organic/organic interfaces is the accurate calculation of quantum state energies and the coupling between different electronic states. Of course, the ground state (S_0) energy is always calculated to provide the baseline for the rest of the states of interest. The next logical state to discuss is the lowest excited singlet state (S_1). Linear response time-dependent DFT [70–72] (TDDFT) can calculate excited state energies to within ± 0.3 eV and is the most commonly used excited-state method [73–75]. Recently, another excited state method based on enforcing non-Aufbau occupations of the orbitals during a typical ground-state-type calculation, called ΔSCF, was also shown to give S_1 energies with accuracy similar to those of TDDFT [76].

As discussed in the Introduction, the HOMO and LUMO energies are also important values. The HOMO and LUMO energies in Fig. 1 are exactly equivalent to the ionization potential (IP) and electron affinity (EA) of the material, respectively. For non-polymeric systems we can typically make the reasonable approximation that the disorder in an OSC material and the low coupling between molecules causes very localized states, and as such we can use the IP and EA of a single molecule. Koopmans theorem allows us to approximate the first IP of a molecule as the HOMO energy obtained from a ground state calculation, but for most approximate schemes, like HF and DFT, this is a very poor approximation. The estimate of the EA of a molecule from its LUMO energy using DFT or HF is even worse. In most approximate exchange-correlation functionals in DFT, there exists a common error that the electron interacts and repels itself [77, 78].

This self-interaction error (SIE) is what causes DFT to over-delocalize, and therefore greatly reduces its estimate of the HOMO and LUMO. For polymers this becomes an even bigger problem, since it greatly underestimates the band gap of the polymer. Therefore, to calculate a more accurate IP and EA, one needs to calculate the anion and cation energies and use $\mathrm{IP} = E(\mathrm{cation}) - E(\mathrm{S}_0)$ and $\mathrm{EA} = E(\mathrm{S}_0) - E(\mathrm{anion})$. It is important to emphasize, however, that the IP/HOMO and EA/LUMO in the bulk can vary substantially from what a gas-phase QM calculation predicts, due to the environment and delocalization effects.

Although the difference between the EA of the acceptor and the IP of the donor can give a preliminary estimate of the interface CT energy, the electrostatic interaction between the donor and acceptor must be included for an accurate value. Thus, it is better to calculate CT state energies explicitly. In addition to calculating singlet excited state energies, TDDFT can also calculate triplet excited states and CT states. Unfortunately, most DFT functionals are plagued by a problem in which the CT excitation energies obtained from TDDFT can be underestimated by more than 1 eV, partly due to insufficient long-range exchange in the functional [72, 79]. The LRC functionals discussed above help alleviate this problem in TDDFT calculations and achieve more accurate CT state energies [80]. Another accurate method for calculating CT states is the constrained DFT (CDFT) method [81–83], which works by applying a potential across the system in order to constrain specified regions with specified amounts of charge and spin. Therefore, a CT state can be easily formed by constraining one extra electron on the acceptor molecule and one less electron on the donor molecule.

Last, but not least, QM methods are used to obtain couplings $V_{\mathrm{fi}} = \langle \mathrm{f}|\mathrm{H}|\mathrm{i}\rangle$ relevant to OPVs, which are

$$\text{Exciton diffusion} : \langle \mathrm{D1}^{*}\mathrm{D2}|H|\mathrm{D1D2}^{*}\rangle$$

$$\text{CT-state formation} : \langle \mathrm{D}^{*}\mathrm{A}|H|\mathrm{D}^{+}\mathrm{A}^{-}\rangle$$

$$\text{CT-state recombination} : \langle \mathrm{D}^{+}\mathrm{A}^{-}|H|\mathrm{DA}\rangle$$

$$\text{Charge diffusion} : \langle \mathrm{D}^{+}\mathrm{D}|H|\mathrm{DD}^{+}\rangle(\langle \mathrm{A}^{-}\mathrm{A}|H|\mathrm{AA}^{-}\rangle)$$

A number of methods, such as fragment excitation difference [84] and CDFT with configuration interactions [85, 86], are capable of calculating these couplings both affordably and quantitatively [87]. In addition, semi-empirical methods can also calculate these couplings – typically by computing the coupling between the relevant HOMO and LUMO orbitals involved in the electronic transition [16, 88–90].

Semi-empirical methods are particularly appealing methods for treating large OPV systems. While there exists a wide variety of semi-empirical methods, many of them focus on accurately treating the π-conjugated, or at most the valence electrons, which are largely responsible for the relevant properties of an OPV [91–95]. The spirit of semi-empirical methods is to ignore or approximate partially

(or fully) the two-electron integrals of HF theory, which are by far the most expensive part of the calculation. Most semi-empirical methods parameterize some aspect of the calculation, using parameter values tuned to reproduce experimental or high-level computational data. While the mean-field nature of exact HF results in the exclusion of dynamic correlation, the parameterization of semi-empirical methods to reproduce data can account, in a sense, for correlation without having to go beyond the basics of HF.

Speed is the main advantage of semi-empirical methods and allows them to be used on systems considerably larger than those treatable through QM, making calculations on large arrays of molecules and even large polymers tractable. Of course, their speed comes at a cost. They are typically less accurate than DFT and correlated wavefunction methods, and, just like choosing the proper functional in DFT, their performance can depend on which type of semi-empirical approximation is used [96–98]. They are reasonably accurate at predicting charge distribution in a large system and can be used to determine the energetics of a charge or CT state in a polarizable environment [99, 100], such as an interface [101, 102].

While semi-empirical models simplify QM by parameterizing certain values of an HF calculation, their approximations are meant for treating a broad range of problems. When dealing with a narrower range of problems, however, it is often possible to make more extreme approximations that simplify the solution even further. Such an approach has been taken towards treating charge transport in OPVs [103]. At a basic level, an excess charge moving through an organic semiconductor results in nuclear displacements and electronic polarization of the surrounding molecules. To be able to determine quickly and accurately the changes in the different molecular properties at the organic/organic interface, one can neglect nuclear displacements, which occur mainly on the molecule on which the charge is localized, and consider only the purely electrostatic interactions between the charge and its environment. These types of models are referred to as micro-electrostatic models, and they approximate each molecule by a chosen number of polarizable sites (dipoles and/or quadrupoles) and calculate the polarization-induced dipoles resulting from excess charges in the system [104–106]. The number of polarizable sites and where they are placed have many possibilities, but a few dominant prescriptions exist. For instance, each molecule in the system can be represented by a single polarizable site, or polarizable sites could be placed at the center of the conjugated rings of each molecule. In effect, the electrons of a molecule are course-grained into multipole moments.

Micro-electrostatic methods are not built based on HF theory and are even cheaper than semi-empirical treatments. They do require self-consistent solutions, since each polarizable entity is polarized by the charge and all the other polarizable sites in its surroundings, but, as a result, screening effects are accounted for. Systems as large as 2,806 [100] molecules have been treated with micro-electrostatic models. In general, they are useful in determining how a molecular environment impacts charge dynamics, and they have been used to characterize interfacial dipoles [107], determine how the size and orientation of molecular quadrupolar moments affect interface energetics [108], and determine the effects

of crystal defects on charge mobility [103]. On the other hand, micro-electrostatic methods are limited and cannot be used to calculate couplings or excitation energies, and they can only obtain absolute charge energies by including an energy shift that accounts for the energy of the charged molecule in the gas phase. Thus, they are often times used as part of a multi-scale approach.

2.2 Multi-Scale Methods

Semi-empirical and micro-electrostatic methods have the advantage of being cheap enough to treat large systems and thus incorporate some effects from the molecular environment and also calculate ensemble averages, but simulation cells large enough to acquire enough samples for a sufficient ensemble average are hard to come by. Instead of performing an average over molecules in a giant system, one often runs a dynamics simulation on a smaller system, calculates the quantity of interest for one or a few molecules in the system during different points in the dynamic trajectory, and performs a time average [109, 110]. This time average is equal to the ensemble average in the limit of an infinitely long dynamics trajectory by the ergodic hypothesis.

The most common method for performing a dynamics simulation is molecular dynamics (MD). In MD, Newton's equations of motion are solved at a finite temperature using a molecular mechanics (MM) force field to calculate the system's energy. Instead of explicitly treating all the electrons of a system, MM force fields treat each atom as a particle with a van der Waals radius, constant effective charge, and polarizability. The force field contains potential energy functions that define the energy of bonds, angles, and dihedrals within a molecule. Additionally, force field parameters are not generally transferable between different molecules. Currently, force fields exist for very few OPV molecules, so one must usually create a new force field for a given OSC molecule [36]. The typical scheme for creating force fields involves matching the parameters to QM calculations and, sometimes, available experimental data (such as the material density) [111]. Difficulties arise in the parameterization of force fields for polymers, because QM is too expensive and experimental data can be difficult to trust, due to the existence of multiple possible structures and morphologies, which can depend on the molecular weight and even how the material was processed (e.g., two known crystal phases of poly (3-hexylthiophene-2,4-diyl) (P3HT) exist [112, 113]).

Another issue with MD is that certain regions of phase space (the molecular configurations available for the system to explore at a chosen temperature) will be favored, and the regions favored can depend on the force field [114, 115]. While this is not as big an issue for OSCs as it is for simulations of protein folding, it can still play a role for polymer MD simulations. Certain regions of phase space contain deep local minima, making a simulation highly dependent on the initial ($t = 0$) configuration, and it is therefore important to include any available experimental information during the setup [116–119]. In most cases, experimental

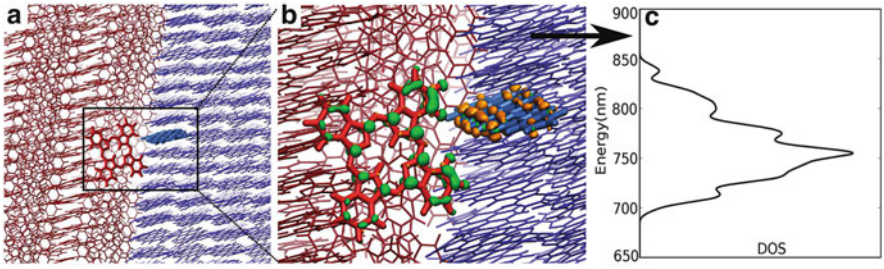

Fig. 3 Illustration of the QM/MM method. (**a**) Disordered cell of the H_2 Pc/PTCBI system described by MM. (**b**) Selection of an H_2 Pc and PTCBI dimer pair at the interface used for a calculation of the charge transfer state energy. (**c**) Density of states plot obtained by repeating the calculation over different snapshots of a MM trajectory. Reprinted with permission from [110] Copyright 2011 American Chemical Society

data on the interfacial packing is not available to guide the initial generation of the simulation interface. So instead, as a starting point, the isolated systems are placed next to one another with the desired interface orientation. While this might not be an ideal initial geometry, it gives a good starting point and can still capture most of the relevant physics at the organic/organic interface.

By calculating energies using force fields, rather than approximate solutions to the Schrödinger equation, MD simulations can handle extremely large system sizes with thousands to millions of atoms, depending on the complexity of the force field, just like the micro-electrostatic calculations. Unfortunately, the accuracy of MM force fields can be quite low compared to QM methods, and energies of excited states and couplings cannot be calculated through MM. However, MM simulations do provide snapshots of nuclear geometries that can be used in QM or semi-empirical calculations. Of course, high-level calculations cannot be run on the large system cell, so a method known as QM/MM is typically used to incorporate the effects of the molecular environment and disorder. In the QM/MM method, the simulation is divided into system and bath regions, the chosen system being small enough to afford the use of an accurate QM calculation. The bath then interacts with the system during the QM calculation through electrostatic and van der Waals interactions, unless the system and bath regions are divided across a bond (e.g., for a large polymer), in which case linker atoms are necessary [120]. MM atoms are represented in the QM calculation as static charges and oscillating dipoles, the specifics of which are determined by the force field.

QM/MM calculations can be combined with MD to calculate an ensemble average for a quantity of interest. The typical procedure for such a study is as follows [110], and is illustrated in Fig. 3. An MD trajectory is calculated at constant pressure and temperature. A snapshot is taken from the trajectory (Fig. 3a). A molecule or dimer (the solute) of the simulation cell are selected. QM is used on the solute to calculate the quantity of interest under the influence of the solvent (Fig. 3b). This procedure is then repeated for many different dimer pairs and/or snapshots from the trajectory, yielding an overall density of states for the calculated state (Fig. 3c).

There are a few different things to consider with the QM/MM method. First, as mentioned above, more care needs to be taken when dividing the system across a covalent bond. Another major issue is selecting the set of MM parameters to represent the MM region, since only a few molecules related with OPVs have existing parameters, for example C_{60} [121] and P3HT [122]. The choice of MM parameters, especially the polarizability parameters, can greatly alter the results. Finally, the results can depend on the size of the QM region. Delocalization can only occur in the QM region, and so one must be careful that delocalization in the system and states is not a significant effect, otherwise a large QM region is needed.

A simpler option for incorporating effects from the environment into a QM calculation is to use a dielectric continuum model [123–125]. Since the molecules in an OPV are relatively static, charge solvation comes nearly entirely from the high-frequency dielectric resulting from the response of the electrons. Even though the actual charge solvation is due to non-continuous surroundings, using a continuous dielectric can actually capture quite a lot of the important effects. Similar to a QM/MM calculation, the electronic structure calculation is solved self-consistently in response to the surrounding dielectric, but the calculation only requires the input geometry of the QM system and a few parameters, such as the effective dielectric constant of the surroundings. Unfortunately, an effective dielectric constant of the system is not always available, and the calculated energy can be sensitive to the choice of dielectric, especially for cation/anion and CT states. In addition, a continuous dielectric is a poor model for the environment of a molecule very near to an interface, since there are two different types of polarizable molecules surrounding it.

With the exception of semi-empirical calculations on large systems, the methods discussed so far do not provide access to properties of delocalization of the electronic states in a material. One way to obtain delocalization is by first computing the energy of each molecule, or in the case of a polymer, each monomer unit, and the electronic coupling between them. Then one can construct a Hamiltonian, the eigenstates of which are the delocalized states of the system [99]. This is exemplified by the work of McMahon et al. in which they compute the electronic structure of P3HT at the interface with amorphous phenyl-C61-butyric acid methyl ester (PCBM) [109] through the use of a localized molecular orbital method [126] to obtain the eigenstates of a system containing thousands of atoms with a quantum chemical level of detail. To make things simpler and drastically cheaper, one can take a Hückel-type approach and consider only nearest-neighbor couplings. These types of simulations can provide a good qualitative estimate of the amount of delocalization within an OPV device.

Each of the different methods discussed here have their own sets of advantages and disadvantages. In order to select the right type of method one needs to ask many questions like how large is the system I want to calculate? What electronic properties do I want to calculate? Is delocalization important for my system? The answer to these types of questions will help in selecting the type of method(s) required for modeling a given organic/organic interface.

3 What Can Computations Tell Us?

The lack of understanding of the charge-formation and separation processes at the organic/organic interface makes it difficult to know whether a new OSC material will perform well in an OPV device. There are many papers that describe how to optimize the properties of organic semiconductors in order to achieve a better OPV device [20, 127–129]. Almost all of these studies, however, focus on optimizing the HOMO and LUMO levels of the donor and acceptor materials, and even more so on optimizing the bulk hetero-junction polymer/PCBM OPV device. Polymer chemists work on systematically modifying the energy levels in polymers in order to maximize the HOMO and LUMO levels with respect to those of PCBM. Optimization of the bulk HOMO and LUMO levels is a straightforward goal, but in actual devices factors such as polymer morphology and charge recombination complicate the optimization [130]. To avoid unforeseen problems when making an OPV device with a new material, we need an improved understanding of the processes occurring at the organic/organic interface.

In the rest of this section we discuss some of the more recent and important work on organic/organic interfaces. While not comprehensive, we cover key research on different molecular properties of OSCs at the organic/organic interface. As a point of reference, we start by discussing the performance of different methods on bulk-phase OSC materials and then lead into characterizing organic/organic interfaces. At the organic/organic interface we start with how the HOMO level, LUMO level, and exciton energy do or do not change when approaching the interface, followed by a review of charge transfer states at the interface. Finally, we discuss calculations of electronic couplings and the overall rate of charge separation and recombination.

3.1 Band Offsets

The generally-used optimization strategy of OPVs based on HOMO and LUMO levels can be difficult using experimental techniques. It can take a significant amount of time to synthesize new molecules or polymers, and the measurement of the HOMO level and, even more so, the LUMO level has limited accuracy. The experimental measurements are typically worse and less reliable than DFT estimates, due to the accuracy of the experimental techniques – on the order of 0.2–0.5 eV [131, 132]. Changes in the HOMO and LUMO on the order of 0.1 eV can make a difference in device efficiencies of a couple of percent. Therefore, having a set of simulations that yield fast and more reliable HOMO and LUMO levels of OSCs is very valuable.

There are two main methods used to compute the HOMO and LUMO levels of monomers or polymer fragments – DFT and semi-empirical methods. Hill et al. used the intermediate neglect of differential overlap (INDO) Hamiltonian

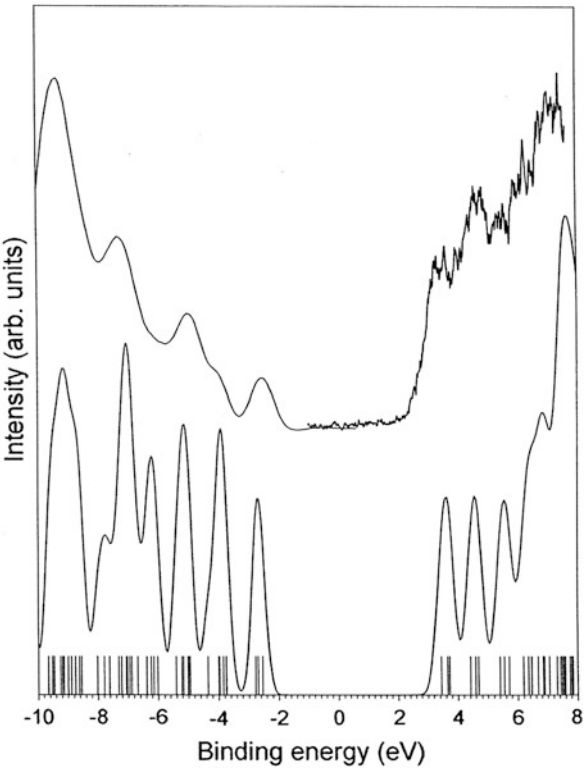

Fig. 4 Comparison between UPS and IPES spectra measured from an Alq_3 thin film (*top*) and INDO-simulated UPS and IPES spectra (*bottom*). The energy scale is referenced to the Fermi level. A compression factor of 1.2 is used to simulate the UPS spectrum and the FWHM is set to 0.5 eV prior to compression. The *vertical bars* at the bottom of the graph refer to the calculated energies of the molecular orbitals. Reprinted with permission from [133]. Copyright 2000 Elsevier B.V.

and a number of empirical corrections to simulate the density of states of an Alq_3 monomer [133]. Figure 4 shows that the experimental and theoretical density of states have similar shapes, but due to the corrections that must be added after the INDO calculations, this method cannot predict HOMO and LUMO levels of Alq_3. The first correction is a compression of the INDO Hamiltonian energy levels by a factor of 1.2–1.3, which is performed in order to compensate for the lack of electron correlation [98]. To correct for the lack of a polarizable environment, the theoretical HOMO and LUMO are shifted to match the HOMO and LUMO from the experiment. Similar results were obtained by Zhan et al. for the density of states of an Alq_3 monomer [134], but in this case, no compression factor was needed, because the authors used DFT. They did, however, still need to shift their peaks to correct for the lack of an environment and match the experimental HOMO and LUMO. While these fast calculations in the gas phase can be used for quick screening of molecules that vary by the addition of side-groups, the main drawback for prediction purposes is the neglect of environment effects.

The simplest approach to correcting for the effects of a polarizable environment and toward more predictive capabilities is to use a polarizable continuum model to simulate the environment. The simplest polarizable continuum model is the Born model [135], where the environment is approximated by a continuous dielectric

medium that solvates a charge in a spherical cavity. Most quantum chemistry programs have more sophisticated models built into them, which also require the specification of a dielectric. If no experimental data on the dielectric of a molecular crystal is available, one can use a calculation of the molecular polarizability and the Clausius–Mossotti equation to approximate the dielectric. DFT methods embedded in a polarizable continuum environment can achieve a mean absolute error between theory and experiment of 0.2 eV for both the HOMO and LUMO levels [136, 137]. This provides a relatively quick and simple technique for screening the HOMO and LUMO values of OSC materials.

Recently, a more accurate treatment of the environment using the mixed QM/MM method was performed on an Alq_3 crystal [36] using a force field of the OPLS-type with parameters derived from experimental values and monomer calculations as outlined in Difley et al. [36]. As described in the previous section, one or two molecules are selected out of a larger system and treated with DFT, while the rest of the system is treated classically. The calculations were performed on snapshots obtained from a constant pressure and temperature dynamics trajectory on a large crystal cell of Alq_3. The calculated thermal averages obtained for the HOMO, LUMO, singlet, and charge transfer states all agreed with experimental values to within a few tenths of an eV. By turning on and off the polarizable environment, they found that it stabilizes the HOMO and LUMO levels by 0.55 and 0.65 eV, respectively. Averaging over the thermal trajectory showed thermal fluctuations in the HOMO and LUMO energies of only 50 meV, which for the HOMO and LUMO is significantly smaller than the widths of the experimental curves shown in Fig. 4. One reason for the disagreement is that there is no delocalization between the molecules, since each calculation is done with a quantum region of one molecule. Also, during the dynamic trajectory, the bond lengths of the monomers were constrained, which caused them to be very rigid throughout the simulations, which in return created much smaller fluctuations in the HOMO and LUMO levels. Due to the significant time and effort required to parameterize the corresponding force field and to obtain a sufficiently thermally sampled system, this type of simulation is not likely to become a useful technique for screening OSC materials in the foreseeable future. Nevertheless, this QM/MM study on Alq_3 demonstrates the importance of including a more detailed environment and proper sampling of the system in order to obtain more quantitative results.

3.2 Band Bending

The discontinuity at the organic/organic interface makes it even more important to account accurately for the environment, and as such, any model of the organic/organic interface needs to have some way of modeling the interfacial geometry between the donor and acceptor regions. As mentioned earlier, the choice of initial geometry for any dynamics simulation has a large impact on the final geometry of the simulation, due to the very large energy barriers for molecular rearrangement

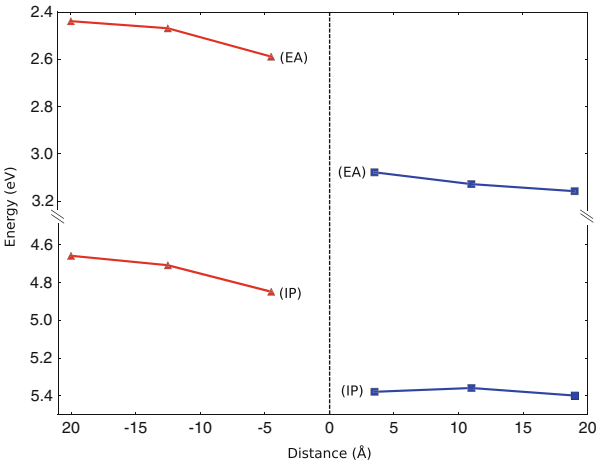

Fig. 5 Band diagram for the H_2Pc (*left*) and PTCBI (*right*) interface. The HOMO (IP) and LUMO (EA) levels decrease in H_2Pc when approaching the interface by over 0.2 eV, while the HOMO and LUMO levels spread apart in PTCBI by 0.1 eV. Reprinted with permission from [110]. Copyright 2011 American Chemical Society

in OSCs. Furthermore, the lack of experimental structural information at the organic/organic interface makes this problem even more difficult to undertake. Most models of the organic/organic interface assume some sort of initial crystalline geometry [107–110, 138]. However, there are a number of different ways to pack the molecules at the interface which, as we will discuss later, can be very important. If experimental data are available, this can aid in making the choice of what initial packing orientations to use. Otherwise, the choice of packing at the interface can be made to minimize the amount of empty space at the interface. For further information on construction of organic/organic interface geometries, we direct the reader to the chapter by Zannoni and co-workers in this book and other review papers on the subject [139–141]. The majority of works reviewed in the rest of this chapter utilize initial crystalline geometries for modeling the organic/organic interfacial structure.

Using the polarizable QM/MM method Yost et al. modeled the interface between metal-free phthalocyanine H_2 Pc and 3,4,9,10-perylenetetracarboxylic bisbenzimidazole PTCBI [110]. The authors chose the interfacial orientations of the donor and acceptor molecules based on the criteria of picking the crystal interfaces that had the maximum overlap with each other and then placed them 0.4 nm apart. A 1-ns constant pressure and temperature dynamics simulation was run to obtain thermal sampling. The polarizable QM/MM method obtained quantitative agreement with the experimental E_{gap} of the OPV system. All the HOMO and LUMO values, however, were too low by about 0.4 eV due to the choice of a small basis set. Using the interfacial simulation cell, the authors selected one or two molecules at different locations relative to the organic/organic interface to create a band diagram like that in Fig. 1. The band diagram obtained for the H_2 Pc/PTCBI interface, shown in Fig. 5, shows that the HOMO and LUMO levels are, in fact, not the same at different locations in the interface system, and as such, the system displays some amount of band bending. The observed band bending is very important, because it increases the energy of any charge transfer state at the interface by more than 0.2 eV.

Due to the nature of the QM/MM simulations used on the H_2 Pc/PTCBI interface system, the band bending observed cannot be due to charge transfer across the interface. When only one molecule is treated by quantum mechanics, there is no way to have any type of partial charge transfer, which is the main effect people think of when they think of shifts in the HOMO and LUMO levels. Inspired by work on the strong donor tetrathiafulvalene (TTF) and strong acceptor tetracyanoquinodimethane (TCNQ) interface that found a vacuum level shift at the organic/organic interface on the order of 0.6 eV [142], Avilov and coworkers modeled the partial charge transfer in a TTF/TCNQ dimer using a variety of methods [143]. By applying an external electric field across the dimer, the authors looked at the amount of electron transfer using restricted and unrestricted DFT and HF, as well as the complete active space self consistent field (CASSCF) method. The restricted HF and DFT methods perform similarly to the CASSCF method for charge transfer less than 0.1 electrons, but soon above this threshold, CASSCF quickly jumps up to one electron transferred, indicating ionization of TTF. Neither restricted HF nor DFT undergo an ionization event; instead, they both slowly increase the number of electrons transferred to more than 1.5 electrons. Unrestricted HF and DFT, however, do predict ionization, but at a much lower potential than CASSCF and, furthermore, they tend to under-predict the amount of electron transfer at all applied fields. The authors found that the maximum amount of charge transfer in the TTF/TCNQ dimer was 0.12 electrons, and so they used the more affordable restricted DFT method. Any partial charge transfer greater than 0.1 electrons should be investigated using a high level method like CASSCF in order to make sure it is not an artifact of the method being used.

Partial charge transfer in organic molecules occurs when the lowest energy state, which is the neutral ground state, mixes with higher energy charge transfer states. In a donor (D) and acceptor (A) system with a neutral ground state, $\Psi_0(\mathrm{DA})$, and excited charge transfer states, $\Psi_{\mathrm{CA}}(\mathrm{D^+A^-})$ and $\Psi_{\mathrm{AC}}(\mathrm{D^-A^+})$, the ground state wavefunction $\Psi(\mathrm{DA})$ will be

$$\Psi(\mathrm{DA}) = a\Psi_0(\mathrm{DA}) + b\Psi_{\mathrm{CA}}(\mathrm{D^+A^-}) + c\Psi_{\mathrm{AC}}(\mathrm{D^-A^+}) \tag{2}$$

where, from first order perturbation theory, the mixing coefficients, b and c, are just $V_{\mathrm{CA}}/E_{\mathrm{CA}}$ and $V_{\mathrm{AC}}/E_{\mathrm{AC}}$, respectively. Here V is the coupling between the ground state and the corresponding charge transfer state and E_i is the excitation energy of the charge transfer state. The amount of partial charge transferred is then just the difference between the forward charge transfer from the $\mathrm{D^+A^-}$ state and the backward charge transfer from the $\mathrm{D^-A^+}$:

$$q = \left(\frac{V_{\mathrm{CA}}}{E_{\mathrm{CA}}}\right)^2 - \left(\frac{V_{\mathrm{AC}}}{E_{\mathrm{AC}}}\right)^2 \tag{3}$$

However, the charge transfer state where the anion is on the donor and the cation is on the acceptor is usually significantly higher in energy and, as such, does not contribute any significant amount of back charge transfer. Therefore, the amount

of partial charge transfer predicted by a method will depend on the coupling between the ground and charge transfer states, as well as the excitation energy of the charge transfer state. When using DFT to analyze the amount of charge transfer, one then needs to be careful when choosing a functional, because most functionals, except for those with very large amounts of exact HF exchange or long range corrected functionals, grossly underestimate the charge transfer state energy and, as such, will overestimate the amount of partial charge transfer in the ground state [72]. Semi-empirical methods will have exactly the opposite problem; they typically overestimate the charge transfer state energy. Finally, the amount of partial charge transfer will also depend on the relative molecular orientation, because of the orientational dependence of the coupling and charge transfer state energy.

Given some partial charge transfer between the donor and acceptor molecule, q, and a separation distance, r, the dipole moment is then qr. Avilov and co-workers used the BHandHLYP functional in DFT, which has 50% exact HF exchange, to compute the induced dipole moment of the TTF/TCNQ dimer. By comparing the induced dipole moment computed through DFT and the dipole moment created by the partial charge transfer for the TTF/TCNQ dimer, shown in Fig. 6a, it was found that a significant portion of the induced dipole moment originates from induced polarization of the two molecules and not partial charge transfer. The faster-than r^{-1} decay of the charge transfer contribution to the dipole moment is due to the coupling's dependence on the overlap between the ground and charge transfer states. In fact, the partial charge transfer quickly drops to zero after 0.5 nm. The dipole moment created by the polarization of the two molecules lasts longer than 0.8 nm, and is therefore a very significant effect.

The induced dipole moment creates an electric field that will shift the HOMO and LUMO levels of the two molecules, and this effect is plotted in Fig. 6b. Here, the TCNQ/TTF dimer was placed 0.35 nm A apart and then translated in a direction perpendicular to the separation direction, yielding shifts in the HOMO and LUMO as large as 0.4 eV. The oscillations in the energy shifts between 0.0 and 0.4 nm come from oscillations in the coupling that are due to the overlap's sensitivity to relative molecular orientation. Interestingly, the shift in the HOMO and LUMO due to induced polarization changes sign past 0.8 nm While this is not important for a dimer, in a condensed phase system, such as an OPV, there will be a number of molecules at this relative location, making it important to model the condensed phase conditions properly. While the partial charge transfer in this strong donor/acceptor system is non-negligible, for many OPV systems the induced polarization effect will be much more important for any HOMO and LUMO level shifts.

A number of electrostatic effects besides partial charge transfer or induced polarization can induce changes in the HOMO and LUMO levels of an OSC. Significant band bending at the pentacene/C_{60} donor/acceptor interface has been predicted by a number of groups [102, 107, 108]. C_{60} and its derivatives are widely used acceptor materials because of their high electron mobility and low LUMO level. The high symmetry of C_{60} makes it much less susceptible to disorder and, as such, it is much simpler to model when constructing an organic/organic interface. The donor, pentacene, is a planar molecule, and its interactions are much more

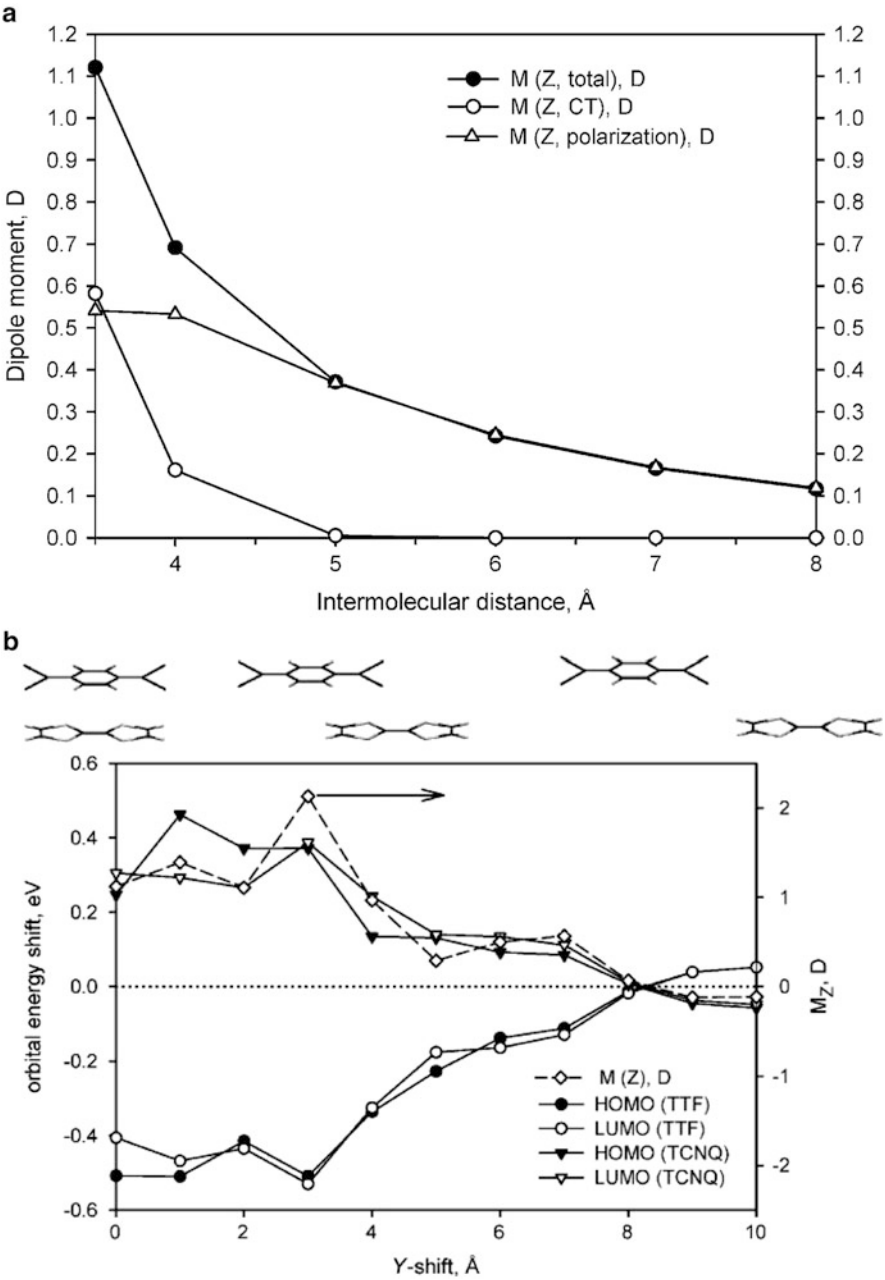

Fig. 6 (**a**) Evolution of the component of the dipole moment normal to the molecular planes of TTF/TCNQ dimer obtained from the DFT calculations (*filled circles*), the Mulliken charges (*open circles*), and the polarization component (*open triangles*). (**b**) Evolution of the shift of the HOMO (*filled*) and LUMO (*open*) levels of TTF (*circles*) and TCNQ (*triangles*) and the dipole moment (*open diamonds*) as a function of the lateral translation along the *Y* molecular axis. Adapted with permission from [143]. Copyright 2009 WILEY-VCH Verlag GmbH and Co. KGaA, Weinheim

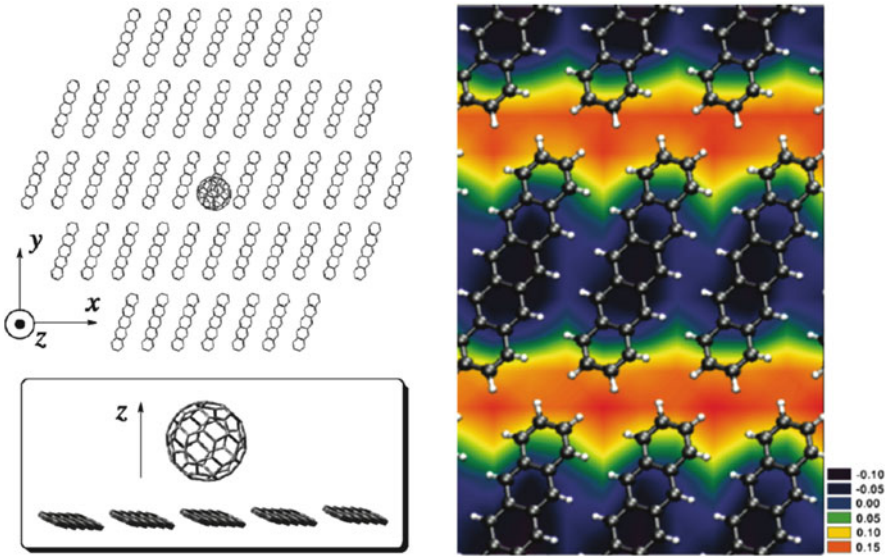

Fig. 7 C_{60} molecule above a plane of pentacene units (*left*) and amplitude of the *z*-component of the induced dipole on the C_{60} molecule as a function of its position on the (*x*,*y*) plane, as calculated using the VB/HF-AM1 model (*right*). Reprinted with permission from [107]. Copyright 2010 American Chemical Society

dependent on its relative orientation with its surroundings. An important aspect of pentacene that makes it very desirable is that the singlet excited state undergoes a process called fission and breaks up into two triplet states, which can result in two charges from one photon [144]. The ability to create two charges per photon is very appealing, since it pushes the Schockley–Queisser limit from 33% to above 40% [144]. This will not matter, though, if the triplet state does not have enough energy to break up at the organic/organic interface, which is why many models have been used on this interface to understand it better.

Linares and co-workers studied the pentacene/C_{60} interface using both the valence bond/Hartree–Fock (VB/HF) model and micro-electrostatic methods [107]. When a C_{60} molecule was placed above the plane of a pentacene molecule, the authors found that the HOMO and LUMO levels shifted in C_{60} by about 0.1 eV, though not due to any charge transfer. The measured change is due to another type of electrostatic interaction, the quadrupolar field created by pentacene interacting with the C_{60} molecule. Dipolar C–H bonds in the pentacene molecule create a strong quadrupolar field, with the negative end on the more electronegative C atoms in the core of the molecule and the positive end of the quadrupole on less electronegative H atoms on the outer part of the pentacene molecule. The effect of the quadrupolar field was modeled by placing a C_{60} molecule over a single layer of the (01–1) plane of pentacene and calculating the induced dipole moment in C_{60} as a function of location over the pentacene plane. The resulting plot is shown in Fig. 7. The magnitude of the induced dipole is smaller in the 2D array than in the dimer

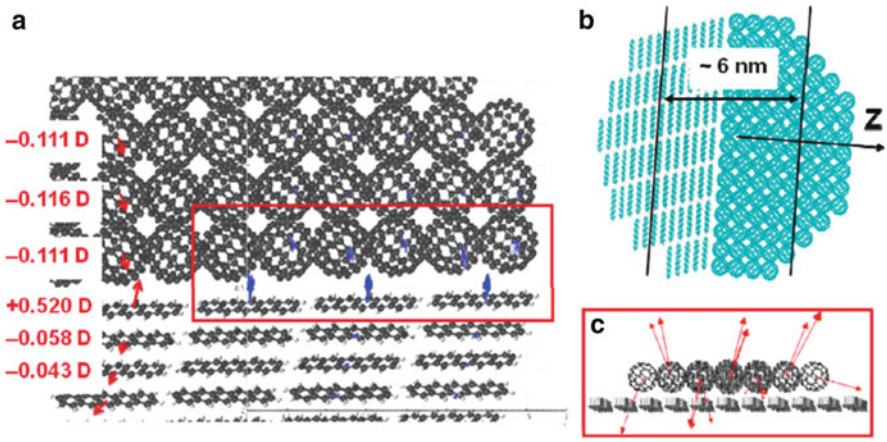

Fig. 8 Quadrupole-induced dipoles at the pentacene(01–1)/C_{60} (001) interface (**a**, **b**) individual induced dipoles (*blue*) and layer-averaged induced dipoles (*red*), as calculated using the micro-electrostatic model. The dispersion of the induced dipole moments on the C_{60} molecules at the interface is highlighted in the *inset* (**c**). Adapted with permission from [107]. Copyright 2010 American Chemical Society

picture, because in the 2D array the positive end of the surrounding pentacene molecules subtract from the effect of the negative pentacene core. While the cause of the negative-to-positive shift in the HOMO and LUMO level in the pentacene/C_{60} system is different from the TTF/TCNQ system, both studies show the importance of including a detailed environment.

Finally, Linares and co-workers created a 3D crystalline interface between the (01–1) face of pentacene and the (001) interface of C_{60}, shown in Fig. 8b. The induced dipole in the C_{60} molecules in the 3D system are no longer in a simple repeated pattern. As shown in Fig. 8c, the magnitude and the orientation of the induced dipole in C_{60} has large fluctuations depending on the location in the crystal. In fact, some C_{60} molecules have induced dipoles pointing exactly in the opposite direction of the average induced dipole at the interface (see Fig. 8a), which shows a more consistent behavior. As the C_{60} molecules get further away from the pentacene interface, their induced dipole decreases. A little surprising, though, is the positive dipole in the first layer of pentacene. This effect is due to the positive part of the quadrupolar field produced from the second layer of the pentacene interacting with the interfacial layer. This does not exist in any of the other pentacene layers, because there is an equal field above and below the pentacene molecules; only at the interface does this trend get broken. Therefore, in the pentacene/C_{60} interface crystal, an induced dipole that shifts the HOMO and LUMO levels of the materials is created from the quadrupolar field of the pentacene molecule. As is the common theme throughout this section, the large fluctuations in the C_{60} induced dipole and the change in the average induced dipole in pentacene stress the importance of modeling a 3D interfacial structure and sampling different locations within the simulation cell.

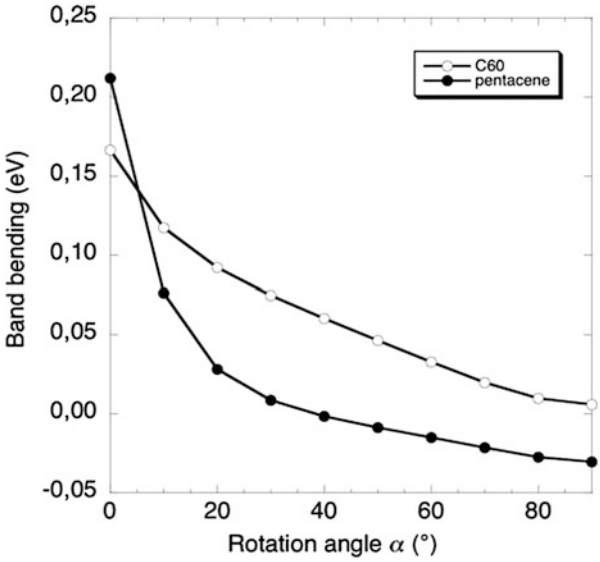

Fig. 9 Bending of the energy levels of pentacene and C_{60} as a function of the rotation angle α Reprinted with permission from [102] Copyright 2012 Wiley Periodicals, Inc

The sampling of the (01–1)/(001) interface by [107] does not consider the effect of different relative orientations between the pentacene and C_{60} molecules. Experimental studies have found that pentacene typically packs along the (001) plane [145], which has the pentacene molecule placed in a direction almost perpendicular to the (01–1) plane. The study by Verlaak et al. used a micro-electrostatic method to analyze the difference between these two packing directions and how the polarization, charge-dipole, and charge-quadrupole interactions differ [108]. The authors found essentially no significant shifts in the HOMO and LUMO levels for the (001)/(001) interface system, while in the (01–1)/(001) interface there was a shift of around 0.2–0.3 eV, in agreement with Linares et al. [107]. To investigate further the difference in the band bending based on the relative orientation of the pentacene molecules with respect to C_{60}, a more recent study modeled many 1D chains of pentacene and C_{60} and rotated the pentacene molecules to varying degrees in each 1D chain [102]. Using the VB/HF-AM1 model, the authors calculated the amount of band bending as a function of rotation angle for the pentacene molecules, shown in Fig. 9. The band bending in both pentacene and C_{60} slowly decay as the pentacene plane goes from being flat against C_{60} to perpendicular to the C_{60} molecules. The pentacene HOMO level actually bends in the opposite direction when it is rotated to 90°, again due to the positive end of the quadrupolar field from the pentacene molecule in the second layer inducing a negative change in the HOMO energy. As Fig. 9 shows, it is important to consider the most probable orientation of the molecules at the organic/organic interface, or attempt to sample them through some sort of dynamics.

In a similar manner to how the quadrupole of pentacene can induce changes in the HOMO and LUMO levels at the organic/organic interface, other molecular multipole moments can create a static electric field at the interface. A recent study

from the Van Voorhis group used the QM/MM method to model the 4-(dicyanomethylene)-2-methyl-6-(4-dimethylaminostyryl)-4*H*-pyran (DCM)/C_{60} interface system [138]. DCM has a significant dipole moment, 14 Debye, due to a number of strongly polar bonds in the molecule. In the unit cell, however, the molecule stacks such that there is no net dipole, and so in a perfect crystal there will be no net dipole at the interface. To simulate a net dipole from molecular dipole moments, only half of the unit cell of DCM was placed in the first layer at the organic/organic interface. This gives two different systems: a (010)/(001) interface system with no net dipole at the interface, and a $(0\frac{1}{2}\ 0)$/(001) interface system with a net dipole at the interface, shown in Fig. 10a, b, respectively. Extra C_{60} molecules were added to the $(0\frac{1}{2}\ 0)$/(001) interface in order to fill in the empty space created by deleting some of the DCM molecules. By using the same dielectric in both DCM and C_{60}, the solvation of the charges remained the same throughout the cell, and the HOMO and LUMO values for both molecules were obtained, as shown in Fig. 10c. Since the dipole of DCM is significantly larger than the quadrupole of pentacene, it creates a stronger electric field at the organic/organic interface, and as such it creates a much larger shift, 1.0 eV, in the HOMO and LUMO levels for the $(0\,\frac{1}{2}\ 0)$/(001) interface. The change in the HOMO and LUMO levels at the (010)/(001) interface are much smaller because there is no net dipole at the interface.

The little difference in the molecular packing makes a huge difference in the HOMO and LUMO levels at the interface. In a real molecular system it is very unlikely that the dipoles of the DCM molecule will align perfectly, like that in Fig. 2b, but there will be a distribution of molecular orientations and local regions that may have a number of dipoles pointed in the same direction. These types of effects can be created by any multipole moment of a molecule, but as one goes from dipole, to quadrupole, to octupole, and so on, the magnitude of the electric field reduces and becomes more complex. The electric field created by a multipole moment will also depend very much upon the direction of the molecule at the interface (see Fig. 9).

So far, only molecular multipole moments have been discussed as a non-charge transfer effect that can create potential changes in the HOMO and LUMO levels at the organic/organic interface. The studies on the bulk HOMO and LUMO values showed how inclusion of a polarizable environment is key to obtaining correct energy levels, and this is still the case at the organic/organic interface. Only now, at the interface, there are two different materials with two different dielectric constants stabilizing the charges. At the interface, a charge is being solvated by approximately equal contributions from both the donor material and the acceptor material. If the dielectric of the acceptor is higher than the dielectric of the donor, then charges in the donor material at the interface will be partially solvated by the higher dielectric, which will stabilize them near the interface. Similarly, charges in the acceptor material will be destabilized at the interface due to the partial solvation by the lower dielectric in the donor material. The effect this has on the HOMO and LUMO levels at the organic/organic interface is shown in Fig. 11. To generate Fig. 11, an interface between rubrene, dielectric of 2.7, and C_{60}, dielectric of 3.6,

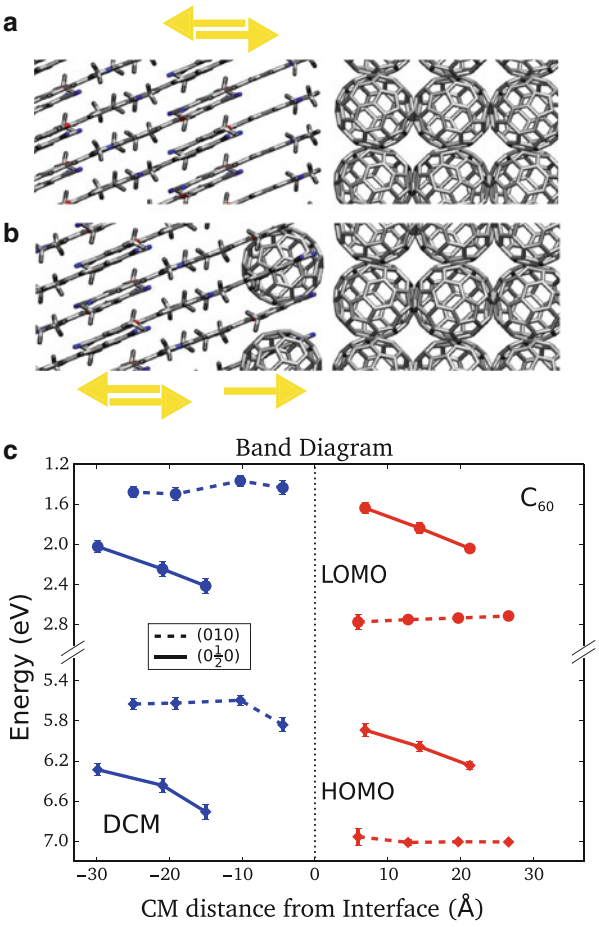

Fig. 10 Picture of the interfacial geometry of the DCM/C_{60} interface for the (010)/(001) (**a**) and $(0\frac{1}{2}0)$/(001) (**b**) interface. (**c**) The HOMO and LUMO levels for DCM and C_{60} shift by over 1.0 eV at the interface in the $(0\frac{1}{2}0)$/(001) interface system, while shifting by less than 0.2 eV in the (010)/(001) interface. Adapted with permission from [138]. Copyright 2013 American Chemical Society

was created and modeled using the QM/MM technique [138]. The HOMO and LUMO level in the lower-dielectric rubrene become pinched together by 0.1 eV because of the increased solvation by the C_{60} molecules at the interface, while the HOMO and LUMO level of C_{60} are pushed apart by 0.15 eV due to the poorly solvating rubrene molecules. Band bending due to differences in dielectric constants is relevant to almost all organic/organic interfaces in OPVs and cannot be reproduced by a continuous dielectric constant model.

The dielectric constant of an OSC is determined by the polarizability of the molecules and the packing density. The larger the polarizability and the tighter the packing density, the larger the dielectric constant will be for the material. The polarizability will not change for a molecule depending on its location in an OPV, but the packing density will most likely change throughout an OPV device because of the large amounts of disorder that can exist. Because any molecular rearrangements in organic crystals have a very large energy barrier, it is very difficult to simulate accurately the amount of disorder one would find in an OPV

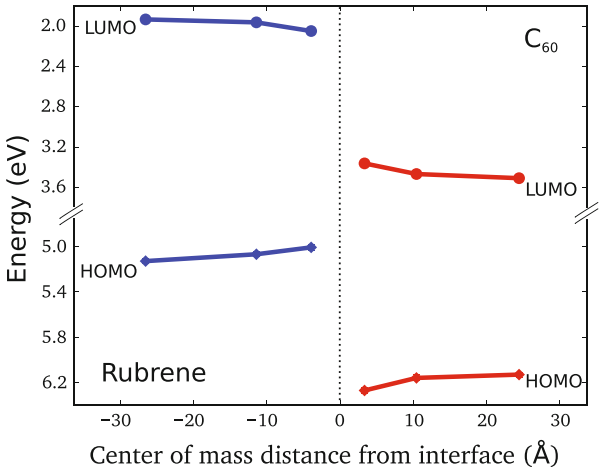

Fig. 11 HOMO and LUMO energies for the rubrene/C_{60} interface system for different locations relative to the interface. The dielectric mismatch at the interface causes the rubrene HOMO and LUMO levels to pinch together and the C_{60} HOMO and LUMO levels to pull apart. Reprinted with permission from [138]. Copyright 2013 American Chemical Society

device at the organic/organic interface using MM methods. If at least one layer of either the donor or the acceptor at the interface has significant disorder causing its packing density to decrease, then both materials will experience a smaller dielectric at the interface, since the charges at the interface are solvated by both materials. To model the affect of disorder Yost et al. chose and interface system containing copper phthalocyanine (CuPc) and PTCBI. Two interface systems were studied, one normal system, and one system where the CuPc and PTCBI cells were pulled apart by 0.6 nm to emphasize the impact of poor packing at the organic/organic interface.

Using the QM/MM method, the HOMO and LUMO levels for the two interface systems were computed at different locations in the simulation cells. Inspection of Fig. 12 shows that the HOMO and LUMO levels of the two different materials are pulled apart at the interface. Much larger changes in the HOMO and LUMO energies occurred in the interface system where CuPc and PTCBI were pulled apart. Interestingly, the LUMO levels in both materials appear relatively constant, while the HOMO levels shift by as much as 0.2 eV. The differences in HOMO and LUMO level shifts have been observed in an experimental study on the CuPc/C_{60} interface [146]. The main reason behind this odd behavior is that excess positive and negative charges concentrate on different regions of a molecule, so a molecule's orientation to the interface determines the asymmetric solvation of the electron/hole densities. In most OSC materials, the excess positive charge from the hole will tend to be more localized on the less electronegative hydrogen atoms that surround the edges of the molecule, while the excess negative charge from the electron will tend to be located at the more electronegative carbon atoms in the middle of the molecule. The CuPc and PTCBI molecules at the organic/organic interface used to produce Fig. 12 are arranged in such a way that the edges of the molecules are the only part exposed to the interface. Thus, the HOMO levels are more susceptible to the environment at the organic/organic interface and so they shift more when the environment changes. Solvation effects from different dielectrics and poor packing will display this kind of dependence on the relative orientation of the molecules.

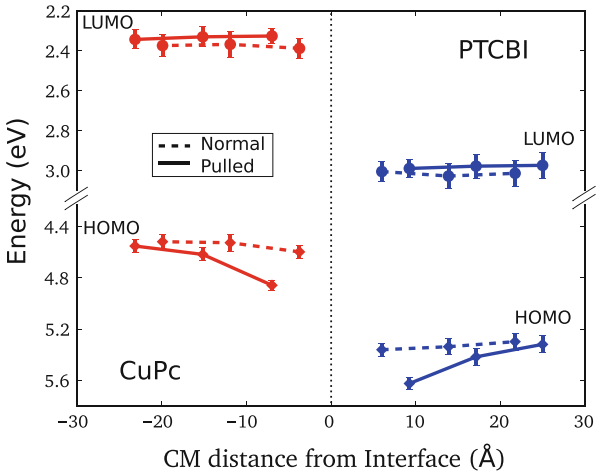

Fig. 12 HOMO and LUMO levels for different locations in the CuPc/PTCBI interface system. The normal interface cell (*dashed*) shows some changes in the HOMO energies near the interface, while the pulled interface cell (*solid*) has much larger HOMO and LUMO changes near the interface. Reprinted with permission from [138]. Copyright 2013 American Chemical Society

The discussed studies on the HOMO and LUMO levels at the organic/organic interface show that they are far from constant. Charge transfer, molecular multipole moments, changes in the dielectric constant, and packing disorder can all play a significant role in altering the HOMO and LUMO levels at the interface. These different effects change the HOMO and LUMO levels in different ways and can depend on the relative orientation of the molecules at the interface. Increased disorder at the interface compared to the bulk is capable of shifting the energy of the HOMO and LUMO levels at the interface and will increase the tendency for the electronic states to be more localized. In polymer systems the energy of the HOMO and LUMO levels greatly depend on the amount of delocalization over the polymer backbone. In a recent study on the P3HT/PCBM interface system it was found that the HOMO and LUMO levels in P3HT shifted by over 0.2 eV due to the change in the localization length in the polymer [109]. The effect of delocalization of the charges can also lessen the amount of band bending created by an electrostatic environment. If the charge is able to spread out over a number of molecules, it can average out the variations in the energies, making the HOMO and LUMO levels more constant. However, due to the amount of disorder in typical small-molecule OPV devices, this will usually not be a significant effect, except in polymers and crystalline systems. These results emphasize the importance of sampling different parts of phase space and properly accounting for the environment when modeling the HOMO and LUMO levels at the organic/organic interface.

3.3 Singlet Excited State

The lowest energy bright excited state in an OSC is typically a HOMO-to-LUMO transition from a bonding to anti-bonding set of π orbitals. So, to a simple

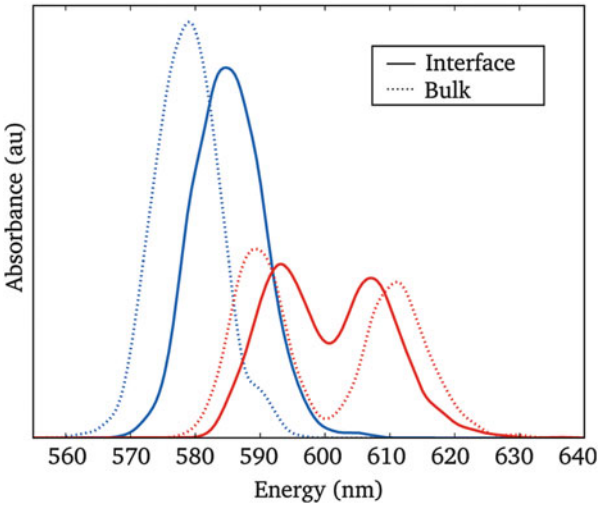

Fig. 13 Calculated absorption spectrum of H_2 Pc (*red*) and PTCBI (*blue*) at the organic–organic interface (*solid*) and in the bulk (*dashed*). Each curve was constructed from 750 different values sampled from 15 molecules each over 50 snapshots and given a Gaussian distribution with FWHM of 1.7 nm. Reprinted with permission from [110]. Copyright 2011 American Chemical Society

approximation, one could consider the singlet excited state energy as the difference between the HOMO and LUMO energy, minus the coulombic binding energy between the electron and hole. Under this simple assumption, one could then expect the singlet excited state energy to change similarly to the HOMO and LUMO energies discussed above. However, this is typically not the case, and the energy of the singlet excited state in an OSC is more complex than just the difference between the HOMO and LUMO. As shown in a study on the H_2 Pc/PTCBI interface, the singlet excited state does not change significantly [110] at the interface. Despite the changes in the HOMO and LUMO levels found in Fig. 5, the results for the singlet excited state in Fig. 13 show that almost no change occurs. The changes in the HOMO and LUMO levels happen because the energies of the individual holes and electrons are highly susceptible to any external electric field or polarization change in the environment. For the singlet excited state, the hole and electron are both localized on the same molecule, forming an electrically neutral quasiparticle that is not affected as significantly as an individual electron or hole. The electrostatic effects that have been found to be important for the HOMO and LUMO energy levels are therefore not important for the singlet excited state energies, so it is possible to change the carrier energy levels without altering the singlet excited state energy.

While electrostatic effects from the environment might not change the singlet excited state energy, the amount of delocalization can. It is well known that when singlet excited states couple in a thin film environment, they can significantly decrease in energy [12] due to the state delocalizing over many molecules, or monomer units in a polymer. A recent study by McMahon and coworkers looked at the singlet excited state in the P3HT/PCBM interface system [109]. The authors created an initial system by placing crystalline P3HT near an amorphous PCBM phase and then ran long constant pressure and temperature dynamics to sample

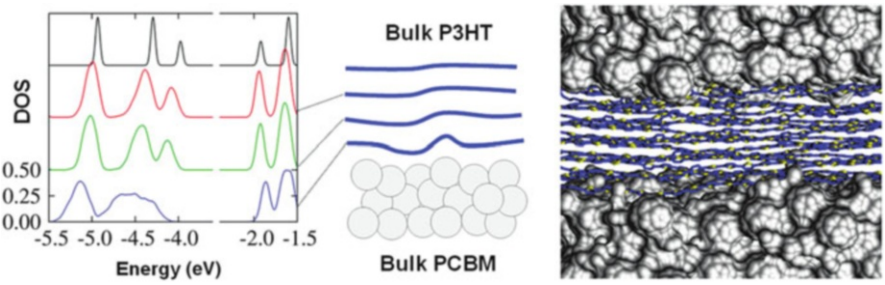

Fig. 14 *Left*: DOS (states monomer^{-1} eV^{-1}) of P3HT for layers at different distances from the interface with PCBM. The plots are offset for clarity. This panel also illustrates that the increased band gap near the interface is mostly due to a reduction of the valence band edge energy. The black curve is the (rescaled) DOS for an idealized isolated chain with no disorder. *Center*: A schematic of the interface with increased chain disorder near the interface. *Right*: A snapshot from the simulation showing that for the two P3HT/PCBM interfaces per snapshot, the P3HT chains are more disordered near the interface. Reprinted with permission from [109] Copyright 2011 American Chemical Society

the thermal fluctuations in the system. Using an ad hoc molecular orbital method [126] they computed the density of states (DOS) of the P3HT polymers at different locations in the simulation cell. Figure 14 shows how the average molecular geometry changes near the interface due to P3HT trying to pack favorably with the PCBM molecules. Due to the increased free volume at the interface, there is an increase in the structural disorder of the polymer, leading to a decrease in the crystallinity and a tendency for the geometry of the backbone to move away from planarity. This change in planarity due to a decreased packing density can be seen in the change of the DOS near the interface. The decreased planarity decreases the conjugation length and leads to a decrease in delocalization length, which increases the separation between the HOMO and LUMO levels. These simulations revealed that the exciton formed in the P3HT layer is repelled by the interface due to the increased disorder in the polymer backbone of the chains at the interface. Further verification was performed by using the ZINDO Hamiltonian to compute the singlet excited states of the P3HT polymers. In these simulations, it is not the environment that causes more than a 0.1 eV change in the singlet state energy, but the structural disorder and decreased conjugation length.

The study of the H_2 Pc/PTCBI system was unable to incorporate any changes in the delocalization length, because for the QM/MM calculation only one or two moleucles are included in the QM region. For the small-molecule OPV based systems, the disorder in the packing and weak coupling between the excited states causes them to be fairly localized. However, changes in singlet excited state energies near the organic/organic interface will be mainly due to delocalization of the states. Therefore, to get a more accurate model of the absorption spectrum and changes in the singlet excited state energies, delocalization should be included for both small-molecule and polymer systems.

3.4 Charge Transfer States

A major question about the changes in the HOMO and LUMO levels is whether the changes are as large as the binding energy of the charge transfer state and/or larger than kT. The binding energy (E_{bind}) of the charge transfer state (E_{CT}) is just $E_{\text{bind}} = E_{\text{CT}} - \left(E_{\text{IP}}^{\text{Donor}} - E_{\text{EA}}^{\text{Acceptor}}\right)$, where $E_{\text{IP}}^{\text{Donor}}$ and $E_{\text{EA}}^{\text{Acceptor}}$ are just the ionization potential of the donor and the electron affinity of the acceptor, respectively. If the binding energy for the charge transfer state is significantly larger than the changes observed in the different interface systems, then the HOMO and LUMO level changes will not greatly impact the charge separation rate at the interface. Computing the binding energy of a charge transfer state can be difficult, since most of the quantum chemistry based methods either give inaccurate answers or are very costly. As mentioned in the previous section, TDDFT calculates charge transfer state energies that are significantly too low, and linear response time dependent Hartree–Fock and semi-empirical methods calculate charge transfer state energies that are too high [72], though some recent promise has been shown using range-separated functionals to calculate charge transfer state energies [68, 80]. In addition, most current computational package implementations of TDDFT allow gas phase calculations only, so they are incapable of including environmental effects, such as the dielectric, in the estimation of the charge transfer state or its binding energy. One method that can incorporate the environment in a similar fashion to calculations used to calculate the HOMO and LUMO levels is the constrained DFT (CDFT) method [81–83], which has been applied to numerous systems to model charge transfer states in many different environments [110, 147–149].

In the pentacene/C_{60} interface, the charge transfer state is very important, since it will determine whether the triplet states formed in pentacene from singlet fission are able to break up into electrons and holes at the interface. To answer this question, the charge transfer state for both the (001)/(010) and (01–1)/(010) interface systems were calculated using CDFT with the QM/MM method. For the (01–1)/(010) interface system, where there exists significant band bending due to the quadrupole of pentacene, the charge transfer state energy is roughly 1.2 eV, while the (001)/(010) interface system charge transfer state energy is roughly 1.0 eV. Without consideration of the changes in the HOMO and LUMO levels shown in Fig. 9, it would appear that the binding energy for the perpendicular system is larger. In actuality, the binding energy for the (01–1)/(010) is over 0.2 eV larger, but because the quadrupolar field of pentacene pushes the LUMO level of C_{60} up, the overall charge transfer state energy is higher [150]. If the triplet excited state in pentacene wants to form a charge transfer state, it must encounter a region where the pentacene is in the (001) direction. Again, we see that the relative orientation of the molecules is an important factor when modeling the energetics at the organic/organic interface, but this time it is the binding energy of the charge transfer state that varies.

In Difley et al. [36] the authors use the QM/MM method combined with CDFT to model the thermal fluctuations in the charge transfer state between two Alq_3 dimers.

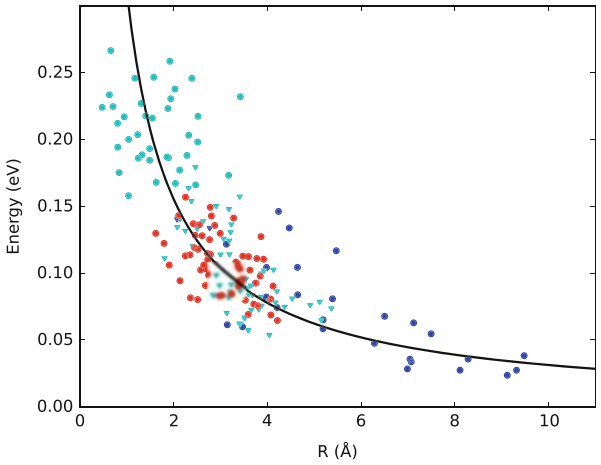

Fig. 15 Distribution of binding energies for the charge transfer state at the H_2 Pc/PTCBI interface. Each color/shape combination represents a unique H_2 Pc/PTCBI dimer at the interface. The binding energy shows an R^{-1} dependence (*black*). The R coordinate is taken as a linear combination of intermolecular distances in order to wash out the effect of the relative molecular orientation. Reprinted with permission from [110]. Copyright 2011 American Chemical Society

The charge transfer state in this system has much larger energy fluctuations than the HOMO and LUMO levels because the small changes in separation distance and relative orientation have a large effect on the binding energy of the charge transfer state. The effects of disorder, packing, and the environment were further studied in the H_2 Pc/PTCBI interface system in [110]. The charge transfer state was computed for a number of different dimer pairs at the organic/organic interface, as well as the binding energy for the charge transfer states. The average binding energy for the samples was 0.10 eV, smaller than the change in the HOMO and LUMO levels at the interface (0.2 eV) shown in Fig. 5. Thus, the charge transfer states at the interface were higher in energy than the fully separated electrons and holes. The average binding energy does not tell the whole story, however; the distribution of binding energies at the organic/organic interface, plotted in Fig. 15, has a large variation. A given dimer pair has thermal fluctuations in the binding energy of 0.1 eV, which is very significant when compared to the total binding energy. The main reasons for the large fluctuations are the fluctuations in the relative distances between the donor and acceptor molecules and the R^{-1} dependence of the binding energy. The distance coordinate, R, required to produce a R^{-1} like behavior in Fig. 15 is not the center of mass separation or the closest contact distance; it is a linear combination of different distances between the donor and acceptor molecule, and is chosen so that the effect of the relative orientation is wiped out. This study emphasizes the impact of the relative molecular orientation on the charge transfer state and its binding energy. To understand better charge formation and separation, more studies of the size of the fluctuations and orientational dependence of the charge transfer state and its binding energy need to be performed.

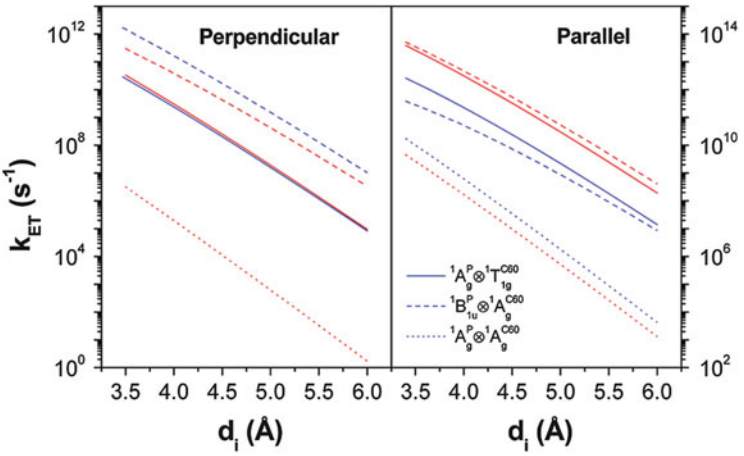

Fig. 16 Dependence of the CT rates [from local-excited states $^1A_g^P \otimes {}^1T_{1g}^{C_{60}}$ (*solid lines*) and $^1B_{1u}^P \otimes {}^1A_g^{C_{60}}$ (*dashed lines*) to the CT_0 state, $^2B_{2g}^{P^+} \otimes {}^2T_{1u}^{C_{60}^-}$] and CR rates [from the lowest CT state to the ground state, $^2B_{2g}^{P^+} \otimes {}^2T_{1u}^{C_{60}^-} \rightarrow {}^1A_g^P \otimes {}^1A_g^{C_{60}}$ (*dotted lines*)] as a function of intermolecular distance. The *blue* and *red* lines refer to different orientations given in [152] Reprinted with permission from [152]. Copyright 2009 American Chemical Society

3.5 Coupling and Rates

After calculating the energies of the singlet excited state, charge transfer state, HOMO level, and LUMO level, the final steps needed to get the charge formation, separation, and recombination rates are to compute the reorganization energy and coupling between the states. All of these values can be combined using the Marcus equation shown in Eq. (1) to obtain rates for the formation, recombination, and separation of charge transfer states. Typically, the reorganization energy for all of these processes is around 0.2–0.5 eV, with the major contributions coming from the relaxation of the molecules. Not many studies have focused on the charge transfer state formation rate or coupling between the singlet excited state and the charge transfer state. One recent study used CDFT in combination with TDDFT to compute the coupling between the singlet excited state and the charge transfer state, and they found the coupling for the zinc phthalocyanine (ZnPc)/PTCBI dimer system to range from 1 to 7 meV [151]. Similarly, Yi and co-workers calculated the coupling between the singlet excited state and the charge transfer state for pentacene/C_{60} dimers using the INDO method [152]. Just like the HOMO level, LUMO level, and charge transfer state energy, the couplings are also highly dependent on the relative orientation of pentacene to C_{60}. The largest coupling for the perpendicular orientation (7 meV) is much smaller than the largest coupling for the parallel orientation (70 meV), again showing the impact of molecular orientation. In both these cases the coupling to the pentacene triplet excited state is much larger than the coupling with the C_{60} excited state,

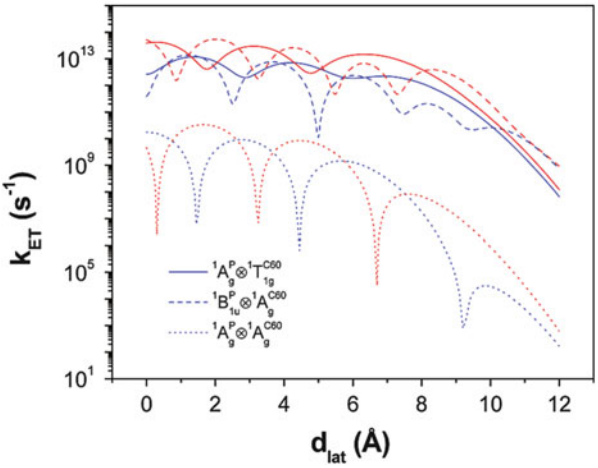

Fig. 17 Dependence of the CT formation rates [from local-excited states $^1A_g^P \otimes {}^1T_{1g}^{C_{60}}$ (*solid lines*) and $^1B_{1u}^P \otimes {}^1A_g^{C_{60}}$ (*dashed lines*) to the CT_0 state, $^2B_{2g}^{P+} \otimes {}^2T_{1u}^{C_{60}-}$] and CR rates [from the lowest CT state to the ground state, $^2B_{2g}^{P+} \otimes {}^2T_{1u}^{C_{60}-} \rightarrow {}^1A_g^P \otimes {}^1A_g^{C_{60}}$ (*dotted lines*)] as a function of lateral displacement of pentacene. The molecules are separated in the *z* direction by 0.35 nm. The *blue* and *red* lines refer to different orientations given in [152]. Reprinted with permission from [152]. Copyright 2009 American Chemical Society

which is beneficial for energy transfer from C_{60} to pentacene, where singlet fission can take place.

Also modeled in the study of pentacene/C_{60} dimers are the couplings and rates for charge recombination. The rates for charge recombination and formation follow the trends of the couplings and are plotted in Figs. 16 and 17. Figure 16 shows how the rates depend on the separation distance of the molecules for both orientations. Most notably, all of the rates are over 100 times faster for the parallel dimer because of the significantly increased overlap between pentacene and C_{60}. The linear slope in the log-linear plot is due to the dependence of the couplings on the overlap of the wavefunctions, which is exponentially dependent on the separation distance between the two molecules. Since the HOMO and LUMO levels on pentacene are located in the π orbitals that are extended in the direction parallel to the normal of the plane of the molecule, there is very little overlap with the C_{60} orbitals in the perpendicular orientation. Any planar π-conjugated molecule will have this type of orientational dependence on the rate of charge transfer state formation, recombination, and separation.

Inspection of the charge transfer formation and charge recombination rates in Fig. 17 reveals that there is an oscillatory nature to the decay of these rates upon lateral displacement of the pentacene molecule about C_{60}. The π-conjugated backbone of the HOMO and LUMO of both pentacene and C_{60} have specific nodal structures. Figure 17 also shows that in the (01–1)/(001) orientation the pentacene/C_{60} charge recombination rate (dotted blue line) is near its maximum

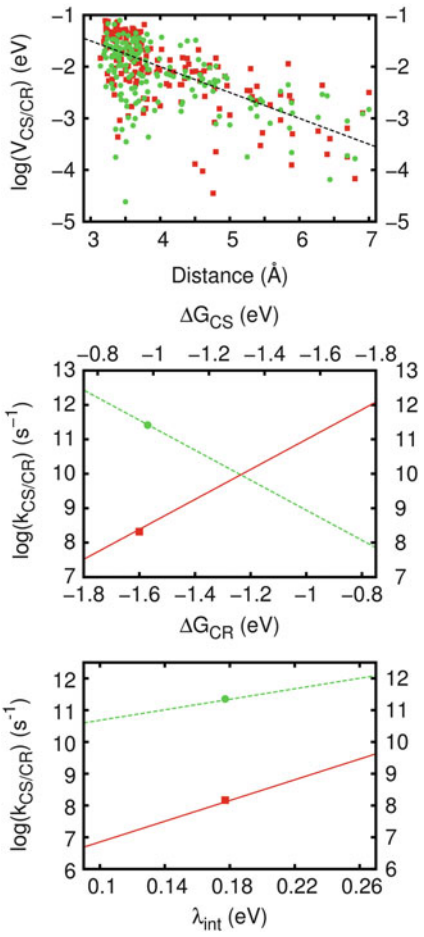

Fig. 18 *Top*: Variation of the electronic coupling $\log(V_{CR/CS})$ (*box/circle*) vs donor/acceptor distance for 210 P3HT/PCBM geometries arising from a simulation of the P3HT/PCBM interface at simulation times of 0.5, 5,5, 9.5 ns. *Middle*: Calculated $\log(k_{CR})$ and $\log(k_{CS})$ as a function of $\Delta G_{CR}/\Delta G_{CS}$ (*red/green*). *Bottom*: $\text{Log}(k_{CR})$ and $\log(k_{CS})$ as a function of λ_{int} (*red/green*). The points in the middle and bottom plots show an average representative value of log $(k_{CR/CS})$. Data taken from [153]

when the pentacene triplet to charge transfer state formation rate (dashed blue line) is near its minimum. This is because the pentacene triplet to charge-transfer-state rate depends on the overlap of the pentacene LUMO and the C_{60} LUMO, while the charge recombination rate depends on the overlap of the pentacene HOMO and the C_{60} LUMO. While it would be extremely difficult to control the packing of molecules down to the angstrom, it is useful to note how drastically the charge formation and recombination rates can vary because of the nodal structure of a molecule's π-conjugated backbone.

All of the studies dealing with the coupling between electronic states that have been mentioned so far contain only a single dimer pair with no environment or sampling of disorder included. These effects were investigated in a study from Liu et al. on the P3HT/PCBM interface [153]. Using different dimer pairs in many different snapshots from an MD trajectory the authors calculated the coupling between P3HT/PCBM, shown plotted in Fig. 18, top. The authors add an exponential

decay to the curve to show that there is a slight general trend for the couplings to decay exponentially, as one might expect. However, fluctuations occurring over several orders of magnitude indicate how sensitive the couplings can be to disorder. In fact, the smallest coupling is at 0.35 and not 0.65 nm as one might expect. Looking at the dependence of the rates on the reorganization energy, shown in Fig. 18, bottom, the charge recombination (CR) rate displays a much larger dependence on changes in the reorganization energy than the rate of charge separation (CS). As the charge transfer state energy increases, the charge recombination rate goes further into the inverted Marcus regime, causing it to slow down, while the charge separation rate increases as the charge transfer state energy increases. Therefore, the two rates will shift in opposite directions as the charge transfer state energy increases, as shown in Fig. 18, middle. This shows that increasing the charge transfer state energy in an OPV device will increase the amount of charges per photon it creates. Combining these rates with an estimation of the free energy and reorganization energy, the authors obtain a distribution of charge separation and recombination rates. The rates can vary from 10^{-10} to 10^{-5} s but, because the molecular dynamics that created this large fluctuation in the rates is on the order of nanoseconds (10^{-8}), the observed rates will then only range from 10^{-10} to 10^{-8} s.

The ratio of the charge separation and charge formation process is key to the performance of OPVs. The studies on the organic/organic interface have shown a number of important properties. Including the surroundings in any model is vital to getting accurate HOMO and LUMO energies at the organic/organic interface, since effects from molecular multipoles and changes in the solvating dielectric environment can occur. The disorder introduced at the organic/organic interface can cause a decrease in the delocalization length and an increase in the energy of the singlet excited state, HOMO level, and LUMO level. Changes in the energies of the HOMO and LUMO can be larger than the binding energy of the charge transfer state, which itself can have significant fluctuations. All of these properties, including the electronic coupling, are very dependent on the relative orientation of the molecules, and as such, either prior knowledge of the approximate interfacial structure or accurate sampling of the interface will lead to more reliable simulations.

4 Device Implications

In order to be able to reliably improve the efficiency of OPVs to levels that compete with inorganic PVs, there is a need to move away from design by trial and error to a more rational approach. The first and major step towards achieving this aim is careful consideration of the interfacial properties when designing new OPV devices, since this is where the exciton is converted into an electron and hole. The efficiency of the interface at forming free charges is reflected in two important device properties, namely, the open circuit voltage (V_{OC}) and the short circuit

current (J_{SC}). The device efficiency, $\eta = \frac{J_{SC} \cdot V_{OC} \cdot FF}{P_{IN}}$, depends on the V_{OC}, the fill factor FF, which is a measure of the actual power relative to the theoretical power, and the input power P_{IN}. The fill factor is dependent on the mobility of the charge carriers, the internal electric field, and the carrier recombination rate. For these reasons, the fill factor for OPVs is usually in the range 0.5–0.7, although recently a fill factor of >0.8 has been reported for a P3HT/PCBM blend incorporating a fixed charge layer at the donor acceptor interface [154].

It has been shown in numerous devices that the V_{OC} is linearly dependent on the band offset (E_{gap}), or charge transfer state energy [155–159]. The maximum achievable V_{OC} is equivalent to the band offset (E_{gap}), but this is rarely realized, due to losses arising from, for example, charge recombination leading to a decrease in the value of V_{OC}. A linear decrease in V_{OC} is also found at high temperatures; for low temperatures, V_{OC} saturates, due to an injection barrier at the contact [160]. Additionally, maximizing the band offset tends to reduce the driving force for charge separation at the donor-acceptor interface and requires a staggered alignment of the bands on the donor and acceptor with sufficient energy gain in order to overcome the exciton binding energy [161]. This requirement that the bands be staggered for efficient charge separation reduces the maximum achievable V_{OC}, as in Fig. 1. Work by Faist et al. quantifies the maximum achievable V_{OC} for an efficient solar cell as being limited by the smaller of the donor or acceptor optical bandgap minus losses due to charge separation and non-geminate recombination, with minimal values of 0.35 and 0.31 eV, respectively, giving a maximum value of $V_{OC} = E_{gap,min} - 0.66$ eV [162]. Minimizing the driving force required for charge separation by raising the energy of the CT state at the interface is one design strategy to target when looking for new donor and acceptor materials with high V_{OC}. However, reducing this driving force below 0.35 eV is likely to result in a reduced photocurrent due to charge carrier recombination [162]. This variation in V_{OC} at high temperature will serve to limit the efficiency at room temperature.

Recombination of the charge carriers is made up of two types of recombination, geminate and non-geminate, and can be the major cause of decreases in OPV efficiency, reducing the V_{OC} and J_{SC}. Geminate recombination predominantly occurs due to the inability of the charge transfer state at the interface to overcome its binding energy. Non-geminate recombination occurs as a result of poor charge mobility, which is often due to poor device morphology leading to charge recombination within the bulk [163, 164]. Losses by non-geminate charge recombination may be reduced by increasing the crystallinity of the material to reduce the number of traps and increase the charge mobility [165]. This is not necessarily the case for geminate recombination, where there is a complex interplay between a number of different features at the organic/organic interface that determine how efficiently the exciton can dissociate and the likelihood of subsequent recombination. To increase the efficiency of an OPV, one then needs to engineer donor/acceptor interfaces in which the charges are repelled, in order to reduce the rate of charge recombination relative to charge separation. Therefore, the properties of the states formed from the exciton at the organic/organic interface are very important in determining the efficiency of an OPV.

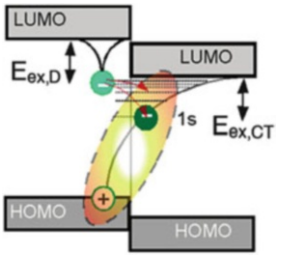

Fig. 19 Dissociation of an exciton in the donor to form the 1 s or hot CT excitons across the donor/acceptor interfaces. Reprinted with permission from [28]. Copyright 2009 American Chemical Society

The different studies on the organic/organic interface have pointed to a number of important molecular properties. The relative orientation of the molecules at the organic/organic interface significantly alters both the coupling between the electronic states and the charge transfer state energy. For polymeric systems, the ability of the material to support delocalized wavefunctions allows for a reduction in the driving force for separation of the exciton. For small molecules, on the other hand, the role played by the electrostatic environment at the interface is key, due to the small amount of delocalization of the electronic states. It is important to note that, while the impact of delocalization and the electrostatic environment have been studied independently, there is no reason that they cannot both exist for a given organic/organic interface. All of the different molecular properties have important implications for the mechanism of charge formation, recombination, and separation at the organic/organic interface.

4.1 Hot Charge Transfer

The complex nature of the organic/organic interface, coupled with the lack of accurate experimental techniques with which to probe the interface, necessitates the use of simulations and theory in order to help reconcile experimentally observed performances of different devices. One major question to be answered is, is the state formed from the exciton initially bound? Basic physics tells us that the electron and hole formed in the acceptor and donor material, respectively, must be bound by some amount of energy. However, this might not be the whole story. The observation that there needs to be a LUMO/LUMO offset at the organic/organic interface of at least 0.2 eV for efficient OPV performance has led some to believe that the excess energy from the exciton goes into vibrationally [28, 166] or electronically [167, 168] exciting the charge transfer state. Figure 19 shows a schematic of how the proposed dissociation mechanism might work from a simple Hamiltonian that Zhu and co-workers used to model the hot CT mechanism [28]. The excess vibrational energy effectively lowers the barrier to charge dissociation and creates a fast pathway for free charge formation. Later work by Tamura and co-workers on a TFB/F8BT dimer used a 3-electronic-state, 28-vibrational-mode Hamiltonian to model exciton dissociation in the dimer and found that a significant increase in the free charge formation rate is obtained when going through a higher energy, vibrationally excited CT state [169].

While the hot CT mechanism can explain the fast CT state separation at the organic/organic interface, it also relies on the formation of free charges before the electronic states can relax. The excited CT state needs to separate sufficiently that the binding energy is on the order of kT before it relaxes, otherwise there will be a high probability that the charge transfer state will recombine at the interface. One experimental study on the formation of hot CT states showed that there was no significant difference in the separation rate when the CT state was formed with excess energy [30]. Another study found the same thing for OPV devices that were already efficient, though they did show that when they vibrationally excited the CT state of poor-performing OPV devices they got an improvement in the device performance [31].

4.2 Localization/Delocalization

Another possible explanation for efficient charge separation is that the excess energy in the initially formed charge transfer state is not vibrationally exciting the charge transfer state but is instead being used to create an initially delocalized charge transfer state [170]. If the charge transfer state is more delocalized, then it will have a much smaller binding energy, making it easier to separate. A recent study by Jailaubekov and co-workers used both experimental and computational methods to probe the dynamics of the CuPc/C_{60} interface [168]. The computational model treated only the π-electrons for the electronic states and a surface hopping algorithm to propagate an initial excited state wavefunction on the electronic potential energy surfaces. Both experiment and theory found that charge formation occurs on the order of 10^{-13} s and relaxation from the initial charge transfer state occurs on the order of 10^{-12} s. The initial charge transfer state that leads to quick charge transfer formation is one where the electron and hole are not located on nearest-neighbors, and are therefore delocalized. This can be seen in Fig. 20a and d, where CT_3 and CT_4 are delocalized charge transfer states whose energies are similar to those of the singlet excited state. The similarity in energy between the high energy charge transfer state and the singlet excited state makes the energy transfer rate between these two states significantly faster.

The work of McMahon et al. provides a similar view through the use of an atomistic model of the interface between a crystalline P3HT phase with an amorphous PCBM phase. This study proposed that the exciton undergoes direct dissociation into relatively delocalized charge carriers, in an almost barrier-less process [109]. Additionally, due to an increase in the disorder of the polymer at the interface relative to the bulk, there was an increase in the band-gap of the polymer at the interface [109]. This led the authors to suggest that the increased efficiency and low charge recombination rate observed in devices based on P3HT/PCBM blends are due to the stability of the charge carriers away from the interface and their delocalized nature. Due to the fact that the increase in disorder at the interface

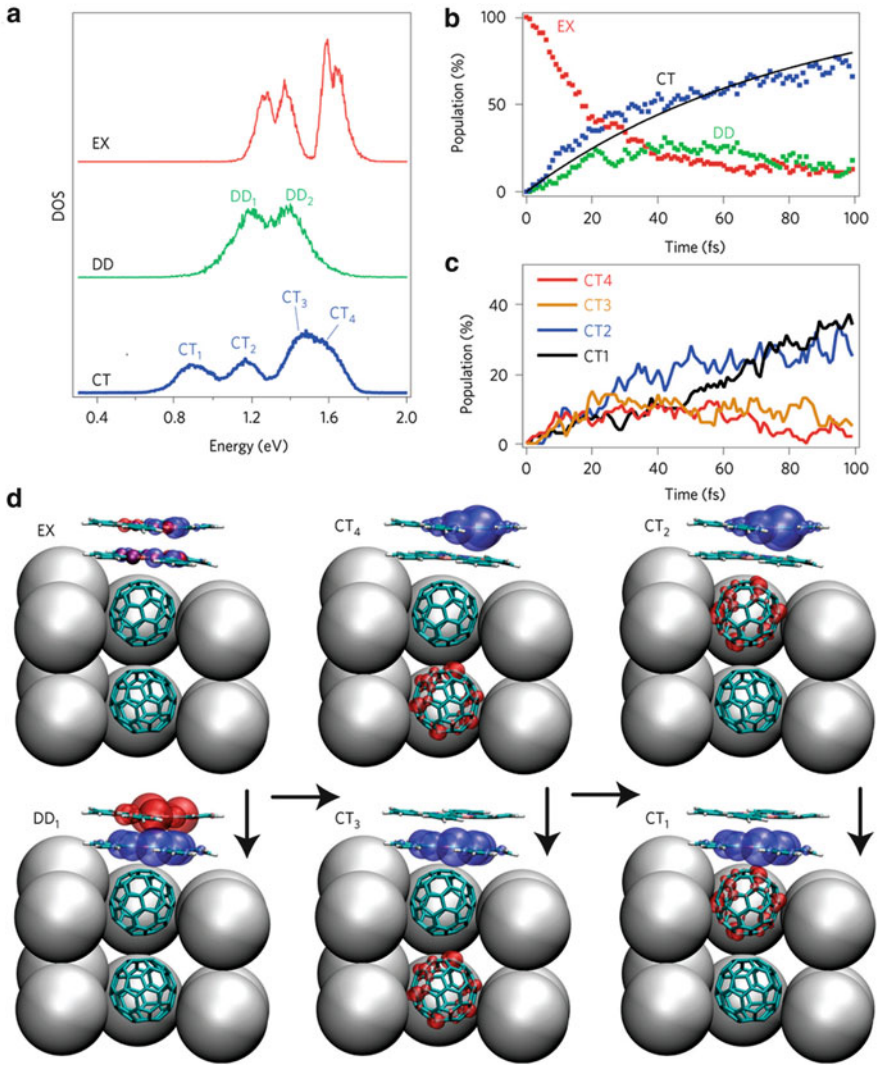

Fig. 20 (**a**) Time-averaged DOS distributions for the S_1 exciton in donors (*red*), the interfacial CT exciton (*blue*), and the inter-donor exciton (*green*) for the two H_2 Pc/two C_{60} face-on configuration. The exciton delocalizes into a CT state over the H_2 Pc dimer, the energy of which splits into a lower-energy DD_1 state that corresponds to positive charge on the H_2 Pc closest to the interface (see image below) and the higher-energy DD_2 state in the reverse configuration (not shown). The interfacial CT exciton splits into four, CT_n ($n = 1$–4) with increasing e–h distance. (**b**) Time-dependent populations of S_1 in H_2 Pc (*red*), the inter-donor exciton (*green*), and the total CT exciton (*blue*). (**c**) Time-dependent sub-populations of the four interfacial CT excitons: CT_1 (*black*), CT_2 (*blue*), CT_3 (*orange*), and CT_4 (*red*). (**d**) Snapshots of selected excitonic state charge distributions (*red*, electron; *blue*, hole). Two of the C_{60} molecules (larger *gray spheres*) that were treated classically have been removed in the picture for clarity. Reprinted with permission from [168]. Copyright 2013 Macmillan Publishers Limited

is a result of an increase in the free volume, this might be a general feature of systems in which one of the components tends to form crystalline phases.

This idea is backed up by the findings of Guo who, in an experimental study on regio-regular P3HT and regio-random P3HT, found that most excitons can dissociate at the interface, but only in regio-regular P3HT do the majority of excitons lead to free carriers [171]. Further work by Bakulin et al. [31], in which a combined experimental and computational study was performed on various conjugated macromolecules with a wide range of external quantum efficiencies, suggests that charge-separation in highly efficient devices occurs through delocalized band states, as opposed to energy-gradient driven intermolecular hopping [31]. Here the energetic driving force for charge separation is the energy needed to reach the delocalized band states, as opposed to the energy required to overcome the coulombic binding energy in the aforementioned theories. These delocalized states help suppress charge-recombination due to the increased distance between the charge carriers and the reduced binding energy of the resultant delocalized states. The extent of the delocalization experienced by the exciton is material dependent but is, nevertheless, likely to be an important general design consideration for both small molecule and polymeric-based devices. The ability of the exciton to form delocalized states is essential for long-range exciton dissociation and the consequent increased device efficiency.

4.3 Band Bending

Another possible explanation for the fast separation of charge transfer states at the organic/organic interface is that the HOMO and LUMO levels bend in such a way that they drive the electrons and holes away from the interface. This idea is similar to how inorganic PVs function and, as in inorganic PVs, partial charge transfer has been measured in organic/organic interfaces to match what are called the charge neutral levels (CNL) of the materials [172, 173]. The amount of charge transferred at the organic-inorganic interface can be significant, while very little to no charge transfer typically occurs at organic/organic interfaces [174]. The lack of partial charge transfer at organic/organic interfaces does not mean that the HOMO and LUMO levels in an OPV are the same throughout the device. As the numerous studies mentioned in the previous section show, band bending at an organic/organic interface is indeed quite prevalent. The dielectric of the surrounding medium can influence the HOMO and LUMO levels present in a material, since in any material the presence of a large dielectric will act to lower the energy of the charges. Stabilization of an electron increases the energy gained on its formation, such that the electron affinity increases. Similarly for the hole, stabilization reduces the energy required to remove an electron to leave a hole, leading to a reduction in the ionization potential. Since the electron affinity and ionization potential are just the LUMO and HOMO levels, respectively, this means that the bands in a typical band diagram compress together as the dielectric is increased. However, placing a high dielectric material next to a low dielectric material will not prove to be a useful

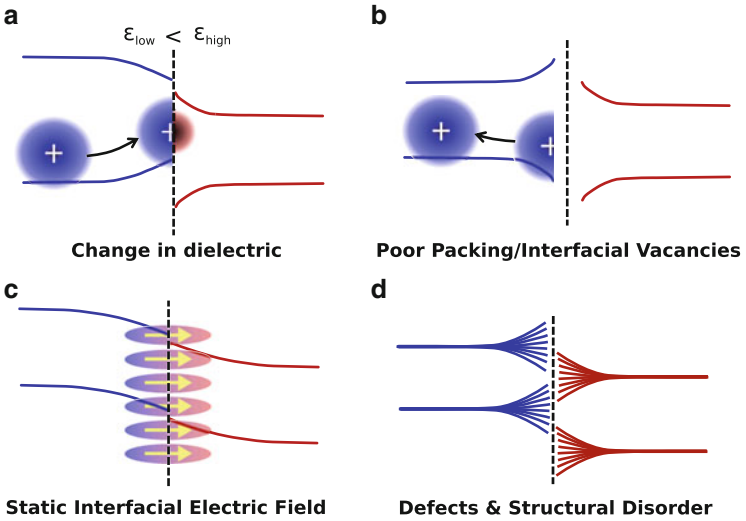

Fig. 21 A schematic representation of four different environmental effects on the organic/organic band structure: (**a**) a difference in dielectrics, (**b**) poor molecular packing at the interface, (**c**) a molecular multipole moment creating an electric field at the interface, and (**d**) a rough depiction of general disorder at the interface. Reprinted with permission from [138]. Copyright 2013 American Chemical Society

strategy to improve OPV performance, since the charges in the low dielectric material will be attracted to the interface, where they can be partially solvated by the high dielectric material, as in Fig. 21a.

Recently, a study with a CuPc/C_{60} interface probed the energetics of the interface through UPS measurements on different layer thicknesses of the organic materials to probe the changes in the HOMO and LUMO levels [146]. The authors suggest two major reasons for the shifts seen in the HOMO and LUMO levels at the interface, the first being a change in the vacuum level due to partial charge transfer across the organic/organic interface. The second results from a change in the effective dielectric of the donor and acceptor materials with respect to the location of the molecules. The solvation energy gained from the dielectric of an OSC material can be expressed as

$$8.25(e)^2 \alpha N^{4/3} \tag{4}$$

where e is the charge of an electron, α is the polarizability of the OSC molecule, and N is the number density of molecules [175]. While changing α can induce changes in the HOMO and LUMO levels, it will typically yield shifts that are not beneficial to OPV performance, reminiscent of the previous example of low and high dielectric materials. Changing the number density, on the other hand, will force a favorable change in the band bending for charge separation in both the donor and acceptor, similar to that shown in Fig. 21c. At the interface, both materials help solvate one

another, and if the number density is lower for one of the materials, then both materials will have a decreased effective dielectric constant, which will destabilize the charges in both materials at the organic/organic interface. This is exactly what is observed in the CuPc/C_{60} interface system, where there is a change of up to 0.3 eV in both the HOMO and LUMO bands [146].

One strategy to achieve reduced charge recombination and better charge separation is the use of poor packing at the interface to decrease the dielectric constant. Not only will the decreased dielectric at the interface create a driving force for charge separation, but it will also increase the charge transfer state energy, reducing charge recombination. This leads to the notion that the efficiency of OPV devices with charge recombination losses can be improved by introducing inert guest materials near the interface of one or both organic layers in order to reduce the number density through disruptions in the crystal packing. In a study by Ray and Alam, they introduced a fixed donor/acceptor layer at the interface and observed an increase in the maximum achievable fill factor [154].

The pentacene/C_{60} interface provides an excellent example of the significant role the orientation and molecular multipole moments play in device performance [107]. Pentacene has no net dipole but does possess a significant quadrupolar field, while C_{60} has neither. In pentacene, the singlet exciton quickly undergoes fission to form two triplet states, which have an energy of about 0.9 eV. The difference between the pentacene HOMO and the C_{60} LUMO is only around 0.9–1.0 eV, and so there is very little excess energy when the triplet breaks up. The pentacene molecules stack in the (001) direction on the SiO_2 surface [145], and as such, the pentacene molecules at the organic/organic interface are perpendicular to C_{60}, causing little to no change in the HOMO and LUMO levels of each material. This means that the triplet is still capable of breaking up near the organic/organic interface. The many simulations on the pentacene/C_{60} interface tell us that if, on the other hand, pentacene were parallel to C_{60} at the interface, then the LUMO of C_{60} would be greatly destabilized, thus causing the charge transfer state energy to increase to above that of the triplet state. While the typical packing of pentacene at the C_{60} interface is not optimal for charge collection at the electrode, it is instead essential for efficient charge formation at the organic/organic interface. This demonstrates the important function that changes in the morphology can have on the electronic structure and consequently on efficient device operation, and whilst it is a more difficult task to undertake, modifying the orientation of the molecules at the organic/organic interface can be very beneficial for improving device performance.

As the previous example shows, if the molecules have any sort of net dipole or quadrupole, then the orientation can play a big role in how much or how little band bending occurs. If a solution of a donor material with a small percent of a guest material with a net dipole was spin cast onto a surface with an electric field pointing perpendicular to the surface, then the final material could have a permanent net dipole pointing in the same direction once solidified. This net electric field would create a driving force for charge separation at the organic/organic interface. One experimental study was done using a donor/acceptor pair of CuPc/$CuPcF_{16}$ [176]. The dipolar natures of the C–H and C–F bonds were used to create shifts in the HOMO and

LUMO levels of the materials. When the molecules were subsequently placed with their faces next to each other, little to no changes in their HOMO and LUMO levels were observed, but when placed in a head to tail configuration, significant shifts occurred in the HOMO and LUMO levels, demonstrating the important role the molecular orientation can play in band bending.

There are many important effects arising due to the complex interplay between the materials at the interface. The significance of a given effect is dependent on the choice of materials used. For small molecules it is seen that electrostatic effects play a key role in modulating the energetic landscape experienced by the HOMO and LUMO levels of the molecules forming the interface. In polymers, on the other hand, the extent of delocalization of the electronic states is key to increasing the driving force for charge separation. This has implications for the design considerations applicable when selecting materials for use in a device. For polymeric materials, a degree of delocalization of the charge carrier wavefunction in the bulk relative to the interface is beneficial to enhancing the rate of charge separation whilst simultaneously reducing the rate of charge recombination, so materials should be selected which can support delocalization of the wavefunction in either one, two, or three dimensions. For small molecules, due to the smaller degree of coupling between molecules, delocalization of the wavefunction is much less significant and is expected to play a much smaller role. All of the potential mechanisms of charge separation are not mutually exclusive, and in the end, the role of each may depend on the materials used and the device architecture.

5 Conclusion

As the demand for solar energy increases, so does the demand for more efficient solar panels. Single-junction silicon solar panels have nearly reached their maximum theoretical efficiency at 30%, but due to their high cost and weight they are still less attractive than the non-renewable alternatives. On the other hand, cheaper and lighter organic solar panels have still to reach their maximum efficiency, with the most efficient organic solar panel currently at 12%. One of the major losses in organic photovoltaics that greatly reduces the efficiency is charge recombination. Charge recombination can decrease the V_{OC}, J_{SC}, and fill factor for an organic solar panel, all of which need to be maximized to get the most out of the solar panel. Rational design of organic materials and photovoltaics with less charge recombination is a challenge, because probing the electronic processes occurring at the organic/organic interface is difficult at best. Accurate computations of the organic/organic interface have shown their ability to fill in some missing details about what is happening at the organic/organic interface, the outcome of which is very important for the progression of organic solar panels.

Models of the organic/organic interface have their own set of problems. Due to the disordered and widely varying environment present in these materials, it is important to account for as many aspects of the environment as possible to obtain

reliable results. The most common way this is done is by treating some or all of the system in a classical way to include explicitly the multipole moments and polarizability of the OSC molecules. The complexity of the environment also makes obtaining ensemble averages of different properties, such as energies and rates, very problematic, due to the computational cost involved in obtaining sufficiently well sampled simulations from which to build the ensemble average. Proper sampling of the different molecular orientations is very important in obtaining the correct ensemble average, but large energy barriers for molecular rearrangement make this a difficult task.

Current state-of-the-art simulations use either low cost semi-empirical methods or some sort of multi-scale method that splits up the organic/organic interface into a system and surroundings. The system is then treated with higher level quantum chemistry while interacting with what is typically purely classical surroundings. These types of methods have shown that numerous environmental factors create shifts in the HOMO and LUMO levels of the organic molecules at the interface. Higher disorder at the interface lowers the delocalization length of electronic states, causing the energies to increase near the interface. The numerous studies on the pentacene/C_{60} interface, as well as other systems, have shown that energies and couplings are highly dependent on the molecular orientations. The variation of the electronic couplings continues to be an important area of study in the field of organic semiconductors, and it is in these systems that thermal fluctuations of the material lead to a distribution of electronic couplings. Fluctuations in the electronic couplings are capable of modulating the mechanism of charge transfer state formation and separation.

The different models presented here of the organic/organic interface have all helped to shed some light on the processes of charge formation, separation, and recombination. The fundamental goal in all these simulations is determining what are the important electronic and geometric features that the materials, and the interface formed between them, must possess in order to maximize the rate of charge separation relative to that of charge recombination. Current work suggests increased interfacial disorder may help in reducing the charge recombination rate, especially in polymeric systems where long-range exciton dissociation may become favorable. Other strategies that might prove fruitful in maximizing the charge separation rate relative to the charge recombination rate are the introduction of an impurity gradient to create a gradient in the local dielectric constant, or gaining more control over the molecular packing orientations to try and align molecular multipole moments such that they drive away charges formed at the interface. It is important to note that the different theories for charge separation are not exclusive, but could in fact be correct for different OPV devices and just depend on the OSC materials used. In the end, one wants a charge transfer state at the interface that is close to the singlet state energy for fast charge transfer state formation, and then a small energy barrier for charge dissociation. These features could be realized by vibrationally/electronically-excited charge transfer states, delocalized charge transfer states, or band bending at the organic/organic interface. All of these potential mechanisms for efficient charge separation have been modeled at the organic/organic interface, and to date there is no dominant mechanism.

In the future it would appear advantageous to pin down a list of the key structural and electronic properties of the molecules in order to identify candidate molecules without the need to obtain first proper ensemble averages. Further studies are also needed in order to determine additional means through which the energetics of the HOMO and LUMO for molecules at the interface can be manipulated in order to maximize the device efficiency. A more detailed treatment of the charge transfer states at the interface necessitates improvements in both the methodology by which they are calculated and the environment in which they are computed. Another question to be answered is how these different molecular properties affect the relationship between the V_{OC} of an OPV device and the charge transfer state energy at the organic/organic interface. Going forward, further expansion on the existing studies of organic/organic interfaces to new experimental systems, as they become available, will prove beneficial in trying to rationalize experimental data and to understand whether any dominant mechanism exists for enabling efficient charge separation.

References

1. Goetzberger A, Hebling C, Schock H-W (2003) Mater Sci Eng R 40:1–46
2. Forrest SR (2004) Nature 428:911–918
3. Zhao J, Wang A, Green MA, Ferrazza F (1998) Appl Phys Lett 73:1991–1993
4. Petermann JH, Zielke D, Schmidt J, Haase F, Rojas EG, Brendel R (2012) Prog Photovolt Res Appl 20:1–5
5. Repins I, Contreras MA, Egaas B, DeHart C, Scharf J, Perkins CL, To B, Noufi R (2008) Prog Photovolt Res Appl 16:235–239
6. Kim JY, Lee K, Coates NE, Moses D, Nguyen T-Q, Dante M, Heeger AJ (2007) Science 317:222–225
7. Park SH, Roy A, Beaupré S, Cho S, Coates N, Moon JS, Moses D, Leclerc M, Lee K, Heeger AJ (2009) Nat Photonics 3:297–302
8. Grätzel M (2003) J Photochem Photobiol C 4:145–153
9. Hardin BE, Snaith HJ, McGehee MD (2012) Nat Photonics 6:162–169
10. Fenna RE, Matthews BW (1975) Nature 258:573–577
11. Nelson J (2003) The physics of solar cells, vol 57. Imperial College Press, London
12. Pope M, Swenberg CE (1999) Electronic processes of organic crystals and polymers, 2nd edn. Oxford University Press, Oxford
13. Knupfer M (2003) Appl Phys A 77:623–626
14. Gregg BAJ (2003) Phys Chem B 107:4688–4698
15. Gregg BA, Hanna MCJ (2003) Appl Phys 93:3605–3614
16. Brédas J-L, Norton JE, Cornil J, Coropceanu V (2009) Acc Chem Res 42:1691–1699
17. Hoppe H, Sariciftci NSJ (2011) Mater Res 19:1924–1945
18. Yella A, Lee H-W, Tsao HN, Yi C, Chandiran AK, Nazeeruddin MK, Diau EW-G, Yeh C-Y, Zakeeruddin SM, Grätzel M (2011) Science 334:629–634
19. Shockley W, Queisser HJJ (1961) Appl Phys 32:510–519
20. Koster LJA, Shaheen SE, Hummelen JC (2012) Adv Energy Mater 2:1246–1253
21. Günes S, Neugebauer H, Sariciftci NS (2007) Chem Rev 107:1324–1338
22. Gebeyehu D, Maennig B, Drechsel J, Leo K, Pfeiffer M (2003) Sol Energy Mater Sol Cells 79:81–92

23. Halls JJM, Walsh CA, Greenham NC, Marseglia EA, Friend RH, Moratti SC, Holmes AB (1995) Nature 376:498–500
24. Yang F, Shtein M, Forrest SR (2004) Nat Mater 4:37–41
25. Armstrong NR, Wang W, Alloway DM, Placencia D, Ratcliff E, Brumbach M (2009) Macromol Rapid Commun 30:717–731
26. Veldman D, Ipek O, Meskers SCJ, Sweelssen J, Koetse MM, Veenstra SC, Kroon JM, van Bavel SS, Loos J, Janssen RAJJ (2008) Am Chem Soc 130:7721–7735
27. Ohkita H, Cook S, Astuti Y, Duffy W, Tierney S, Zhang W, Heeney M, McCulloch I, Nelson J, Bradley DDC, Durrant JRJ (2008) Am Chem Soc 130:3030–3042
28. Zhu X-Y, Yang Q, Muntwiler M (2009) Acc Chem Res 42:1779–1787
29. Muntwiler M, Yang Q, Tisdale W, Zhu X-Y (2008) Phys Rev Lett 101:196403
30. Lee J, Vandewal K, Yost SR, Bahlke ME, Goris L, Baldo MA, Manca JV, Van Voorhis TJ (2010) Am Chem Soc 132:11878–11880
31. Bakulin AA, Rao A, Pavelyev VG, van Loosdrecht PHM, Pshenichnikov MS, Niedzialek D, Cornil J, Beljonne D, Friend RH (2012) Science 335:1340–1344
32. Credgington D, Hamilton R, Atienzar P, Nelson J, Durrant JR (2011) Adv Funct Mater 21:2744–2753
33. Marcus RAJ (1956) Chem Phys 24:966
34. Dang MT, Wantz G, Bejbouji H, Urien M, Dautel OJ, Vignau L, Hirsch L (2011) Sol Energy Mater Sol Cells 95:3408–3418
35. Krebs FC (2009) Sol Energy Mater Sol Cells 93:394–412
36. Difley S, Wang L-P, Yeganeh S, Yost SR, Van Voorhis T (2010) Acc Chem Res 43:995–1004
37. Milman V, Winkler B, White JA, Pickard CJ, Payne MC, Akhmatskaya EV, Nobes RH (2000) Int J Quantum Chem 77:895–910
38. Kresse G (1996) Phys Rev B 54:11169–11186
39. Anderson PW (1958) Phys Rev 109:1492–1505
40. Szabo A, Ostlund NS (1996) Modern quantum chemistry: introduction to advanced electronic structure theory. Dover Publications, Mineola
41. Scott AP, Radom LJ (1996) Phys Chem 100:16502–16513
42. Bauschlicher CW (1995) Chem Phys Lett 246:40–44
43. Bartlett R, Musiaå M (2007) Rev Mod Phys 79:291–352
44. Purvis GD, Bartlett RJJ (1982) Chem Phys 76:1910
45. Knowles PJ, Hampel C, Werner H-JJ (1993) Chem Phys 99:5219–5227
46. Löwdin P-O (1955) Phys Rev 97:1474–1489
47. Krylov AI (2001) Chem Phys Lett 350:522–530
48. Knowles PJ, Werner H-J (1988) Chem Phys Lett 145:514–522
49. Roos BO, Taylor PR, Siegbahn PE (1980) Chem Phys 48:157–173
50. Siegbahn PEM, Almlöf J, Heiberg A, Roos BOJ (1981) Chem Phys 74:2384–2396
51. Head-Gordon M, Pople JA, Frisch MJ (1988) Chem Phys Lett 153:503–506
52. Hampel C, Peterson KA, Werner H-J (1992) Chem Phys Lett 190:1–12
53. Kohn W, Sham LJ (1965) Phys Rev 140:A1133–A1138
54. Parr RG, Weitao Y (1994) Density-functional theory of atoms and molecules, vol 16. Oxford University Press, New York
55. Kohn W, Becke AD, Parr RGJ (1996) Phys Chem 100:12974–12980
56. Perdew JP, Kurth S (2003) In: Foilhais C, Nogueira F, Marques M (eds) Density functionals for non-relativistic coulomb systems in the new century. Springer Verlag, Berlin, Chap. 1, pp 1–55
57. Scuseria GE, Staroverov VN (2005) Theory Appl Comput Chem First Forty Years 40:669–724
58. Perdew JP, Burke K, Ernzerhof M (1996) Phys Rev Lett 77:3865–3868
59. Zhao Y, Truhlar DG (2007) Theor Chem Acc 120:215–241
60. Zhao Y, Truhlar DGJ (2004) Phys Chem A 108:6908–6918
61. Becke ADJ (1993) Chem Phys 98:1372–1377
62. Zhang Y, Yang W (1998) Phys Rev Lett 80:890–890

63. Adamo C, Barone VJ (1999) Chem Phys 110:6158–6169
64. Becke ADJ (1993) Chem Phys 98:5648–5652
65. Iikura H, Tsuneda T, Yanai T, Hirao KJ (2001) Chem Phys 115:3540–3544
66. Vydrov OA, Scuseria GEJ (2006) Chem Phys 125:234109
67. Baer R, Livshits E, Salzner U (2010) Annu Rev Phys Chem 61:85–109
68. Rohrdanz MA, Martins KM, Herbert JMJ (2009) Chem Phys 130:054112
69. Sousa SF, Fernandes PA, Ramos MJA (2007) J Phys Chem A 111:10439–10452
70. Runge E, Gross EKU (1984) Phys Rev Lett 52:997–1000
71. Gross E, Kohn W (1985) Phys Rev Lett 55:2850–2852
72. Dreuw A, Head-Gordon M (2005) Chem Rev 105:4009–4037
73. Jacquemin D, Wathelet V, Perpéte EA, Adamo CJ (2009) Chem Theory Comput 5:2420–2435
74. Jacquemin D, Perpéte EA, Ciofini I, Adamo C, Valero R, Zhao Y, Truhlar DGJ (2010) Chem Theory Comput 6:2071–2085
75. Song J-W, Tokura S, Sato T, Watson MA, Hirao KJ (2009) Chem Phys 131:059901
76. Kowalczyk T, Yost SR, Van Voorhis TJ (2011) Chem Phys 134:054128
77. Perdew JP, Zunger A (1981) Phys Rev B 23:5048–5079
78. Cohen AJ, Mori-Sánchez P, Yang W (2008) Science 321:792–794
79. Dreuw A, Weisman JL, Head-Gordon MJ (2003) Chem Phys 119:2943
80. Tawada Y, Tsuneda T, Yanagisawa S, Yanai T, Hirao KJ (2004) Chem Phys 120:8425–8433
81. Wu Q, Van Voorhis T (2005) Phys Rev A 72:024502
82. Wu Q, Van Voorhis TJ (2006) Chem Phys 125:164105
83. Wu Q, Van Voorhis TJ (2006) Chem Theory Comput 2:765–774
84. Hsu C-P, You Z-Q, Chen H-CJ (2008) Phys Chem C 112:1204–1212
85. Wu Q, Cheng C-L, Van Voorhis TJ (2007) Chem Phys 127:164119
86. Wu Q, Kaduk B, Van Voorhis TJ (2009) Chem Phys 130:034109
87. Hsu C-P (2009) Acc Chem Res 42:509–518
88. Coropceanu V, Cornil J, da Silva Filho DA, Olivier Y, Silbey R, Brédas J-L (2007) Chem Rev 107:926–952
89. Brédas J-L, Beljonne D, Coropceanu V, Cornil J (2004) Chem Rev 104:4971–5004
90. Brédas JL, Calbert JP, da Silva Filho DA, Cornil J (2002) Proc Natl Acad Sci U S A 99:5804–5809
91. Pople JAJ (1967) Chem Phys 47:2026–2033
92. Zerner MC, Loew GH, Kirchner RF, Mueller-Westerhoff UTJ (1980) Am Chem Soc 102:589–599
93. Bingham RC, Dewar MJS, Lo DHJ (1975) Am Chem Soc 97:1285–1293
94. Dewar MJS, Thiel WJ (1977) Am Chem Soc 99:4899–4907
95. Stewart JJPJ (1989) Comput Chem 10:209–220
96. Stewart JJPJ (2004) Mol Model 10:6–12
97. Sattelmeyer KW, Tirado-Rives J, Jorgensen WLJ (2006) Phys Chem A 110:13551–13559
98. Cornil J et al(1999) Chem Mater 11:2436–2443
99. Castet F, Aurel P, Fritsch A, Ducasse L, Liotard D, Linares M, Cornil J, Beljonne D (2008) Phys Rev B 77:115210
100. Tsiper E, Soos Z (2003) Phys Rev B 68:085301
101. Sreearunothai P, Morteani A, Avilov I, Cornil J, Beljonne D, Friend R, Phillips R, Silva C, Herz L (2006) Phys Rev Lett 96:117403
102. Idé J, Mothy S, Savoyant A, Fritsch A, Aurel P, Méreau R, Ducasse L, Cornil J, Beljonne D, Castet F (2013) Int J Quantum Chem 113:580–584
103. Verlaak S, Heremans P (2007) Phys Rev B 75:115127
104. Tsiper E, Soos Z (2001) Phys Rev B 64:195124
105. Knowles D, Munn RJ (1940) Mater Sci Mater Electron 5:89–93
106. Bounds P, Munn R (1981) Chem Phys 59:47–53
107. Linares M, Beljonne D, Cornil J, Lancaster K, Brédas J-L, Verlaak S, Mityashin A, Heremans P, Fuchs A, Lennartz C, Idé J, Me Ì, Reau R, Aurel P, Ducasse L, Castet F (2010) J Phys Chem C 114:3215–3224

108. Verlaak S, Beljonne D, Cheyns D, Rolin C, Linares M, Castet F, Cornil J, Heremans P (2009) Adv Funct Mater 19:3809–3814
109. McMahon DP, Cheung DL, Troisi AJ (2011) Phys Chem Lett 2:2737–2741
110. Yost SR, Wang L-P, Van Voorhis TJ (2011) Phys Chem C 115:14431–14436
111. Jorgensen WL, Maxwell DS, Tirado-Rives JJ (1996) Am Chem Soc 118:11225–11236
112. Kline RJ, DeLongchamp DM, Fischer DA, Lin EK, Richter LJ, Chabinyc ML, Toney MF, Heeney M, McCulloch I (2007) Macromolecules 40:7960–7965
113. Prosa TJ, Winokur MJ, McCullough RD (1996) Macromolecules 29:3654–3656
114. Mu Y, Kosov DS, Stock GJ (2003) Phys Chem B 107:5064–5073
115. Hornak V, Abel R, Okur A, Strockbine B, Roitberg A, Simmerling C (2006) Proteins 65:712–725
116. Aasmundtveit KE, Samuelsen EJ, Guldstein M, Steinsland C, Flornes O, Fagermo C, Seeberg TM, Pettersson LAA, Inganäs O, Feidenhans'l R, Ferrer S (2000) Macromolecules 33:3120–3127
117. Grévin B, Rannou P, Payerne R, Pron A, Travers J-P (2003) Adv Mater 15:881–884
118. Thurn-Albrecht T, Thomann R, Heinzel T, Hugger S (2004) Colloid Polym Sci 282:932–938
119. Sirringhaus H, Brown PJ, Friend RH, Nielsen MM, Bechgaard K, Langeveld-Voss BMW, Spiering AJH, Janssen RAJ, Meijer EW, Herwig P, de Leeuw DM (1999) Nature 401: 685–688
120. Singh UC, Kollman PAJ (1986) Comput Chem 7:718–730
121. Huang DM, Faller R, Do K, Moulé AJJ (2010) Chem Theory Comput 6:526–537
122. Moreno M, Casalegno M, Raos G, Meille SV, Po RJ (2010) Phys Chem B 114:1591–1602
123. Tomasi J, Persico M (1994) Chem Rev 94:2027–2094
124. Klamt A, Schüürmann G (1993) J Chem Soc Perkin Trans 2:799–805
125. Cossi M, Rega N, Scalmani G, Barone VJ (2003) Comput Chem 24:669–681
126. McMahon DP, Troisi A (2009) Chem Phys Lett 480:210–214
127. Scharber MC, Mühlbacher D, Koppe M, Denk P, Waldauf C, Heeger AJ, Brabec CJ (2006) Adv Mater 18:789–794
128. Servaites JD, Yeganeh S, Marks TJ, Ratner MA (2010) Adv Funct Mater 20:97–104
129. Li G, Nitzan A, Ratner MA (2012) Phys Chem Chem Phys 14:14270–14276
130. Kroon R, Lenes M, Hummelen JC, Blom PWM, de Boer B (2008) Polym Rev 48:531–582
131. Hüfner S (2003) Photoelectron spectroscopy: principles and applications, 3rd edn. Springer Verlag, Berlin
132. Zahn DR, Gavrila GN, Gorgoi M (2006) Chem Phys 325:99–112
133. Hill I, Kahn A, Cornil J, dos Santos D, Brédas J (2000) Chem Phys Lett 317:444–450
134. Zhan X, Risko C, Amy F, Chan C, Zhao W, Barlow S, Kahn A, Brédas J-L, Marder SRJ (2005) Am Chem Soc 127:9021–9029
135. Born MZ (1920) Physik 1:45–48
136. Nayak PK, Periasamy N (2009) Org Electron 10:532–535
137. Nayak PK, Periasamy N (2009) Org Electron 10:1396–1400
138. Yost SR, Van Voorhis T (2013) J Phys Chem C 2013
139. Beljonne D, Cornil J, Muccioli L, Zannoni C, Brédas J-L, Castet F (2011) Chem Mater 23:591–609
140. Dunitz JD, Gavezzotti A (2009) Chem Soc Rev 38:2622–2633
141. Price SSL (2009) Acc Chem Res 42:117–126
142. Murdey RJ, Salaneck WR (2005) Jpn J Appl Phys 44:3751–3756
143. Avilov I, Geskin V, Cornil J (2009) Adv Funct Mater 19:624–633
144. Smith MB, Michl J (2010) Chem Rev 110:6891–6936
145. Fritz SE, Martin SM, Frisbie CD, Ward MD, Toney MFJ (2004) Am Chem Soc 126:4084–4085
146. Akaike K, Kanai K, Ouchi Y, Seki K (2010) Adv Funct Mater 20:715–721
147. Van Voorhis T, Kowalczyk T, Kaduk B, Wang L-P, Cheng C-L, Wu Q (2010) Annu Rev Phys Chem 61:149–170

148. Wang L-P, Wu Q, Van Voorhis T (2010) Inorg Chem 49:4543–4553
149. Kowalczyk T, Lin Z, Van Voorhis TJ (2010) Phys Chem A 114:10427–10434
150. Jadhav PJ, Brown PR, Thompson N, Wunsch B, Mohanty A, Yost SR, Hontz E, Van Voorhis T, Bawendi MG, Bulović V, Baldo MA (2012) Adv Mater 24:6169–6174
151. Difley S, Van Voorhis TJ (2011) Chem Theory Comput 7:594–601
152. Yi Y, Coropceanu V, Brédas J-LJ (2009) Am Chem Soc 131:15777–15783
153. Liu T, Cheung DL, Troisi A (2011) Phys Chem Chem Phys 13:21461–21470
154. Ray B, Alam MA (2013) IEEE J Photovolt 3:310–317
155. Brabec CJ, Cravino A, Meissner D, Sariciftci NS, Fromherz T, Rispens MT, Sanchez L, Hummelen JC (2001) Adv Funct Mater 11:374–380
156. Gadisa A, Svensson M, Andersson MR, Inganäs O (2004) Appl Phys Lett 84:1609
157. Kietzke T, Egbe DAM, Hörhold H-H, Neher D (2006) Macromolecules 39:4018–4022
158. Kooistra FB, Knol J, Kastenberg F, Popescu LM, Verhees WJH, Kroon JM, Hummelen JC (2007) Org Lett 9:551–554
159. Vandewal K, Tvingstedt K, Gadisa A, Inganäs O, Manca JV (2009) Nat Mater 8:904–909
160. Rauh D, Wagenpfahl A, Deibel C, Dyakonov V (2011) Appl Phys Lett 98:133301
161. Nevil N, Ling Y, Van Mierloo S, Kesters J, Piersimoni F, Adriaensens P, Lutsen L, Vanderzande D, Manca J, Maes W et al(2012) Phys Chem Chem Phys 14:15774–15784
162. Faist MA, Kirchartz T, Gong W, Ashraf RS, McCulloch I, de Mello JC, Ekins-Daukes NJ, Bradley DD, Nelson J (2011) J Am Chem Soc 134:685–692
163. Walker B, Tamayo AB, Dang X-D, Zalar P, Seo JH, Garcia A, Tantiwiwat M, Nguyen T-Q (2009) Adv Funct Mater 19:3063–3069
164. van Bavel SS, Bärenklau M, de With G, Hoppe H, Loos J (2010) Adv Funct Mater 20:1458–1463
165. Ma W, Yang C, Gong X, Lee K, Heeger AJ (2005) Adv Funct Mater 15:1617–1622
166. Clarke TM, Ballantyne AM, Nelson J, Bradley DDC, Durrant JR (2008) Adv Funct Mater 18:4029–4035
167. Liu T, Troisi A (2013) Adv Mater 25:1038–1041
168. Jailaubekov AE, Willard AP, Tritsch JR, Chan W-L, Sai N, Gearba R, Kaake LG, Williams KJ, Leung K, Rossky PJ, Zhu X-Y (2013) Nat Mater 12:66–73
169. Tamura H, Ramon J, Bittner E, Burghardt I (2008) Phys Rev Lett 100:107402
170. Deibel C, Strobel T, Dyakonov V (2009) Phys Rev Lett 103:036402
171. Guo J, Ohkita H, Benten H, Ito SJ (2010) Am Chem Soc 132:6154–6164
172. Vázquez H, Oszwaldowski R, Pou P, Ortega J, Pérez R, Flores F, Kahn A (2004) Europhys Lett 65:802–808
173. Vázquez H, Gao W, Flores F, Kahn A (2005) Phys Rev B 71:041306
174. Braun S, Salaneck WR, Fahlman M (2009) Adv Mater 21:1450–1472
175. Sato N, Seki K, Inokuchi H (1981) J Chem Soc Faraday Trans 2(77):1621–1633
176. Chen W, Qi DC, Huang H, Gao X, Wee ATS (2011) Adv Funct Mater 21:410–424

Top Curr Chem (2014) 352: 151–236
DOI: 10.1007/128_2013_468

Published online: 25 October 2013

Modeling Materials and Processes in Dye-Sensitized Solar Cells: Understanding the Mechanism, Improving the Efficiency

Mariachiara Pastore and Filippo De Angelis

Abstract We present a review of recent first-principles computational modeling studies on dye-sensitized solar cells (DSCs), focusing on the materials and processes modeling aspects which are key to the functioning of this promising class of photovoltaic devices. Crucial to the DSCs functioning is the photoinduced charge separation occurring at the heterointerface(s) between a dye-sensitized nanocrystalline, mesoporous metal oxide electrode and a redox shuttle. Theoretical and computational modeling of isolated cell components (e.g., dye, semiconductor nanoparticles, redox shuttle, etc...) as well as of combined dye/semiconductor/redox shuttle systems can successfully assist the experimental research by providing basic design rules of new sensitizers and a deeper comprehension of the fundamental chemical and physical processes governing the cell functioning and its performances. A computational approach to DSCs modeling can essentially be cast into a stepwise problem, whereby one first needs to simulate accurately the individual DSCs components to move to relevant pair (or higher order) interactions characterizing the device functioning. This information can contribute to enhancing further the target DSCs characteristics, such as temporal stability and optimization of device components. After presenting selected results for isolated dyes, including the computational design of new dyes, and model semiconductors, including realistic nanostructure models, we focus in the remainder of this review on the interaction between dye-sensitizers and semiconductor oxides, covering organic as well as metallorganic dyes.

Keywords Aggregation · Co-sensitized TiO_2 · DSCs · FT/TDDFT · Organic dyes · Ruthenium dyes · TiO_2 · ZnO

M. Pastore (✉) and F. De Angelis (✉)
Computational Laboratory for Hybrid Organic Photovoltaics (CLHYO), Istituto CNR di Scienze e Tecnologie Molecolari, via Elce di Sotto 8, I-06123, Perugia, Italy
e-mail: chiara@thch.unipg.it; filippo@thch.unipg.it

Contents

1 Introduction

1.1 Device Functioning and Conversion Efficiency

Dye-sensitized solar cells (DSCs) are photoelectrochemical cells that directly convert sunlight into electrical energy at low cost and with high efficiency [1–4]. Those appealing characteristics have stimulated intensive academic and industrial research, with the recent launch of the first DSCs-based commercial product (http://www.g24i.com/pages,g24i-wireless-keyboard,109.html) highlighting the DSCs market potential. Crucial to the DSCs functioning is the photoinduced charge separation occurring at the heterointerface(s) between a dye-sensitized nanocrystalline, mesoporous metal oxide electrode and a redox shuttle in an electrolyte solution or hole conductor, generally referred to hereafter as a redox shuttle.

The heart of the device consists of a mesoporous oxide layer, which is deposited onto a transparent conducting oxide (TCO) on a glass or plastic substrate (see Fig. 1). Grafted onto the surface of the nanocrystalline oxide is a monolayer of sensitizing dye, which absorbs the solar radiation and injects the ensuing photo-excited electrons into the manifold of unoccupied semiconductor states, consisting of both trap and conduction states, which we hereafter refer to generically as a conduction band (CB). The charge hole which is created on the dye upon excited state charge injection into the semiconductor CB is transferred to the redox shuttle, which is regenerated by a catalyst at the counter-electrode, closing the circuit (Fig. 1).

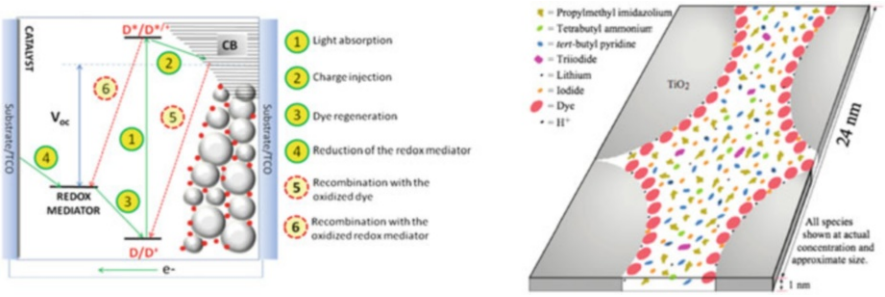

Fig. 1 *Left*: Schematic representation of the constituent materials, energy levels and processes in a DSC. *Green lines* correspond to forward electron transfer steps, *red lines* to parasitic recombination reactions. *Right*: Diagram of a 1 nm slab sliced from a pore in a typical DSC, Adapted from [51]. Copyrigt (2013) American Chemical Society

The (dye-sensitized) solar cell efficiency is defined as

$$\eta = \frac{V_{\mathrm{oc}} J_{\mathrm{SC}} \mathrm{FF}}{P_I} \tag{1}$$

where V_{oc} (the open circuit voltage of the cell) is the difference between the quasi-Fermi level of the semiconductor under illumination and the redox potential of the mediator (Fig. 1); J_{SC} is the photocurrent density at short circuit, FF is the fill factor, and PI is the intensity of the incident light. The overall DSCs performance is strongly determined by the efficiency of the various desired electron transfer and charge transport processes (1–4 in Fig. 1) against the recombination losses occurring between electrons in the semiconductor and oxidized dyes and/or oxidized species in the redox shuttle (5 and 6 in Fig. 1).

The short circuit photocurrent, J_{SC}, is defined as integral over the solar spectrum of the monochromatic incident photon to current conversion efficiency (IPCE) of the solar cell under short circuit conditions:

$$\mathrm{IPCE} = \mathrm{LHE} \times \phi_{\mathrm{INJ}} \times \phi_{\mathrm{COLL}} \tag{2}$$

where LHE is the light harvesting efficiency of the photoelectrode, ϕ_{INJ} is the quantum yield of electron injection, and ϕ_{COLL} is the electron collection efficiency at the TCO. Thus, the charge generation (LHE $\times$ ϕ_{INJ}) contribution to J_{sc} depends directly on the dye, while the collection efficiency depends on the ratio between diffusion of electrons in the semiconductor and recombination losses. In particular, the LHE is directly related to the dye optical properties (absorption spectrum, molar extinction coefficient), according to (3):

$$\mathrm{LHE}(\lambda) = 1 - 10^{-\alpha d} \tag{3}$$

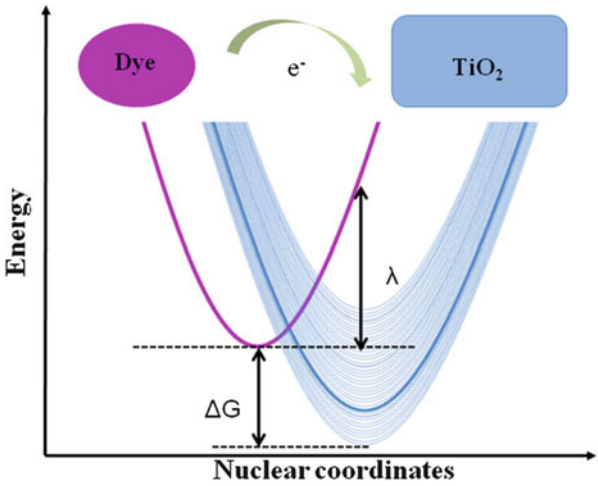

Fig. 2 Energetics of the electron transfer process between a donor (*left side*) and a quasi-continuum of acceptor states (*right side*) typical of dye-sensitization of a semiconductor. Reprinted with permission of [141]. Copyright (2013) American Chemical Society

where α is the reciprocal absorption length, given by the product of the optical absorption cross section of the sensitizer and its concentration in the mesoporous film, and d is the thickness of the film.

The injection efficiency ϕ_{INJ} is defined in terms of the ratio between the injection rate k_{INJ} and the possible radiative (k_{F}) and non radiative (k_{NR}) deactivation processes for the excited states of the surface adsorbed dye:

$$\phi_{\mathrm{INJ}} = k_{\mathrm{INJ}}/(k_{\mathrm{INJ}} + k_{\mathrm{F}} + k_{\mathrm{NR}}) \tag{4}$$

Considering the charge injection as a non-adiabatic radiationless process [5], k_{INJ}, expressed by (5), depends on two factors: (1) the squared electronic coupling matrix element between the donor and the acceptor ($|\mathrm{H}|^2$ in (5) and (2) the Franck–Condon weighted density of states (FCWD), which is a function of the reorganization energy λ and of the driving force ΔG, see Fig. 2, and equation (6) [5]:

$$k_{\mathrm{et}} = \frac{2\pi}{\hbar}|H|^2\mathrm{FCWD} = \frac{2\pi}{\hbar}|H|^2\rho(E) \tag{5}$$

$$\mathrm{FCWD} = \frac{1}{\sqrt{4\pi\lambda k_b T}}\exp\left(-\frac{(\lambda+\Delta G)^2}{4\lambda k_b T}\right) \tag{6}$$

The coupling is a function of the spatial overlap between donor and acceptor states. The driving force is related to the alignment of dye/semiconductor energy levels and the density of unoccupied semiconductor states, which therefore both contribute to the effectiveness of the electron injection process. The reorganization energy, together with the driving force, defines the probability of reaching an isoenergetic nuclear configuration where the donor–acceptor electronic states have

the same energy. Note that for a large number of acceptor states, which is typical of semiconductors (Fig. 2), the FCDW reduces to a pure density of states; see right hand side of equation (5) [5, 6].

Based on the above considerations, a potential highly-efficient dye sensitizer should be endowed with a wide and intense optical absorption spectrum, associated with a long-lived charge-separated excited state strongly coupled to the oxide CB states, and ground and excited state oxidation potentials which properly match the redox potential of the mediator and the semiconductor CB, respectively (Fig. 1). On the one hand, most current research on dye sensitizers has been focused on extending the dye spectral response, either in terms of stronger or more extended absorption, although these two requirements are usually difficult to get within a single molecule. On the other hand, an appealing strategy to overcome the limits of a single dye was the employment of a dye cocktail of co-sensitization strategies, whereby different dyes were used to absorb different portions of the solar spectrum [7–21]. As a matter of fact, the new DSCs efficiency record, close to 13%, was obtained by the combination of a Zn(II)-porphyrin and an organic dye showing complementary absorption [22].

The DSC open circuit voltage, V_{OC} in (1), represents the difference between the quasi-Fermi level of the semiconductor under illumination and the redox potential of the electrolyte (see Fig. 1), the latter being nearly constant under operation conditions due to the high concentration of redox species [23]. The quasi-Fermi level ($E_{F,n}$) of the semiconductor depends "statically" on the semiconductor conduction band (CB) energy and "dynamically" on the charge density (n) accumulated in the semiconductor [24], according to (7):

$$E_{F,n} = E_{CB} + k_B T \ln[n/N_c] \tag{7}$$

where N_c is the density of states in the semiconductor. Accordingly, charge density accumulation in the semiconductor provides an increase of the quasi-Fermi level; a shift in E_{CB} also provides a shift in the quasi-Fermi energy. Clearly, V_{oc} depends only indirectly on the nature of the dye, which can affect either the rate of recombination reactions (both with the oxidized dye and oxidized species in the electrolyte) and/or change the energetics of the semiconductor CB states.

Dye sensitizers give dense packing on the titania surface, usually described as surface monolayers [25–29], which may inhibit the parasitic recombination reactions between TiO_2-injected electrons and oxidized species in the electrolyte: a compact dye monolayer would act as an insulating layer towards the approach of the electrolyte to the TiO_2 surface. It was also suggested that particular atoms or chemical groups can also provide binding sites for oxidized species in the redox shuttle (I_2 or I_3^-), increasing their concentration close to the TiO_2 surface and thus accelerating the recombination and/or dye regeneration processes [30–36]. Recently, Mosconi et al. [37] reported on the interaction between Co(III) ions in the redox shuttle and the anionic N719 dye, which led to a strong efficiency loss due to enhanced recombination.

The energetics of the TiO_2 CB are known to depend on several factors, such as the local pH [38–40], the concentration of potential determining ions (e.g., Li^+) [40, 41], and, possibly in relation to acid/base equilibria, the nature of the electrolyte solvent [41, 42]. The role of surface adsorbed molecules, including the dye, in determining the TiO_2 CB energetics is much less clear [23, 43–49]. Some authors have shown a correlation between the dye protonation state and the DSCs performance for homologous ruthenium dyes [45, 46, 49], with dyes carrying a higher number of protons leading to higher J_{sc} but lower V_{oc}. An interesting correlation between the dipole moment of co-adsorbing species, mainly substituted benzoic acids, and the corresponding DSCs V_{oc} was observed by Rühle et al. [44] who pointed out a linear relationship between the dye coverage (N), the dipole (μ) component normal to the surface (θ is the molecule tilting angle), and the potential shift (ΔV) at the interface affecting the TiO_2 CB energy:

$$\Delta V = \frac{N\mu \cos\theta}{\varepsilon\varepsilon_0} \tag{8}$$

Work on solid-state DSCs has clearly shown a >100 mV TiO_2 conduction band shift between a heteroleptic ruthenium dye and an organic dye, which was interpreted in terms of a dipole-induced TiO_2 CB shift of different sign [50]. Such shifts are generally more difficult to observe in DSCs based on a liquid electrolyte [31], in which the high ion strength and the effect of thermal motion may hinder the role of interface dipoles. Nevertheless, Kusama et al. reported a combined experimental and theoretical study which showed a clear correlation between the dipole moment of electrolyte additives and their DSC V_{oc}.[48].

The fill factor FF of the cell is an adimensional parameter which reflects the shape of the JV curve compared to the ideal rectangular $J_{SC} \times V_{OC}$ product shape. The fill factor is mainly a measure of the (internal and external) cell resistance, including the contacts, and as such is quite difficult to map into the properties of the dye/semiconductor/electrolyte constituents.

1.2 First Principles DSCs Modeling

DSCs can be schematized as being formed by three fundamental components (i.e., the dye, the metal oxide, and the redox shuttle), which, to a first approximation, can be individually optimized in the continuing search for higher photovoltaic efficiency or longer device temporal stability. One has to recognize, however, that the DSC is an inherently complex system, since in most real cases the interdependencies among the various components dictate the overall device performances. A schematic representation of a 1-nm slab sliced from a pore in a DSC made by the N719 dye in contact with an iodine-based electrolyte of typical composition is reported in Fig. 1. As it can be noticed, the ideal optimization of the individual DSCs components is very hardly mapped into the realistic picture of Fig. 1, whereby strong interdependencies are likely to occur. Relevant pair interactions include, but

are possibly not limited to (1) dye–semiconductor; (2) redox shuttle–semiconductor; (3) dye–redox shuttle; and (4) dye–dye and dye–co-adsorbent interactions.

Theoretical and computational modeling of isolated cell components (e.g., dye, semiconductor nanoparticles, redox shuttle, etc...) as well as of combined dye/semiconductor/redox shuttle systems [52, 53] can successfully assist experimental research by providing basic design rules of new sensitizers and a deeper understanding of the fundamental chemical and physical processes governing the cell functioning and its performances. A computational approach to DSCs modeling can be essentially casted into a stepwise problem, whereby one first needs to simulate the individual DSCs components accurately to move to the relevant pair (or higher order) interactions discussed above. This information can constitute the basis for an integrated multiscale computational description of the device functioning which may further boost the DSCs efficiency along with providing the basic understanding of the device, necessary for further enhancing target DSCs characteristics, such as temporal stability and optimization of device components.

The fundamental information amenable to basic simulation tools are: (1) the dye geometrical structures, ground state oxidation potential, optical absorption spectra, and excited state oxidation potential; (2) the semiconductor CB energy and/or density of states and its band gap; and (3) the electrolyte/hole conductor redox properties. For the interacting dye/semiconductor system, one needs to calculate the dye adsorption modes onto the semiconductor, the nature and localization of the dye semiconductor excited states, and the alignment of ground and excited state energy levels at the dye/semiconductor heterointerface, which, along with an estimate of the electronic coupling, constitute the fundamental parameters controlling the electron injection and dye regeneration processes. A further step implies the simulation of the dye-sensitized semiconductor in the presence of the electrolyte solution and/or redox species, which allows one to gain insight into possible interactions between these constituting materials which might be key to the device efficiency.

Modern first principles computational methodologies, such as those based on Density Functional Theory (DFT) and its Time Dependent extension (TDDFT), provide the theoretical/computational framework to describe most of the desired properties of the individual dye/semiconductor/electrolyte systems and of their relevant interfaces. The information extracted from these calculations constitutes the basis for the explicit simulation of photo-induced electron transfer by means of quantum or non-adiabatic dynamics. The dynamics introduces a further degree of complexity in the simulation, due to the simultaneous description of the coupled nuclear/electronic problem. Various combinations of electronic structure/excited states and nuclear dynamics descriptions have been applied to dye-sensitized interfaces [54–57]. In most cases these approaches rely either on semi-empirical Hamiltonians [58, 59] or on the time-dependent propagation of single particle DFT orbitals [60, 61], with the nuclear dynamics being described within mixed quantum-classical [54, 55, 59, 60] or fully quantum mechanical approaches [61]. Real time propagation of the TDDFT excited states [62] has

also emerged as a powerful tool to study photoinduced electron transfer events, with applications to dye-sensitized interfaces based on mixed quantum-classical dynamics [57, 63].

Inclusion of solvation effects is mandatory to provide a direct connection of the calculated properties with the corresponding experimental quantities [64]. While explicit inclusion of solvent molecules is obviously the "exact" way of treating solvation effects, it involves a huge increase in the dimensions of the system and associated computational overhead. The inclusion of solvation effects is therefore usually introduced by means of continuum solvation models (PCM, CPCM) [65–67].

In light of the anticipated DSCs complexity, a working simulation tool should also include an accurate description of multiple dye-adsorption on TiO_2 relevant to aggregate properties and the simulation of co-sensitized patterns involving both different dyes and dye-coadsorbent interactions. Despite their huge potential and large scope for application, DFT methods usually substantially fail in reproducing weak intermolecular interactions, such as those occurring among surface-adsorbed dyes. This requires the accurate treatment of dispersion forces (often referred to as van der Waals forces), arising entirely from fine long-range electron correlation effects [68–71]. In ab initio wavefunction-based approaches, correlated methods are necessary to recover the dispersion energy: usually the second-order Møller–Plesset perturbation (MP2) and Coupled-Cluster methods deliver accurate interaction energies for weakly-bounded systems but present slow convergence with respect to the number of basic functions and (highly) unfavorable scaling of the computational cost as the system size increases. All standard DFT methods yield repulsive interactions between dispersion-bound adducts at large separations rather than the $1/R^6$ behavior typical of dispersion attraction, where R is the interatomic distance. The development of DFT-based methods which accurately account for weak intermolecular interactions is becoming one of the most active research lines in computational chemistry, physics, and materials science [72]. Various Meta-Generalized Gradient Approximation DFTs, expressly parameterized to give better van der Waals binding energies, have been recently developed and implemented in the most used quantum chemistry codes: the M05, M05-2X, M06, and M06-2X functionals [73–75]. An alternative and simpler approach, known as the DFT-D method, is to correct the DFT energy by adding an empirical potential of the form C_6R^{-6}, where C_6 are the dispersion coefficients; in the framework of DFT-D methods, various strategies have been developed to obtain the empirical dispersion coefficients [76–82]. When the binding energies of more than two dye-sensitizers (dimer) have to be evaluated, MP2 calculations become unfeasible and one needs to resort to DFT-based approach, such as the D3 correction by Grimme and co-workers [80, 83], which has been shown to provide reliable results [33, 84].

In this review we want to offer a unified view of recent activity on the computational modeling of DSCs, with the aim of establishing the conceptual modeling basis to design and further optimize the DSCs efficiency, along with providing a basic understanding on the cells functioning. In particular, after briefly describing the methodological aspects underlying the computational description of DSCs,

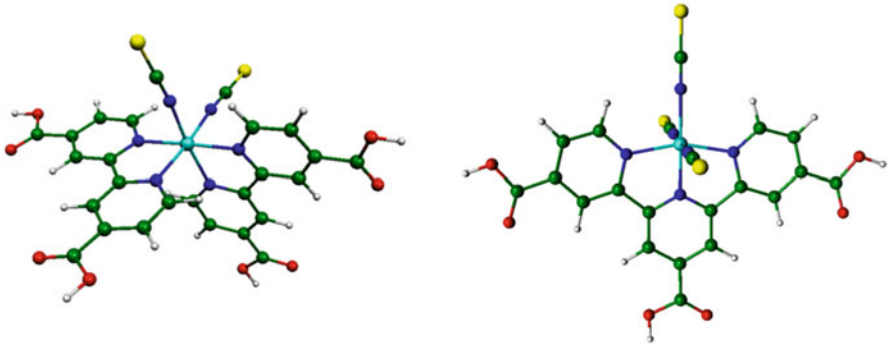

Fig. 3 Molecular structures of the doubly protonated N3 dye (*left*) and of the N749 black dye (*right*)

we will concisely provide an overview of first principles modeling of the fundamental DSCs constituting materials, e.g., dyes, metal oxide semiconductors, and redox shuttles. We will then focus on what we believe are the main physicochemical processes underlying the DSCs functioning, i.e., (1) dye adsorption onto the semiconductor surface; (2) light absorption and charge injection; (3) recombination with oxidized dyes and electrolytes; (4) regeneration of the oxidized dye; and (5) supramolecular effects, including formation of dye aggregates on the semiconductor surface and co-sensitization modeling.

2 Materials

2.1 Dyes

2.1.1 Ruthenium Dyes

Ru(II)-polypyridyl complexes have been primarily employed as dye sensitizers [85–89]. The remarkable performance of the N3 dye [85], of its doubly protonated analogue (N719) [86], and of the so-called black dye or N749 [87, 88] (see Fig. 3), had a central role in significantly advancing the DSCs technology, with solar to electric power efficiencies exceeding 11% [86, 89].

In the last few years a flourishing family of new generation Ru(II)-dyes have been designed and synthesized to provide higher molar extinction coefficient or peculiar supramolecular interactions compared to N719 or N749, thus enhancing the DSCs overall stability and/or efficiency [90–94]. Fully organic sensitizers have been developed as metal-free dyes because of their increased molar extinction coefficient, compared to Ru(II)-dyes, spectral tunability, and reduced environmental impact [95, 96]. When employing the most common I^-/I_3^- redox shuttle,

organic dyes have delivered very high photovoltaic efficiencies, exceeding 10% [97]. Functionalized donor-acceptor Zn(II)-porphyrins have recently emerged as a new class of sensitizers with high performance potential, due to the extended absorption spectrum in the red up to near IR region [22, 98, 99].

Due to the success of the N3/N719 sensitizer in DSCs, most of early theoretical/computational investigations have been initially devoted to these complexes. These works have been followed by a vast number of studies on various ruthenium complexes, which will not be reviewed here, where we briefly comment on the early studies. The first theoretical investigation performed on N3 (and related complexes) dates back to the work by Rensmo et al. of 1997 [100]. These authors have surprisingly found that, unlike $[Ru(bpy)_3]^{2+}$, the HOMOs of N3 were not pure Ru-t_{2g} states but rather they resulted from the admixture of Ru-t_{2g} states with sulfur lone pairs and π orbitals of the thiocyanate ligands. The presence of thiocyanate character in the N3 HOMOs has important consequences for the DSCs functioning: since upon adsorption of the complex onto TiO_2, the thiocyanate groups point towards the outermost region, which is that exposed to the I^-/I_3^- electrolyte, a charge hole partially delocalized over the thiocyanate ligands should help regeneration of the oxidized dye by the electrolyte redox couple. The first TDDFT study on the N3 complex, specifically on its tetradeprotonated form, was reported by Monat et al. [101], while a semiempirical investigation on the analogous $[Ru(4,4'\text{-COOH-}2,2'\text{-bpy})_2(Cl)_2]$ complex was reported in 2000 by Nazeeruddin et al. [102]. Soon after the work by Monat et al., two papers reporting TDDFT calculations appeared, one by us on the N3 complex [64] and one by Guilemoles et al. [103], who addressed the ground and excited-state properties of $[M(bpy)_2L_2]$ complexes (M = Ru, Os, L = CN, SCN). In our earlier work, we considered the tetra-protonated N3 species [64], which corresponds to the experimental species observed at low pH (<1.5), where the four carboxylic groups are entirely protonated. A sizable variation of the N3 electronic properties was observed by varying the protonation of the anchoring carboxylic groups. We thus systematically investigated the impact of acid/base chemistry on the electronic and optical properties of the N3 dye [86].

The results show an overall destabilization of the occupied and unoccupied energy levels. The LUMOs destabilization, however, offsets the HOMOs destabilization, leading to increased HOMO–LUMO gaps for the deprotonated species. As a matter of fact, the fully deprotonated N3 [104–106], which is found at pH > 11, exhibits its main spectral features in the visible and UV region at 2.48, 3.33, and 4.07 eV; the bands in the visible are blue-shifted by ca. 0.2 eV going from pH < 1.5 to pH 11. The related complex in which the NCS^- groups are replaced by Cl^- ligands complex has attracted considerable interest due to its red-shifted visible absorption bands (2.38, 3.25, and 4.03 eV) (see Fig. 4).

As can be seen, the calculated data (B3LYP/DGDZVP/PCM) in Fig. 4 are in excellent agreement with the experimental spectra, both in terms of band separations and relative intensities of the main spectral features. Most notably, our calculations reproduce the observed red-shift of the visible and near-UV bands in the Cl-complex spectrum, as well as the appearance of a low-energy shoulder

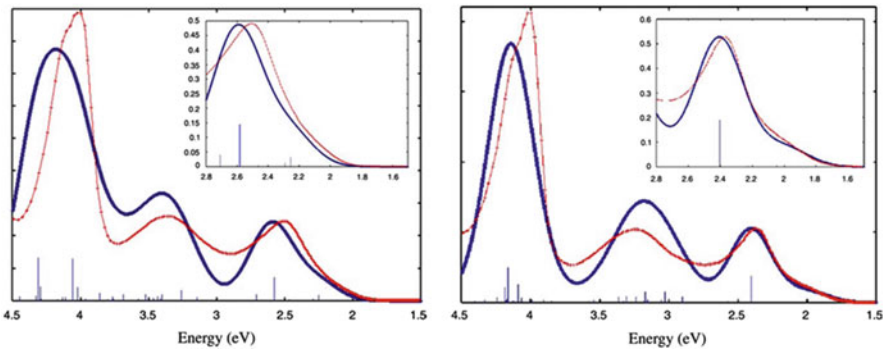

Fig. 4 Comparison of the calculated (*blue lines*) absorption spectrum of the same complexes, X=NCS (*left*), Cl (*right*), with the corresponding experimental spectra (*red lines*) in water solution. *Inset*: detail of the low-energy spectral region. Energies in eV. The intensity of the experimental spectrum has been rescaled so that the intensity of the experimental and calculated absorption maxima of low-energy bands match. Reprinted from [104] with kind permission of Elsevier

(inset of Fig. 4). Also in agreement with the experiment, the calculated absorption maxima of the band in the UV are at essentially the same energy in the two complexes [104].

Similarly to the N3 dye, various theoretical studies were reported for the black dye (BD) [107–116]. In particular, a few computational pieces of work have been focused on the electronic structure of the BD [108] and on the optical properties of the monoprotonated [110] and fully protonated, di- and mono-protonated and fully deprotonated forms of BD [109]. Notably, the interaction of the BD with iodine and the formation of hydrogen-bonded dimers of the BD and chenodeoxycholic acid have also been recently computationally explored [113, 117].

We recently reported on the variation of the electronic and optical properties of the BD as a function of the protonation of the terminal carboxylic groups [118], finding a similar orbital pattern and energetic trend to that found for the N3 dye. A comparison of the experimental and TDDFT-calculated UV–vis absorption spectrum for the mono-protonated BD in solution is shown in Fig. 5. As can be seen, also applying to the BD, TDDFT with the standard hybrid B3LYP functional delivers an excellent agreement with the experimental data, allowing a precise assignment of the main absorption features.

2.1.2 Zinc Porphyrins

A class of compounds which has recently emerged as very efficient dye sensitizers is represented by asymmetric push–pull porphyrins, which reached 11% efficiency as single dye absorbers [119, 120] and exceeded 12% efficiency in combination with an organic co-absorber [22]. Several DFT and TDDFT investigations have been reported for substituted Zn(II)-porphyrins [98, 119–128], with the main target of designing and screening new candidate molecules and rationalizing their observed photovoltaic behavior.

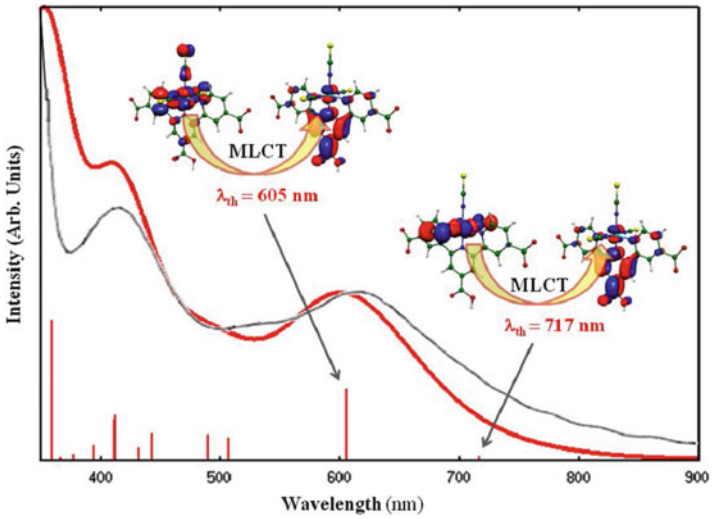

Fig. 5 Comparison between computed spectra of mono-protonated BD_1H (*red lines*) in water solution and experimental absorption data recorded in ethanolic solution (*black lines*). *Red vertical lines* correspond to calculated excitation energies and oscillator strengths. Reprint from [118] with permission of the Swiss Chemical Society

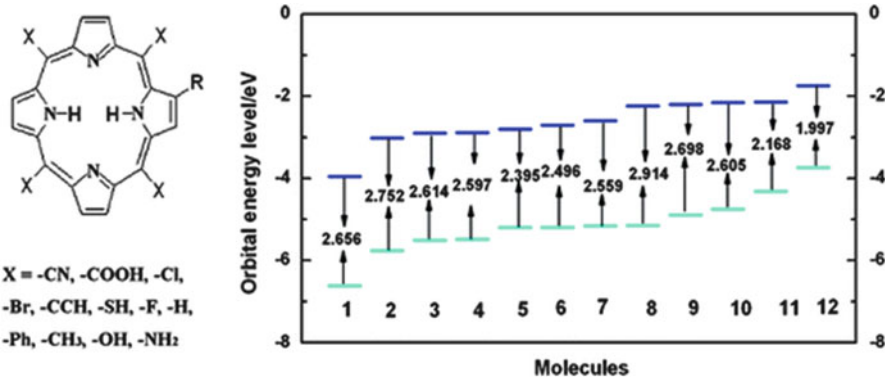

Fig. 6 Chemical structures and orbital energy levels of the HOMO and LUMO and the HOMO–LUMO gaps for a series of meso-substituted porphyrins. From [126]. Adapted with permission of [127]. Copyright (2009) American Chemical Society

As an example of the computational screening/design work we mention an early paper by Ma et al. where a large series of meso-substituted porphyrins was computationally assessed based on their HOMO–LUMO gap, nature of the frontier molecular orbitals, and simulation, by TDDFT, of their spectral properties. A survey of the investigated systems and the main results in terms of modulation of the energy levels and HOMO–LUMO gap are reported in Fig. 6. As can be seen,

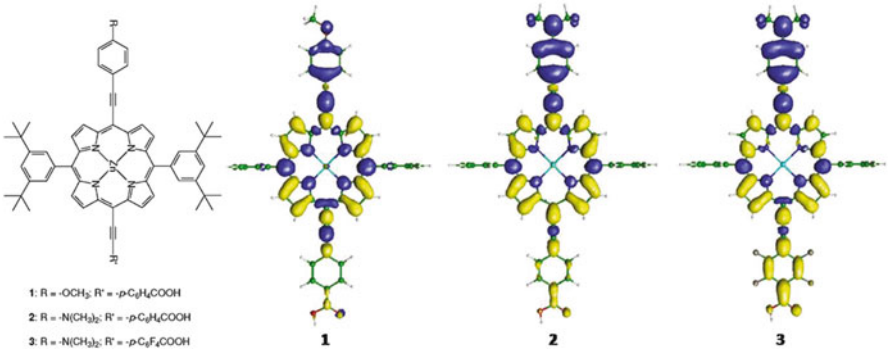

Fig. 7 Chemical structures of the investigated Zn(II) push–pull porphyrinates (*left*) and electron density difference plots between the ground and lowest excited state for dyes **1**–**3**. A *blue* (*yellow*) color signals a charge depletion (accumulation) in a given molecular region. For the sake of simplicity, in position 10, 20, simple phenyl substituents, not carrying two *tert*-butyl groups in the meta position, were taken into account in the calculations. Adapted with permission of [127]. Copyright (2011) American Chemical Society

modulation of the energy levels by ca. 2 eV could be achieved, demonstrating the huge flexibility of this class of compounds.

Another particularly interesting aspect of porphyrin sensitizers is the modulation of the charge separation occurring in the excited state by changing the nature of the electron donating and accepting units in asymmetric push–pull meso-substituted porphyrins. An example of this effect was reported by us [127] by considering two variants of the prototype push–pull system originally introduced by Diau and co-workers [119] (see Fig. 7). The considered systems were obtained by replacing the $–NMe_2$ donor by a weaker OMe group and the C_6H_4–COOH group by a stronger C_6F_4–COOH group. For these systems the standard B3LYP functional provided optical absorption spectra in excellent agreement with the experimental data, both in terms of absolute transition energies and relative intensities of the Q and B bands typical of porphyrins. To visualize the spatial localization of the charge separation occurring in the excited state, we plot in Fig. 7 the charge density difference between the lowest optically active TDDFT-calculated excited state, characterizing the Q band absorption at ca. 680 nm, and the ground state. As can be seen, maintaining the same acceptor group, the weaker −OMe donor leads to a decrease of the excited state charge accumulation on the acceptor region (compare plots for 1 and 2 in Fig. 7). Similarly, maintaining the same $–NMe_2$ donor but shifting to the stronger fluorinated acceptor, i.e., moving from 2 to 3 in Fig. 7, leads to a sizable increase in the excited state charge separation. These results illustrate the full potential of this type of porphyrin dyes in achieving an almost optimal electronic and optical response.

To summarize, for metallorganic dyes (either ruthenium polypyridyl complexes or zinc porphyrins), standard DFT/TDDFT methods have been shown to reproduce accurately most of the relevant electronic and optical properties of the investigated systems, with reference to their use in DSCs.

2.1.3 Organic Dyes

For push–pull organic sensitizers the calculation of the optical absorption spectra still represents a challenge for standard TDDFT approaches [129–132]. Conventional exchange-correlation (*x*-*c*) functionals yield large underestimations for excited states with a significant long-range CT character and in the case of molecules with spatially-extended π systems [132–134]. For Ru(II)-complexes the CT problem is limited to some extent by the substantial overlap of metal and ligand states characterizing the constituting starting and arriving orbitals in MLCT excitations typical of these complexes. The use of tailored hybrid functionals, incorporating a variable amount of non-local Hartree–Fock (HF) exchange, partially corrects the wrong asymptotic behavior [96, 132, 135]. Alternative methodological approaches use an increasing fraction of HF exchange as the interelectronic separation increases; the long-range corrected (LC) functionals [136–139] and the Coulomb-attenuating B3LYP (CAM-B3LYP) method [140] belong to this family of range-separated functionals.

Here we shall present the TDDFT results for two representative dye sensitizers which we recently reported [141], selected among the highest-efficient ones and having different electron donor and acceptor groups: the JK2 [142] dye has a TPA-like (*N*,*N*-bis(9,9-dimethylfluorene-2-yl)phenyl]donor), with a cyanoacrylic acid as anchoring unit, while the D102 dye [143, 144] has indoline and rhodanine-3-acetic acid as electron donor and acceptor groups respectively (see Fig. 8).

In Table 1 we report the calculated lowest excitation energies for the protonated (1H) and deprotonated (0H) JK2 and D102 in gas phase and ethanol solution along with the corresponding experimental absorption maxima. We notice that, going from the gas phase to ethanol solution, a decrease of the lowest excitation energy is observed; such a red-shift, regardless of the x-c functional employed, is in the range 0.15–0.35 eV and arises from the stabilization of the charge-separated excited state by the solvent. On the other hand, deprotonation of the carboxylic moiety may lead to a substantial blue-shift of the lowest excitation energy. Deprotonation of the conjugated cyanoacrylic acid in JK2 gives rise to a large blue-shift, by ca. 0.3–0.4 eV, compared to that predicted for the non-conjugated rhodanine-3-acetic acid in D102, which is ca. 0.1 eV. For JK2 we expect spectral data in ethanol to be somehow intermediate between those calculated for protonated and deprotonated species. With reference to solution data, we calculate 2.45/2.81 eV (MPW1K) and 2.79/2.94 (CAM-B3LYP) excitation energies for protonated/deprotonated species (1H or 0H in Table 1), in good agreement with the experimental absorption maximum of 2.84 eV. The MPW1K functional slightly underestimates the electronic transitions for JK2, possibly due to the static description of Hartree–Fock exchange with the interelectronic distance, which introduces a rigid system-independent shift of the transition energies [145, 146].

Looking at the calculated data for the D102 sensitizer, we find a somehow similar trend although in this case both MPW1K and CAM-B3LYP seem to overshoot the experimental absorption maximum of 2.53 eV, with 1H/0H values

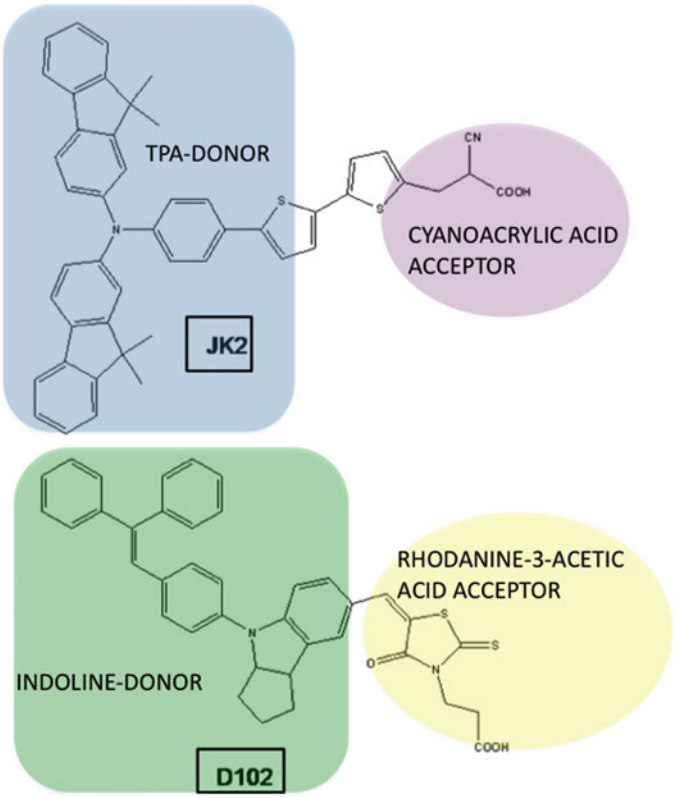

Fig. 8 Molecular structures of the JK2 and D102 dye sensitizers. Reprinted with permission of [141]. Copyright (2013) American Chemical Society

Table 1 Computed and experimental excitation energies (in eV) of the lowest excited state of JK2 and D102 in gas phase and EtOH solution

	B3LYP			MPW1K			CAM-B3LYP			
	1H		*0H*	*1H*		*0H*	*1H*		*0H*	
Dye	*vac*	*solv*	*solv*	*vac*	*solv*	*solv*	*vac*	*solv*	*solv*	Exp. (EtOH)
JK2	1.99	1.82	2.26	2.60	2.45	2.81	2.78	2.62	2.94	2.84 (143)
D102	2.61	2.29	2.37	3.07	2.78	2.89	3.11	2.86	2.90	2.53 (144)

Data from [141]

of 2.78/2.89 and 2.86/2.90 eV, respectively. The B3LYP functional, on the other hand, delivers a lowest excitation of 2.29–2.37 eV for 1H/0H cases, thus underestimating the experimental absorption maximum energy. Clearly the two dyes

have quite a different response to the choice of the x-c functional. This system-dependent variability imposes a careful a priori calibration of the computational protocol, including solvent effects and a careful analysis of the anchoring group acid–base chemistry.

2.2 Semiconductor Metal Oxides: TiO_2 and ZnO

2.2.1 TiO_2 Models Relevant for DSCs

TiO_2 is established as the most performing semiconductor metal oxide in DSCs, both in the form of the commonly employed sintered nanoparticles and nanotubes/nanorods [147, 148]; alternative metal oxides to TiO_2, such as ZnO and SnO_2, are also actively investigated [149–152].

Many theoretical/computational investigations on TiO_2 have been performed, due to the wide breadth of interesting technological applications of this material. In this section we necessarily limit our attention to some of the more interesting results obtained from theoretical/computational investigations on TiO_2 surfaces or nanoparticles of direct relevance to DSCs. Most of theoretical/computational results on TiO_2 have been obtained in the context of surface science and solid state physics. The natural framework in which to describe TiO_2 surfaces is clearly that of calculations employing periodic boundary conditions (PBC), in which an infinite and periodic solid can be effectively modeled. As a consequence, most of the calculations focused on periodic slabs, composed typically by three–four TiO_2 layers. In the case of DFT calculations, this translates in most cases into the use of non-hybrid xc functionals, which are most common in PBC codes using plane waves basis sets.

For bulk anatase TiO_2 non-hybrid functionals provide a band-gap of ca. 2.7 eV [153], compared to an experimental value of 3.2 eV. A dramatic case is that of bulk ZnO, for which a 0.8–1.0 eV band gap is predicted by local or semi-local (i.e., GGA) functionals [154], against a 3.4-eV experimental band gap. Hybrid functionals correct this inadequacy delivering essentially the experimental band-gap values for both TiO_2 and ZnO [155]. Despite this drawback, non-hybrid functional are widely used because of their efficiency and because they deliver geometrical structures which are in good agreement with experimental and hybrid functionals values. A case against this argument is that of oxygen vacancies in TiO_2, for which the two sets of functionals provide distinctly different geometries, B3LYP delivering the correct answer [156].

Probably the most significant body of work on computational TiO_2 surface science has been reported by Selloni and coworkers. The structural properties of the bulk phase and of the low-index surfaces of the anatase and rutile polymorphs of TiO_2 were recently reviewed by Vittadini et al. [153] and we refer the reader to that paper and references therein for details. Here we just mention that PBC calculations deliver the (101) as the most stable surface, consistent with the experimental evidence, and that geometrical relaxation greatly lowers the energy of all surfaces

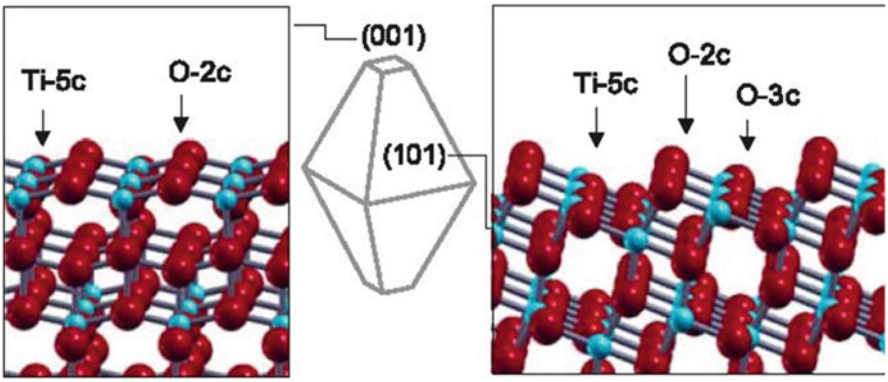

Fig. 9 Equilibrium shape of the anatase crystal. The atomic structures of the minority (001), *left*, and the majority (101) surfaces are also shown. With kind permission of Springer Science +Business Media: [153] (Fig. 1 therein)

except the (001) one; see Fig. 9. A salient characteristic of the majority anatase (101) surface is that of showing alternate rows of 6-coordinated and 5-coordinated titanium atoms, the latter representing the adsorption sites for dye binding (Fig. 9).

A major computational effort in devising suitable cluster models of TiO_2 surfaces or nanoparticles has been performed by Persson et al. [157, 158] who investigated the structural and electronic properties of bare and dye-sensitized TiO_2 clusters and nanoparticles with sizes of ca. 2 nm by DFT calculations. The electronic structures of optimized 1–2-nm nanoparticles showed well developed band structures with essentially no electronic band-gap defect states. In all cases the anatase crystal form was largely intact with at most a few Ti–O bonds broken and a few defect sites formed. Another interesting aspect, which was investigated by these authors, regards the convergence of the electronic properties with increasing cluster size. The calculated band edges were found to vary by less than 1 eV regardless of computational method. Also, the density of states (DOS) plots display gradually emerging quasi-continuous valence and conduction bands with no apparent defect states in the band-gap. According to the B3LYP/VDZ calculations, the calculated band-gap slowly decreases monotonically from 5 to 4.6 eV passing from $(TiO_2)_{16}$ to $(TiO_2)_{60}$, roughly corresponding to a doubling of the nanocrystal size. The lowest calculated TDDFT excitations follow the trend in the HOMO–LUMO energy gaps, but are consistently lower by ca. 1 eV.

In efficient DSCs, electron collection at the electrode competes with recombination at the TiO_2/electrolyte interface, so that slow electron transport can limit the charge-collection efficiency and eventually lead to an overall diminished DSC's conversion efficiency [159, 160]. For nanostructured TiO_2 films commonly employed in DSCs, effective diffusion coefficient values in the range 10^{-8} to 10^{-4} cm^2/s have been measured, depending on the light intensity. These values are orders of magnitude smaller than those observed for TiO_2 single crystals [161–164], suggesting a high concentration of electron-trapping sites in the semiconductor film [165–172].

Intense research efforts have been devoted to characterize the electronic trap states in single crystal and colloidal TiO_2 [173–176], although it is still unclear whether these states originate from defects in the bulk and surface regions, from the grain boundaries of the particles, from Coulomb trapping due to interactions of electrons with the cations of the electrolyte, or from a combination of all these factors.

In contrast to the numerous studies of anatase and rutile low index surfaces [177–182], computational investigations of the structural and electronic properties of large by TiO_2 nanocrystals (NCs) of realistic shape are still scarce. Larger NCs, constituted by up to 455 TiO_2 units with a tetragonal bipyramidal shape, were investigated by Tight-Binding (TB) calculations [183]. More recently, DFT calculations have been employed to characterize the geometrical and electronic properties of anatase TiO_2 nanoparticles having up to 449 TiO_2 units [184]. In another DFT study, the electronic structure of pure and Li-doped rutile TiO_2 nanoparticles of up to 61 TiO_2 units, saturated by water molecules, was investigated [185]. The interfaces between two TiO_2 NCs have also been studied, but only via classical molecular dynamics simulations [186, 187].

We recently reported DFT and DFT Tight-Binding (DFTB) calculations on the nature of trap states in realistic anatase TiO_2 NCs of ca. 3 nm diameter and investigated the interaction between two sintered TiO_2 NCs across different interfaces [188]. We generated our starting NC structures by cleaving bulk anatase TiO_2 according to the typical bipyramidal Wulff shape. The resulting NCs expose (101) surfaces on the lateral facets, (001) surfaces on the truncation facets, and (100) surfaces at the junction of the two pyramids (see Fig. 10). We considered NC models of various sizes, up to 3 nm. After verifying the impossibility to generate perfectly crystalline and stoichiometric $(TiO_2)_n$ truncated bipyramidal NCs, we chose to focus on two types of models, obtained by (1) saturating all the under-coordinated dangling oxygen atoms on the (001) surfaces by hydrogen atoms and (2) removing selected atoms from the (101) surfaces to keep the cluster neutral and stoichiometric. In particular, two specific models are discussed in detail in the following: (1) a $(TiO_2)_{411}$-H_{16} NC (structure **1** in Fig. 10c) with perfectly crystalline (101) surfaces and OH-saturated (001) surfaces and (2) a $(TiO_2)_{367}$ cluster (structure **2** in Fig. 10d), with some missing atoms ("holes") on the (101) surfaces.

Upon geometry optimization of **1** and **2**, the largest structural distortions with respect to the bulk crystalline structures occur at the Ti_{4c} under-coordinated sites, which rearrange from the under-coordinated octahedral configuration characteristic of the bulk-truncated structure to a distorted tetragonal configuration. The electronic structure for NCs **1** and **2** computed at the PBE-PW [189–191] level are compared in terms of DOS in Fig. 11, focusing on the manifold of unoccupied states. Similar band gaps of 1.68 (2.71) and 1.79 (2.83) eV were computed for **1** and **2** by PBE-PW (DFTB), respectively. As mentioned above, the PBE-PW calculated band gaps are considerably underestimated compared to the 3.2 eV experimental band gap of anatase TiO_2.

The unoccupied states of lowest energy for NC 1, of titanium t_{2g} character, are localized within the central part of the NC, mainly at the intersection of the (100) and (101) surfaces (left panel of Fig. 12). At higher energy, the unoccupied

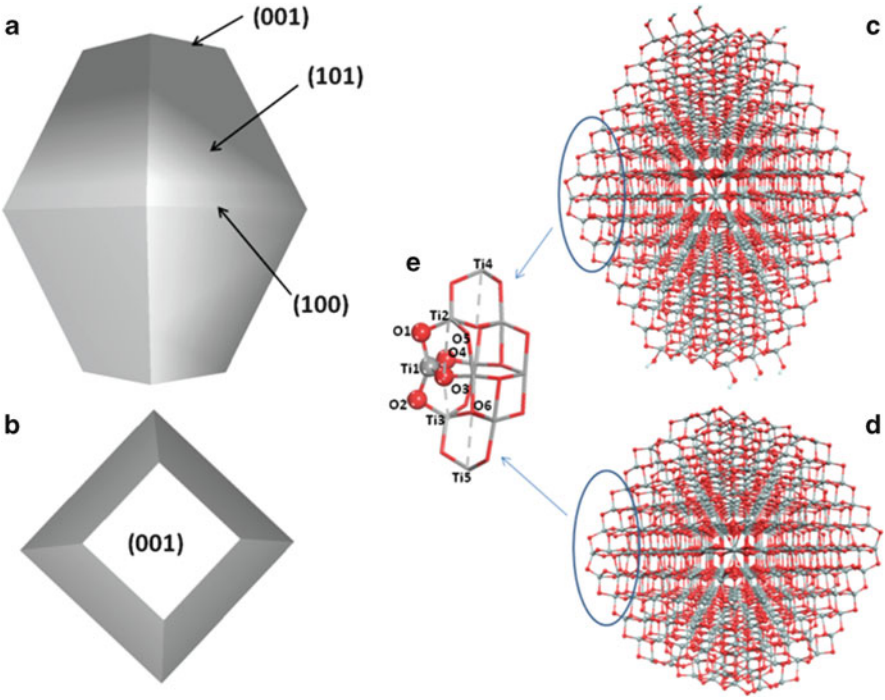

Fig. 10 (**a**, **b**) Schematics of the truncated bipyramidal NCs, showing (101), (100), and (001) surfaces from different views. (**c**) Optimized geometry of the TiO_2 NC model **1**. (**d**) Optimized geometry of the TiO_2 NC model **2**. Ti atoms are in *gray*, O in *red*, and H in *white*. Reproduced from [188] by permission of The Royal Society of Chemistry (http://pubs.rsc.org/en/content/articlelanding/2013/EE/C3EE24100A)

states are progressively more delocalized, with the lowest energy state completely delocalized over the NC structure (right panel of Fig. 12) being found ca. 0.3–0.4 eV above the LUMO, in agreement with both electrochemical and spectro-electrochemical results [169–171, 192]. These results suggest the presence of inherent trap states in perfectly stoichiometric and crystalline TiO_2 NCs due to under-coordinated surface Ti(IV) ions at the (100) facets.

To investigate whether the boundaries between sintered NCs can introduce electronic trap states at the bottom of the unoccupied states manifold, we constructed models of sintered NCs by attaching two TiO_2 NCs at their available surfaces. The optimized structures of two NCs of type 2 (see Fig. 10d) with 101/101, 101/001, 001/001, and 100/001 interfaces are shown in Fig. 13. The same picture holds for NCs of type 1. The computed DOS for the sintered configurations confirms that the shape of the DOS tail is largely not affected by the NCs boundaries, while subtle differences in the distribution of the trap states are found for those configurations where some under-coordinated Ti sites are saturated, such as in the 101/101 and 100/001 models in Fig. 13. These results indicate that, upon full relaxation, the structure of two interacting NCs tends to become similar to a bulk like structure.

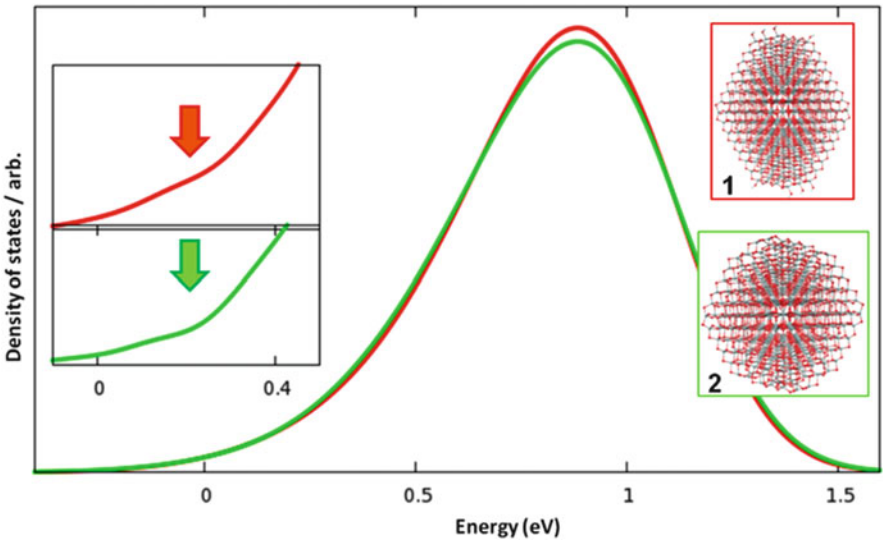

Fig. 11 DOS profile (300 lowest unoccupied states) for models **1** (*red line*) and **2** (*green line*) calculated at the DFTB optimized geometry with PBE/PW level of theory ($\sigma = 0.18$ eV). The two DOSs have been aligned at their maximum. The zero of the energy is set at the LUMO of **1**. The *inset* shows a magnification of the bottom region ($\sigma = 0.08$ eV). The *arrows in the inset* show the region of maximally localized states. Reproduced from [188] by permission of The Royal Society of Chemistry (http://pubs.rsc.org/en/content/articlelanding/2013/EE/C3EE24100A)

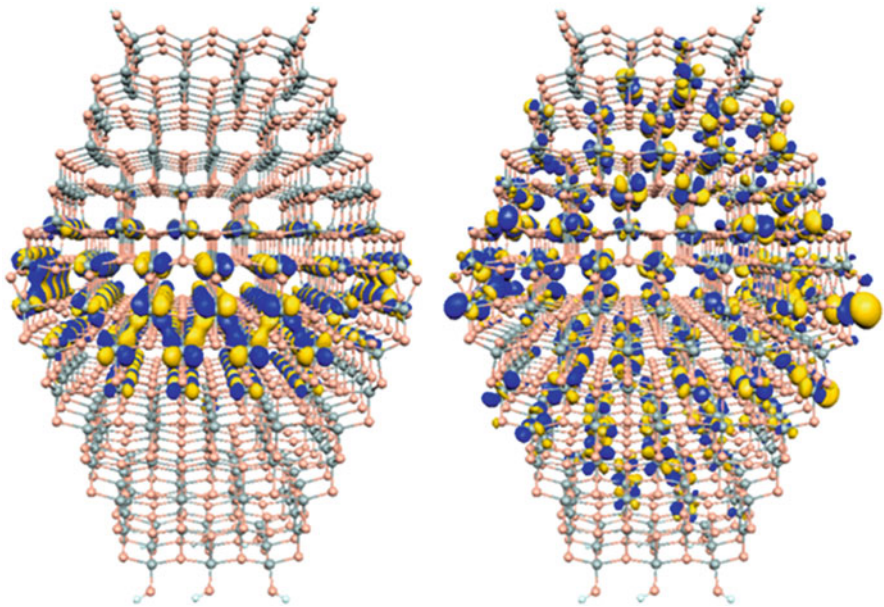

Fig. 12 Representative unoccupied states characterizing the LUMO (*left*) and the higher energy CB states, at ca. 0.3–0.4 eV above the LUMO (*right*). Reproduced from [188] by permission of The Royal Society of Chemistry (http://pubs.rsc.org/en/content/articlelanding/2013/EE/C3EE24100A

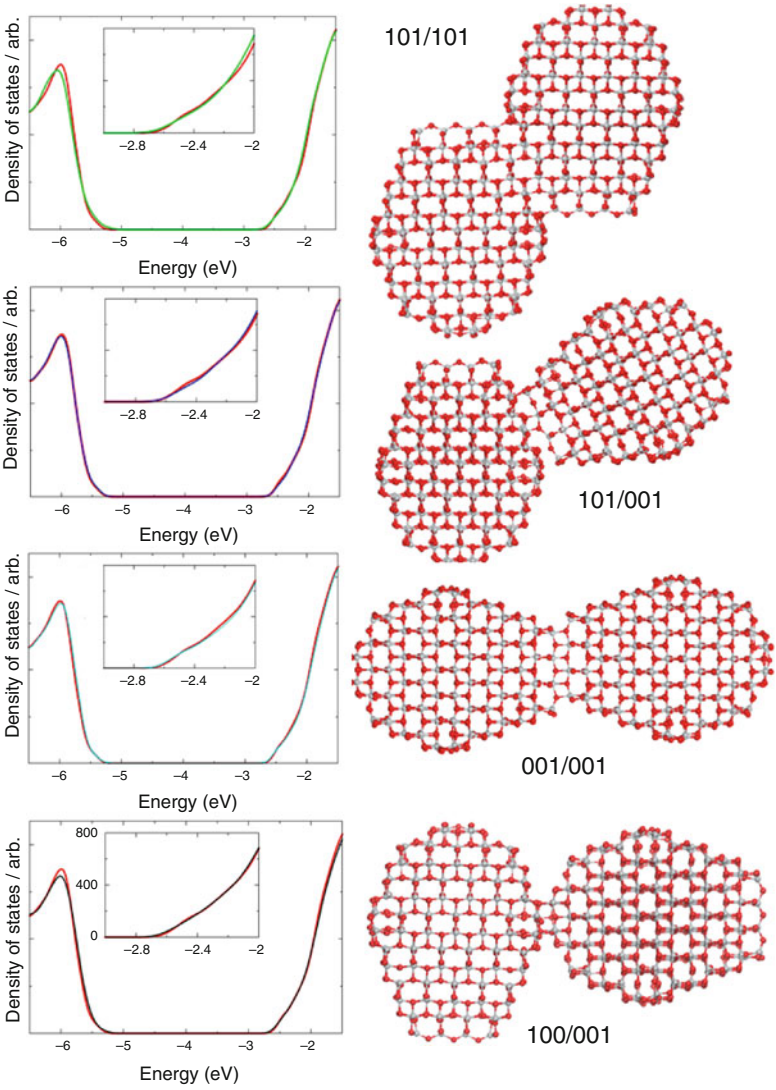

Fig. 13 Optimized geometries for two interacting NCs (model **2**) with the 101/101, 101/001, 001/001 and 100/001 interfaces, along with the corresponding DOS (*curves of different colors*) compared to that of the isolated model 2 (*red curves*) calculated at the DFTB level of theory ($\sigma = 0.18$ eV). Reproduced from [188] by permission of The Royal Society of Chemistry (http://pubs.rsc.org/en/content/articlelanding/2013/EE/C3EE24100A

Obviously, this might not always be the case under the high temperature/short time conditions used experimentally for NC film sintering (500°C for 30 min), also considering that at that temperature the ligands surrounding the NCs are destroyed, thus adding an additional level of disorder to the NCs interactions.

2.2.2 ZnO Models Relevant to DSCs

As mentioned above, TiO_2 clusters of sizable but finite size can provide electronic properties comparable to those of extended systems. This is a general property of the material, which is independent of the adopted level of theory, and which translates into size-independent electronic properties above a size of ca. 1–2 nm. The situation is completely different for ZnO and for related ZnX materials (with X = S, Se, and Te), which all exhibit strong quantum confinement effects [193–195]. As examples of this behavior we mention that 0.7–1.5 nm radii colloidal ZnO particles show absorption onsets in the range 3.7–3.8 eV, which are found to shift towards the bulk band-gap value of 3.3–3.4 eV with increasing particle size [193–195]. The interesting and tunable optoelectronic properties of these materials have thus been exploited in various applications, including semiconductor substrates for DSCs and components of inorganic hybrid heterojunctions [196–199].

Following the work on TiO_2 cluster substrates, we devised several different models of ZnX nanostructures, ranging from 0D to 3D systems [200–202]. Here we briefly illustrate the basic computational strategy adopted for ZnO nanostructures and the main results relevant in the DSCs framework. Various computational investigations of dye sensitized ZnO have been reported [203–206], although to the best of our knowledge a full quantum mechanical study of such a system including a description of the interacting excited states and the effect of quantum confinement on realistic nanostructures was reported only recently by us [207]. While band-gap transition energies of bulk ZnO can be reasonably approximated by differences of the Kohn–Sham (KS) single-particle molecular orbital energies [155, 208, 209], excitation energies in confined nanostructures can be accurately computed by TDDFT, in which Coulomb and exchange-correlation effects, as well as configurational mixing of single excitations, are properly taken into account [210]. A further effect, which should be taken into account to simulate realistically the optical properties of ZnO nanostructures, is the inclusion of solvation effects on the calculated quantities. Solvation effects have been observed to lead to ca. 0.2 eV red-shift in the luminescence of ZnO particles in solution compared to dry ones [211].

1D, 2D, and 3D ZnO clusters of various dimensions have been set up starting from the bulk wurtzite structure. As previously noted, the polarity of the Zn- and O- terminated (0001) and (0001) surfaces induces the simulated ZnO to become metallic unless proper saturation of the polar surfaces is taken into account [209, 212]; this in turn is associated with establishment of an unrealistic net dipole moment along the *c* axis, which diverges with increasing dimension along this axis. Moreover, structural instability of ZnO clusters exposing unsaturated polar surfaces has been observed [212, 213], leading to a phase transition from the wurtzite to the rock-salt structure [213]. We confirmed these results and therefore saturated the polar surfaces of our nanostructures by dissociating water molecules at those surfaces, with H^+ (OH^-) adsorbing on the O-terminated (Zn-terminated) surfaces [212]. The number and adsorption sites of dissociated water

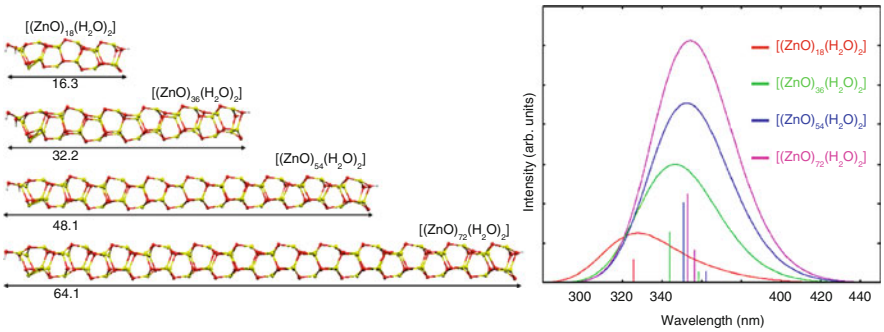

Fig. 14 *Left*: Optimized geometrical structure of the $[(ZnO)_{18}(H_2O)_2]$, $[(ZnO)_{36}(H_2O)_2]$, $[(ZnO)_{54}(H_2O)_2]$, and $[(ZnO)_{72}(H_2O)_2]$ nanowires. The wire lengths (Å) are also reported. *Red*=O, *yellow*=Zn, *white*=H atoms. *Right*: Calculated TDDFT absorption spectra for the $[(ZnO)_{18}(H_2O)_2]$, $[(ZnO)_{36}(H_2O)_2]$, $[(ZnO)_{54}(H_2O)_2]$, and $[(ZnO)_{72}(H_2O)_2]$ nanowires. Adapted from [200] by permission of the PCCP Owner Societies

molecules was varied until minimization of the energy and of the dipole along the c axis is achieved. Dissociative water adsorption is found to take place at the hollow sites on the Zn-terminated surface, in agreement with previous results, which showed this process to be exothermic by ca. 0.8 eV per water molecule for one monolayer coverage [212].

A calibration of the computational set-up based on realistic structures showed that employing the B3LYP functional modified to contain 27.5% of Hartree–Fock exchange together with a SVP basis set led to reasonably converged results for the optical band gap of realistic ZnO nanoparticles compared to experimental values [200]. With this set-up we investigated the electronic and optical properties of 1D and 2D ZnO nanostructures to compare them to the 3D model constituted by the $(ZnO)_{111}$ cluster. 1D nanowires have previously been investigated by Shen et al. [214] and were found to be stable compared to nanotubes for large diameters. Here we restrict our investigation to the smallest nanowire/nanotube possible while preserving the wurtzite structure, and explore the variation of the electronic and optical properties as a function of the wire length along the c axis for systems saturated by two water molecules, with tube/wire lengths of 1.6, 3.2, 4.8, and 6.4 nm; see Fig. 14. Also reported in Fig. 14 are the simulated TDDFT absorption spectra, obtained by a Gaussian convolution with FWHM of 0.48 eV, calculated for the wire series in solution, taking into account the lowest three excited states. As can be seen, the absorption maxima shift substantially upon increasing the wire/tube length, to essentially saturate for the longest structures. The fact that the excitation energy saturates for a system of 6.4 nm dimension is consistent with reported values for the exciton radius in ZnO of the order of 3–4 nm [215, 216].

The 2D nanostructures, or surface slabs, are suitable for the simulation of the apolar ZnO surfaces and might constitute the basis for the investigation of adsorption of dye-sensitizers onto ZnO [203] which are of interest for dye-sensitized solar cells. Here we performed a systematic investigation of the electronic and optical properties

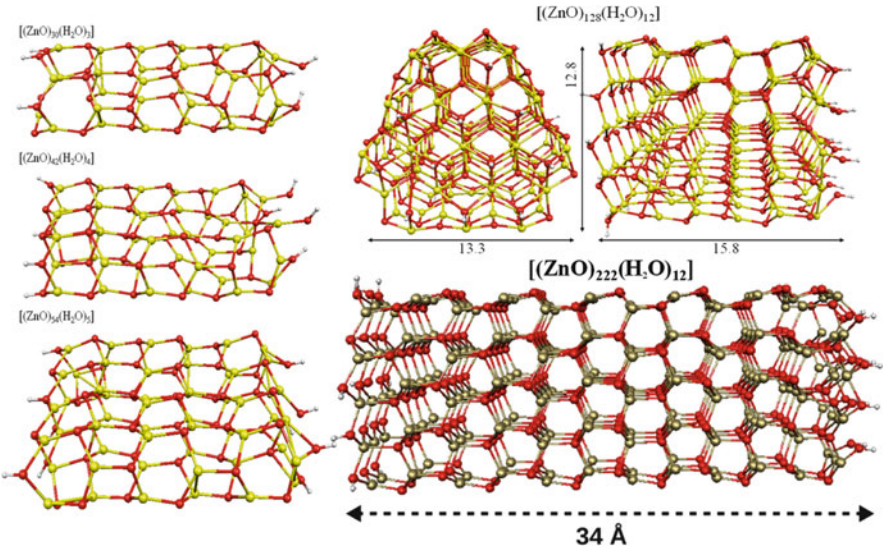

Fig. 15 *Left*: Optimized geometrical structure of the $[(ZnO)_{30}(H_2O)_3]$, $[(ZnO)_{42}(H_2O)_4]$, and $[(ZnO)_{54}(H_2O)_5]$ 2D nanostructures. *Red*=O, *yellow*=Zn, *white*=H atoms. *Right*: Optimized geometrical structure of the $[(ZnO)_{128}(H_2O)_{12}]$ and $[(ZnO)_{222}(H_2O)_{12}]$ 3D nanostructures. The *dashed arrow* indicates the *c* axis along the [1210] direction. Adapted from [200] by permission of the PCCP Owner Societies

of such 2D structures, by keeping fixed the length along the *c* axis to that of the $(ZnO)_{111}$ cluster and varying the length along the [1210] axis. Starting from the unidimensional $[(ZnO)_{18}(H_2O)_2]$ structure, we investigated the $[(ZnO)_{30}(H_2O)_3]$, $[(ZnO)_{42}(H_2O)_4]$, and $[(ZnO)_{54}(H_2O)_5]$ 2D nanostructures, formally obtained from the former by enlarging the surface by a factor 2, 3, and 4, respectively (see Fig. 15).

For the considered 2D nanostructures, we find the lowest TDDFT excitation energy in solution to be almost independent of the surface extension, with calculated values of 3.93, 3.97, and 3.96 eV for $[(ZnO)_{30}(H_2O)_3]$, $[(ZnO)_{42}(H_2O)_4]$, and $[(ZnO)_{54}(H_2O)_5]$, respectively, which are, as expected, higher than the lowest excitation energy for the reference $(ZnO)_{111}$ cluster (3.59 eV). Altogether, these results suggest that the main directions responsible for quantum confinement correspond to the [1010] and [0001] crystal axes.

The optimized geometries of the $[(ZnO)_{111}(H_2O)_{12}]$ and $[(ZnO)_{222}(H_2O)_{12}]$ 3D nanostructures (Fig. 15), preserve the wurtzite structure with a conduction band width exceeding 10 eV. The investigated 2D and 3D systems show a progressively lower conduction band edge energy, which alters the distribution of dye/semiconductor molecular orbitals and the nature of the excited states, strongly affecting the electronic coupling across the dye-sensitized semiconductor interface. As an example, for $[(ZnO)_{111}(H_2O)_{12}]$ and $[(ZnO)_{222}(H_2O)_{12}]$ 3D nanostructures, we calculate the lowest

TDDFT excitation energies in solution at 3.59 and 3.50 eV, which are both in good agreement with the experimental values for similar size nanoparticles [193, 194]. Our results highlight the very relevant role and the challenge of properly describing the nature and the alignment of excited state energy levels at the dye/ZnO interface.

3 Dye Adsorption on Semiconductor Surfaces

The primary dye/semiconductor interactions are mediated by the dye adsorption mode onto the semiconductor surface. The simulation of the adsorption mode of a single adsorbent on TiO_2 and ZnO is thus briefly reviewed here. A crucial characteristic for efficient dyes is the presence of suitable functional groups able to bind strongly to the semiconducting oxide surface. To favor ultrafast electron injection, the anchoring group should indeed coincide with, or be very close (conjugated) to, the dye acceptor unit, where the photo-excited electrons are spatially confined. This promotes electronic coupling between the donor levels of the excited dye and the delocalized acceptor levels of the semiconductor conduction band, and helps the charge injection process [217]. The orientation and packing of adsorbed dyes on the semiconductor surface also strictly depend on the binding motif, possibly affecting the rate and effectiveness of parasitic recombination reactions [47, 218, 219]. Finally, the sensitizer's anchoring group should provide stable grafting of the dye onto semiconductor surface, thus leading to long-term device stability [220–222].

In an effort to design new and more stable and efficient dyes, it is then clear how fundamental it is to disclose the adsorbing mode shown by the most commonly employed sensitizers and by the newly designed ones, with the ultimate goal of individualizing and optimizing many aspects that affect the DSCs' performance, such as the solvent used for the sensitization process [223, 224], the use of co-adsorbent species [225, 226], and the electrolyte composition [227].

3.1 Organic Dyes on TiO_2

3.1.1 Binding Modes: Theory vs Experiment

From an experimental standpoint, information on the dye binding modes at the semiconductor/dye interface, are conventionally accessed by vibrational spectroscopy [Fourier Transform InfraRed (FT-IR) spectroscopy and Surface-Enhanced Raman Spectroscopy (SERS)] [228–237]. These techniques can provide structural details about the adsorption modes as well as information on the relative orientation of the molecules anchored onto the oxide surface. Photoelectron Spectroscopy (PES) has also been successfully employed to characterize the dye/oxide interface for a series of organic dyes [238–242]. The analysis of the PES spectra yields information on the molecular and electronic structures at the interface, along with basic indications of the dye coverage and of the distance of selected atoms from the

surface. More recently, X-ray reflectometry has also been employed to unravel the orientation of dye molecules adsorbed onto TiO_2 surfaces [29].

The anchoring mechanism of the largely employed carboxylic acid group to the TiO_2 surface can be exemplified by referring to the coordination modes of the carboxylate fragment (COO^-) to metal ions; there are basically three typical coordination schemes: monodentate, bidentate chelating, and bidentate bridging [243]. An empirical rule, derived by Deacon and Philips [244], correlates the difference between the asymmetric and symmetric stretching frequencies ($\Delta\nu_{as}$) of COO^- and the type of coordination: if the measured $\Delta\nu_{as}$ for the adsorbed species is larger than that measured for the neat salt, a monodentate coordination is supposed to take place; otherwise if $\Delta\nu_{as}$ is similar or smaller than that of the corresponding salt, a bidentate bonding mode is hypothesized. Identification of the COO^- symmetric and asymmetric vibrational frequencies is usually possible for simple carboxylic acids, but often realistic dyes show a plethora of overlapping absorptions in the 1,400–1,600 cm^{-1} range, which hinder identification and/or assignment of the diagnostic carboxylic modes.

Along with experimental investigations, a number of theoretical studies of the dye adsorption modes on the TiO_2 surface have been published,[46, 47, 50, 53, 105, 219, 230, 236, 245–253] starting from the pivotal work by Vittadini et al. on formic acid adsorption on the TiO_2 anatase (101) surface [254]. In some cases, calculations showed that for organic dyes bearing a carboxylic acid as anchoring group, the preferred adsorption mode was bidentate bridging, with one proton transferred to a nearby surface oxygen [50, 219, 255, 256], while monodentate anchoring is usually predicted to be less stable, although some dependency of the relative stability of these two anchoring modes on the employed computational methodology has been outlined [254, 257, 258].

Recently [237] an integrated experimental/computational strategy, combining FT-IR measurements with DFT computer simulations, has been applied to find the most energetically favorable adsorption mode for a carboxylic acid probe, followed by calculation of the IR spectra and structure validation by comparison with experimental data. In particular, the work has been focused on the adsorption of prototypical dyes, exploiting the typical diagnostic symmetric and asymmetric stretching frequencies of the carboxylic group, and choosing the structural simplicity of acetic acid as a meaningful model for realistic organic dyes. Acetic acid offers the advantage of having the most commonly employed carboxylic acid group of realistic dyes, coupled to a single methyl group, substantially simplifying the IR spectrum.

The carboxylic group was initially considered to be protonated, as required by the dye solution charge neutrality. The acidic proton can then be either transferred to the oxide surface (both in a bidentate and monodentate anchoring mode) or be retained on the dye and possibly interact with a surface oxygen via hydrogen-bonding. We considered here two different monodentate binding modes (M1 and M2) and a bridged bidentate (BB) anchoring (see Fig. 16). In M1 the –OH group interacts with a surface oxygen which is not directly bound to the adsorption-involved Ti atom, while in M2 the interaction is instead established with the adjoining surface oxygen; see optimized geometries in Fig. 16.

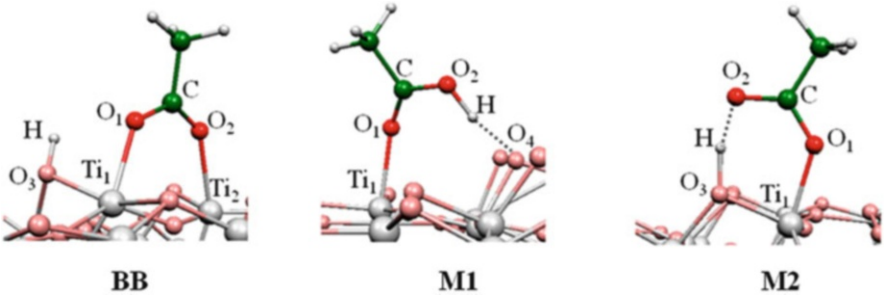

Fig. 16 Optimized geometrical structures of the investigated adsorption modes of acetic acid onto the TiO_2 surface. Reproduced from [237] by permission of the PCCP Owner Societies

For the description of the TiO_2 semiconductor we used two stoichiometric $(TiO_2)_n$ clusters, with $n = 38$ and 82, which have been demonstrated to reproduce to a good degree of accuracy the DOS of periodic TiO_2 surfaces [248]. The two cluster models are used to gauge the stability of the various adsorption modes, allowing for the comparison of hybrid and GGA DFT functionals. We then resorted

Table 2 Relative stabilities (kcal/mol) of the various investigated adsorption modes of AcH on TiO_2

Geometry optimization	Energy evaluation		BB	M1	M2
CL/ADF/PBE/DZ(TZ)VP	PBE/DZ(TZ)VP	*Vac*	0.0	+10.1	−4.1
	PBE/PWs	*Vac*	0.0	+8.9	−4.1
	PBE/6-311G**	*Vac*	0.0	+7.3	−1.6
		Solv	0.0	+4.2	+1.4
	B3LYP/6-311G**	*Vac*	0.0	+10.8	−0.9
		Solv	0.0	+6.5	+1.3
PBC/CP/PBE/PWs	PBE/PWs	*Vac*	0.0	−12.1	−10.8

Both results obtained with a cluster (CL) and a periodic (PBC) TiO_2 model are reported. PBE/DZ(TZ)VP data were obtained by the ADF code and PBE/PWs by the CP code; PBE/6-311G** and B3LYP/6-311G** have been obtained by the Gaussian code

to a $(TiO_2)_{32}$ periodic slab for comparison purposes. It was recently shown that TiO_2 anatase slabs, with a thickness similar to our cluster or periodic models, nicely reproduce the electronic structure of thicker films [250]. In all cases, our TiO_2 models expose the majority (101) surfaces. We refer the reader to [237] for technical details on the cluster/periodic calculations and FT-IR measurements discussed in the following.

For the interacting AcOH/TiO_2 system, the relative energies of the M1, M2, and BB adsorption modes (see Table 2) were calculated. Different calculation levels were employed and the effect of water solvent on the adsorption stability was also taken in account on the geometries optimized in vacuo. Considering the PBE/DZ(TZ)VP [259]

Table 3 Calculated (unscaled) and experimental IR frequencies for AcOH adsorbed onto TiO_2

Frequencies	BB	M1	M2	Exp.
$\nu_{as\ COO}$	1,543	1,614	1,748	1,558
$\nu_{sym\ COO}$	1,432	1,425	1,377	1,424
δ_{CH3}	1,351	1,335	1,416	1,335
$\Delta(\nu_{as}-\nu_{sym})$	111	189	371	134

level used for geometry optimization on the cluster-adsorbed systems, at least two structures should be taken into account in terms of relative energy, i.e., BB and M2. Data in 2 suggest M2 to be the most stable structure, as previously found for acetic acid adsorption on the (110) TiO_2 surface in [260]. On the same (ADF) optimized cluster geometries, the relative stabilities calculated by the PBE functional by ADF [261], Car–Parrinello (CP) [191], and Gaussian03 [262] programs in vacuo are totally consistent, despite the different basis sets (Slater, Gaussian, and Plane Waves), showing a similar description of the dye/TiO_2 interaction by all such computational approaches. M2 is predicted to be the most stable structure, with BB lying very close in energy and M1 much higher. B3LYP data in vacuo are consistent with the corresponding PBE data, suggesting a marginal effect of the functional. Moving to the solution environment, BB was calculated to be the most stable structure both with B3LYP and PBE, with M2 and M1 lying, respectively, 1.3 (1.4) and 6.5 (4.2) kcal/mol higher in energy at the B3LYP [263] (PBE) level. These results are in line with previous calculations, showing a sizable sensitivity of the more stable adsorption mode for carboxylic acids and organic dyes onto the (101) TiO_2 surface in the presence of explicit solvent molecules [257, 264, 265].

Surprisingly, a totally different stability order is calculated if one considers the CP optimized geometries within PBC TiO_2 description (PBE/PWs entries in Table 2), which show the M1 adsorption mode to be the most stable structure, in line with the results of Vittadini et al. on the prototype formic acid system [254]. Considering the large variability of computed stabilities with the employed geometry optimization method and, since based on the relative energies alone it was not possible to discriminate clearly among the possible AcOH adsorption modes, for each of the considered structures, the IR vibrational frequencies at the same PBE/DZ(TZ)VP level of theory used for geometry optimization were calculated. A summary of the main IR peaks and their assignment is reported in Table 3.

Looking at the calculated frequencies, the BB adsorption mode well reproduces the three main spectral features, showing three intense signals at 1,543, 1,432, and 1,351 cm^{-1}, compared to experimental signatures at 1,558, 1,435 and 1,340 cm^{-1}, respectively. The assignment of the 1,543 cm^{-1} feature to the asymmetric COO^- stretching is straightforward, while the two modes calculated at 1,432 and 1,351 cm^{-1} result from the admixture of the symmetric COO^- stretching and of the δCH_3 mode. For the BB structure, the separation between the asymmetric and symmetric COO stretching is 111, comparing reasonably with the 134 cm^{-1} value found experimentally. Based on the simulated IR spectra, the presence of the monodentate species M1 and M2 (either dissociated or undissociated) can be ruled out, due to the significant discrepancies found in their IR spectra compared

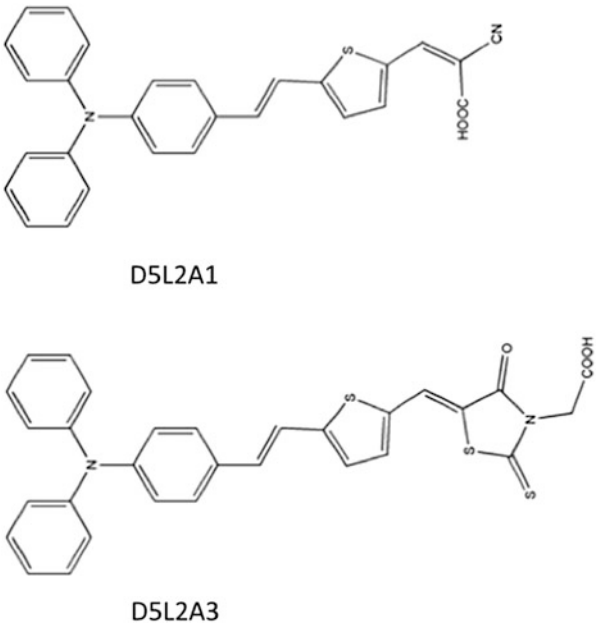

Fig. 17 Molecular structures of the D5L2A1 and D5L2A3 dye sensitizers

to the experimental data. The experimental spectra show no trace of peaks of the characteristic carbonyl stretching belonging to the M2 adsorption mode (~1,760 cm^{-1}). For M1 the feature at ~1,550 cm^{-1} is missing, so even if the low-lying carbonyl stretching (1,614 cm^{-1}) were overlapping with the residual water peak, found at 1,630 cm^{-1}, this mode can be excluded. It has to be noted that frequency assignment in these two cases is complicated by the admixture of several modes, including OH stretchings, so that for M1 and M2 the mode assignments in Table 3 should be taken with some care, although the listed frequencies are those displaying the highest intensity in the investigated energy range. Summarizing, combined experimental and computational modeling of acetic acid adsorption on TiO_2 points at the BB structure as the most likely AcOH adsorption mode, consistent with the calculated energetics in solution.

3.1.2 Effect of Different Anchoring Groups on the Electron Injection/Recombination Dynamics

As already stated, the bonding type and the extent of electronic coupling between the dye excited state and the semiconductor unoccupied states can directly influence the cell performances [1]. An emblematic case is represented by the D5L2A1 (also known as D5) [266, 267] and D5L2A3 [239] dyes, which only differ in the anchoring unit, namely a conjugated cyanoacrylic acid in the former and non-conjugated rhodanine-3-acetic acid in the latter; see molecular structures in Fig. 17. The loss of electron conjugation between the donor-linker moiety and the

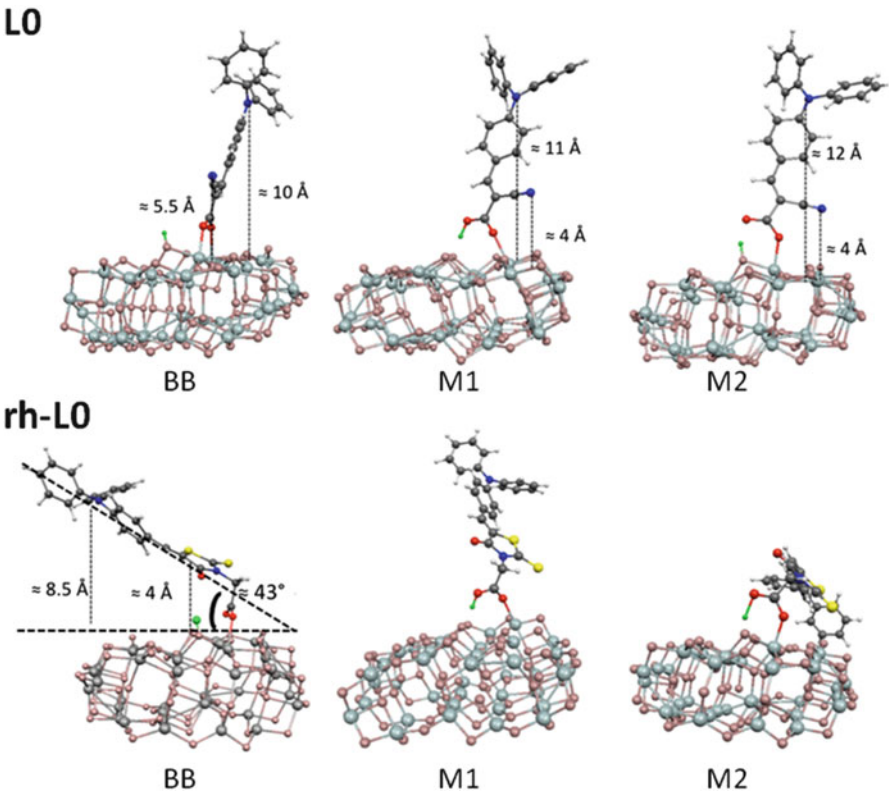

Fig. 18 *Left*: Optimized structures of the L0 (*upper panel*) and rh-L0 (*lower panel*) dyes on TiO_2. *Right*: Chemical structures of L0 (*top*) and rh-L0 (*bottom*). Adapted from [237] by permission of the PCCP Owner Societies

anchoring –COOH group passing from the cyanoacrylic acid to the rhodanine-3-acetic acid, seems to be the cause of the drastic drop in the photovoltaic conversion efficiency of D5L2A3 (~2%) [239] compared to D5L2A1 (~6%) [266, 267]. Wiberg et al. [218] reported that the two different sensitizers showed unitary electron injection efficiency but substantially different rates of charge recombination between the photo-injected electrons and the oxidized dye, with estimated losses of 80% and 50% of injected electrons for D5L2A3 and D5L2A1, respectively, within 1.4 ns.[218]

Thus we discuss here the possible anchoring modes to the TiO_2 surface of two representative organic dyes employed in DSSC devices [239, 268], hereafter referred as L0 and rh-L0 (optimized structures grafted on the TiO_2 slab in Fig. 18). These two dyes are interesting in themselves, being experimentally employed in DSSC and, having TPA donor groups and cyanoacrylic and rhodanine-3-acetic acids acceptor moieties, respectively, representing valuable models for the D5L2A1 and D5L2A3 dyes, subjects of the investigation of Wiberg

Table 4 Relative energies (kcal/mol) of BB, M1 and M2 adsorption modes of L0 and rh-L0 on $(TiO_2)_{38}$

Energy evaluation		BB	M1	M2
L0 dye				
PBE/DZ(TZ)VP	*Vac*	0.0	+10.9	−1.5
PBE/6-311G**	*Vac*	0.0	+10.8	+2.6
	*Solv**	0.0	+8.4	+7.4
B3LYP/6-311G**	*Vac*	0.0	+14.9	+3.6
	Solv	0.0	+10.9	+7.7
rh-L0 dye				
PBE/DZ(TZ)VP	*Vac*	0.0	+7.1	−1.9
PBE/6-311G**	*Vac*	0.0	+6.7	−5.6
	*Solv**	0.0	+0.4	+5.0
B3LYP/6-311G**	*Vac*	0.0	+8.1	+2.9
	Solv	0.0	+0.4	+7.7

From [47] PBE results in water (Solv* entry) solution were obtained with the 6-311G** basis set

et al. [218]. We consider here both monodentate and bidentated binding: see optimized structures in Fig. 18 and the relative energies of BB, M1, and M2 adsorption modes in Table 4. The calculated data follow the trend outlined above for acetic acid adsorption, whereby at the PBE/DZ(TZ)VP/vac level of theory, M2 is slightly more stable, by 1.5 kcal/mol, than the bidentate structure, BB, while the M1 configuration seems to be strongly destabilized (ca. +10 kcal/mol) with respect to BB. Single point calculations on the optimized structures in solution, however, always indicate the bidentate configuration as the preferred one, giving the stability ordering BB > M2 > M1. Although all three investigated structures would be compatible with the PES data for the related D5L2A1 dye [238], which indicate that the molecule lies with the donor (TPA) group pointing out from the surface and the acceptor CN group close to the TiO_2, our calculated stabilities are suggestive of a bidentate coordination mode for L0 and analogous dyes bearing a cyanoacrylic anchoring group [50]. Similar remarks can be made for rh-L0: at the PBE/DZ(TZ)VP/vac level of optimization, the bidentate structure is the most stable adsorption mode. Although small energy differences are calculated between different levels of theory, these data indicate overall that the bidentate coordination is also favored for the rhodanine dyes, and therefore we conclude that rh-L0 as well as the related D149 and D102 [219] dyes lie almost flat with an inclination of about 45° with respect to the TiO_2 plane, as also found in previous works [27, 269].

As discussed by Wiberg et al. [218], the substitution of the cyanoacrylic anchoring group with the rhodanine-3-acetic acid one, by breaking the electron conjugation between the donor-linker moiety and the COOH anchoring unit, should drastically reduce the coupling between the dye and the TiO_2. This is effectively retrieved both experimentally and theoretically for perylene dye-sensitized TiO_2 [252, 270–272], for which a substantially different coupling was found by varying the nature of the anchoring group leading to associated different measured injection dynamics. A qualitative analysis of this different dye/semiconductor coupling for L0@TiO_2

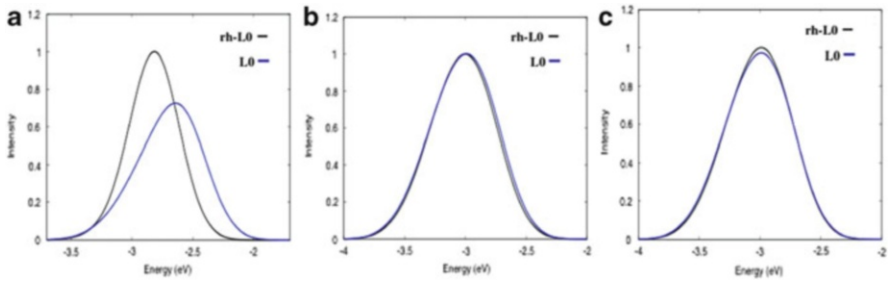

Fig. 19 Plots of density of states (DOS) for the L0 (*blue lines*) and rh-L0 (*black lines*) dyes. (**a**) Dyes contribution. (**b**) $(TiO_2)_{38}$ cluster contribution. (**c**) Total DOS. Reproduced from [47] by permission of the PCCP Owner Societies

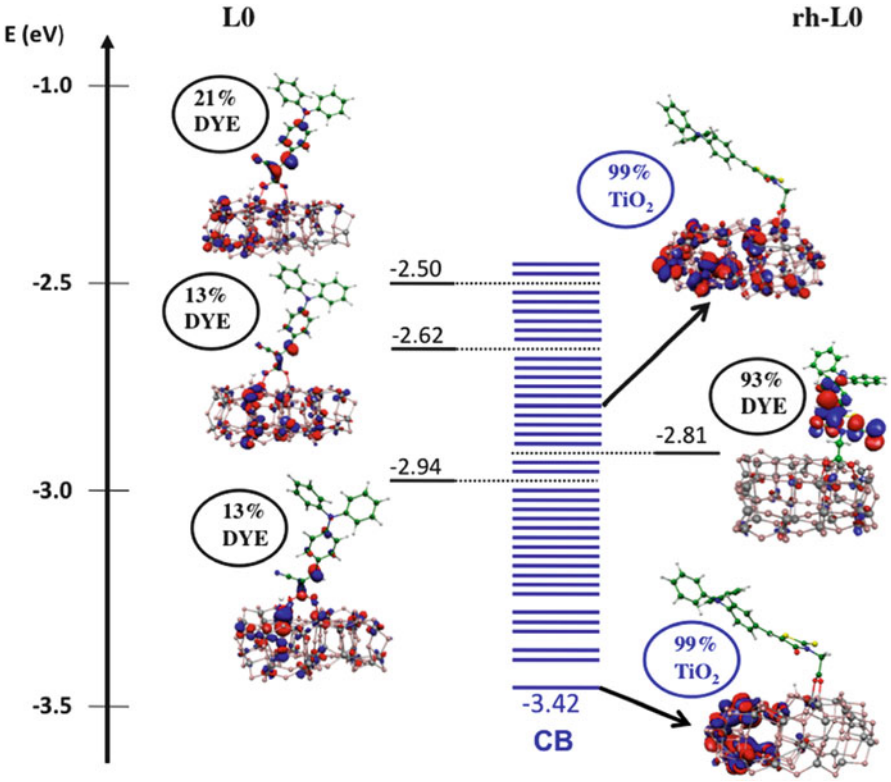

Fig. 20 Isodensity surface plots of some representative molecular orbitals of the L0@TiO_2 (*left side*) and rh-L0@TiO_2 (*right side*) systems and their relative energy alignment. Reproduced from [47] by permission of the PCCP Owner Societies

and rh-L0@TiO_2 systems is reported in Figs. 19 and 20, where a comparison between the DOS profiles and an energy level alignment diagram with the plots of the representative molecular orbitals are reported, respectively. As can be seen, while

the two systems show a marked difference in the dye projected DOS (a in Fig. 19), no appreciable shift in the TiO_2 and total DOS is observed (b and c in Fig. 19, respectively). The narrow projected DOS peak of rh-L0 clearly indicates a negligible mixing between the excited state of the dye and the manifold of the TiO_2 CB, as is in fact shown in Fig. 20, where we found at −2.81 eV a molecular orbital essentially corresponding to the pure LUMO of the dye (93% of electron density localized on the dye molecule). Conversely, for the conjugated L0@TiO_2 system, the dye-projected DOS exhibits a broader shape, being indicative of a considerable mixing between the dye excited state and the TiO_2 CB states. Considering a window of 40 unoccupied orbitals, in Fig. 20, we report only the three molecular orbitals with a contribution to the electron density from the dye larger than 10%: these are located at −2.94 (13%), −2.62 (13%), and −2.50 eV (21%); the remaining 53% of dye LUMO character is spread over the other CB states considered here. In Fig. 20 we also report the energy distribution of the TiO_2 unoccupied states, with the lower-energy and less-dense region, corresponding to more localized trap states and the higher-energy states which are, as expected, completely delocalized. It is worth mentioning that our calculated alignment of energy levels is in excellent agreement with spectro-electrochemical data showing essentially the same energy of the dye excited state, with D5L2A1 [268] only slightly higher than D5L2A3 [239]. Moreover, taking for the TiO_2 conduction band edge a typical value of ca. −0.5 vs NHE [1], a "driving force" for electron injection of 0.86 (D5L2A1) and 0.54 V (D5L2A3) is inferred from the spectro-electrochemical data, compared to a ~0.5–0.6 eV difference calculated in Fig. 20.

How can such a different electronic coupling influence the ET kinetics? In [218] for the analogous D5L2A3 and D5L2A1 dyes, no difference in the rate of electron injection <100 fs (the instrument set up limit) could be measured, but rather when the rhodanine-3-acetic anchoring group was considered (D5L2A3) the back recombination reaction between photo-injected electrons and the oxidized dyes was accelerated. A difference in the location of the injected electrons was invoked to justify such differences in the back recombination rates: the electrons injected by D5L2A3 are supposed to be located at the semiconductor surface to a higher extent than those injected by D5L2A1. Therefore, the electron injection reactions for the two classes of dyes turn out to be comparably fast and efficient, even if intimately different in the mechanism: in L0 (D5L2A1), given the strong coupling, the photo-excited electron has a large probability to be directly injected into the CB states or if a long-lived charge-separated dye excited state is formed it is immediately and adiabatically transferred to the oxide acceptor states; in the case of rh-L0 (D5L2A3) the non-adiabatic electron injection from the dye excited state also follows ultrafast kinetics owing to the high-density of accessible acceptor isoenergetic states (see Fig. 20) as well as a modest donor-acceptor separation, being approximately 5 Å (see BB1 structure in Fig. 18).

To discuss the differences in the recombination reactions [169, 273] it is worth remembering that the kinetics of recombination between the injected electrons and the dye cations are strongly dependent upon the electron density in the conduction band/trap states (the rate accelerates as the cell voltage is increased), the electrolyte

composition [274–276], and the spatial separation of the charge hole localized on the oxidized dye, which can be assimilated to the HOMO of the neutral dye, and the TiO_2 surface [173, 277]. Solely on the basis of the discussed results, i.e., of the different charge injection mechanisms, it is not straightforward to hypothesize a different location of the injected electrons as one should take into account the complex dynamics of the delocalization of the electrons into the oxide bulk as well as their relaxation pathways to the CB edge [278]. We can however speculate that for the rh-L0 dye, and in general for those dyes characterized by a weak electronic coupling with the semiconductor CB, the prevalence of a non-adiabatic electron injection mechanism implies an exponential dependence of the electron transfer rate upon the dye donor/semiconductor acceptor states, i.e., the electronic coupling is determined by the tunneling probability, with the associated exponential decay. It can therefore be conceived that a high probability of electron injection would correspond to semiconductor CB states localized close to the dye LUMO, i.e., CB states localized at the semiconductor surface rather than within the bulk, from which a faster recombination with oxidized dyes can be expected. One can furthermore elaborate that the different orientation of the dyes with respect to the surface, determined by the different anchoring unit, results in a different dye HOMO/TiO_2 CB separation even considering the same nature of the CB states involved in the electron injection from L0 and rh-L0 dyes. Looking at the bidentate structures reported in Fig. 18, and considering the TPA donor unity, the dye HOMO/TiO_2 distance can be roughly estimated to be 8–10 Å for L0 and 6–8 Å for the rh-L0 dye. By extrapolating this data for the longer D5L2A1 and D5L2A3 dyes examined by Wiberg et al. [218], we calculate a dye HOMO/TiO_2 separation of 14–16 Å and 9–11 Å for the two dyes, respectively. These results might also account for the measured differences in the recombination rates, whereby a closer proximity of the hole localized on the dye to the semiconductor surface would lead to higher recombination rates [279]. This hypothesis also seems to be corroborated by the recombination kinetic data recently reported by Long et al. [280] which, despite a reversed HOMO energy compared to the present case, showed an increased recombination rate between injected electrons and the oxidized sensitizer for the dye bearing the rhodanine-3-acetic acid (D205, more positive oxidation potential) compared to that having the cyanoacrylic acid group (C218, less positive oxidation potential).

A large body of theoretical investigations has been specifically devoted to the effect of the dye anchoring and spacer groups in determining the efficiency of the electron injection steps and the minimization of parasitic recombination processes [47, 217, 251, 252, 281–290]. The effect of the anchoring group on the electron injection dynamics in dye-sensitized semiconductor surfaces was pioneered by Persson and co-workers in a series of papers [217, 281–283, 291]. These authors exploited the Newns–Anderson model framework to estimate the lifetime of an electron initially residing on the dye LUMO when it comes into contact with the manifold of unoccupied semiconductor states. The resulting state broadening is an estimate of the injection time. The main findings of these studies are that a conjugated anchoring group, e.g., a perylene dye featuring a double bond

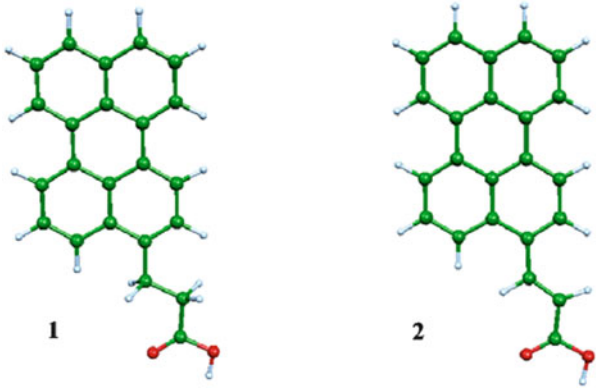

Fig. 21 Optimized molecular structures of the perylene dyes **1** and **2**. Reprinted from [252] with kind permission of Elsevier

connecting the donor and acceptor moieties (1 in Fig. 21), exhibits a much stronger interfacial coupling and shorter electron injection time than the same system with a non-conjugated anchoring group (2 in Fig. 21).

Persson, Thoss and co-workers later performed quantum dynamics simulations on the same perylene systems, confirming the static electronic structure picture [284]. We also reported on the same conjugated and non-conjugated perylene dyes of Fig. 21, performing TDDFT excited state calculations for the dyes adsorbed on a model TiO_2 nanoparticle.

An interesting contribution to the "anchoring group" issue came recently from the Troisi group, who systematically investigated electron injection times in a series of different dyes. They set up a new computational strategy, which allows one to compute the injection times by simply investigating the TiO_2-anchoring group interface, without the need to compute the entire dye/semiconductor system. For dyes carrying the same anchoring groups this clearly represents an advantage, since a single calculation on the anchoring group/TiO_2 is needed, followed by simple molecular investigations on the isolated dyes. The ET rate is expressed in terms of coupling and overlap matrix elements, and the semiconductor's energy-dependent density matrix. Here we briefly review the results for the search for the optimal dye anchoring group. The authors investigated a series of possible anchoring groups, reported in Fig. 22, in combination with a perylene donor moiety.

The authors investigated the attachment chemistry and computed the binding energies of 15 different anchoring groups on both anatase (101) and rutile (110) surfaces. Periodic calculations using the B3LYP functional were performed. Most of the groups were found to have multiple stable adsorption modes, with a total of 35 adsorption modes on anatase (101) and 26 adsorption modes on rutile (110). For each anchoring group and each observed adsorption geometry, the authors computed the electron injection time for a perylene molecule bearing the selected group on anatase (101) and rutile (110). Here we just comment on the injection times for the most stable adsorption geometries, which are reported in Fig. 23. The representation of Fig. 23 allows for an immediate visualization, in the top left quadrant of the diagram, of the anchoring groups that can be considered promising alternatives to the

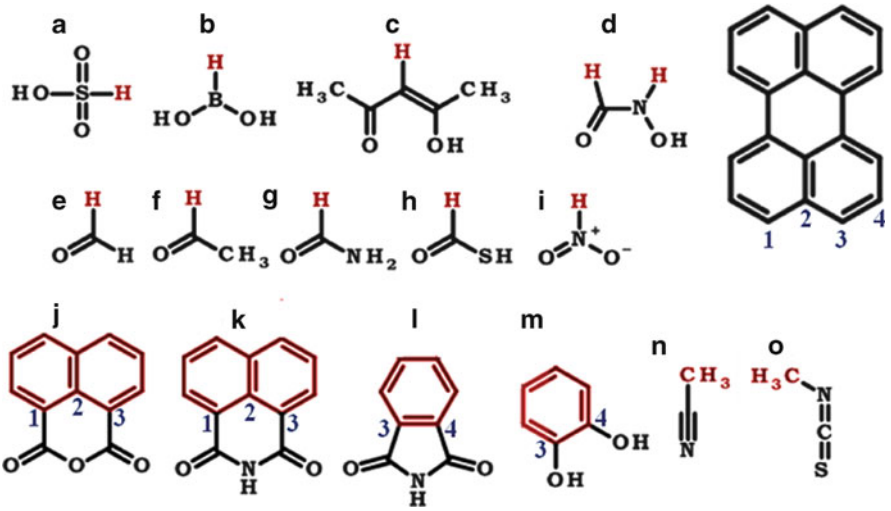

Fig. 22 (**a**–**o**) Molecules with model anchoring groups studied in [290]. Reprinted with permission of [290]. Copyright (2012) American Chemical Society

common carboxylic acid in terms of good properties for both anchoring stability and injection. Various interesting alternatives to the most common carboxylic or phosphonic acid anchoring were pointed out by this computational investigation, such as acetylacetone (c) and hydroxamic acid (d) anchors, which both display good computed binding and injection characteristics. A main conclusion of this study is that the results are not easily predictable on the basis of chemical intuition alone because the electron injection rate is determined by the delicate balance between weights of the dye LUMO and the orbital couplings. While the former is due to the electron distribution of the dye, which can be intuitively predicted, the latter is influenced by the adsorption geometry and the surface electronic structure, which are much harder to guess.

3.2 Ruthenium-Dyes on TiO_2

Similarly to what has been discussed for modeling studies on the isolated dyes, the success of the N3/N719 sensitizer in DSCs has led to several theoretical/computational investigations being devoted to studying the adsorption and electronic/optical properties of this complex on TiO_2 [46, 105, 118, 246–248, 291–294]. In parallel, various computational investigations have been reported for the adsorption of the black dye on TiO_2, using both cluster and PBC approaches [114–116], including recent work from our lab [118].

The first DFT investigation of a Ru(II)-dye adsorbed onto TiO_2 was reported by Persson et al. in 2005 [295]. The adsorption mode occurred via a single bipyridine ligand, which was binding to TiO_2 in a bidentate dissociative way. The lowest

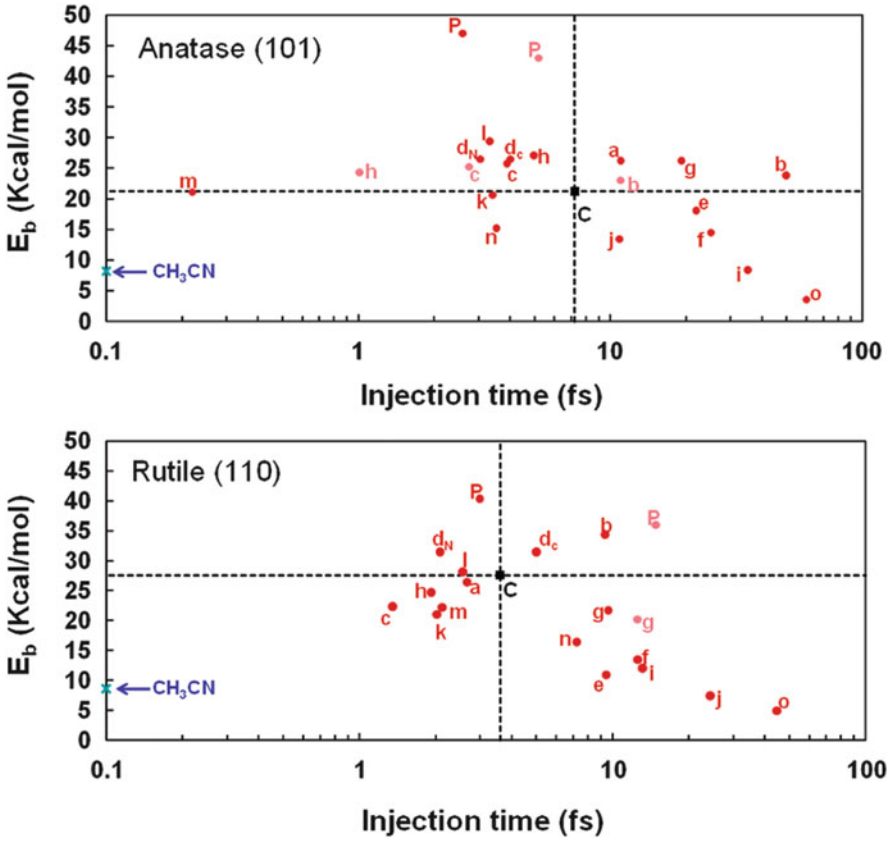

Fig. 23 Electron injection times vs adsorption energy for different anchoring groups (a−o) for anatase (101) and rutile (110). Reprinted with permission of [290]. Copyright (2012) American Chemical Society

TDDFT excited states for the combined system were calculated and an injection time of 10 fs was estimated [291]. The effect of TiO_2 protonation and of the dye adsorption mode for the N719 system on TiO_2 was later simulated by us [46, 105]. In an effort to optimize the overall device conversion efficiency, it was found that the sensitizer's carboxylic groups, the photocurrent, and the open-circuit voltage significantly increase and decrease by increasing the number of protons carried by the sensitizer's carboxylic groups respectively. Optimal performances were obtained for dyes carrying one to two protons over a possible range of zero to four [104, 105]. Since some of the sensitizer's protons can be transferred to the TiO_2 surface [105], these observations indicate that protonation of the sensitizer and/or of the surface can have an important influence on the electronic dye/semiconductor coupling and on the position of the TiO_2 conduction band in DSCs [234].

Moreover, unexpectedly, experiments have shown that V_{OC} for DSCs employing heteroleptic dyes is significantly lower compared to that observed using homoleptic sensitizers containing the same number of protons [46]. This difference is likely to

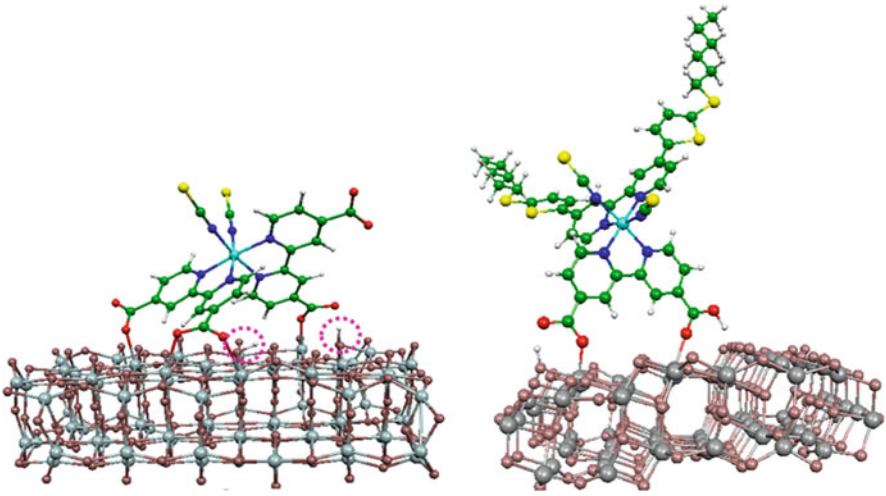

Fig. 24 Adsorption geometries of two prototypical Ru(II)-complexes: (*left*) N719 with three points anchoring (one bidentate bridging and two monodentate) and (*right*) C106 with two monodentate points anchoring

originate from the different adsorption modes of the two types of complexes onto the TiO_2 surface. Indeed, while homoleptic dyes, such as N3 or N719, can adsorb on TiO_2 using carboxylic anchoring groups residing on different bipyridine ligands and hence using up to three carboxylic groups [246, 247], Fig. 24 (left side), heteroleptic dyes, e.g., N621, C106, or Z907, necessarily adsorb via carboxylic groups residing on the same bipyridine (two carboxylic groups) [28, 84], Fig. 24 (right side). For the related black dye, carrying a carboxy-substituted terpyridine ligand, various anchoring modes were reported, depending on the protonation of the dye [114], similar to what is found for the N719 dye [246].

3.2.1 N3/N719 Dyes

We have recently reported on the influence of the molecular adsorption geometry, counterions, and surface protonation on the electronic structure of the dye/semiconductor systems by means of Car–Parrinello molecular dynamics combined with single point hybrid functional calculations of the electronic properties [247] Our results show that the homoleptic N719 and YE05 dyes, both bearing two bipyridine ligands functionalized with four carboxylic groups, adsorb onto the TiO_2 surface by exploiting *three* carboxylic groups. A subsequent paper by Schiffmann et al. [246] has confirmed that this adsorption mode is the more stable when protons are present in the combined dye/semiconductor system.

The bulky TBA counterions employed in N719 cause a modest energy down-shift of the TiO_2 conduction band, while the smaller Na^+ counterions, which can access the surface more closely, lead to a larger conduction band energy perturbation. Our

results also confirm that the surface protonation plays a fundamental role in determining the DSSC efficiency, with a strong impact on both short circuit photocurrent and open circuit voltage. Altogether, our study provides evidence that adsorption of the sensitizer via "three anchoring sites" is a key requisite to obtain high open circuit potentials when employed in DSSC devices, thus paving the route to the design of new and more efficient sensitizers.

Labat et al. [293] also reported a periodic DFT investigation of the N3 dye on TiO_2, considering binding through a single bipyridine ligand. This study confirmed a highly favored electron injection step from the dye LUMO, with an estimated injection time of 22 fs. An interesting study by the same authors was reported later [292] in which the effect of the different binding and anchoring mode of the N3 dye onto TiO_2 on the electronic and optical properties of the joint system was presented. Although, due to the limited available surface area, the authors considered only binding via two carboxylic groups (see Fig. 25), they found that adsorption mode BB, which exploits two anchoring groups from two different bipyridine ligands, was the favored adsorption mode, similar to what was previously found by us [46]. Most notably, the calculated injection times showed the BB adsorption mode to exhibit the shortest value (3 fs), followed by the mixed monodentate-bidentate, MB, and by the mixed monodentate bidentate with additional NCS interaction, MB′ (22 and 100 fs, respectively). These results clearly highlight the importance of the dye adsorption mode on TiO_2 in mediating the interfacial electronic coupling and therefore the injection time.

Almost at the same time, Martsinovich et al. [294] investigated the N3 dye adsorption on the rutile (110) surface rather than on the anatase (101) surface as from previous studies. These authors systematically investigated several dye adsorption modes, as reported in Fig. 26, evaluating the energetics of the different anchoring modes and the related electronic structures and injection times.

On the basis of the calculated adsorption energies, it was not possible to identify a single adsorbed structure, which is more favorable than others. Instead, the authors found several configurations with similar stabilities, which may co-exist or convert into one another. The authors calculated injection times from the LUMO of the N3 molecule to the TiO_2 conduction band for all the studied configurations; see last column of Table 5. Injection from the molecule adsorbed via just one carboxylic group (configuration 1) is slower (12–26 fs), similar to what was found by Labat et al. [292]. The injection times for configuration 1 are also longer than the experimental upper limit for the injection time for N3 on rutile and anatase, 12 and 20 fs [296–300], and therefore the one-carboxylate configuration was ruled out. Among the configurations adsorbed via two or three carboxylic groups, the structures with only MH adsorption showed slower injection, above the experimental value of 12 fs [300]; purely M adsorption also gives relatively slower injection. Configurations with BB adsorption showed the fastest injection, similar to or faster than the experimental upper limit, again in line with previous results [292].

The large body of studies on N3/N719 on TiO_2 revealed that several adsorption modes are energetically feasible, including anchoring by one, two, or three carboxylic groups depending on the conditions (solvent, presence of acids/bases) and the type of

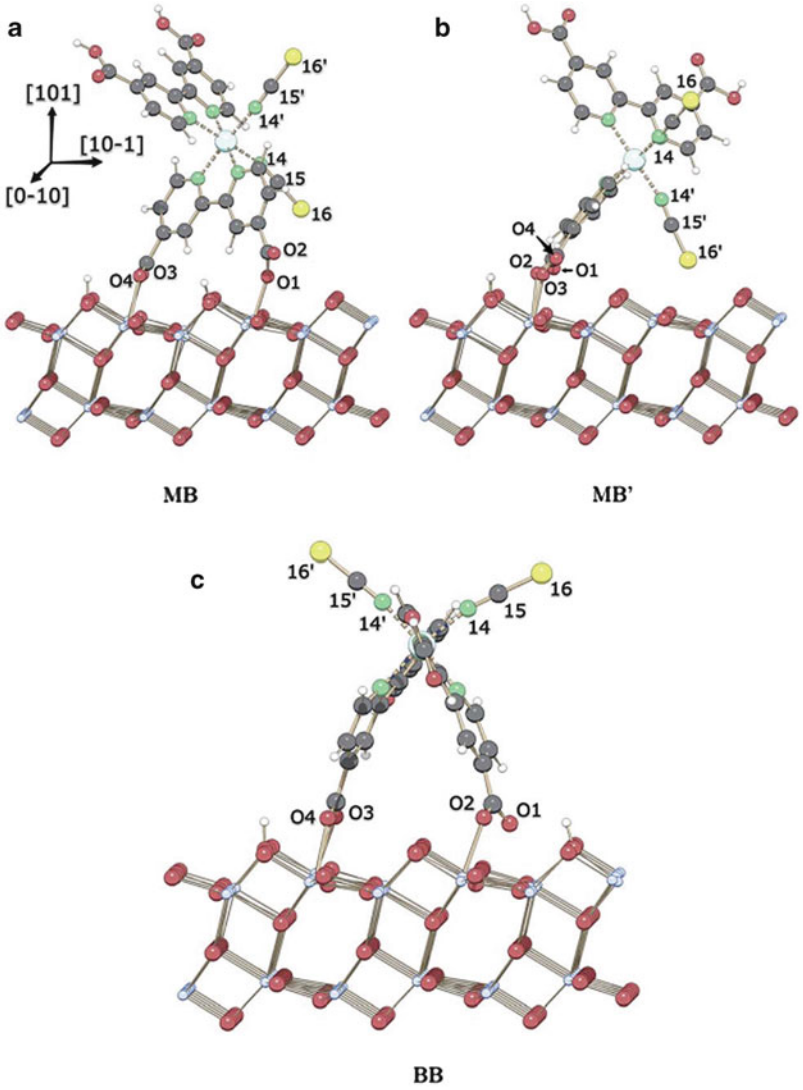

Fig. 25 Side views of the (**a**) MB, (**b**) MB′ and (**c**) BB adsorption modes of N3 on TiO_2 anatase (101). *Black*, *red*, *green*, *yellow*, and *white* spheres represent C, O, N, S, and H atoms, respectively. Ru and Ti atoms are shown as light blue spheres. Because of an approximate C2 axis along the bisector of the N14–Ru–N14′ and N8–Ru–N8′ angles in the isolated N3 molecule, symmetry-related atoms are designated with a prime. Reprinted from [292] by permission of Royal Society of Chemistry

substrate (anatase vs rutile). What is also noticeable is the substantial dependence of the calculated electronic properties on the adsorption mode, with a peculiar sensitivity of injection time from the latter. On a different note, the calculated optical properties for various adsorption modes are less sensitive to the precise adsorption

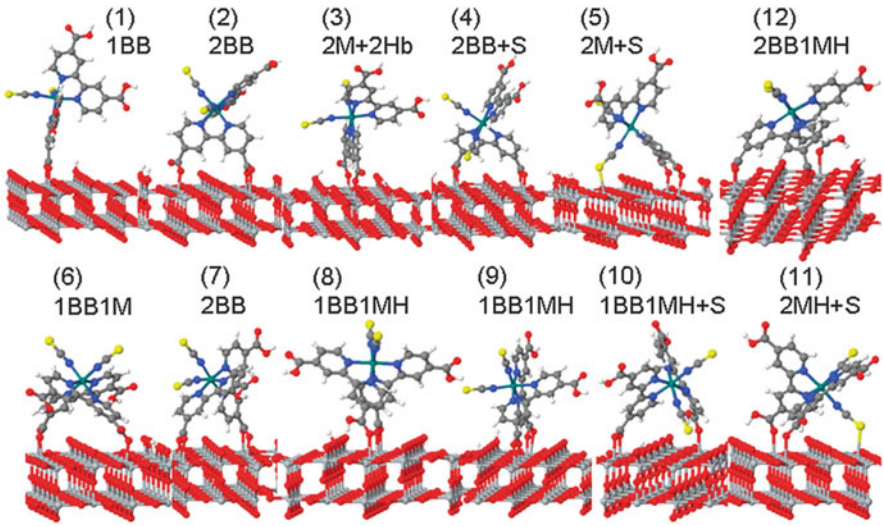

Fig. 26 Most stable adsorption geometries of N3 on rutile (110) slab (see also Table 5). Reprinted from [294] by permission of the PCCP Owner Societies

features [46], suggesting that the N3 dye might experience a heterogeneous environment when bound to the TiO_2 surface which might be reflected in a spread of injection times but not revealed by UV–vis spectroscopy.

As a final application for modeling the N3/N719 dye on TiO_2, we report in Fig. 27 the comparison between the experimental and TDDFT-calculated optical absorption spectra for N719 bound to a large $(TiO_2)_{82}$ cluster. The TDDFT calculations were performed on the GGA-optimized geometries, employing the hybrid B3LYP functional with a 3-21G* basis set. The effect of the surrounding water solvent is included by employing a polarizable continuum model of solvation (C-PCM). To calculate the absorption spectrum up to ca. 2.5 eV, corresponding to the entire first visible absorption band, a large number of singlet excited states were computed (the 50 lowest transitions) with an associated large computational overhead. We also calculated the lowest 25 triplet excited states (inset of Fig. 27).

The agreement between the calculated and experimental spectra in Fig. 27 is excellent over the investigated energy range. The calculated spectral profile shows a shape comparable to the experimental one, with the absorption maximum being calculated at 552 nm (2.25 eV), compared to an experimental band maximum at 531 nm (2.34 eV). The small discrepancy between theory and experiment ($<$0.1 eV) seems to confirm the accuracy of the employed model and adsorption geometry. Since the use of cluster models for TiO_2 could lead to some cluster size dependency of the results [158], we compared the present data, obtained by N719 adsorbed onto a $(TiO_2)_{82}$ cluster, with our previous data for the same dye adsorbed on the smaller $(TiO_2)_{38}$ cluster [105]. For N719@$(TiO_2)_{38}$ the TDDFT absorption maximum was calculated at 2.07 and 2.27 eV, depending on the position of the dye

Table 5 Adsorption configurations of N3 on the rutile (110) slab, their adsorption energies and injection times

Number	Configuration	Structure		Adsorption energy (eV)	Injection time (fs)
		Starting	Final		
1	1COOH-*trans*	1BB	1BB	−1.07	11.8
	1COOH-*cis*	1BB	1BB	−1.08	26.3
2	2COOH-same-2rows	2BB	2BB	−0.99	4.1
3	2COOH-same-1row	2BB	2M+2Hbonds	−0.90	4.4
		2BB	2M	−0.62	23.2
		2MH	2MH	−0.68	19.6
4	2COOH-same-2rows-S	2BB+S	2BB+S	−1.01	4.6
5	2COOH-same-1row-S	2BB+S	2M+S	−0.96	11.4
		2MH+S	2MH+S	−0.84	90.7
6	2COOH-diff(2*trans*)-2rows	2BB	1BB1M	0.09	8.9
7	2COOH-diff(*cis*,*trans*)-2rows	2BB	2BB	−0.86	26.9
8	2COOH-diff(2*trans*)-1row	2BB	2BB	−0.04	6.0
		1BB1MH	1BB1MH	−0.67	11.9
		2MH	2MH	−0.63	26.7
9	2COOH-diff(*cis*,*trans*)-1row	2BB	1BB1M	−0.51	10.2
		1BB1MH	1BB1MH	−0.80	3.0
		2MH	2MH	−0.76	10.8
10	2COOH-diff(*cis*,*trans*)-2rows-S	2BB+S	1BB1M+S	−0.91	6.5
		1BB1MH+S	1BB1MH+S	−0.95	7.3
		2MH+S	2MH+S	−0.83	17.0
11	2COOH-diff(*cis*,*trans*)-1row-S	2BB+S	1BB1M+S	−0.91	5.9
		1BB1MH+S	1BB1MH+S	−0.79	4.7
		2MH+S	2MH+S	−1.04	14.0
12	3COOH	2BB1MH	2BB1MH	−1.04	7.3
	3COOH	3BB	3BB	−0.26	3.3

Data from [294], courtesy of the authors

protons, suggesting a moderate role of the TiO_2 cluster size in determining the optical absorption of the joint dye/semiconductor system.

For N719@$(TiO_2)_{82}$, the lowest 17 TDDFT transitions, spanning an energy range between 1.58 ($S_0 \rightarrow S_1$) and 1.88 ($S_0 \rightarrow S_{17}$) eV, correspond to direct excitations from the dye HOMOs to the lowest unoccupied states of TiO_2, with negligible oscillator strength (<0.001), i.e., a vanishingly small probability of being populated in absorption. The lowest excitation with a sizable oscillator strength is the 18th ($S_0 \rightarrow S_{18}$) excited state, which is calculated at 649 nm (1.91 eV). This transition is clearly responsible for the shoulder exhibited by the experimental absorption spectrum in exactly the same energy range; see Fig. 27.

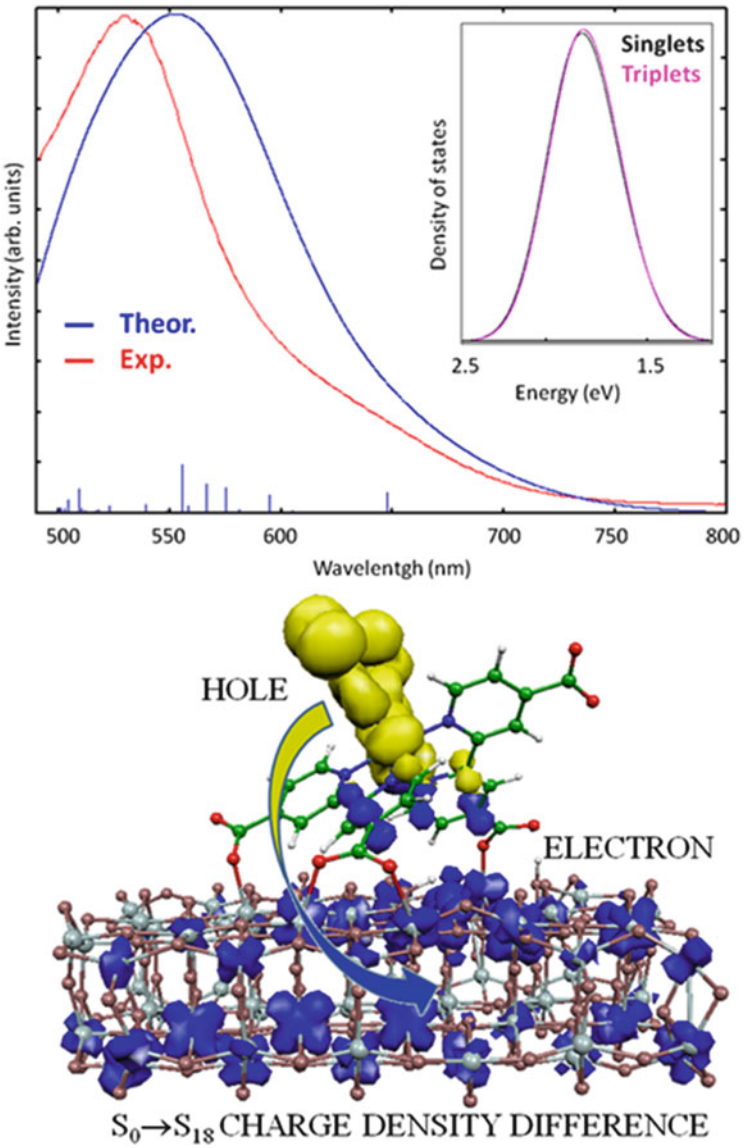

Fig. 27 *Top*: Comparison between the experimental (*red*) and calculated (*blue*) absorption spectra of N719 on TiO_2. The intensity of the experimental spectrum has been rescaled so that the absorption maxima match. The *inset* shows the calculated density of singlet (*black*) and triplet (*magenta*) excited states (energy in eV) for the same system. *Bottom*: Charge density difference between the ground state (S_0) and the S_{18} excited state. A *blue* (*yellow*) color signifies and increase (decrease) of charge density upon electron excitation. Reprinted with permission of [141]. Copyright (2013) American Chemical Society

Also shown in the bottom panel of Fig. 27 is the charge density difference between the S_0 ground state and the S_{18} excited state. Considering the strong admixture of dye/semiconductor unoccupied states, the ultrafast electron injection times measured for the N3/N719 dyes on TiO_2 are not surprising [301, 302]. Following visible light absorption, the excited electron is already partly delocalized into the semiconductor and only weakly interacting through the dye π^* orbitals with the charge hole localized on the Ru-NCS moieties (Fig. 27). This seems an almost "direct" injection mechanism [295], partly mediated by the dye contribution to the excited states which provides a sizable transition probability, but without the appearance of a new or shifted absorption band in the combined systems spectrum.

We now turn to the alignment of the energy levels in the combined N719@TiO_2 system. In the following we report the single particle energies (HOMO/LUMO) together with the TDDFT many-particle energies of the entire system, which can be directly compared on the same diagram under the assumption that the HOMO and LUMO energies are a reasonable estimate of the corresponding oxidation/reduction potentials. For such a purpose, we have fixed the relative energy scale of our system by taking as a reference the energy of the dye HOMO, which, for the isolated dye, represents a good approximation to the dye Ground State Oxidation potential (GSOP). In the combined N719@TiO_2 case, the dye-based HOMO is calculated at -5.34 eV, essentially coinciding with that of the tetraprotonated N3 dye in solution (-5.39 eV). With the estimate of dye GSOP, we can thus locate the position of the lowest TiO_2-based excited state level simply by adding the energy of the TDDFT $S_0 \rightarrow S_1$ transition (1.58 eV) to the HOMO energy (-5.34 eV), obtaining -3.76 eV for the lowest excited state localized on the TiO_2. The lowest dye-based excited state is accordingly calculated at -3.43 eV, with a corresponding lowest driving force for electron injection of ca. 0.3 eV. Considering a Nernstian behavior for TiO_2, at pH $= 7$ a TiO_2 flatband energy of -0.82 V vs SCE (-0.58 vs NHE) can be estimated [38, 41]. Converting the energy of the NHE reference electrode in water to the vacuum scale, we can position the TiO_2 manifold of unoccupied levels at -3.86 eV vs vacuum, which is almost coincident with our estimate, although, due to the limitations of our model, a comparison should be performed with some caution. Having located the dye-sensitized TiO_2 absorption onset on an absolute energy scale, we can further superimpose the density of unoccupied states in the dye-sensitized and unsensitized TiO_2 on the excited state energy diagram to provide a picture of the alignment of the absorption spectrum (mainly due to the dye transitions) and the density of TiO_2 unoccupied states. Such information is reported in Fig. 28, where the energy of the lowest unoccupied TiO_2 molecular orbital of the combined system, yielding the DOS on the right-side of Fig. 28, has been aligned to the lowest transition of the combined N719@TiO_2 system. As can be seen, the absorption spectrum of the combined system matches very well with the density of unoccupied states in both sensitized and unsensitized TiO_2, with all the most intense transitions of the absorption spectrum taking place in a region of high TiO_2 density of unoccupied states. This is an essential requirement, along with the spatial excited state coupling, ensured by the nature of the excited states, to have the very efficient ultrafast electron injection observed in this system.

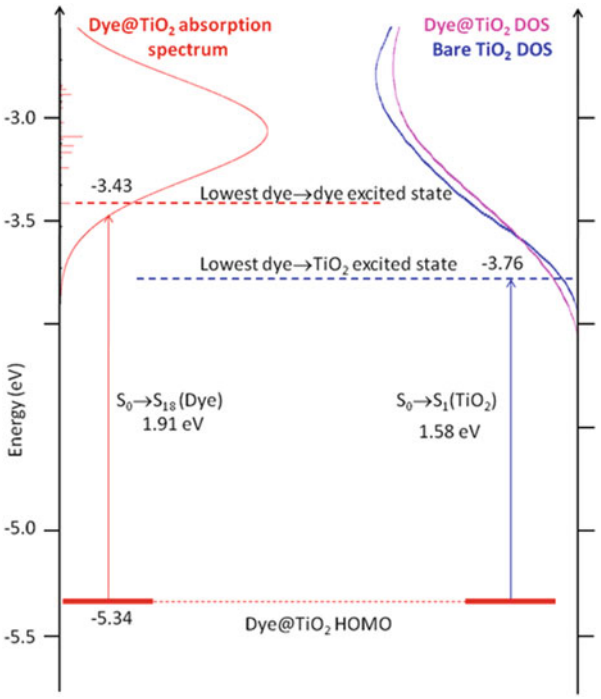

Fig. 28 *Left*: Alignment of the ground and excited state energy levels for the interacting N719@TiO_2 system. *Right*: The calculated density of unoccupied TiO_2 states has been aligned to the energy of the lowest TiO_2 state in the combined system. Reprinted with permission of [141]. Copyright (2013) American Chemical Society

3.2.2 Black Dye

The optical absorption spectrum of the black dye (BD) adsorbed onto TiO_2 clusters (BD@TiO_2) has also been calculated [115], although a simplified $(TiO_2)_{28}$ model was employed which did not allow full exploration of the possible dye binding modes [116]. Despite the limited size of the TiO_2 cluster used, the TDDFT-calculated optical absorption spectrum of BD@TiO_2 in various protonation states were in good agreement with experimental data; see a comparison of the entire data set in Fig. 29.

A slight dependency of the calculated absorption spectrum on the number of protons initially carried by the dye was observed, which led to a slight red-shift when increasing the proton content in the model.

The work by Sodeyama et al., on the other hand, explored in detail the possible BD binding modes on TiO_2 using a periodic model considering the fully protonated dye [114]; see Fig. 30 for a survey of the calculated structures. The same authors also reported the TDDFT-simulated optical properties for the isolated dye at their adsorption geometry [114].

The authors concluded that, for the fully protonated BD, a molecular monodentate adsorption mode is the more stable structure, in contrast to most previous reports concerning carboxylic anchoring groups. This conclusion was also supported by the

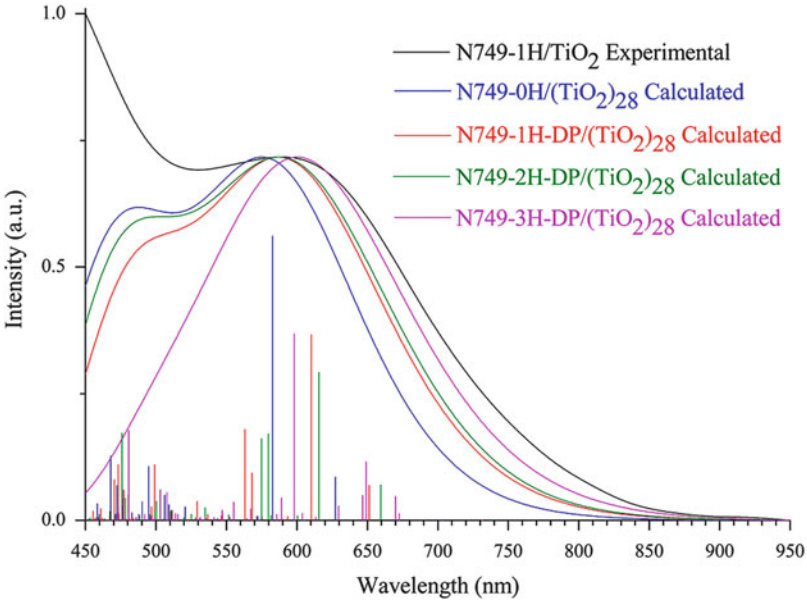

Fig. 29 The experimental N749-1H/TiO_2 and calculated absorption spectra of the four N749-DP/$(TiO_2)_{28}$ surface models in acetonitrile. The label DP indicates the deprotonation of anchored dye. The *blue*, *red*, *green*, and *pink vertical lines* at the bottom of the graph represent the relative oscillator strengths. Reprinted with permission of [115]. Copyright (2012) American Chemical Society

best match between the calculated and experimental optical spectra for the isolated dyes.

Very recently we also investigated the BD adsorption mode on a $(TiO_2)_{82}$ cluster, considering the species with two protons [118]. We calculated three structures in which the two dye protons were located in the proximity of the TiO_2 surface. In all cases the BD adsorbs on TiO_2 using two of the three available carboxylic groups; see Fig. 31. The starting structure we considered, (a) in Fig. 31, originates from that calculated for N719 and is characterized by dissociated bridged bidentate and monodentate anchoring of the two carboxylic groups. In this structure, one of the three NCS groups points towards the TiO_2 surface. Structure (b) is, on the other hand, similar to the typical adsorption mode found for heteroleptic ruthenium dyes [28, 84] and features two deprotonated monodentate carboxylic groups. Structure (c) is somehow intermediate between (a) and (c), showing a similar orientation with respect to the TiO_2 surface to (b) but an anchoring pattern close to that of (a). Our calculations indicate structure (b) to be the more stable structure, followed by (c) and (a). This data differ from what is reported by Sodeyama et al. [114] for the fully protonated BD on a periodic TiO_2 slab in vacuo, who found a single bidentate carboxylic anchoring as the most stable structure. The different number of protons, the cluster vs periodic approach and the

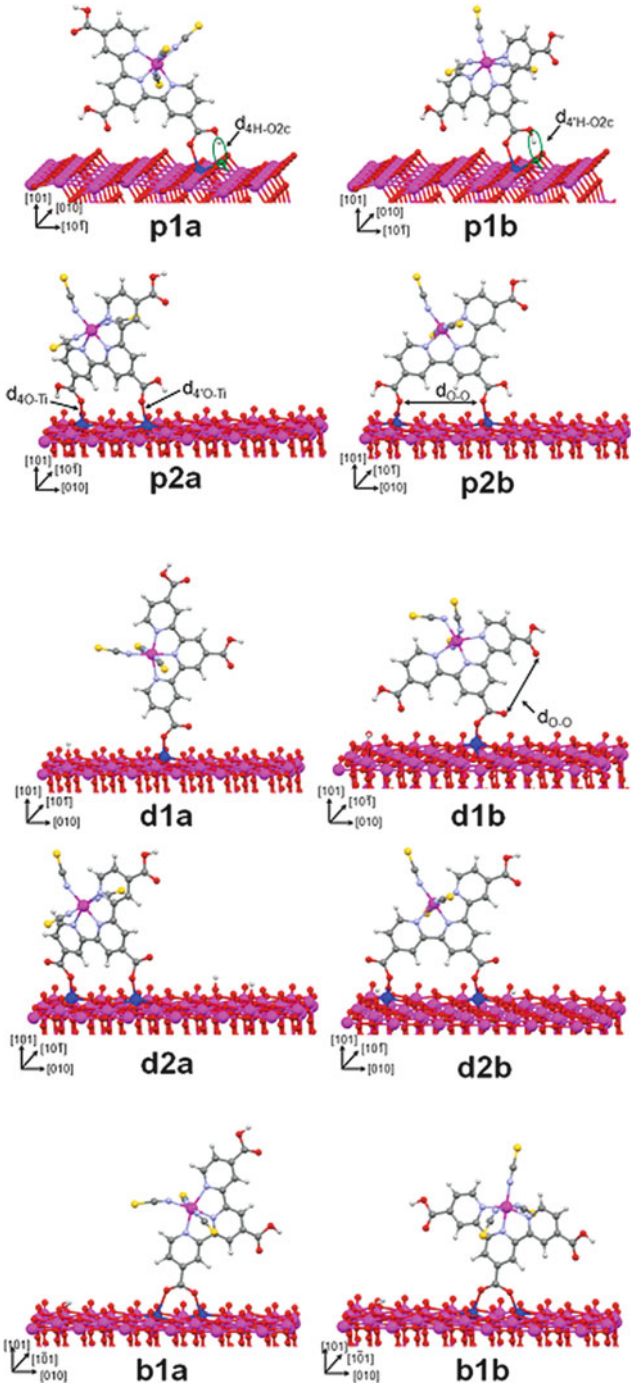

Fig. 30 Optimized adsorbed structures of black dye on the TiO_2 anatase (101) surface. Protonated adsorptions with one and two protonated anchors are labeled as **p1x** and **p2x**, respectively (**x** = **a**,**b**), while **d1x** and **d2x** (**x** = **a**,**b**) indicate the structures with deprotonated one and two anchors, respectively. **b1x** (**x** = **a**,**b**) indicates the bidentate bridging adsorptions with one anchor. Reprinted with permission of [114]. Copyright (2012) American chemical Society

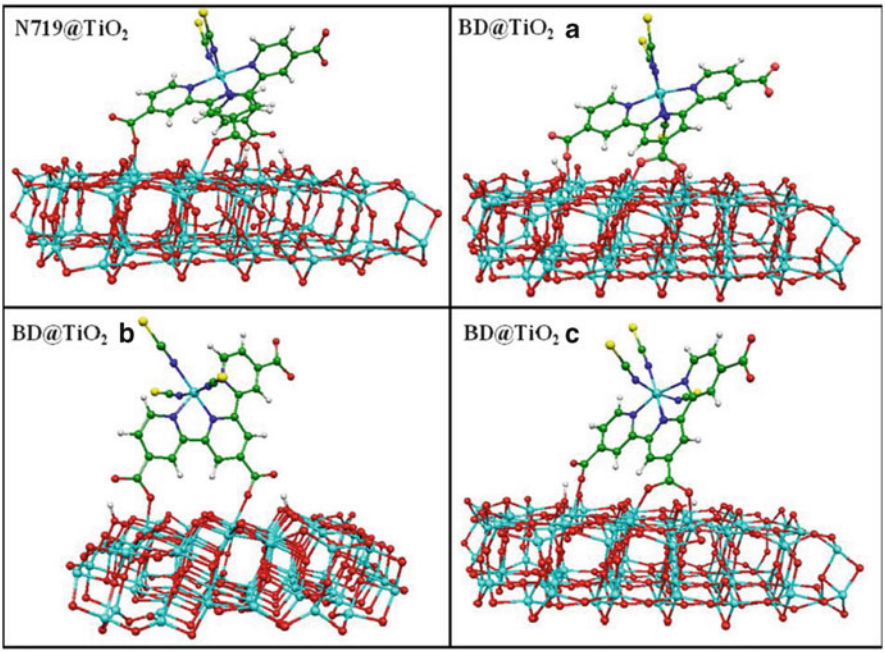

Fig. 31 Adsorption geometry of N719 on TiO2 (*top*, *left*) and of BD on TiO_2 in the configuration **a**, **b**, and **c** as described in the text. From [118]. Reprint from [118] with permission of the Swiss Chemical Society

inclusion of solvation effects in our calculations, are most likely the reasons for the different adsorption modes.

3.3 Dye Binding to ZnO: Quantum Size Effect on the DSCs Properties

As an example of quantum size effects on the DSCs properties, we report recent work by our lab on the electronic structure and optical properties of a perylene dye with a conjugated acrylic acid anchoring group, adsorbed onto ZnO (see Fig. 32) [207]. This system has been investigated by time-resolved spectroscopic techniques [303], finding a sizable dye/semiconductor coupling, as signaled by the broader and partly unstructured steady-state absorption spectrum measured for the dye anchored to the semiconductor compared to the dye in solution. Consistently with this observation, a 190 fs fast electron injection component was measured for the dye@ZnO. Stronger coupling and shorter injection times were found for TiO_2 compared to ZnO [303].

Various computational investigations of dye sensitized ZnO have been reported [203–206], but to our knowledge a full quantum mechanical study of such a system including a description of the interacting excited states and the effect of quantum

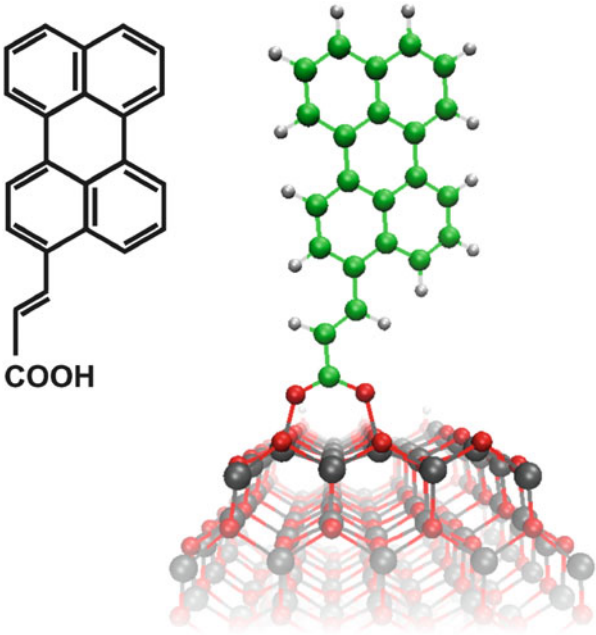

Fig. 32 Structure of the investigated perylene dye and its optimized adsorption geometry onto ZnO. The anchoring Zn–O (C–O) distances are calculated 2.05/1.93 (1.41/1.32) Å. Reprinted from [207] by permission of the PCCP Owner Societies

confinement on realistic nanostructures has only recently been reported by us. For simplicity, we considered the dye to adsorb on ZnO in its deprotonated state in a bridged bidentate configuration on the apolar (1010) surface (see Fig. 32) which, despite being less reactive than the polar surfaces, is the major surface exposed by ZnO nanostructures used in DSCs [304]. The investigation of the precise dye adsorption mode on ZnO is not expected to vary with the dimension of the nanostructures, so we limited our attention to the bridged bidentate binding, which was found to be favored over other adsorption modes in previous model studies [204, 205].

The electronic structure of the perylene dye and of three $(ZnO)_n$ models of increasing size, with $n = 42$, 84, and 222, and of the corresponding dye@$(ZnO)_n$ systems are reported in Fig. 33. For the dye in solution we find HOMO and LUMO values of -5.09 and -2.41 eV, in good agreement with photoelectron spectroscopy and spectroscopic data for a similar perylene dye (-5.0 and -2.28 eV) [305]. Comparing the isolated $(ZnO)_n$ systems, we immediately notice that the ZnO conduction band edge, corresponding to the systems LUMO, substantially down-shifts on going from $n = 42$ to 84 and to 222 ZnO units, with 0.18 and 0.62 eV shifts, respectively. For the largest dye@$(ZnO)_{222}$ case investigated here the bottom of the ZnO conduction band lies at -2.8 eV, i.e., still substantially higher than the expected value for the bulk [1].

For the non-interacting dye and $n = 42$ and 84 systems, the lowest semiconductor unoccupied state lies above or is almost coincident with the dye-based LUMO, making electron injection energetically unfavorable. For the large $(ZnO)_{222}$ cluster,

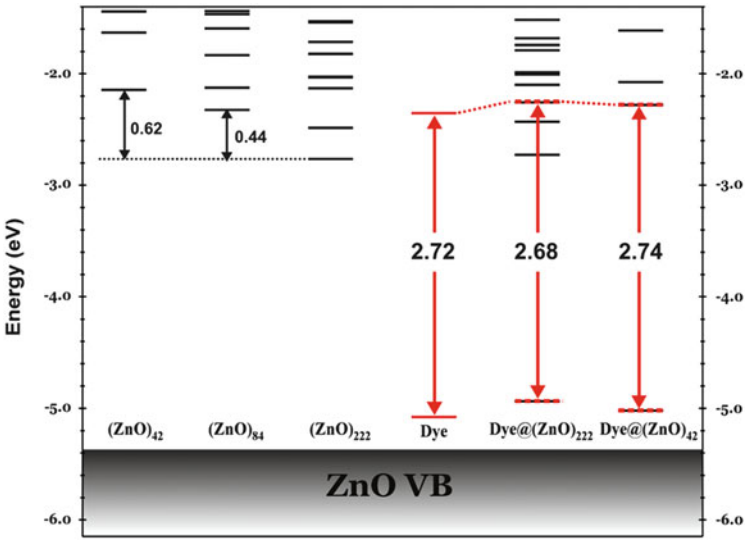

Fig. 33 Schematic energy levels of the isolated Dye and $(ZnO)_n$ clusters ($n = 42$, 84, and 222) and of the interacting Dye@$(ZnO)_n$ ($n = 42$ and 222) systems. Levels which are maximally localized on the dye are in *red*. Reprinted from [207] by permission of the PCCP Owner Societies

on the other hand, the ZnO-based LUMO lies ca. 0.4 eV below the dye-based LUMO, reverting to the dye/semiconductor energetics and making electron injection a favorable process. For the interacting dye/ZnO system we find a similar alignment of energy levels as for the non-interacting systems (Fig. 33).

For both dye@$(ZnO)_{42}$ and dye@$(ZnO)_{222}$ we calculate the almost pure dye HOMO to insert within the semiconductor band-gap; this level is only marginally affected by the size of the ZnO cluster. On the contrary, as found for the non-interacting systems, the position of the semiconductor-based LUMO is strongly dependent on the system size. For dye@$(ZnO)_{42}$, the LUMO is mainly localized on the dye, with the lowest unoccupied level localized on the ZnO lying 0.11 eV above. For dye@$(ZnO)_{222}$, on the other hand, the LUMO is manly located on the semiconductor, with the first unoccupied orbital localized on the dye being the LUMO+2, found 0.47 eV above the LUMO. Furthermore, while for dye@$(ZnO)_{42}$ the dye-based LUMO has only a 5% mixing with ZnO states, for dye@$(ZnO)_{222}$ a 13% contribution to the dye-based LUMO+2 comes from the semiconductor.

To gain further insight on the dye@$(ZnO)_n$ excited state nature beyond a simple one-electron picture, we performed TDDFT excited state calculations for both the $n = 42$ and $n = 222$ cases. For the latter system, TDDFT calculations were particularly heavy due to the large system size (518 atoms, 4,362 occupied orbitals, and 11,951 basis functions), and still we were able to calculate the lowest seven excited states in the fully interacting orbital space. The computed absorption spectra for the dye@$(ZnO)_n$ systems ($n = 42$ and 222) are compared to results for the isolated dye in solution and to experimental data in Fig. 34.

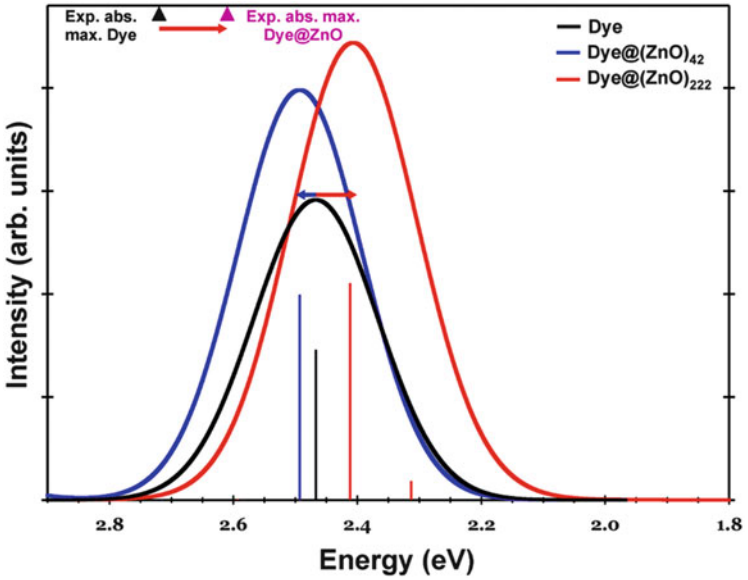

Fig. 34 TDDFT-calculated absorption spectra for the isolated dye (*black line*), the Dye@$(ZnO)_{42}$ (*blue line*), and the Dye@$(ZnO)_{222}$ (*red-line*) systems. *Vertical lines* correspond to unbroadened excitation energies and oscillator strengths. Reprinted from [207] by permission of the PCCP Owner Societies

Experimentally, an absorption maximum at 2.72 eV is measured for the isolated dye in methanol solution, while dye anchoring onto the ZnO surface produces an absorption maximum red-shift of ~0.1 eV [303]. The computed absorption spectrum of the isolated dye is formed by a single HOMO→LUMO excitation computed at 2.47 eV, i.e., 0.25 eV red-shifted compared to the experimental data [252, 303]. The absorption spectrum of the dye@$(ZnO)_{42}$ system is dominated by a single transition ($S_0 \rightarrow S_1$) computed at 2.49 eV, of essentially (80%) HOMO→LUMO character. The nature of the orbitals involved in the TDDFT transitions can be used to gauge qualitatively the character of the excited state. For ($S_0 \rightarrow S_1$) of $n = 42$ we find essentially a charge redistribution taking place within the dye, with negligible coupling to semiconductor unoccupied states. Furthermore, the absorption maximum is slightly blue-shifted with respect to the isolated dye, contrary to the experimental findings. For the dye@$(ZnO)_{222}$ system, we calculate an absorption maximum at 2.41 eV, i.e., 0.06 eV red-shifted compared to the isolated dye molecule in solution, as experimentally retrieved, and 0.08 eV red-shifted compared to the $n = 42$ case. The spectrum is mainly formed by two transitions: (1) $S_0 \rightarrow S_2$, computed at 2.31 eV, characterized by a small but sizable oscillator strength (0.09), and (2) the more intense $S_0 \rightarrow S_4$ excitation, computed at 2.41 eV, with an oscillator strength of 1.05. The lowest excitation, $S_0 \rightarrow S_1$, is calculated at 2.04 eV with zero oscillator strength, and corresponds to a direct charge-transfer excitation from the dye-based HOMO to the ZnO-based LUMO. The $S_0 \rightarrow S_2$ excitation is made of contributions from four major

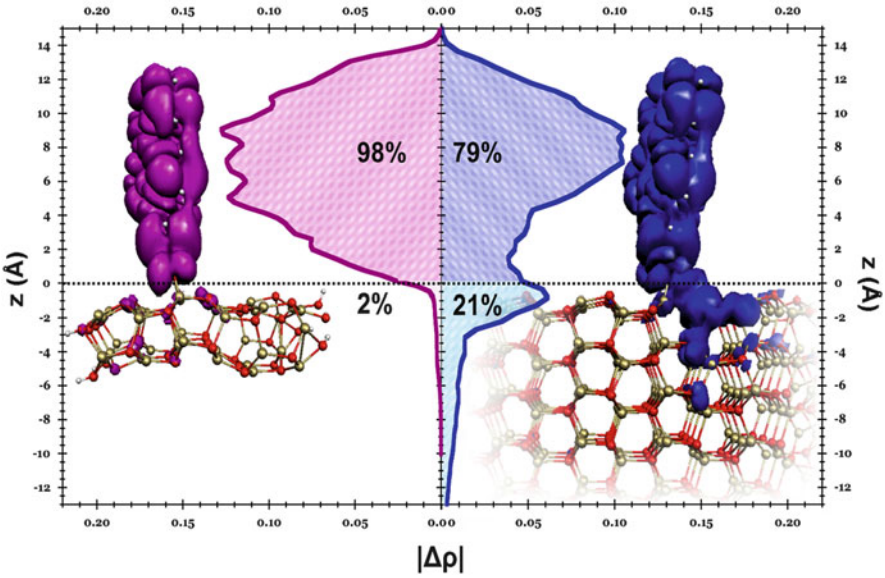

Fig. 35 Isodensity plot of the absolute charge difference differences ($|\Delta\rho|$) between S_0-S_1 of Dye@$(ZnO)_{42}$ (*left*, *magenta*) and S_0-S_4, of Dye@$(ZnO)_{222}$ (*right*, *blue*). *Center*: Integral of $|\Delta\rho$ along the *x* and *y* directions plotted as a function of *z*. The zero is in all cases set in the middle of the O–Zn bonds between the dye and the semiconductor. Reprinted from [207] by permission of the PCCP Owner Societies

orbital excitations; these are mainly localized within the semiconductor, although they are characterized by a small admixture with dye states. The intense $S_0 \rightarrow S_4$ excitation is mainly formed by a HOMO→LUMO+2 transition, with the latter orbital showing 87% and 13% localization within the dye and semiconductor, respectively.

A more complete vision of the overall character and localization of the excited state at the dye/semiconductor interface for $n = 42$ and 222 can be obtained by plotting the absolute values of the charge differences between the excited states involved in the main excitations and the ground state, $|\Delta\rho| = |\rho(S_n) - \rho(S_0)|$. This quantity allows for the visualization of the excited state localization, whereby the absolute value serves to exclude possible $\Delta\rho$ cancellations due to sign changes within a given region of space which would show up upon $\Delta\rho$ integration. In the plane we have computed $|\Delta\rho|$ curves for the $S_0 \rightarrow S_1$ and $S_0 \rightarrow S_4$ transitions of dye@$(ZnO)_{42}$ and dye@$(ZnO)_{222}$, respectively, and the results are reported in Fig. 35. For each system, we define the *z* coordinate as the dye axis normal to the semiconductor surface and integrate the charge differences along the *x* and *y* directions.

As can be seen from Fig. 35, for both $n = 42$ and $n = 222$ the most intense excitations are primarily located in the dye space region. Noticeable differences are however found at the dye/semiconductor interface for the two systems. The dye@$(ZnO)_{42}$ system exhibits a negligible excited state spreading into the semiconductor, as it can be quantitatively seen from the isodensity $|\Delta\rho|$ plot and from the integrated

$|\Delta\rho|$ curve. In contrast, for dye@$(ZnO)_{222}$ the isodensity $|\Delta\rho|$ plot clearly shows a sizable contribution from the semiconductor, being characterized by a 79%/21% dye/semiconductor localization.

Our results clearly show that a substantial coupling between the dye and the large ZnO model exists. This is due both to orbital and to excited state configuration mixing, which contribute to imparting a substantial semiconductor character to the otherwise dye optical transitions.

4 Dye Effect on the TiO_2 Conduction Band

When a dye binds to a semiconductor surface, two effects might be at work: (1) the electrostatic (EL) effect, due to the dye dipole moment and (2) the effect of the charge transfer (CT) between the dye and the semiconductor which may accompany the dye/semiconductor bond formation. More recently, some of us [306], employing the so-termed Charge Displacement (CD) analysis [307], have investigated the adsorption of several prototypical organic dyes and co-adsorbents (see Fig. 36) on TiO_2 models, quantifying and rationalizing the effects of EL and CT contributions to the TiO_2 CB energetics. The compounds described above have been anchored on the titania surface by the carboxylic group in both dissociative bridged bidentate (BB) and molecular monodentate (M), adsorption modes [306].

A key approach in this analysis is the study of the electron density changes taking place upon formation of the dye-TiO_2 adducts. The electron density change ($\Delta\rho$) is defined as the density difference between the interacting complex and the isolated, non-interacting, partners placed at the same position they have in the bonded adduct. To analyze the electron density rearrangement, we define the charge displacement (CD) along the z direction as

$$\Delta q(z) = \int_{-\infty}^{\infty} dx \int_{-\infty}^{\infty} dy \int_{-\infty}^{z} \Delta\rho(x, y, z')dz' \tag{9}$$

where $\Delta\rho$ is the electron density difference as defined above. $\Delta q(z)$ measures at each point z along the chosen axis the electron charge that, upon formation of the adduct, is transferred from the right to the left side of the perpendicular plane through z [307] (a negative value thus corresponds to electron flow from left to right). In Fig. 37 we show the isodensity contour plot of the electron density difference and the CD curve, calculated by (9) for the prototypical L0 dye adsorbed onto TiO_2 in the BB configuration. We can see significant charge depletion lobes in the areas around the carboxylic group, the nitrogen atom of the nitrile group, and the phenyl bound to the cyanoacrylic moiety. Charge accumulation lobes can be seen instead on the central carbon of the cyanoacrylic anchoring group of the sensitizer, in proximity to the proton detached from the dye and adsorbed on the TiO_2 surface and, in particular, in regions of the semiconductor cluster. Note that the curve is largely positive across the entire adduct, implying a continuous charge

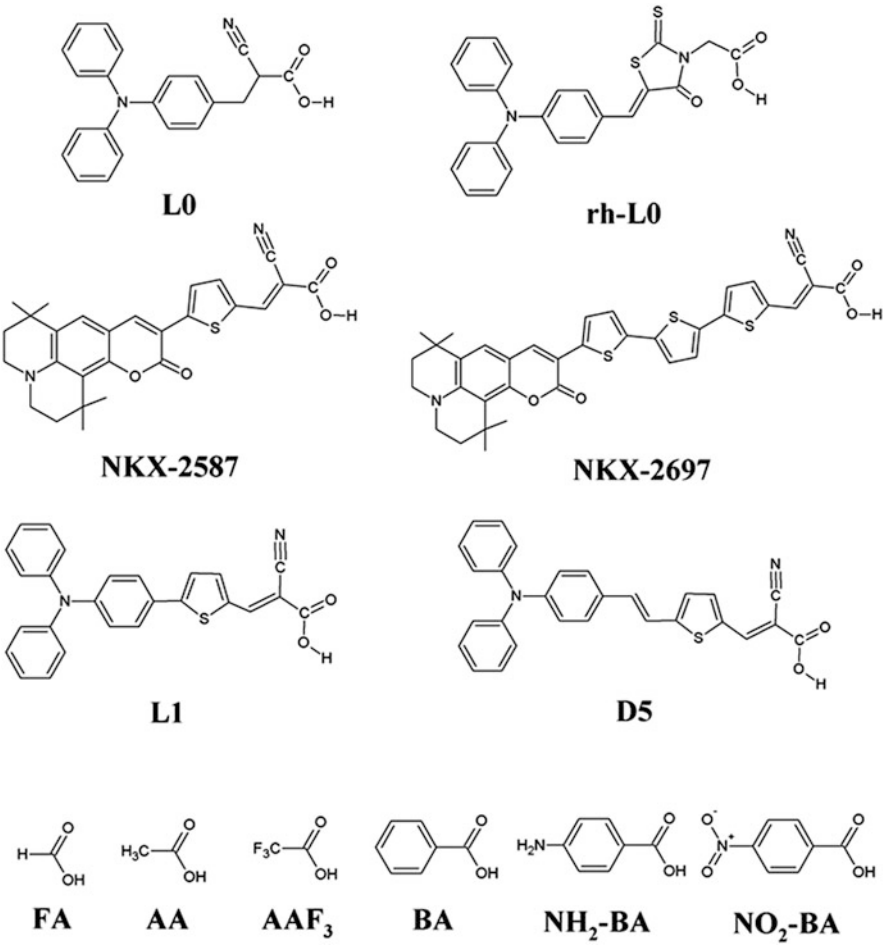

Fig. 36 Molecular structures of the L0, rh-L0, NKX-2587, NKX-2697, L1, and D5 dyes, and of benzoic acid (BA), 4-aminobenzoic acid (NH_2-BA), nitrobenzoic acid (NO_2-BA), acetic acid (AA), trifluoroacetic acid (AAF_3), and formic acid (FA). Reproduced from [306] by permission of The Royal Society of Chemistry

transfer from the dye to the TiO_2. The maximum of the CD curve in the inter-fragment region is 0.36 electrons.

Assuming that this marked charge redistribution, along with a pure electrostatic (EL) contribution, due to the dye dipole, induces significant modifications on the TiO_2 CB edge, one can formulate a simple interpretative model by expressing the total TiO_2 CB shift, ΔCB_{TOT}, as the sum of the two main effects strictly related to the dye sensitizer [306]:

$$\Delta CB_{TOT} = \Delta CB_{EL} + \Delta CB_{CT} \tag{10}$$

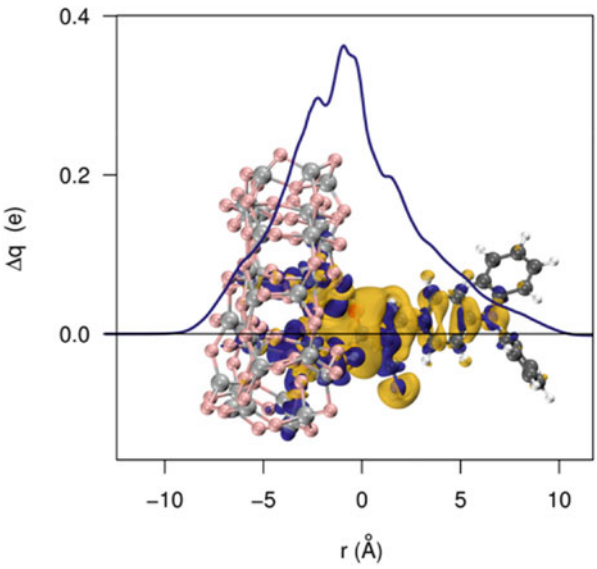

Fig. 37 Isodensity contour plot and charge displacement curve for L0 adsorbed onto TiO_2 in a BB configuration. *Yellow* surfaces identify regions in which the electron density decreases whereas zones of density accumulation are marked by *dark blue* surfaces. The density value at the surfaces is ± 0.0005 e/au^3. Reproduced from [306] by permission of The Royal Society of Chemistry

Note that the contributions due to the solvent and to the various additives can be assumed to be approximately constant for DSCs fabricated under comparable conditions and hence left out.

Concerning the EL effect, we evaluate the CB shift in relation to the electrostatic potential generated by the dye molecule rather than with its standalone dipole moment:

$$V_{\mathrm{EL}} = \frac{1}{n_{\mathrm{Ti}}} \sum_{i=1}^{n_{\mathrm{Ti}}} \sum_{j=1}^{n_q} \frac{q_j}{r_{ij}} \tag{11}$$

where q_j is the jth of the n_q dye point charges and r_{ij} represents the distances of these charges from each of the n_{Ti} titanium atoms constituting the superficial layer of the TiO_2 cluster. This quantity represents the effective average electrostatic potential generated by the dye charge distribution in the region of the first semiconductor titanium layer. The relation between the TiO_2 CB shift and the electrostatic potential of (11) is reported for the dye series shown in Fig. 38. Looking at the main panel we immediately notice an approximately linear relation between the electrostatic potential and the CB shift for the dyes adsorbed on TiO_2 in a monodentate way. Including the dyes anchored on TiO_2 in the BB geometry, we can see that the linear trend persists and actually the fit quality improves. It is of course eye-catching that the BB dyes generate a significantly higher potential on the TiO_2 surface with consequent larger shifts. This behavior can be explained simply by considering that, as pointed out earlier, the species adsorbed on the semiconductor in BB geometry are charged. Our results then suggest that to obtain conduction band shifts comparable with those measured experimentally we need to consider charged molecules adsorbed on TiO_2. In comparison with the M-adsorbed dyes, the BB systems show a larger deviation

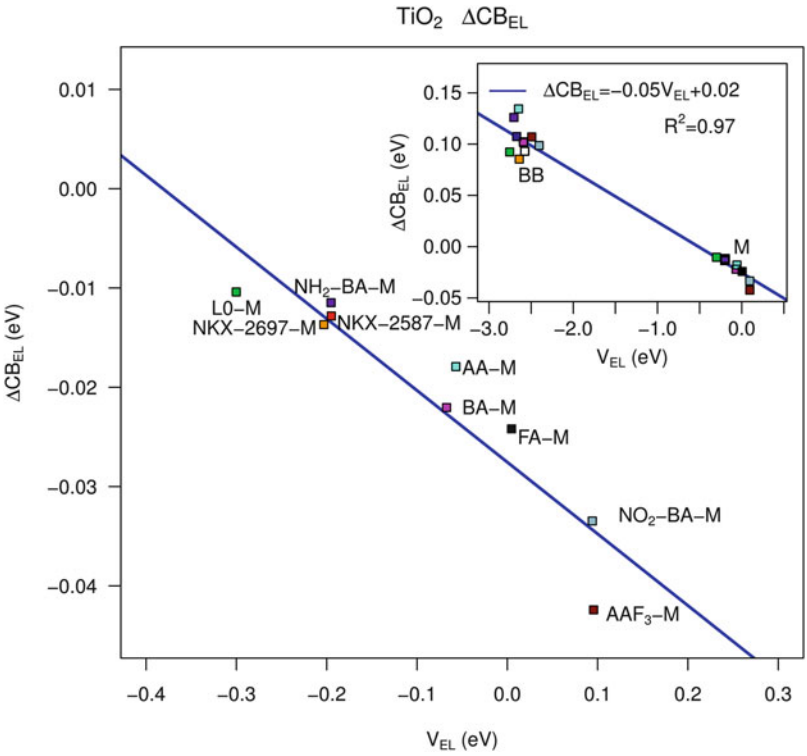

Fig. 38 CB shift due to the electric field generated by the adsorbed dye molecule as a function of the electrostatic potential (11) generated by the dye point charges for all the dyes in their monodentate adsorption mode. *Inset*: same but including the charged dyes in the bidentate adsorption mode. Reproduced from [306] by permission of The Royal Society of Chemistry

from the linear trend. This can be explained by taking into account the irregularities in the low energy DOS profile due to the presence of the proton adsorbed on the surface and the larger perturbation generated by a charged species on the semiconductor.

The above results confirm the direct proportionality between the electrostatic component of the CB shift and the electrostatic potential generated by the sensitizer. We now move to discuss the relation between the residual CB shift ($\Delta CB_{TOT} - \Delta CB_{EL}$) and the CT amount predicted by the charge displacement analysis along the series of dye-TiO_2 systems. This is displayed in Fig. 39, which shows beyond doubt a surprisingly accurate linear correlation between the two computed quantities (R^2=1.00).

As expected, the complexes at hand cluster in two distinct groups, one corresponding to the neutral M-bound dyes, at smaller shifts and CT values, and the other to the charged BB-anchored systems. The linear correlation appears to fit both groups equally accurately. This finding clearly strengthens that the additional CB shift component must be attributed to CT, besides confirming the adequacy of the charge displacement analysis as a tool to measure CT and supporting our estimate of the

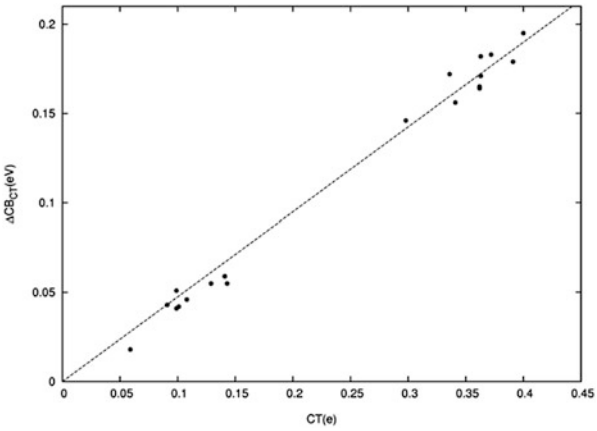

Fig. 39 Difference in eV between the total CB energy shift and its electrostatic component plotted vs the amount of CT (electrons). The *top right part* of the graph refers to BB-anchored dyes, the *bottom left part* of the graph to M-anchored dye. Reproduced from [306] by permission of The Royal Society of Chemistry

electrostatic contribution to the band shift. On the basis of the above results, it may be safely concluded that, in the dye-TiO_2 interaction, CT effects induce a CB shift which for BB anchored systems is much larger than for the M-bound ones, and this, as well as the electrostatic effect, contributes to their larger upward CB shift. It thus turns out that the CT component of the CB shift may in fact be the dominant one (60–70% of the total), with a relative variability comparable to that exhibited by the electrostatic component.

5 Multiple-Dye Adsorption on TiO_2: Dye Aggregation and Aggregate Properties

Taking as a starting point the optimized geometry of a single dye molecule adsorbed on TiO_2, one can try to model the dye packing on the surface employing a simple topological approach and assuming that in the sensitization process the dye/TiO_2 interactions, which result from the chemical bonds between the dye anchoring groups and the semiconductor surface, are stronger than the intermolecular ones, thus guiding the formation of the dye monolayer [32, 84, 219]. The dye molecular structure, on the other hand, reflects the peculiar dye/dye interactions, which determine the energetically favored aggregation motifs among all the possible ones. In other words, one can assume that the five-coordinated Ti atoms on the surface dictate the possible adsorption sites, the dye/surface interactions govern the binding mode and the adsorption geometry, and the interactions among adsorbed dye molecules give the particular aggregation patterns. This assumption is grounded on the observation that dye/TiO_2 binding energies are usually ~3 times larger [257] than intermolecular binding energies for highly interacting organic dyes [219].

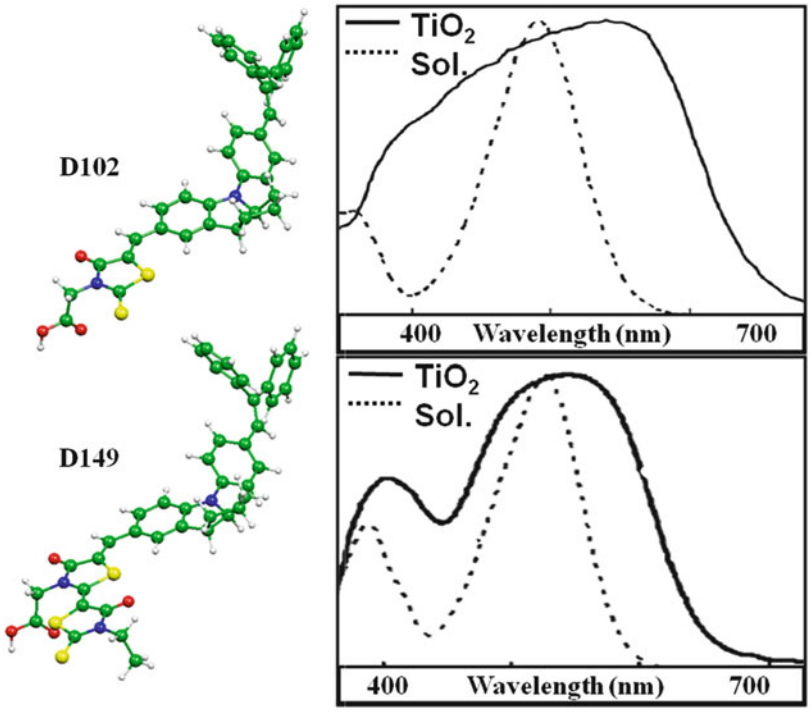

Fig. 40 Molecular structures of D102 (top) and D149 (bottom); note the second rhodanine ring in the molecular structure of D149. Right side: Absorption spectra of D102 (top) and D149 (bottom) in solution (*dashed line*) and on TiO_2 (*solid line*). Reprinted with permission of [219]. Copyright (2010) American Chemical Society

5.1 Organic Dyes

To model the formation of possible aggregates of two indoline dyes, termed D102 [144] and D149 [308], and to investigate the relation existing between the molecular structure of the dye and its tendency to form aggregates on the TiO_2 surface (see Fig. 40), we employed a TiO_2 nanoparticle model consisting of a (101) $(TiO_2)_{82}$ anatase slab of approximately 4 nm^2 area, with three rows of five- and six-coordinated surface Ti sites and sufficient coordination sites to accommodate the considered dimeric arrangements.

On this TiO_2 slab we have modeled the dye-aggregation for both D102 and D149, initially selecting among all possible dimeric arrangements the closest interacting ones with no explicit superposition of atomic structures. After this preliminary screening, a set of six configurations was selected for D102, while, due to the steric hindrance introduced by the presence of the second rhodanine moiety, only three of them were retained as possible candidates for the D149 molecule. The nomenclature we use to label the dimer configurations is depicted in Fig. 41: keeping fixed the

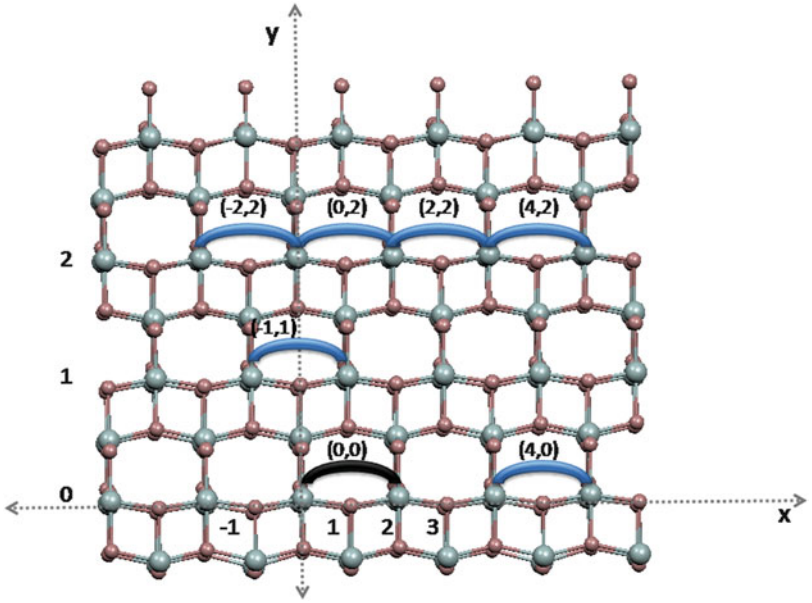

Fig. 41 Graphical representation of the (101) TiO_2 anatase surface. The scheme illustrates the convention adopted to indicate the relative positions of two molecules: each couple is labeled with the (*x*,*y*) coordinates of the second molecule, being the first one conventionally fixed in (0,0). Reprinted with permission of [219]. Copyright (2010) American Chemical Society

position of the molecule placed in (0,0), each dimer is labeled by the (*x*,*y*) coordinates of the second molecule. Therefore, the six dimers of D102 examined in this study are labeled as (4,0), (−1,1), (−2,2), (0,2), (2,2), and (4,2); for D149 only the (0,2), (2,2), and (4,2) configurations are considered.

To take into account the effect of the geometry relaxation as a consequence of the interaction between the molecules upon their adsorption on the surface, for each configuration, we performed geometry optimizations of various dye dimers adsorbed onto TiO_2 by means of the Car–Parrinello (CP) method [309] using the PBE exchange-correlation functional [259], a plane-wave basis set, and ultrasoft pseudopotentials [310, 311]. To evaluate the relative stability of the various optimized configurations, we carried out single point MP2 as well as DFT calculations on the deprotonated dimers (i.e., after removing the TiO_2 slab) in solution taking the optimized geometries of the dyes adsorbed onto TiO_2 [73].

Table 6 lists the MP2 and B3LYP relative energies of the deprotonated dimers in ethanol solution, computed with respect to the most stable configuration, using a 6-31G* basis set. An extremely interesting picture emerges from MP2 results: the lowest-energy configuration for D102 is that termed (0,2), having the two molecules aligned along the y direction with the π systems almost perfectly stacked. Most notably, this arrangement turns out to be the highest in energy for D149 (by 4.5 kcal/mol), while the preferred configuration is (2,2), with the molecules

Table 6 B3LYP and MP2 relative energies (kcal/mol) of a series of dimers of D149 and D102 extracted from the corresponding optimized geometries on TiO_2

	D102		*D149*	
Dimer	B3LYP	MP2	B3LYP	MP2
(0,2)	6.80	**0.00**	12.49	4.50
(2,2)	5.57	3.94	3.23	**0.00**
(4,2)	**0.00**	4.47	**0.00**	3.62
(−2,2)	4.14	4.81	–	–
(4,0)	10.03	1.64	–	–
(−1,1)	11.23	1.23	–	–

The nomenclature (*x*,*y*) adopted to indicate the position of the second molecule on the TiO_2 surface is illustrated in Fig. 41.
Bold values indicate the most stable configuration

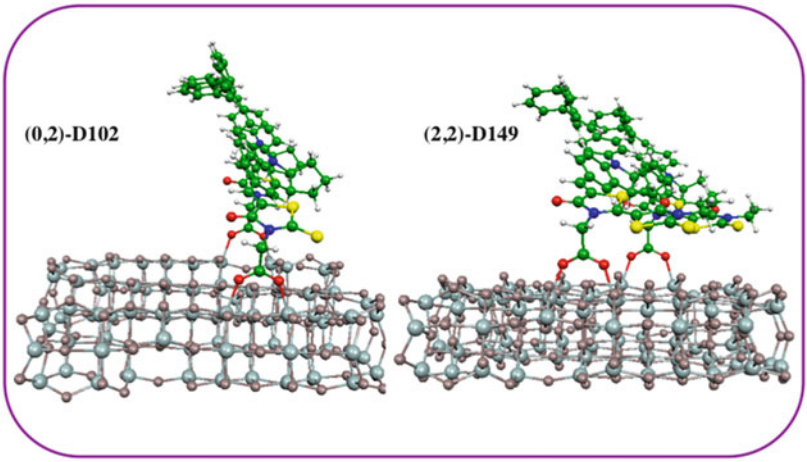

Fig. 42 Optimized molecular structures of the most stable (0,2)-D102@TiO_2 and (2,2)-D149@TiO_2

separated by one Ti atom along the x axis. It should also be noted that for D102 there are at least two other arrangements, namely (4,0) and (−1,1), precluded to D149 because of the presence of the second rhodanine ring, which are very close in energy to the (0,2) dimer (see Fig. 42). As is also apparent, the energetics obtained by DFT and MP2 are rather different. For both dyes, DFT does not predict dye aggregation, delivering an increasing stability as the distance between the two dye molecules increases: the (4,2) configuration is predicted to be more stable for both D102 and D149.

Since MP2 calculations can easily become very computationally expensive as the number of atoms and basis set dimensions increase, we have benchmarked the more computationally affordable "dispersion-corrected" B3LYP-D3 (see Sect. 1.2) method against B3LYP and MP2 methods for the favored (2,0)-D102 and (2,2)-D149 dimers. The results are in this case obtained in vacuo for the protonated dyes at their optimized adsorption mode on TiO_2. The results, reported in Table 7, show a similar description of the inter-chromophore interaction by B3LYP-D3 and MP2

Table 7 B3LYP, B3LYP-D3 and MP2 binding energies (kcal/mol) for the most stable D102 and D149 dimeric arrangements

System	B3LYP	B3LYP-D3	MP2
(0,2)-D102	−0.10	−16.27	−14.08
(2,2)-D149	+1.42	−10.02	−8.04

Table 8 Computed TDDFT(B3LYP)/6-31G* excitation energies (eV) and oscillator strengths for the four lowest excited states of the most stable dimers of D102 and D149. The corresponding shifts of the lowest excited state (eV) with respect to the reference monomers are listed in the last column

Dimer	Exc.	*f*	Shift
(0,2)-D102	**1.96**	0.022	**−0.15**
	2.10	1.016	
	2.18	0.537	
	2.28	0.001	
(4,0)-D102	**2.13**	0.075	**+0.02**
	2.14	0.077	
	2.21	1.195	
	2.27	0.048	
(−1,1)-D102	**2.00**	0.028	**−0.11**
	2.09	0.535	
	2.23	0.698	
	2.30	0.283	
(2,2)-D149	**1.97**	0.007	**−0.08**

Bold values indicate the most stable configuration

methods (a rigid increase of the binding energy by ca. 2 kcal/mol is found by B3LYP-D3 compared to MP2), while B3LYP does not predict any binding between the two monomers. Also in line with our previous results, the (0,2)-D102 dimeric arrangement is substantially favored compared to the (2,2)-D149 case, with ca. 6 kcal/mol higher binding energies, testifying to the greater tendency of the D102 dye to form aggregates. As expected, lower binding energies are calculated in solution for the deprotonated dyes, which for the D102 case amount to 9.0 kcal/mol.

On the basis of the stability order discussed above, we report in Table 8 the excitation energies and the oscillator strengths of the lowest excited states for the relevant dimeric configurations: (0,2), (4,0), and (−1,1) for D102 and (2,2) for D149. The energy shifts are computed with respect to the lowest excited states of the standalone D102 and D149 dyes.

The results show that the different aggregation schemes investigated for D102 have different, and even opposite, effects on the excited states. In fact, the (4,0) configuration with the molecules placed side-by-side and the π-systems almost parallel produces a blue-shift of the excited states, typical of so-called H-aggregates. If one looks at the excited state with the largest oscillator strength (1.195), located at 2.21 eV, the blue-shift of the absorption maximum for the (4,0) dimer is even more pronounced, amounting to ca. 0.1 eV, so this aggregation pattern can be reasonably disregarded on the basis of the experimentally observed

red-shift. On the other hand, the two D102 dimeric arrangements which induce a sizable π–π stacking, (0,2) and (−1,1), imply the appearance of new bands in the absorption spectra which are substantially red-shifted compared to the monomer spectrum (0.15 and 0.11 eV, compared to a 0.23 eV experimental shift), a characteristic signature of J-aggregates. Notably, the most stable (0,2) dimer shows also the largest red-shift. If we now compare the calculated data for D102 and D149, this model almost quantitatively reproduces the different spectroscopic behavior of the two dyes adsorbed on the TiO_2 surface. Selecting the most stable configurations, the red-shifts computed upon aggregation are 0.15 and 0.08 eV for D102 and D149, respectively, compared to the experimentally measured values of 0.23 [144] and 0.07 eV [308]. Most notably, the computed oscillator strengths for the dimer excited states further reveal a stronger interaction in the case of the (0,2)-D102 configuration, with ca. a threefold reduction of the J-band oscillator strength calculated in (2,2)-D149. Overall, the larger shift and higher intensity of the new spectroscopic feature appearing in D102 as a function of dye aggregation is perfectly in line with the available experimental information.

Having modeled the dye adsorption and the formation of surface aggregates, in principle one possesses a realistic model to investigate and reproduce a series of interfacial phenomena which are strictly related to the dye packing on the TiO_2 surface, such as, for instance, the occurrence of spectral shifts on the ground state absorption spectrum of the semiconductor-adsorbed dyes [256, 269, 312–318]. These effects manifest themselves as absorbance changes occurring for the neutral, non-oxidized, adsorbed dyes, which have been detected by both transient absorption and PIA spectroscopy. Various interpretations have been introduced to explain the observed band shifts and intensity changes: Staniszewski et al. [314] attributed the spectral changes to a marked change occurring in the dye environment after electron injection and regeneration by iodide, essentially due to slow cation transfer; basically, electron injection perturbs the electrostatic environment surrounding the dye, which slowly responds by displacing positive charges in solution or surface-adsorbed Li^+ ions or protons. The appearance of similar or related peak bleaches in the adsorbed dye absorption spectrum has also been ascribed to possible phenomena of electron accumulation into the semiconductor affecting the LUMO of the dye [316] or electron extraction [317] from the TiO_2 as well as to the presence of long-lived photoreduced dye molecules [315]. However, more recently, some authors have argued [269, 312, 313] that the measured spectral changes are consistent with first order transient Stark effects [319–321]. Such local electric fields, which show maximum amplitude at the initial observation times after electron injection, are expected to be associated to the electron transfer from the dye to the TiO_2 film and to the consequent formation of oxidized dye molecules. Exploiting the work on the aggregation of the indoline dyes and employing a model which "statically" simulates the oxidation/electron injection and regeneration steps and the associated optical responses, we also provided [256] a computational framework to interpret the Stark shifts experimentally observed by Cappel et al. for D149-sensitized solar cells [269].

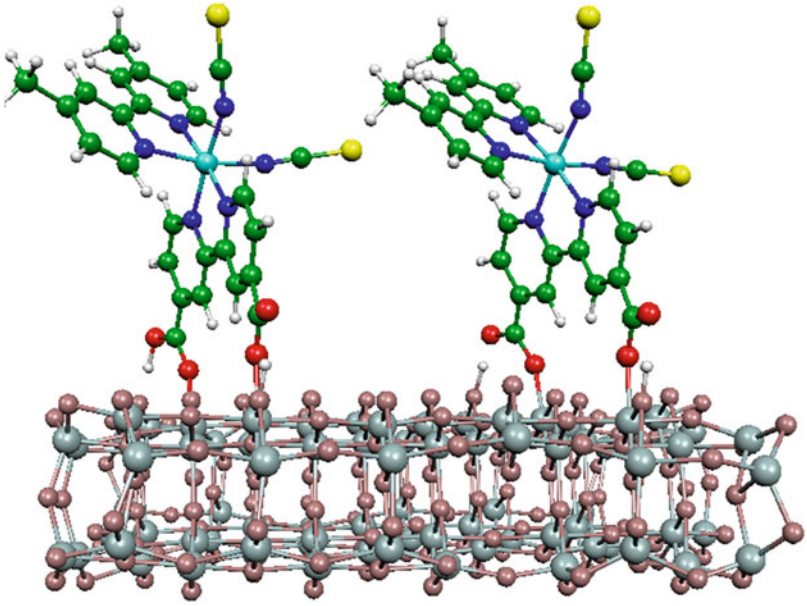

Fig. 43 Optimized molecular structure of a dimeric configuration of the Z907 dye with nonyl chains replaced by methyl groups, adsorbed on the $(TiO_2)_{82}$ cluster. Reprinted with permission of [329]. Copyright (2013) American Chemical Society.

5.2 Ruthenium Dyes

To the best of our knowledge, the aggregation of ruthenium dyes on TiO_2 has never been computationally investigated beyond the work of Patrick et al. on the hydrogen bonding of TiO_2-adsorbed N3 [322]. Here we report preliminary results obtained for the heteroleptic Z907 dye with nonyl chains replaced by methyl groups, which was investigated by Wang et al. [323]. We report in Fig. 43 the DFT optimized geometry of a TiO_2-adsorbed ruthenium dye dimer.

The two dyes were considered to be adsorbed on the same two rows of Ti atoms, which ensures a close interaction distance avoiding explicit atomic superimposition. Although this interaction geometry might not be the most stable dimeric arrangement, yet this is a useful model to provide an estimate of the strength of intermolecular interactions for this type of dye. We also notice that this adsorption mode corresponds to a surface coverage of ca. 0.5 dye molecules/nm^2, which is quite typical for this class of ruthenium dyes [28, 324].

For the ruthenium dye dimer reported in Fig. 43 we calculated a B3LYP-D3 interaction energy in vacuo of 9.0 kcal/mol, which is smaller than the 16.3 kcal/mol value computed for the D102 organic dye at the same level of theory; see Table 7. As an estimate of the electronic coupling occurring between the two TiO_2-adsorbed dyes, we evaluated by DFT (B3LYP/3-21G*) the dye-based HOMO splitting for the surface adsorbed dimer, finding a value of 0.02 eV, and thus a coupling of

0.01 eV. This value is consistent with the very efficient hole transfer measured for this dye upon adsorption onto TiO_2 [323] and, as suggested by the same authors, is most likely the consequence of the proximity of the NCS ligands of the two interacting dyes.

6 Co-sensitization of TiO_2

For the simulation of more complex aggregation patterns, comprising, for instance, three or more dye sensitizers, one needs to extend this model further and to increase the TiO_2 surface available for the dye adsorption. Obviously the computational overhead associated to the growing size of the system becomes quickly unaffordable. We recall indeed that a doubling of the system size implies, with standard DFT implementations, ca. one order of magnitude growth of the computational demand. The strategy we thus propose for the modeling of complex co-adsorption schemes [84], and that we shall widely discuss in the next section, consists in taking the structures of the sensitizers optimized alone on the $(TiO_2)_{82}$ cluster, removing the TiO_2 slab, and placing them on a grid of Ti atoms with the same geometrical arrangement calculated for the $(TiO_2)_{82}$ cluster, in such a way to obtain a map of actual anchoring positions to place the dyes [84]. This model, based on a simple replication of the structure of the isolated anchored dye, clearly neglects the geometrical relaxation due to the intermolecular interactions as well as possible local relaxation of the TiO_2 surface due to the dye anchoring. The basic idea consists in considering the dye adsorption mode as essentially determined by the specific dye–TiO_2 interactions, supposed to be identical for each surface Ti atom, and to calculate dye–dye intermolecular interactions a posteriori.

6.1 TiO_2 Co-sensitized by Different Dyes

The mixture of sensitizers having complementary absorption spectra, one of them possibly possessing high light-harvesting capability in the red and near infrared (NIR) regions, represents an appealing strategy to obtain panchromatic TiO_2sensitization [7–18]. An alternative approach is that of exploiting Fluorescence (Förster) Resonance Energy Transfer (FRET) [325] from an energy relay dye (ERD) to the sensitizing dye (SD) to produce additional photocurrent [326, 327]. FRET is mediated by the coupling of two resonant dipoles in the presence of an electric field [326]. The geometry of the ERD donor–SD acceptor system directly determines the energy transfer rate.

Hardin et al. [328] have reported on the energy transfer between a zinc naphthalocyanine ERD (AS02) and an Ru(II) SD (C106), both grafted onto the TiO_2 surface. Motivated by this study, we have modeled the co-sensitization process by taking the optimized structures of the TiO_2-adsorbed standalone dyes, and replicating these structures on the grid of Ti atoms presented above [84]. Although we have developed this strategy for the particular case illustrated

Table 9 Computed binding energies (kcal/mol) of the co-adsorption configurations of AS02 and C106. For each 1:n AS02:C106 ratio the energy of the most stable configuration is highlighted in bold.

	Stabilization energy (kcal/mol)	
Configurations	B3LYP	B3LYP+D3
1:1 AS02:C106 structures		
1_A	−2.4	−2.7
1_B	−7.7	−9.7
1_C	−6.8	**−12.6**
1_D	**−7.7**	−10.1
1_E	+5.7	−1.0
1_F	−2.9	−10.4
1_G	+14.0	−3.3
1_H	**−8.9**	**−18.1**
1:2 AS02:C106 structures		
2_A	**+4.6**	**−10.6**
1:3 AS02:C106 structures		
3_A	−9.1	−26.7
3_B	−3.0	−20.0
3_C	**−10.3**	−27.2
3_D	+0.3	**−27.5**
1:4 AS02:C106 structures		
4_A	−2.5	−32.3
4_B	**−3.4**	**−33.9**
4_C	+10.4	−18.3

Bold values indicate the most stable configuration

here, the methodology is absolutely general and as such it can be extended to any cocktail of co-sensitizing dyes, provided one knows the relative surface coverage of each species.

Starting from 1:1 AS02:C106 arrangements and arriving at 1:4 AS02:C106 co-adsorbed schemes, which mimic the reference experimental coverage of ≈80% (C106) and ≈20% (AS02), we selected the set of the most closely interacting configurations; the relative stabilization energies are listed in Table 9. To limit the variables in the co-adsorption pattern selection, we followed a stepwise procedure: we started by selecting the two most stable "back" (1_A–E in Fig. 44) and "front" (1_F–H in Fig. 44) 1:1 dimeric structures, to provide a suitable 1:2 trimeric aggregate. We then explored various possible positions for the third C106 molecule (Fig. 45) selecting the most stable configuration. Finally, we looked for the most stable 1:4 AS02/C106 co-adsorption aggregate (Fig. 46), which reproduces the experimental relative coverage of the two species. The stability of the various configurations was evaluated by B3LYP single point calculations in the gas phase with the DGDZVP basis set adding the D3 correction [80, 83] (B3LYP-D3). We label the aggregate structures as n_X, with n ranging from 1 to 4 representing the number of SDs surrounding the ERD, and X (A–H), representing the different investigated interaction patterns. On the technical side we again note the different interaction energies obtained by B3LYP and D3-B3LYP [219]; the inclusion of the D3 correction, accounting for dispersion interactions, provides a coherent trend within the calculated values, with an interaction energy increasing as the number of

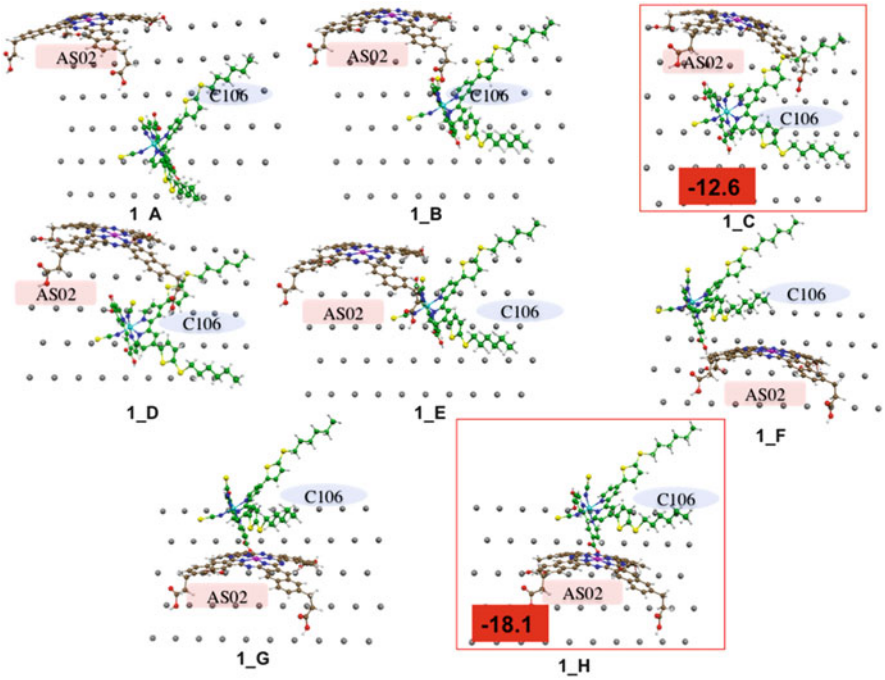

Fig. 44 Top view of the 1:1 co-adsorption schemes; the most stable structures are shown within *red frames* along with their interaction energies in kcal/mol in vacuo. Reprinted with permission of [84]. Copyright (2013) American Chemical Society

SD molecules increases the only exception being the 1:2 structure, given by combining the most stable 1_C and 1_H 1:1 (SD:ERD) assemblies, which turns out to be less stable than both the constituents 1:1 structures due to a repulsive interaction between the two C106 molecules. Moving to the 1:3 co-sensitization patterns (Fig. 45), we find three assemblies (3_A, 3_C, and 3_D) to be very close in energy with a stabilization energy of about 27 kcal/mol and relative differences within 0.8 kcal/mol. For the 1:4 aggregates (Fig. 46), the 4_B structure is the most stable, with a B3LYP-D3 stabilization energy of almost 34 kcal/mol. Our co-adsorption scheme also predicts an average SD-ERD separation very close to the experimentally estimated value of ca. 0.914 nm: [328] for the closest interacting AS02-C106 couple (1_H) we obtained a Zn–Ru distance of 0.908 nm, while for the 1_C configuration the calculated Zn–Ru separation was 1.221 nm.

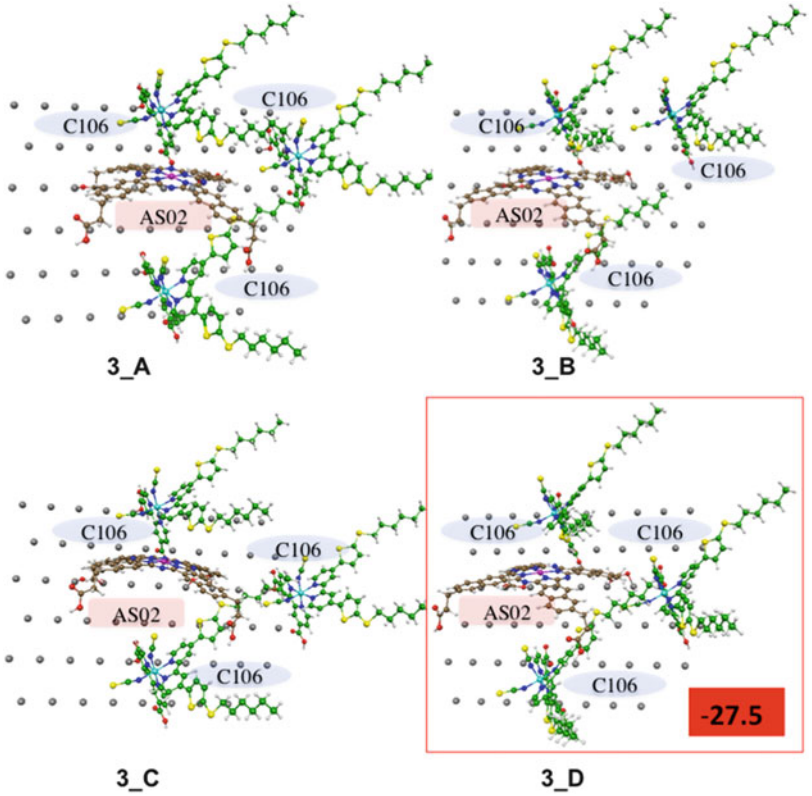

Fig. 45 Top view of the 1:3 co-adsorption schemes; the most stable structure is shown within a *red frame* along with its interaction energies in kcal/mol in vacuo. Reprinted with permission of [84]. Copyright (2013) American Chemical Society

7 Conclusions

Thanks to the advent of Density Functional Theory and Time-Dependent Density Functional Theory, the scope of computational modeling of complex systems, such as dye-sensitized solar cells (DSCs), has been considerably expanded in the last few years. We have reviewed selected applications of quantum mechanical modeling of DSCs materials and processes, with emphasis on the interaction between dye-sensitizers and inorganic semiconductor oxides. Standard DFT/TDDFT approaches provide accurate results for metallorganic Ru(II)-polypyridine and Zn(II)-porphyrin dyes, while the description of push-pull organic dyes is somehow more problematic due to the high degree of charge-transfer characterizing the excited states of such systems. The accurate description of realistic semiconductor nanostructures is also possible, with (tailored) hybrid DFT approaches leading to a reliable description of the electronic and other properties of large systems consisting of several hundred atoms. The simulation of the interaction of dye

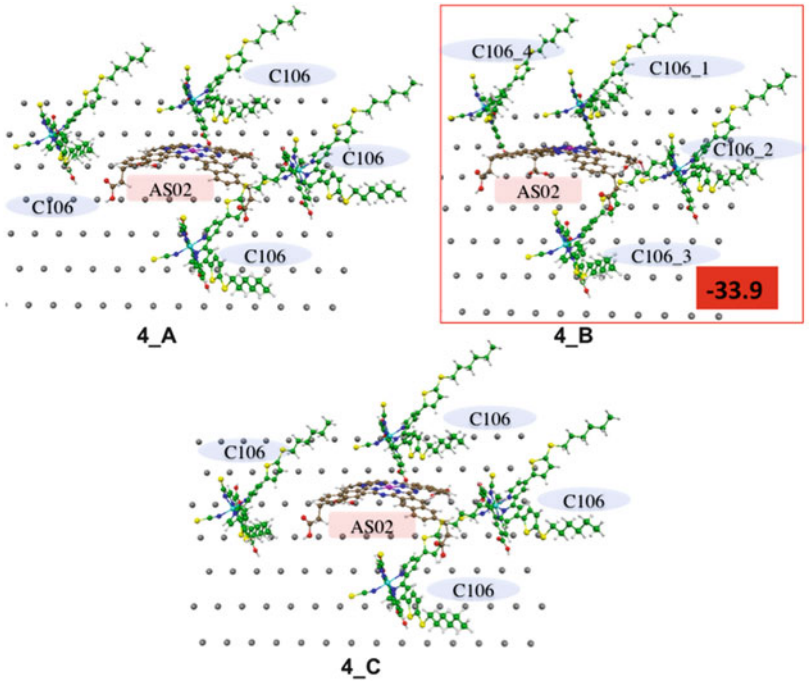

Fig. 46 Top view of the 1:4 co-adsorption schemes; the most stable structure is shown within a *red frame* along with its interaction energies in kcal/mol in vacuo. Reprinted with permission of [84]. Copyright (2013) American Chemical Society

sensitizers with semiconductor oxides is also delivering results consistent with available experimental information, although in complex cases, such as those involving multiple dye anchoring modes, modeling approaches cannot be taken as "black box" tools, but need to be checked a posteriori and possibly integrated by experimental information. In the case of organic dyes the systematic investigation of dye/semiconductor interactions has also allowed researchers to establish new design rules for alternative binding groups with improved characteristics. A further increase in complexity is embodied in the simulation of multiple dye adsorption on semiconductor surfaces or the description of semiconductors co-sensitized by different dyes. In these cases some model simplifications might be needed, such as to consider the single dye binding mode on the semiconductor and to replicate it to obtain the dye packing motif. Still, in some explorative calculations, the results are successful in explaining some experimental evidence, such as those related to fluorescence resonance energy transfer among surface-adsorbed energy relay and sensitizing dyes.

The fundamental information acquired from these studies might constitute the basis for an integrated multiscale computational description of the device functioning, including all the possible interdependencies among the DSC constituents. This may further boost the DSCs efficiency along with providing the basic understanding of the

device necessary for further enhancing priority DSCs requirements, such as temporal stability and optimization of device components. We believe this should be the direction of future computational modeling research in the DSCs field.

Acknowledgments We thank FP7-NMP-2009 project 246124 "SANS" and FP7-ENERGY-2010 project 261920 "ESCORT" for financial support.

References

1. O'Regan B, Grätzel M (1991) A low-cost, high-efficiency solar cell based on dye-sensitized colloidal TiO_2 films. Nature 353(6346):737–740
2. Grätzel M (2009) Recent advances in sensitized mesoscopic solar cells. Acc Chem Res 42(11): 1788–1798
3. Hagfeldt A, Boschloo G, Sun L, Kloo L, Pettersson H (2010) Dye-sensitized solar cells. Chem Rev 110(11):6595–6663
4. Hardin BE, Snaith HJ, McGehee MD (2012) The renaissance of dye-sensitized solar cells. Nat Photonics 6:162
5. Moser JE (2010) Dynamics of interfacial and surface electron transfer processes. In: Kalyanasundarame K (ed) Dye-sensitized solar cells. EPFL, Lausanne, pp 403–456
6. Lanzafame JM, Palese S, Wang D, Miller RJD, Muenter AA (1994) Ultrafast nonlinear optical studies of surface reaction dynamics: mapping the electron trajectory. J Phys Chem 98(43): 11020–11033
7. Clifford JN, Forneli A, Chen H, Torres T, Tan S, Palomares E (2011) Co-sensitized DSCs: dye selection criteria for optimized device Voc and efficiency. J Mater Chem 21(6): 1693–1696
8. Sayama K, Tsukagoshi S, Mori T, Hara K, Ohga Y, Shinpou A, Abe Y, Suga S, Arakawa H (2003) Efficient sensitization of nanocrystalline TiO_2 films with cyanine and merocyanine organic dyes. Sol Energy Mater Sol Cells 80(1):47–71
9. Martínez-Díaz MV, de la Torre G, Torres T (2010) Lighting porphyrins and phthalocyanines for molecular photovoltaics. Chem Commun 46(38):7090–7108
10. Chen Y, Zeng Z, Li C, Wang W, Wang X, Zhang B (2005) Highly efficient co-sensitization of nanocrystalline TiO_2 electrodes with plural organic dyes. New J Chem 29(6):773–776
11. Yum J-H, Jang S-R, Walter P, Geiger T, Nüesch F, Kim S, Ko J, Grätzel M, Nazeeruddin MK (2007) Efficient co-sensitization of nanocrystalline TiO_2 films by organic sensitizers. Chem Commun (44):4680–4682
12. Lan C-M, Wu H-P, Pan T-Y, Chang C-W, Chao W-S, Chen C-T, Wang C-L, Lin C-Y, Diau EW-G (2012) Enhanced photovoltaic performance with co-sensitization of porphyrin and an organic dye in dye-sensitized solar cells. Energy Environ Sci 5(4):6460–6464
13. Yum J-H, Baranoff E, Wenger S, Nazeeruddin MK, Grätzel M (2011) Panchromatic engineering for dye-sensitized solar cells. Energy Environ Sci 4(3):842–857
14. Brown MD, Parkinson P, Torres T, Miura H, Herz LM, Snaith HJ (2011) Surface energy relay between cosensitized molecules in solid-state dye-sensitized solar cells. J Phys Chem C 115(46): 23204–23208
15. Siegers C, Würfel U, Zistler M, Gores H, Hohl-Ebinger J, Hinsch A, Haag R (2008) Overcoming kinetic limitations of electron injection in the dye solar cell via coadsorption and FRET. Chem Phys Chem 9(5):793–798
16. Clifford JN, Palomares E, Nazeeruddin MK, Thampi R, Grätzel M, Durrant JR (2004) Multistep electron transfer processes on dye co-sensitized nanocrystalline TiO_2 films. J Am Chem Soc 126(18):5670–5671
17. Fan S-Q, Kim C, Fang B, Liao K-X, Yang G-J, Li C-J, Kim J-J, Ko J (2011) Improved efficiency of over 10% in dye-sensitized solar cells with a ruthenium complex and an organic

dye heterogeneously positioning on a single TiO_2 electrode. J Phys Chem C 115(15): 7747–7754
18. Ogura RY, Nakane S, Morooka M, Orihashi M, Suzuki Y, Noda K (2009) High-performance dye-sensitized solar cell with a multiple dye system. Appl Phys Lett 94(7):073308
19. Ozawa H, Shimizu R, Arakawa H (2012) Significant improvement in the conversion efficiency of black-dye-based dye-sensitized solar cells by cosensitization with organic dye. RSC Adv 2(8):3198–3200
20. Kuang D, Walter P, Nüesch F, Kim S, Ko J, Comte P, Zakeeruddin SM, Nazeeruddin MK, Grätzel M (2007) Co-sensitization of organic dyes for efficient ionic liquid electrolyte-based dye-sensitized solar cells. Langmuir 23(22):10906–10909
21. Nguyen LH, Mulmudi HK, Sabba D, Kulkarni SA, Batabyal SK, Nonomura K, Grätzel M, Mhaisalkar SG (2012) A selective co-sensitization approach to increase photon conversion efficiency and electron lifetime in dye-sensitized solar cells. Phy Chem Chem Phys. doi:10.1039/C2CP42959D
22. Yella A, Lee H-W, Tsao HN, Yi C, Chandiran AK, Nazeeruddin MK, Diau EW-G, Yeh C-Y, Zakeeruddin SM, Grätzel M (2011) Porphyrin-sensitized solar cells with cobalt (II/III)-based redox electrolyte exceed 12 percent efficiency. Science 334(6056):629–634
23. Rühle S, Cahen D (2004) Electron tunneling at the TiO_2/substrate interface can determine dye-sensitized solar cell performance. J Phys Chem B 108(46):17946–17951
24. Liu J, Zhou D, Xu M, Jing X, Wang P (2011) The structure–property relationship of organic dyes in mesoscopic titania solar cells: only one double-bond difference. Energy Environ Sci 4:3545–3551
25. Xu M, Zhang M, Pastore M, Li R, De Angelis F, Wang P (2012) Joint electrical, photophysical and computational studies on D-p-A dye sensitized solar cells: the impacts of dithiophene rigidification. Chem Sci 3:976–983
26. Dualeh A, De Angelis F, Fantacci S, Moehl T, Yi C, Kessler F, Baranoff E, Nazeeruddin MK, Grätzel M (2012) Influence of donor groups of organic D-π-A dyes on open-circuit voltage in solid-state dye-sensitized solar cells. J Phys Chem C 116:1572–1578
27. Howie WH, Claeyssens F, Miura H, Peter LM (2008) Characterization of solid-state dye-sensitized solar cells utilizing high absorption coefficient metal-free organic dyes. J Am Chem Soc 130(4):1367–1375
28. De Angelis F, Vitillaro G, Kavan L, Nazeeruddin MK, Grätzel M (2012) Modeling ruthenium-dye-sensitized TiO_2 surfaces exposing the (001) or (101) faces: a first-principles investigation. J Phys Chem C 116(34):18124–18131
29. Griffith MJ, James M, Triani G, Wagner P, Wallace GG, Officer DL (2011) Determining the orientation and molecular packing of organic dyes on a TiO_2 surface using X-ray reflectometry. Langmuir 27(21):12944–12950
30. O'Regan BC, Walley K, Juozapavicius M, Anderson AY, Matar F, Ghaddar T, Zakeeruddin SM, Klein C, Durrant JR (2009) Structure/function relationships in dyes for solar energy conversion: a two-atom change in dye structure and the mechanism for its effect on cell voltage. J Am Chem Soc 131(10):3541–3548
31. Miyashita M, Sunahara K, Nishikawa K, Uemura Y, Koumura N, Hara K, Mori A, Abe T, Suzuki E, Mori S (2008) Interfacial electron-transfer kinetics in metal-free organic dye-sensitized solar cells: combined effects of molecular structure of dyes and electrolytes. J Am Chem Soc 130:17874–17881
32. Planells M, Pellejà L, Clifford JN, Pastore M, De Angelis F, López N, Marder SR, Palomares E (2011) Energy levels, charge injection, charge recombination and dye regeneration dynamics for donor–acceptor π-conjugated organic dyes in mesoscopic TiO_2 sensitized solar cells. Energy Environ Sci 4:1820–1829
33. Pastore M, Mosconi E, De Angelis F (2012) Computational investigation of dye–iodine interactions in organic dye-sensitized solar cells. J Phys Chem C 116(9):5965–5973
34. Bai Y, Zhang J, Zhou D, Wang Y, Zhang M, Wang P (2011) Engineering organic sensitizers for iodine-free dye-sensitized solar cells: red-shifted current response concomitant with

attenuated charge recombination. J Am Chem Soc 133(30):11442–11445. doi:10.1021/ja203708k
35. Tuikka M, Hirva P, Rissanen K, Korppi-Tommola J, Haukka M (2011) Halogen bonding—a key step in charge recombination of the dye-sensitized solar cell. Chem Commun 47: 4499–4501
36. Li X, Reynal A, Barnes P, Humphry-Baker R, Zakeeruddin SM, De Angelis F, O'Regan BC (2012) Measured binding coefficients for iodine and ruthenium dyes; implications for recombination in dye sensitised solar cells. Phy Chem Chem Phys 14(44):15421–15428
37. Mosconi E, Yum J-H, Kessler F, García CJG, Zuccaccia C, Cinti A, Nazeeruddin MK, Grätzel M, De Angelis F (2012) Cobalt electrolyte/dye interactions in dye-sensitized solar cells: a combined computational and experimental study. J Am Chem Soc 134(47): 19438–19453
38. Rothenberger G, Fitzmaurice D, Grätzel M (1992) Spectroscopy of conduction band electrons in transparent metal oxide semiconductor films: optical determination of the flatband potential of colloidal titanium dioxide films. J Phys Chem 96(14):5983–5986
39. O'Regan B, Grätzel M, Fitzmaurice D (1991) Optical electrochemistry. 2. Real-time spectroscopy of conduction band electrons in a metal oxide semiconductor electrode. J Phys Chem 95 (26): 10525–10528
40. Boschloo G, Fitzmaurice D (1999) Electron accumulation in nanostructured TiO_2 (anatase) electrodes. J Phys Chem B 103(37):7860–7868
41. Redmond G, Fitzmaurice D (1993) Spectroscopic determination of flatband potentials for polycrystalline titania electrodes in nonaqueous solvents. J Phys Chem 97(7):1426–1430
42. Enright B, Redmond G, Fitzmaurice D (1994) Spectroscopic determination of flatband potentials for polycrystalline TiO_2 electrodes in mixed solvent systems. J Phys Chem 98: 6195–6200
43. Westermark K, Henningsson A, Rensmo H, Södergren S, Siegbahn H, Hagfeldt A (2002) Determination of the electronic density of states at a nanostructured TiO_2/Ru-dye/electrolyte interface by means of photoelectron spectroscopy. Chem Phys 285(1):157–165
44. Rühle S, Greenshtein M, Chen S-G, Merson A, Pizem H, Sukenik CS, Cahen D, Zaban A (2005) Molecular adjustment of the electronic properties of nanoporous electrodes in dye-sensitized solar cells. J Phys Chem B 109(40):18907–18913
45. Yan SG, Hupp JT (1996) Semiconductor-based interfacial electron-transfer reactivity: decoupling kinetics from pH-dependent band energetics in a dye-sensitized titanium dioxide aqueous solution system. J Phys Chem 100(17):6867–6870
46. De Angelis F, Fantacci S, Selloni A, Grätzel M, Nazeeruddin MK (2007) Influence of the sensitizer adsorption mode on the open-circuit potential of dye-sensitized solar cells. Nano Lett 7(10):3189–3195
47. Pastore M, De Angelis F (2012) Computational modelling of TiO_2 surfaces sensitized by organic dyes with different anchoring groups: adsorption modes electronic structure and implication for electron injection/recombination. Phy Chem Chem Phys 14(2):920–928
48. Kusama H, Orita H, Sugihara H (2008) TiO_2 band shift by nitrogen-containing heterocycles in dye-sensitized solar cells: a periodic density functional theory study. Langmuir 24(8): 4411–4419
49. Tachibana Y, Haque SA, Mercer IP, Moser JE, Klug DR, Durrant JR (2001) Modulation of the rate of electron injection in dye-sensitized nanocrystalline TiO_2 films by externally applied bias. J Phys Chem B 105(31):7424–7431
50. Chen P, Yum JH, De Angelis F, Mosconi E, Fantacci S, Moon S-J, Baker RH, Ko J, Nazeeruddin MK, Grätzel M (2009) High open-circuit voltage solid-state dye-sensitized solar cells with organic dye. Nano Lett 9(6):2487–2492
51. O'Regan BC, Durrant JR (2009) Kinetic and energetic paradigms for dye-sensitized solar cells: moving from the ideal to the real. Acc Chem Res 42(11):1799–1808

52. De Angelis F, Fantacci S, Sgamellotti A (2007) An integrated computational tool for the study of the optical properties of nanoscale devices: application to solar cells and molecular wires. Theor Chem Acc 117(5–6):1093–1104
53. Lee DH, Lee MJ, Song HM, Song BJ, Seo KD, Pastore M, Anselmi C, Fantacci S, De Angelis F, Nazeeruddin MK, Gräetzel M, Kim HK (2011) Organic dyes incorporating low-band-gap chromophores based on π-extended benzothiadiazole for dye-sensitized solar cells 91(2):192–198
54. Stier W, Prezhdo OV (2002) Nonadiabatic molecular dynamics simulation of light-induced electron transfer from an anchored molecular electron donor to a semiconductor acceptor. J Phys Chem B 106(33):8047–8054
55. Rego LGC, Batista VS (2003) Quantum dynamics simulations of interfacial electron transfer in sensitized TiO_2 semiconductors. J Am Chem Soc 125(7989–7997)
56. Kondov I, Čížek M, Benesch C, Wang H, Thoss M (2007) Quantum dynamics of photoinduced electron-transfer reactions in dye−semiconductor systems: first-principles description and application to coumarin 343–TiO_2. J Phys Chem C 111(32):11970–11981
57. Meng S, Ren J, Kaxiras E (2008) Natural dyes adsorbed on TiO_2 nanowire for photovoltaic applications: enhanced light absorption and ultrafast electron injection. Nano Lett 8(10): 3266–3272
58. Rego LGC, Batista VS (2003) Quantum dynamics simulations of interfacial electron transfer in sensitized TiO_2 semiconductors. J Am Chem Soc 125:7989–7997
59. Abuabara SG, Rego LGC, Batista VS (2005) Influence of thermal fluctuations on interfacial electron transfer in functionalized TiO_2 semiconductors. J Am Chem Soc 127:18234–18242
60. Duncan WR, Stier WM, Prezhdo OV (2005) Ab initio nonadiabatic molecular dynamics of the ultrafast electron injection across the alizarin−TiO_2 interface. J Am Chem Soc 127(21): 7941–7951
61. Li J, Wang H, Persson P, Thoss M (2012) Photoinduced electron transfer processes in dye-semiconductor systems with different spacer groups. J Chem Phys 137:22A529
62. Marques MAL, López X, Varsano D, Castro A, Rubio A (2003) Time-dependent density-functional approach for biological chromophores: the case of the green fluorescent protein. Phys Rev Lett 90(25):258101–258104
63. Meng S, Kaxiras E (2010) Electron and hole dynamics in dye-sensitized solar cells: influencing factors and systematic trends. Nano Lett 10:1238–1247
64. Fantacci S, De Angelis F, Selloni A (2003) Absorption spectrum and solvatochromism of the [Ru(4,4'-COOH-2,2'-bpy)2(NCS)2] molecular dye by time dependent density functional theory. J Am Chem Soc 125(14):4381–4387
65. Klamt A, Schüürmann G (1993) COSMO: a new approach to dielectric screening in solvents with explicit expressions for the screening energy and its gradient. J Chem Soc Perkin Trans 2:799–805
66. Cossi M, Barone V (2001) Time-dependent density functional theory for molecules in liquid solutions. J Chem Phys 115(10):4708–4717
67. Barone V, Cossi M, Tomasi J (1997) A new definition of cavities for the computation of solvation free energies by the polarizable continuum model. J Chem Phys 107:3210
68. Kristyán S, Pulay P (1994) Can (semi)local density functional theory account for the london dispersion forces? Che Phys Lett 229(3):175–180
69. Tkatchenko A, Romaner L, Hofmann OT, Zojer E, Ambrosch-Draxl C, Scheffler M (2010) Van der Waals interactions between organic adsorbates and at organic/inorganic interfaces. MRS Bulletin 35(6):435–442
70. Johnson ER, Mackie ID, DiLabio GA (2009) Dispersion interactions in density-functional theory. J Phys Org Chem 22(12):1127–1135
71. Johnson ERJ, Wolkow RA, DiLabio GA (2004) Application of 25 density functionals to dispersion-bound homomolecular dimers. Chem Phys Lett 394:334–338
72. Klimeš J, Michaelides A (2012) Perspective: advances and challenges in treating van der Waals dispersion forces in density functional theory. J Chem Phys 137(12):120901

73. Zhao Y, Truhlar DG (2005) Benchmark databases for nonbonded interactions and their use to test density functional theory. J Chem Theor Comp 1(3):415–432
74. Zhao Y, Schultz NE, Truhlar DG (2006) Design of density functionals by combining the method of constraint satisfaction with parametrization for thermochemistry, thermochemical kinetics, and noncovalent interactions. J Chem Theor Comp 2(2):364–382
75. Zhao Y, Truhlar DG (2008) The M06 suite of density functionals for main group thermochemistry, thermochemical kinetics, noncovalent interactions, excited states, and transition elements: two new functionals and systematic testing of four M06-class functionals and 12 other functionals. Theor Chem Acc 120:215–241
76. Wu Q, Yang W (2002) Empirical correction to density functional theory for van der Waals interactions. J Chem Phys 116(2):515
77. Grimme S (2004) Accurate description of van der Waals complexes by density functional theory including empirical corrections. J Comp Chem 25(12):1463–1473
78. Elstner M, Hobza P, Frauenheim T, Suhai S, Kaxiras E (2001) Hydrogen bonding and stacking interactions of nucleic acid base pairs: a density-functional-theory based treatment. J Chem Phys 114:5149
79. Zimmerli U, Parrinello M, Koumoutsakos P (2004) Dispersion corrections to density functionals for water aromatic interactions. J Chem Phys 120(6):2693
80. Grimme S, Antony J, Ehrlich S, Krieg H (2010) A consistent and accurate ab initio parametrization of density functional dispersion correction (DFT-D) for the 94 elements H-Pu. J Chem Phys 132(15):154104
81. Grimme S (2006) Semiempirical GGA-type density functional constructed with a long-range dispersion correction. J Comp Chem 27(15):1787–1799
82. Chai J-D, Head-Gordon M (2008) Long-range corrected hybrid density functionals with damped atom–atom dispersion corrections. Phys Chem Chem Phys 10(44):6615–6620
83. Grimme S, Ehrlich S, Goerigk L (2011) Effect of the damping function in dispersion corrected density functional theory. J Comp Chem 32(7):1456–1465
84. Pastore M, De Angelis F (2012) First-principles computational modeling of fluorescence resonance energy transfer in co-sensitized dye solar cells. J Phys Chem Lett 3(16):2146–2153
85. Nazeeruddin MK, Kay A, Rodicio I, Humphry-Baker R, Mueller E, Liska P, Vlachopoulos N, Graetzel M (1993) Conversion of light to electricity by cis-X2bis(2,2'-bipyridyl-4,4'-dicarboxylate)ruthenium(II) charge-transfer sensitizers (X=Cl−, Br−, I−, CN−, and SCN−) on nanocrystalline titanium dioxide electrode. J Am Chem Soc 115(14):6382–6390
86. Nazeeruddin MK, De Angelis F, Fantacci S, Selloni A, Viscardi G, Liska P, Ito S, Takeru B, Grätzel M (2005) Combined experimental and DFT-TDDFT computational study of photoelectrochemical cell ruthenium sensitizers. J Am Chem Soc 127:16835–16847
87. Nazeeruddin MK, Péchy P, Grätzel M (1997) Efficient panchromatic sensitization of nanocrystalline TiO_2 films by a black dye based on atrithiocyanato–ruthenium complex. Chem Commun (18):1705–1706
88. Nazeeruddin MK, Péchy P, Renouard T, Zakeeruddin SM, Humphry-Baker R, Comte P, Liska P, Cevey L, Costa E, Shklover V, Spiccia L, Deacon GB, Bignozzi CA, Grätzel M (2001) Engineering of efficient panchromatic sensitizers for nanocrystalline TiO_2-based solar cells. J Am Chem Soc 123(8):1613–1624
89. Han L, Islam A, Chen H, Malapaka C, Chiranjeevi B, Zhang S, Yang X, Yanagida M (2012) High-efficiency dye-sensitized solar cell with a novel co-adsorbent. Energy Environ Sci 5(3): 6057–6060
90. Wang P, Zakeeruddin SM, Exnar I, Grätzel M (2002) High efficiency dye-sensitized nanocrystalline solar cells based on ionic liquid polymer gel electrolyte. Chem Commun (24):2972–2973
91. Chen C-Y, Wu S-J, Wu C-G, Chen J-G, Ho K-C (2006) A ruthenium complex with superhigh light-harvesting capacity for dye-sensitized solar cells. Angew Chem Int Ed 45(35): 5822–5825

92. Gao F, Wang Y, Shi D, Zhang J, Wang M, Jing X, Humphry-Baker R, Wang P, Zakeeruddin SM, Grätzel M (2008) Enhance the optical absorptivity of nanocrystalline TiO_2 film with high molar extinction coefficient ruthenium sensitizers for high performance dye-sensitized solar cells. J Am Chem Soc 130(32):10720–10728
93. Bessho T, Yoneda E, Yum J-H, Guglielmi M, Tavernelli I, Imai H, Rothlisberger U, Nazeeruddin MK, Grätzel M (2009) New paradigm in molecular engineering of sensitizers for solar cell applications. J Am Chem Soc 131(16):5930–5934
94. Bomben PG, Koivisto BD, Berlinguette CP (2010) Cyclometalated Ru complexes of type [RuII(NN)2(CN)]z: physicochemical response to substituents installed on the anionic ligand. Inorg Chem 49(11):4960–4971
95. Mishra A, Fischer M, Bäuerle P (2009) Metal-free organic dyes for dye-sensitized solar cells: from structure: property relationships to design rules. Angew Chem Int Ed 48(14):2474–2499
96. Pastore M, Mosconi E, Fantacci S, De Angelis F (2012) Computational investigations on organic sensitizers for dye-sensitized solar cells. Curr Org Synth 9(2):215–232
97. Zeng W, Cao Y, Bai Y, Wang Y, Shi Y, Zhang M, Wang F, Pan C, Wang P (2010) Efficient dye-sensitized solar cells with an organic photosensitizer featuring orderly conjugated ethylenedioxythiophene and dithienosilole blocks. Chem Mater 22(5):1915–1925
98. Wu S-L, Lu H-P, Yu H-T, Chuang S-H, Chiu C-L, Lee C-W, Diau EW-G, Yeh C-Y (2010) Design and characterization of porphyrin sensitizers with a push–pull framework for highly efficient dye-sensitized solar cells. Energy Environ Sci 3(7):949–955
99. Chang Y-C, Wang C-L, Pan T-Y, Hong S-H, Lan C-M, Kuo H-H, Lo C-F, Hsu H-Y, Lin C-Y, Diau EW-G (2011) A strategy to design highly efficient porphyrin sensitizers for dye-sensitized solar cells. Chem Commun 47(31):8910–8912
100. Rensmo H, Södergren S, Patthey L, Westermark K, Vayssieres L, Kohle O, Brühwiler PA, Hagfeldt A, Siegbahn H (1997) The electronic structure of the *cis*-bis(4,4′-dicarboxy-2, 2′-bipyridine)-bis(isothiocyanato)ruthenium(II) complex and its ligand 2,2′-bipyridyl-4, 4′-dicarboxylic acid studied with electron spectroscopy. Chem Phys Lett 274(1–3):51–57
101. Monat JE, Rodriguez JH, McCusker JK (2002) Ground- and excited-state electronic structures of the solar cell sensitizer bis(4,4′-dicarboxylato-2,2′-bipyridine)bis(isothiocyanato)ruthenium(II). J Phys Chem A 106:7399–7406
102. Nazeeruddin MK, Zakeeruddin SM, Humphry-Baker R, Gorelsky SI, Lever ABP, Grätzel M (2000) Synthesis, spectroscopic and a ZINDO study of *cis*- and *trans*-(X2)bis(4,4′-dicarboxylic acid-2,2′-bipyridine)ruthenium(II) complexes (X=Cl−, H2O, NCS−). Coord Chemi Rev 208 (1):213–225
103. Guillemoles J-F, Barone V, Joubert L, Adamo C (2002) A theoretical investigation of the ground and excited states of selected Ru and Os polypyridyl molecular dyes. J Phys Chem A 106(46):11354–11360
104. De Angelis F, Fantacci S, Selloni A (2005) Time dependent density functional theory study of the absorption spectrum of the [Ru(4,4′-COO–2,2′-bpy)(2)(X)(2)](4-) (X=NCS, Cl) dyes in water solution. Chem Phys Lett 415(1–3):115–120
105. De Angelis F, Fantacci S, Selloni A, Nazeeruddin MK, Grätzel M (2007) Time-dependent density functional theory investigations on the excited states of Ru(II)-dye-sensitized TiO_2 nanoparticles: the role of sensitizer protonation. J Am Chem Soc 129(46):14156–14157
106. De Angelis F, Fantacci S, Selloni A (2004) Time-dependent density functional theory study of the absorption spectrum of [Ru(4,4′-COOH-2,2′-bpy)(2)(NCS)(2)] in water solution: influence of the pH. Chem Phys Lett 389(1–3):204
107. Aiga F, Tada T (2003) Molecular and electronic structures of black dye; an efficient sensitizing dye for nanocrystalline TiO_2 solar cells. J Mol Struc 658(1–2):25–32
108. Ghosh S, Chaitanya GK, Bhanuprakash K, Nazeeruddin MK, Grätzel M, Yella RP (2006) Electronic structures and absorption spectra of linkage isomers of trithiocyanato (4,4',4''-tricarboxy-2,2':6,2''-terpyridine) ruthenium(II) complexes: a DFT Study. Inorg Chem 45(19): 7600–7611

109. Li M-X, Zhou X, Xia B-H, Zhang H-X, Pan Q-J, Liu T, Fu H-G, Sun C-C (2008) Theoretical studies on structures and spectroscopic properties of photoelectrochemical cell ruthenium sensitizers, [Ru (Hmtcterpy)(NCS)3]n- (m = 0, 1, 2, and 3; n = 4, 3, 2, and 1). Inorg Chem 47(7): 2312–2324
110. Li M-X, Zhang H-X, Zhou X, Pan Q-J, Fu H-G, Sun C-C (2007) Theoretical studies of the electronic structure and spectroscopic properties of [Ru(Htcterpy)(NCS)3]3–. Eur J Inorg Chem 2171–2180
111. Govindasamy A, Lv C, Tsuboi H, Koyama M, Endou A, Takaba H, Kubo M, Del Carpio CA, Miyamoto A (2007) Theoretical investigation of the photophysical properties of black dye sensitizer [(H3-tctpy)M(NCS)3]− (M = Fe, Ru, Os) in dye sensitized solar cells. Jpn J Appl Phys 46:2655–2660
112. Kusama H, Sugihara H, Sayama K (2011) Theoretical study on the interactions between black dye and iodide in dye-sensitized solar cells. J Phys Chem C 115(18):9267–9275
113. Bang SY, Ko MJ, Kim K, Kim JH, Jang I-H, Park N-G (2012) Evaluation of dye aggregation and effect of deoxycholic acid concentration on photovoltaic performance of N749-sensitized solar cell. Synth Metals 162(17–18):1503–1507
114. Sodeyama K, Sumita M, O'Rourke C, Terranova U, Islam A, Han L, Bowler DR, Tateyama Y (2012) Protonated carboxyl anchor for stable adsorption of Ru N749 dye (black dye) on a TiO_2 anatase (101) surface. J Phys Chem Lett 3(4):472–477
115. Liu S-H, Fu H, Cheng Y-M, Wu K-L, Ho S-T, Chi Y, Chou P-T (2012) Theoretical study of N749 dyes anchoring on the $(TiO_2)28$ surface in DSSCs and their electronic absorption properties. J Phys Chem C 116(31):16338–16345
116. Chen J, Bai F-Q, Wang J, Hao L, Xie Z-F, Pan Q-J, Zhang H-X (2012) Theoretical studies on spectroscopic properties of ruthenium sensitizers adsorbed to TiO_2 film surface with connection mode for DSSC. Dyes Pigm 94(3):459–468
117. Kusama H, Sugihara H, Sayama K (2011) Effect of cations on the interactions of Ru dye and iodides in dye-sensitized solar cells: a density functional theory study. J Phys Chem C 115(5): 2544–2552
118. Fantacci S, Lobello MG, De Angelis F (2013) Everything you always wanted to know about the black dye (but were afraid to ask): a DFT/TDDFT investigation. Chimia. doi:10.2533/chimia.2013.1
119. Lee C-W, Lu H-P, Lan C-M, Huang Y-L, Liang Y-R, Yen W-N, Liu Y-C, Lin Y-S, Diau EW-G, Yeh C-Y (2009) Novel zinc porphyrin sensitizers for dye-sensitized solar cells: synthesis and spectral, electrochemical, and photovoltaic properties. Chem Eur J 15(6):1403–1412
120. Bessho T, Zakeeruddin SM, Yeh C-Y, Diau EW-G, Grätzel M (2010) Highly efficient mesoscopic dye-sensitized solar cells based on donor–acceptor-substituted porphyrins. Angew Chem Int Ed 49(37):6646–6649
121. Wang Q, Campbell WM, Bonfantani EE, Jolley KW, Officer DL, Walsh PJ, Gordon K, Humphry-Baker R, Nazeeruddin MK, Grätzel M (2005) Efficient light harvesting by using green Zn-porphyrin-sensitized nanocrystalline TiO_2 films. J Phys Chem B 109(32): 15397–15409
122. Walsh PJ, Gordon KC, Officer DL, Campbell WM (2006) A DFT study of the optical properties of substituted Zn(II)TPP complexes. J Mol Struct THEOCHEM 759(1–3):17–24
123. Santhanamoorthi N, Lo C-M, Jiang J-C (2013) Molecular design of porphyrins for dye-sensitized solar cells: a DFT/TDDFT study. J Phys Chem Let 4(3):524–530
124. Lind SJ, Gordon KC, Gambhir S, Officer DL (2009) A spectroscopic and DFT study of thiophene-substituted metalloporphyrins as dye-sensitized solar cell dyes. Phys Chem Chem Phys 11(27):5598–5607
125. Hsieh C-P, Lu H-P, Chiu C-L, Lee C-W, Chuang S-H, Mai C-L, Yen W-N, Hsu S-J, Diau EW-G, Yeh C-Y (2010) Synthesis and characterization of porphyrin sensitizers with various electron-donating substituents for highly efficient dye-sensitized solar cells. J Mater Chem 20(6): 1127–1134

126. Ma R, Guo P, Cui H, Zhang X, Nazeeruddin MK, Grätzel M (2009) Substituent effect on the meso-substituted porphyrins: theoretical screening of sensitizer candidates for dye-sensitized solar cells. J Phys Chem A 113(37):10119–10124
127. Orbelli Biroli A, Tessore F, Pizzotti M, Biaggi C, Ugo R, Caramori S, Aliprandi A, Bignozzi CA, De Angelis F, Giorgi G, Licandro E, Longhi E (2011) A multitechnique physicochemical investigation of various factors controlling the photoaction spectra and of some aspects of the electron transfer for a series of push–pull Zn(II) porphyrins acting as dyes in DSSCs. J Phys Chem C 115(46):23170–23182
128. Balanay MP, Kim DH (2008) DFT/TD-DFT molecular design of porphyrin analogues for use in dye-sensitized solar cells. Phys Chem Chem Phys 10(33):5121–5127
129. Pastore M, Mosconi E, De Angelis F, Grätzel M (2010) A computational investigation of organic dyes for dye-sensitized solar cells: benchmark, strategies, and open issues. J Phys Chem C 114(15):7205–7212
130. Pastore M, Fantacci S, De Angelis F (2010) Ab Initio determination of ground and excited state oxidation potentials of organic chromophores for dye-sensitized solar cells. J Phys Chem C 114(51):22742–22750
131. Jacquemin D, Perpète EA, Ciofini I, Adamo C (2009) Accurate simulation of optical properties in dyes. Acc Chem Res 42(2):326–334
132. Jacquemin D, Perpete EA, Scuseria GE, Ciofini I, Adamo C (2008) TD-DFT performance for the visible absorption spectra of organic dyes: conventional versus long-range hybrids. J Chem Theor Comp 4(1):123–135
133. Dreuw A, Weisman JL, Head-Gordon M (2003) Long-range charge-transfer excited states in time-dependent density functional theory require non-local exchange. J Chem Phys 119(6): 2943–2946
134. Tozer DJ (2003) Relationship between long-range charge-transfer excitation energy error and integer discontinuity in Kohn–Sham theory. J Chem Phys 119(24):12697–12699
135. Dev P, Agrawal S, English NJ (2012) Determining the appropriate exchange-correlation functional for time-dependent density functional theory studies of charge-transfer excitations in organic dyes. J Chem Phys 136:224301
136. Tawada Y, Tsuneda T, Yanagisawa S, Yanai T, Hirao K (2004) A long-range-corrected time-dependent density functional theory. J Chem Phys 120(18):8425–8433
137. Kamiya M, Sekino H, Tsuneda T, Hirao K (2005) Nonlinear optical property calculations by the long-range-corrected coupled-perturbed Kohn–Sham method. J Chem Phys 122(23): 234111
138. Iikura H, Tsuneda T, Yanai T, Hirao K (2001) A long-range correction scheme for generalized-gradient-approximation exchange functionals. J Chem Phys 115(8):3540–3544
139. Chai J-D, Head-Gordon M (2008) Systematic optimization of long-range corrected hybrid density functionals. J Chem Phys 128(8):084106
140. Yanai T, Tew DP, Handy NC (2004) A new hybrid exchange-correlation functional using the Coulomb-attenuating method (CAM-B3LYP). Chem Phys Lett 393(1–3):51–57
141. Pastore M, Fantacci S, De Angelis F (2013) Modeling excited states and alignment of energy levels in dye-sensitized solar cells: successes, failures, and challenges. J Phys Chem C 117(8): 3685–3700
142. Kim S, Lee JK, Kang SO, Ko J, Yum JH, Fantacci S, De Angelis F, Di Censo D, Nazeeruddin MK, Grätzel M (2006) Molecular engineering of organic sensitizers for solar cell applications. J Am Chem Soc 128(51):16701–16707
143. Schmidt-Mende L, Bach U, Humphry-Baker R, Horiuchi T, Miura H, Ito S, Uchida S, Grätzel M (2005) Organic dye for highly efficient solid-state dye-sensitized solar cells. Adv Mater 17(7): 813–815
144. Horiuchi T, Miura H, Uchida S (2003) Highly-efficient metal-free organic dyes for dye-sensitized solar cells. Chem Commun 3036–3037
145. Magyar RJ, Tretiak S (2007) Dependence of spurious charge-transfer excited states on orbital exchange in TDDFT: large molecules and clusters. J Chem Theor Comp 3:976–987

146. Preat J, Michaux C, Jacquemin D, Perpete EA (2009) Enhanced efficiency of organic dye-sensitized solar cells: triphenylamine derivatives. J Phys Chem C 113:16821–16833
147. Ito S, Chen P, Comte P, Nazeeruddin MK, Liska P, Pechy P, Grätzel M (2007) Fabrication of screen-printing pastes from TiO_2 powders for dye-sensitised solar cells. Progr Photovoltaics 15:603–612
148. Shankar K, Mor GK, Prakasam HE, Yoriya S, Paulose M, Varghese OK, Grimes CA (2007) Highly-ordered TiO_2 nanotube arrays up to 220 μm in length: use in water photoelectrolysis and dye-sensitized solar cells. Nanotechnology 18(6):065707
149. Saito M, Fujihara S (2008) Large photocurrent generation in dye-sensitized ZnO solar cells. Energy Environ Sci 1(2):280–283
150. Keis K, Lindgren J, Lindquist S-E, Hagfeldt A (2000) Studies of the adsorption process of Ru complexes in nanoporous ZnO electrodes. Langmuir 16(10):4688–4694
151. Ferrere S, Zaban A, Gregg BA (1997) Dye sensitization of nanocrystalline tin oxide by perylene derivatives. J Phys Chem B 101(23):4490–4493
152. Kay A, Grätzel M (2002) Dye-sensitized core−shell nanocrystals: improved efficiency of mesoporous tin oxide electrodes coated with a thin layer of an insulating oxide. Chem Mater 14(7):2930–2935
153. Vittadini A, Casarin M, Selloni A (2007) Chemistry of and on TiO_2-anatase surfaces by DFT calculations: a partial review. Theor Chem Acc 117(5–6):663–671
154. Kohan AF, Ceder G, Morgan D, Van de Walle CG (2000) First-principles study of native point defects in ZnO. Phys Rev B 61(22):15019–15027
155. Muscat J, Wander A, Harrison NM (2001) On the prediction of band gaps from hybrid functional theory. Chem Phys Lett 342(3–4):397–401
156. Di Valentin C, Pacchioni G, Selloni A (2006) Electronic structure of defect states in hydroxylated and reduced rutile TiO_2(110) surfaces. Phys Rev Lett 97(16):166803–166806
157. De Angelis F, Tilocca A, Selloni A (2004) Time-dependent DFT study of [Fe(CN)6](4-) sensitization of TiO_2 nanoparticles. J Am Chem Soc 126(46):15024–15025
158. Lundqvist MJ, Nilsing M, Persson P, Lunel S (2006) DFT study of bare and dye-sensitized TiO_2 clusters and nanocrystals. Int J Quantum Chem 106(15):3214–3234
159. van de Lagemaat J, Park N-G, Frank AJ (2000) Influence of electrical potential distribution, charge transport, and recombination on the photopotential and photocurrent conversion efficiency of dye-sensitized nanocrystalline TiO_2 solar cells: a study by electrical impedance and optical modulation techniques. J Phys Chem B 104(9):2044–2052
160. Schlichthörl G, Park NG, Frank AJ (1999) Evaluation of the charge-collection efficiency of dye-sensitized nanocrystalline TiO_2 solar cells. J Phys Chem B 103(5):782–791
161. Cao F, Oskam G, Meyer GJ, Searson PC (1996) Electron transport in porous nanocrystalline TiO_2 photoelectrochemical cells. J Phys Chem B 100(42):17021–17027
162. Dloczik L, Ileperuma O, Lauermann I, Peter LM, Ponomarev EA, Redmond G, Shaw NJ, Uhlendorf I (1997) Dynamic response of dye-sensitized nanocrystalline solar cells: characterization by intensity-modulated photocurrent spectroscopy. J Phys Chem B 101(49):10281–10289
163. Solbrand A, Lindström H, Rensmo H, Hagfeldt A, Lindquist S-E (1997) Electron transport in the nanostructured TiO_2 – electrolyte system studied with time-resolved photocurrents. J Phys Chem B 101(14):2514–2518
164. Kopidakis N, Schiff EA, Park N-G, van de Lagemaat J, Frank AJ (2000) Ambipolar diffusion of photocarriers in electrolyte-filled, nanoporous TiO_2. J Phys Chem B 104(16):3930–3936
165. Fabregat-Santiago F, Mora-Sero I, Garcia-Belmonte G, Bisquert J (2003) Cyclic voltammetry studies of nanoporous semiconductors. Capacitive and reactive properties of nanocrystalline TiO_2 electrodes in aqueous electrolyte. J Phys Chem B 107(3):758–768
166. Bisquert J, Fabregat-Santiago F, Mora-Sero I, Garcia-Belmonte G, Barea EM, Palomares E (2008) A review of recent results on electrochemical determination of the density of electronic states of nanostructured metal-oxide semiconductors and organic hole conductors. Inorg Chim Acta 361(3):684–698

167. Montero JM, Bisquert J (2011) Trap origin of field-dependent mobility of the carrier transport in organic layers. Solid-State Electron 55(1):1–4
168. Bisquert J, Fabregat-Santiago F, Mora-Seró I, Garcia-Belmonte G, Giménez S (2009) Electron lifetime in dye-sensitized solar cells: theory and interpretation of measurements. J Phys Chem C 113(40):17278–17290
169. Bisquert J, Zaban A, Salvador P (2002) Analysis of the mechanisms of electron recombination in nanoporous TiO_2 dye-sensitized solar cells. Nonequilibrium steady-state statistics and interfacial electron transfer via surface states. J Phys Chem B 106(34):8774–8782
170. Bisquert J, Cahen D, Hodes G, Ruhle S, Zaban A (2004) Physical chemical principles of photovoltaic conversion with nanoparticulate, mesoporous dye-sensitized solar cells. J Phys Chem B 108(24):8106–8118
171. Zaban A, Greenshtein M, Bisquert J (2003) Determination of the electron lifetime in nanocrystalline dye solar cells by open-circuit voltage decay measurements. Chem Phys Chem 4(8):859–864
172. Bailes M, Cameron PJ, Lobato K, Peter LM (2005) Determination of the density and energetic distribution of electron traps in dye-sensitized nanocrystalline solar cells. J Phys Chem B 109(32):15429–15435
173. Ardo S, Meyer GJ (2009) Photodriven heterogeneous charge transfer with transition-metal compounds anchored to TiO_2 semiconductor surfaces. Chem Soc Rev 38(1):115–164
174. Hagfeldt A, Peter L (2010) Dye-sensitized solar cells dye-sensitized solar cells. EPFL, Lausanne
175. Moser JE (2010) Dye-sensitized solar cells dye-sensitized solar cells. EPFL, Lausanne
176. Thompson TL, Yates JT (2006) Surface science studies of the photoactivation of TiO_2 new photochemical processes. Chem Rev 106(10):4428–4453
177. Diebold U, Ruzycki N, Herman GS, Selloni A (2003) One step towards bridging the materials gap: surface studies of TiO_2 anatase. Catal Today 85(2–4):93–100
178. Vittadini A, Selloni A, Rotzinger FP, Grätzel M (1998) Structure and energetics of water adsorbed at TiO_2 anatase (101) and (001) surfaces. Phy Rev Lett 81(14):2954–2957
179. Diebold U (2003) Surf Sci Rep 48:53–229
180. Finazzi E, Di Valentin C, Pacchioni G, Selloni A (2008) Excess electron states in reduced bulk anatase TiO(2): comparison of standard GGA, GGA plus U, and hybrid DFT calculations. J Chem Phys 129(15):154113
181. Finazzi E, Di Valentin C, Pacchioni G (2009) Nature of Ti interstitials in reduced bulk anatase and rutile TiO_2. J Phys Chem C 113(9):3382–3385
182. Krüger P, Bourgeois S, Domenichini B, Magnan H, Chandesris D, Le Fèvre P, Flank AM, Jupille J, Floreano L, Cossaro A, Verdini A, Morgante A (2008) Defect states at the TiO_2 (110) surface probed by resonant photoelectron diffraction. Phys Rev Lett 100(5):055501
183. Barnard AS, Erdin S, Lin Y, Zapol P, Halley JW (2006) Modeling the structure and electronic properties of TiO_2 nanoparticles. Phys Rev B 73(20):205405
184. Li Y-F, Liu Z-P (2011) Particle size, shape and activity for photocatalysis on titania anatase nanoparticles in aqueous surroundings. J Am Chem Soc 133(39):15743–15752
185. Zhang JF, Hughes T, Steigerwald M, Brus LA, Friesner R (2012) Realistic cluster modeling of electron transport and trapping in solvated TiO_2 nanoparticles. J Am Chem Soc 134(29): 12028–12042
186. Koparde VN, Cummings PT (2008) Phase transformations during sintering of titania nanoparticles. ACS Nano 2(8):1620–1624
187. Alimohammadi M, Fichthorn KA (2009) Molecular dynamics simulation of the aggregation of titanium dioxide nanocrystals: preferential alignment. Nano Lett 9(12):4198–4203
188. Nunzi F, Mosconi E, Storchi L, Ronca E, Selloni A, Gratzel M, De Angelis F (2013) Inherent electronic trap states in TiO_2 nanocrystals: effect of saturation and sintering. Energy Environ Sci 6:1221–1229
189. Baerends EJ, Ellis DE, Ros P (1973) Self-consistent molecular Hartree–Fock–Slater calculations I. The computational procedure. Chem Phys 2:41–51

190. Fonseca Guerra C, Snijders JG, te Velde G, Baerends EJ (1998) Towards an order-N DFT method. Theor Chem Acc 99(6):391–403
191. Giannozzi P, Baroni S, Bonini N, Calandra M, Car R, Cavazzoni C, Ceresoli D, Chiarotti GL, Cococcioni M, Dabo I, Dal Corso A, De Gironcoli S, Fabris S, Frates G, Gebauer R, Gerstmann U, Gougoussis C, Kokalj A, Lazzeri M, Martin-Samos L, Marzari N, Mauri F, Mazzarello R, Paolini S, Pasquarello A, Paulatto L, Sbraccia C, Scandolo S, Sclauzero G, Seitsonen AP, Smogunov A, Umaril P, Wentzcovitch RM (2009) QUANTUM ESPRESSO: a modular and open-source software project for quantum simulations of materials. J Phys Condens Matter 21:395502
192. Bisquert J, Zaban A, Greenshtein M, Mora-Serò I (2004) Determination of rate constants for charge transfer and the distribution of semiconductor and electrolyte electronic energy levels in dye-sensitized solar cells by open-circuit photovoltage decay method. J Am Chem Soc 126 (41):13550–13559
193. Monticone S, Tufeu R, Kanaev AV (1998) Complex nature of the UV and visible fluorescence of colloidal ZnO nanoparticles. J Phys Chem B 102(16):2854–2862
194. van Dijken A, Meulenkamp EA, Vanmaekelbergh D, Meijerink A (2000) The kinetics of the radiative and nonradiative processes in nanocrystalline ZnO particles upon photoexcitation. J Phys Chem B 104(8):1715–1723
195. Kahn ML, Cardinal T, Bousquet B, Monge M, Jubera V, Chaudret B (2006) Optical properties of zinc oxide nanoparticles and nanorods synthesized using an organometallic method. Chem Phys Chem 7(11):2392–2397
196. Schrier J, Demchenko DO, Wang L-W, Alivisatos AP (2007) Optical properties of ZnO/ZnS and ZnO/ZnTe heterostructures for photovoltaic applications. Nano Lett 7(8):2377–2382
197. Galoppini E, Rochford J, Chen H, Saraf G, Lu Y, Hagfeldt A, Boschloo G (2006) Fast electron transport in metal organic vapor deposition grown dye-sensitized ZnO nanorod solar cells. J Phys Chem B 110(33):16159–16161
198. Quintana M, Edvinsson T, Hagfeldt A, Boschloo G (2007) Comparison of dye-sensitized ZnO and TiO_2 solar cells: studies of charge transport and carrier lifetime. J Phys Chem C 111(2): 1035–1041
199. Martinson ABF, Elam JW, Hupp JT, Pellin MJ (2007) ZnO nanotube based dye-sensitized solar cells. Nano Lett 7(8):2183–2187
200. De Angelis F, Armelao L (2011) Optical properties of ZnO nanostructures: a hybrid DFT/TDDFT investigation. Phys Chem Chem Phys 13:467–475
201. Azpiroz JM, Mosconi E, De Angelis F (2011) Modeling ZnS and ZnO nanostructures: structural, electronic, and optical properties. J Phys Chem C 115:25219–25226
202. Azpiroz JM, Infante I, Lopez X, Ugalde JU, De Angelis F (2012) A first-principles study of II–VI (II = Zn; VI = O, S, Se, Te) semiconductor nanostructures. J Mater Chem 22: 21453–21465
203. Labat F, Ciofini I, Hratchian HP, Frisch M, Raghavachari K, Adamo C (2009) First principles modeling of eosin-loaded ZnO films: a step toward the understanding of dye-sensitized solar cell performances. J Am Chem Soc 131(40):14290–14298
204. Westermark K, Rensmo H, Siegbahn H (2002) PES studies of Ru(dcbpyH2)2(NCS)2 adsorption on nanostructured ZnO for solar cell applications. J Phys Chem B 106(39):10102–10107
205. Persson P, Lunell S, Ojamäe L (2002) Quantum chemical prediction of the adsorption conformations and dynamics at HCOOH-covered ZnO(1010) surfaces. Int J Quantum Chem 89(3):172–180
206. Persson P, Ojamäe L (2000) Periodic Hartree–Fock study of the adsorption of formic acid on ZnO(1010). Chem Phys Lett 321(3.4):302–308
207. Amat A, De Angelis F (2012) Challenges in the simulation of dye-sensitized ZnO solar cells: quantum confinement, alignment of energy levels and excited states nature at the dye/semiconductor interface. Chem Phys Phys Chem 14:10662–10668
208. Patterson CH (2006) Role of defects in ferromagnetism in Zn1xCoxO: a hybrid density-functional study. Phys Rev B 74(14):144432

209. Wander A, Harrison NM (2001) The stability of polar oxide surfaces: the interaction of H_2O with ZnO(0001) and ZnO(000). J Chem Phys 115(5):2312
210. Matxain JM, Mercero JM, Fowler JE, Ugalde JM (2003) Electronic excitation energies of ZniOi clusters. J Am Chem Soc 125(31):9494–9499
211. Liu D-P, Li G-D, Su Y, Chen J-S (2006) Highly luminescent ZnO nanocrystals stabilized by ionic-liquid components. Angew Chem Int Ed 45(44):7370–7373. doi:10.1002/anie.200602429
212. Meyer B (2004) First-principles study of the polar O-terminated ZnO surface in thermodynamic equilibrium with oxygen and hydrogen. Phys Rev B 69(4):045416
213. Li C, Guo W, Kong Y, Gao H (2007) First-principles study on ZnO nanoclusters with hexagonal prism structures. Appl Phys Lett 90(22):223102–223103
214. Shen X, Allen PB, Muckerman JT, Davenport JW, Zheng J-C (2007) Wire versus tube: stability of small one-dimensional ZnO nanostructures. Nano Lett 7(8):2267–2271
215. Djurišić AB, Leung YH (2006) Optical properties of ZnO nanostructures. Small 2(8–9): 944–961
216. Armelao L, Pascolini M, Biasiolo E, Tondello E, Bottaro G, Dalle Carbonare MD, D'Arrigo A, Leon A (2008) Innovative metal oxide-based substrates for DNA microarrays. Inorg Chim Acta 361(12–13):3603–3608
217. Lundqvist MJ, Nilsing M, Lunell S, Åkermark B, Persson P (2006) Spacer and anchor effects on the electronic coupling in ruthenium-bis-terpyridine dye-sensitized TiO_2 nanocrystals studied by DFT. J Phys Chem B 110(41):20513–20525
218. Wiberg J, Marinado T, Hagberg DP, Sun L, Hagfeldt A, Albinsson B (2009) Effect of anchoring group on electron injection and recombination dynamics in organic dye-sensitized solar cells. J Phys Chem C 113(9):3881–3886
219. Pastore M, De Angelis F (2010) Aggregation of organic dyes on TiO_2 in dye-sensitized solar cells models: an ab initio investigation. ACS Nano 4(1):556–562
220. Grätzel M (2004) Conversion of sunlight to electric power by nanocrystalline dye-sensitized solar cells. J Photochem Photobiol A 164(1–3):3–14
221. Odobel F, Blart E, Lagrée M, Villieras M, Boujtita H, El Murr N, Caramori S, Bignozzi CA (2003) Porphyrin dyes for TiO_2 sensitization. J Mater Chem 13(3):502–510
222. Abbotto A, Manfredi N, Marinzi C, De Angelis F, Mosconi E, Yum J, Xianxi Z, Nazeeruddin MK, Grätzel M (2009) Di-branched di-anchoring organic dyes for dye-sensitized solar cells. Energy Environ Sci 2(10):1094. doi:10.1039/b910654e
223. Argazzi R, Bignozzi CA (2002) Solvatochromic dye sensitized nanocrystalline solar cells. Nano Lett 2(6):625–628
224. Katoh R, Kasuya M, Furube A, Fuke N, Koide N, Han L (2009) Quantitative study of solvent effects on electron injection efficiency for black-dye-sensitized nanocrystalline TiO_2 films. Sol Energy Mater Sol Cells 93(6–7):698–703
225. Hara K, Dan-oh Y, Kasada C, Ohga Y, Shinpo A, Suga S, Sayama K, Arakawa H (2004) Effect of additives on the photovoltaic performance of coumarin-dye-sensitized nanocrystalline TiO_2 solar cells. Langmuir 20:4205–4210
226. Kay A, Gratzel M (1993) Artificial photosynthesis. 1. Photosensitization of TiO_2 solar cells with chlorophyll derivatives and related natural porphyrins. J Phys Chem 97:6272–6277
227. Liu Y, Hagfeldt A, Xiao X-R, Lindquist S-E (1998) Investigation of influence of redox species on the interfacial energetics of a dye-sensitized nanoporous TiO_2 solar cell. Sol Energy Mater Sol Cells 55(3):267–281
228. Falaras P (1998) Synergetic effect of carboxylic acid functional groups and fractal surface characteristics for efficient dye sensitization of titanium oxide. Sol Energy Mater Sol Cells 53 (1–2):163–175
229. Finnie KS, Bartlett JR, Woolfrey JL (1998) Vibrational spectroscopic study of the coordination of (2,2′-bipyridyl-4,4′-dicarboxylic acid)ruthenium(II) complexes to the surface of nanocrystalline titania. Langmuir 14:2744–2749
230. Srinivas K, Yesudas K, Bhanuprakash K, Rao VJ, Giribabu L (2009) A combined experimental and computational investigation of anthracene based sensitizers for DSSC:

comparison of cyanoacrylic and malonic acid electron withdrawing groups binding onto the TiO_2 anatase (101) surface. J Phys Chem C 113:20117–20126
231. Hara K, Sato T, Katoh R, Furube A, Yoshihara T, Murai M, Kurashige M, Ito S, Shinpo A, Suga S (2005) Novel conjugated organic dyes for efficient dye sensitized solar cells. Adv Funct Mater 15(2):246–252
232. Hara K, Sato T, Katoh R, Furube A, Ohga Y, Shinpo A, Suga S, Sayama K, Sugihara H, Arakawa H (2003) Molecular design of coumarin dyes for efficient dye-sensitized solar cells. J Phys Chem B 107:597–606
233. Ganbold E-O, Lee Y, Lee K, Kwon O, Joo S-W (2010) Interfacial behavior of benzoic acid and phenylphosphonic acid on nanocrystalline TiO_2 surfaces. Chem Asian J 5:852–858
234. Nazeeruddin MK, Humphry-Baker R, Liska P, Grätzel M (2003) Investigation of sensitizer adsorption and the influence of protons on current and voltage of a dye-sensitized nanocrystalline TiO_2 solar cell. J Phys Chem B 107(34):8981–8987
235. Lee KE, Gomez MA, Elouatik S, Demopoulos GP (2010) Further understanding of the adsorption mechanism of N719 sensitizer on anatase TiO_2 films for DSSC applications using vibrational spectroscopy and confocal Raman imaging. Langmuir 26(12):9575–9583
236. Pérez León C, Kador L, Peng B, Thelakkat M (2006) Characterization of the adsorption of Ru-bpy dyes on mesoporous TiO_2 films with UV−vis, Raman, and FTIR spectroscopies. J Phys Chem B 110(17):8723–8730
237. Anselmi C, Mosconi E, Pastore M, Ronca E, De Angelis F (2012) Adsorption of organic dyes on TiO_2 surfaces in dye-sensitized solar cells: interplay of theory and experiment. Phy Chem Chem Phys 14(46):15963–15974
238. Johansson EMJ, Edvinsson T, Odelius M, Hagberg DP, Sun L, Hagfeldt A, Siegbahn H, Rensmo H (2007) Electronic and molecular surface structure of a polyene-diphenylaniline dye adsorbed from solution onto nanoporous TiO_2. J Phys Chem C 111:8580–8586
239. Marinado T, Hagberg D, Hedlund M, Edvinsson T, Johansson E, Boschloo G, Rensmo H, Brinck T, Sun L, Hagfeldt A (2009) Rhodanine dyes for dye-sensitized solar cells: spectroscopy, energy levels and photovoltaic performance. Phys Chem Chem Phys 11(1):133–141
240. Hahlin M, Johansson E, Plogmaker S, Odelius M, Sun L, Siegbahn H, Rensmo H (2010) Electronic and molecular structures of organic dye/TiO_2 interfaces for solar cell applications: a core level photoelectron spectroscopy study. Phys Chem Chem Phys 12:1507–1517
241. Karlsson KM, Jiang X, Eriksson SK, Gabrielsson E, Rensmo H, Hagfeldt A, Sun L (2011) Phenoxazine dyes for dye-sensitized solar cells: relationship between molecular structure and electron lifetime. Chem Eur J 17(23):6415–6424
242. Wang M, Plogmaker S, Humphry-Baker R, Pechy P, Rensmo H, Zakeeruddin SM, Grätzel M (2012) Molecular-scale interface engineering of nanocrystalline titania by co-adsorbents for solar energy conversion. Chem Sus Chem 5(1):181–187
243. Nara M, Torii H, Tasumi M (1996) Correlation between the vibrational frequencies of the carboxylate group and the types of its coordination to a metal ion: an ab initio molecular orbital study. J Phys Chem 100:19812–19817
244. Deacon GB, Phillips RJ (1980) Relationships between the carbon–oxygen stretching frequencies of carboxylato complexes and the type of carboxylate coordination. Coord Chem Rev 33(3):227–250
245. Shklover V, Ovchinnikov YE, Braginsky LS, Zakeeruddin SM, Grätzel M (1998) Structure of organic/inorganic interface in assembled materials comprising molecular components. Crystal structure of the sensitizer bis[(4,4′-carboxy-2,2′-bipyridine)(thiocyanato)]ruthenium(II). Chem Mater 10(9):2533–2541
246. Schiffmann F, VandeVondele J, Hutter J, Wirz R, Urakawa A, Baiker A (2010) Protonation-dependent binding of ruthenium bipyridyl complexes to the anatase(101) surface. J Phys Chem C 114(18):8398–8404
247. De Angelis F, Fantacci S, Selloni A, Nazeeruddin MK, Grätzel M (2010) First-principles modeling of the adsorption geometry and electronic structure of Ru(II) dyes on extended TiO_2 substrates for dye-sensitized solar cell applications. J Phys Chem C 114(13):6054–6061

248. De Angelis F, Fantacci S, Mosconi E, Nazeeruddin MK, Grätzel M (2011) Absorption spectra and excited state energy levels of the N719 dye on TiO_2 in dye-sensitized solar cell models. J Phys Chem C 115(17):8825–8831
249. Rocca D, Gebauer R, De Angelis F, Nazeeruddin MK, Baroni S (2009) Time-dependent density functional theory study of squaraine dye-sensitized solar cells. Chem Phys Lett 475: 49–53
250. Martsinovich N, Jones DR, Troisi A (2010) Electronic structure of TiO_2 surfaces and effect of molecular adsorbates using different DFT implementations. J Phys Chem C 114(51): 22659–22670
251. Martsinovich N, Troisi A (2011) High-throughput computational screening of chromophores for dye-sensitized solar cells. J Phys Chem C 115(23):11781–11792
252. De Angelis F (2010) Direct vs indirect injection mechanisms in perylene dye-sensitized solar cells: a DFT/TDDFT investigation. Chem Phys Lett 493(4–6):323–327
253. Persson P, Bergstrom R, Lunell S (2000) Quantum chemical study of photoinjection processes in dye-sensitized TiO_2 nanoparticles. J Phys Chem B 104(44):10348–10351
254. Vittadini A, Selloni A, Rotzinger FP, Grätzel M (2000) Formic acid adsorption on dry and hydrated TiO_2 anatase (101) surfaces by DFT calculations. J Phys Chem B 104(6):1300–1306
255. Tian H, Yang X, Chen R, Zhang R, Hagfeldt A, Sun L (2008) Effect of different dye baths and dye-structures on the performance of dye-sensitized solar cells based on triphenylamine dyes. J Phys Chem C 112:11023–11033
256. Pastore M, De Angelis F (2011) Computational modeling of stark effects in organic dye-sensitized TiO_2 heterointerfaces. J Phys Chem Lett 2(11):1261–1267
257. Mosconi E, Selloni A, De Angelis F (2012) Solvent effects on the adsorption geometry and electronic structure of dye-sensitized TiO_2: a first-principles investigation. J Phys Chem C 116(9):5932–5940
258. Nunzi F, De Angelis F (2011) DFT investigations of formic acid adsorption on single-wall TiO_2 nanotubes: effect of the surface curvature. J Phys Chem C 115(5):2179–2186
259. Perdew JP, Burke K, Ernzerhof M (1996) Generalized gradient approximation made simple. Phy Rev Lett 77(18):3865–3868
260. Foster AS, Nieminen RM (2004) Adsorption of acetic and trifluoroacetic acid on the TiO_2(110) surface. J Chem Phys 121(18):9039
261. te Velde G, Bickelhaupt FM, Baerends EJ, Fonseca Guerra C, van Gisbergen SJA, Snijders JG, Ziegler T (2001) Chemistry with ADF. J Comp Chem 22(9):931–967
262. Frisch MJ, Trucks GW, Schlegel HB, Scuseria GE, Robb MA, Cheeseman JR, Montgomery JA, Vreven JT, Kudin KN, Burant JC, Millam JM, Iyengar SS, Tomasi J, Barone V, Mennucci B, Cossi M, Scalmani G, Rega N, Petersson GA, Nakatsuji H, Hada M, Ehara M, Toyota K, Fukuda R, Hasegawa J, Ishida M, Nakajima T, Honda Y, Kitao O, Nakai H, Klene M, Li X, Knox JE, Hratchian HP, Cross JB, Adamo C, Jaramillo J, Gomperts R, Stratmann RE, Yazyev O, Austin AJ, Cammi R, Pomelli C, Ochterski JW, Ayala PY, Morokuma K, Voth GA, Salvador P, Dannenberg JJ, Zakrzewski VG, Dapprich S, Daniels AD, Strain MC, Farkas O, Malick DK, Rabuck AD, Raghavachari K, Foresman JB, Ortiz JV, Cui Q, Baboul AG, Clifford S, Cioslowski J, Stefanov BB, Liu G, Liashenko A, Piskorz P, Komaromi I, Martin RL, Fox DJ, Keith T, Al-Laham MA, Peng CY, Nanayakkara A, Challacombe M, Gill PMW, Johnson B, Chen W, Wong MW, Gonzalez C, Pople JA (2003) Gaussian 03. Revision B05 edn. Gaussian Inc., Pittsburgh
263. Becke AD (1993) A new mixing of Hartree–Fock and local density-functional theories. J Chem Phys 98(2):1372–1377
264. Miller KL, Musgrave CB, Falconer JL, Medlin JW (2011) Effects of water and formic acid adsorption on the electronic structure of anatase TiO_2(101). J Phys Chem C 115(6): 2738–2749
265. Miller KL, Falconer JL, Medlin JW (2011) Effect of water on the adsorbed structure of formic acid on TiO_2 anatase (1 0 1). J Catalysis 278(2):321–328

266. Hagberg DP, Yum J-H, Lee H, De Angelis F, Marinado T, Karlsson KM, Humphry-Baker R, Sun L, Hagfeldt A, Grätzel M, Nazeeruddin MK (2008) Molecular engineering of organic sensitizers for dye-sensitized solar cell applications. J Am Chem Soc 130:6259–6266
267. Hagberg DP, Edvinsson T, Marinado T, Boschloo G, Hagfeldt A, Sun LC (2006) A novel organic chromophore for dye-sensitized nanostructured solar cells. Chem Comm 21: 2245–2247
268. Hagberg DP, Marinado T, Karlsson KM, Nonomura K, Qin P, Boschloo G, Brinck T, Hagfeldt A, Sun L (2007) Tuning the HOMO and LUMO energy levels of organic chromophores for dye sensitized solar cells. J Org Chem 72(25):9550–9556
269. Cappel UB, Feldt SM, Schoneboom J, Hagfeldt A, Boschloo G (2010) The influence of local electric fields on photoinduced absorption in dye-sensitized solar cells. J Am Chem Soc 132: 9096–9101
270. Nilsing M, Persson P, Lunell S, Ojamäe L (2007) Dye-sensitization of the TiO_2 rutile (110) surface by perylene dyes: quantum-chemical periodic B3LYP computations. J Phys Chem C 111(32):12116–12123
271. Li J, Nilsing M, Kondov I, Wang H, Persson P, Lunell S, Thoss M (2008) Dynamical simulation of photoinduced electron transfer reactions in dye – semiconductor systems with different anchor groups. J Phys Chem C 112(32):12326–12333
272. Persson P, Lundqvist MJ, Ernstorfer R, Goddard WA III, Willig F (2006) Quantum chemical calculations of the influence of anchor-cum-spacer groups on femtosecond electron transfer times in dye-sensitized semiconductor nanocrystals. J Chem Theor Comp 2(2):441–451
273. Moser JE, Grätzel M (1993) Observation of temperature independent heterogeneous electron transfer reactions in the inverted Marcus region. Chem Phys 176(2–3):493–500
274. O'Regan B, Moser J, Anderson M, Grätzel M (1990) Vectorial electron injection into transparent semiconductor membranes and electric field effects on the dynamics of light-induced charge separation. J Phys Chem 94(24):8720–8726
275. Haque SA, Tachibana Y, Willis RL, Moser JE, Grätzel M, Klug DR, Durrant JR (2000) Parameters influencing charge recombination kinetics in dye-sensitized nanocrystalline titanium dioxide films. J Phys Chem B 104(3):538–547
276. Haque SA, Tachibana Y, Klug DR, Durrant JR (1998) Charge recombination kinetics in dye-sensitized nanocrystalline titanium dioxide films under externally applied bias. J Phys Chem B 102(10):1745–1749
277. Haque SA, Handa S, Peter K, Palomares E, Thelakkat M, Durrant JR (2005) Supermolecular control of charge transfer in dye-sensitized nanocrystalline TiO_2 films: towards a quantitative structure-function. Angew Chem Int Ed 44:5740–5744
278. Prezhdo OV, Duncan WR, Prezhdo VV (2008) Dynamics of the photoexcited electron at the chromophore–semiconductor interface. Acc Chem Res 41(2):339–348
279. Haque SA, Palomares E, Cho BM, Green ANM, Hirata N, Klug DR, Durrant JR (2005) Charge separation versus recombination in dye-sensitized nanocrystalline solar cells: the minimization of kinetic redundancy. J Am Chem Soc 127(10):3456–3462
280. Long H, Zhou D, Zhang M, Peng C, Uchida S, Wang P (2011) Probing dye-correlated interplay of energetics and kinetics in mesoscopic titania solar cells with 4-tert-butylpyridine. J Phys Chem C 115(29):14408–14414
281. Nilsing M, Persson P, Ojamäe L (2005) Anchor group influence on molecule-metal oxide interfaces: periodic hybrid DFT study of pyridine bound to TiO_2 via carboxylic and phosphonic acid. Chem Phys Lett 415(4–6):375–380
282. Pal SK, Sundstrom V, Galoppini E, Persson P (2009) Calculations of interfacial interactions in pyrene-Ipa rod sensitized nanostructured TiO_2. Dalton Trans (45):10021–10031
283. Persson P, Lundqvist MJ, Ernstorfer R, Goddard WA, Willig F (2006) Quantum chemical calculations of the influence of anchor-cum-spacer groups on femtosecond electron transfer times in dye-sensitized semiconductor nanocrystals. J Chem Theory Comput 2(2):441–451
284. Li J, Wang H, Persson P, Thoss M (2012) Photoinduced electron transfer processes in dye-semiconductor systems with different spacer groups. J Chem Phys 137(22):22A529-516

285. Ambrosio F, Martsinovich N, Troisi A (2012) Effect of the anchoring group on electron injection: theoretical study of phosphonated dyes for dye-sensitized solar cells. J Phys Chem C 116(3):2622–2629
286. Maggio E, Martsinovich N, Troisi A (2012) Evaluating charge recombination rate in dye-sensitized solar cells from electronic structure calculations. J Phys Chem C 116(14): 7638–7649
287. Jones DR, Troisi A (2010) A method to rapidly predict the charge injection rate in dye sensitized solar cells. Phys Chem Chem Phys 12(18):4625–4634
288. Maggio E, Martsinovich N, Troisi A (2012) Theoretical study of charge recombination at the TiO_2-electrolyte interface in dye sensitised solar cells. J Chem Phys 137(22):22A508
289. Maggio E, Martsinovich N, Troisi A (2013) Using orbital symmetry to minimize charge recombination in dye-sensitized solar cells. Angew Chem Int Ed 52(3):973–975
290. Ambrosio F, Martsinovich N, Troisi A (2012) What is the best anchoring group for a dye in a dye-sensitized solar cell? J Phys Chem Lett 3(11):1531–1535
291. Persson P, Lundqvist MJ (2005) Calculated structural and electronic interactions of the ruthenium dye N3 with a titanium dioxide nanocrystal. J Phys Chem B 109(24):11918–11924
292. Labat F, Ciofini I, Adamo C (2012) Revisiting the importance of dye binding mode in dye-sensitized solar cells: a periodic viewpoint. J Mater Chem 22(24):12205–12211
293. Labat FDR, Ciofini I, Hratchian HP, Frisch MJ, Raghavachari K, Adamo C (2011) Insights into working principles of ruthenium polypyridyl dye-sensitized solar cells from first principles modeling. J Phys Chem C 115(10):4297–4306
294. Martsinovich N, Ambrosio F, Troisi A (2012) Adsorption and electron injection of the N3 metal-organic dye on the TiO_2 rutile (110) surface. Phys Chem Chem Phys 14(48): 16668–16676
295. Persson P, Lundqvist MJ (2005) Calculated structural and electronic interactions of a titanium dioxide nanocrystal sensitized with the ruthenium dye N3. J Phys Chem B 109: 11918
296. Benkö G, Kallioinen J, Korppi-Tommola JEI, Yartsev AP, Sundström V (2001) Photo-induced ultrafast dye-to-semiconductor electron injection from nonthermalized and thermalized donor states. J Am Chem Soc 124(3):489–493. doi:10.1021/ja016561n
297. Wenger B, Grätzel M, Moser J-E (2005) Rationale for kinetic heterogeneity of ultrafast light-induced electron transfer from Ru(II) complex sensitizers to nanocrystalline TiO_2. J Am Chem Soc 127(35):12150–12151
298. Kuang D, Ito S, Wenger B, Klein C, Moser J-E, Humphry-Baker R, Zakeeruddin SM, Grätzel M (2006) High molar extinction coefficient heteroleptic ruthenium complexes for thin film dye-sensitized solar cells. J Am Chem Soc 128(12):4146–4154
299. Mayor LC, Taylor JB, Magnano G, Rienzo A, Satterley CJ, O'Shea JN, Schnadt J (2008) Photoemission, resonant photoemission, and X-ray absorption of a Ru(II) complex adsorbed on rutile TiO_2 (110) prepared by in situ electrospray deposition. J Chem Phys 129(11): 114701–114709
300. Weston M, Britton AJ, O'Shea JN (2011) Charge transfer dynamics of model charge transfer centers of a multicenter water splitting dye complex on rutile TiO_2 (110). J Chem Phys 134(5): 054705–054710
301. Benkö G, Kallioinen J, Korppi-Tommola JEI, Yartsev AP, Sundström V (2002) Photo-induced ultrafast dye-to-semiconductor electron injection from nonthermalized and thermalized donor states. J Am Chem Soc 124(3):489–493
302. Bräm O, Cannizzo A, Chergui M (2012) Ultrafast fluorescence studies of dye sensitized solar cells. Phy Chem Chem Phys 14:7934–7937
303. Szarko JM, Neubauer A, Bartelt A, Socaciu-Siebert L, Birkner F, Schwarzburg K, Hannappel T, Eichberger R (2008) The ultrafast temporal and spectral characterization of electron injection from perylene derivatives into ZnO and TiO_2 colloidal films. J Phys Chem C 112(28):10542–10552

304. Gonzalez-Moreno R, Cook PL, Zegkinoglou I, Liu X, Johnson PS, Yang W, Ruther RE, Hamers RJ, Tena-Zaera R, Himpsel FJ, Ortega JE, Rogero C (2011) Attachment of proto-porphyrin dyes to nanostructured ZnO surfaces: characterization by near edge X-ray absorption fine structure spectroscopy. J Phys Chem C 115(37):18195–18201
305. Burfeindt B, Hannappel T, Storck W, Willig F (1996) Measurement of temperature-independent femtosecond interfacial electron transfer from an anchored molecular electron donor to a semiconductor as acceptor. J Phys Chem 100(41):16463–16465. doi:10.1021/jp9622905
306. Ronca E, Pastore M, Belpassi L, Tarantelli F, De Angelis F (2013) Influence of the dye molecular structure on the TiO_2 conduction band in dye-sensitized solar cells: disentangling charge transfer and electrostatic effects. Energy Environ Sci 6:183–193
307. Belpassi L, Infante I, Tarantelli F, Visscher L (2008) The chemical bond between Au(I) and the noble gases. Comparative study of NgAuF and NgAu+ (Ng = Ar, Kr, Xe) by density functional and coupled cluster methods. J Am Chem Soc 130(3):1048–1060
308. Horiuchi T, Miura H, Sumioka K, Uchida S (2004) High efficiency of dye-sensitized solar cells based on metal-free indoline dyes. J Am Chem Soc 126(39):12218–12219
309. Car R, Parrinello M (1985) Unified approach for molecular dynamics and density-functional theory. Phys Rev Lett 55(22):2471–2474
310. Pasquarello A, Laasonen K, Car R, Lee C, Vanderbilt D (1992) Ab initio molecular dynamics for d-electron systems: liquid copper at 1500 K. Phys Rev Lett 69(13):1982–1985
311. Giannozzi P, Angelis FD, Car R (2004) First-principle molecular dynamics with ultrasoft pseudopotentials: parallel implementation and application to extended bioinorganic systems. J Chem Phys 120(13):5903–5915
312. Ardo S, Sun Y, Castellano FN, Meyer GJ (2010) Excited-state electron transfer from ruthenium-polypyridyl compounds to anatase TiO_2 nanocrystallites: evidence for a stark effect. J Phys Chem B 114:14596–14604
313. Ardo S, Sun Y, Staniszewski A, Castellano FN, Meyer GJ (2010) Stark effects after excited-state interfacial electron transfer at sensitized TiO_2 nanocrystallites. J Am Chem Soc 132:6696–6709
314. Staniszewski A, Ardo S, Sun Y, Castellano FN, Meyer GJ (2008) Slow cation transfer follows sensitizer regeneration at anatase TiO_2 interfaces. J Am Chem Soc 130(35):11586–11587
315. Snaith HJ, Karthikeyan CS, Petrozza A, Teuscher J, Moser JE, Nazeeruddin MK, Thelakkat M, Grätzel M (2008) High extinction coefficient "Antenna" dye in solid-state dye-sensitized solar cells: a photophysical and electronic study. J Phys Chem C 112(20):7562–7566
316. Cappel UB, Gibson EA, Hagfeldt A, Boschloo G (2009) Dye regeneration by spiro-MeOTAD in solid state dye-sensitized solar cells studied by photoinduced absorption spectroscopy and spectroelectrochemistry. J Phys Chem C 113:6275–6281
317. Anderson AY, Barnes PRF, Durrant JR, O'Regan B (2010) Simultaneous transient absorption and transient electrical measurements on operating dye-sensitized solar cells: elucidating the intermediates in iodide oxidation. J Phys Chem C 114:1953–1958
318. Cappel UB, Smeigh AL, Plogmaker S, Johansson EMJ, Rensmo H, Hammarström L, Hagfeldt A, Boschloo G (2011) Characterization of the interface properties and processes in solid state dye-sensitized solar cells employing a perylene sensitizer. J Phys Chem C 115:4345–4358
319. Stark J (1914) Observation of the separation of spectral lines by an electric field. Nature 401:401
320. Boxer SG (2009) Stark realities. J Phys Chem B 113:2972–2983
321. Bublitz GU, Boxer SG (1997) Stark spectroscopy: applications in chemistry, biology, and materials science. Ann Rev Phys Chem 48:213–242
322. Patrick CE, Giustino F (2011) O 1s core-level shifts at the anatase TiO_2 (101)/N3 photovoltaic interface: signature of H-bonded supramolecular assembly. Phys Rev B 84:085330

323. Wang Q, Zakeeruddin SM, Nazeeruddin MK, Humphry-Baker R, Grätzel M (2006) Molecular wiring of nanocrystals: NCS-enhanced cross-surface charge transfer in self-assembled Ru-complex monolayer on mesoscopic oxide films. J Am Chem Soc 128:4446–4452
324. Ellis-Gibbings L, Johansson V, Walsh RB, Kloo L, Quinton JS, Andersson GG (2012) Formation of N719 dye multilayers on dye sensitized solar cell photoelectrode surfaces investigated by direct determination of element concentration depth profiles. Langmuir 28(25): 9431–9439
325. Föster T (1959) 10th Spiers memorial lecture. Transfer mechanisms of electronic excitation. Discuss Faraday Soc 27:7–17
326. Hoke ET, Hardin BE, McGehee MD (2010) Modeling the efficiency of Förster resonant energy transfer from energy relay dyes in dye-sensitized solar cells. Opt Exp 18(4): 3893–3904
327. Mor GK, Basham J, Paulose M, Kim S, Varghese OK, Vaish A, Yoriya S, Grimes CA (2010) High-efficiency Förster resonance energy transfer in solid-state dye sensitized solar cells. Nano Lett 10(7):2387–2394
328. Hardin BE, Sellinger A, Moehl T, Humphry-Baker R, Moser J-E, Wang P, Zakeeruddin SM, Grätzel M, McGehee MD (2011) Energy and hole transfer between dyes attached to titania in cosensitized dye-sensitized solar cells. J Am Chem Soc 133(27):10662–10667
329. Pastore F, De Angelis F (2013) Intermolecular interactions in dye-sensitized solar cells: a computational modeling perspective. J Phys Chem Lett 4:956–974

Top Curr Chem (2014) 352: 237–256
DOI: 10.1007/128_2013_472

Published online: 13 November 2013

Monte Carlo Studies of Electronic Processes in Dye-Sensitized Solar Cells

Alison B. Walker

Abstract This topic reviews random walk Monte Carlo simulation models of charge transport in DSSC. The main electron transport approaches used are covered. Monte Carlo methods and results are explained, addressing the continuous time random walk model developed for transport in disordered materials in the context of the large number of trap states present in the electron transporting material. Multiple timescale MC models developed to look at the morphology dependence of electron transport are described. The concluding section looks at future applications of these methods and the related MC models for polymer blend cells.

Keywords Charge transport · Dye-sensitized · Excitonic · Monte Carlo · Simulation · Solar power · Transport

Contents

A.B. Walker (✉)
Department of Physics, University of Bath, Bath BA2 7AY, UK
e-mail: a.b.walker@bath.ac.uk

1 Introduction

Together with organic photovoltaics, dye-sensitized solar cells, DSSCs, comprise the third generation of solar technologies which are expected to provide added functionality and lowered costs compared to previous generations. DSSCs were invented by O'Regan and Grätzel in 1988 [1] and their potential impact on the quality of life and on sustainable development acknowledged by the award of the 2010 Millennium Technology Grand Prize to Grätzel. DSSCs, an example of which is pictured in Fig. 1, that can be processed at low temperature in air, are semi-flexible and semi-transparent so have possible applications in building integrated photovoltaics and consumer electronics not applicable to glass-based systems, and they employ low-cost and sustainable materials to a considerable extent.

Conventional DSSCs work by mimicking photosynthesis, where all the processes of solar energy collection and charge transport are physically separated [2]. The sensitizer – a monolayer of dye or quantum dots – absorbs a photon to create a tightly bound Frenkel exciton that dissociates rapidly (ps) due to injection of the electron into the mesoporous oxide layer consisting of grains ~10 nm in diameter which, in the case of the widely used TiO_2, films have the anatase structure. Oxidation of iodide ions to tri-iodide ions regenerates the excited dye molecule through transferring its positive charge to the redox system. The photogenerated electrons flow through the micron thick oxide layer toward the collector electrode, a transparent conducting oxide, TCO, where they are collected to power a load. They re-enter the device via a Pt coated counterelectrode, the Pt being required to catalyse the reduction of tri-iodide ions to iodide ions, completing the circuit.

Figure 2 illustrates the energy levels at which these processes occur [3] and how the open circuit voltage V_{oc} is obtained from the difference between the quasi Fermi level E_F for the injected electrons in the TiO_2 film and the redox potential for the I_3^-/I^- reaction in the electrolyte.The electron injection overpotential required to drive electron transfer to the TiO_2 film is approximately 0.1–0.15 V and the dye regeneration overpotential is around 0.6 V, over half this value coming from reactions within the electrolyte. As can be seen from Fig. 2, the minimum bandgap dictating the onset of light absorption of the sensitizing dye required to overcome these losses is 0.75 V. Despite the disdvantage of the large dye regeneration overpotential, the iodide/triiodide system is popular because of the slow recombination kinetics discussed in Sect. 2.

Solid-state DSSCs (SS-DSSCs) use solid hole conductors instead of a liquid electrolyte and are also capable of delivering high voltages [3]. The hole conductor is typically made from either wide-bandgap small molecules such as 2,2′,7,7′-tetrakis-(*N*,*N*-di-*p*-methoxyphenylamine)-9,9′-spirobifluorene, spiro-OMeTAD, or semiconducting polymers such as poly(3-hexylthiophene-2,5-diyl), P3HT. SS-DSSCs overcome the disadvantage that their liquid counterparts possess of requiring careful packaging that is resistant to corrosion, and so are easier to exploit. A recent development of the solid state DSSC is the meso-superstructured solar cell [4]. These cells replace the dye monolayer with a highly crystalline perovskite absorber with a large

Fig. 1 DSSC made at the University of Bath Chemistry Department. Reproduced with permission from the University of Bath

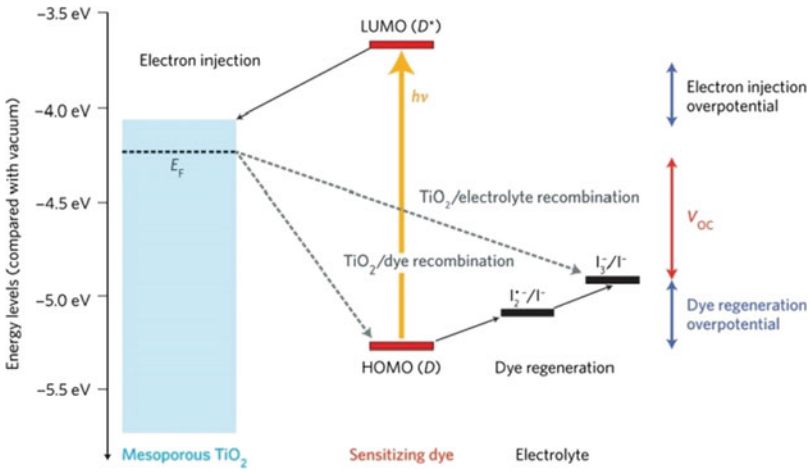

Fig. 2 Schematic diagram showing energy levels in conventional DSCs [3]. Reprinted with permission from Nature Photonics © 2012 Nature Publishing Group

visible to near-infrared absorptivity. High efficiencies are obtained by replacing the TiO_2 film with alumina, Al_2O_3, which acts as an inert scaffold, forcing the electrons to remain within and be transported through an extremely thin absorber layer [4]. Low temperature processable cells with this structure and the perovskite compound $CH_3NH_3PbI_{3-x}Cl_x$ have now achieved power conversion efficiencies up to 12.3% [5]. Cells employing mesoporous TiO_2, with $CH_3NH_3PbI_3$ perovskite as their light harvester, have a similar power conversion efficiency, 12.0% [6].

DSSCs are similar to organic bulk heterojunction solar cells (for which Monte Carlo models have been reviewed by Groves and Greenham [7]) in that in both technologies tightly bound excitons are the first step following light absorption. This similarity was first documented by Gregg [8] who coined the term "excitonic cell" for

cells with these characteristics. The driving force for the movement of charge carriers is the gradient of the free energy and so they are sensitive not only to changes in their potential energy arising from the electrical potential, but also to their concentration via the entropic term in the Gibbs energy. In DSSC, the entropic contribution, small in a typical silicon solar cell but important in all excitonic cells, dominates over electrostatic field gradients since the injected electron charge is screened by the cations in the electrolyte, which eliminates the internal field except very close to the electrodes.

For DSSCs to be marketable and to compete with their inorganic counterparts, fundamental science has to be used to find ways of enhancing cell and module life time and stability without sacrificing performance and scalability. These cells possess a complex structure with disparate materials. Predictive models, validated and improved by continuous feedback from experimental measurements, are needed to decouple and study the many competing mechanisms found in the working cell. With this tool we can discover how cell performance and cell design are related to its material parameters and then systematically search for and arrive at the design specifications that will optimize the cell operation. The need for systematic research in DSSC has been stressed by Peter [9].

In this chapter I will review random walk Monte Carlo, MC, simulation models of electron transport in DSSC. In Sect. 2, I will place these studies in the context of DSSC transport models. MC methods and results are covered in Sect. 3 The concluding section, Sect. 4, looks at future applications of these methods and the related MC models for polymer blend cells that are covered in [7].

2 Electrical Transport Models in DSSC

Electrical transport models predict the device current–voltage characteristics and response to impulse, step and frequency modulated illumination. The power conversion efficiency of the cell η is determined by the open circuit voltage V_{oc}, the short circuit current J_{sc}, and the fill factor FF. FF is calculated from the maximum obtainable power max (JV) as shown in Fig. 3:

$$\mathrm{FF} = \frac{\max\,(JV)}{J_{sc}\,V_{oc}}, \quad \eta = \frac{\mathrm{FF}\,J_{sc}\,V_{oc}}{P_{in}}. \tag{1}$$

The input power P_{in} is obtained from the illumination spectrum. An optical model is required to determine the photon absorption profile in cases where this profile is engineered through encouraging photon scattering by a disperse distribution of TiO_2 particles or the use of photonic band gap materials [10], but the profile usually follows the Beer-Lambert law where the intensity varies exponentially with distance from the illuminated electrode.

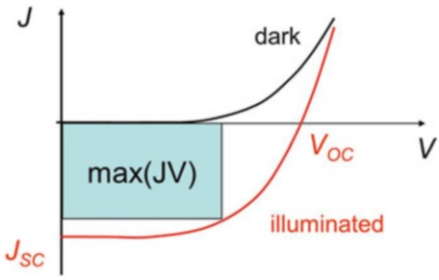

Fig. 3 Schematic diagram showing how the power efficiency η is determined by the shape of the current–voltage characteristic

Length and timescales dominate the physics of electrical transport in a DSSC. In conventional DSSCs, the electrolyte permeates the mesoporous network and is highly conductive through a large concentration of mobile ions. Over a length scale larger than the 10 nm typical grain size and at times longer than the time required for these mobile ions to adjust to changes in electric fields, all electric fields are screened by the electrolyte ions. This screening exists but is less effective in SS-DSSCs as the hole concentration is much lower than the ion concentration in the electrolytes, leading to lower conductivities. Electron–electron interactions at length scales of less than 10 nm are determined by the number of free electrons per grain. The wide bandgap (3.2 eV) of TiO_2 rules out contributions from direct excitation across the bandgap for illumination by a standard solar spectrum such as AM1.5. Free electrons can come from accidental dopants, typically n-type and with a density $\sim 10^{17}$ cm^{-3}. The main source of free charge is photogenerated electrons. At open circuit and 1 sun illumination, the density of these free electrons is $\sim 10^{17}$ cm^{-3} corresponding to one free electron per particle. At these free electron concentrations, the band bending is less than $\approx$40 meV and can be ignored [2]. Even when there is more than one electron in a grain, interactions between electrons in the grain are shielded by the highly polar TiO_2 which has a relative dielectric constant of 12 [11].

The most important form of charge–charge interaction that influences DSSC performance is recombination. DSSCs work because geminate recombination, where the photogenerated exciton recombines before it can dissociate, is reduced by the much faster processes of charge injection and dye regeneration as shown in Fig. 4 [12]. Bimolecular recombination, where the electrons injected from the dye molecules reduce tri-iodide ions to iodide (electrolyte DSSCs) or recombine with a hole (SS-DSSCs), is a major source of loss since electron transport to the collector electrode is slow and takes place on similar timescales to these recombination processes. It is hence essential for the success of the dye-sensitized cell that this back reaction is rendered slow enough that electrons injected by the photoexcited dye can be collected efficiently.

Electron transport is slow because of the large density of traps in TiO_2 that act as a bottleneck for charge transport and has therefore attracted extensive literature. Alternative pictures of electron transport in DSSC studies are hopping and multiple

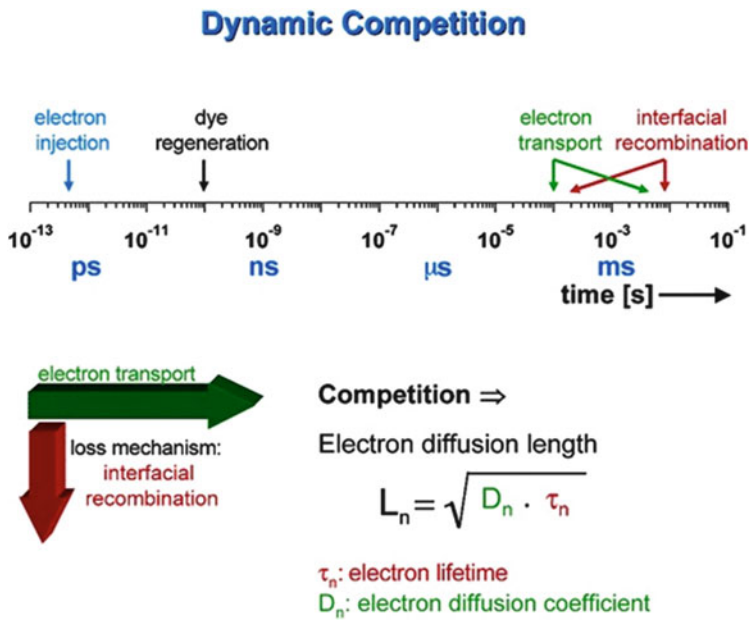

Fig. 4 Timescales of the processes involved in the conversion of light to electric power by DSSCs [12]. © 2005 American Chemical Society

trapping. In the hopping model, charge transport is instead assumed to take place through thermally assisted tunneling between the traps, with hopping rates that depend on the difference in energies and distance [13]. This picture is rarely used because typical trap densities in mesoporous TiO_2 are of the order of one trap per grain [14]. Since grains are typically 10 nm in diameter, distances between traps are too large for significant tunneling to take place by the trapped electrons. In the more widely used multiple trapping picture, illustrated in Fig. 5, the photoinjected electrons are assumed to be in extended states in the conduction band as they execute a random walk through the mesoporous film and their passage is interrupted by a succession of events consisting of rapid trapping into localized states followed by thermally assisted detrapping events. Detrapping from a trap at energy E is assumed to take place by thermal activation at a rate determined from the trapping rate k_t (typically 10^9 s^{-1}) by detailed balance:

$$k_{\mathrm{d}}(E) = \frac{k_{\mathrm{t}} N_{\mathrm{c}}}{N_{\mathrm{t}}} \exp\left[-\frac{(E_{\mathrm{C}} - E)}{k_{\mathrm{B}} T}\right]. \tag{2}$$

Here E_{C} is the conduction band energy, N_{c} is the density of conduction band states, N_{t} is the volume trap density, 10^{20}–10^{21} cm^{-3}, corresponding to a mean distance between traps of 1–3 nm [15], T is the temperature, and k_{B} is Boltzmann's constant. The effective mass of anatase TiO_2 is not well known, in fact not even

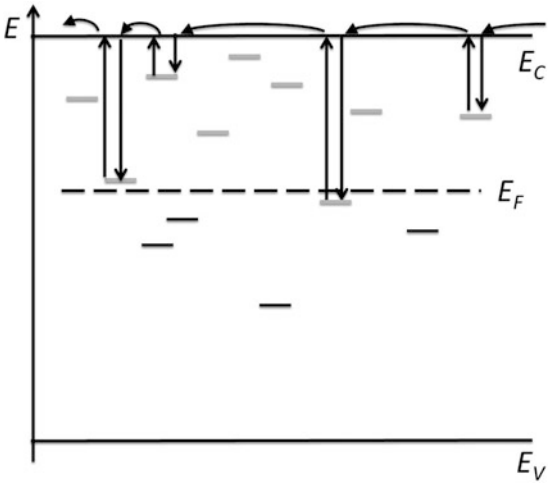

Fig. 5 Schematic illustration of the multiple trapping model. The traps are shown as localized states in the bandgap, where filled states are *black lines* and empty states are *grey lines*. The conduction band E_C, valence band E_V and quasi Fermi level E_F are also shown. The path of an electron trapping into empty states and subsequent detrapping by thermal excitation into the conduction band is shown by the *arrows*

whether it is valid to obtain N_c from the effective mass, so N_c is treated as a fitting parameter with a typical value of 10^{21} cm^{-3}.

The exponential distribution of trap states specifies that the number of trap states per volume in an energy range E to $E + dE$ is given by $g(E)dE$ where

$$g(E) = \frac{N_t}{k_B T_0} \exp\left[-\frac{(E_C - E)}{k_B T_0}\right]. \tag{3}$$

This distribution is almost always used in the absence of experimental data on the trap states that is detailed enough to generate a trap density of state. The width parameter T_0 characterizes this distribution: a low value of T_0 corresponds to almost all traps lying just below E_C. Values of T_0 usually range between 500 and 900 K, depending on preparation and measurement conditions.

Most of the detrapping occurs from traps at energies closest to the quasi Fermi energy E_F (the word quasi is used as the cell is not in equilibrium under illumination) which depends on the light intensity I_0. The steady state photogenerated charge density n_{css} is sufficiently small to assume nondegenerate statistics. At open circuit, where the rate of photocharge generation is balanced by recombination and n_{css} is a constant value across the cell, if linear recombination is assumed, the recombination rate varies linearly with n_{css} with a rate constant k_{rec}:

$$n_{CSS} = N_C \exp\left[\frac{-(E_C - E_F)}{k_B T}\right] = \frac{\alpha_{abs} I_o}{k_{rec}}. \tag{4}$$

Here α_{abs} is the light absorption coefficient (typically 10^3 cm^{-1}). The higher the value of I_0, the closer E_F is to E_C so from (2), the detrapping time is reduced as I_0 increases.

Figure 4 also shows the typical length travelled by an electron before recombination, L_n, whose square is the product of the effective electron diffusion coefficient and lifetime D_n and τ_n, respectively, in the presence of traps. D_n is reduced by the free electrons participating in the multiple trapping processes illustrated in Fig. 5 as it takes longer for the electrons to diffuse through the device in the net direction in which the concentration of electrons is lowered from Fick's first law. By contrast, τ_n is increased by the trapping processes since the electrons have to reach the grain surfaces before bimolecular recombination can take place. In the steady state, trapping/detrapping processes do not influence the electron flow since the carriers will always detrap even if it takes a long time, unless recombination takes place in the trapped states. Therefore it is necessary to measure the response of the DSSC to transient optical or electrical perturbation of the system to probe the effect of traps on electron transport.

D_n depends on the detrapping times. As argued above, the detrapping times are very sensitive to the illumination intensity and will be long at low illumination levels. Experimental measurements using intensity modulated photocurrent spectroscopy, IMPS, backed up by a model that explicitly accounts for the trapped electron density [16] show that D_n decreases from 0.4 cm^2s^{-1} for bulk anatase TiO_2 to below 10^{-8} cm^2s^{-1} at an illumination intensity of 10^{-3} sun [2]. Recently, steady state microwave reflectance measurements on illuminated DSSCs have been shown to be dominated by trapped electrons in the TiO_2 film, contrary to the standard interpretation that only free electrons contribute to the microwave response [11]. In most device models, recombination from trapped states is ignored. Although it has been argued that the trap states are at the surface, e.g., by Kopidakis et al. [17], there is insufficient information available to determine the recombination rates in this case.

If the free and trapped electrons are in local quasi-static equilibrium, it is possible to combine the continuity equations for free and trapped electrons into a single equation for the free electrons with values of the effective electron diffusion coefficient and lifetime D_n and τ_n, respectively, that depend strongly on the free electron density due to trapping and detrapping as described above [18]. L_n [2], however, is independent of the free electron density. The quasistatic approach, though elegant and widely used, is only valid at or close to open circuit where the electron concentration does not vary much with distance unless the electron density is approximated by its average across the cell.

A full macroscopic device model [19] is required to examine the influence of cell geometry and electrode configuration. Extensions for electrolyte mass transport are needed to predict the performance of cells with other redox systems, especially systems less corrosive than the conventional iodide/tri-iodide system [20]. The most common way of implementing this approach is to treat the cell as a quasi-homogeneous system by solving the steady state coupled continuity equations in one and two dimensions for free (conduction band) electrons in the TiO_2 phase, and the iodide/triiodide ions and cation in the electrolyte phase [21]. A similar approach was adopted by Barnes et al. [22] but here, instead of the cations, the oxidized dye molecule profile was solved for and the response to time varying illumination considered by accounting for the trapped electrons in the TiO_2 phase.

Random walk MC is an alternative technique for studying charge transport in electronic devices; see, for example, the book by Hockney and Eastwood [23]. In terms of lengthscales, MC studies lie between a microscopic level description of electronic and optical properties at organic/oxide interfaces where charge separation and recombination occur, discussed in this volume by De Angelis [24], and a device model.

Electron transport is sensitive to morphology so oxide films comprising nanoporous networks, crystalline nanowires/rods, and single crystals will show different behaviors. Geminate and bimolecular recombination rates are sufficiently slow in DSSCs in optimized cells based on mesoporous TiO_2, standard ruthenium-based dyes, and the conventional redox electrolyte that L_n exceeds the thickness of the TiO_2 film, normally around 10 μm. The electron collection efficiency is hence close to 100% in this case and, therefore, improvement is possible only for suboptimal cells or other materials [2]. ZnO has also been studied in depth because fabrication of many different morphologies is easy. Light harvesting in one-dimensional ZnO nanostructures is not noticeably reduced by the lower surface area, suggesting that the best way to improve ZnO is to treat its surface to improve injection and reduce corrosion [25]. The higher relative permittivity of anatase TiO_2 compared to ZnO reduces the electrostatic interaction between injected electrons and oxidized dye molecules, and hence the losses due to geminate recombination of electrons and oxidized dye molecules immediately after electron injection. The lower injection efficiencies in the case of ZnO films arise from formation of bound electron/oxidized dye pairs arising from the lower relative permittivity of the oxide [26]. This picture has been confirmed by THz spectroscopy measurements backed up by MC calculations as discussed below [27]. SnO_2 is an alternative that continues to attract interest because of electron mobilities, over two orders of magnitude higher in the bulk than in bulk TiO_2, although this mobility improvement has not been seen in mesoporous SnO_2 film and SS-DSSCs made with SnO_2 and the polymer P3HT show high leakage current and low shunt-resistance [28].

3 Monte Carlo Methods and Results

In random walk MC simulations, trajectories of an ensemble of particles are obtained by a sequence of random numbers and used to calculate quantities such as the photocurrent and charge recombination transients. For electron transport in DSSC, MC is more realistic than continuum transport models because the continuity equations assume all electrons have the same diffusion coefficient, whereas MC can address transport in disperse systems where the diffusion coefficient is a poorly defined quantity as shown in more detail in Sect. 3.1. MC can also be implemented for complex geometries and so can separate out the effect of morphology on electron transport noted in Sect. 1.1. Section 3.2 describes simulations that explicitly consider the morphology of the oxide.

3.1 Continuous Time Random Walk Model of Dispersive Transport

The CTRW model developed by Scher and others to interpret transient photocurrents in amorphous semiconductors recognized the subtleties of transport in disordered materials such as the lack of a well-defined charge mobility [29]. Application of this approach to electron transport in DSSC has been reviewed recently [30] so this topic is only addressed briefly here. In the CTRW model, illustrated in the left panel of Fig. 6, the hopping picture described above was adopted in which moves are between trap sites. Moves are confined to nearest neighbor sites on a 3D cubic lattice and have a waiting time distribution. In the CTRW, the time for each step is taken from a waiting time distribution $\psi(t)$ where

$$\psi\,(t)\,\alpha\,t^{1-\alpha}. \tag{5}$$

The dispersion parameter α takes a value between 0.1 and 0.3 and is obtained from optical density measurements which vary with time t as $\exp[-(t/\tau)^{\alpha}]$ for a characteristic time τ. For an exponential distribution of trap states of width T_0, $\alpha = T/T_0$. In a development of these ideas, the multiple trapping model was used to explain the variation of experimental cation absorption decay data as a function of applied bias using spectral information to obtain the initial electron number density per nanoparticle [31].

This work was further extended by Barzykin et al. [32]. Here there was a random choice of the next trapping site for an electron within the nanoparticle after detrapping and diffusion in the conduction band as illustrated in the right panel of Fig. 6. The waiting time distribution used to generate detrapping times t_i is given by

$$\psi_i(t) = k_d(E_i)\exp[-k_d(E_i)\ t]. \tag{6}$$

The nanoparticle is modeled as a sphere containing a regular cubic lattice of electron acceptor sites. A fraction φ of these sites are traps with energies E drawn from the distribution function $g(E)$; the remainder are conduction band sites with energy E_c. Initially n sites are populated with electrons and one site is occupied by a dye cation. For consistency with Fermi Dirac statistics, each site can be occupied only once. Recombination occurs whenever an electron arrives on a site occupied by the dye cation. An electron with the shortest detrapping time is detrapped, then the current time is advanced by that detrapping time and the detrapping times for the rest of the electrons are updated. The fate of the freed electron is decided immediately; it is placed at random either on one of the vacant trap sites or on a cation where it immediately recombines.

This model was used to explain the kinetics of charge recombination in dye-sensitized TiO_2 nanoparticles from measurements of the decay of the cation state of $Ru(dcbpy)_2(NCS)_2$ adsorbed on a nanocrystalline TiO_2 electrode with an ethanol/0.1 M tetrabutylammonium triflate electrolyte [33], as shown in Fig. 7.

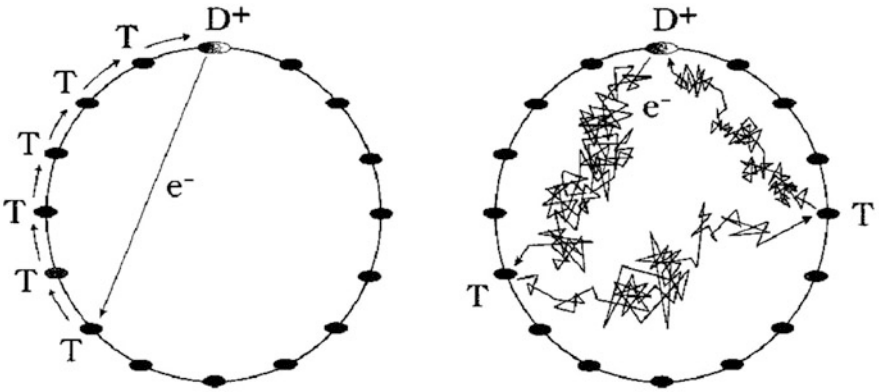

Fig. 6 Two models of charge recombination in a semiconductor particle. *T* are the trap sites, D^+ is the excited dye molecule following electron injection In both cases cations are immobile, while electrons can move between trap sites on the surface of the nanoparticle by thermal activation to the conduction band. The model of [31] ([32]) is shown on the *left* (*right*). Reproduced with permission from [32]. Left figure © (2001) The American Physical Society Right figure © 2002 American Chemical Society

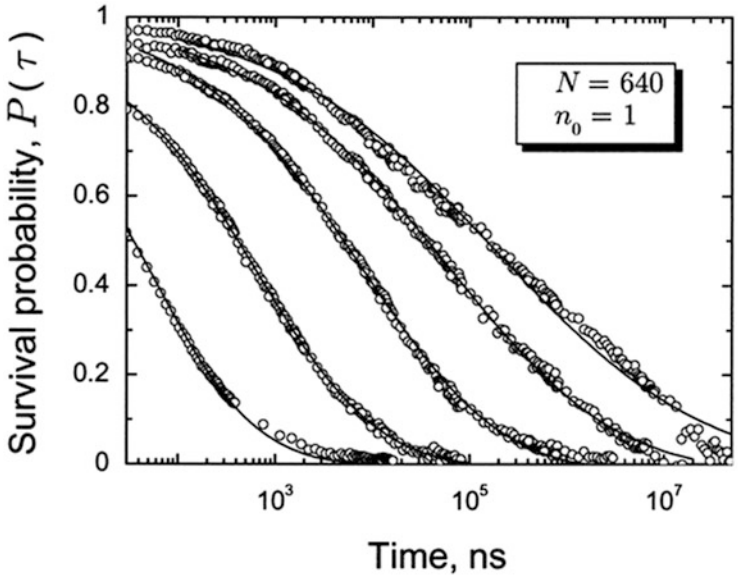

Fig. 7 Transient absorption data showing the decay of the cation state of $Ru(dcbpy)_2(NCS)_2$ adsorbed on a nanocrystalline TiO_2 electrode with an ethanol/0.1 M tetrabutylammonium triflate electrolyte for different applied potentials: 0, 100, 200, 300, and 400 mV (*circles*, *right to left*) [33]. *Lines* were calculated using the simulation procedure described in [32] assuming one cation per nanoparticle. The parameters obtained from fitting are $\alpha = 0.37, 0.4, 0.47, 0.58, 0.81$ and quasi Fermi energy E_F as a ratio of k_BT of 25.1, 21.1, 17.9, 15.5, 13.1 (*right to left*). Reproduced with permission from [32] © 2002 American Chemical Society

The curves are for different illumination intensities. Each curve is characterized by the quasi Fermi energy E_F. The good agreement with experiment combined with the conclusion that long-time behavior of the recombination kinetics is determined solely by the trap energy distribution has led to widespread acceptance of the trapping model.

Experimental data on the variation of L_n with electron quasi Fermi level [34] suggests that nonlinear recombination occurs in DSSC and so a continuum implementation of the multiple trapping model has been extended to this case [35]. Whilst there is insufficient experimental evidence to be certain about the origin of the nonlinear recombination, it is likely that it is due to recombination from trap states [17].

A combined experimental and MC simulation was made into the charge transport and recombination in dye-sensitized mesoporous TiO_2 at temperatures between 110 and 295 K [36]. The MC simulations employed the multiple trapping model and assumed traps were distributed on a 3-dimensional cubic lattice. As the temperature was lowered, the mobility at first increased and then decreased at any given charge density. These observations were shown to be consistent with the multiple-trapping model if the average trap depth becomes shallower and the density of states more ordered as the temperature is decreased. Their analysis also suggested that at room temperature the recombination is mainly influenced by the recombination reaction and the cation density and only weakly influenced by the charge transport. The implications drawn for material design were that, if the mobility can be enhanced without increasing the charge density in the film, for instance by reducing the average trap depth, then there would not necessarily be enhanced recombination, and so the mobility enhancement could greatly increase the charge carrier diffusion lengths in dye-sensitized or mesoscopic solar cells. These conclusions are interesting in the light of the perovskite cells mentioned in Sects. 1 and 4.

3.2 *MC Models Testing Morphology Dependence of Electron Transport*

The CTRW methodology described in Sect. 2.1 was used to compare the tracer diffusion coefficient D_{tracer} in the presence of electron trapping for different porosities and nanoparticle sizes and for trap locations on the surface or extended throughout the nanoparticles, as illustrated in Fig. 8 [37]. D_{tracer} describes the diffusion of a single electron and is obtained from the mean-squared electron displacement using

$$\left\langle r\,(t)^2 \right\rangle = 6D_{\text{tracer}}\,t. \tag{7}$$

This type of diffusion can be followed using isotopic tracers, hence the name. As shown in [35], D_{tracer} depends on the porosity of the film determined by the

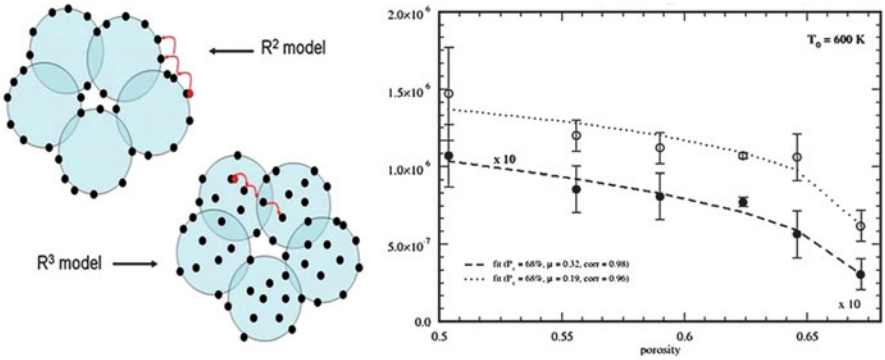

Fig. 8 In the R^2 model, electron traps are located on the surface of the nanoparticles, whereas in the R^3 model the traps occupy the whole volume. Each nanoparticles has a diameter of 10 nm. Results for D_{tracer} as a function of the porosity of the film are shown (*circles*) with exponential distribution of trap energies with $T_0 = 600$ K. A constant number of traps per nanoparticle is assumed in the calculations so that the total number of traps decreases as the porosity increases. *Open* and *filled* circles are used to represent the data from the R^2 and the R^3 model respectively. R^3 data have been multiplied by 10 to facilitate comparison. Reproduced with permission from [37]. © 2008 American Chemical Society

fraction of the volume of voids compared to the total volume. The simulated data reproduce the observed porosity dependence and suggest that only if the traps are located on the surface of the nanoparticles is it possible to reproduce the experimental decrease of the diffusion coefficient with grain size [17]. Connectivity and porosity are related quantities that show the importance of percolation on electron transport. Recent work [37] has separated out this link with percolation from there being fewer nanoparticles per unit volume in films of higher porosity. A similar approach has recently been used to show that partial ordering of the grains in the oxide film can almost double the collection efficiency with respect to a disordered film [38]. Whilst D_{tracer} is an easy parameter to understand, it does not allow for changes in trap occupancy. The effective diffusion coefficient D_{n} which takes these effects into account is more helpful when comparing diffusion coefficients deduced from the response to time varying illumination [39]. Nevertheless, the following useful conclusions were made from this study [37]: D_{tracer} decreases with porosity and is ten times larger for surface traps (R^2) than for bulk traps (R^3) for the same trap concentration, favoring transport in the former case. This result can be understood from the larger mean coordination number in the R^3 model compared to the R^2 model. Electrons in the R^3 model tend to hop within small clusters of traps with high connectivity instead of percolating throughout the network of nanoparticles. This approach also has the advantage of being less demanding of computational resources than the more detailed description of electron transport below and so easier to extend to consider recombination from traps when more information is available on recombination rates from experiment and/or microscopic theory.

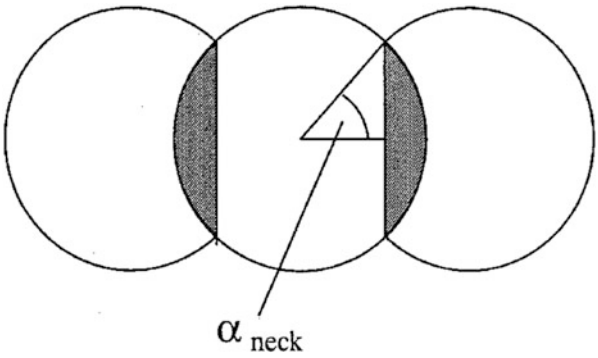

Fig. 9 Schematic diagram showing how the grains are linked and the angle α_{neck} is defined. The *shaded areas* indicate the regions in which an electron is deemed to have moved from the middle grain to a side grain. Reproduced with permission from [40]. © 2003 American Chemical Society

Fig. 10 Grain connectivity in the voided three-dimensional network. The *red grains* are in the top layer, the *yellow grains* in the middle layer, and the *blue grains* in the bottom layer. Otherwise the grains are identical. These colors are used to make it easier to see the grain connectivity [42]. Reproduced with permission of The Royal Society of Chemistry

To allow a direct comparison between MC simulation for systems with different morphologies and experimental measurements of macroscopic quantities such as photocurrent transients and extracted charge, the multi-timescale approach illustrated in Fig. 9 was developed [40–42]. This work was motivated by the IMPS measurements of [43] which showed that electron transport is slower in rutile TiO_2 films than in the more commonly used anatase TiO_2 films due to differences in interparticle connectivity giving rise to different particle packing densities. Two timescales, namely nanoseconds (intragrain motion) and milliseconds (intergrain, across the 2-μm TiO_2 film) are needed because the electron transport in the grains is governed by scattering events on a femtosecond timescale, whereas the electrons take approximately milliseconds to reach the collector electrode after photoinjection. In these simulations, 10 nm radius grains were simulated whose connectivity was controlled by the angle α_{neck} defined in Fig. 9. In addition to transport along linear chains of grains, transport through a three-dimensional grain network in which atoms were removed from a simple cubic lattice to ensure the measured nearest neighbor coordination of four [44] was simulated and is shown in Fig. 10. The grains are placed on a simple cubic lattice to reduce the computing time involved in calculating intergrain transport and it is not evident that using this

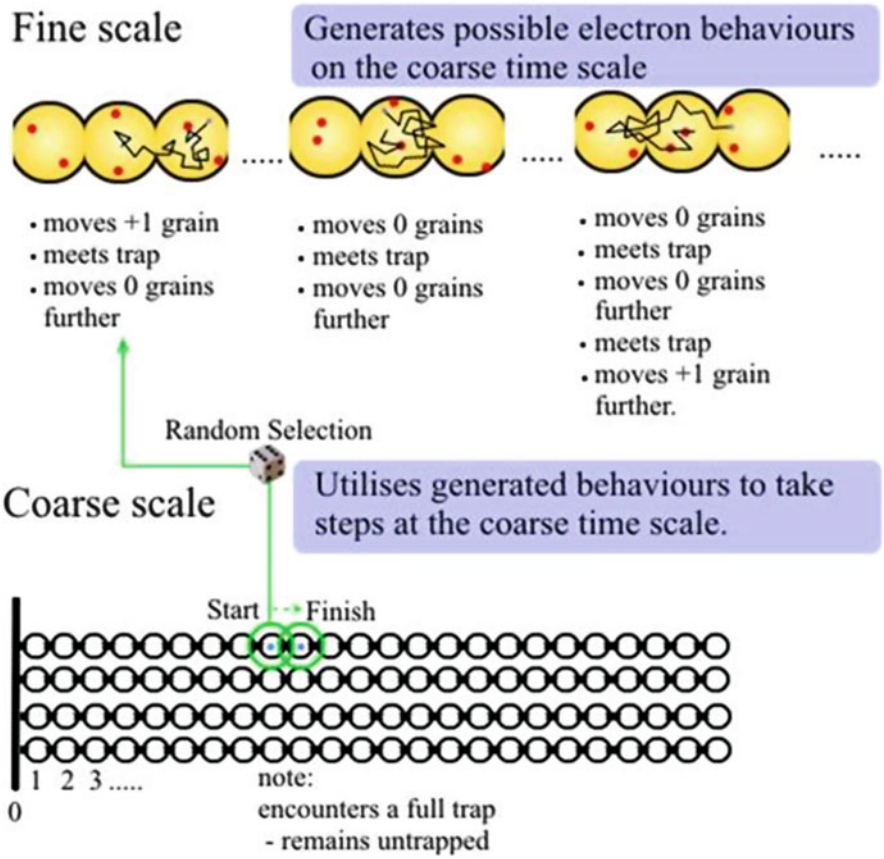

Fig. 11 Schematic diagram showing showing how the simulation is divided into fine and coarse timescales. This illustration is for linear chain coordination [42]. Reproduced with permission of The Royal Society of Chemistry

simplification will have a large effect on the electron transport, whereas it is important to have the correct nearest coordination to ensure sufficient connectivity between the grains.

In these Monte Carlo simulations the electrons move in straight lines until they are scattered. On scattering, a random direction is chosen for their subsequent motion. The average temporal and spatial separation of scattering events experienced by the electrons can be approximated from the electron diffusion coefficient in bulk anatase TiO_2, to give us a length (0.1 nm) and duration (~fs) for the steps made by electrons in the random walk. Electrons require milliseconds or longer to exit the TiO_2 film so $\sim 10^{12}$ steps of 2 fs duration would need to be taken in each random walk, requiring unrealistically large computational resources. Thus in order to simulate the passage of electrons through the grains, we split the simulation into two stages as illustrated in Fig. 11. First, a fine scale simulation, where an electron

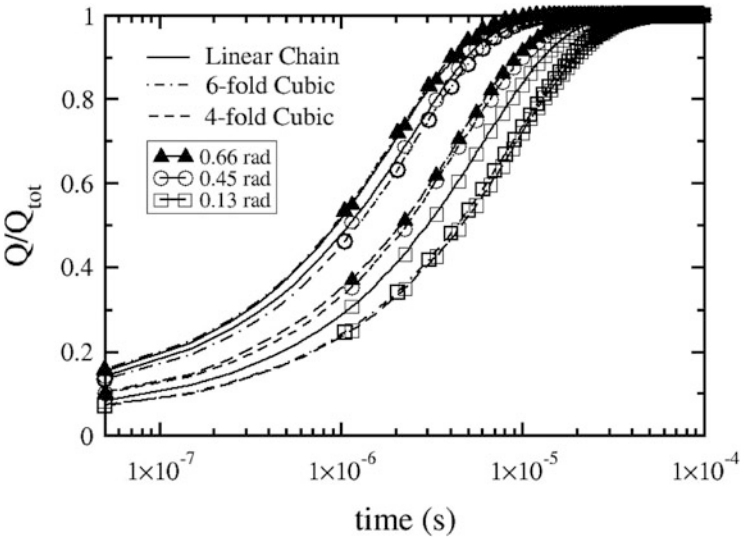

Fig. 12 Comparison between total charge extracted Q as a ratio of injected charge Q_{tot} with no traps present for linear chains with twofold coordination (*solid lines*) and a cubic network with sixfold coordination (*chained lines*) and fourfold coordination (*dashed lines*) and in grains with neck angles of 0.66 rad (*filled triangles*), 0.45 rad (*empty circles*), and 0.13 rad (*empty squares*). An electron density of 3.84×10^{23} m^{-3} is assumed, corresponding to four electrons/grain. Reproduced with permission from [41]. © 2005 American Chemical Society

makes a random walk using steps of size 0.1 nm is allowed to continue for a number of steps that is sufficiently large that the electron could move a few grains along the chain but sufficiently small that many walks are simulated in a reasonable time frame. A walk of 10^5 steps taking 0.2 ns fulfills these requirements. By repeating such a walk many times, we have obtained probabilities for the number of grains moved and the likelihood of trapping. These can then be used in a coarse scale simulation, in which the position of each electron is recorded only in terms of which grain it is in and at each time interval the electron moves or is trapped according to the generated probabilities.

Figure 12 [38] shows that the constrictions at the grain necks slow the electrons, making trapping more likely and hence further delaying their passage to the extracting electrode and that transport is slower in the three-dimensional network than the linear chain of grains due to the additional paths available to the electrons. The reason for the above observations is that in linear chains the electrons move only up and down the chain. The electrode is therefore reached in a much shorter time than in the 3D systems where electrons can take more tortuous paths, especially in the fourfold coordinated system where the reduced coordination makes it even less likely than for the sixfold coordinated system that the electrons can reach the electrode in a given time. As the neck size increases for a given film thickness, the number of grains in the direction normal to the electrodes increases, thus enhancing the number of possible necks through which the electrons have to pass on each path

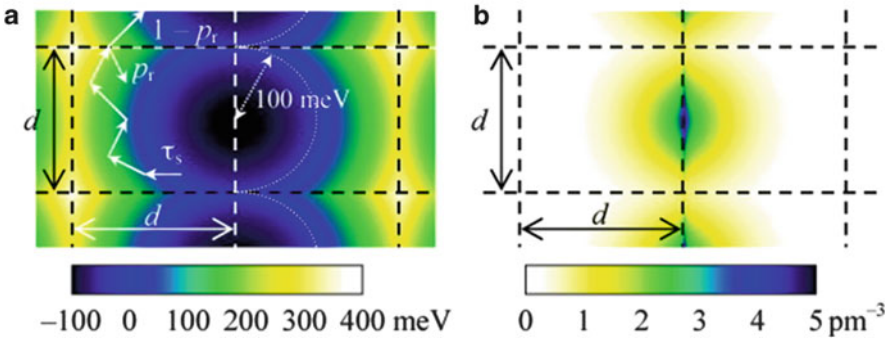

Fig. 13 (**a**) Geometry employed in the MC simulations of electrons interacting with dye cations in ZnO. The *cation* is located in the center of the picture. The *colors* show the potential contours and the *dashed lines* indicate nanoparticle surfaces. The *arrows* show a typical electron trajectory. Its momentum p_r at a position r is changed through scattering with a mean time τ_s. (**b**) Calculated electron density distribution whose contours are shown by the colors for the configuration sketched in (**a**). Reproduced with permission from [27]. © (2010) The American Physical Society

and the number of paths available to them. This effect compensates to some extent for the easier passage due to the wider necks.

The work reported in [37] quantified electron transport through the single particle diffusion coefficient D_{tracer} whereas that in [41] was done to calculate currents through the use of the multi-timescale approach. An effective diffusion coefficient D_{eff} was found by fitting the charge transients to analytical expressions obtained by solving the continuity equation for the electron density in the absence of traps [41]. When traps are present, the competition between slowing down due to trapping and extraction of charge at the extracting electrode provides transients that are quite different in shape to the analytical solutions and so a value for D_{eff} cannot be fitted, suggesting that the TiO_2 film is a disperse medium, consistent with the CTRW approach described above.

The strong influence of nanoparticle connectivity on electron transport has been seen in time-resolved spectroscopic measurements in the THz and visible spectral regions interpreted by MC simulations of electron transport within a grain and its neighbors [27]. Transient conductivity measurements at 9 GHz, where the transport over several nanoparticles was probed, found an order of magnitude lower mobility than at THz frequencies. The MC simulations illustrated in Fig. 13 taken from [27] showed that charge transport in the active solar cell material can be very different from that in non-sensitized semiconductors, due to strong electrostatic interactions between injected electrons and dye cations at the surface of the semiconductor nanoparticle. These interactions localize the electron in the vicinity of the cation.

4 Summary, Conclusions, Outlook

MC simulations are an essential tool for understanding electron transport in the mesoporous oxide films employed in DSSC. There are many implementations of the underlying random walk method, dictated by the phenomena being investigated, from the use of the CTRW to look at energetic disorder due to the traps described in Sect. 2.1 to simulations with an explicit morphology and in some cases multiple timescales looking at the subtle influence of connectivity and electrostatic interactions described in Sect. 2.2. Many papers have been published on DSC that try to improve the cell efficiency by altering the morphology of the nanoporous film, for example by using TiO_2 nanotubes [16]. For these studies, a Monte Carlo modeling approach that can examine the effects of the morphology such as the models reviewed in Sect. 3.2 is important. One caveat is that without detailed experimental measurements, the less computationally demanding approach of solving one-dimensional continuity equations for the free and trapped electrons using averaged parameters is just as effective as shown in [39] where predictions for the transient photocurrent for multi-timescale MC and the continuity equations were compared with experiment.

There are many applications of MC related to the examples I have provided above. Kinetic MC, reviewed in [7], is a generalization of MC that can handle interacting particles in complex three-dimensional morphologies. For example, the hole conductivity in SS-DSSC has been studied [45] with this approach. Such studies are important to tease out the role of additives [45]. By generalizing the methodology of [38] to kinetic MC to treat interacting particles the device current–voltage curves can be predicted for the meso-superstructured cells described in Sect. 1, [4]. The hole transport occurs on the surfaces of the grains and so the geometry is likely to influence the cell output. To identify the role of bimolecular recombination in these cells, and to predict how the performance differs between the devices based on the structures shown, it is important to consider interactions between the holes moving through the transporter medium and the electrons moving through the TiO_2 film as well as the perovskite layer (or just the latter for cells where Al_2O_3 replaces TiO_2).

Acknowledgments The research leading to these results has received funding from the European Union Seventh Framework Programme [FP7/2007–2013] under grant agreement 316494 and from the UK Engineering and Physical Sciences Research Council Supergen Excitonic Solar Cell Consortium and Supergen Supersolar Hub.

References

1. O'Regan B, Grätzel M (1991) A low-cost, high-efficiency solar cell based on dye-sensitized colloidal TiO_2 films. Nature 353:737–740
2. Peter LM (2007) Characterization and modeling of dye-sensitized solar cells. J Phys Chem C 111:6601–6612

3. Hardin B, Snaith HJ, McGehee MD (2012) The renaissance of dye-sensitized solar cells. Nat Photon 6:162–169
4. Lee MM, Teuscher J, Miyasaka TN, Snaith HJ (2012) Efficient hybrid solar cells based on meso-superstructured organometal halide perovskites. Science 338:643–647
5. Ball JM, Lee MM, Hey A, Snaith HJ (2013) Low-temperature processed meso-superstructured to thin-film perovskite solar cells. Energy Environ Sci 6:1739–1743
6. Heo HH, Im SH, Noh JH, Mandal TN, Lim C-S, Chang JA, Lee YH, Sarkar A, Nazeeruddin MK, Grätzel M, Seok SI (2013) Efficient inorganic–organic hybrid heterojunction solar cells containing perovskite compound and polymeric hole conductors. Nat Photon doi:10.1038/nphoton.2013.80
7. Groves C, Greenham NC (2013) Monte Carlo simulations of organic photovoltaics. Top Curr Chem. doi:10.1007/128_2013_467
8. Gregg BA (2013) Excitonic solar cells. J Phys Chem B 107:4688–4698
9. Peter LM (2011) The Grätzel cell: where next? J Phys Chem Lett 2:1861–1867
10. Tétreault N, Grätzel M (2012) Novel nanostructures for next generation dye-sensitized solar cells. Energy Environ Sci 5:8506–8516
11. Dunn HK, Peter LM, Bingham SJ, Maluta E, Walker AB (2012) In situ detection of free and trapped electrons in dye-sensitized solar cells by photo-induced microwave reflectance measurements. J Phys Chem C 116:22063–22072
12. Grätzel M (2005) Solar energy conversion by dye-sensitized photovoltaic cells. Inorg Chem 44:6841–6851
13. Nelson J (1999) Continuous time random walk model of electron transport in nanocrystalline TiO_2 electrodes. Phys Rev B 59:15374
14. Van de Laagemaat J, Frank AJ (2001) Nonthermalized electron transport in dye sensitized nanocrystalline TiO_2 films. J Phys Chem C 105:11194–20005
15. Fabregat-Santiago F, Mora-Sero I, Garcia-Belmonte G, Bisquert J (2003) Cyclic voltammetry studies of nanoporous semiconductors. Capacitive and reactive properties of nanocrystalline TiO_2 electrodes in aqueous electrolyte. J Phys Chem B 107:758–768
16. Jennings JR, Ghicov A, Peter LM, Schmuki P, Walker AB (2008) J Am Chem Soc 130:13364
17. Kopidakis N, Neale NR, Zhu K, van de Lagemaat J, Frank AJ (2005) Spatial location of transport-limiting traps in TiO_2 nanoparticle films in dye-sensitized solar cells. Appl Phys Lett 87:202106
18. Bisquert J, Vikhrenko VS (2004) Interpretation of the time constants measured by kinetic techniques in nanostructured semiconductor electrodes and dye-sensitized solar cells. J Phys Chem B 108:2313–2322
19. Bisquert J, Marcus RA (2013) Device modeling of dye-sensitized solar cells. Top Curr Chem. doi:10.1007/128_2013_471
20. Mosconi E, Yum J-H, Kessler F, Gómez Garcia J, Zuccaccia C, Conti A, Nazeeruddin MK, Grätzel M, De Angelis F (2012) J Am Chem Soc 134:19438–19453
21. Gagliardi A, Mastroianni S, Gentilini D, Giordano F, Reale A, Brown TM, Di Carlo AD (2010) Multiscale modelling of dye solar cells and comparison with experimental data. IEEE J Sel Top Quantum Electron 16:1611–1618
22. Barnes P, Anderson AY, Durrant JR, O'Regan BC (2011) Simulation and measurement of complete dye sensitized solar cells. Phys Chem Chem Phys 13:5798–5816
23. Hockney RW, Eastwood JW (1988) Computer simulation using particles. Adam Hilger, London
24. Pastore M, De Angelis F (2013) Modeling materials and processes in dye-sensitized solar cells: understanding the mechanism, improving the efficiency. Top Curr Chem. doi:10.1007/128_2013_468
25. Anta JA, Guillén E, Tena-Zaera R (2012) ZnO-based dye-sensitized solar cells. J Phys Chem C 116:11413–11425

26. Stockwell D, Yang Y, Huang J, Anfuso C, Huang Z, Lian T (2010) Comparison of electron-transfer dynamics from coumarin 343 to TiO_2, SnO_2, and ZnO nanocrystalline thin films. J Phys Chem C 114:6560–6566
27. Nemec H, Rochford J, Taratula O, Galoppini E, Kuzel P, Polívka T, Yartsev A, Sundstrom V (2010) Impact of electron–cation interaction on electron mobility in dye-sensitized ZnO and TiO_2 nanocrystals. Phys Rev Lett 104:197401
28. Sadoughi G, Sivaram V, Gunning R, Docampo P, Bruder I, Pschirer N, Irajizad A, Snaith HJ (2013) Enhanced electronic contacts in SnO_2–dye–P3HT based solid state dye sensitized solar cells. Phys Chem Chem Phys 13:2075–2080
29. Scher H, Shlesinger MF, Bendler JT (1991) Time-scale invariance in transport and relaxation. Phys Today 1991:26–34
30. Anta JA (2009) Random walk numerical simulation for solar cell applications. Energy Environ Sci 2:387–392
31. Nelson J, Haque SA, Klug DR, Durrant JR (2001) Trap-limited recombination in dye-sensitized nanocrystalline metal oxide electrodes. Phys Rev B 63:205321
32. Barzykin AV, Tachiya M (2002) Mechanism of charge recombination in dye-sensitized nanocrystalline semiconductors. J Phys Chem B 106:4356–4363
33. Haque SA, Tachibana Y, Willis RL, Moser JE, Grätzel M, Klug DR, Durrant JR (2000) Parameters influencing charge recombination kinetics in dye-sensitized nanocrystalline titanium dioxide films. J Phys Chem B 104:538–547
34. Jennings JR, Li F, Wang Q (2010) Reliable determination of electron diffusion length and charge separation efficiency in dye-sensitized solar cells. J Phys Chem C 114:14665–14674
35. Ansari-Rad M, Abdi Y, Arzi E (2012) Simulation of non-linear recombination of charge carriers in sensitized nanocrystalline solar cells. J Appl Phys 112:074319
36. Petrozza A, Groves C, Snaith HJ (2008) Electron transport and recombination in dye-sensitized mesoporous TiO_2 probed by photo induced charge-conductivity modulation spectroscopy with Monte Carlo modeling. J Am Chem Soc 130:12912–12920
37. Anta JA, Morales-Florez V (2008) Combined effect of energetic and spatial disorder on the trap-limited electron diffusion coefficient of metal-oxide nanostructures. J Phys Chem C 112:10287–10293
38. Gonzalez-Vazquez JP, Morales-Flórez V, Anta JA (2012) How important is working with an ordered electrode to improve the charge collection efficiency in nanostructured solar cells? J Phys Chem Lett 3:386–393
39. Bisquert J (2004) Chemical diffusion coefficient of electrons in nanostructured semiconductor electrodes and dye-sensitized solar cells. J Phys Chem B 108:2323–2332
40. Cass MJ, Qiu FL, Walker AB, Fisher AC, Peter LM (2003) Influence of grain morphology on electron transport in dye sensitized nanocrystalline solar cells. J Phys Chem B 107:113–119
41. Cass MJ, Walker AB, Martínez D, Peter LM (2005) Grain morphology and trapping effects on electron transport in dye sensitized nanocrystalline solar cells. J Phys Chem B 109:5100–5107
42. Walker AB, Peter LM, Cass MJ, Cameron PJ, Martínez D (2005) Grain morphology and trapping effects on electron transport in dye sensitized nanocrystalline solar cells. J Mater Chem 15:1–5
43. Park NG, van de Lagemaat J, Frank AJ (2000) Comparison of dye-sensitized rutile- and anatase-based TiO_2 solar cells. J Phys Chem B 104:8989–8994
44. Benkstein KD, Kopidakis N, van de Lagemaat J, Frank AJ (2003) Influence of the percolation network geometry on electron transport in dye-sensitized titanium dioxide solar cells. J Phys Chem B 107:7759–7767
45. Abate A, Staff DR, Hollman DJ, Snaith HJ, Walker AB (2013) Influence of ionizing dopants on charge transport in organic semiconductors Phys Chem Chem Phys submitted

Top Curr Chem (2014) 352: 257–278
DOI: 10.1007/128_2013_467

Published online: 12 July 2013

Monte Carlo Simulations of Organic Photovoltaics

Chris Groves and Neil C. Greenham

Abstract Monte Carlo simulations are a valuable tool to model the generation, separation, and collection of charges in organic photovoltaics where charges move by hopping in a complex nanostructure and Coulomb interactions between charge carriers are important. We review the Monte Carlo techniques that have been applied to this problem, and describe the results of simulations of the various recombination processes that limit device performance. We show how these processes are influenced by the local physical and energetic structure of the material, providing information that is useful for design of efficient photovoltaic systems.

Keywords Monte Carlo simulation · Organic semiconductors · Photovoltaics

Contents

C. Groves
School of Engineering and Computing Sciences, Durham University, Durham DH1 3LE, UK

N.C. Greenham (✉)
Cavendish Laboratory, University of Cambridge, J. J. Thomson Avenue, Cambridge CB3 0HE, UK
e-mail: ncg11@cam.ac.uk

1 Introduction

Organic photovoltaic devices are different from conventional photovoltaics not only in their materials, structure, and method of manufacture, but also in the techniques that must be applied to model their operation successfully. One obvious difference is the complex nanostructure of donor and acceptor materials that forms the basis of the bulk heterojunction devices that are commonly used. Accurate modeling of device function therefore requires microscopic simulation of the motion of charges and other excited states on appropriate lengthscales within the nanostructure. However, even within a single organic semiconductor material, there are important differences in the underlying physics compared with conventional semiconductors, and these already require a microscopic approach to modeling. Charge transport in organic semiconductors occurs by hopping between localized sites that may represent individual molecules or segments of a conjugated polymer chain. These sites are typically not arranged in a regular crystalline lattice, and the different environments experienced by charges on different sites lead to a range of energies of those charges. This energetic disorder is key to understanding the transport properties. Furthermore, due to the localized nature of excited states and the low dielectric constants of organic semiconductors (ε~3–4), Coulombic interactions between charges are much more important than in typical inorganic semiconductors. Photoexcitation of an organic semiconductor leads to the creation of a bound, neutral excited state known as an exciton which itself can hop between sites in a diffusive process. Even once the exciton has diffused to an interface with a second material where charge transfer can occur, Coulomb interactions between the electron and hole remain very important and can make it difficult to separate the electron and hole before they recombine geminately (i.e., the recombination is of an electron and a hole originating from the same exciton). To model these local interactions between pairs of carriers, together with the nanoscale morphology and the site-to-site disorder in energy, requires a model that can keep track of the motion of individual charge carriers and their interactions within a device. Monte Carlo (MC) simulations are the natural approach to this, and recent improvements in computing power mean that it is now feasible to model devices under realistic conditions. The essence of MC simulations is that excited states are introduced into a model of a device comprising an array of hopping sites, and are allowed to move and react in a probabilistic fashion. The models can be used to track the collection of photogenerated charges at the electrodes, and to identify the recombination processes taking place. To simulate device characteristics accurately it is necessary to integrate over many photogeneration events, and also sometimes to average over different random implementations of morphology and energetic disorder.

Monte Carlo simulations of charge transport in organic semiconductors have a long history, including the pioneering work of Bässler [1] which allowed the characteristics of the macroscopically measured mobility to be related to

the microscopic hopping processes. By simulating the hopping of individual charge carriers within a lattice of hopping sites in the presence of Gaussian energetic and spatial disorder he was able to parameterize the temperature and field dependence of the mobility in terms of the amount of disorder present. Importantly, this work explained the Poole–Frenkel-type dependence of mobility, μ, on electric field E [$\mu \propto \exp(\gamma E^{0.5})$] which is often observed in organic semiconductors. The importance of simulations increased with the explosion of interest in organic light-emitting diodes (OLEDs). In these devices electrons and holes are injected into a thin film of organic semiconductor from metallic electrodes. Monte Carlo simulations proved invaluable in understanding the injection of charge carriers in these systems by considering carriers moving within a disordered energy landscape but in the presence of an image force drawing them back to the electrode [2, 3].

More recently, it has become apparent that modeling carriers as moving independently between hopping sites is not necessarily a good approximation under the conditions typically encountered in organic devices such as LEDs and field-effect transistors. Once the carrier concentration becomes significant (site occupancy >1 in 10^3 for typical disorder widths at room temperature), the fact that two carriers cannot occupy the same site means that the carriers on average must occupy higher-energy sites within the Gaussian distribution than they would under thermal equilibrium in the low-density limit. Since carriers on higher-energy sites can more easily hop to neighboring sites, the mobility increases with carrier density. Incorporation of these state-filling effects led to the development of the "extended Gaussian disorder model" (EGDM) which allowed the dependence of mobility on both electric field and carrier density to be parameterized [4], and more recently Coulombic repulsion between the charge carriers has been considered [5]. These models have led to greatly improved predictive ability in the simulation of OLEDs, and have resolved some important questions about the form of the temperature dependence of mobility [6]. However this remains an open area of research, since there are important questions about whether simple uncorrelated Gaussian disorder is the best model to describe the properties of all organic semiconductors, and to what extent the parameterization of mobilities from the EGDM can be transferred directly into macroscopic "effective medium" models for device operation.

In this chapter we focus directly on the application of Monte Carlo simulations in the modeling of organic photovoltaics. Key questions that we want to answer are as follows. (1) Can we predict macroscopic device performance, i.e., the current–voltage curve of a device under illumination, from microscopic models? (2) How does nanoscale morphology influence device performance and what would the optimum morphology be? (3) What recombination mechanisms dominate under different regimes of device operation? (4) How do charges separate efficiently in the best OPV devices despite the strong Coulomb attraction between them, and what are the microscopic requirements to achieve this?

2 Model Implementation

Kinetic Monte Carlo (KMC) models are an attempt to describe the behavior in time of individual charges and excitons that give rise to OPV performance. The key ingredient in any kind of KMC model is the set of rates, R_i, which describe the various competing processes which may happen to the particles in a system, such as hopping in different directions. In most KMC simulations, for a given configuration of particles these rates are assumed to be independent of time. In one commonly-used implementation of KMC, once the rates are defined the total rate $R = \Sigma R_i$ is calculated, and a random hopping time is calculated using (1):

$$\tau = -\frac{\ln(X)}{R}. \tag{1}$$

Here X is a random number which is uniformly distributed between 0 and 1. The time τ is then added to the simulation clock. The process which occurs is then chosen according to a uniform random distribution, with the probability of a process occurring being proportional to its rate R_i. It is the use of random numbers that gives MC models their name. In an alternative, but equivalent, implementation, random waiting times are generated corresponding to the rates of all the processes R_i in a similar manner to (1), and the process with the shortest waiting time is chosen to occur, with the simulation clock then being advanced by this waiting time. For a system with interacting particles, once an event has occurred it is in principle necessary to recalculate the rates for all possible events in the new configuration. The choice and efficient computational realization of KMC methods is a complex area, particularly for interacting particles, and is reviewed in detail by Jansen [7].

A key ingredient in any MC model is the equation used to calculate the rates, R_i. In organic materials, the intermolecular electronic interactions are usually weak, and coupling of charges to intramolecular vibrations is strong. This leads to transport proceeding by non-adiabatic tunneling events, or hops. Hopping transport can be described by a Marcus-type equation:

$$R_{\text{hop}} = \frac{|J|^2}{\hbar}\sqrt{\frac{\pi}{\lambda kT}}\exp\left(-\frac{(\Delta E + \lambda)^2}{4\lambda kT}\right). \tag{2}$$

Here J is the electronic transfer integral associated with the hop, λ is the reorganization energy (equal to half the polaron binding energy), ΔE is the change in energy associated with the hop, $\hbar$ is the reduced Planck's constant, k is Boltzmann's constant, and T is the temperature. ΔE includes a number of different contributions. First we consider the device empty of charges, with a uniform electric field arising from the presence of charges (considered as a continuous sheet) on the electrodes, producing a linear drop in potential across the device.

We then add on the effects of energetic disorder at each hopping site. Finally we consider the Coulomb interactions between a charge on the hopping site and other individual localized carriers within the device. A further complication arises since the presence of a localized charge in the vicinity of a metal electrode will modify the charge distribution on the electrode in order to maintain the boundary condition that the in-plane electric field at the electrode surface must be zero. Rather than calculating the electrode charge distribution directly, these effects can conveniently be reproduced using the "method of images." In this approach, the potential distribution due to a charge in front of an electrode is found by adding on the potential from a hypothetical opposite "image charge" placed an equal distance behind the electrode. Coulomb interactions must therefore be calculated not just between the actual charges within the device, but also between the actual charges and all the image charges.

There are a range of KMC models which differ in their treatment of the electronic coupling, J. The ultimate goal would be to simulate or measure an exact molecular structure for the solid, to use electronic structure calculations to determine the nature of the hopping sites, and then to calculate the electronic coupling for each possible (or likely) hop. Although there has been some progress towards this goal in molecular systems with artificially generated morphologies [8], the calculation of the set of J values is laborious and so restricts the use of this method to simulations of simple processes in relatively small systems. In the models we describe here a number of simplifications are made. The hopping sites are assumed to be arranged on a Cartesian lattice, and the electronic coupling is assumed to be independent of time. Additionally, J is often assumed to be isotropic [9–11], although in some cases anisotropic coupling is assumed [12]. These assumptions significantly reduce the time required to calculate hopping rates, and so permit the examination of larger problems, such as the current–voltage characteristic of an OPV. This of course implies some loss of fidelity in charge transport, as might be important for example if charge transport is anisotropic [13] or if the molecular geometry of the chains thermally fluctuates [14]. However, the isotropic, time-averaged electronic coupling is usually determined by fitting to experimental mobility data [11, 15, 16] or chosen to give mobilities similar to those seen in experiment [9, 10, 17, 18]. Likewise, the distribution of energetic disorder, which in turn will influence ΔE in (2), is fitted to experimental data. Taking this approach has resulted in KMC models which show quantitative agreement with experimental data for all-polymer [15, 16] and polymer–fullerene [11] OPV devices. Given that J falls off very rapidly with distance, we normally consider only nearest-neighbor hops, although in principle longer-range hops can be included. These long-range hops are likely to be more important at low temperatures. KMC should be considered to be intermediate between MC models which calculate the electronic coupling between molecules and parts of molecules, and other modeling techniques which consider charges in terms of local populations [19] or occupation probabilities [4].

To model photovoltaic device operation it is important to include the recombination events that compete with charge transport and eventual charge extraction. Since electrons and holes reside predominantly within the acceptor and donor

materials respectively, recombination events are assumed to occur for opposite charges located on neighboring sites on either side of a heterojunction interface. The rate for this process can in principle be calculated from Marcus theory, left as a fitting parameter, or ideally measured by experiment [15, 16]. Usually the rate is aggregated over all possible decay routes from the charge pair to the ground state, although KMC is capable of including multiple decay routes to the ground state if greater detail is required.

Photogenerated charge is usually introduced via excitons. Excitons can be created at random positions within the film [9], or at random positions weighted by the expected optical profile within the device [15]. Excitons are typically assumed to move via Förster resonant energy transfer (FRET), which is described by the following equation [20]:

$$R_{\mathrm{FRET}} = w_{\mathrm{e}} \left(\frac{R_0}{r} \right)^6 f(\Delta E), \tag{3}$$

where w_e is proportional to the attempt-to-hop frequency, R_0 is the exciton localization or Förster radius, r is the hop distance, ΔE is the associated change in energy, and $f(\Delta E)$ is given by a Boltzmann-type rate:

$$f(\Delta E) = \begin{cases} \exp\left(-\frac{\Delta E}{kT}\right) & : \Delta E > 0 \\ 0 & : \Delta E < 0 \end{cases}. \tag{4}$$

However, it has been shown that a simple random walk approximates the behavior of (3) relatively well [21]. Exciton transport competes with exciton decay, which again is taken to occur at a rate measured by spectroscopy [10]. An exciton incident upon a donor–acceptor interface is typically assumed to dissociate immediately into an electron–hole pair either side of the heterojunction, in accordance with experimental findings showing that exciton dissociation in charge transfer pairs is fast.

In order to calculate the current–voltage characteristic of an OPV, it is also necessary to consider charge injection and extraction at the electrodes. This can be achieved by considering an array of charges at the contact and calculating their hopping rate into the device, remembering that ΔE in (2) is determined by the energy difference between the electrode workfunction and the HOMO or LUMO of the material in question [2, 9], as well as by Coulomb interactions with charges and image charges. Unless there is a strong electric field pulling carriers away from the interface, many of the injected carriers will rapidly hop back into the electrode. Indeed, for a device in the dark at zero voltage the current must be zero, so the rates of hopping in and out at the electrodes must balance and the carriers inside the device must obey Fermi–Dirac statistics. Once carrier extraction is properly implemented it can also deal with removal of photogenerated carriers from the device, as required to collect a photocurrent. Extraction of carriers diffusing to the "wrong" contact must also be considered; this process can be thought of as interface recombination and can be a significant loss mechanism in thin OPVs (<50 nm) [22].

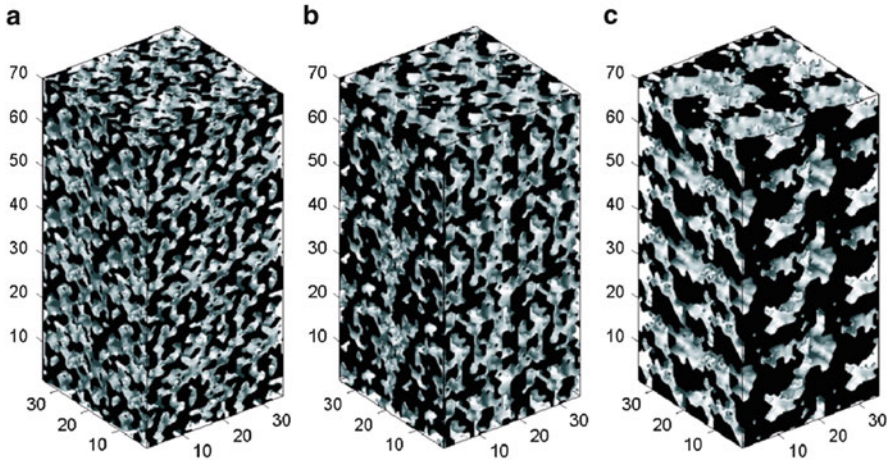

Fig. 1 Evolution of a binary blend structure by simulated annealing, giving characteristic feature sizes of 2.5, 3.0, and 4.3 units (**a–c**, respectively). Reproduced with permission from [9]. © American Institute of Physics

Now we move on to consider the morphological and energetic structure of the OPV. Of greatest practical importance are bulk heterojunction (BHJ) OPVs, since these allow simultaneously good optical absorption (i.e., thick films) and good exciton dissociation (i.e., distributed donor–acceptor heterojunctions). Ideally, the device simulation would start with a three-dimensional BHJ morphology determined by experiment, but it is extremely difficult to image the three-dimensional structure with sufficient resolution. Electron tomography is beginning to provide suitable data in certain materials systems [23, 24], but in general it is necessary to simulate the BHJ morphology instead. There are two commonly used techniques. The first involves "simulated annealing" using an Ising Hamiltonian to relax an initially fine donor–acceptor structure into a coarser state [9, 10, 25]. Examples of morphologies simulated using this technique are shown in Fig. 1.

The technique is straightforward but neglects the thermodynamics and kinetics of morphology formation. Another technique involves using a modified Cahn–Hilliard equation to describe blend formation [17]. This approach takes better account of the physical processes of blend formation, with the additional benefit of being able to include further processes, such as differing surface energies [17] or solvent evaporation [26] as appropriate, as shown in Fig. 2.

The morphology itself is usually represented by a Cartesian grid in either two [27] or three [9, 10] dimensions which is assigned donor or acceptor character in accordance with the method above. Additionally, each site is assigned a HOMO or LUMO energy drawn from a probability distribution function (pdf) to emulate the effects of energetic disorder. Typically this pdf is chosen to be Gaussian, but other investigations suggest the pdf may be exponential [28], or have multiple components [29], and so the pdf can be modified as necessary. The site energies

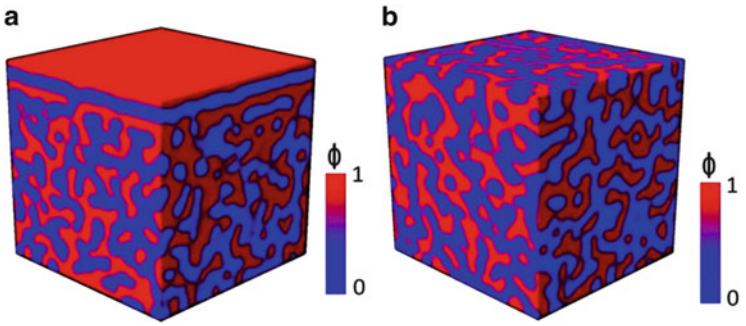

Fig. 2 Simulated blend structures using a modified Cahn–Hilliard equation to describe blend formation, illustrating the ability to control the formation of surface wetting layers (present in (**a**) but not in (**b**)). Reproduced with permission from [17]. © American Chemical Society

may also be spatially correlated by use of a correlation function [30, 31], as may be appropriate for crystalline polymers or for molecules with significant dipolar disorder, for example. There are no prohibitions on the complexity of the energetic structure in KMC provided one can represent them within the code. For example, energy cascades in the region of the donor–acceptor heterojunction have also been examined using KMC models [32].

An important concern in KMC models is how to execute the calculations efficiently. One of the principal problems is efficient calculation of the Coulomb interactions required to define ΔE in (2). For greatest accuracy, all Coulomb interactions between charges and image charges should be considered. In turn this means that the calculation time of hopping rates should scale at least as n, where n is the number of charges in the simulation. In actuality, coding will not be perfect and so the time taken to calculate Coulomb interactions scales superlinearly with n, meaning simulations around open circuit where carrier densities are high become very time-consuming. A number of strategies to overcome this issue have been reported.

The first involves only including Coulomb interactions up to a certain mutual distance, called the cut-off radius r_c. This limits the sphere of influence of charges and so limits the computational burden. Values of r_c have been chosen from a range spanning from the Debye screening length [10] to the Coulomb capture radius [9] (defined as the mutual separation at which the Coulomb attraction between an electron–hole pair is $\sim kT$). However, this may lead to errors in short-circuit current depending upon the value of r_c [33]. Another approach involves coupling a Poisson solver into the MC model, such that charges are treated explicitly at short distances, and treated as one-dimensional sheets of charge at long distances [34, 35]. While an effective method of handling Coulomb interactions, it is necessary to make sure that charges are not double-counted [34]. A further method is to calculate Coulomb interactions only as needed rather than calculating and storing the Coulomb potentials everywhere [36, 37]. This approach allows all Coulomb interactions to be

calculated explicitly, and can be effective in reducing run-time when the charge density is small. The calculation of image charge potentials can likewise be improved by making use of the periodicity of image charge spacing (i.e., in a device spanning between 0 and l, a charge at position x will produce image charges at $-x$, $2l - x$, $-(2l - x)$, $(2l + x)$, and so on) using the so-called Ewald sum technique [33].

Another noteworthy technique to improve the efficiency of KMC simulations applies when waiting times of all possible events are calculated and the event with the shortest waiting time is selected, known as the First Reaction Method (FRM) [38]. If one were to obtain the maximum accuracy in a KMC model, whenever a charge moves, the behaviors of all the remaining charges should be recalculated since the Coulomb interactions will have changed. Practically this can lead to simulation run time scaling as $\sim n^2$ (since for each hop the behavior of n charges must be determined, and for each charge, the Coulomb contributions of the other $n - 1$ charges must be added together). The FRM reduces this problem by calculating the waiting time for events only once, and storing these times in an ordered list. Once an event occurs, only the waiting times for possible events for that particle are recalculated and reinserted in the queue, making simulation time scale as $\sim n$. For interacting particles this is physically equivalent to making the assumption that the behavior of a charge does not change after it has been calculated, even if the local potential environment changes in the interim. One type of situation in which the FRM might be expected to lead to errors is in the simulation of geminate pair separation, since the Coulombic environment of the geminate charges changes significantly as the charges hop around on either side of the donor–acceptor interface [36, 39]. However, even when considering geminate recombination, the predictions of the FRM are in quantitative agreement with the full calculation (where charge behavior is updated after each hop), both in terms of dynamics [9] and absolute separation efficiency [37].

3 Losses in OPVs

An important target in OPV research is to reduce the recombination of charges which competes with carrier extraction that generates the photocurrent. Recombination can be either geminate (where the electron and hole involved were generated from the same photoexcitation event), or non-geminate (where a carrier encounters an oppositely charged carrier from a different photoexcitation event before it has the chance to be extracted from the device). The relative importance of these losses, and the mechanisms which influence this balance, have been the subject of lively debate within the community [40]. On the one hand, one may expect geminate recombination to dominate due to the typically low dielectric constant in the materials used ($\varepsilon \sim 3$–4), and the consequently strong Coulomb interactions between geminate charge pairs. These expectations

are reinforced by findings from Onsager–Braun (O–B) [41, 42] type models which, when parameters from experiment are used, typically predict small, and field-dependent, separation efficiencies, η_{GS}. While small and field-dependent separation efficiencies are reported in some systems [43–45], in others it appears that separation efficiencies are large and field-independent [44, 46–48]. A significant factor appears to be whether geminate charges are formed via a transiently hot delocalized charge transfer (CT) state [49–51], although it is not yet clear where the measured dependence of OPV performance upon morphology fits into this picture [52, 53]. However, efficient charge dissociation via hot CT states carries a significant penalty in lost energy, and therefore open-circuit voltage, when the hot CT state cools. Therefore the charge separation process through lower, more-localized CT states still warrants attention. Indeed, there are many other mechanisms by which geminate charge separation may still be efficient, such as charge delocalization [43, 54], cascaded energy heterojunctions [54, 55], and exciton delocalization [56]. These processes cannot be captured by an effective medium approach such as O–B or its later refinements to account better for a finite recombination rate [57] and energetic disorder [58]. KMC is better able to include detailed morphological and energetic structure than is possible with an analytical approach.

Non-geminate recombination can also limit the performance of an OPV [44, 59, 60]. On the nanoscale, the degree of non-geminate recombination is perhaps most conveniently described by the non-geminate rate constant, β (such that βnp is the total rate of non-geminate recombination, where n and p are the local electron and hole densities respectively). Expectations of the non-geminate recombination rate often stem from the Langevin equation:

$$\beta = \frac{q(\mu_e + \mu_h)}{\varepsilon\varepsilon_0}. \tag{5}$$

Here μ_e and μ_h are the electron and hole mobilities respectively. Equation (5) was derived on the assumption that charge transport was isotropic, trap-free and that both electrons and holes move in the same material. These are not good descriptions of the transport environment within an OPV, and so perhaps unsurprisingly, the measured non-geminate rate constant, β_m, often does not agree the predictions of (5). In OPVs it is common that $\beta_m < \beta$, and that β_m is additionally dependent on charge density [61–63]. KMC models allow the opportunity to predict the rate of non-geminate recombination in the context expected to occur within OPVs, namely including trapping, morphology, and anisotropic transport.

This section will review KMC findings relating to geminate and non-geminate recombination in OPVs, and, in doing so, will discuss the effect that energetic and morphological structure has on OPV devices.

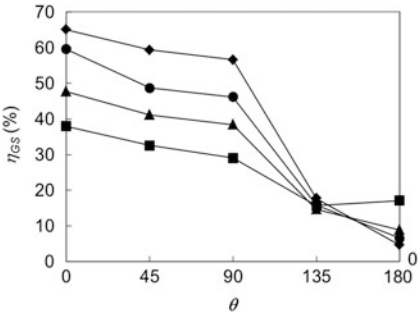

Fig. 3 Geminate separation efficiency for charge pairs in a bilayer structure as a function of the angle between the electric field and the normal to the heterojunction. Modified with permission from [39]. © American Institute of Physics

3.1 Geminate Recombination

3.1.1 Morphology

As discussed previously, O–B models omit many details pertaining to charge transport which KMC offers the opportunity to examine. First we will consider the effect of morphology. The simplest morphology to consider is a donor–acceptor bilayer. Peumans and Forrest [64] examined the effect of a bilayer on the charge separation efficiency and found that constraining the motion of the electron to the acceptor and hole to the donor significantly reduced the separation efficiency when compared to O–B. This was examined further by Groves et al. [39] who also considered the effect of heterojunction alignment to an electric field, thereby examining the effect of random heterojunction orientation which occurs in bulk heterojunction devices (Fig. 3). It was found that the separation efficiency of charges was minimally affected provided there was no component of the electric field forcing the charges into (rather than away from) the heterojunction.

These investigations are useful to begin understanding the role of donor–acceptor morphology, but OPVs of greatest practical importance have heterojunctions distributed throughout the device to give efficient exciton dissociation. KMC simulations have been used to examine a variety of distributed heterojunction devices, including bulk heterojunctions [9, 10, 18, 65, 66], gyroids [36], and columns [9, 10]. These investigations have shown that, generally, increasing the feature size of the donor or acceptor domains increases geminate separation efficiency. This can be thought of as a result of increasing entropy driving charge separation as the domains get larger [67]. However, OPVs also have to transport excitons efficiently to donor/acceptor interfaces, a process which is favored by smaller feature sizes. Hence KMC simulations typically show a characteristic peak in the photocurrent provided by a blend when the domain size is around the exciton diffusion length, in agreement with experiment [68]. This was first illustrated by Watkins et al. [10], who simulated exciton diffusion and charge separation in the absence of energetic disorder for BHJ structures with various feature sizes and found an optimum feature size of 20 nm (Fig. 4).

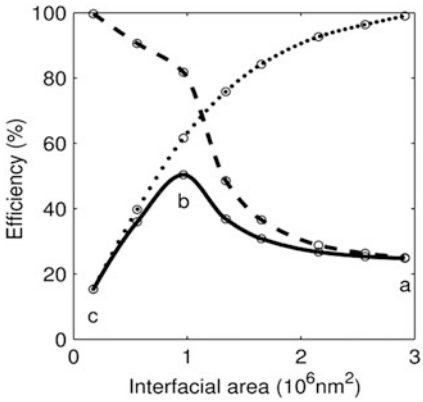

Fig. 4 Exciton dissociation efficiency (*dotted line*), charge collection efficiency (*dashed line*), and internal quantum efficiency in blend structures of different lengthscales (quantified in terms of heterojunction interfacial area per unit volume). Modified with permission from [10]. © American Chemical Society

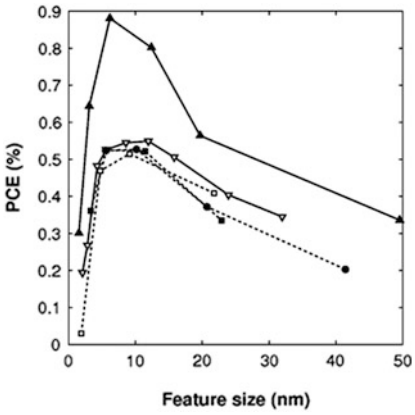

Fig. 5 Predicted power conversion efficiency (PCE) as a function of feature size for bulk heterojunction (*open triangles*), columnar (*solid triangles*), gyroid (*circles*), double gyroid (*solid squares*), and double-diamond (*open squares*) morphologies. Modified with permission from [36] by permission of The Royal Society of Chemistry

The effect of BHJ feature size on the charge separation was further investigated in the presence of energetic disorder by Marsh et al. [9]. The general picture emerging from these simulations is that charge generation is strongly field-dependent and rather inefficient. Using hopping rates and disorder widths designed to reproduce bulk mobility values from experiments, it was found that to generate even modest yields of free carriers (20–50%), surprisingly long recombination times needed to be used for carriers at the heterojunction interface (2 μs in [9] and 10 ms in [10]). These times are much longer than the recombination times for charge-transfer states in these systems measured spectroscopically, which are typically in the range 1–100 ns. Clearly these MC models are not capturing the full physics present in real devices, and we discuss possible resolutions for this issue in the following sections.

When comparing the performance of different morphology types, gyroids and bulk heterojunctions have been shown to give similar performance for equivalent domain sizes [36], whereas columns give better performance than either for equivalent domain sizes [9, 10], as shown in Fig. 5. The performance of columnar structures can be explained by the work of Groves et al. [39], who showed that

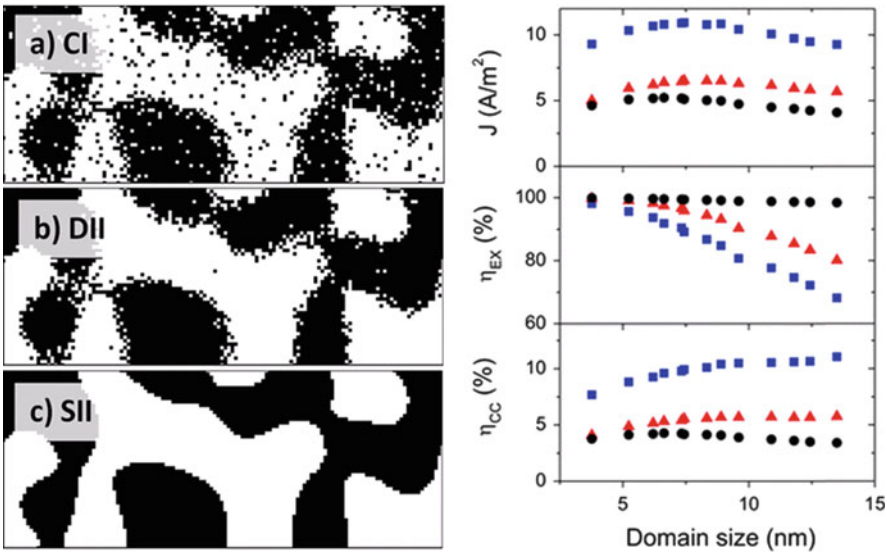

Fig. 6 *Left*: Two-dimensional slices through representative structures with diffuse interfaces (CI), pure domains with diffuse interfaces (DII) and pure domains with abrupt interfaces (SII). *Right*: KMC predictions of short-circuit current density (*top*), exciton dissociation efficiency (*middle*), and carrier collection efficiency (*bottom*) for the CI (*circles*), DII (*triangles*), and SII (*squares*) morphologies. Adapted from [18] by permission of The Royal Society of Chemistry

the (optimized) separation efficiency in bilayer donor–acceptor heterojunctions does not change much as the electric field is rotated from the conventional orientation perpendicular to the plane of the heterojunction to an orientation parallel to the plane. Thus all the interfaces in a columnar structure can contribute efficiently to charge generation. This provides further impetus to fabricate structures with this morphology [69].

However, bulk heterojunction morphologies are described by much more than just a characteristic domain size. Further morphological features which may determine the performance of a bulk heterojunction OPV include the purity of the domains, the interfaces between these domains, the connectivity of the domains, and more. Lyons et al. [18] tried to deconvolve the effects of these morphological features by comparing simulation results on a range of morphologies with different characteristics, namely impure domains with diffuse interfaces (CI), pure domains with diffuse interfaces (DII), and pure domains with abrupt interfaces (SII), as shown in Fig. 6.

All of these morphologies showed the expected characteristic peak in photocurrent when the domain size was approximately equal to the exciton diffusion length. However, what was more pronounced was the influence of the interfacial morphology. A morphology with domains of only ~4 nm and sharp heterojunction interfaces was found to out-perform a morphology with "optimal" sized domains of ~8 nm with diffuse interfaces. This suggests that the environment around the

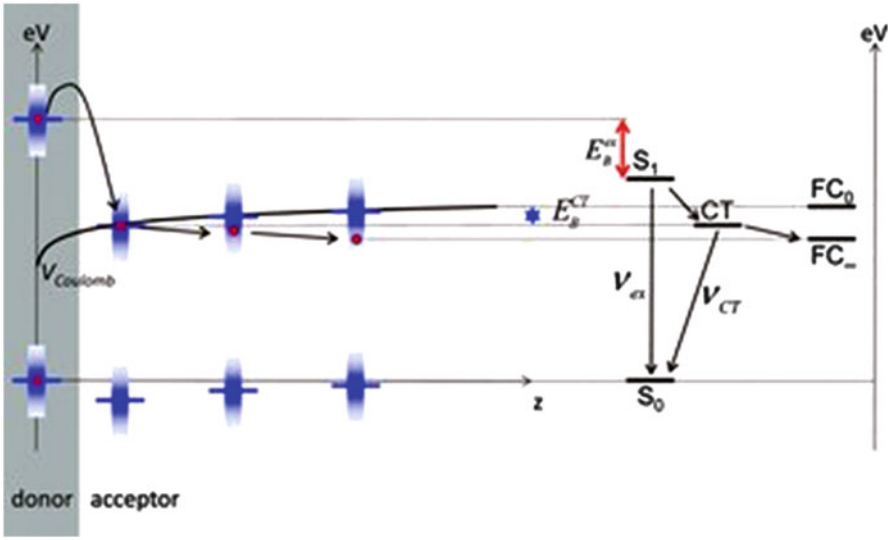

Fig. 7 *Left*: Schematic diagram of the dissociation process for charge-transfer (CT) states. *Horizontal lines* indicate the center of the donor and acceptor HOMO and LUMO energy distributions, and the *vertical gradient bars* indicate the broadened density of states. Here the hole is assumed to be immobile. The CT state is dissociated via downward hops, as the electron relaxes towards its equilibrium energy while overcoming the remaining Coulomb energy (*thick black line*). *Right*: Corresponding Jablonsky diagram. Reproduced with permission from [11]. © 2012 WILEY-VCH Verlag GmbH & Co. KGaA, Weinheim

heterojunction interface is of greater importance to geminate charge separation than the long-range "bulk" morphology.

3.1.2 Energetic Structure at the Donor–Acceptor Interface

One of the first KMC investigations into the geminate separation process in OPVs was by Albrecht and Bässler [70]. They showed that energetic disorder leads to greater than expected charge separation efficiency when compared to the predictions of O–B, and that this difference was especially large when the availability of energy to drive charge separation (i.e., field and temperature) was low. The mechanism for this process is simply that charges are created with a non-equilibrium energy distribution. While the charges cool, hops apart from one another can be energetically favored, as shown in Fig. 7, leading to relaxation-assisted separation. As might be expected, the efficacy of this mechanism depends strongly upon the energy with which charges are generated. In contrast to the situation considered by Albrecht and Bässler [70], charges generated trapped within the bottom of the density of states have far lower separation efficiencies [31, 37].

Relaxation-assisted charge separation was later shown to explain the J-V characteristics of MDMO-PPV:PCBM OPVs very well using experimentally

reasonable recombination times of 1 ns [11]. Although these effects are in principle included within the earlier simulations of Marsh et al. [9], a key issue appears to be the hopping distance between lattice sites. Where this distance is large (2.5 nm as assumed in [11]), a small number of hops away from the interface driven by relaxation within the density of states is sufficient to reduce the Coulomb attraction considerably. When a hopping distance of 1 nm is assumed [9], more hops are required to overcome the Coulomb potential and this is less likely to occur during the relaxation process. This is highlighted by contrasting the findings of [11] with those of Groves et al. [31], in which a lattice constant of 1 nm is assumed. In Groves et al. [31], KMC was used to predict the performance of OPVs in systems where the energetic disorder was spatially correlated, i.e., where the energy of a site is correlated with that of its neighbors. This may occur in real materials due to the presence of molecular dipoles, or due to packing effects where the conformation, and hence the energy, of neighboring polymer chain segments is likely to be similar. The effect is to reduce the chance of separating charges being trapped at low-energy sites from which there are no easy escape routes. In the presence of correlated disorder it was shown that charge separation was efficient and only had a weak dependence on electric field. Hence, in [31] where the lattice constant is 1 nm, energetic disorder can lead to charge trapping, while in [11] where the lattice constant is 2.5 nm, energetic disorder leads to relaxation-assisted separation. Another important point to note is that Groves et al. [31] showed that charge separation was primarily a function of the spatial distribution of traps, rather than of the density of states function or the charge mobility, highlighting the difficulty in describing OPV performance in terms of average quantities.

Quantum chemical calculations have recently suggested that the variation in morphological order at various distances from the donor–acceptor interface gives rise to a cascaded energy heterojunction structure, which is expected to encourage the separation of geminate charges [55]. This in turn may help explain experimental data for polymer–fullerene devices which correlate the onset of PCBM crystallization/aggregation with increased OPV performance [54]. Groves [32] used KMC to relate the form of the cascaded energy heterojunction quantitatively to charge separation. It was found that cascades very similar to those which might be expected for P3HT:PCBM solar cells do indeed give very large separation efficiencies (in excess of 70% over the operating field range of OPVs). Essentially cascades perform the same function as energetic disorder as examined by van Eersel et al. [11], namely allowing relaxation within the energy landscape to overcome mutual Coulomb attraction.

3.1.3 Delocalization

A further consideration absent in simple models of charge separation is the possibility of delocalization of charges or of the exciton. Analytical calculations have considered the effect of efficient charge transport in one dimension upon charge separation [71], but this did not include the effect of the morphology around the

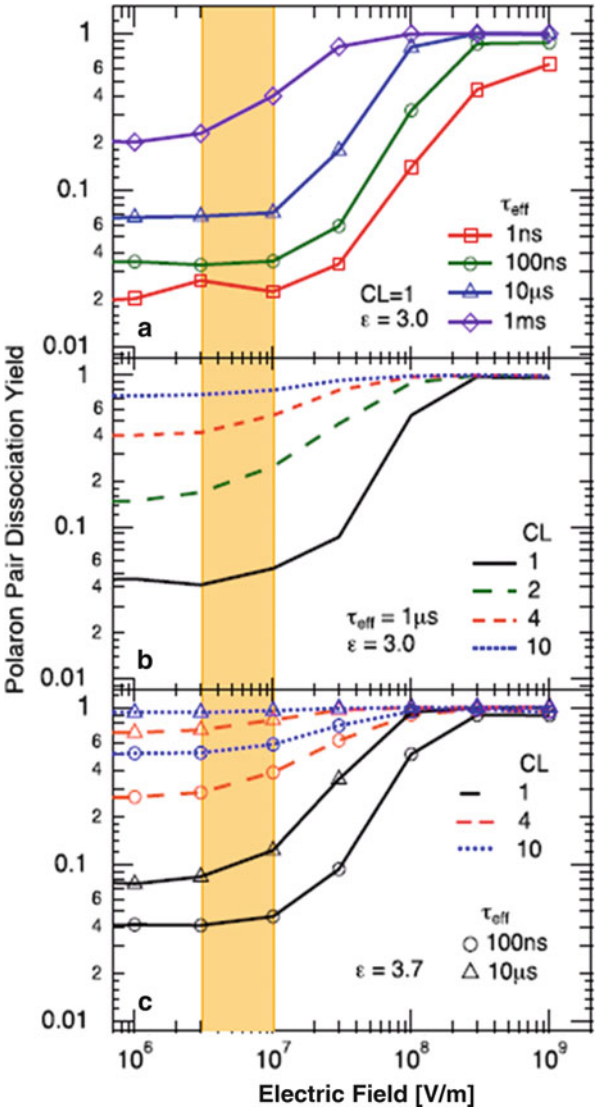

Fig. 8 Predicted dissociation yield as a function of electric field, from KMC simulations, showing: (**a**) the effect of recombination rate ($1/\tau_{\text{eff}}$) for a hopping system without delocalization (CL = 1), (**b**) the effect of changing delocalization length (CL), (**c**) the effect of varying CL for a variety of experimentally observed recombination rates. Reproduced from [72]. © American Physical Society

polymer chain. Deibel et al. [72] used a KMC model to examine the effect of charge delocalization along a polymer chain on geminate charge separation in the context of a polymer:fullerene-like morphology. The morphology was generated considering intermolecular interactions between polymer chains after the technique of Frost et al. [73]. Charge delocalization was incorporated by "sharing" the charge along the polymer chain, which varied in length between one (i.e., no delocalization) and ten lattice units. The results of KMC simulations are shown in Fig. 8. It was found that only modest increases in the polymer chain length from one to four lattice units could increase the separation efficiency by roughly an order of magnitude. This has relevance to recent data relating to hot, delocalized CT states [49–51], showing that

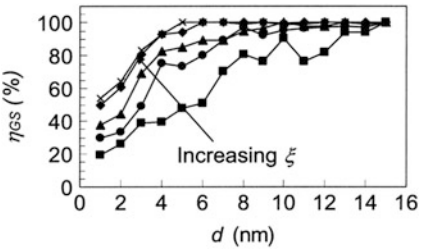

Fig. 9 Separation efficiency (η_{GS}) in a bilayer structure as a function of separation (d) for geminate pairs present in the simulation after 100 ns. The electric field, ξ is 0 V m^{-1} (*squares*), 5 $\times$ 10^6 V m^{-1} (*circles*), 10^7 V m^{-1} (*triangles*), 2 $\times$ 10^7 V m^{-1} (*diamonds*), and 2.4 $\times$ 10^7 V m^{-1} (*crosses*). Reproduced with permission from [39]. © American Institute of Physics

delocalization can indeed substantially increase geminate separation efficiency (although in the case of the KMC model, delocalization occurs in the lowest CT state, and so is "always there," whereas the hot delocalized CT state is only transient).

One effect which delocalization has is to increase the effective distance between the geminate electron–hole pair. However, there are other processes that can yield similar results, namely exciton delocalization. Caruso and Troisi [56] have shown that, for some circumstances (here P3HT lamellae), exciton delocalization is expected to yield charges which are separated by at least ~2 nm, in turn increasing the separation efficiency. Both Peumans and Forest [64] and Groves et al. [39] showed that charges with small separations (of the order of 4 nm) have substantially higher separation efficiencies than charges which are separated by only 1 nm, as shown in Fig. 9. This is in spite of the Coulomb capture radius for these simulations being of the order of 15–20 nm. The commonly reported Coulomb capture radius does not therefore appear to be the defining lengthscale for charge separation, since successful charge separation can occur on lengthscales less than 10 nm.

3.1.4 Summary

KMC models have examined the effect of a range of OPV properties upon geminate separation efficiency. It is found that, counter to the expectations of O–B, separation efficiency can be large when energetic disorder, charge or exciton delocalization, or cascaded energy heterojunctions are present. Furthermore, it is shown that viable charge separation efficiencies can be obtained within morphologies with small feature sizes if the interface between donor and acceptor is sharp. These results affirm the importance of the area immediately surrounding the donor–acceptor interface in determining separation efficiency, rather than long-range order. As a final word on the use of O–B models, it should be noted that quantitative agreement between O–B and KMC can be obtained [31, 70], but the parameters used in O–B to obtain these fits often have little relation with KMC

values. O–B therefore appears to be useful in fitting to experimental data, but the values obtained from such fits should be viewed as indicators of the separation process rather than quantitative metrics of the physical parameters.

3.2 Non-Geminate Recombination

3.2.1 Morphology

The Langevin equation describes the non-geminate recombination rate in a featureless morphology, within which both electron and hole are free to move. To begin examining the effects of the bulk heterojunction in OPVs upon non-geminate recombination it is convenient to begin with a bilayer, since this represents the simplest donor–acceptor morphology. Greenham and Bobbert [74] used a KMC and Master Equation approach to measure the rate of non-geminate recombination at interfaces where the electrons were mobile in a 2-D plane but holes were immobile, in the presence of energetic disorder. It was found that under these circumstances the non-geminate rate constant varied as $n^{0.43}$, making the recombination kinetics superlinear with electron density. This helps explain one of the commonly observed behaviors of non-geminate recombination in blended devices, namely that the non-geminate recombination kinetics increase more quickly with charge density than would be expected on the basis of the Langevin expression [61, 62]. The charge density dependence appears to be due to two mechanisms, namely the filling of low-energy states [61, 75] and the altered nature of charge transport in confined volumes [12]. While the former may always be expected to play a role in bulk heterojunction OPVs, the latter may also be relevant in P3HT:PCBM devices where P3HT forms two-dimensional lamellae within the larger bulk heterojunction morphology [76].

More generally, charge transport is constrained to a distributed donor–acceptor bulk heterojunction within an OPV. This case was considered by Groves and Greenham [12]. It was shown that the measured non-geminate recombination rate was generally lower than the predictions of the Langevin equation by factors of more than 2, depending upon the difference in electron and hole mobilities, degree of charge trapping, and size of domains as shown in Fig. 10. The reason for the reduction is that both charges need to be present at the donor–acceptor interface in order to recombine, and so, on average, there is some degree of waiting involved since the arrivals of charges at the interface are not synchronized. Hence factors that increase the average wait, namely larger domains, increased charge trapping, or larger mismatches between mobilities, all reduce the rate of non-geminate recombination.

Frost et al. [73] also examined the effect of morphology on non-geminate recombination, but, in this case, considered more explicitly the link between molecular interactions and the degree of non-geminate recombination. In this paper it was assumed that the morphology comprised a series of polymer donor

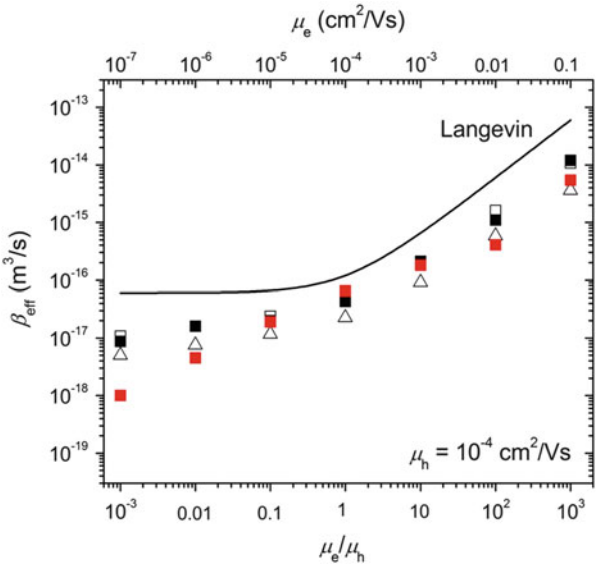

Fig. 10 KMC prediction of the bimolecular recombination rate constant (*symbols*) for bulk heterojunctions with 4 nm (*black*) and 35 nm (*red/grey*) domains. *Squares* correspond to no energetic disorder, while *triangles* assume Gaussian-distributed energetic disorder with $\sigma = 75$ meV. The *solid line* shows the prediction of the Langevin equation. Modified from [12]. © American Physical Society

"snakes" embedded within a "sea" of fullerene acceptor molecules. The blends were annealed assuming either heterophilic or homophilic interactions, giving rise to either well-dispersed or aggregated morphologies, respectively. It was found that heterophilic interactions lead to greater recombination due to increased surface area between donor and acceptor, over which recombination can occur.

3.2.2 Transport

The previous section considered the case in which the characteristics of charge transport were defined by isotropic charge transport and a spatially uniform density of states function. These assumptions may not always be appropriate for OPVs.

For instance, experiments on organic transistors in which the polymer chains have been uniformly aligned suggest that the rate of intra-molecular hopping along the polymer backbone axis is faster than hopping radial to the backbone [13, 77]. This circumstance was considered by Groves and Greenham by introducing anisotropic hopping prefactors in an MC simulation [12]. As perhaps might be expected, the non-geminate recombination rate was between the predictions of the Langevin equation when the axial and perpendicular mobilities, μ_{axial} and μ_{perp}, respectively, were used. Interestingly, KMC data showed that the measured non-geminate rate coefficient could be predicted quite well if an effective mobility was used in the Langevin equation of $\mu_{\text{eff}} = \sqrt{\mu_{\text{axial}}\mu_{\text{perp}}}$.

Given that OPV morphology is spatially heterogeneous [78], it is possible that the density of states function is also spatially heterogeneous. This was considered by Nelson [75], when a variant of KMC was used where sites could be from one of

two populations: "transport levels," where charges moved by diffusion, and "trap levels," where charges escaped by thermal activation. The relative density of trap and transport levels, as well as the density of states function for the traps, were varied to fit transient spectroscopy data for MDMO-PPV:PCBM OPVs at temperatures between 220 and 300 K. It was shown that the dynamic behavior of charge populations, which decay via non-geminate recombination, was sensitive to both the density of states function and the trap density. Quantitative fits to experimental data could only be obtained for a trap density of 10^{17} cm^{-3} with a characteristic trap depth of 750 K. This in turn shows that KMC models in combination with experiment can provide useful quantitative information about trapping behavior of charges in OPVs.

4 Conclusions

We have shown that KMC models can obtain quantitative agreement with experimental OPV data, as well as provide qualitative understanding of the effect of nanoscale morphology and electronic structure on OPV performance. A number of investigations were reviewed that can help explain commonly observed inefficient geminate and non-geminate recombination in OPVs. Although the presence of delocalized states formed directly after charge transfer appears to be a significant factor in the efficient formation of free charges, one may not need to be too pessimistic about the performance of devices in which delocalized CT states do not form, since local variations in site energies can assist the charge separation process.

In many cases models predict that variation of quantities on the nanoscale results in large changes in the recombination processes that limit OPV performance. Given that morphology can be heterogeneous, and that donor and acceptor materials can be present in a number of phases at various positions, this calls into question the appropriateness of modeling OPVs in term of average parameters. However, this presents a challenge to KMC modeling as well. Since KMC has shown that losses in OPVs are sensitive to their nanostructure, predictive models now require a greater quality of detailed information about both the electronic and morphological structure of OPVs.

References

1. Bässler H (1993) Phys Status Solidi B Basic Res 175:15–56
2. Wolf U, Arkhipov VI, Bässler H (1999) Phys Rev B 59:7507–7513
3. Barth S, Wolf U, Bässler H (1999) Phys Rev B 60:8791–8797
4. Pasveer WF, Cottaar J, Tanase C, Coehoorn R, Bobbert PA, Blom PWM, de Leeuw DM, Michels MAJ (2005) Phys Rev Lett 94:206601
5. Zhou J, Zhou YC, Zhao JM, Wu CQ, Ding XM, Hou XY (2007) Phys Rev B 75:153201

6. Coehoorn R, Pasveer WF, Bobbert PA, Michels MAJ (2005) Phys Rev B 72:155206
7. Jansen APJ (2012) An introduction to kinetic Monte Carlo simulations of surface reactions. Springer, Berlin, Heidelberg
8. Athanasopoulos S, Kirkpatrick J, Martinez D, Frost JM, Foden CM, Walker AB, Nelson J (2007) Nano Lett 7:1785–1788
9. Marsh RA, Groves C, Greenham NC (2007) J Appl Phys 101:083509
10. Watkins PK, Walker AB, Verschoor GLB (2005) Nano Lett 5:1814–1818
11. van Eersel H, Janssen RAJ, Kemerink M (2012) Adv Funct Mater 22:2700–2708
12. Groves C, Greenham NC (2008) Phys Rev B 78:155205
13. Crossland EJW, Tremel K, Fischer F, Rahimi K, Reiter G, Steiner U, Ludwigs S (2012) Adv Mater 24:839–844
14. Liu T, Cheung DL, Troisi A (2011) Phys Chem Chem Phys 13:21461–21470
15. Yan H, Swaraj S, Wang C, Hwang I, Greenham NC, Groves C, Ade H, McNeill CR (2010) Adv Funct Mater 20:4329–4337
16. Kimber RGE, Wright EN, O'Kane SEJ, Walker AB, Blakesley JC (2012) Phys Rev B 86:235206
17. Lyons BP, Clarke N, Groves C (2011) J Phys Chem C 115:22572–22577
18. Lyons BP, Clarke N, Groves C (2012) Energy Environ Sci 5:7657–7663
19. Koster LJA, Smits ECP, Mihailetchi VD, Blom PWM (2005) Phys Rev B 72:085205
20. Athanasopoulos S, Emelianova EV, Walker AB, Beljonne D (2009) Phys Rev B 80:195209
21. Feron K, Zhou X, Belcher WJ, Dastoor PC (2012) J Appl Phys 111:044510
22. Feron K, Fell CJ, Rozanski LJ, Gong BB, Nicolaidis N, Belcher WJ, Zhou X, Sesa E, King BV, Dastoor PC (2012) Appl Phys Lett 101:193306
23. Oosterhout SD, Wienk MM, van Bavel SS, Thiedmann R, Koster LJA, Gilot J, Loos J, Schmidt V, Janssen RAJ (2009) Nat Mater 8:818–824
24. Hindson JC, Saghi Z, Hernandez-Garrido J-C, Midgley PA, Greenham NC (2011) Nano Lett 11:904–909
25. Peumans P, Uchida S, Forrest SR (2003) Nature 425:158–162
26. Wodo O, Ganapathysubramanian B (2012) Comput Mater Sci 55:113–126
27. Gagorik AG, Mohin JW, Kowalewski T, Hutchison GR (2013) J Phys Chem Lett 4:36–42
28. Nelson J, Kwiatkowski JJ, Kirkpatrick J, Frost JM (2009) Acc Chem Res 42:1768–1778
29. MacKenzie RCI, Shuttle CC, Chablinyc ML, Nelson J (2012) Adv Energy Mater 2:662–669
30. Gartstein YN, Conwell EM (1995) Chem Phys Lett 245:351–358
31. Groves C, Blakesley JC, Greenham NC (2010) Nano Lett 10:1063–1069
32. Groves C (2013) Energy Environ Sci 6:1546–1551
33. Casalegno M, Raos G, Po R (2010) J Chem Phys 132:094705
34. van der Holst JJM, van Oost FWA, Coehoorn R, Bobbert PA (2011) Phys Rev B 83:085206
35. Meng LY, Wang D, Li QK, Yi YP, Bredas JL, Shuai ZG (2011) J Chem Phys 134:124102
36. Kimber RGE, Walker AB, Schroder-Turk GE, Cleaver DJ (2010) Phys Chem Chem Phys 12:844–851
37. Groves C, Kimber RGE, Walker AB (2010) J Chem Phys 133:144110
38. Lukkien JJ, Segers JPL, Hilbers PAJ, Gelten RJ, Jansen APJ (1998) Phys Rev E 58:2598–2610
39. Groves C, Marsh RA, Greenham NC (2008) J Chem Phys 129:114903
40. Clarke TM, Durrant JR (2010) Chem Rev 110:6736–6767
41. Onsager L (1938) Phys Rev 54:554
42. Braun CL (1984) J Chem Phys 80:4157–4161
43. Veldman D, Ipek O, Meskers SCJ, Sweelssen J, Koetse MM, Veenstra SC, Kroon JM, van Bavel SS, Loos J, Janssen RAJ (2008) J Am Chem Soc 130:7721–7735
44. Dibb GFA, Jamieson FC, Maurano A, Nelson J, Durrant JR (2013) J Phys Chem Lett 803–808
45. Keivanidis PE, Clarke TM, Lilliu S, Agostinelli T, Macdonald JE, Durrant JR, Bradley DDC, Nelson J (2010) J Phys Chem Lett 1:734–738
46. Park SH, Roy A, Beaupre S, Cho S, Coates N, Moon JS, Moses D, Leclerc M, Lee K, Heeger AJ (2009) Nat Photon 3:297–302

47. Howard IA, Mauer R, Meister M, Laquai F (2010) J Am Chem Soc 132:14866–14876
48. Jamieson FC, Agostinelli T, Azimi H, Nelson J, Durrant JR (2010) J Phys Chem Lett 1:3306–3310
49. Bakulin AA, Rao A, Pavelyev VG, van Loosdrecht PHM, Pshenichnikov MS, Niedzialek D, Cornil J, Beljonne D, Friend RH (2012) Science 335:1340–1344
50. Grancini G, Maiuri M, Fazzi D, Petrozza A, Egelhaaf HJ, Brida D, Cerullo G, Lanzani G (2013) Nat Mater 12:29–33
51. Jailaubekov AE, Willard AP, Tritsch JR, Chan WL, Sai N, Gearba R, Kaake LG, Williams KJ, Leung K, Rossky PJ, Zhu XY (2013) Nat Mater 12:66–73
52. Brabec CJ, Heeney M, McCulloch I, Nelson J (2011) Chem Soc Rev 40:1185–1199
53. McNeill CR, Greenham NC (2009) Adv Mater 21:3840–3850
54. Jamieson FC, Domingo EB, McCarthy-Ward T, Heeney M, Stingelin N, Durrant JR (2012) Chem Sci 3:485–492
55. McMahon DP, Cheung DL, Troisi A (2011) J Phys Chem Lett 2:2737–2741
56. Caruso D, Troisi A (2012) Proc Natl Acad Sci USA 109:13498–13502
57. Sano H, Tachiya M (1979) J Chem Phys 71:1276–1282
58. Tachiya M, Seki K (2010) Phys Rev B 82:085201
59. Koster LJA, Mihailetchi VD, Blom PWM (2006) Appl Phys Lett 88:052104
60. Maturova K, van Bavel SS, Wienk MM, Janssen RAJ, Kemerink M (2009) Nano Lett 9:3032–3037
61. Shuttle CG, O'Regan B, Ballantyne AM, Nelson J, Bradley DDC, Durrant JR (2008) Phys Rev B 78:113201
62. Juška G, Arlauskas K, Stuchlik J, Osterbaka R (2006) J Non Crystal Solids 352:1167–1171
63. Pivrikas A, Sariciftci NS, Juška G, Österbacka R (2007) Progress in Photovolt Res Appl 15:677–696
64. Peumans P, Forrest SR (2004) Chem Phys Lett 398:27–31
65. Yang F, Forrest SR (2008) ACS Nano 2:1022–1032
66. Meng LY, Shang Y, Li QK, Li YF, Zhan XW, Shuai ZG, Kimber RGE, Walker AB (2010) J Phys Chem B 114:36–41
67. Gregg BA (2011) J Phys Chem Lett 3013–3015
68. McNeill CR, Westenhoff S, Groves C, Friend RH, Greenham NC (2007) J Phys Chem C 111:19153–19160
69. He XM, Gao F, Tu GL, Hasko D, Huttner S, Steiner U, Greenham NC, Friend RH, Huck WTS (2010) Nano Lett 10:1302–1307
70. Albrecht U, Bassler H (1995) Chem Phys Lett 235:389–393
71. Rubel O, Baranovskii SD, Stolz W, Gebhard F (2008) Phys Rev Lett 100:196602
72. Deibel C, Strobel T, Dyakonov V (2009) Phys Rev Lett 103:036402
73. Frost JM, Cheynis F, Tuladhar SM, Nelson J (2006) Nano Lett 6:1674–1681
74. Greenham NC, Bobbert PA (2003) Phys Rev B 68:245301
75. Nelson J (2003) Phys Rev B 67:155209
76. Juška G, Genevičius K, Nekrašas N, Sliaužys G (2010) Phys Status Solidi (C) 7:980–983
77. Zaumseil J, Groves C, Winfield JM, Greenham NC, Sirringhaus H (2008) Adv Funct Mater 18:3630–3637
78. Groves C, Reid OG, Ginger DS (2010) Acc Chem Res 43:612–620

Top Curr Chem (2014) 352: 279–324
DOI: 10.1007/128_2013_473

Published online: 28 September 2013

Device Modelling of Organic Bulk Heterojunction Solar Cells

Thomas Kirchartz and Jenny Nelson

Abstract We review the methods used to simulate the optoelectronic response of organic solar cells and focus on the application of one-dimensional drift-diffusion simulations. We discuss how the important physical processes are treated and review some of the experiments necessary to determine the input parameters for device simulations. To illustrate the usefulness of drift-diffusion simulations, we discuss several case studies, addressing the influence of charged defects on transport in bipolar and unipolar devices, the influence of defects on recombination, device performance and ideality factors. To illustrate frequency domain simulations, we show how to determine the validity range of Mott–Schottky plots for thin devices. Finally, we discuss an example where optical simulations are used to calculate the parasitic absorption in contact layers.

Keywords Polymer:fullerene blends · Photovoltaics · Poisson equation · Traps · Doping · Density of states · Disordered semiconductor

Contents

T. Kirchartz and J. Nelson (✉)
Department of Physics and Centre for Plastic Electronics, Imperial College London, London SW7 2AZ, UK
e-mail: jenny.nelson@imperial.ac.uk

1 Introduction

1.1 Introducing Organic Bulk Heterojunction Solar Cells

In recent years, much of the research effort in the area of novel photovoltaic absorber materials has been directed towards developing solution processable materials consisting of either π-conjugated molecules [1, 2] or inorganic nanoparticles [3–7]. These materials have in common that they are disordered materials of rather low electronic quality but with reasonable absorption coefficients enabling effective light harvesting with absorber thicknesses of order 100 nm. Among the most widely studied absorber materials for solution processed thin-film solar cells are organic semiconductors such as conjugated polymers and small molecules. The efficiencies of solar cells based on these organic materials have increased [8–16] in the last years up to values of around 10% which are comparable to efficiencies for thin-film silicon solar cells [17]. The semiconducting properties of organic semiconductors are distinguished by the fact that all electronic states, including photoexcited and charged states, are localized on individual molecules or conjugated segments of a few cubic nanometers in volume, and the

energies of these states vary due to the intrinsic disorder in molecular packing. The localized nature of the excited states has led to the particular design of most organic solar cells, where the light absorbing medium is made up of a blend of different organic semiconductors that are mixed together on the nanoscale and form a so-called "bulk heterojunction" [18–20]. This heterojunction between the two types of molecules is non-planar and extends through the whole bulk of the absorber. The small volume of the exciton combined with the low dielectric permittivity of organic semiconductors means that the binding energy of the electron and hole in the photogenerated exciton exceeds the thermal energy kT at room temperature. The heterojunction provides a sufficient free energy difference to encourage the dissociation of the exciton into an electron–hole pair. After exciton dissociation at the heterojunction, the electron will be on the acceptor molecule (high electron affinity) and the hole on the donor molecule (low ionization potential). The challenge of creating a good bulk-heterojunction is to optimize simultaneously the energetics and the microstructure of the blend. The energetic offsets at the heterojunction need to be high enough to allow efficient exciton dissociation but as low as possible to reduce the loss in energy and, consequently, open-circuit voltage that is associated with the energetic offsets [21–24]. The microstructure of the film needs to be engineered such that it is fine enough to allow every exciton to find an interface for dissociation and at the same time it has to be sufficiently segregated to allow the charge carriers to travel efficiently to the respective electrode without recombining [25]. While the exciton dissociation and charge generation are surprisingly efficient in blends of electron-donating polymers and electron-accepting fullerenes [26–28], charge collection is a challenge due to the relatively low mobilities and low permittivities of organic materials. Only in a few cases [29–31] are absorber thicknesses above 100 nm possible without substantially reducing the efficiency of collecting the photogenerated charge carriers.

The low dielectric constant, high exciton binding energy and the subsequent use of the bulk-heterojunction concept sets organic solar cells apart from inorganic solar cells. However, in many ways, organic solar cells have similarities to amorphous or microcrystalline silicon solar cells. In both cases, the absorber layer is a relatively disordered semiconductor that contains localized states that slow down charge carrier transport. In both cases the device consists of an intrinsic or lowly doped absorber sandwiched between two contact layers that create a built-in electric field that helps to separate the charge carriers.

Due to these similarities, device modelling of organic solar cells has many similarities to device modelling in inorganic thin-film solar cells. In particular the underlying differential equations are the same and the treatment of disorder is based on the same mathematics as for inorganic solar cells. However, there have been several models and concepts that are specific to organic solar cells that we will briefly discuss in the following. However, most of the following theory will be relevant for all kinds of thin-film solar cells and is not specific to organic molecules. In this review we will discuss the simulation of organic solar cells based on the concept of one-dimensional drift-diffusion simulations. We will discuss the underlying differential equations, the description of physical phenomena such as transport

and recombination in organic solar cells and the measurements used to determine necessary parameters. Finally, we present examples of situations where device modelling can give useful insights that would otherwise be difficult to obtain.

1.2 Differential Equations

In any semiconductor device the charge densities are governed by three differential equations, Poisson's equation which expresses the minimization of electrostatic potential energy and continuity equations that express the conservation of charges. Typically, multilayer stacks of thin-film solar cells are simulated in the dimension parallel to the surface normal of the stack. For such a one-dimensional device model, these equations become

$$\frac{\partial^2 \varphi}{\partial x^2} = -\frac{\rho}{\varepsilon}, \tag{1}$$

relating the electrical potential φ to the space charge density ρ,

$$\frac{\mathrm{d}n}{\mathrm{d}t} = G - R + \frac{1}{q}\frac{\mathrm{d}J_\mathrm{n}}{\mathrm{d}x} \tag{2}$$

expressing the conservation of electron density n in terms of charge pair volume generation rate G, charge recombination rate R, and electron current density J_n, and

$$\frac{\mathrm{d}p}{\mathrm{d}t} = G - R - \frac{1}{q}\frac{\mathrm{d}J_\mathrm{p}}{\mathrm{d}x} \tag{3}$$

expressing the conservation of hole density p in terms of the hole current density J_p, G and R. Here, x is the coordinate normal to the surface of the device, t is the time and q is the elementary charge. In (1), ε is the absolute permittivity, i.e. the product of relative permittivity ε_r and vacuum permittivity ε_0.

In steady state ($\mathrm{d}n/\mathrm{d}t = 0$ and $\mathrm{d}p/\mathrm{d}t = 0$), the continuity equations can be rewritten as

$$-\frac{1}{q}\frac{\mathrm{d}J_\mathrm{n}(x)}{\mathrm{d}x} = -D_\mathrm{n}\frac{\mathrm{d}^2 n(x)}{\mathrm{d}x^2} - F\mu_\mathrm{n}\frac{\mathrm{d}n(x)}{\mathrm{d}x} = G(x) - R(x,n,p) \tag{4}$$

for electrons and

$$\frac{1}{q}\frac{\mathrm{d}J_\mathrm{p}(x)}{\mathrm{d}x} = -D_\mathrm{p}\frac{\mathrm{d}^2 p(x)}{\mathrm{d}x^2} + F\mu_\mathrm{p}\frac{\mathrm{d}p(x)}{\mathrm{d}x} = G(x) - R(x,n,p) \tag{5}$$

for holes. In (4) and (5) the current densities have been split into a diffusion and a drift term, where $D_\mathrm{n,p} = kT\mu_\mathrm{n,p}/q$ is the diffusion constant and F is the electric field.

Note that since the charge concentrations n and p in (4) and (5) are the concentrations of free carriers and μ_n and μ_p are the mobilities of free charge carriers, the classical Einstein relation ($D_{n,p} = kT\mu_{n,p}/q$) is applicable. Only if we were to define n and p as the concentration of free and trapped carriers would we have to use the generalized Einstein relation [32, 33].

In order to solve the above equations, suitable boundary conditions have to be defined that fix the difference in electrostatic potential at the two contacts (boundary condition for the Poisson equation) and a set of equations that connects the electron and hole currents flowing out of the devices with the charge carrier concentrations. In Sect. 2.5 we will discuss these boundary conditions in more detail.

This set of equations is the basis for the simulation of any optoelectronic device in one spatial dimension and they are not specific to organic solar cells. In order to make meaningful simulations, the challenge for the simulation of any solar cell technology is to determine the form of the mobilities μ_n and μ_p, the recombination rate R and the generation rate G. In the simple case of a crystalline inorganic semiconductor like Si, the mobilities can be measured (e.g. with Hall effect measurements), the recombination rate in most of the bulk of the material is (nearly) proportional to the minority carrier concentration and light intensity and, because the devices are optically thick, the generation rate can be calculated with the simple exponential Lambert–Beer law. In addition, the largest part of the volume of c-Si solar cells is usually the p-type base in which the electric field is negligible and the only relevant equation to solve is the diffusion equation for minority carriers, which can be done analytically [34–36]. In contrast, in organic solar cells the mobilities are a function of carrier density [37, 38] and low. In addition, the devices are so thin that the carrier concentration gradients are large [39, 40], meaning that both carrier types have to be considered and the recombination rates are therefore nonlinear [41, 42]. Low thickness also means that the optical generation rates depend on optical interference [43–45]. Moreover, the optical generation rate is not identical to the generation rate for free charge carriers because of the variable efficiency of the intermediate stages of exciton dissociation and charge separation [46, 47]. Because of the low dielectric constant in organic materials, space charge effects are likely to matter more than in similarly thin inorganic thin-film solar cells. This will mean that the shape of the band diagram depends strongly on space charge effects due to, e.g. asymmetric mobilities of electrons and holes and is therefore a function of charge carrier concentration and often not reliably known [48–50]. Finally, because of the disordered nature of the films the density of states cannot be approximated by two bands of delocalized states for electrons and holes. Instead, there is evidence for a continuous distribution of localized states in the band gap of the semiconductor that affects transport and recombination [51–54].

In describing solar cell response, different approximations can be made to solutions of the device equations. In the next sections we review how some of the common approximate models are used and adapted for organic solar cells.

1.3 Equivalent Circuit Models

One of the most popular models to describe a solar cell is the equivalent circuit model. In this case, the dark current/voltage curve of most solar cells is described by the classical diode equation

$$J_{\mathrm{d}} = J_0 \left[\exp\left(\frac{q(V - J_{\mathrm{d}} R_{\mathrm{s}})}{n_{\mathrm{id}} kT} \right) - 1 \right] + \frac{V - J_{\mathrm{d}} R_{\mathrm{s}}}{R_{\mathrm{p}}} \tag{6}$$

including a series resistance R_{s} and a parallel resistance R_{p}. Equation (6) is the mathematical description of an ideal diode, characterized only by a saturation current density J_0 and an ideality factor n_{id}, connected in parallel to a resistor R_{p} and both are connected in series to a resistor R_{s}. These parameters, J_0 and n_{id}, relate to the device parameters and can be derived from solving the continuity and Poisson equations [55]. While the diode parameters, J_0 and n_{id}, describe the recombination of electrons and holes as a function of applied voltage, the series resistance considers all resistive effects in series with the diode. These resistive effects can be internal, i.e. due to the finite conductivity of the semiconductor causing a voltage drop to drive majority carriers through the device, or external, i.e. due to the finite conductivity of the contacts. The shunt resistance is due to local defects in the material that allows unipolar electrical transport through the device that is ohmic or nearly ohmic.

Different ideal circuit elements (diode, shunt and series resistance) dominate at different applied voltages. For low voltages, the current $(V-JR_{\mathrm{s}})/R_{\mathrm{p}}$ over the shunt resistance is dominant. For intermediate voltages, the current increases exponentially with voltage before – at high voltages – the slope starts to decrease again because of the voltage drop over the series resistance.[1]

For inorganic pn-junction solar cells the J_{l}/V curve under illumination follows from the dark J/V curve by subtraction of the short-circuit current density J_{sc} (the "superposition principle") giving

$$J_l = J_0 \left[\exp\left(\frac{q(V - J_l R_{\mathrm{s}})}{n_{\mathrm{id}} kT} \right) - 1 \right] + \frac{V - J_l R_{\mathrm{s}}}{R_{\mathrm{p}}} - J_{\mathrm{sc}}. \tag{7}$$

Thus, the J_{l}/V curve under illumination is described as a superposition of the dark current and a current source that takes into account the photovoltaic effect in the device. The superposition means that this current source is independent of applied voltage and depends only on illumination. In addition, it is often implicitly

[1] The description of the dark current density with (8) is typically sufficient for most solar cell technologies. In some cases, especially for crystalline Si solar cells, a second diode has to be taken into account because different recombination mechanisms with different ideality factors dominate at different voltages (recombination in the space charge region at low voltages and recombination in the neutral zone at higher voltages).

assumed that it scales linearly with illumination. This approximation is reasonable for pn-junction solar cells where charge carrier collection is driven mostly by diffusion in a field free base.

For thin-film solar cells with absorber layer thicknesses of the order of the space charge regions, a substantial part of the absorber layer will be depleted of free charge carriers. Thus, collection will be (at least partly) field driven and, additionally, non-geminate recombination will be nonlinear. Under these circumstances, the superposition principle will cease to be valid and (7) has to be rephrased:

$$J_l = J_0\left[\exp\left(\frac{q(V - J_l R_\mathrm{s})}{n_\mathrm{id} kT}\right) - 1\right] + \frac{V - J_l R_\mathrm{s}}{R_\mathrm{p}} - J_\mathrm{ph}(V, \phi). \tag{8}$$

We call J_ph the photocurrent which may now depend on voltage V and which may scale nonlinearly with the photon flux ϕ because the recombination depends nonlinearly on light intensity. For devices with high mobility and good collection independent of voltage, J_ph would be a constant as a function of voltage.[2] In organic solar cells J_ph may depend on voltage because the charge carrier mobilities are low and collection is sensitive to the electric field and therefore to the term $(V_\mathrm{bi}{-}V)$ [58]. Here, V_bi is the built-in voltage (at short circuit) and $(V_\mathrm{bi}{-}V)$ is the potential difference between cathode and anode at an applied voltage V. One approach to incorporate this effect is described next.

1.4 Approximations Based on the Mobility-Lifetime Product

In the case of a thin absorber layer such that the electric field in the device is uniform, an analytical approximation can be used to describe the voltage dependent photocurrent in thin-film solar cells at least around short circuit and for small forward bias. The equation for the photocurrent

$$J_\mathrm{ph} = 2q\overline{G}\mu\tau\frac{V_\mathrm{bi} - V}{d}\left(1 - \exp\left(-\frac{d^2}{2\mu\tau(V_\mathrm{bi} - V)}\right)\right) \tag{9}$$

is based on the Hecht equation from the 1930s [59] and has been adapted for the case of amorphous Si solar cells by Crandall in the 1980s [60]. Equation (9) and similar equations based on the concept of a mobility-lifetime ($\mu\tau$) product have been introduced to the field of organic solar cells in recent years [8, 21, 53, 61–63]. Equation (9) captures two main features of the photocurrent J_ph. It depends

[2] However, note that J_ph is not equal to $J_\mathrm{d}{-}J_\mathrm{l}$, which would *not* be a constant as a function of voltage even for infinite mobilities as long as there is a finite series resistance in the device. This is due to the fact that the voltage drop over the series resistance is $J_\mathrm{l}R_\mathrm{s}$ under illumination and $J_\mathrm{d}R_\mathrm{s}$ in the dark (i.e. not the same), meaning $J_\mathrm{d}{-}J_\mathrm{l}$ is affected by the series resistance at larger forward bias [56, 57].

on voltage, with higher forward voltage V leading to a lower electric field $(V_{bi}-V)/d$ and therefore a less efficient charge carrier collection. In addition, the photocurrent J_{ph} depends on a representative mobility μ and lifetime τ such that higher mobilities and lifetimes lead to better collection and higher photocurrents. Note that the mobility μ is assumed to be representative of both electrons and holes, which is reasonable because (9) is not valid for highly asymmetric mobilities and the lifetime τ is assumed equal for both carrier types. Equal lifetimes would result for the recombination of free charges via midgap defects [60], which is a reasonable assumption for amorphous Si solar cells. Equation (9) predicts J_{ph} to be linear with light intensity, which is not necessarily correct for organic solar cells [41].

Some more complicated analytical models have been applied to inorganic thin-film solar cells mostly by the amorphous Si community [64–67]. However, little work in this context has been done by the organic photovoltaics community [68].

1.5 Trap Free Drift-Diffusion Models

The next step up in complexity for the organic solar cell community was a trap-free effective medium drift-diffusion model. Koster et al. [69] solved the continuity, current and Poisson equations, essentially as for a crystalline semiconductor but with a modified generation term for free charge carriers. While in inorganic solar cells at room temperature all recombination is non-geminate (between separated electrons and holes), in organic solar cells there might also be a substantial amount of prompt recombination of either excitons or unseparated charge pairs, known as geminate recombination. To take geminate recombination into account, the generation term was weighted by a field dependent charge separation probability. The probability is calculated with a model developed by Onsager [70] and modified by Braun [71]. In these drift diffusion models, the two phase blend is treated like one effective medium with the conduction band of the effective semiconductor representing the energy of free electrons in the acceptor and the valence representing the energy of the free holes in the donor, so that the exciton diffusion is not considered. Similar trap-free drift-diffusion models have been used by other authors [43, 72–76].

Disadvantages of the model are that it only yields ideality factors of one, which is in contrast to what is mostly found experimentally [77] and that it is unable to reproduce transient device response since trap states are neglected [54]. In addition, the model makes it difficult to discriminate between different effects that have a similar influence on the shape of the current/voltage curve under illumination. For instance, similar current/voltage curves may be assigned to space charge effects on non-geminate recombination [78] or to field dependent geminate recombination [79]. Indeed, several studies [80–82] suggest that effects of field dependent geminate recombination can be small, at least in some relevant systems.

1.6 Drift Diffusion Including Localized States

The capability of drift-diffusion models can be increased by introducing localized states into the band gap. Recently, several studies have introduced single trap levels [83] as well as distributions of localized states in order to describe the results of transient and steady state experiments on polymer:fullerene solar cells [54, 84–89]. Most of these models use a Shockley–Read–Hall type occupation statistics for the localized states, which we will discuss in more detail in Sect. 2.3 and the Appendix 2 before discussing some of the implications of this model in the case studies in Sect. 4.1.

1.7 1D Versus 2D Simulations

While most literature on device simulations of organic solar cells is on one-dimensional simulations, there are also some examples of two- and three-dimensional simulations [90–93]. Adding one more dimension brings the option of studying the effect of blend microstructure on device performance. Maturova et al. studied the relation between device performance and microstructure in polymer:fullerene solar cells as measured with various microscopic techniques such as atomic force microscopy (AFM), scanning Kelvin probe microscopy (SKPM), scanning tunnelling microscopy (STM) and transmission electron microscopy (TEM) by using a two-dimensional drift-diffusion model [94–97]. One of the main features of this model as shown in Fig. 1 is that it consists of layers containing a mixed donor:acceptor phase and layers containing a pure acceptor phase. Using this assumption, the model reproduces the dependence of photocurrent on the measured phase separation in MDMO-PPV:PCBM where the polymer-rich phases are usually believed to contain fullerene. If we assume that exciton diffusion in the mixed donor:acceptor layer is efficient but that the electron mobility is much smaller as compared to the pure acceptor phase, the trends in photocurrent vs domain size can be explained quantitatively [94].

1.8 Monte Carlo Simulations

Drift-diffusion treatments are ideal for multilayer devices with one-dimensional variations in structure and where the density of electronic states is sufficiently sharp near the band edges that an effective density of states and a quasi Fermi level can be defined for each carrier type. As we shall see below, part of the challenge in applying drift-diffusion simulations to organic semiconductors has been handling the influence of electronic states that lie within the electrical gap and can act as charge traps and recombination centers. An alternative approach to materials with

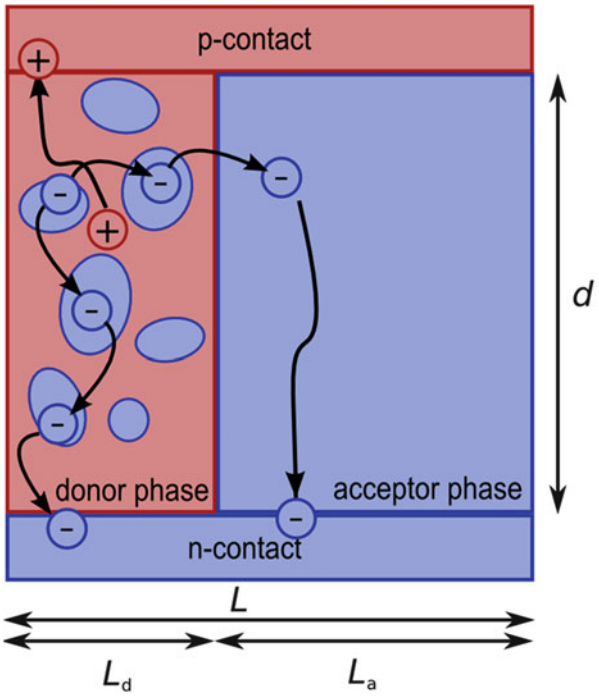

Fig. 1 Layout of the unit cell simulated by Maturova et al. [94]. The active layer between the two contacts consists of a pure acceptor phase and a donor-rich phase that contains some acceptor molecules as well. The donor phase has a lower electron mobility than the acceptor phase. Thus, photogenerated electrons may either diffuse to the interface to the pure acceptor phase where it is transported with a high mobility towards the electron contact or it may drift in the donor-rich phase to the electron contact. Modelling the microstructure of the device as shown in the figure allows one to explain the trends in device performance vs domain size in MDMO-PPV:PCBM and to reproduce the shape of the current/voltage curves

high disorder in the electronic state energies is to use Monte Carlo simulations, where a disordered medium possessing some density of states is generated at random, and physical processes of charge generation, separation, transport, recombination and injection can be simulated microscopically. The response of a material can then be modelled by averaging over a large number of realizations of the material and of the situation being simulated. A master equation method where different rates for different charge transfer events are incorporated using different coupling coefficients in a nonlinear matrix equation can alternatively be used to model transport in a disordered assembly of transport sites [98].

Monte Carlo approaches are attractive for disordered organic semiconductors because they incorporate the disorder in energy levels in a natural way. This is because the chemical nature can be incorporated explicitly through the energy levels and interactions between different molecules and because the effects of 3D variations in structure (such as in molecular packing and phase segregation) can be

modelled explicitly. The method is also easily compatible with adaptive time steps, which allows rare events (such as release from a deep trap) to be modelled efficiently. The disadvantages for device simulation are that a very large number of simultaneous or competing processes need to be handled, making the simulation rather slow, especially since multiple repeats of the simulation are needed to generate good statistics and that it is an inefficient way to model the behaviour of charge carriers in bands. For device simulation, MC approaches are probably most useful when used in combination with continuum approaches to simulate parts of the problem – for example injection from an electrode [99], or when simulating highly energetically disordered systems where continuum approaches do not work, or when used to develop the appropriate functional form of some physical process such as the local charge density dependence of recombination or transport.

Given the limitations in computer time, MC has proved extremely useful in understanding organic photovoltaic materials and has been used successfully to study charge transport [100] charge recombination [101] geminate pair separation at a heterojunction [102, 103], phase segregation [104–106] current generation [105, 106], charge injection from electrodes [99] and at heterojunctions [107] and entire device simulation [108]. A separate chapter of this volume is devoted to a review of this subject [109].

2 Description of Physical Phenomena

2.1 Optical Generation

Optical modelling of absorption in organic and inorganic thin-film solar cells is widely used in device design, diagnosis and interpretation of measurements [43–45, 76, 110, 111]. It is useful to estimate the maximum photocurrent that a certain system may provide, for the estimation of losses due to parasitic absorption in contact layers (like ITO or PEDOT:PSS) or for the calculation of the internal quantum efficiency [112–115]. It is also helpful to understand how the electrostatics in the device will affect the amount of charge that will be collected [58]. In the previous sections we learned that the collection efficiency in organic solar cells is not necessarily independent of position. For example, if the device is doped sufficiently highly that the space charge region is much thinner than the cell, collection efficiency will depend on where the charge is generated. The same happens if space charge results from asymmetric mobilities [78]. In these cases, optical modelling allows us to determine whether at a given thickness most light is absorbed close to the front contact or more homogeneously distributed over the whole thickness.

The thickness of organic solar cells is comparable to the wavelength of light that is absorbed in the device. Thus, optical absorption cannot be calculated with a simple Beer–Lambert approach. Instead, optical interference effects have to be

taken into account. This can be done easily in the normal case of flat interfaces using a transfer matrix formalism (see appendix 1). Modelling rough interfaces and effects of scattering or diffraction of light requires more complex methods possibly involving solution of Maxwell's equations in two or three dimensions. Such approaches lie beyond the scope of this review but we refer the reader to the literature on this topic in the context of thin-film silicon solar cells, where light trapping concepts have already been studied for decades from both an experimental [116–119] and recently also theoretical point of view [120–123].

2.2 Distribution of Localized States

In trap free models we describe the density of states in the bands with an effective density of states N_C and N_V for conduction and valence band, and no distribution in state energy is considered. However, organic semiconductors contain distributions of energy levels for electrons and holes as a result of the disorder in molecular conformation, intermolecular interactions, and physical and chemical defects as well as disorder in conjugation length in the case of conjugated polymers. The fraction of these states that lie at lower energies than the average LUMO or HOMO levels act as trap states. The shape of the density of subgap states in organic solar cells is in general unknown. It is often assumed that around the peak of the density of states the shape is Gaussian. Further down in the band gap it has been suggested to continue to be Gaussian [124] or to be exponentially decaying towards midgap [54]. Sometimes evidence for deep defects is found that can often be modelled as a second Gaussian feature [52, 53]. When simulating the effect of localized states on transport and recombination, it is therefore usually sufficient to model the density of states with a combination of exponential tails and additional Gaussian defects. Typically, the tails are characterized by a characteristic tail slope E_{chC} or E_{chV} and a density N_{0CBT} or N_{0VBT} of tail states at the conduction or valence band edge (unit typically in $1/(cm^3\ eV)$) [40, 54, 58]. Thus, we can write the density N_{CBT} of states in the conduction band tail as

$$N_{CBT} = N_{0CBT} \exp\left(\frac{E - E_C}{E_{chC}}\right) \tag{10a}$$

and the density N_{VBT} of states in the valence band tail as

$$N_{VBT} = N_{0VBT} \exp\left(-\frac{E - E_V}{E_{chV}}\right). \tag{10b}$$

Any Gaussian shaped defect is characterized by the position E_t of the center of the Gaussian, the width σ_t and the absolute concentration N_t. Thus the density of states for a Gaussian defect can be written as

$$N_{\mathrm{GD}}(E) = N_{\mathrm{t}} \frac{1}{\sigma_{\mathrm{T}}\sqrt{2\pi}} \exp\left(-\frac{(E-E_{\mathrm{t}})^2}{2\sigma_{\mathrm{t}}^2}\right). \tag{11}$$

2.3 Transport and Recombination

In models of transport in crystalline semiconductors all charge carriers are mobile and their transport properties are characterized by the mobilities of electrons and holes. Transport in amorphous or nanocrystalline semiconductors is often described using a multiple trapping model, where some carriers are mobile and some are trapped in localized states. In organic semiconductors, charge carrier transport is typically described as a hopping process between localized sites. Hopping can be approximated by a multiple trapping model [125] by assigning a low mobility to the most delocalized states and treating more localized states as traps. Such a multiple trapping model is easy to implement in a drift-diffusion solver and therefore a good choice to handle disorder and localization while still maintaining simplicity and computational speed. While the traps slow down transport, they might also affect the recombination rate if charges on traps can recombine with free charges of opposite polarity.

The effect of traps can easily be added to a drift-diffusion simulation by modifying the recombination rate R and the space charge ρ. In Appendix 2, we describe how the modified R can be obtained. The final result of the derivation is that the net recombination rate R via the trap or indeed any distribution $N_{\mathrm{t}}(E)$ of traps can be expressed via ($\beta_{\mathrm{n,p}}$ are the capture coefficients and $e_{\mathrm{n,p}}$ are the emission coefficients for electrons and holes)

$$R = \int_{E_{\mathrm{v}}}^{E_{\mathrm{c}}} N_{\mathrm{t}}(E)\beta_{\mathrm{n}}\beta_{\mathrm{p}} \frac{np - n_{\mathrm{i}}^2}{n\beta_{\mathrm{n}} + p\beta_{\mathrm{p}} + e_{\mathrm{n}} + e_{\mathrm{p}}} \mathrm{d}E. \tag{12}$$

Equation (12) is all the information we need to modify the continuity equations to take trapping, detrapping and recombination via traps into account. However, what is still missing is the influence of the trap levels on the space charge and subsequently the Poisson equation.

When we add up all the space charge in the device for the calculation of the electrostatic potential via the Poisson equation, we have to know what the charge states of our trap levels are. Initially, one might assume that a trap is negatively charged when filled with a trapped electron and neutral when empty. However, although this is sometimes implicitly assumed [126], it is not necessarily true. In general, we consider the two most relevant cases of an acceptor-like or a donor-like trap. An acceptor-like trap is a trap that behaves like an acceptor dopant. An acceptor dopant creates free holes if ionized and it is therefore negatively charged if ionized or neutral if occupied with a hole. In contrast a donor like trap is positively charged when ionized and neutral when occupied with an electron. Usually, donor-like traps do not affect the space charge much if they are close to the valence band; likewise for acceptor-like traps if they are close to the conduction

band. Only if donor-like traps are close to the conduction band or acceptor-like traps are close to the valence band will they be charged either negatively (acceptor-like trap) or positively (donor-like trap) and therefore act in the same way as classical dopants in inorganic semiconductors. They will change the electrostatics and have an influence on the current/voltage curves as we will show in Sect. 4.1.1.

Traditionally, exponential tails of disordered semiconductors like amorphous Si have been modelled using acceptor-like conduction band tail states and donor-like valence band tail states. Thus, the space charge due to free carriers and tails can simply be calculated by adding the free and trapped holes and subtracting the free and trapped electrons (i.e. $\rho = q(p + p_{\mathrm{tail}} - n - n_{\mathrm{tail}})$.). When using the multiple trapping model and exponential tails in the context of organic solar cells [40, 54, 86, 88], this definition of the charge states of band tails has been assumed to be valid as well.

However, there is experimental evidence for deep defects in organic semiconductors that cannot easily be described by exponential tails and whose charge states are currently unknown [53, 127]. They may be acceptor-like, donor-like or even amphoteric, which means that they can be positively charged, neutral or negatively charged depending on the occupation of the trap with electrons. No matter what type, these defects can easily be included in the space charge and recombination via these states can be modelled using Shockley–Read-Hall statistics for singly charged defects and Sah–Shockley [128, 129] statistics for doubly charged (amphoteric states). Currently, however, there is a lack of knowledge about the properties of defects and experimental data that could help to assess how to model these defects, how to assess their influence on device performance and how to passivate them and to eliminate their negative influence on device performance.

2.4 Doping

In contrast to inorganic semiconductors, organic semiconductors are seldom intentionally doped. This is because of negative effects of dopant impurities on electronic properties, and difficulties achieving doping in a solution process. The exception is in the case of vacuum deposited small molecular organic devices where doping levels can be tuned carefully through vacuum co-deposition of semiconductor molecules and dopants [130]. Some nominally intrinsic organic semiconductors have turned out to be unintentionally doped when probed using capacitance voltage profiling [49, 58, 131–133]. Early work on poly (3-hexylthiophene) (P3HT):1-(3-methoxycarbonyl)propyl-1-phenyl-[6,6]-methano fullerene (PCBM) gave evidence for the blend to be p-type [131], which could result from the influence of molecular oxygen and partial charge transfer [134–136]. While capacitance-voltage measurements are in principle a simple way of analyzing the width of space charge regions in organic solar cells, one has to exercise caution to get values that are not affected by the device thickness.

To ensure this, the film thickness should always be sufficiently high so that the space charge region due to doping is much smaller than the cell thickness [49].

Doping adds to the space charge ρ in Poisson's equation. Therefore, the electrostatic potential changes as a function of the doping concentration and the type (n-type or p-type). Sufficiently high doping would lead to the creation of a neutral region where the electric field is low and a space charge region where the electric field is high. Because the magnitude of the electric field affects the collection probability of charges, doping will change this probability and make it position dependent. This effect can control the thickness dependence of device performance [58], it can favour photocurrent collection from one side over the other [137] and it complicates the interpretation of device data [40, 138].

The origin of unintentional doping is not known in general [139]. Synthetic routes and exposure of samples can influence the phenomenon. As described above, effective doping may result from the existence of acceptor type defect states that lie below the Fermi level for electrons or donor type defects lying above the Fermi level for holes. In many ways the effects of dopants on band profiles and device behaviour are similar to those of the space charge; see above.

2.5 Band Diagram and Boundary Conditions

The three differential equations (1), (2) and (3) have to be solved with a set of boundary conditions that define the properties of cathode and anode. The boundary conditions have to specify the values of the electrical potential and the current densities for electrons and holes at front and back contact. Figure 2 shows the schematic band-diagram of a thin organic solar cell with the anode on the left and the cathode on the right. The donor:acceptor blend appears in the band diagram like a classical semiconductor with a conduction band with the electron affinity of the acceptor and a valence band with the ionization potential of the donor. The conduction and valence band edge are separated by the interfacial band gap:

$$E_{\mathrm{gi}} = E_{\mathrm{c}} - E_{\mathrm{v}} = IP_{\mathrm{don}} - EA_{\mathrm{acc}}. \tag{13}$$

From the band diagram, we can directly define the boundary condition for the electrical potential φ, which is

$$\varphi(d) - \varphi(0) = V_{\mathrm{bi}} - V. \tag{14}$$

The absolute value of the electrical potential is of no interest for the simulation, only the difference between the front and back contact, which is given by the built-in voltage V_{bi} and the applied voltage V. Figure 2 shows an example where the Fermi-level at anode and cathode is in the band gap. This is the case if the workfunction WF_{a} of the anode is smaller than the ionization potential IP_{don} of

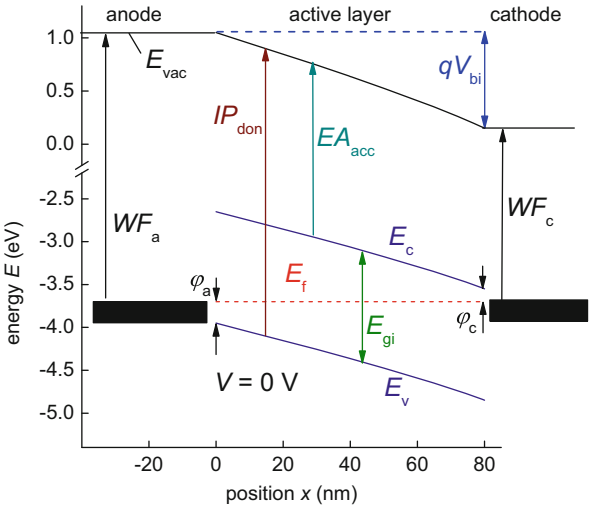

Fig. 2 Schematic band diagram of an organic solar cell at $V = 0$ V in the dark introducing relevant quantities like the built-in voltage, the workfunctions of anode and cathode, the electron affinity of the acceptor and the ionization potential of the donor that are represented by conduction and valence band in the simulation. From the difference between the contact workfunctions and conduction and valence band edges at the two contacts one may calculate the contact barriers φ_a and φ_c. Note that the zero on the energy axis is arbitrary

the donor and if the workfunction WF_c of the cathode is larger than the electron affinity EA_{acc} of the acceptor. In this case, we can define two contact barriers φ_a and φ_c at the anode and cathode that are given by

$$\varphi_a = IP_{don} - WF_a \tag{15}$$

and

$$\varphi_c = WF_c - EA_{acc}. \tag{16}$$

If the right hand sides of (15) and (16) were to get negative, the barriers are usually set to zero, implying that we expect the Fermi-level to pin to the conduction or valence band edge instead of being in the band. The resulting situation is then essentially equivalent to a zero contact barrier that results from a fixed, voltage independent dipole that should not change the result of the simulation. The situation of the essentially zero contact barrier is especially relevant for the cathode if made from low workfunction metals like Ca or Ba. The workfunctions of these materials are substantially lower than the electron affinities of typical acceptors.

The fixed contact barriers φ_a and φ_c can be used to calculate the equilibrium concentrations of electrons at the cathode (assumed to be at $x = d$):

$$n_0(x = d) = N_C \exp\left(-\frac{\varphi_c}{kT}\right) \tag{17}$$

and the equilibrium concentration of holes at the anode (assumed to be at $x = 0$):

$$p_0(x = 0) = N_V \exp\left(-\frac{\varphi_a}{kT}\right). \tag{18}$$

Thus, in this model the equilibrium concentrations of majority carriers are fixed at the contacts by the properties of the contact. The equilibrium concentrations of minorities (electrons at the anode and holes at the cathode) are fixed as well via ${n_i}^2 = n_0 p_0$ and ${n_i}^2 = N_C N_V \exp(-E_{gi}/kT)$. Under applied bias or under illumination, the majority carrier concentrations will usually still be close to their equilibrium values at the electrode but the minority carrier concentrations might be much higher. When minority carriers approach a contact (electrons the anode, holes the cathode), they might recombine with a charge in the electrode. For instance a hole reaching the metal cathode might recombine with an electron in the metal. This process will decrease the concentration of holes and will therefore lead to losses in photocurrent and open-circuit voltage. To describe this interaction of charges at the contact, we use boundary conditions given in form of surface recombination currents [54]:

$$J_n(0) = qS_{nf}(n(0) - n_0(0)) \tag{19a}$$

$$J_p(0) = qS_{pf}(p(0) - p_0(0)) \tag{19b}$$

$$J_n(d) = qS_{nb}(n(d) - n_0(d)) \tag{19c}$$

$$J_p(d) = qS_{pb}(p(d) - p_0(d)). \tag{19d}$$

Here $S_{nf,b}$ is the surface recombination velocity for electrons at the front or back respectively, while $s_{pf,b}$ is the analogous quantity for the holes.[3]

[3] Within the framework of this model, the concentrations of majority carriers at the contacts are essentially fixed by the workfunctions of the contact materials. The minority carrier concentrations may or may not be fixed depending on how high the surface recombination velocity is chosen. This model will lead to a built-in field that is distributed rather homogeneously over the thin (100 nm or less) absorber layers that are typical for most organic solar cells and will lead to a substantial relevance of the electric field to charge carrier collection. An alternative suggestion comes from the group of Juan Bisquert which promotes a model based on an interfacial dipole at the cathode. This interfacial dipole is not fixed but changes as a function of voltage and accommodates part of the voltage drop under forward bias and reduces the electric field in the absorber layer relative to the case without a dipole. This would mean that charge collection would depend less on the electric field and transport would be mostly controlled by diffusion which will also play a role in the classical model when the device is thick enough and doped as we will discuss later. While the

2.6 Solving Continuity and Poisson Equation in Steady State

In the case of trap-free systems (Sect. 1.5), standard methods are used to solve the system of coupled differential equations (1)–(5) subject to the boundary conditions (Sect. 2.5). Usually a finite difference method is used where first a grid is generated and then the equations are discretized on the chosen grid. Typically, the equations are solved for three independent variables: the electron concentration n, the hole concentration p and the electrostatic potential φ. Each of these three variables is an array with the number of grid points as length. All derivatives are written as difference equations instead. Interpolation is usually done linearly for the Poisson equation. The same is not possible for the continuity equations because the equations are stiff, i.e. the carrier concentrations may vary drastically between grid-points. To have a numerically stable solver without requiring massive numbers of grid points, the Scharfetter–Gummel method is usually used [141].

The discretization of the three independent variables leads to a set of $3 \times N$ nonlinear algebraic equations, where N is the number of grid points. These are then either solved iteratively (Gummel-method [142]) or fully coupled. Both methods use the Newton iteration method to solve the set of equations. To get the best convergence, we usually use the Gummel method for the first few iterations and then switch to the fully coupled method for the rest. For more information on the numerical details of drift-diffusion solvers see the book by Siegfried Selberherr [143].

The distribution of localized states that we usually take into account needs to be discretized in energy to calculate the contribution of the trapped charge to the space charge and to calculate the recombination via these traps. We usually discretize the states with at least 20 levels to make sure our result is not influenced by the discretization. A typical number of gridpoints for the discretization in the spatial dimension is 200.

2.7 Solving Continuity and Poisson Equation for Transient Simulations

In the approach to trapped states described in Sect. 2.6 above, the traps are occupied according to a steady state occupation probability that resembles a Fermi–Dirac function, which allows one to define a quasi-Fermi level for the trapped charge. In transient simulations, the occupation function evolves as a function of time through capture, emission and recombination, which means that the differential equations

influence of interfacial dipoles on the device physics is a highly interesting topic, currently we are not aware of any publications reporting on (numerical) device simulations studying this effect. Therefore, we want to refer the reader to current literature on experimental evidence and analytical modeling that deals with interface dipoles such as for instance those in [48, 140].

for the charge carrier densities need to be solved for each discretized energy level individually. To describe such a system numerically, a set of coupled difference equations has to be solved simultaneously. For a simulation space of M spatial mesh points, $3 \times M$ equations need to be solved in steady state. For transient simulations the number of coupled difference equations increases to $3 \times M + M \times (N_{\mathrm{hDoS}} + N_{\mathrm{eDoS}})$ when the electron and hole DoS are discretized into N_{hDoS} and N_{eDoS} levels. This can be done practically with a Newton method where all equations are solved self consistently, and strategies are used to encourage convergence [86].

3 Experimental Methods Relevant to Device Modelling

To implement the drift-diffusion models for organic photovoltaic devices, we need a way to determine the parameters describing transport, generation and recombination and their functional form. It is not yet possible to predict these parameters from the chemical structure of the materials; they should therefore be determined experimentally for the materials under investigation. Here, we give a brief overview of the experimental methods that are used to determine input parameters for optical or electrical modelling and to validate the model.

3.1 Methods to Determine Optical Properties of Layers

In order to calculate the optical generation rates in the organic absorbers (see appendix 1), it is necessary to determine the complex refractive index $\widetilde{n} = n + ik$ of all layers. The most useful method to obtain this data is spectroscopic ellipsometry, which allows us to determine the real part n and imaginary part k of the refractive index. The general measurement principle of ellipsometry is to measure the polarization of an output beam after the polarized input beam has interacted with the sample. From the change in polarization we derive the optical properties of the layer by fitting the measured output polarization to a model of the optical response of the material [144].

While the real part of $\widetilde{n}$ is usually taken as determined from ellipsometry, the data for the imaginary part, i.e. the extinction coefficient k, can be improved through complementary measurements of absorption. Low absorption coefficients can be measured accurately using photothermal deflection spectroscopy (PDS) where the change in temperature of a liquid in response to heating the sample through light absorption is measured. During the measurement, the sample is placed in a liquid that changes its refractive index with temperature. The sample is illuminated with monochromatic light and, at the same time, the refractive index is monitored with a laser that is deflected by the refractive index gradient in the liquid. The deflection of the laser is measured with a position detector. From the

refractive index change, the temperature change is derived. Because the change in temperature at each wavelength must be due to absorption of light in the sample, the absorptance can be derived. From the measured absorptance, the absorption coefficient α and the extinction coefficient $k = \alpha\lambda/(4\pi)$ can be derived when the layer thickness of the sample is known (λ is the wavelength of light). This method is very sensitive and is usually able to measure down to absorption coefficients of $\alpha = 10\ \mathrm{cm}^{-1}$ [115]. One of the applications of PDS beyond modelling is to study the absorption edge and the absorption of the CT state [145–147] as well as to calculate the internal quantum efficiency of a solar cell with high precision in the range of low absorption [115].

3.2 Methods to Measure Recombination

Recombination is either characterized using steady state measurements, for instance in the dark or under open-circuit conditions, or transient methods where the decay of the concentration of charges is used to analyze the strength and type of recombination. To determine the recombination rate itself is not useful because the continuity equations are solved in terms of the charge densities of electrons and holes on which the recombination rate is strongly dependent. Therefore, we need to measure directly a recombination lifetime τ or an effective recombination prefactor k, which is usually defined as $k = R/n^2$, where n is the average excess electron and hole concentration. Typically, these measurements are done by transient photovoltage measurements [31, 42, 148–152], by transient absorption measurements [148, 153] or by impedance measurements [154–156].

3.3 Methods to Measure the Density of States

The density of states of the molecules used in organic photovoltaics is not known in general, but at least for commonly studied systems such as P3HT:PCBM there is a variety of experimental data that gives us some information about its shape. The most important part of the density of states is the density of localized states or traps in the forbidden gap of a bulk-heterojunction solar cell between the donor HOMO and the acceptor LUMO. To probe the density of states in the gap, one can probe optical transitions between the states in absorption [51, 53, 127] and emission [157]. This has proved to be a useful method to detect changes in trap density and correlate them with device performance [53, 127]. An alternative method is to use a transient photocurrent or time of flight experiment, where the transient response of electrons can be correlated with the depth of the localized states they occupied [52, 86, 158–160]. In addition, a device can be filled with charges optically and the amount of charge can be measured as a function of light intensity by draining the device at short-circuit. By measuring the V_{oc} generated by the same

light intensity, we can obtain information about the states the charges were stored in [54, 85, 150, 161]. Additional information on the density of localized states can also be obtained by other experiments like thermally stimulated currents [161–164], electron spin resonance measurements [165], space charge limited current measurements [126, 166–168], transient absorption spectroscopy [89, 101, 169] and admittance measurements [136, 170]. Most of these experiments hint at a band tail that may be characterized by an exponential decay. The origin of this energetic disorder is not known in general but it has been proposed to originate from disorder in the arrangement of the molecules [171]. In addition, some experiments [53, 136] give evidence for additional states that are roughly Gaussian in shape and that may in some cases [136] also act as p-type dopants.

3.4 Methods to Measure Transport

One of the most frequently used methods for the determination of mobilities of organic photovoltaic absorber materials is the space charge limited current method [126, 167, 172–182]. The advantage of this method is the ease of device fabrication and the fact that the sample used for the measurement is – with the exception of the contacts – the same sample as used for an organic solar cell and importantly has the same thickness. The measurement is done by measuring the current/voltage curve of a single carrier device, i.e. a device with two ohmic contacts for electrons or for holes. The resulting current should depend on the square of the net applied voltage $V-V_{\mathrm{bi}}$ if the device is reasonably intrinsic and trap free. The main disadvantage of this method is that organic semiconductors used for solar cells are typically neither intrinsic nor trap free. This situation creates an interesting problem for device modelling which will be further discussed in one of our case studies in Sect. 4.2. A less frequently used alternative to space charge limited current measurements is the use of admittance spectroscopy to determine the mobility [183–186].

Another classical method to determine the mobility of low mobility semiconductors is the time-of-flight (TOF) measurement [187–192]. In TOF, the movement of a sheet of charges through a thick device is determined by measuring the displacement current induced by the transport of the charges. By using a device thickness that is much larger than the absorption length of light, one of the two charge carriers will be collected rapidly by the adjacent contact while the other type may drift through the whole device. From the transit time of the charges travelling through the device, the mobility is calculated. A disadvantage of the TOF method is that the TOF samples have to be thicker (>1 μm) than the samples typically used for organic solar cells. This means that the microstructure of the active layer is not necessarily the same in a TOF sample as it is in a solar cell. Among the advantages of the method is that the influence of diffusion can be reduced by applying a larger bias during extraction [132] and that it is easily possible to distinguish electron and

hole mobilities. In addition, the post-transit decay can also be interpreted in terms of a density of states [193].

In recent years, large signal transient photocurrent experiments like TOF have been adapted to the study of thin solar cells and the interpretation of the data is less straightforward. These experiments are either called charge extraction at linearly increasing voltages (CELIV) [192, 194–198] or just charge extraction at short circuit [37, 199]. In the case of CELIV, the transient photocurrent is measured while the bias is switched from a forward bias around 0.5 V to a reverse bias with a linear voltage ramp. Then the peak (time and current) of the transient current is used to calculate the mobility. In the case of the charge extraction method, the excess charge density at short circuit is measured as a function of light intensity and is compared to the short-circuit current at the same light intensity. From the ratio and the electric field a drift-mobility can be calculated.

3.5 *Methods to Measure Doping*

One way of analyzing the doping concentration and the electrostatic properties of a semiconductor is to measure the capacitance as a function of voltage, frequency or temperature [48, 133, 140, 154, 155, 170, 200–204]. The simplest measurement to carry out is the so-called Mott–Schottky analysis, which consists of measuring the capacitance as a function of voltage and then using analytical approximations to determine the width of the space charge region and the concentration of charged defects. The solar cell is approximated as a plate capacitor with capacitance

$$C = \frac{\varepsilon_0 \varepsilon_r A}{w} \tag{20}$$

where A is the area and w is the width between the capacitor plates. This width w may be either the thickness of the semiconductor layer sandwiched between cathode and anode or it may be the width of the space charge region depending on which is the smaller. If we assume the space charge width is smaller, we can express w as

$$w = \sqrt{\frac{2\varepsilon_0 \varepsilon_\mathrm{r}(V_\mathrm{bi} - V)}{qN_\mathrm{A}}}, \tag{21}$$

when using the depletion approximation. Here, N_A is the concentration of charged defects and within the depletion approximation it is assumed that the charge density in the space charge region can be approximated by qN_A and that the concentration of free carriers is negligible.

Combining (20) and (21) leads to a dependence of capacitance on the square root of the concentration of charged defects. To be able to determine the defect concentration by fitting a straight line to the data, the Mott–Schottky analysis involves the plot of C^{-2} vs applied d.c. voltage. The intersect of C^{-2} with the voltage axis yields

the built-in voltage of the analyzed space charge region while the slope provides N_A via [205]

$$N_A(x) = -\frac{2}{q\varepsilon_0\varepsilon_r A}\left(\frac{dC(x)^{-2}}{dV}\right)^{-1}, \tag{22}$$

Obviously this analysis is only possible if the width of the space charge region is much smaller than the device thickness. The consequences of using the Mott–Schottky analysis in insufficiently thick devices are discussed in one of the case studies in Sect. 4.4.

An alternative way of measuring the doping concentration is to counter-dope for instance a p-type material with known quantities of n-type dopants and measure the conductivity of the material at the same time. This method has recently been applied to P3HT:PCBM diodes by Liang and Gregg [139].

4 Case Studies of the Use of Device Simulation

Whilst organic solar cell device models may be intended ultimately to help design the most efficient solar cells [206–210], they have proved very useful in exploring fundamental mechanisms [177, 211–214] and in helping to interpret experimental data [47, 50, 54, 58, 74, 88, 215–219]. In the following we will present a series of case studies where simulations of experimental results have allowed us to interpret experimental data better and to understand fundamental physical phenomena. Please see Appendix 3 for a short description of the used software.

4.1 Current/Voltage Curves

Current/voltage curves are the most important characterization technique for any solar cell technology, because they define the power conversion efficiency of the device. However, despite the simplicity of the measurement, current/voltage curves are challenging to interpret. This is because they are rather featureless and depend on a variety of different physical phenomena. Thus, current/voltage curves usually represent the start but rarely also the end of any investigation of the device physics of organic solar cells.

4.1.1 The Effect of Diffusion on the Photocurrent in Organic Solar Cells

As mentioned in the introduction, due to the low relative permittivities in organic semiconductors, the high levels of charged defects often found in organic solar cell

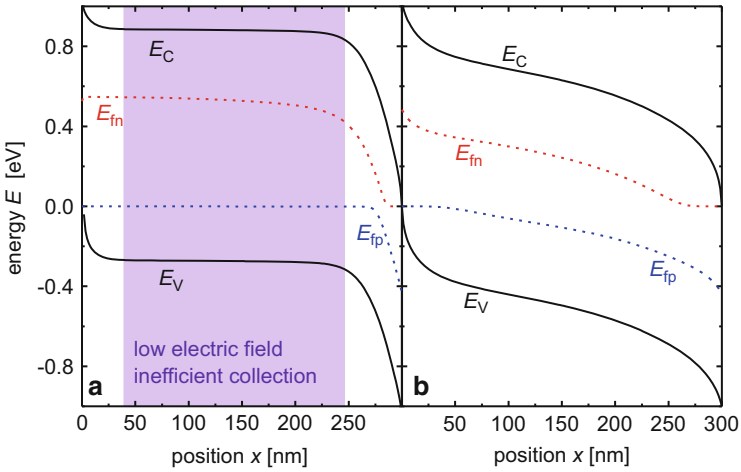

Fig. 3 Band diagrams of a 300 nm thick active layer (**a**) with doping ($N_A = 10^{17}$ cm^{-3}) and (**b**) without doping. In case of doping, a small space charge region and a larger field free region are created. It can be shown that in the field free region, charge carrier collection is reduced

materials [58, 126, 136, 139] and sometimes due to asymmetric mobilities [220, 221], the assumption of constant electric fields in organic solar cells is not necessarily valid. In addition, due to the typically nonlinear recombination mechanisms in organic solar cells [42], the light intensity dependence of the photocurrent may be nonlinear as well. In these conditions the superposition principle is violated and analytical approximations are no longer feasible. Drift-diffusion simulations are then helpful in understanding the shape of solar cell current/voltage curves.

An example of an effect where simulations help to explain where analytic approximations fail is that of reduced mobilities or lifetimes on the current/voltage curve under illumination for non-uniform electric field. To study this we choose two limiting situations, one with a high doping concentration and one without any doping. In each case we simulate the band diagrams of a device with a relatively thick absorber (300 nm) to amplify the effect of the space charge. In the high doping case the electric field is low in parts of the device and high in the depletion region, which has an extension much smaller than the cell thickness as shown in Fig. 3a. In the neutral (field-free) region, charge carrier collection is driven by diffusion and in the space charge region it is driven by drift and is therefore more efficient. In the case without doping (Fig. 3b) the electric field is more uniform, i.e. the built-in voltage drops more homogeneously over the absorber layer. That means that the collection efficiency should be less dependent on position but more dependent on applied voltage then in the case with doping. This is because without doping the electric field helps in collecting the charges but it does so only at low applied bias and therefore high average electric field $(V_{bi}-V)/d$. With doping, charge collection in the neutral region will be equally (in)efficient no matter how high the applied bias. Thus, the photocurrent will be expected to depend less on voltage.

Table 1 Parameters used for the simulations (Figs. 3, 4 and 5)

Name	Symbol	Doping and mobility	Deep defects
Electron mobility	μ_n (cm^2/Vs)	Variable	10^{-3}
Hole mobility	μ_p (cm^2/Vs)	Variable	10^{-3}
p-Type doping density	N_A (cm^{-3})	0 or 10^{17}	0
Effective density of states of the conduction band	N_C (cm^{-3})	10^{20}	10^{20}
Effective density of states of the of the valence band	N_V (cm^{-3})	10^{20}	10^{20}
Total density of tail states (conduction band tail)	N_{Ctail} (cm^{-3})	1.6×10^{18}	1.6×10^{18}
Total density of tail states (valence band tail)	N_{Vtail} (cm^{-3})	1.6×10^{18}	1.6×10^{18}
Tail slope (conduction band tail)	E_{chC} (meV)	80	80
Tail slope (valence band tail)	E_{chV} (meV)	80	80
Capture coefficients	β_n^+ ($cm^3\ s^{-1}$)	2.5×10^{-12}	2.5×10^{-12}
	β_p^0 ($cm^3\ s^{-1}$)	10^{-10}	10^{-10}
	β_p^- ($cm^3\ s^{-1}$)	2.5×10^{-12}	2.5×10^{-12}
	β_n^0 ($cm^3\ s^{-1}$)	10^{-10}	10^{-10}
Capture coefficient deep defects	β_{deep} ($cm^3\ s^{-1}$)	–	10^{-10}
Gaussian width deep defects	σ_t (meV)	–	150
Band gap	E_g (eV)	1.1	1.1
Surface recombination velocity	S (cm/s)	10^5	10^5
Contact barrier	φ_b (meV)	0	0

Note that the mobilities given are band mobilities and apply only to the untrapped fraction of the charge carrier population

To study whether our predictions from the band diagrams are true, we simulate the current /voltage curve under illumination (for simulation parameters see Table 1). The result is presented in Fig. 4, where we varied the mobility as a means to study different collection efficiencies without strongly affecting the electrostatics of the two cases. Without doping (Fig. 4a, b), a reduction in mobility will indeed lead to a strong voltage dependence of photocurrent collection, seen in the low fill factor. The photocurrent around the maximum power point will be more strongly reduced by lower mobilities than the current under reverse bias or short circuit. With doping (Fig. 4c, d), the photocurrent decreases with reduced mobilities as well, but the decrease depends less on applied voltage. Thus, the *FF* will stay reasonably high even for low mobilities while the short-circuit current will decrease already at much higher mobilities than without doping. Figure 4b, d shows the current voltage curves on a log/log plot. This way of presenting the data has been used frequently in the past [78, 79, 94] as a way to analyze the field dependence of the photocurrent. The voltage axis is meant to be (roughly) proportional to the electric field and is defined either as $V_{oc}-V$ if the current under illumination is plotted on the *y*-axis or as $V_{bi}-V$ if the photocurrent is plotted on the *y*-axis. In Fig. 4b, the current has essentially two slopes. Close to V_{oc} at low electric fields the current goes to zero and towards large negative bias the current saturates, leading to a flat part for high electric fields and a steep part for low electric fields. In Fig. 4d we

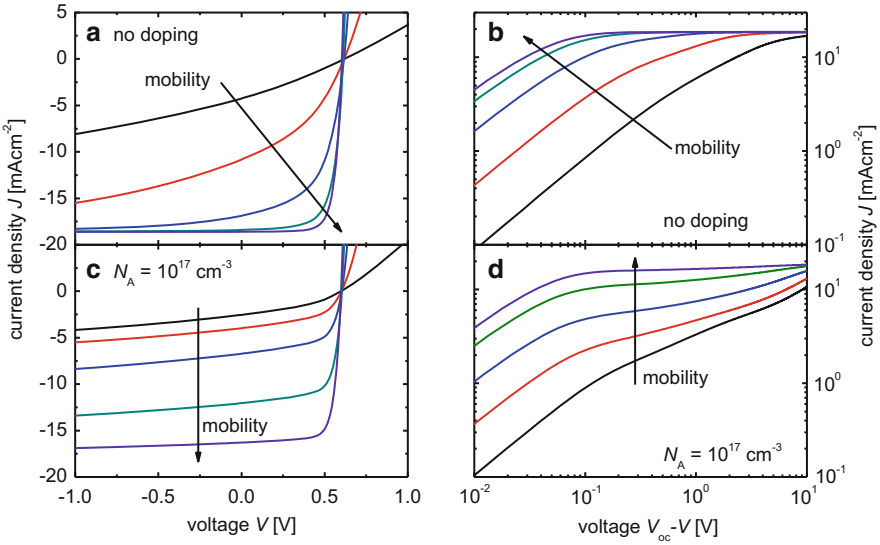

Fig. 4 Effect of mobility on the current/voltage curve of an organic solar cell ($d = 300$ nm) if (**a**, **b**) the absorber is completely intrinsic and (**c**, **d**) the absorber is strongly p-type ($N_A = 10^{17}$ cm^{-3}). In the case with doping, diffusion of charges through the neutral region is more important and so the photocurrent is less voltage dependent (FF is high but J_{sc} decreases strongly with mobility). If the current is plotted on a log-log scale, diffusion leads to a third intermediate slope (**d**), between the saturation region at large reverse bias and the region at around V_{oc}. For parameters see Table 1

see a third slope for intermediate voltages that becomes more pronounced for lower mobilities. This intermediate region has been interpreted alternatively as due to field dependent geminate recombination [74, 79] or due to spatial effects, where electrons have to diffuse through a mixed amorphous phase before they are transported through a fullerene-rich phase to the cathode [94]. Figure 4d shows that a third slope also occurs whenever charges have to diffuse through parts of the device with low electric fields. Although diffusion is completely field independent, the whole collection process is still slightly field dependent, as seen in Fig. 4d because the reverse bias slowly depletes the absorber and decreases the width of the field free zone.

The differences described in Fig. 4 are rather fundamental for photovoltaic devices. They show how to accommodate low mobilities or charge carrier lifetimes in different geometries. From an electrostatic point of view the major difference between different solar cells is the position of the main capacitor (the region where the built-in voltage drops), i.e. whether it lies on the periphery of the device or makes up a large part of the device volume. For low mobility solar cells it is usually beneficial to design the device such that the whole absorber is the capacitor, while for materials with long diffusion lengths, it is beneficial to have the space charge region on the periphery of the device to minimize the amount of recombination in the space charge region. Recombination in the space charge region is usually higher

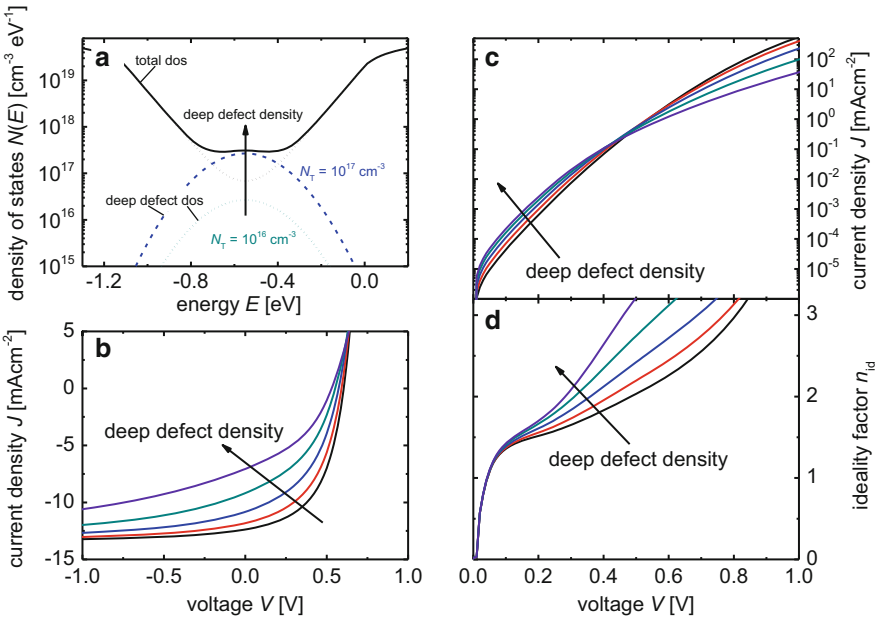

Fig. 5 Effect of the increase of the density of deep defects on the (**a**) total density of states, (**b**) the solar cell current voltage curve under illumination, (**c**) the current/voltage curve in the dark and (**d**) the ideality factor. For parameters, see Table 1

than in the neutral region (for a given density of traps), because the Shockley Read Hall statistics lead to maximum recombination if electron and hole concentration are of similar magnitude, as they are in the space charge region.

4.1.2 Relation Between the Density of Traps and the Current/Voltage Curve

Another example where numerical simulations bring additional benefit relative to analytical equations is when a direct relation is sought between the shape and magnitude of the subgap density of states and device performance. In a recent experimental study, Street and coworkers examined the effect of different trap states on the performance of PCDTBT:PCBM solar cells [53]. Using subgap quantum efficiency measurements they found that prolonged illumination leads to an increase in deep defects, which then leads to a decreased *FF* and device performance as well as increased ideality factors as derived from the dark current/voltage curve.

Figure 5 shows that these observations are consistent with generic simulations, where we add a deep defect at midgap and change the defect density (for simulation parameters see Table 1). Figure 5a shows the density of states used in the simulation. $E = 0$ eV is defined as the conduction band edge and $E = -1.1$ eV is the

valence band edge. In the middle at $E_t = -0.55$ eV, we add a defect of Gaussian shape with a width $\sigma_t = 0.15$ eV. At low defect densities $N_t < 10^{16}$ cm^{-3}, recombination via the exponential band tails dominates. At higher trap density, recombination via midgap defects becomes dominant and we observe that the performance is reduced (see Fig. 5b). The reduction in performance is due to a reduction in all three characteristic parameters, J_{sc}, V_{oc} and FF. Figure 5c shows the effect of the additional defects on the dark current voltage curve. More defects lead to an increased series resistance at high voltages and to a smaller slope of the exponential part at lower voltages (the shunt is chosen to have infinite resistance in the simulation). The increased series resistance shows that the deep defects have a detrimental effect on transport. The smaller slope at low bias can be interpreted as increased ideality factor (see Fig. 5d), as expected from a transition from recombination via band tails to recombination via deep traps. A detailed analysis of the relation between the density of states and the ideality factor has been published in [40].

4.2 Space Charge Limited Current Measurements

The preceding sections addressed the current/voltage curves of solar cells, i.e. two carrier devices. In organic photovoltaics, the measurement of single carrier devices with two electron or two hole injecting and extracting contacts is also relevant as a way of characterizing transport properties. By injecting only one type of carrier, the current voltage curve depends entirely on majority carrier properties, i.e. concentration and mobility of one carrier type. Recombination with the other carrier type is irrelevant as are the transport properties of the minorities. Thus, single carrier devices are a means to isolate certain properties of the material from others.

Contacting an n-type semiconductor with two electron injecting contacts, for instance, would lead to ohmic conduction with the current depending linearly on voltage, on mobility and on the concentration of free carriers as determined by the concentration of ionized dopants. In an intrinsic semiconductor with ohmic contacts, the injected charge carriers dominate the transport. The injected charge will determine the space charge, which will then, via Poisson's equation, control the band bending and the current density in the device. In this situation, the current will depend only on mobility and dielectric constant and is called space charge limited current. The current/voltage dependence is usually called the Mott–Gurney law:

$$J = \frac{9}{8}\varepsilon_0\varepsilon_r\mu\frac{V^2}{d^3}. \tag{23}$$

and is applicable to trap free and intrinsic semiconductors only. Although organic semiconductors are in general neither trap free nor intrinsic, the Mott–Gurney equation or variations of it like the Murgatroyd [222] or the Mark–Helfrich [223] equation are frequently used to determine the mobility in organic semiconductors [126, 167, 172–182, 224].

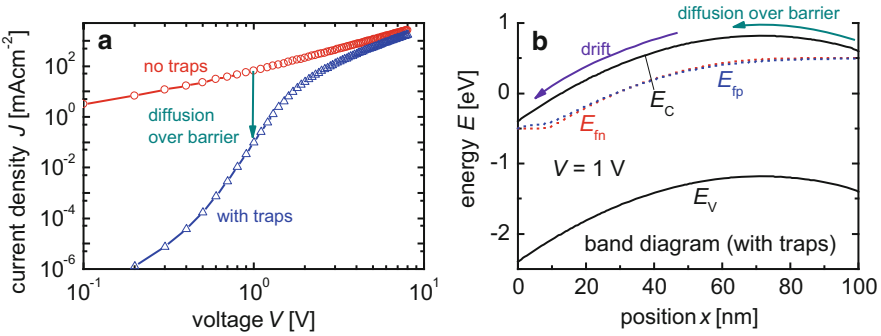

Fig. 6 (**a**) Simulated current/voltage curve of an electron-only device with and without p-type doping ($N_A = 10^{17}$ cm^{-3}). (**b**) Band diagram of the simulated electron-only device with doping. The diffusion over the barrier created by the negative charge of the ionized dopants is visible in the current/voltage curve as an increased voltage needed to get the same current. The effect disappears at higher voltages, when the voltage needed to overcome the barrier is negligible relative to the voltage dropping over the drift-dominated part of the device. E_{fn} and E_{fp} are the quasi-Fermi levels for electrons and holes and E_C and E_V are the conduction and valence band edge

The main assumptions that enter (23) are that the current is controlled purely by drift and not by diffusion, that the concentration of minority carriers is negligible and that the concentration of majority carriers is controlled only by the contacts and not by the properties of the semiconductor. Numerical simulations of single carrier devices become interesting, especially if some of these assumptions are no longer valid. One example is the situation where diffusion, rather than drift, becomes dominant. There are two obvious and relevant situations where diffusion might have a major impact on the current/voltage curve. If the two contacts have different work functions, the device has a built-in voltage while it may still be a single carrier device. That means one contact might inject electrons well and one contact has a slightly larger barrier for electron injection and extraction but still doesn't inject or extract holes. If the device is biased such that injection occurs at the contact with the smaller contact barrier, the electric field due to the built-in voltage will impede the transport of charges. Thus, charges first have to overcome this barrier by diffusion before drift dominated current sets in. An alternative case is if, for instance, a p-type semiconductor contacted with two electron injecting contacts. For current to flow, the electrons would have to diffuse over the barrier created by the negative charge of the p-type dopants and then only after overcoming the barrier space charge limited conduction would set in. Both configurations will therefore result in a current/voltage curve that could be described by a series connection of a diode with a perfect SCLC-type device.

Figure 6 shows the current/voltage curve (Fig. 6a) and the band diagram for an electron only device with a p-type dopant (Fig. 6b). Figure 6a shows that, relative to the undoped case, the current is greatly reduced at low voltages. This is due to the fact that part of the voltage is used to overcome the barrier that can be seen in

Fig. 6b. Only when the barrier is overcome does the current approach the situation without doping. Using numerical simulations like these might allow a correct determination of the properties of the defects (like depth and concentration) [126] and the mobility at the same time [138]. However, because the effect of a barrier due to doping is difficult to discriminate from a barrier due to a variation in workfunctions (a non-zero V_{bi}), the properties of the contacts have to be known precisely.

4.3 Transient Measurements

As mentioned in Sects. 3.2 and 3.3, transient electrical measurements are frequently used to characterize charge generation, recombination and transport in organic bulk-heterojunction solar cells. These techniques include transient photocurrent [37, 51, 52, 80, 81, 132, 148–150, 159, 196, 225–227] or transient photovoltage [31, 42, 148–152] methods and can be classified as either small or large signal perturbation techniques. One example is a large signal transient photocurrent technique called charge extraction that is used to analyze the density of states [54] by extracting the integrated photogenerated charge at different light intensities and bias conditions. In this method it is assumed that the spatial distribution of charge carriers is uniform, so that the measured photovoltage at a given light intensity can be considered as the Fermi level position within a representative density of states. Steady-state device simulations can be used to evaluate this method of obtaining a density of states from the extracted charge data. In a recent study [40] we have shown that the spatial distribution of charge carriers in the device has a major influence on the charge density vs open-circuit voltage relationship, which can make an interpretation of charge extraction data in terms of a density of states impossible.

Transient electrical data collected under different bias conditions contain enough information to determine the density of states with the aid of a transient device model. One study has shown that by simultaneously fitting a number of transient current measurements, as well as steady-state device response, a non-trivial best fit for the densities of sub gap electron and hole states could be obtained [86]. In a further application of the transient device simulation it has been shown that in certain conditions the transient current extracted from a solar cell device accurately reflects the density of states of the carrier type with the greater density of deep trap states [160]. In those conditions where this approximation is true, then transient current data can be modelled with a simple expression for current due to thermally emitted charge carriers, and the current transient mapped onto a density of states function [51, 52]. However, the approximation fails in the limit of significant recombination or low electric fields.

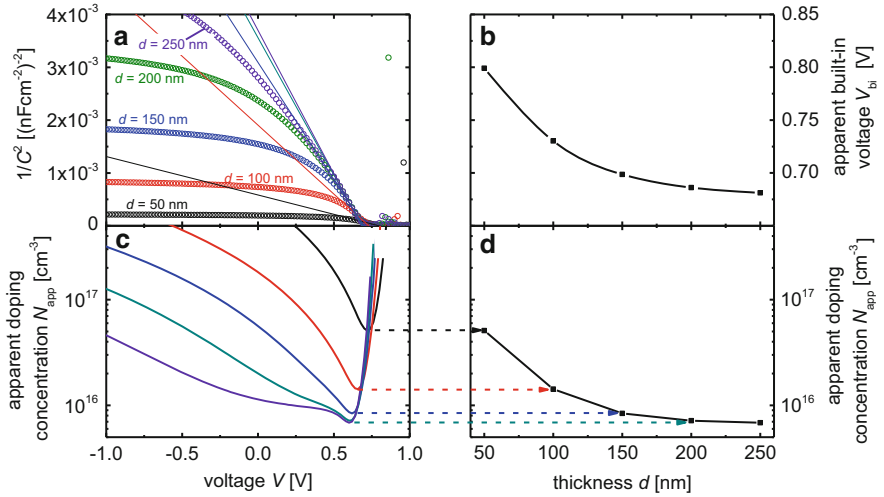

Fig. 7 (**a**) Mott–Schottky plot of a device with $N_A = 10^{16}$ cm^{-3} p-type doping and different thicknesses d between 50 and 250 nm. From the Mott–Schottky plot we derive (**b**) an apparent built-in voltage V_{bi} and from the derivative of C^{-2} vs V, we determine the apparent doping concentration N_{app} (**c**, **d**). (**c**) shows the derivative at every position while (**d**) shows only the minimum. These plots show that device thicknesses that are small relative to the width of the space charge region lead to erroneous values for the doping and the built-in voltage because of the influence of the geometric capacitance. In both cases, the values will be too high in thin devices

4.4 Capacitance/Voltage Measurements

We have seen above in our discussion of current/voltage curves both in diodes and single carrier devices that the concentration of defects and the presence of space charge due to charged defects or dopants have a major influence on the behaviour of thin-film solar cells. The measurement of the capacitance as a function of voltage is a useful way to analyze the fixed space charge as described in Sect. 3.5. These measurements of voltage dependent capacitance have to be done with devices that are sufficiently thick to ensure that the device is not fully depleted in the measurement range (say from −1 V to forward bias). Figure 7 shows how numerical simulations can help to explain what happens if this requirement is not met and the width of the space charge region is comparable to the device thickness [49] (for parameters used in the simulation see Table 2). This is relevant, because for normal device thicknesses of 100 nm the device would be fully depleted at short circuit and an analysis of the capacitance in terms of a doping concentration becomes impossible. It is therefore important to know how thick devices need to be for a correct analysis of the data and what the capacitance of an insufficiently thick solar cell looks like.

If the device thickness is sufficiently high, the Mott–Schottky plot [i.e. C^{-2} vs voltage; see (22)] yields a straight line over a considerable voltage range. At larger reverse bias, C^{-2} may saturate to a constant value. This indicates that the device is

Table 2 Parameters used for Fig. 7

Name	Symbol	
Electron mobility	μ_n (cm^2/Vs)	10^{-3}
Hole mobility	μ_p (cm^2/Vs)	10^{-3}
p-Type doping density	N_A (cm^{-3})	10^{16}
Effective density of states of the conduction band	N_C (cm^{-3})	10^{19}
Effective density of states of the conduction band of the valence band	N_V (cm^{-3})	10^{19}
Band gap	E_g (eV)	1.1
Surface recombination velocity	S (cm/s)	10^5
Contact barrier	φ_b (meV)	0

now fully depleted and the capacitance will approach the value of a plate capacitor with the plates separated by the device thickness. Figure 7a shows that the smaller the device thickness the lower the saturation value of C^{-2} and the higher the voltage at which the saturation happens. This saturation value also affects the slope of the linear part of C^{-2} vs voltage that is used to determine the doping and the built-in voltage. If we always fit a straight line precisely to the inflection point of the C^{-2}/V curve as shown in Fig. 7a, we obtain the built-in voltages as shown in Fig. 7b. Because of the influence of the saturation region on the slope, the V_{bi} increases for small thicknesses. The same happens for the doping concentration. If we apply (22) to the Mott–Schottky plots in Fig. 7a, we obtain the data shown in Fig. 7c. The inflection points of the Mott–Schottky plot correspond to the minima in Fig. 7c. These minima also decrease with increasing thickness as shown in Fig. 7d. Thus, a reasonable representation of the doping concentration is only possible at greater thicknesses. For the current example of $N_A = 10^{16}$ cm^{-3} we need thicknesses of $d > 200$ nm to get a result that is no longer affected by the geometrical capacitance.[4]

4.5 Optical Losses and Parasitic Absorption

In Sect. 2.1 we discussed the many applications of optical modelling for organic solar cells. The case study we chose to present as one application of optical modelling of organic solar cells is the analysis of parasitic absorption losses in the different layers of the solar cell stack. One example is shown in Fig. 8. We calculated the absorptance of each layer in a layer stack glass/ITO (160 nm)/poly(3,4-ethylenedioxythiophene):poly(styrenesulfonate) (PEDOT:PSS) (30 nm)/poly[(4,40-bis (2-ethylhexyl)dithieno [3,2-*b*:20,30-*d*]silole)-2,6-diyl-alt-(4,7-bis(2-thienyl)-2,1,3-benzothiadiazole)-5,50-diyl] (SiPCPDTBT):[6,6]-phenyl C71-butyric acid methyl ester ($PC_{71}BM$) (100 nm)/Ca (20 nm)/Al(100 nm). The transfer matrix formalism

[4] The frequency domain simulations done for Fig. 7 have been performed using the drift-diffusion simulator SCAPS, which is available from Prof. Marc Burgelman at the University of Ghent in Belgium [228, 229].

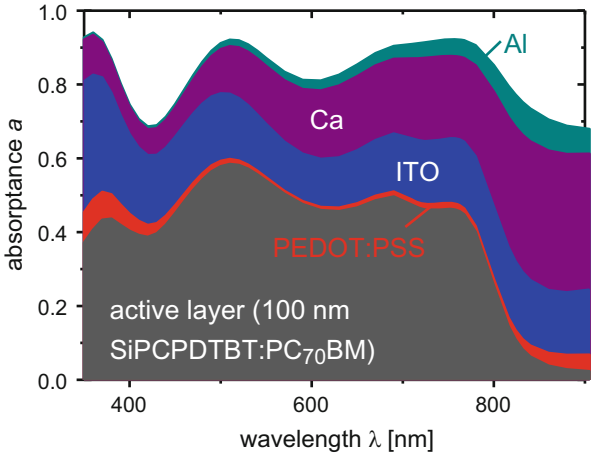

Fig. 8 Absorptance per layer, calculated for a layer stack glass/ITO (160 nm)/PEDOT:PSS (30 nm)/SiPCPDTBT:PC70BM (100 nm)/Ca (20 nm)/Al(100 nm). Note that the glass substrate is assumed to be perfectly transparent; thus, only the reflection at the air/glass and glass/ITO interfaces have been taken into account. Except for the glass substrate, the layers were modelled with a transfer matrix formalism to take interferences into account

allows us to calculate and visualize the parasitic absorption losses in the different layers. Calculations like this can be used for a variety of purposes. One would be to quantify the losses in the different layers other than the polymer:fullerene layer and to optimize their thickness such that the absorption in the active layer is maximized. Other applications would be to repeat this simulation for various thicknesses and to integrate the absorption in the active layer to obtain an estimate of the maximum possible photocurrent as a function of thickness. This can help to show the optimum thicknesses of the active layer based on the optics of the system. The more complex the system, the more simulations will be able to help the design by reducing the amount of trial and error necessary for optimization of devices. Thus, simulations of absorption in individual layers of tandem cells should be of great help for optimizing the layer thicknesses. If parameters for the electronic properties of the devices are available, the optical modelling can be combined with electrical modelling to produce a predictive tool for modelling the device performance of multijunction solar cells. This has been done before for thin-film silicon solar cells [230]), but not yet for organic multijunction solar cells.

Moreover, we can use the calculated absorptance of the active layer to determine the internal quantum efficiency (IQE) of a device and thereby quantify the electronic losses relative to the optical losses [112–114]. The IQE is the ratio of the measured external quantum efficiency to the absorptance of the active layer of the solar cell. However, because absorptance of the active layer alone cannot easily be measured, the most effective way to determine IQE is to calculate the absorptance of the active layer using the experimentally determined complex refractive indices of all layers (obtained using ellipsometry and sometimes photothermal deflection spectroscopy [230]).

5 Conclusions

In conclusion, we have shown that optical and electrical device modelling of organic bulk heterojunction solar cells is a useful tool to improve the interpretation of electrical and optoelectronic measurements. For organic solar cells, numerical simulations often give additional insight relative to simpler analytical approaches because of the large variations of charge density as a function of position and energy that are due to the presence of traps and doping as well as the small thicknesses typical for organic solar cells. Because optoelectronic device modelling requires the knowledge of a substantial amount of parameters, we discuss the characterization methods of relevance. These characterization methods will either allow us to determine some of the unknown parameters or the simulations may be used to determine parameters from the experimental data, because there may be no analytical model to determine the data otherwise. To illustrate some applications of optical and electrical device modelling we chose a series of relevant case studies discussing the effect of changes in parameters such as doping, trap concentration, thickness and mobility on simulated electrical measurements like current/voltage or capacitance/voltage measurements. Future developments in the field of device simulations might involve simulating a larger variety of more complex experiments. While currently simulations are often steady-state simulations used to analyze current/voltage curves, in future we will use more frequency domain and time-domain drift-diffusion simulations to simulate directly complex experiments like transient photocurrent measurements or impedance measurements.

Acknowledgements T. K. acknowledges support by an Imperial College Junior Research Fellowship. J. N. acknowledges support from the Engineering and Physical Sciences Research Council (EP/J500021/1 and EP/G031088/1) and the Royal Society through an Industry Fellowship.

Appendix 1: Transfer Matrix Formalism

There have been plenty of descriptions in the literature of the transfer matrix formalism for computing the position dependent generation rate in a multilayer stack with flat interfaces [43–45, 115, 231]. Thus, we will not repeat the whole derivation, but instead give a short summary of the underlying idea. The situation most relevant for organic solar cells is that of normal incidence of light on a glass substrate with a thickness much larger than the wavelength of light followed by several layers with thicknesses comparable or smaller than the wavelength of light. Thus, the glass substrate is first treated incoherently with Lambert–Beer and then the following multi-layer stack is treated with the transfer matrix formalism. Figure 9 shows the general layout of the problem. Light is incident from the left, perpendicular to the surface of the solar cell. To calculate the left and right going electric fields in any layer as a function of the electric fields at the interface between

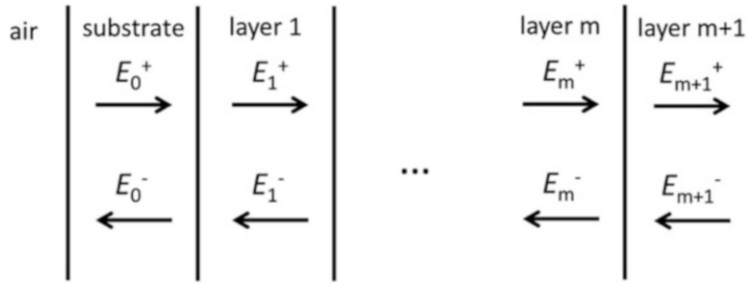

Fig. 9 Definition of the electric fields in a multilayer stack consisting of m layers. The matrix transfer formalism uses a matrix for every interface and every layer to express the in- and outgoing electric field on the left of the stack to the in- and outgoing electric field on the right of the stack. With this formalism we can calculate the electric field everywhere in the device and finally the position dependent generation rate

substrate and first layer, we need to define matrices for each interface and each layer. The interface between layers j and k is represented by one interface matrix [43, 44]

$$M_{\mathrm{jk}}^{\mathrm{I}} = \frac{1}{t_{\mathrm{jk}}} \begin{pmatrix} 1 & r_{\mathrm{jk}} \\ r_{\mathrm{jk}} & 1 \end{pmatrix}. \tag{24}$$

where

$$r_{\mathrm{jk}} = \frac{\widetilde{n}_{\mathrm{j}} - \widetilde{n}_{\mathrm{k}}}{\widetilde{n}_{\mathrm{j}} + \widetilde{n}_{\mathrm{k}}} \tag{25}$$

and

$$t_{\mathrm{jk}} = \frac{2\widetilde{n}_{\mathrm{j}}}{\widetilde{n}_{\mathrm{j}} + \widetilde{n}_{\mathrm{k}}} \tag{26}$$

are the Fresnel reflection and transmission coefficients for the special case of normal incidence. The layers are characterized by their complex refractive index $\widetilde{n}_{\mathrm{j}} = n_{\mathrm{j}} + ik_{\mathrm{j}}$ and their thickness d_{j}. The thickness becomes relevant for the calculation of the layer matrix [43, 44]

$$M_{\mathrm{j}}^{\mathrm{L}} = \begin{pmatrix} \exp\left(-i\dfrac{2\pi\widetilde{n}_{\mathrm{j}}d_{\mathrm{j}}}{\lambda}\right) & 0 \\ 0 & \exp\left(i\dfrac{2\pi\widetilde{n}_{\mathrm{j}}d_{\mathrm{j}}}{\lambda}\right) \end{pmatrix}. \tag{27}$$

Using the interface and layer matrices, we can express the electric field everywhere in the device as a function of the incoming and outgoing electric field E_0 at the interface between substrate and first layer via

$$\begin{pmatrix} E_0^+ \\ E_0^- \end{pmatrix} = M_{01}^{\mathrm{I}} M_1^{\mathrm{L}} M_{12}^{\mathrm{I}} \ldots M_m^{\mathrm{L}} M_{mm+1}^{\mathrm{I}} \begin{pmatrix} E_{m+1}^+ \\ E_{m+1}^- \end{pmatrix}. \tag{28}$$

Using this concept the electric field everywhere in the device can be calculated which we can use for the calculation of the generation rate at any position x.

The group of Prof. McGehee in Stanford offers a free transfer matrix modelling code on their homepage. The code is available in Matlab and Python and contains a database with the complex refractive indices of common materials of relevance for photovoltaics. More information is available on http://www.stanford.edu/group/mcgehee/transfermatrix/ (accessed 3/1/2013).

Appendix 2: Shockley–Read–Hall Recombination

Let us assume we are dealing with a trap level in the band gap as shown in Fig. 10. To understand how much recombination would be caused by this trap level we would need to know the occupation of that trap level. Initially we would not know which quasi-Fermi level (electrons or holes) would control the occupation of that trap level. This would also depend on how much interaction that trap level has with the conduction band and the valence band. It would depend on whether the trap level is a trap in the fullerene phase, in the polymer phase or at the interface of both. In addition, especially, if the trap can easily interact with both conduction and valence band, we will see that neither the electron nor hole quasi-Fermi level will be able to control the occupation probability of this trap. Instead, we would have to define a new occupation statistics for the trap that is different from that of both conduction and valence band. This new occupation statistics would not necessarily look like a Fermi–Dirac statistics so we might not be able to define a quasi-Fermi level for a trap at all.

To find the occupation statistics for a trap – the Shockley–Read–Hall statistics [232, 233] – we need to consider the four processes shown in Fig. 10. A single trap can capture and emit an electron and capture and emit a hole. If the same trap captures a hole and an electron, one recombination event happens. If a trap captures and emits an electron *or* a hole, the trap will have slowed down transport only. Table 3 summarizes the four rates that we need to consider. However, the four rates are not independent of each other in quasi-equilibrium. Because in equilibrium, detailed balance between inverse processes must be obeyed, the capture and emission processes must be connected. In addition, in thermal equilibrium the occupation function for all charge carriers (free or trapped, electrons or holes) must be the Fermi–Dirac function in thermal equilibrium, i.e.

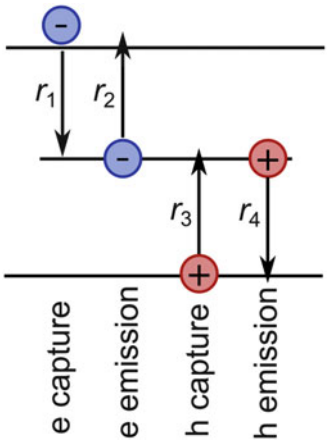

Fig. 10 Definition of the four rates of capture and emission of electrons and holes by a single trap level. These four rate equations are the basis of Shockley–Read–Hall statistics, which defines the occupation probability and the recombination rate via this trap

$$f_{\text{theq}} = \frac{1}{\left[1 + \exp\left(\frac{E - E_{\text{F}}}{kT}\right)\right]}. \tag{29}$$

Thus, we can connect the capture coefficients $\beta_{\text{n,p}}$ and the emission coefficients $e_{\text{n,p}}$ using the conditions $r_1(f_{\text{theq}}) = r_2(f_{\text{theq}})$ and $r_3(f_{\text{theq}}) = r_4(f_{\text{theq}})$. This leads to the conditions

$$\begin{aligned} e_{\text{n}} &= \beta_{\text{n}} N_{\text{c}} \exp\left(\frac{E_{\text{t}} - E_{\text{c}}}{kT}\right) \\ e_{\text{p}} &= \beta_{\text{p}} N_{\text{v}} \exp\left(\frac{E_{\text{v}} - E_{\text{t}}}{kT}\right), \end{aligned} \tag{30}$$

where we used $n = N_{\text{c}} \exp(-(E_{\text{c}} - E_{\text{F}})/kT)$ and $p = N_{\text{v}} \exp((E_{\text{v}} - E_{\text{F}})/kT)$. Now, we can compute the steady-state but non-equilibrium solution for the occupation probability f. Steady state means that the occupation probability of the trap does not change over time. Therefore, the rates need to obey

$$r_1 - r_2 = r_3 - r_4. \tag{31}$$

Using (30) and (31) and the rates defined in Table 3, we can calculate the occupation probability f_{srh} of our trap level as

$$f_{\text{srh}} = \frac{n\beta_{\text{n}} + e_{\text{p}}}{n\beta_{\text{n}} + p\beta_{\text{p}} + e_{\text{n}} + e_{\text{p}}} \tag{32}$$

Note that this occupation probability has indeed no longer the same shape as a Fermi–Dirac distribution. Instead of one inflection point (the Fermi level in Fermi–Dirac statistics), there are two inflection points that are sometimes called quasi-Fermi levels for trapped charge [234, 235].

Table 3 Capture and emission rates of single electron trap states

Process	Symbol	Rate
Electron capture	r_1	$\beta_n n p_t = \beta_n n N_t (1 - f)$
Electron emission	r_2	$e_n n_t = e_n N_t f$
Hole capture	r_3	$\beta_p p n_t = \beta_p p N_t f$
Hole emission	r_4	$e_p p_t = e_p N_t (1 - f)$

The rates are defined in Fig. 10. Note that the occupation probability f is defined by Fermi–Dirac statistics in thermal equilibrium but by Shockley–Read–Hall statistics in non-equilibrium. The capture coefficients are denoted by $\beta_{n,p}$ and the emission coefficients by $e_{n,p}$

Either from r_1 to r_2 or from r_3 to r_4, we can now calculate the net recombination rate R via the trap or indeed any distribution $N_t(E)$ of traps via

$$R = \int_{E_v}^{E_c} N_t(E) \beta_n \beta_p \frac{np - n_i^2}{n\beta_n + p\beta_p + e_n + e_p} \mathrm{d}E. \tag{33}$$

Thus, in the case of a single trap level with concentration N_t, the recombination rate would be

$$R = N_t \beta_n \beta_p \frac{np - n_i^2}{n\beta_n + p\beta_p + e_n + e_p}. \tag{34}$$

which is the result often found in textbooks.

Appendix 3: Software

In the following, we will briefly discuss some programs the authors have used and found helpful for doing simulations of thin-film solar cells. The first two programs (ASA, SCAPS) are developed for inorganic solar cells but provide the basic functionality necessary for one-dimensional effective medium simulations. In all cases, detailed information is available on the respective homepages, so the main aim of this section is to make the reader aware of the existence of certain tools rather than to give a detailed assessment of the capabilities of the programs.

ASA (Zeman Group, Delft)

ASA (Advanced Semiconductor Analysis) has been developed by the group of Prof. Miro Zeman at the Technical University of Delft in the Netherlands as simulation software optimized for amorphous silicon solar cells [236]. Because of this focus on amorphous silicon, the software has several features that make it advantageous for

one-dimensional drift-diffusion simulations of organic semiconductors as well. ASA can simulate both the spatially resolved generation rate based on a transfer matrix formalism and the electrical transport and recombination of charges in a multilayer system with a distribution of subgap defects. ASA allows the use of two exponential band tails and one amphoteric Gaussian defect. The inclusion of optical models means that electro-optical simulations are very simple. ASA works by reading in scripts containing the input parameters. It is therefore possible to change variables in these scripts using external programming languages or software like Matlab and therefore control the whole software via external scripts. Figures for this review have been made mostly using ASA and loops to change variables were written in Matlab. This flexibility allows users to use ASA in innovative ways that have nothing to do with the original application of amorphous Si solar cells. One option is to include field dependent photogeneration [75]. This can be done by running ASA once using field independent photogeneration, then reading in the optical generation and the electric field calculated by ASA and finally repeating the electrical calculation until the field no longer changes. Using this technique it is possible to use a commercially available drift-diffusion simulator and concentrate on adding extra features without needing to access the source code of ASA.

Because of the focus of thin-film silicon research on light trapping schemes to optimize light absorption, ASA also contains models to deal with light trapping and to allow the calculation of photogeneration rates with rough scattering surfaces. This may be advantageous for future work on light trapping in organic solar cells as well [237]. In addition, ASA is well suited to model tandem solar cells, also a typical application for thin-film silicon solar cells [230] and likely to be of increasing relevance for organic photovoltaics [15, 238, 239].

ASA is sold by the TU Delft. More information on ASA can be found under the following URL: http://www.ewi.tudelft.nl/en/the-faculty/departments/electrical-sustainable-energy/photovoltaic-materials-and-devices/asa-software/ (accessed 3/1/2013)

SCAPS (Burgelman Group, Ghent)

SCAPS (Solar Cell Capacitance Simulator) is software developed by the group of Prof. Marc Burgelman at the University of Ghent in Belgium. It was originally developed for use with compound semiconductor thin-film photovoltaics, i.e. for devices based on Cu(In,Ga)Se_2 or CdTe absorbers [228, 229, 240, 241]. However, the electrical models provide a basic functionality similar to that of ASA without having sophisticated optical models. Generation rates calculated with a transfer matrix formalism (which can be done with freeware as shown below) can be imported. The main advantage of SCAPS is that not only steady-state simulations but also frequency domain simulations can be performed. This option allows one to model the capacitance as a function of voltage, frequency and temperature and to use SCAPS for interpretation of impedance spectra [136] and Mott–Schottky plots

[49]. In addition, SCAPS is comparatively easy to learn and intuitive to control. More information on SCAPS can be found under the following URL: http://users.elis.ugent.be/ELISgroups/solar/projects/scaps/

References

1. Li G, Zhu R, Yang Y (2012) Nat Photonics 6:153
2. Nelson J (2011) Mater Today 14:462
3. Graetzel M, Janssen RAJ, Mitzi DB, Sargent EH (2012) Nature 488:304
4. Sargent EH (2009) Nat Photonics 3:325
5. Ip AH, Thon SM, Hoogland S, Voznyy O, Zhitomirsky D, Debnath R, Levina L, Rollny LR, Carey GH, Fischer A, Kemp KW, Kramer IJ, Ning ZJ, Labelle AJ, Chou KW, Amassian A, Sargent EH (2012) Nat Nanotechnol 7:577
6. Semonin OE, Luther JM, Choi S, Chen HY, Gao JB, Nozik AJ, Beard MC (2011) Science 334:1530
7. Rath AK, Bernechea M, Martinez L, de Arquer FPG, Osmond J, Konstantatos G (2012) Nat Photonics 6:529
8. Li G, Shrotriya V, Huang JS, Yao Y, Moriarty T, Emery K, Yang Y (2005) Nat Mater 4:864
9. Kim Y, Cook S, Tuladhar SM, Choulis SA, Nelson J, Durrant JR, Bradley DDC, Giles M, McCulloch I, Ha CS, Ree M (2006) Nat Mater 5:197
10. Peet J, Kim JY, Coates NE, Ma WL, Moses D, Heeger AJ, Bazan GC (2007) Nat Mater 6:497
11. Park SH, Roy A, Beaupre S, Cho S, Coates N, Moon JS, Moses D, Leclerc M, Lee K, Heeger AJ (2009) Nat Photonics 3:297
12. Chen HY, Hou JH, Zhang SQ, Liang YY, Yang GW, Yang Y, Yu LP, Wu Y, Li G (2009) Nat Photonics 3:649
13. He ZC, Zhong CM, Huang X, Wong WY, Wu HB, Chen LW, Su SJ, Cao Y (2011) Adv Mater 23:4636
14. Small CE, Chen S, Subbiah J, Amb CM, Tsang SW, Lai TH, Reynolds JR, So F (2012) Nat Photonics 6:115
15. Dou LT, You JB, Yang J, Chen CC, He YJ, Murase S, Moriarty T, Emery K, Li G, Yang Y (2012) Nat Photonics 6:180
16. He ZC, Zhong CM, Su SJ, Xu M, Wu HB, Cao Y (2012) Nat Photonics 6:591
17. Green MA, Emery K, Hishikawa Y, Warta W, Dunlop ED (2012) Prog Photovoltaics 20:606
18. Halls JJM, Walsh CA, Greenham NC, Marseglia EA, Friend RH, Moratti SC, Holmes AB (1995) Nature 376:498
19. Yu G, Gao J, Hummelen JC, Wudl F, Heeger AJ (1995) Science 270:1789
20. Brabec CJ, Gowrisanker S, Halls JJM, Laird D, Jia SJ, Williams SP (2010) Adv Mater 22:3839
21. Scharber MC, Wuhlbacher D, Koppe M, Denk P, Waldauf C, Heeger AJ, Brabec CL (2006) Adv Mater 18:789
22. Vandewal K, Gadisa A, Oosterbaan WD, Bertho S, Banishoeib F, Van Severen I, Lutsen L, Cleij TJ, Vanderzande D, Manca JV (2008) Adv Funct Mater 18:2064
23. Vandewal K, Ma Z, Bergqvist J, Tang Z, Wang E, Henriksson P, Tvingstedt K, Andersson MR, Zhang F, Inganas O (2012) Adv Energy Mater 22:3480
24. Faist MA, Kirchartz T, Gong W, Ashraf RS, McCulloch I, de Mello JC, Ekins-Daukes NJ, Bradley DDC, Nelson J (2012) J Am Chem Soc 134:685
25. Brabec CJ, Heeney M, McCulloch I, Nelson J (2011) Chem Soc Rev 40:1185
26. Deibel C, Strobel T, Dyakonov V (2009) Phys Rev Lett 103
27. McMahon DP, Cheung DL, Troisi A (2011) J Phys Chem Lett 2:2737

28. Grancini G, Maiuri M, Fazzi D, Petrozza A, Egelhaaf HJ, Brida D, Cerullo G, Lanzani G (2013) Nat Mater 12:29
29. Price SC, Stuart AC, Yang LQ, Zhou HX, You W (2011) J Am Chem Soc 133:4625
30. Peet J, Wen L, Byrne P, Rodman S, Forberich K, Shao Y, Drolet N, Gaudiana R, Dennler G, Waller D (2011) Appl Phys Lett 98:043301
31. Credgington D, Hamilton R, Atienzar P, Nelson J, Durrant JR (2011) Adv Funct Mater 21:2744
32. Roichman Y, Tessler N (2002) Appl Phys Lett 80:1948
33. Roichman Y, Preezant Y, Tessler N (2004) Physica Status Solidi A Appl Res 201:1246
34. Arora ND, Chamberlain SG, Roulston DJ (1980) Appl Phys Lett 37:325
35. Wurfel P, Trupke T, Puzzer T, Schaffer E, Warta W, Glunz SW (2007) J Appl Phys 101:123110
36. Kirchartz T, Helbig A, Rau U (2008) Sol Energ Mat Sol C 92:1621
37. Shuttle CG, Hamilton R, Nelson J, O'Regan BC, Durrant JR (2010) Adv Funct Mater 20:698
38. Montero JM, Bisquert J (2011) Solid State Electron 55:1
39. Deibel C, Wagenpfahl A, Dyakonov V (2009) Phys Rev B 80
40. Kirchartz T, Nelson J (2012) Phys Rev B 86:165201
41. Cowan SR, Roy A, Heeger AJ (2010) Phys Rev B 82:245207
42. Dibb GFA, Kirchartz T, Credgington D, Durrant JR, Nelson J (2011) J Phys Chem Lett 2:2407
43. Sievers DW, Shrotriya V, Yang Y (2006) J Appl Phys 100:114509
44. Pettersson LAA, Roman LS, Inganas O (1999) J Appl Phys 86:487
45. Peumans P, Yakimov A, Forrest SR (2003) J Appl Phys 93:3693
46. Ojala A, Petersen A, Fuchs A, Lovrincic R, Polking C, Trollmann J, Hwang J, Lennartz C, Reichelt H, Hoffken HW, Pucci A, Erk P, Kirchartz T, Wurthner F (2012) Adv Funct Mater 22:86
47. Petersen A, Ojala A, Kirchartz T, Wagner TA, Wurthner F, Rau U (2012) Phys Rev B 85:245208
48. Bisquert J, Garcia-Belmonte G (2011) J Phys Chem Lett 2:1950
49. Kirchartz T, Gong W, Hawks SA, Agostinelli T, MacKenzie RCI, Yang Y, Nelson J (2012) J Phys Chem C 116:7672
50. Mingebach M, Deibel C, Dyakonov V (2011) Phys Rev B 84:153201
51. Street RA, Song KW, Northrup JE, Cowan S (2011) Phys Rev B 83:165207
52. Street RA (2011) Phys Rev B 84:075208
53. Street RA, Krakaris A, Cowan SR (2012) Adv Funct Mater 22:4608
54. Kirchartz T, Pieters BE, Kirkpatrick J, Rau U, Nelson J (2011) Phys Rev B 83:115209
55. Brendel R, Rau U (1999) J Appl Phys 85:3634
56. Kirchartz T, Ding K, Rau U (2011) Fundamental electrical characterization of thin-film solar cells. In: Abou-Ras D, Kirchartz T, Rau U (eds) Advanced characterization techniques for thin film solar cells. Wiley-VCH, Weinheim, Chap 2, p 33
57. Street RA, Song KW, Cowan S (2011) Org Electron 12:244
58. Kirchartz T, Agostinelli T, Campoy-Quiles M, Gong W, Nelson J (2012) J Phys Chem Lett 3:3470
59. Hecht Z (1932) Z Phys A 77:235
60. Crandall RS (1982) J Appl Phys 53:3350
61. Street RA, Schoendorf M, Roy A, Lee JH (2010) Phys Rev B 81:205307
62. Tumbleston JR, Liu YC, Samulski ET, Lopez R (2012) Adv Energy Mater 2:477
63. Waldauf C, Scharber MC, Schilinsky P, Hauch JA, Brabec CJ (2006) J Appl Phys 99:104503
64. Crandall RS (1983) J Appl Phys 54:7176
65. Crandall RS (1984) J Appl Phys 55:4418
66. Taretto K, Rau U, Werner JH (2003) Appl Phys A-Mater 77:865
67. Taretto K (2012) Prog Photovoltaics; doi: 10.1002/pip.2325
68. Savoie BM, Movaghar B, Marks TJ, Ratner MA (2013) J Phys Chem Lett 4:704

69. Koster LJA, Smits ECP, Mihailetchi VD, Blom PWM (2005) Phys Rev B 72:085205
70. Onsager L (1934) J Chem Phys 2:599
71. Braun CL (1984) J Chem Phys 80:4157
72. Gommans HHP, Kemerink M, Kramer JM, Janssen RAJ (2005) Appl Phys Lett 87:122104
73. Deibel C, Wagenpfahl A, Dyakonov V (2008) Phys Status Solidi-R 2:175
74. Limpinsel M, Wagenpfahl A, Mingebach M, Deibel C, Dyakonov V (2010) Phys Rev B 81:085203
75. Kirchartz T, Pieters BE, Taretto K, Rau U (2008) J Appl Phys 104:094513
76. Hausermann R, Knapp E, Moos M, Reinke NA, Flatz T, Ruhstaller B (2009) J Appl Phys 106:104507
77. Soldera M, Taretto K, Kirchartz T (2012) Phys Status Solidi A 209:207
78. Mihailetchi VD, Wildeman J, Blom PWM (2005) Phys Rev Lett 94:126602
79. Mihailetchi VD, Koster LJA, Hummelen JC, Blom PWM (2004) Phys Rev Lett 93:216601
80. Street RA, Cowan S, Heeger AJ (2010) Phys Rev B 82:121301
81. Shuttle CG, Hamilton R, O'Regan BC, Nelson J, Durrant JR (2010) Proc Natl Acad Sci U S A 107:16448
82. Jamieson FC, Agostinelli T, Azimi H, Nelson J, Durrant JR (2010) J Phys Chem Lett 1:3306
83. Mandoc MM, Kooistra FB, Hummelen JC, de Boer B, Blom PWM (2007) Appl Phys Lett 91
84. Hwang I, McNeill CR, Greenham NC (2009) J Appl Phys 106:094506
85. MacKenzie RCI, Kirchartz T, Dibb GFA, Nelson J (2011) J Phys Chem C 115:9806
86. MacKenzie RCI, Shuttle CG, Chabinyc ML, Nelson J (2012) Adv Energy Mater 2:662
87. Blakesley JC, Neher D (2011) Phys Rev B 84:075210
88. Schafer S, Petersen A, Wagner TA, Kniprath R, Lingenfelser D, Zen A, Kirchartz T, Zimmermann B, Wurfel U, Feng XJ, Mayer T (2011) Phys Rev B 83:165311
89. Tachiya M, Seki K (2010) Phys Rev B 82:085201
90. Ray B, Nair PR, Alam MA (2011) Sol Energ Mat Sol C 95:3287
91. Ray B, Alam MA (2011) Appl Phys Lett 99:033303
92. Ray B, Alam MA (2012) Sol Energ Mat Sol C 99:204
93. Stelzl FF, Wurfel U (2012) Phys Rev B 86:075315
94. Maturova K, van Bavel SS, Wienk MM, Janssen RAJ, Kemerink M (2009) Nano Lett 9:3032
95. Maturova K, Kemerink M, Wienk MM, Charrier DSH, Janssen RAJ (2009) Adv Funct Mater 19:1379
96. Maturova K, Janssen RAJ, Kemerink M (2010) ACS Nano 4:1385
97. Maturova K, van Bavel SS, Wienk MM, Janssen RAJ, Kemerink M (2011) Adv Funct Mater 21:261
98. Yu ZG, Smith DL, Saxena A, Martin RL, Bishop AR (2001) Phys Rev B 63:085202
99. Barth S, Wolf U, Bassler H, Muller P, Riel H, Vestweber H, Seidler PF, Riess W (1999) Phys Rev B 60:8791
100. Bassler H (1993) Physica Status Solidi B-Basic Res 175:15
101. Nelson J (2003) Phys Rev B 67:155209
102. Offermans T, Meskers SCJ, Janssen RAJ (2005) Chem Phys 308:125
103. van Eersel H, Janssen RAJ, Kemerink M (2012) Adv Funct Mater 22:2700
104. Peumans P, Uchida S, Forrest SR (2003) Nature 425:158
105. Watkins PK, Walker AB, Verschoor GLB (2005) Nano Lett 5:1814
106. Frost JM, Cheynis F, Tuladhar SM, Nelson J (2006) Nano Lett 6:1674
107. Greenham NC, Bobbert PA (2003) Phys Rev B 68:245301
108. Groves C, Blakesley JC, Greenham NC (2010) Nano Lett 10:1063
109. Groves C, Greenham NC (2013) Monte Carlo simulations of organic photovoltaics. Top Curr Chem. doi:10.1007/128_2013_467
110. Christ NS, Kettlitz SW, Valouch S, Zufle S, Gartner C, Punke M, Lemmer U (2009) J Appl Phys 105:104513
111. Brenner TJK, Hwang I, Greenham NC, McNeill CR (2010) J Appl Phys 107:114501

112. Slooff LH, Veenstra SC, Kroon JM, Moet DJD, Sweelssen J, Koetse MM (2007) Appl Phys Lett 90:143506
113. Burkhard GF, Hoke ET, McGehee MD (2010) Adv Mater 22:3293
114. Burkhard GF, Hoke ET, Scully SR, McGehee MD (2009) Nano Lett 9:4037
115. Lee J, Vandewal K, Yost SR, Bahlke ME, Goris L, Baldo MA, Manca JV, Van Voorhis T (2010) J Am Chem Soc 132:11878
116. Battaglia C, Escarre J, Soderstrom K, Charriere M, Despeisse M, Haug FJ, Ballif C (2011) Nat Photonics 5:535
117. Battaglia C, Hsu CM, Soderstrom K, Escarre J, Haug FJ, Charriere M, Boccard M, Despeisse M, Alexander DTL, Cantoni M, Cui Y, Ballif C (2012) ACS Nano 6:2790
118. Deckman HW, Wronski C, Witzke H, Yablonovitch E (1982) J Opt Soc Am 72:1745
119. Upping J, Bielawny A, Wehrspohn RB, Beckers T, Carius R, Rau U, Fahr S, Rockstuhl C, Lederer F, Kroll M, Pertsch T, Steidl L, Zentel R (2011) Adv Mater 23:3896
120. Rockstuhl C, Fahr S, Lederer F, Bittkau K, Beckers T, Carius R (2008) Appl Phys Lett 93:061105
121. Fahr S, Rockstuhl C, Lederer F (2008) Appl Phys Lett 92:171114
122. Rockstuhl C, Fahr S, Bittkau K, Beckers T, Carius R, Haug FJ, Soderstrom T, Ballif C, Lederer F (2010) Opt Express 18:A335
123. Fahr S, Kirchartz T, Rockstuhl C, Lederer F (2011) Opt Express 19:A865
124. Garcia-Belmonte G, Bisquert J (2010) Appl Phys Lett 96:113301
125. Stallinga P (2011) Adv Mater 23:3356
126. Nicolai HT, Kuik M, Wetzelaer GAH, de Boer B, Campbell C, Risko C, Bredas JL, Blom PWM (2012) Nat Mater 11:882
127. Street RA, Northrup JE, Krusor BS (2012) Phys Rev B 85:205211
128. Sah C-T, Shockley W (1958) Phys Rev 109:1103
129. Pieters BE (2008) Characterization of thin-film silicon materials and solar cells through numerical modelling. PhD Thesis, Delft University of Technology, Delft
130. Riede M, Mueller T, Tress W, Schueppel R, Leo K (2008) Nanotechnology 19
131. Glatthaar M, Mingirulli N, Zimmermann B, Ziegler T, Kern R, Niggemann M, Hinsch A, Gombert A (2005) Phys Status Solidi A 202:R125
132. Morfa AJ, Nardes AM, Shaheen SE, Kopidakis N, van de Lagemaat J (2011) Adv Funct Mater 21:2580
133. Bisquert J, Garcia-Belmonte G, Munar A, Sessolo M, Soriano A, Bolink HJ (2008) Chem Phys Lett 465:57
134. Abdou MSA, Orfino FP, Son Y, Holdcroft S (1997) J Am Chem Soc 119:4518
135. Boix PP, Garcia-Belmonte G, Munecas U, Neophytou M, Waldauf C, Pacios R (2009) Appl Phys Lett 95:233302
136. Khelifi S, Decock K, Lauwaert J, Vrielinck H, Spoltore D, Piersimoni F, Manca J, Belghachi A, Burgelman M (2011) J Appl Phys 110:094509
137. Dibb GFA, Muth M, Kirchartz T, Engmann S, Hoppe H, Gobsch G, Thelakatt M, Orozco MC, Durrant JR, Nelson J (2013) Influence of space charge and doping on charge carrier collection in normal and inverted geometry polymer:fullerene solar cells (Unpublished)
138. Kirchartz T (2013) Beilstein J Nanotechnol 4:180
139. Liang ZQ, Gregg BA (2012) Adv Mater 24:3258
140. Guerrero A, Marchesi LF, Boix PP, Ruiz-Raga S, Ripolles-Sanchis T, Garcia-Belmonte G, Bisquert J (2012) ACS Nano 6:3453
141. Scharfetter DL, Gummel HK (1969) IEEE Trans Electron Devices 16:64
142. Gummel HK (1964) IEEE Trans Electron Devices 11:455
143. Selberherr S (1984) Analysis and simulation of semiconductor devices. Springer-Verlag, Wien
144. Marsillac S, Sestak MN, Li J, Collins RW (2011) Spectroscopic ellipsometry. In: Abou-Ras D, Kirchartz T, Rau U (eds) Advanced characterization techniques for thin film solar cells. Wiley-VCH, Weinheim, Chap 6, p 125

145. Goris L, Poruba A, Hod'akova L, Vanecek M, Haenen K, Nesladek M, Wagner P, Vanderzande D, De Schepper L, Manca JV (2006) Appl Phys Lett 88:052113
146. Goris L, Haenen K, Nesladek M, Wagner P, Vanderzande D, De Schepper L, D'Haen J, Lutsen L, Manca JV (2005) J Mater Sci 40:1413
147. Holcombe TW, Norton JE, Rivnay J, Woo CH, Goris L, Piliego C, Griffini G, Sellinger A, Bredas JL, Salleo A, Frechet JMJ (2011) J Am Chem Soc 133:12106
148. Shuttle CG, O'Regan B, Ballantyne AM, Nelson J, Bradley DDC, de Mello J, Durrant JR (2008) Appl Phys Lett 92:093311
149. Shuttle CG, O'Regan B, Ballantyne AM, Nelson J, Bradley DDC, Durrant JR (2008) Phys Rev B 78:113201
150. Shuttle CG, Maurano A, Hamilton R, O'Regan B, de Mello JC, Durrant JR (2008) Appl Phys Lett 93:183501
151. Credgington D, Jamieson FC, Walker B, Nguyen TQ, Durrant JR (2012) Adv Mater 24:2135
152. Credgington D, Durrant JR (2012) J Phys Chem Lett 3:1465
153. Etzold F, Howard IA, Mauer R, Meister M, Kim TD, Lee KS, Baek NS, Laquai F (2011) J Am Chem Soc 133:9469
154. Boix PP, Guerrero A, Marchesi LF, Garcia-Belmonte G, Bisquert J (2011) Adv Energy Mater 1:1073
155. Guerrero A, Marchesi LF, Boix PP, Bisquert J, Garcia-Belmonte G (2012) J Phys Chem Lett 3:1386
156. Boix PP, Ajuria J, Pacios R, Garcia-Belmonte G (2011) J Appl Phys 109
157. Gong W, Faist MA, Ekins-Daukes NJ, Xu Z, Bradley DDC, Nelson J, Kirchartz T (2012) Phys Rev B 86:024201
158. Christ N, Kettlitz SW, Zuefle S, Valouch S, Lemmer U (2011) Phys Rev B 83:195211
159. Shuttle CG, Treat ND, Douglas JD, Frechet JMJ, Chabinyc ML (2012) Adv Energy Mater 2:111
160. MacKenzie RCI, Shuttle CG, Dibb GFA, Treat ND, von Hauff E, Robb M, Hawker CJ, Chabinyc ML, Nelson J (2013) J Phys Chem C 117:12407
161. Foertig A, Rauh J, Dyakonov V, Deibel C (2012) Phys Rev B 86:115302
162. Schafferhans J, Deibel C, Dyakonov V (2011) Adv Energy Mater 1:655
163. Schafferhans J, Baumann A, Wagenpfahl A, Deibel C, Dyakonov V (2010) Org Electron 11:1693
164. Schafferhans J, Baumann A, Deibel C, Dyakonov V (2008) Appl Phys Lett 93
165. Carati C, Bonoldi L, Po R (2011) Phys Rev B 84:245205
166. Schmechel R, von Seggern H (2004) Physica Status Solidi A-Appl Res 201:1215
167. Beiley ZM, Hoke ET, Noriega R, Dacuna J, Burkhard GF, Bartelt JA, Salleo A, Toney MF, McGehee MD (2011) Adv Energy Mater 1:954
168. Blakesley JC, Clubb HS, Greenham NC (2010) Phys Rev B 81:045210
169. Eng MP, Barnes PRF, Durrant JR (2010) J Phys Chem Lett 1:3096
170. Garcia-Belmonte G, Boix PP, Bisquert J, Lenes M, Bolink HJ, La Rosa A, Filippone S, Martin N (2010) J Phys Chem Lett 1:2566
171. Rivnay J, Noriega R, Northrup JE, Kline RJ, Toney MF, Salleo A (2011) Phys Rev B 83:121306
172. Nicolai HT, Wetzelaer GAH, Kuik M, Kronemeijer AJ, de Boer B, Blom PWM (2010) Appl Phys Lett 96:172107
173. Lenes M, Shelton SW, Sieval AB, Kronholm DF, Hummelen JC, Blom PWM (2009) Adv Funct Mater 19:3002
174. Lenes M, Morana M, Brabec CJ, Blom PWM (2009) Adv Funct Mater 19:1106
175. Mihailetchi VD, Koster LJA, Blom PWM, Melzer C, de Boer B, van Duren JKJ, Janssen RAJ (2005) Adv Funct Mater 15:795
176. Mihailetchi VD, van Duren JKJ, Blom PWM, Hummelen JC, Janssen RAJ, Kroon JM, Rispens MT, Verhees WJH, Wienk MM (2003) Adv Funct Mater 13:43
177. Nicolai HT, Mandoc MM, Blom PWM (2011) Phys Rev B 83:195204

178. Lu MT, Nicolai HT, Wetzelaer GJAH, Blom PWM (2011) J Polym Sci Pol Phys 49:1745
179. Azimi H, Senes A, Scharber MC, Hingerl K, Brabec CJ (2011) Adv Energy Mater 1:1162
180. Dacuna J, Salleo A (2011) Phys Rev B 84:195209
181. Dacuna J, Xie W, Salleo A (2012) Phys Rev B 86:115202
182. Kuik M, Wetzelaer GJAH, Ladde JG, Nicolai HT, Wildeman J, Sweelssen J, Blom PWM (2011) Adv Funct Mater 21:4502
183. Martens HCF, Huiberts JN, Blom PWM (2000) Appl Phys Lett 77:1852
184. Martens HCF, Brom HB, Blom PWM, Schoo HFM (2000) Physica Status Solidi B-Basic Res 218:283
185. Poplavskyy D, So F (2006) J Appl Phys 99:033707
186. Knapp E, Ruhstaller B (2012) J Appl Phys 112:024519
187. Scher H, Montroll EW (1975) Phys Rev B 12:2455
188. Pivrikas A, Juska G, Mozer AJ, Scharber M, Arlauskas K, Sariciftci NS, Stubb H, Osterbacka R (2005) Phys Rev Lett 94:176806
189. Choulis SA, Nelson J, Kim Y, Poplavskyy D, Kreouzis T, Durrant JR, Bradley DDC (2003) Appl Phys Lett 83:3812
190. Tuladhar SM, Poplavskyy D, Choulis SA, Durrant JR, Bradley DDC, Nelson J (2005) Adv Funct Mater 15:1171
191. Tuladhar SM, Sims M, Choulis SA, Nielsen CB, George WN, Steinke JHG, Bradley DDC, Nelson J (2009) Org Electron 10:562
192. Pivrikas A, Sariciftci NS, Juska G, Osterbacka R (2007) Prog Photovoltaics 15:677
193. Seynhaeve GF, Barclay RP, Adriaenssens GJ, Marshall JM (1989) Phys Rev B 39:10196
194. Baumann A, Lorrmann J, Rauh D, Deibel C, Dyakonov V (2012) Adv Mater 24:4381
195. Lorrmann J, Badada BH, Inganas O, Dyakonov V, Deibel C (2010) J Appl Phys 108
196. Albrecht S, Schindler W, Kurpiers J, Kniepert J, Blakesley JC, Dumsch I, Allard S, Fostiropoulos K, Scherf U, Neher D (2012) J Phys Chem Lett 3:640
197. Neukom MT, Reinke NA, Ruhstaller B (2011) Sol Energ 85:1250
198. Neukom MT, Zufle S, Ruhstaller B (2012) Org Electron 13:2910
199. Rauh D, Deibel C, Dyakonov V (2012) Adv Funct Mater 22:3371
200. Bisquert J (2003) Phys Chem Chem Phys 5:5360
201. Mora-Sero I, Bisquert J, Fabregat-Santiago F, Garcia-Belmonte G, Zoppi G, Durose K, Proskuryakov Y, Oja I, Belaidi A, Dittrich T, Tena-Zaera R, Katty A, Levy-Clement C, Barrioz V, Irvine SJC (2006) Nano Lett 6:640
202. Garcia-Belmonte G, Munar A, Barea EM, Bisquert J, Ugarte I, Pacios R (2008) Org Electron 9:847
203. Garcia-Belmonte G, Boix PP, Bisquert J, Sessolo M, Bolink HJ (2010) Sol Energ Mat Sol C 94:366
204. Fabregat-Santiago F, Garcia-Belmonte G, Mora-Sero I, Bisquert J (2011) Phys Chem Chem Phys 13:9083
205. Heath J, Zabierowski P (2011) Capacitance spectroscopy of thin-film solar cells. In: Abou-Ras D, Kirchartz T, Rau U (eds) Advanced characterization techniques for thin film solar cells. Weinheim, Wiley-Vch, Chap 4, p 81
206. Nelson J, Kirkpatrick J, Ravirajan P (2004) Phys Rev B 69
207. Kirchartz T, Mattheis J, Rau U (2008) Phys Rev B 78:235320
208. Koster LJA, Mihailetchi VD, Blom PWM (2006) Appl Phys Lett 88:093511
209. Kirchartz T, Taretto K, Rau U (2009) J Phys Chem C 113:17958
210. Koster LJA, Shaheen SE, Hummelen JC (2012) Adv Energy Mater 2:1246
211. Mandoc MM, Koster LJA, Blom PWM (2007) Appl Phys Lett 90
212. Wehenkel DJ, Koster LJA, Wienk MM, Janssen RAJ (2012) Phys Rev B 85:125203
213. Petersen A, Kirchartz T, Wagner TA (2012) Phys Rev B 85:045208
214. Kirchartz T, Pieters BE, Taretto K, Rau U (2009) Phys Rev B 80:035334
215. Koster LJA, Mihailetchi VD, Ramaker R, Blom PWM (2005) Appl Phys Lett 86:123509
216. Koster LJA, Mihailetchi VD, Xie H, Blom PWM (2005) Appl Phys Lett 87:203502

217. Kuik M, Koster LJA, Wetzelaer GAH, Blom PWM (2011) Phys Rev Lett 107
218. Wagenpfahl A, Rauh D, Binder M, Deibel C, Dyakonov V (2010) Phys Rev B 82:115306
219. Deibel C, Wagenpfahl A (2010) Phys Rev B 82:207301
220. Kotlarski JD, Moet DJD, Blom PWM (2011) J Polym Sci Pol Phys 49:708
221. Kotlarski JD, Blom PWM (2012) Appl Phys Lett 100:013306
222. Murgatroyd PN (1970) J Phys D: Appl Phys 3:151
223. Mark P, Helfrich W (1962) J Appl Phys 33:205
224. Faist MA, Shoaee S, Tuladhar SM, Dibb GFA, Foster S, Gong W, Kirchartz T, Bradley DDC, Durrant JR, Nelson J (2013) Adv Energy Mat 3:744
225. Maurano A, Hamilton R, Shuttle CG, Ballantyne AM, Nelson J, O'Regan B, Zhang WM, McCulloch I, Azimi H, Morana M, Brabec CJ, Durrant JR (2010) Adv Mater 22:4987
226. Maurano A, Shuttle CC, Hamilton R, Ballantyne AM, Nelson J, Zhang WM, Heeney M, Durrant JR (2011) J Phys Chem C 115:5947
227. Cowan SR, Street RA, Cho SN, Heeger AJ (2011) Phys Rev B 83
228. Burgelman M, Nollet P, Degrave S (2000) Thin Solid Films 361:527
229. Burgelman M, Verschraegen J, Degrave S, Nollet P (2004) Prog Photovoltaics 12:143
230. Ding KN, Kirchartz T, Pieters BE, Ulbrich C, Ermes AM, Schicho S, Lambertz A, Carius R, Rau U (2011) Sol Energ Mat Sol C 95:3318
231. Berning PH (1963) Theory and calculations of optical thin films. In: Hass G (ed) Physics of thin films. Academic, New York, Chap 2, p 69
232. Hall RN (1952) Phys Rev 87:387
233. Shockley W, Read WT (1952) Phys Rev 87:835
234. Simmons JG, Taylor GW (1971) Phys Rev B 4:502
235. Pieters BE, Kirchartz T, Merdzhanova T, Carius R (2010) Sol Energ Mat Sol C 94:1851
236. Zeman M, Krc J (2008) J Mater Res 23:889
237. Kim JB, Kim P, Pegard NC, Oh SJ, Kagan CR, Fleischer JW, Stone HA, Loo YL (2012) Nat Photonics 6:327
238. Gevaerts VS, Furlan A, Wienk MM, Turbiez M, Janssen RAJ (2012) Adv Mater 24:2130
239. Kouijzer S, Esiner S, Frijters CH, Turbiez M, Wienk MM, Janssen RAJ (2012) Adv Energy Mater 2:945
240. Decock K, Khelifi S, Buecheler S, Pianezzi F, Tiwari AN, Burgelman M (2011) J Appl Phys 110:063722
241. Pieters BE, Decock K, Burgelman M, Stangl R, Kirchartz T (2011) One-dimensional electro-optical simulations of thin-film solar cells. In: Abou-Ras D, Kirchartz T, Rau U (eds) Advanced characterization techniques for thin film solar cells. Wiley-VCH Verlag GmbH & Co, KGaA, p 501

Top Curr Chem (2014) 352: 325–396
DOI: 10.1007/128_2013_471

Published online: 28 September 2013

Device Modeling of Dye-Sensitized Solar Cells

Juan Bisquert and Rudolph A. Marcus

Abstract We review the concepts and methods of modeling of the dye-sensitized solar cell, starting from fundamental electron transfer theory, and using phenomenological transport-conservation equations. The models revised here are aimed at describing the components of the current–voltage curve of the solar cell, based on small perturbation experimental methods, and to such an end, a range of phenomena occurring in the nanoparticulate electron transport materials, and at interfaces, are covered. Disorder plays a major role in the definition of kinetic parameters, and we introduce single particle as well as collective function definitions of diffusion coefficient and electron lifetime. Based on these fundamental considerations, applied tools of analysis of impedance spectroscopy are described, and we outline in detail the theory of recombination via surface states that is successful to describe the measured recombination resistance and lifetime.

Keywords Dye solar cell · Electron transport · Nanomaterials · Impedance spectroscopy

Contents

J. Bisquert (✉)
Photovoltaics and Optoelectronic Devices Group, Departament de Física, Universitat Jaume I, 12071 Castelló, Spain
e-mail: bisquert@uji.es

R.A. Marcus
Noyes Laboratory of Chemical Physics, California Institute of Technology, Pasadena, CA 91125, USA

1 Introduction

Standard dye-sensitized solar cells (DSCs) [1] are composed of three main elements, as indicated in Fig. 1a: the electron transport material (ETM), the hole transport material (HTM), and the light absorber. The ETM is a mesoporous structured wide band gap metal oxide semiconductor that provides a high internal area framework to maintain the light absorber rigidly anchored or stuck to the surface. We will refer to mesoporous anatase TiO_2 as the archetypal ETM. Conventionally the light absorber is a monolayer of metal-organic dye such as the well known N719 ruthenium bipyridyl dye. In recent years an enormous variety of dyes have been investigated, and porphyrin dyes in particular have shown very powerful results, elevating power conversion efficiency to 12% [2]. In addition, solid light absorbers of different classes, either colloidal quantum dots or uniform nanometer-thick light absorbing layers, have become increasingly investigated [3–5]. Finally, the preferred HTM was a liquid electrolyte containing redox couple I_3^-/I^- and a number of coadsorbents to control the surface conditioning of the TiO_2 metal oxide. Recently, rather effective redox shuttles based on transition metal complexes have been applied to high performance devices [6]. Fully solid hole conductors have been widely used as well. In general the selection of the HTM depends critically on the type of absorber, and these choices also determine the counterelectrode [7].

Device modeling can serve different purposes. It may be used to gain detailed scientific insight into a range of phenomena occurring in the DSC. Or it may be aimed at technical characterization to support the quality of fabrication of devices. Among the two extremes, a widely used type of application of the methods is to compare a set of DSCs prepared with some variation of materials or procedures, in order to extract information about the internal mechanisms. Therefore modeling DSCs and solar cells in general may have a wide variety of purposes.

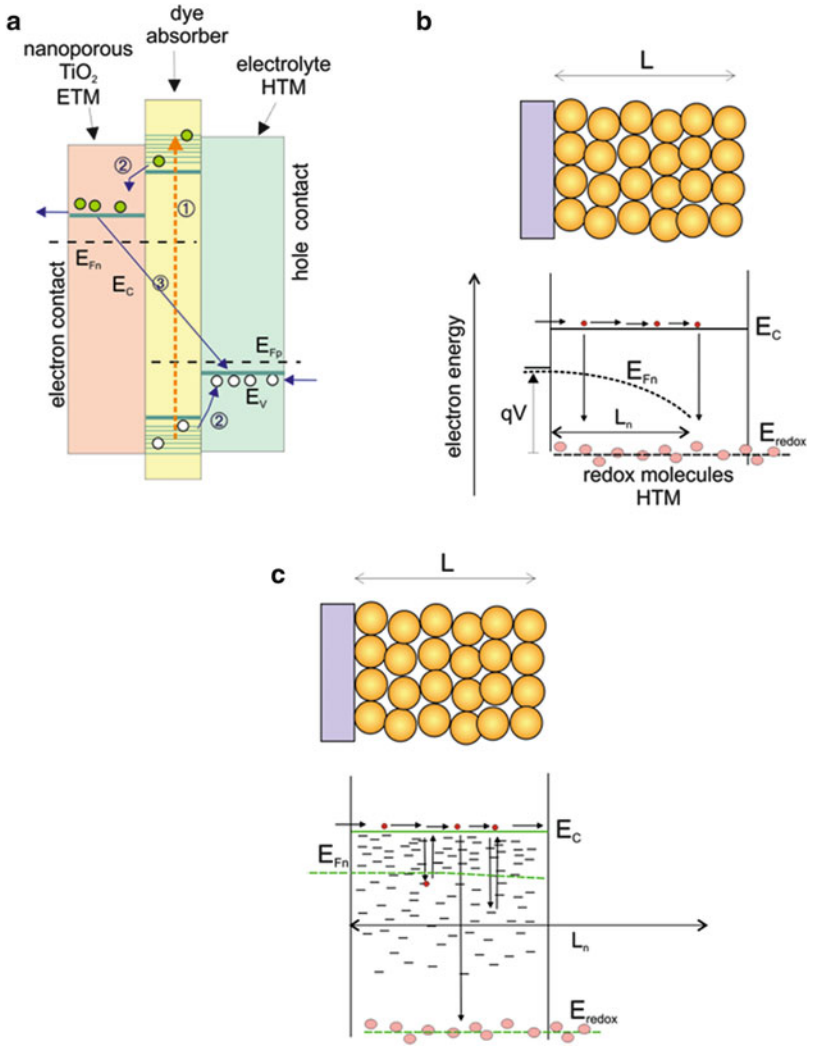

Fig. 1 (**a**) Energy diagram of a DSC, formed by three phases materials that function, as the absorber, the electron (ETM) and hole (HTM) transport materials, or redox electrolyte. Carriers relax to the conduction band of the ETM, E_C, and the valence band (E_V) of the HTM, producing a splitting of the quasi-Fermi levels of electrons (E_{Fn}) in the ETM and holes (E_{Fp}) in the HTM, or redox level in electrolyte E_{redox}. (**a**) The arrows indicate the following processes: (1) absorption of light, generating electrons and holes in the absorber. (2) Charge separation: Injection from the absorber to the ETM and HTM. (3) Recombination of electrons and holes. (**b**) Mesoporous structure that forms the ETM in a DSC. It consists of interconnected particles that allow the transport of electrons via extended states. The potential V at the substrate fixes the electron density at the edge of the nanostructured semiconductor. Injected electrons at the contact have a probability to diffuse and recombine by charge transfer to the acceptor species in the HTM, so that the effective penetration in the layer is governed by the diffusion length L_n. (**c**) In this case transport in the extended level is coupled with trapping and release from localized states in the bandgap. The right contact is reflecting to electrons. If the diffusion length is long with respect to film thickness then the concentration is nearly homogeneous

The following overview aims to present a reasonably short summary of the state-of-the-art and recent exciting developments with a view to broaden the possible applications of these methods. We aim to cover a series of fundamental factors that have appeared crucial to the operation of the DSC over many years of research: causes of fundamental electron transfer rate that govern recombination; energy disorder affecting electronic states in electron conductor; and the general modeling approach incorporating such fundamental properties to small perturbation techniques that have provided outstanding control over the internal state of the device and the mechanisms lying behind the photovoltaic performance. We will include the description of the basis of impedance spectroscopy results, the causes and measurements of the electron lifetime, and how these understandings establish properties of current–voltage curves.

2 The Electron Subsystem

In cells in which the absorber is a molecular dye and the HTM is a liquid conductor with low viscosity, the injection of photogenerated electrons into TiO_2 is very fast, in the picosecond domain, and the main modeling issues are referred to the electron subsystem. Provided that dye regeneration is sufficiently fast, the HTM can be viewed simply as a homogeneous medium that regenerates the oxidized dye and therefore provides (the oxidized) species that may accept electrons from TiO_2. It is therefore assumed in a starting approach that the Fermi level of the hole species is flat and stable and any kind of kinetics in the absorber or HTM can be safely ignored. In contrast, for thin inorganic absorbers of quantum dots, a number of additional issues occur because the carrier dynamics in the absorber cannot be ignored [7–9]. Furthermore, for viscous electrolytes, or solid HTM, it is necessary to describe the transport of the ionic or electronic species [10].

Let us for the moment set aside the problems of dynamics in the absorber and HTM and consider the description of electrons in ETM, which is a central problem to the modeling of dye solar cells.

From the point of view of energetics the basic modeling uses two main levels, indicated in Fig. 1b: a transport level usually identified with a conduction band level, E_c, and the electrochemical potential of electrons that is usually called the Fermi level, E_{Fn}. The energy level E_c is significant for issues of charge transfer as in injection from the dye and recombination [11], while the Fermi level determines the photovoltage in the DSC and establishes how electron transport is driven by diffusion [12]. Normally the TiO_2 nanoparticles (or wires, tubes, etc.) provide a well connected structure and the energy level is defined globally in the nanostructured film as shown in Fig. 1b. Electron density in the transport level n_c is defined as

$$n_c = N_c e^{(E_{Fn}-E_c)/k_B T} \tag{1}$$

where $k_B T$ is thermal energy and N_c is an effective total density of states. The Fermi level in the absence of bias voltage E_{F0} is called the "equilibrium Fermi level". The electron density at equilibrium is

$$n_{c0} = N_c e^{(E_{F0}-E_c)/k_B T} \tag{2}$$

and we may write

$$n_c = n_{c0} e^{(E_{Fn}-E_{F0})/k_B T} \tag{3}$$

Consider for the sake of clarity a pulse of electrons injected from the substrate into the metal oxide nanostructure. The electrons diffuse into the ETM, and the electron motion can be viewed as a random walk process [13], in which a carrier at each step has a chance to either continue random walk or recombine with the acceptor ionic species, or holes in the HTM. The probability of moving away from the injection point is governed by the diffusion length L_n, as suggested in Fig. 1b. This parameter plays a key role in the modeling of DSC [14] since the size of L_n compared to film thickness L critically determines the collection efficiency [15] of the solar cell. In addition, a large $L_n >> L$ implies that carrier gradients are small in most conditions. This feature greatly simplifies modeling, as stated above, because one considers homogeneous distribution of carriers and may focus exclusively on the time dependence of the processes. This case will be developed in the next section to formulate an important description of the performance of a DSC.

3 The Fundamental Diode Model

According to a fundamental conservation argument, in a film where electrons can be generated, diffuse, and recombine, as in Fig. 1b, electron density at position x is shown by the equation

$$\frac{\partial n_c}{\partial t} = -\frac{\partial J_n}{\partial x} + G(x) - U_n(x) \tag{4}$$

where J_n is the electron flux, related to the free electron diffusion coefficient, D_0, by Fick's law:

$$J_n = -D_0 \frac{\partial n_c}{\partial x} \tag{5}$$

G is a local generation rate, and U_n is a recombination rate. At the extraction contact the carrier density is controlled by the voltage. The voltage is given by the rise of the electrons Fermi level, with respect to the redox level, as indicated in Fig. 1b:

$$qV = E_{Fn}(x = 0) - E_{redox} \tag{6}$$

Note that we use a positive voltage for raising the Fermi level of electrons. This convention has an opposite sign with respect to the voltage in electrochemistry, but it is convenient for the description of the DSC, where the active contact is that of electrons and provides a negative voltage. The convention of (6) makes the normal photovoltage positive.

At initial equilibrium we have $E_{F0} = E_{redox}$, and we assume here that the redox level remains stationary even though the electron density may increase. Therefore we have the following expression for the voltage in the device:

$$qV = E_{Fn} - E_{F0} \tag{7}$$

where q is the elementary charge, and therefore

$$n_c(x = 0) = n_{c0}\, e^{qV/k_B T} \tag{8}$$

The selective boundary at $x = L$ imposes the condition

$$J_n(L) = 0 \tag{9}$$

Let us assume reasonably homogeneous carrier distribution in the mesoporous TiO_2 film. This model with fast transport and Fermi levels is shown in Fig. 2. By spatial integration of (4) along the thickness of the device, we obtain

$$\frac{\partial(n_c L)}{\partial t} = J_n(0) + \int_0^L G(x)\mathrm{d}x - LU_n \tag{10}$$

Variations of the total carrier number $n_c L$ correspond to the sum of three effects: electrons going out and into the device through the contact, in the flux $J_n(0)$, generation, and finally, recombination. We start by considering steady state condition, in which $\partial n_c/\partial t = 0$. From (10)

$$-J_n(0) = \int_0^L G(x)\mathrm{d}x - LU_n \tag{11}$$

There is a full balance of the three terms of (10) as suggested in Fig. 2a. The steady state regime is the true domain of operation of a solar cell for electrical power production under sunlight. On the other hand, most characterization

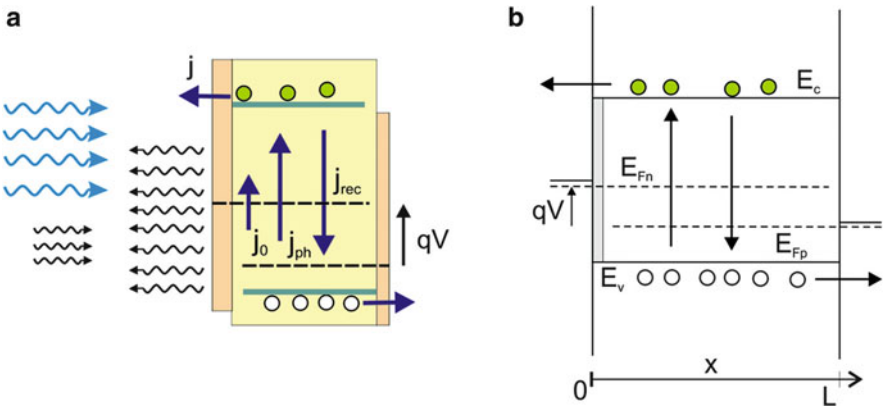

Fig. 2 (**a**) Model energy diagram of a solar cell with an electron selective contact at the left side and a hole selective contact at the right side. Under illumination, absorbed photons promote excitation of the absorber creating an electron-hole pair. Charge separation produces an electron in the ETM conduction band and a hole in the transport level of the HTM. The diagram indicates the balance of radiation in the ideal diode. The diode receives thermal background radiation (even in dark equilibrium), sunlight, and emits photons by radiative recombination. (**b**) Processes of carrier generation, recombination and extraction that lead to the different fluxes indicated in (**a**)

techniques involve time dependence in order to provide detailed kinetic information about the system, and these conditions will be described later.

Working in steady state conditions we have to describe simply two variables: The voltage and the current. The electrical current density in the outer circuit

$$j = qJ_{\mathrm{n}}(0) \tag{12}$$

is a function of the voltage. V is related to concentration by (8). The concentration enters the balance (11) via the recombination term. A phenomenological model that gives good results in many cases is the following [14, 16]:

$$U_{\mathrm{n}} = k_{\mathrm{rec}}\left(n_{\mathrm{c}}{}^{\beta} - n_{\mathrm{c0}}{}^{\beta}\right) \tag{13}$$

Equation (13) represents a power β of the free carrier density and is called the β-recombination model. This parameter usually has experimental values of 0.6–0.75. The recombination rate in (13) is composed of two terms: a dark generation rate that we express as a current density:

$$j_0 = qLk_{\mathrm{rec}}\, n_{\mathrm{c0}}{}^{\beta} \tag{14}$$

and the recombination current

$$j_{\mathrm{rec}} = qLk_{\mathrm{rec}}\, n_c{}^{\beta} \tag{15}$$

The latter term can also be expressed

$$j_{\text{rec}} = j_0 \, \mathrm{e}^{q\beta V/k_{\text{B}}T} \tag{16}$$

Finally, photogeneration in (11) gives the photocurrent as follows:

$$j_{\text{ph}} = q\int_0^d G_\Phi \mathrm{d}x \tag{17}$$

In summary we have that

$$j = j_{\text{ph}} - j_{\text{rec}} + j_0 \tag{18}$$

where j_{rec}, as discussed before, is the recombination current that we have described in (16) as j_0 (the recombination current at thermal equilibrium) enhanced by the applied voltage. Therefore we may write (18) as

$$j = j_{\text{ph}} - j_0\left(\mathrm{e}^{qV/mk_{\text{B}}T} - 1\right) \tag{19}$$

We observe that the diode quality factor relates to the recombination exponent as $m = 1/\beta$ [17]. The balance of currents shown at (18) is indicated in Fig. 2a.

4 Features of Current–Voltage Curves: Photocurrent and Photovoltage

The simple model of Fig. 2 and (19) appears deceptively primitive at first sight but in fact it has important applications as it contains the main features for the description of the current–voltage (jV) curve of the DSC. There are two main assumptions to this model; the first is a total decoupling of photocurrent and recombination – these two features are viewed as independent phenomena; the second is that the carrier density is independent of position. Both assumptions are a good approximation so far as the diffusion length is very large. But how well are they realized?

If the carrier collection efficiency is very good, then the photocurrent, j_{ph}, is determined by the light absorption and charge injection features that are measured by Incident Photon to Current conversion Efficiency (IPCE), also known as the External Quantum Efficiency (EQE) [18]. Examples of the absorption spectra of efficient dyes are shown in Fig. 3 [19], and the corresponding IPCE is shown in the figure together with the final photovoltaic performance. In this type of highly efficient DSC, the measured current can indeed be viewed as completely decoupled from recombination, as in the model of (19). The convolution of IPCE with the solar spectrum describes very well the actual value of j_{ph}. However, in cells with low collection efficiency, one should be careful to calculate correctly the collection

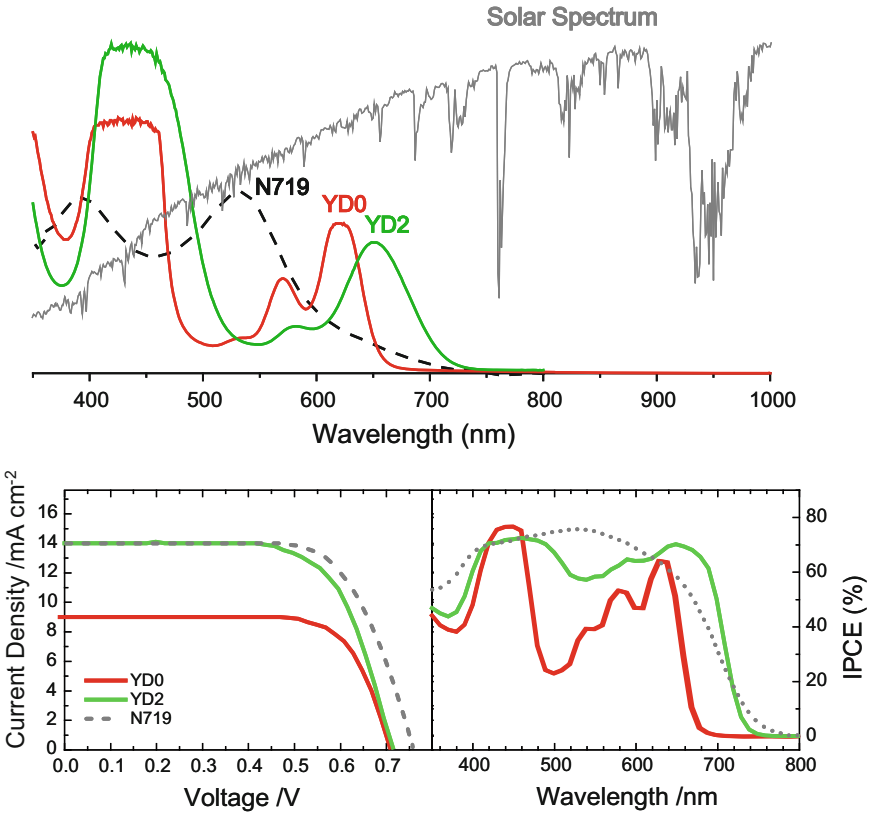

Fig. 3 Absorption coefficient of N719 and two porphyrin dyes, in comparison with the spectral photon flux, and the corresponding photovoltaic performance and IPCE. Adapted from [19] by courtesy of Lu-Lin Li and Eric W. Diau

efficiency starting from diffusion lengths [20]. Another important consideration to describe photocurrent is optical modeling, including features such as glass reflection, scatter layers, and photonic crystal light absorption [21–26].

The next main feature is recombination of electrons, which is described in this simple model by j_{rec} in (16). Now recombination describes the shape of the jV curve apart from the additive j_{ph} term. Therefore recombination determines the fill factor and open-circuit voltage V_{oc} of the solar cell. A vast number of papers and studies have been devoted to obtaining comparative information on DSCs with varying characteristics and we will review here a number of features. As an example we consider the data in Fig. 4a that correspond to a series of DSCs with different electrolytes but otherwise identical conditions of film thickness, dye (N719), and so on [27].

We should first note that experimentally it is usually not possible to obtain j_{rec} from the jV due to complications such as series resistance that is always present and affects the voltage. The voltage associated with separation of Fermi levels is called

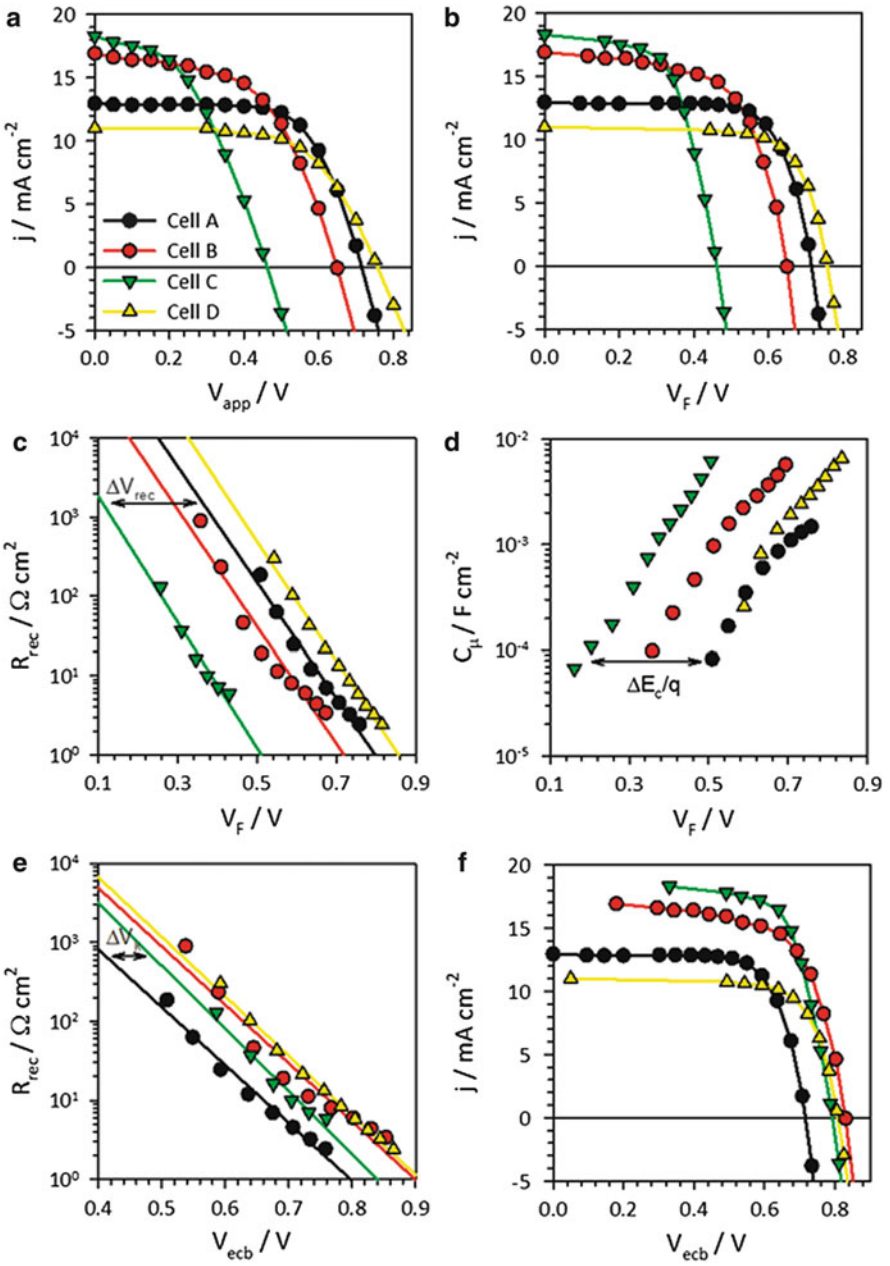

Fig. 4 (**a**) Current density–voltage curves of a set of DSCs with different electrolytes. Points are obtained from Impedance Spectroscopy measurements and lines by an integration procedure. (**b**) Current density–voltage curves with respect to Fermi level voltage V_F, in which the voltage drop due to internal series resistance has been corrected. (**c**) Recombination resistance between the semiconductor and the acceptor species in the electrolyte. (**d**) Chemical capacitance of the TiO_2.

V_F, and it is obtained from the measured voltage V_{app} by correction of the voltage drop at series resistance. In Fig. 4b the jV curve is shown with respect to V_F. In this case the downward bending of the curve towards high voltages must be due to recombination and the curves correspond to (19).

To avoid the common problem of uncertainty of jV curve modeling, it has become widely accepted in the DSC area to use the technique of impedance spectroscopy (IS) that separates different resistive components [28, 29] by means of an equivalent circuit analysis that takes into account the spectral shapes. One key point about IS applicable to DSC is that it provides a direct probe of recombination via the recombination resistance, R_{rec}:

$$R_{rec} = \left(\frac{\partial j_{rec}}{\partial V_F}\right)^{-1} \tag{20}$$

Obviously R_{rec} consists of a derivative of the recombination flux.

Assuming that R_{rec} is measured, as in Fig. 4, we wish to obtain the parameters for recombination in the DSC. For example from the model of (16) we obtain the explicit dependence

$$R_{rec} = R_0 \exp\left[-\frac{\beta q V_F}{k_B T}\right] \tag{21}$$

where

$$R_0 = \frac{k_B T}{\beta q j_0} \tag{22}$$

Therefore from the measurement of impedance spectroscopy the recombination parameters j_0 and β can be derived. In general, as may be seen in Fig. 4b, R_{rec} approaches quite well the single exponential behaviour given in (21). Another example of the recombination resistance in a family of similar DSCs is shown in Fig. 5b. These results provide strong support to the recombination model at (13). Therefore we may aim at a more fundamental discussion of the parameters j_0 and β in terms of electron transfer, depending on surface conditions, TiO_2 properties, etc. [30–34].

Figure 4c shows that the variation of electrolyte conditions produces a very large impact on recombination parameters. This is due to two different factors: the shift of the conduction band and the change of interfacial kinetics, induced by the specific properties of the electrolyte. These questions will be treated in more detail in a later section, after we have introduced the disordered DOS in TiO_2. In all the cells of

Fig. 4 (continued) (**e**) The recombination resistance with respect to equivalent conduction band potential V_{ecb}, in which the voltage V_F is shifted so that all capacitances match to the same line. (**f**) Current density–voltage curves with respect to voltage V_{ecb}. Adapted from [27] by courtesy of Sonia R. Raga and Fran Fabregat-Santiago

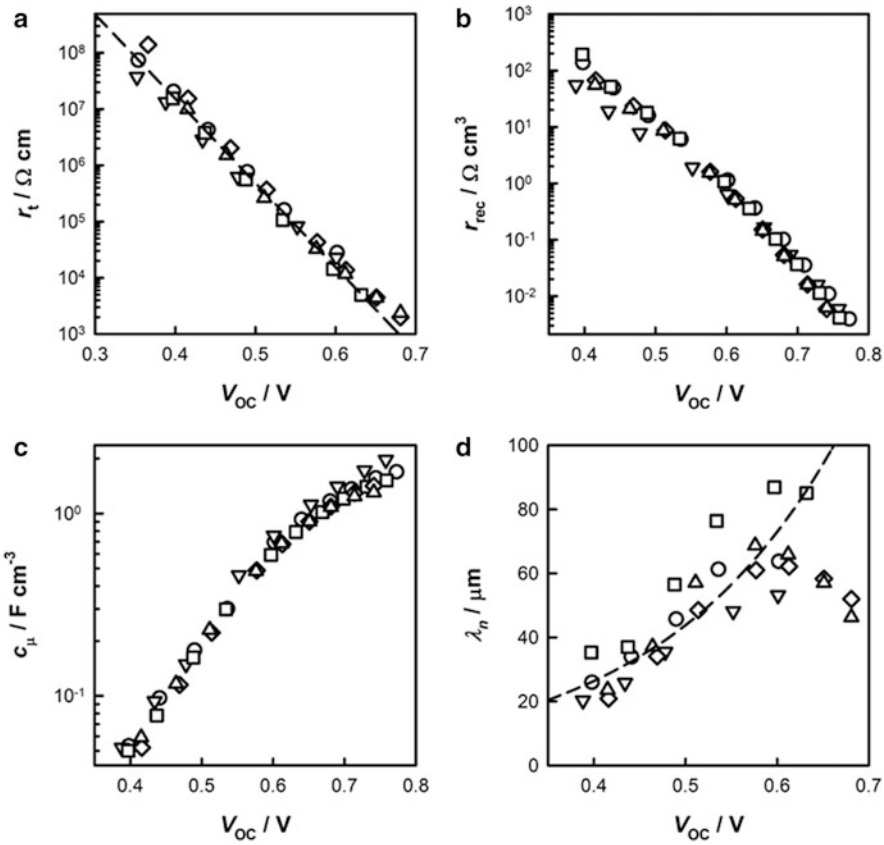

Fig. 5 Plots of distributed transport resistance (**a**), charge transfer resistance (**b**), electrode capacitance (**c**), and electron diffusion length (**d**) vs open-circuit photovoltage for a series of cells with average TiO_2 layer thicknesses of 4 (*circles*), 8 (*downward triangles*), 14 (*squares*), 16 (*upward triangles*), and 18 μm (*diamonds*). The *dashed line* in (**a**) is a fit with a slope of $q/k_BT = 15.2\ V^{-1}$, while the *dashed line* in (**d**) is just a guide to the eye. Adapted from [45] by courtesy of James Jennings and Qing Wang

Fig. 4 the redox couple is the same, but other redox couples based on cobalt or copper can be used and the variations are investigated using similar methods [35–39].

It has been established that we are able to measure recombination with great accuracy, and it is a challenge of great significance, from both fundamental and applied stances, to be able to describe these observations by a comprehensive theory. We will carry out this discussion below, but first we need to develop a number of points concerning the disorder in the electron subsystem. It should be pointed out, however, that the exponential dependence of the recombination resistance on voltage, which is characteristic of high performance liquid electrolyte

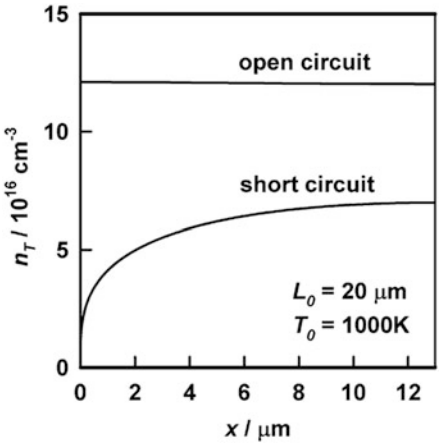

Fig. 6 Trapped carrier density profiles calculated from the steady-state continuity equation for open and short circuit conditions. $N_{L,0} = 10^{19}$ cm^{-3}, $T_0 = 1{,}000$ K, $\tau_0 = 10^{-5}$ s, $\alpha = 500$ cm $- 1$, $L = 13$ μm, diffusion length $L_0 = 20$ μm. Reproduced with permission from [43]

DSC, is not universal, and different types of behavior have occasionally been reported [40, 41].

Another important method of application of the recombination resistance is that, by integration of (20), we can recover j_{rec}. In addition, for the simple model of (16), integration is not even needed as the following expression [27] can be used:

$$j = j_{ph} + j_0 - \frac{k_B T}{\beta q} \frac{1}{R_{rec}(V_F)} \tag{23}$$

Therefore from the impedance data it is possible to reconstruct the jV curve, as shown in Fig. 4a, with great control over the elements that intervene in the curve. A similar method has been derived for organic solar cells [42].

We must also discuss the second assumption of the fundamental diode model of Fig. 2, which is homogeneous carrier density. Clearly this assumption is better realized close to open circuit than in short circuit conditions, as in the latter case the electron Fermi level must come to the equilibrium value, at the contact, while the carrier density is still high in the rest of the device; see Fig. 6 [43]. However, the region of the jV curve close to open circuit is the most significant one, in cells in which the collection efficiency is high, as it is in this voltage region where we wish to measure recombination in order to obtain an understanding of the factors controlling fill factor and V_{oc}. It is therefore important to check that homogeneous distribution is a good hypothesis, and this has been done in the data shown in Fig. 5, that indicate that the distributed transmission line elements [44] (measured at open circuit conditions), that will be discussed in Sect. 12, are independent of the TiO_2 film thickness in the DSC, for a significant variation of film sizes [45]. This result shows that local impedances in the film are independent of thickness, indicating nearly homogeneous carrier distribution.

5 Interfaces and Mass Transport

Let us consider a more detailed modeling of the device operation beyond the homogeneous model discussed in the previous section. Modeling the DSC and in general any complex nanostructured device requires four main aspects to be considered:

1. The number of types of transport species: charged and neutral, ionic and electronic.
2. The spatial distribution of the charge carriers that relates to important properties such as shielding, macroscopic electrical fields and the main transport mechanisms.
3. The structure of interfaces, particularly at the contacts, including a description of interfacial capacitances.
4. The energy axis, governed by disorder at each material [17], and by energy level alignment at interfaces [46].

The device is therefore formed by some geometry and morphology that sets the first constraint in establishing regions where the carriers can be distributed, either in motion or stationary. Such regions have boundaries that are described by suitable boundary conditions, and in particular the contacts, in which electronic carriers communicate with the external circuit, are critically important for the operation of solar cells [47].

Having set morphologies and boundaries, there are two different dimensionalities, namely the *geometric space* which can be described with one or more dimensions, and the *energy space*. At each point an energy diagram gives the allowed energy levels for type of carrier, or their combination, as indicated in Fig. 1a and in quantitative detail in Fig. 7. Energy levels for electronic carriers may be stationary states, also called localized states or traps, or extended states that allow fast transport. Transport may also proceed by hopping between localized states [48], but this formalism is not usually adopted in DSC, in which the transport of electrons is well described by the multiple trapping model [49]. The relative energy alignment at interfaces provides essential constraints for the kinetics of charge or energy transfer.

Based on these general properties that allow one to describe the model, one formulates a series of macroscopic equations and boundary conditions that provide, as a result, carrier densities and carrier dynamics, expressed as output current densities, either for steady state or any desired transient condition. In this chapter we focus our attention on phenomenological modeling using macroscopic equations. A first model, presented in the previous section, contains only one kind of carrier (electrons in TiO_2) and no spatial dimension at all (once the photocurrent is calculated by an integration of the generation term), since all the points are considered at the same density. This model is fairly useful, as discussed above; however, for a deeper understanding of the microscopic electronic phenomena it is necessary to include the energy axis, distinguishing free and trapped electrons,

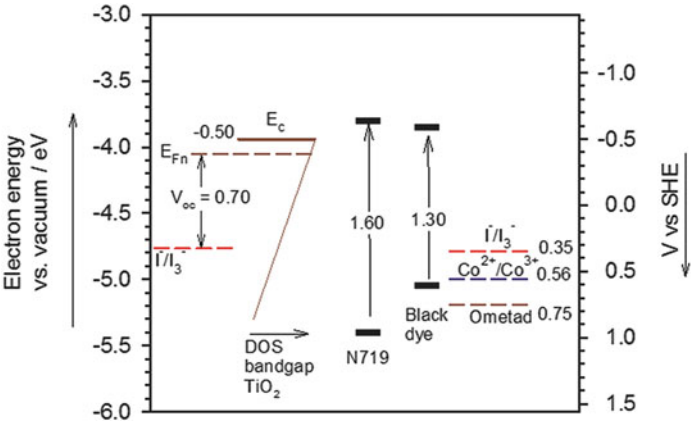

Fig. 7 Energetic scheme of the components of a DSC. The position of the conduction band of TiO_2 and the density of states (DOS) in the bandgap is indicated. Also shown is the photovoltage by difference of the Fermi level of electrons and the redox potential in the electrolyte. At the *right* are shown the redox potential of conventional hole conductors. In the *center* is shown ground and excited state of standard dyes. More accurately, the excited and ground states are spread over an energy interval. Energy differences are expressed in eV

which has a very large effect on all measured kinetic parameters of the DSC. This description is discussed below [49–52].

Instead of the phenomenological transport and conservation equations, one may adopt a more fundamental point of view in which electronic states are modeled individually and the transfer rates between states allow us to analyze the global dynamics by Monte Carlo simulation [13]. These methods have also been widely applied; they permit one to establish arbitrary morphologies and to investigate complex effects such as percolation and nonthermalized electron transport [53–57]. Still a more fundamental approach consists in a simulation of the molecular details of the components of the system. This approach can produce very valuable knowledge about the structure of interfaces and the origin of the observed energy distribution features, and the nature of excited or intermediate states for charge transfer phenomena [58–60]. Microscopic simulation methods have been widely explored in the field of organic materials, and have important applications for the investigation of carrier and energy transport in organic solids [61–63].

A very important aspect of the modeling of a DSC, beyond the zero-dimensional homogeneous model, is to consider a one-dimensional model, adapted to the standard sandwich-type cell, where (4) allows the consideration of gradients like those shown in Fig. 6 to calculate photocurrents and other quantities. In the steady state we have

$$-\frac{\partial J_{\mathrm{n}}}{\partial x} + G(x) - U_{\mathrm{n}}(x) = 0 \tag{24}$$

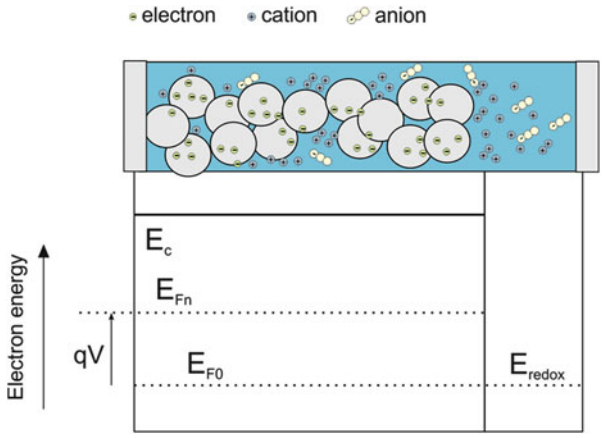

Fig. 8 Scheme showing electron accumulation in a nanocrystalline semiconductor electrode and the compensation by positive charge in the electrolyte to produce local electroneutrality. The electrolyte may contain several species of anions, cations, and redox molecules, as well as molecules that have the role of modifying the surface to produce some beneficial effects. The energy diagram shows the change of electrons Fermi level that causes a photovoltage

This type of model, generally denoted a diffusion-recombination model, has been very widely used, with many extensions and variants [43, 64–72]. It is interesting to recall that (24), and its many extensions, are based on a macrohomogeneous approach [73–75] in which the mixture of nanoporous ETM and the HTM inside the pores is viewed as a unique medium that hosts both species, with certain probabilities of carrier exchanges between ETM and HTM, corresponding to electron injection, regeneration, electron–hole recombination, etc. In a highly concentrated electrolyte, the Debye length is very short, and shielding by electroneutrality prevents the formation of long range electrical fields in the semiconductor nanostructure. When the electrons are injected into a nanostructured metal oxide, positive ions move to the surface of the charged nanoparticles and neutralize long range electrical fields. Therefore electron transport is driven by concentration gradient, i.e., by diffusion [15]. This property is quite general for a number of photovoltaic and electrochemical cells, such as inorganic composite solar cells formed by nanoscale elements [76], classical electrochemical systems when a supporting electrolyte is used [77], and also crystalline p-silicon solar cells, in which injected electrons are much less than the majority carrier holes [78, 79].

The crucial mechanism of shielding of electrical fields which considerably simplifies the modeling tasks is illustrated in Fig. 8. There the increase of electron Fermi level in the nanostructure is permitted by the large quantity of compensating charges in the HTM, so that the holes in the latter medium (or ions) effectively play the role of a majority carrier. If the shielding is effective, then the cell voltage is readily explained by the change of the Fermi level at the left contact; see Fig. 8. It should be emphasized that the *voltage* is the amount of work necessary to carry an electron from one plate of the device to the other. This work involves the

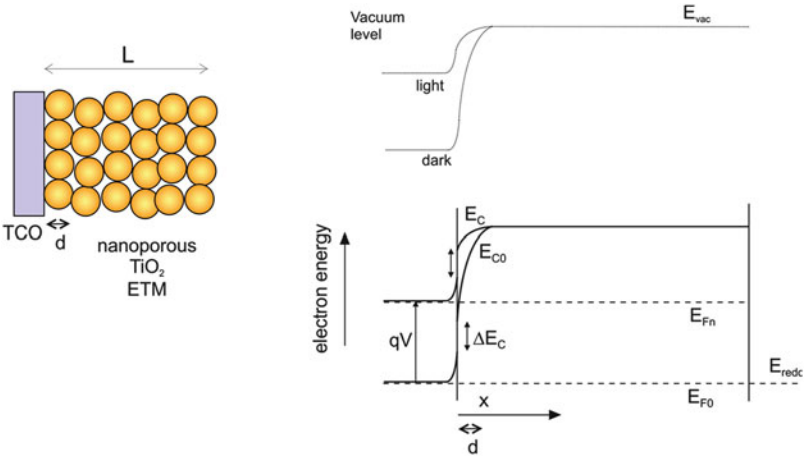

Fig. 9 Energy diagram showing the contact of the nanocrystalline semiconductor electrode with the transparent conducting oxide (TCO) substrate, and the change of Fermi levels and the vacuum level under illumination, with respect to the dark equilibrium. ΔE_c is the energy offset between the conduction band of the TiO_2 and the transparent conducting oxide (TCO)

measurement of an electrical current with an electrometer and is given by the *difference of electron Fermi levels* between the two plates [80, 81], which is the rationale for (6). It is also true that a change of voltage between the contacts requires that somewhere in the device a modification of *electrostatic potentials* (reflected by a change of the vacuum level diagram) occurs as well. There is a widespread tendency to look for a change of *band bending* as a source of photovoltage in a solar cell. In the area of DSC the question of potential barriers was a matter of concern that promoted many discussions [82–84]. It is now well established that the origin of photovoltage is a kinetic balance of excess carriers as expressed by (4), a result that was conclusively demonstrated by Gregg et al. [83]. Monitoring the Fermi level variation is a definitive explanation of photovoltage but still begs the question about the location of the electrical field, and this can be reasoned as shown in Fig. 9. The figure suggests that the change of electrostatic potential, reflected in a change of the vacuum level associated with the photovoltage, i.e., the difference of electrostatic potentials between dark and light, is absorbed at the interface between the SnO_2 transparent conducting oxide (TCO) and the TiO_2. This interface has been repeatedly discussed in the literature [85–91]. Due to effective shielding as mentioned above, the electrical field at the surface of the substrate does not penetrate deeply into the mesostructure.

In principle the diagrams of Figs. 8 and 9 do not seem consistent with the fact that the conduction bands of TiO_2 and SnO_2, are normally reported at −4.3 and −4.8 eV, respectively, with respect to the vacuum level. At acidic pH, corresponding to the DSC electrolytes, the TCO conduction band should be higher, but it achieves equilibrium with the redox level, which is about −4.8 eV vs vacuum for I_3^-/I^- (see Fig. 7) and deeper for other redox couples, that consequently are able to produce a higher photovoltage [92]. The remarkable point is the high position of

the TiO_2 conduction band [84] that is facilitated by specific coadsorbents, which allow a large photovoltage to be achieved [93]. It must be noted, therefore, that the overall picture in Fig. 9 covers the equilibration by interfacial charging at several interfaces: TCO/electrolyte and TiO_2/electrolyte. As a result of these properties the Fermi level in the TCO finally rises under illumination, pulled up by the electrons in TiO_2 so that the TCO/TiO_2 junction forms an excellent selective contact to electrons that is responsible to a large extent for the good operational properties of the DSC. For comparison, the operation of the cathode in bulk heterojunction solar cells seems more problematic, as the initial offset of work functions is shared by both a surface dipole and band bending entering the bulk of the blend [94].

The previous model erases all electrical fields and interfacial barriers in the mesostructure, which is viewed in effect as a homogeneous medium. However, in semiconductor mesostructures, filled with an HTM, one can also allow for the presence of an electrical field and semiconductor barrier at the internal interface ETM/HTM. The prevalence of one approach or the other, i.e., a macrohomogeneous model that only contemplates the Fermi level or the explicit presence of internal interface barriers, depends on doping densities, size of semiconductor particles or wires, and Debye length both in the semiconductor nanostructure and in the HTM [95–97].

The diffusion-recombination model has been developed largely for the liquid electrolyte containing iodide/triiodide that has a very high conductivity and generally introduces no problem for transport. It was shown that improving the conditions of shielding in liquid electrolyte enhances the observed electron diffusion coefficient [98]. A high concentration electrolyte provides excellent shielding and a flat reference E_{redox}. However, energetically the I_3^-/I^- redox level is too high (see Fig. 7); for example measurement of tris(1,10-phenanthroline)cobalt(II/III) show that this redox couple is 230 mV deeper (more positive redox potential) than iodide electrolyte [37]. As a consequence, cobalt electrolytes, and solid organic hole conductors, have been widely explored. It should be noticed in Fig. 7 that Co(II/III) redox couple stands too deep to regenerate oxidized standard ruthenium bipyridyl dye. Therefore both the dye and the redox couple have been simultaneously optimized for strong performance [99, 100] and this approach has provided large rewards in terms of power conversion efficiency [2].

A number of solid electrolytes have been amply investigated, OMETAD being the best known [101–103] but other materials such as CuSCN [104] and P3HT [3, 105] also showed promising results. In such solid conductors the free carrier density is not as high as in the liquid one, and easy shielding and electroneutrality is not warranted but need to be carefully investigated. IS studies of these DSCs with a solid hole conductor using either organic or inorganic absorbers have shown that the transport of holes in these HTMs is usually an issue that introduces a large additional resistance affecting the fill factor of the solar cell [104–106]. Using high extinction solid absorbers such as Sb_2S_3 sensitizer, it was reported that in planar, thin layer configurations, the solid cells provide a sizable photocurrent, but a poor fill factor [105]. It is concluded that the role of mesostructure is not only to provide a large internal area for carrier generation. Charge compensation to satisfy

electroneutrality is also a central property of mesoporous DSC. The questions will very likely be more intensively investigated with perovskite absorbers, which very likely are genuine ambipolar transport materials that do not strictly need fast separation of carriers into different phases [4, 5, 107].

The one-dimensional diffusion-recombination model neglects the transport in the electrolyte and shielding conditions. A standard, more general approach to multiple carrier transport problems [77] is solved using a set of equations that comprises:

- Diffusion-drift equation for each carrier
- Poisson equation that determines the macroscopic electrical fields
- The boundary conditions

These equations must be combined with statements on energy distributions and charge transfer rates. Early models applied the idea of ambipolar diffusion [108], which is based on the coupling of just two types of carriers by electroneutrality [109, 110]. There have been many attempts to develop a general set of equations able to model the DSC behavior, especially with reference to mass transport limitations in liquid electrolytes [111–117]. It is tempting to aim at a simulation tool that will provide a "total" description of the DSC, but one should evaluate very carefully whether this goal is feasible, recognizing the complexity of the system. Many aspects of the DSC need to be studied separately, and simulation by a number of phenomenological equations cannot be a substitute for detailed physical understanding. For example, the structure of the three-phase contact at the base of the substrate, mentioned above, or the detailed rates of charge transfer dependence on energy and density, as well as the interactions at semiconductor/dye/hole conductor interface, are issues that have to be properly controlled when describing the system. New solar cell configurations and absorbers are bound to pose their own subtleties.

There has nevertheless been important progress in the formulation of simulation tools that can bring useful results. The first important question is that two- or three-dimensional modeling [118] is able to deal with effects that are certainly beyond reach of simple one-dimensional modeling, such as the properties of exotic configurations of the solar cell [119] or important practical features such as the distribution of the measured quantities in the solar cell plane due to edge effects [120, 121]. The second relevant line of progress is that the main defect of old approaches, which was to compare a model with dozens of parameters, with a measured jV curve that may be described with just two or three, has been corrected. More sophisticated approaches incorporate the physics that has been learned about DSC, such as nonlinear recombination model [14, 116, 122, 123]. An example of realistic modeling including all carriers present in the DSC, as well as free and trapped electrons, is shown in Fig. 10 [123]. In addition, researchers have recognized that different experimental techniques have to be combined in order to provide a meaningful and reliable characterization for the solar cell performance [124–127]. In particular, the coupling of multidimensional modeling with impedance spectroscopy analysis has become a powerful method in order to establish sound results and interpretation of DSC devices [121, 124].

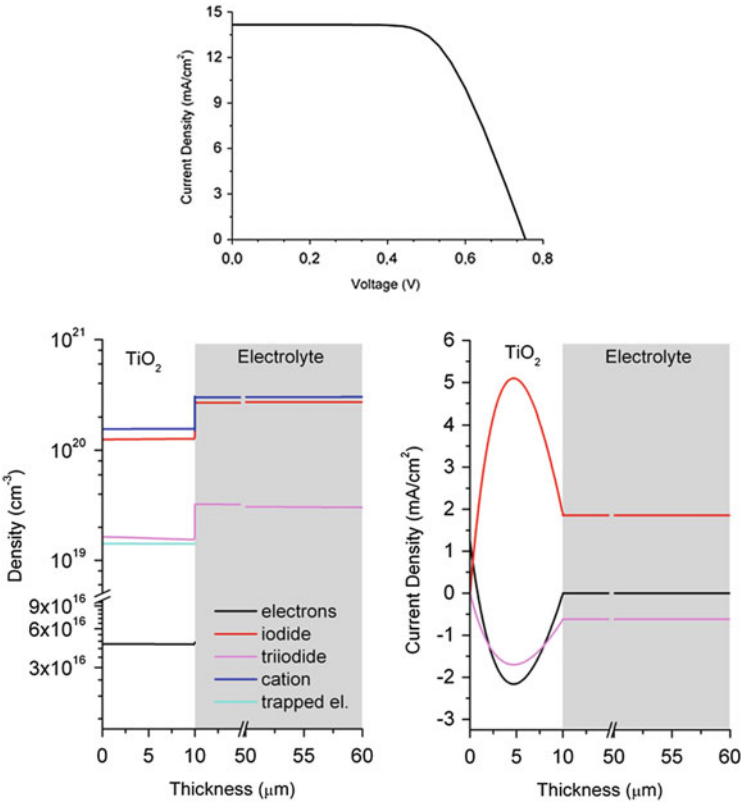

Fig. 10 *Upper panel*: simulation of a current–voltage characteristic for a typical DSC (10 μm of mesoporous TiO_2/electrolyte, 50 μm of pure electrolyte) with N719 dye. *Lower panel*: density distribution (*left*) and current density (*right*) within the cell at 737 mV (close to open-circuit condition). The *left picture* shows all the charged species in the system: electrons (free and trapped), iodide and triiodide, positive counter-ion. For the current density only the charged species which contribute to the total current are shown: free electrons, iodide and triiodide ions. Simulation performed using TiberCAD software, courtesy of Alessio Gagliardi and Aldo di Carlo

6 Energy Disorder in the Semiconductor: Combined Description of Free and Trapped Electrons

In previous sections we have commented on the success of the fundamental diode model, based on electron density in the conduction band, n_c, and phenomenological β-recombination model in Eq. (13), for a first understanding of current voltage curves of high quality DSC. However, it has been well established that electron density restricted to a single level poses important limitations for the description of measurements of DSC, such as recombination resistance, diffusion coefficient, electron lifetime, diffusion length, etc., due to the fact that the localized states in

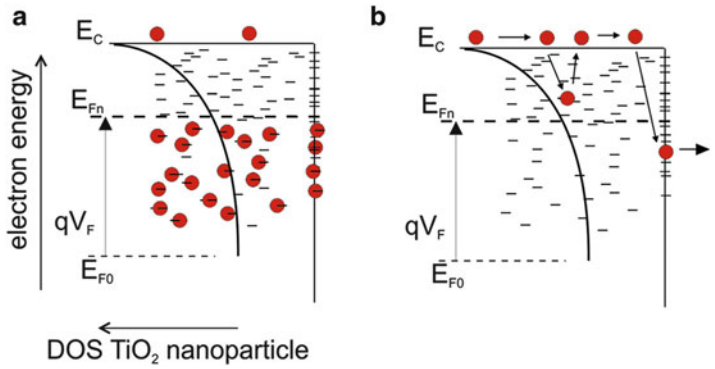

Fig. 11 Characteristic distribution of electronic states in the metal oxide nanoparticulate framework of a DSC, and their role in different electronic processes. (**a**) The electronic states consist of the transport states in the conduction band level, E_c, the localized states in the bandgap, which form an exponential distribution, and the surface states, whose energy distribution depends drastically on surface treatment. For an exponential distribution it is a good approximation to assume that localized states in the bandgap below the Fermi level are occupied and those above nearly empty. The occupation of the transport level is an important consideration as it gives rise to d.c. conductivity. The occupation of surface states depends on their charge transfer properties. (**b**) Electron displacement in transport states is interrupted by trapping and release processes. Trapping occurs mainly to unoccupied states above the Fermi level. Electrons are trapped in surface states from which charge transfer to acceptor species in solution occurs

the bandgap produce strong dynamic effects [17, 128–133]. A model that is successful to account for most observed properties is indicated in Fig. 11a. It is composed of the transport level that was discussed above, at energy E_c, and a density of states (DOS) in the bandgap, $g(E)$. A key feature is that an electron in the transport level can be trapped in a localized state in the bandgap and later be thermally ejected to the conduction band. By thermalization the carrier density in the localized states is found to be

$$n_L = \int_{-\infty}^{+\infty} g(E) f(E - E_{Fn}) dE \tag{25}$$

where $f(E - E_F)$ is the Fermi–Dirac function. The total carrier density is

$$n = n_c + n_L \tag{26}$$

In the DSC as well as in similar devices, the carrier density is measured in steps at different voltages, or by small perturbation methods. It is important to characterize the differential of the carrier density, which is known as the chemical capacitance [134].

In general the differential capacitance that is measured by small perturbation has the expression

$$C = \frac{\mathrm{d}Q}{\mathrm{d}V} \tag{27}$$

The textbook example is a *dielectric capacitor*, in which the charge separation creates an electrical field between the plates. The capacitance, per unit area, is given by

$$C = \frac{\varepsilon\varepsilon_0}{d} \tag{28}$$

We obtain a chemical capacitance when the Fermi level in a semiconductor is displaced with respect to the conduction band edge, because in this case we only change the *chemical potential* of the electrons, and not their electrostatic potential. A structure of selective contacts is also necessary so that the Fermi level variation translates into a voltage as follows:

$$\mathrm{d}V = \mathrm{d}E_{\mathrm{Fn}}/q \tag{29}$$

This structure is presented in Figs. 2 and 11, in which the change of voltage implies that the Fermi level of electrons moves toward the conduction band, as stated before in (6). If L is the thickness of the layer, and A is the area, the charge accumulated in the semiconductor is $Q = -LAnq$. Hence we obtain the *chemical capacitance* [134, 135] per unit area, that is defined as follows:

$$C_\mu = LAq^2 \frac{\mathrm{d}n}{\mathrm{d}E_{\mathrm{Fn}}} \tag{30}$$

A specific chemical capacitance per unit volume is defined as

$$c_\mu = q^2 \frac{\mathrm{d}n}{\mathrm{d}E_{\mathrm{Fn}}} \tag{31}$$

For conduction band carriers the chemical capacitance is

$$c_\mu^{\mathrm{cb}} = \frac{q^2 n_{\mathrm{c}}}{k_{\mathrm{B}}T} \tag{32}$$

This was first calculated by Shockley for crystalline semiconductors [136]. The concept is very useful in the characterization of disordered materials [12, 137]. In the DSC the contribution of trapped electrons is dominant. The calculation of the chemical capacitance for a broad DOS is

$$c_\mu = q^2 \int_{-\infty}^{+\infty} g(E) \frac{\mathrm{d}f}{\mathrm{d}E_{\mathrm{Fn}}} (E - E_{\mathrm{Fn}}) \mathrm{d}E \tag{33}$$

Using the approximation of the zero-temperature limit of the Fermi function, i.e., a step function at $E = E_{\mathrm{Fn}}$ separating occupied from unoccupied states, as suggested in Fig. 11a, it can be shown that (33) reduces to [12]

$$c_{\mu}^{\mathrm{L}} = q^2 g(E_{\mathrm{Fn}}) \tag{34}$$

In this approximation, the Fermi–Dirac function is a unity step function at the Fermi level. Therefore, displacing the Fermi level by $\mathrm{d}E_{\mathrm{F}}$ simply fills with carriers a slice of the DOS: $\mathrm{d}n = g(E_{\mathrm{F}})\mathrm{d}E_{\mathrm{F}}$. c_{μ} is also denoted a *thermodynamic density of states* [138].

Measurements of the chemical capacitance of nanostructured TiO_2 have shown that the localized states are distributed as an exponential distribution that enters the gap of the semiconductor from the conduction band, as suggested in Fig. 11 and indicated by the expression

$$g(E) = \frac{N_{\mathrm{L}}}{k_{\mathrm{B}}T_0} \exp[(E - E_{\mathrm{c}})/k_{\mathrm{B}}T_0] \tag{35}$$

Here N_{L} is the total density of localized states and T_0 is a parameter with temperature units that determines the depth of the distribution, which can be alternatively expressed as a coefficient $\alpha = T/T_0$. The DOS of nanostructured TiO_2 has been well characterized experimentally [139]. The exponential distribution is observed in measurements of chemical capacitance shown in Figs. 4d and 5c. The DOS resulting from such measurements is indicated in Fig. 7.

An important feature of the DOS of the nanostructured metal oxide is that E_{c} can be displaced with respect to the redox level, and this method is frequently used to improve the photovoltage, as mentioned before [93]. The change of position of the conduction band is obvious in Fig. 4d, where a shift ΔE_{c} is marked, with respect to a reference sample. Note that the shift changes the equilibrium density, n_{c0}, by (2), and this affects the dark reverse current, j_0. These variations are more generally discussed in the next section. Therefore a control of the DOS of electrons in titania is essential for the meaningful discussion of recombination and any other electronic parameter of the DSC.

In most conditions of measurement we can assume that $n \approx n_{\mathrm{L}}$. The equilibrium value of the carrier density is given by

$$n_{\mathrm{L0}} = N_{\mathrm{L}} \mathrm{e}^{(E_{\mathrm{F0}} - E_{\mathrm{c}})/k_{\mathrm{B}}T_0} \tag{36}$$

Again, using zero-temperature approximation the total electron carrier density is given by the integration of DOS up to the Fermi level, (25):

$$\begin{aligned} n &= \int_0^{E_{\mathrm{Fn}}} g(E)\, \mathrm{d}E \\ &= N_{\mathrm{L}} \mathrm{e}^{(E_{\mathrm{Fn}} - E_{\mathrm{c}})/k_{\mathrm{B}}T_0} \\ &= n_{\mathrm{L0}} \mathrm{e}^{qV_{\mathrm{F}}/k_{\mathrm{B}}T_0} \end{aligned} \tag{37}$$

Therefore the chemical capacitance of the localized carriers in the exponential distribution can be written as

$$c_{\mu}^{\mathrm{L}} = \frac{q^2 n}{k_{\mathrm{B}} T_0} \tag{38}$$

It should be stated that we now have two density parameters n and n_{c} to describe equations modeling the DSC. We have assumed so far that both densities relate to a single Fermi level. Equations (1) and (37) provide the following condition:

$$\frac{n}{n_{\mathrm{L0}}} = \left(\frac{n_{\mathrm{c}}}{n_{\mathrm{c0}}}\right)^{\alpha} \tag{39}$$

In fact in steady state conditions, such as in the calculation of current voltage curves, one could formulate equations in terms of either three parameters: n, n_c, or V (or more appropriately, V_{F}, to discount any series and shunt resistance) [122]. Which is the best choice? There is not a single answer, but, as shown in Fig. 4, modeling work in DSC often reverts to explaining the components of current-density voltage curves, and therefore the voltage is a very good choice for the x axis representation of different parameters. If different samples have a similar DOS it is also useful to compare quantities plotted vs n. However, if the DOS is variable then V_{F} should be preferred, since a value of the Fermi level is stipulated at each voltage. The special feature of the carriers at the transport level, or free electrons, n_{c}, is that carrier density is simply related to the voltage V_{F} by (see (8))

$$n_{\mathrm{c}} = n_{\mathrm{c0}} \mathrm{e}^{qV_{\mathrm{F}}/k_{\mathrm{B}}T} \tag{40}$$

Therefore actual measurements of carrier density via chemical capacitance or any related stepped technique will provide the total carrier density n, but since actual measurements are often performed as function of voltage, the *free carrier density* (and not total carrier density) is a useful index of the voltage V_{F}. This is the advantage of expressing β-recombination model in terms of free carriers as in (15) [14], as then the exponent β immediately translates into the diode quality factor of (19). Since one can convert from free to total carrier density by the expression at (39), recombination of excess carriers can be phenomenologically modeled as a power-law dependence of the total carrier density:

$$j_{\mathrm{rec}} = qLB[n^{\gamma} - n_0{}^{\gamma}] \tag{41}$$

Comparing (15) we obviously have the relationship $\gamma = \beta/\alpha$. Equations (15) and (41) are equivalent expressions that do not speak about the origin of the recombination mechanism, which will be discussed later.

In summary, for the modeling of steady state quantities one can switch between n and n_{c} by using (39). When plotting different measured quantities, one has the

choice to use V or n. The carrier density n is convenient to remove the shift of the conduction band, but in general it is important to present the voltage as the main parameter that changes in the solar cell. For the description of time-dependent measurements the effects of traps is significant, and it is then important to maintain the distinction between n and n_c. Dynamic effects of traps will be discussed below.

7 Shift of Conduction Band and Change of Redox Level

We have already mentioned that modification of electrolytes and other factors produce a shift in the position of the TiO_2 conduction band, which is an important property of the DSC. E_c affects charge injection from the dye. In addition, the change of the position of the conduction band produces a strong variation of the recombination resistance, because the parameter j_0 is modified. Indeed note that by (2) and (14)

$$j_0 = qLk_{rec}N_c{}^{\beta}e^{\beta(E_{F0}-E_c)/k_BT} \tag{42}$$

Consequently the change of E_c produces a change of R_0, according to (22). It is important to introduce additional kinetic parameters that specify the properties of j_0. The following expression generalizes the suggestions in [28, 30] in order to include the change of redox level [32]. Let us define a kinetic constant j_{0k} that determines the recombination rate, independently of the conduction band position:

$$j_{0k} = qLk_{rec}N_c^{\beta} \tag{43}$$

Therefore

$$j_0 = j_{0k}e^{\beta(E_{F0}-E_c)/k_BT} \tag{44}$$

so that (19) becomes

$$j = j_{sc} - j_{0k}\,e^{\beta(E_{F0}-E_c)/k_BT}\left(e^{q\beta V_F/k_BT} - 1\right) \tag{45}$$

Equation (44) simplifies the treatment of empirical data by separation in the conventional "dark current" parameter (j_0) of two effects that frequently have an important influence on the behavior of DSC: E_c, that tracks possible changes of the position of the conduction band of the n-semiconductor and j_{0k} (or equivalently U_{0k} [32]) that represents changes in the charge transfer rate, e.g., by blocking the TiO_2 surface. The photovoltage gives

$$V_{oc} = \frac{E_c - E_{F0}}{q} - \frac{k_BT}{q\beta}\ln\frac{j_{ph}}{j_{0k}} \tag{46}$$

These variations are well illustrated in Fig. 4c, in which part of the shift of the recombination resistance is due to the change of the conduction band position that is visible in the chemical capacitance of Fig. 4d. An important tool to evaluate correctly the recombination rate is therefore to plot the recombination resistances of different devices at the same equivalent value of the position of the conduction band. Therefore we define a suitable potential,

$$V_{\mathrm{ecb}} = V_{\mathrm{F}} - \Delta E_{\mathrm{c}}/q + \Delta E_{\mathrm{F0}}/q \tag{47}$$

Here "ecb" stands for "common equivalent conduction band," ΔE_{c} is the shift of the conduction band, and ΔE_{F0} is the change of the redox potential of the hole conductor (for example when comparing different electrolytes), both with respect to a reference sample:

$$\Delta E_{\mathrm{c}} = E_{\mathrm{c}} - E_{\mathrm{c,ref}} \tag{48}$$

$$\Delta E_{\mathrm{F0}} = E_{\mathrm{F0}} - E_{\mathrm{F0,ref}} \tag{49}$$

We obtain the following expression for the recombination resistance:

$$r_{\mathrm{rec}} = \frac{k_{\mathrm{B}}T}{q\beta j_{0\mathrm{k}}} \mathrm{e}^{-\beta\left(qV_{\mathrm{ecb}} - E_{\mathrm{c,ref}} + E_{\mathrm{F0,ref}}\right)/k_{\mathrm{B}}T} \tag{50}$$

Therefore, when plotted with respect to V_{ecb}, as shown in Fig. 4e, differences in the recombination resistance correspond exactly to the variation of the reciprocal of the kinetic parameter $j_{0\mathrm{k}}$, removing the influence of change conduction band position. The analysis is more complicated if the samples present different values of the DOS parameter α or recombination exponent β.

8 Electron Lifetime

In general the quantities characterizing the recombination flux cannot be obtained from analysis of steady state measurement, which supplies very limited information. Experimentally one uses a method that applies a small perturbation to obtain the recombination kinetics at each value of stationary voltage. Here we discuss the electron lifetime, τ_{n}, that is a quantity often used to characterize recombination dynamics in DSCs [50, 52, 140]. We review the definition of the lifetime as a first illustration of the small perturbation quantity [52, 140–144].

We take first the simplest recombination model which is that of linear recombination

$$U_{\mathrm{n}} = k_{\mathrm{rec}}(n_c - n_0) \tag{51}$$

The decay of a population of electrons is governed by the equation

$$\frac{\mathrm{d}n_c}{\mathrm{d}t} = -U_\mathrm{n}(n_\mathrm{c}) \tag{52}$$

Excess electrons injected can be written $\Delta n = n - n_0$, and their decay is controlled by the equation

$$\frac{\mathrm{d}(\Delta n_\mathrm{c})}{\mathrm{d}t} = -k_\mathrm{rec}\Delta n_\mathrm{c} \tag{53}$$

Therefore the decay with time takes the form

$$\Delta n_\mathrm{c}(t) = \Delta n_\mathrm{c}(0)e^{-t/\tau_\mathrm{n}} \tag{54}$$

In general we define the lifetime as the constant in the denominator of the exponential decay law. In (54) the lifetime, τ_n, is given by the prefactor of Δn in (53), that is,

$$\tau_\mathrm{n} = k_\mathrm{rec}^{-1} \tag{55}$$

However, we observe that such decay law depends critically on the fact that our starting recombination law in (51) is linear, while we have emphasized before that nonlinear recombination is the general rule in a DSC.

Let us take a system that is determined by any general recombination law $U_\mathrm{n}(n_\mathrm{c})$. A stationary density is maintained by a photogeneration G_Φ or similar process, so that the quasiequilibrium, stable carrier density, is $\bar{n}_\mathrm{c}$. The conservation equation at (4) can be written

$$\frac{\mathrm{d}n_\mathrm{c}}{\mathrm{d}t} = G_\Phi - U_\mathrm{n}(n_\mathrm{c}) \tag{56}$$

which in equilibrium sets the stable carrier density by the equation

$$U_\mathrm{n}(\bar{n}_\mathrm{c}) = G_\Phi \tag{57}$$

Now the small perturbation $\hat{n}$ that is induced on top of the steady state provides the density dependence on time as

$$n_\mathrm{c}(t) = \bar{n}_\mathrm{c} + \hat{n}_\mathrm{c}(t) \tag{58}$$

Using an expansion

$$U_\mathrm{n}(n_\mathrm{c}) = U_\mathrm{n}(\bar{n}_\mathrm{c}) + \frac{\partial U}{\partial n_\mathrm{c}}\hat{n}_\mathrm{c} \tag{59}$$

we obtain from (56)

$$\frac{\mathrm{d}\hat{n}_\mathrm{c}}{\mathrm{d}t} = -\frac{\partial U_\mathrm{n}}{\partial n_\mathrm{c}}\hat{n}_\mathrm{c} \tag{60}$$

The result we obtain in (60) is that the linearization procedure always takes the evolution equation to a form of the type (53) that will provide an exponential decay of the small perturbation excess density. A general feature of small perturbation methods is that all the nonlinear transport-conservation equations become linear.

Let us introduce the free carrier lifetime [52],

$$\tau_\mathrm{f} = \left(\frac{\partial U_\mathrm{n}}{\partial n_\mathrm{c}}\right)^{-1}_{\bar{n}_\mathrm{c}} \tag{61}$$

Hence (60) may be written as

$$\frac{\mathrm{d}\hat{n}_\mathrm{c}}{\mathrm{d}t} = -\frac{1}{\tau_\mathrm{f}}\hat{n}_\mathrm{c} \tag{62}$$

As an example of the small perturbation procedure, consider the nonlinear recombination law introduced in (13). Equation (4) can be written

$$\frac{\mathrm{d}\hat{n}_c}{\mathrm{d}t} = G_\Phi - k_\mathrm{rec}\left[(\bar{n}_\mathrm{c} + \hat{n}_\mathrm{c})^\beta - {n_\mathrm{c0}}^\beta\right] \tag{63}$$

Expanding the sum to first order in $\hat{n}$ and removing the steady state terms (that cancel out) we have

$$\frac{\mathrm{d}\hat{n}_\mathrm{c}}{\mathrm{d}t} = -k_\mathrm{rec}\beta {\bar{n}_\mathrm{c}}^{\beta-1}\hat{n}_\mathrm{c} \tag{64}$$

Therefore the lifetime is

$$\tau_\mathrm{f}(\bar{n}_\mathrm{c}) = \left(k_\mathrm{rec}\beta {\bar{n}_\mathrm{c}}^{\beta-1}\right)^{-1} \tag{65}$$

Obviously the result in (65) can be derived directly by (61). Note that the lifetime is a function of the steady state; this is a general feature of nonlinear systems.

The decay of a small population that serves as a probe of the kinetics of the system has therefore been characterized for any recombination rate law and steady state condition. More generally, the decay may require a number of sequential processes coupled to recombination, for example when prior detrapping of localized carriers is required, as we discuss later on. The free carrier lifetime τ_f in (61) does not yet consider the trapping–detrapping dynamics, but just the charge

transfer kinetics. More generally, the electron lifetime is defined in terms of the recombination rate $U_{\mathrm{n}}(n)$ and total carrier density as [52]

$$\tau_{\mathrm{n}} = \left(\frac{\partial U_{\mathrm{n}}}{\partial n} \right)^{-1}_{\bar{\mathrm{n}}} \tag{66}$$

The relationship with τ_{f} is provided below.

9 Trapping Factors in the Kinetic Constants

The main effects of traps in the dynamics of electrons in a DSC are indicated in Fig. 11b. For the long range transport of electrons in the nanostructure, also outlined in Fig. 1c, we distinguish two classes of electronic states: the transport states above the mobility edge (that may be associated with extended states in the conduction band) and localized states in the bandgap. These assumptions are common in the classical multiple trapping transport [145–147], which describes the effect of trap levels over the rate of displacement through transport states. Another important effect of traps, and more specifically surfaces states is to provide a variety of pathways in the energy axis for interfacial charge transfer, as indicated in Fig. 12b.

Let us consider the retarding effect of traps and how this effect changes the measured kinetic constants [51]. In the presence of traps, the time-dependent conservation equation for free carriers, n_{c}, contains an additional term, due to the net capture and release by traps, which results in a modified concentration of localized electrons n_{L}:

$$\frac{\partial n_{\mathrm{c}}}{\partial t} = G(x) - \frac{\partial J}{\partial x} - U_{\mathrm{n}}(n_{\mathrm{c}}) - \frac{\partial n_{\mathrm{L}}}{\partial t} \tag{67}$$

If we use the small perturbation approach of (54) again, (67) is split into two parts. The first is the steady state equation at (24). Note that the localized states do not introduce any new effect in the *steady state* conservation equation. Therefore quantities such as the electron conductivity are independent of the number and occupation of traps, as described further below.

The second equation is for the small perturbed density:

$$\frac{\partial \hat{n}_{\mathrm{c}}}{\partial t} = -\frac{\partial \hat{J}}{\partial x} - \frac{1}{\tau_{\mathrm{f}}} \hat{n}_{\mathrm{c}} - \frac{\partial \hat{n}_{\mathrm{L}}}{\partial t} \tag{68}$$

where we have included the free carrier lifetime as defined by (61). Equation (68) may be completed by a kinetic equation for the traps that defines the variation $\partial n_{\mathrm{L}}/\partial t$. However, if the trapping kinetics is fast (with respect to time scale of the transient measurement) we may assume that the traps follow the equilibrium relation with the free carriers:

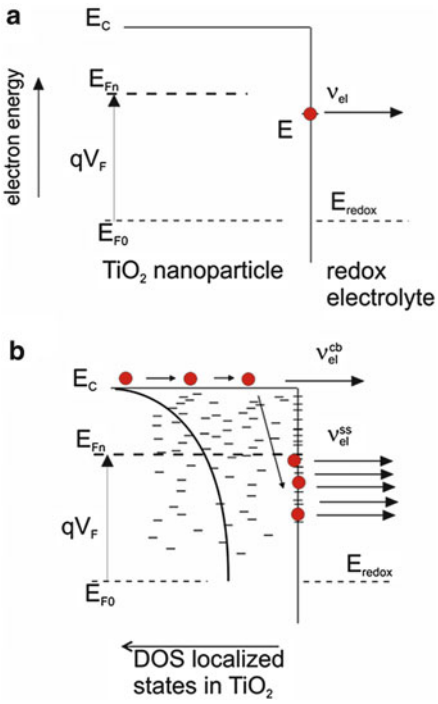

Fig. 12 Energy diagrams indicating recombination events in a DSC of electrons in TiO_2 semiconductor nanoparticle by transfer to the oxidized acceptor species of the redox couple in the electrolyte. E_c is the energy of the conduction band, E_{F0} is the equilibrium Fermi level in the semiconductor, that initially is in equilibrium with the redox level in the electrolyte, and E_{Fn} is the Fermi level in the semiconductor when the TiO_2 photoelectrode is at the potential V_F. (**a**) Electron transfer from a surface state at the energy E to an oxidized ion in electrolyte with probability ν_{el}. (**b**) Model including the various channels for electron transfer between the surface of TiO_2 nanoparticles and the oxidized species in the electrolyte (or hole conductor) in a DSC, namely, the transfer from extended states of the semiconductor conduction band with probability ν_{el}^{cb}, and the transfer from a distribution of surface states, each with a probability $\nu_{el}^{ss}(E)$

$$\frac{\partial n_L}{\partial t} = \frac{\partial n_L}{\partial n_c}\frac{\partial n_c}{\partial t} \tag{69}$$

We developed earlier in (39) the relationship between free and trapped carrier density when the system rests at equilibrium. Equation (69) has a different meaning in that it states that equilibrium will be maintained for any time variation during kinetic measurements. Equation (69) is termed *the quasistatic approximation* and it was introduced to account for the properties of measured time constants in DSC [51].

Applying the quasistatic approximation, (68) becomes

$$\left(1 + \frac{\partial n_L}{\partial n_c}\right)\frac{\partial \hat{n}_c}{\partial t} = -\frac{\partial \hat{J}}{\partial x} - \frac{1}{\tau_f}\hat{n}_c \tag{70}$$

We introduce the trapping factor

$$\Theta_{\mathrm{L}} = \left(1 + \frac{\partial n_{\mathrm{L}}}{\partial n_{\mathrm{c}}}\right) \tag{71}$$

From the previous definition of lifetimes, (61) and (66), we note that

$$\tau_{\mathrm{n}} = \Theta_{\mathrm{L}} \tau_{\mathrm{f}} \tag{72}$$

Equation (72) now gives the measured lifetime τ_{n} as a combination of two effects: trapping and detrapping effects in the bulk, and subsequent charge transfer, by a nonlinear dependence on the free carrier density. More complex theories of the electron lifetime extend this model by a combination of mechanisms and will be described later [50, 148, 149].

Furthermore we show later that the measured (chemical) diffusion coefficient is given by

$$D_{\mathrm{n}} = \frac{1}{\Theta_{\mathrm{L}}} D_0 \tag{73}$$

The trapping factor can also be expressed in terms of the chemical capacitances of the separate electronic states

$$\Theta_{\mathrm{L}} = \frac{c_{\mu}}{c_{\mu}^{\mathrm{cb}}} = \frac{c_{\mu}^{\mathrm{cb}} + c_{\mu}^{\mathrm{L}}}{c_{\mu}^{\mathrm{cb}}} \tag{74}$$

We note that, if the trapped electron density dominates, then

$$\Theta_{\mathrm{L}} \approx \frac{\partial n_{\mathrm{L}}}{\partial n_{\mathrm{c}}} = \frac{c_{\mu}^{\mathrm{L}}}{c_{\mu}^{\mathrm{cb}}} \tag{75}$$

For an exponential distribution,

$$\Theta_{\mathrm{L}} = \frac{T}{T_0} \frac{n_{\mathrm{L}}}{n_{\mathrm{c}}} \tag{76}$$

and we obtain the voltage dependence of the trapping factor as follows:

$$\Theta_{\mathrm{L}} = \frac{T}{T_0} \frac{n_{\mathrm{L0}}}{n_{\mathrm{c0}}} \exp\left[qV\left(\frac{1}{k_{\mathrm{B}}T_0} - \frac{1}{k_{\mathrm{B}}T}\right)\right] \tag{77}$$

Using Fick's law, (5), we convert (70) to

$$\frac{\partial \hat{n}_{\mathrm{c}}}{\partial t} = \frac{D_0}{\Theta_{\mathrm{L}}} \frac{\partial^2 \hat{n}_{\mathrm{c}}}{\partial x^2} - \frac{1}{\Theta_{\mathrm{L}} \tau_{\mathrm{f}}} \hat{n}_{\mathrm{c}} \tag{78}$$

and therefore

$$\frac{\partial \hat{n}_c}{\partial t} = D_n \frac{\partial^2 \hat{n}_c}{\partial x^2} - \frac{1}{\tau_n}\hat{n}_c \tag{79}$$

Equation (79) implies that the system of Fig. 11 can be treated with the dynamic equations of a single level, but with kinetic coefficients (lifetime, diffusion coefficient) that depend on the steady state. The essence of the quasistatic approximation is to describe the kinetic factors associated to trapping and detrapping in terms of occupation of free and localized states. The quasistatic approximation is explained in more detail in [51, 52, 150, 151]. It has been widely used to describe experimental results of DSCs.

Figure 13 shows electron densities and time constants dependence on voltage according to the model developed above, for an exponential distribution of traps. These features are often observed in experiments [16, 33, 43, 152, 153]. One exception is the free carrier density that will be commented on separately later. It is assumed that D_0, the free electron diffusion coefficient, is a constant. The calculation of the chemical diffusion coefficient in (73) for an exponential distribution gives an exponential dependence on the Fermi-level position as follows [154]:

$$D_n = \frac{T_0}{T}\frac{N_c}{N_L}\exp\left[(E_{Fn} - E_c)\left(\frac{1}{k_B T} - \frac{1}{k_B T_0}\right)\right] D_0 \tag{80}$$

Therefore the electron diffusion coefficient increases when the Fermi level rises. This is because the retarding effect of traps is suppressed when traps become increasingly occupied.

On the other hand, the free carrier lifetime, given in (61), depends on the voltage as follows:

$$\tau_f = \frac{{n_{c0}}^{1-\beta}}{\beta k_{rec}}\exp\left[(1-\beta)\frac{qV}{k_B T}\right] \tag{81}$$

and the lifetime has the expression [52]

$$\tau_n = \frac{T}{T_0}\frac{n_{L0}}{{n_{c0}}^{\beta}\beta k_{rec}}\exp\left[(\alpha-\beta)\frac{qV}{k_B T}\right] \tag{82}$$

We observe in Fig. 13 that the lifetime, τ_n, that is measured by the decay of the Fermi level, decreases with increasing potential, but this can be attributed mostly to the trapping factor. The change of position of the Fermi level changes the detrapping time in an exponential fashion. Characteristic experimental results are shown in Fig. 14 [155]. It should be pointed out that the relevant lifetime *for steady state conditions* is the free carrier lifetime, τ_f, which increases with the bias voltage as indicated in (81).

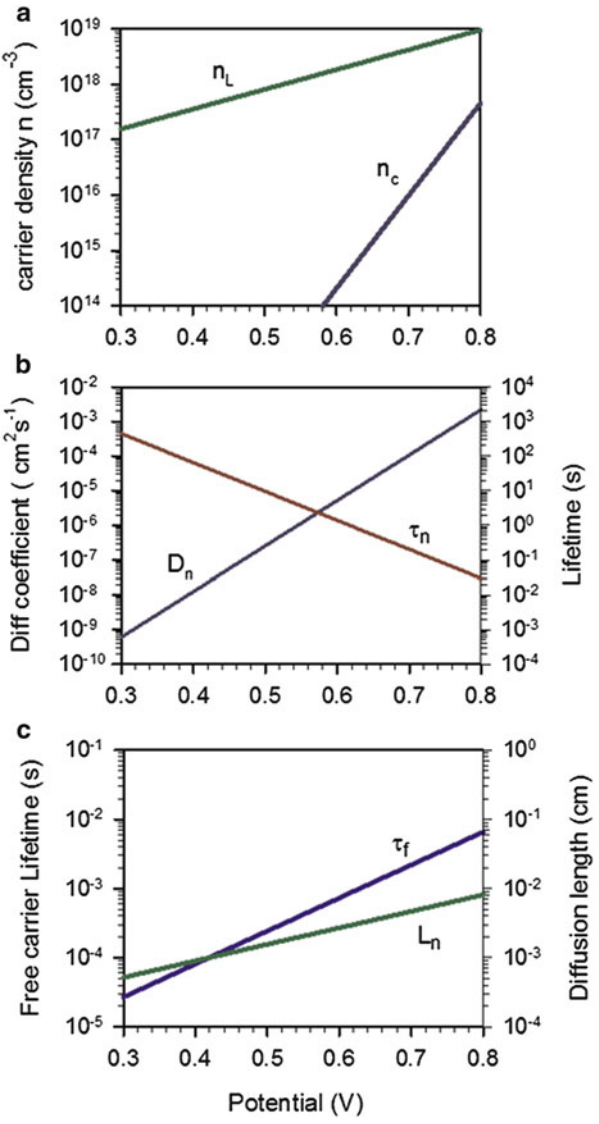

Fig. 13 (**a**) Representation of the free and localized carrier density, as a function of potential (Fermi level position), for an exponential distribution of localized states ($T = 300$ K, $T_0 = 1,400$ K, $\beta = 0.5 + T/T_0 = 0.71$). (**b**) Electron lifetime, τ_n and the diffusion coefficient, D_n measured by small perturbation. (**c**) Free carrier lifetime, τ_f, and diffusion length $L_n = \sqrt{D_n \tau_n} = \sqrt{D_0 \tau_f}$

Another important quantity is the diffusion length, as mentioned before and indicated in Fig. 1:

$$L_n = \sqrt{D_n \tau_n} \tag{83}$$

From (72) and (73) it can be seen that the trapping factors Θ_L compensate in the diffusion length [51]. However, if the free carrier lifetime shows some dependence

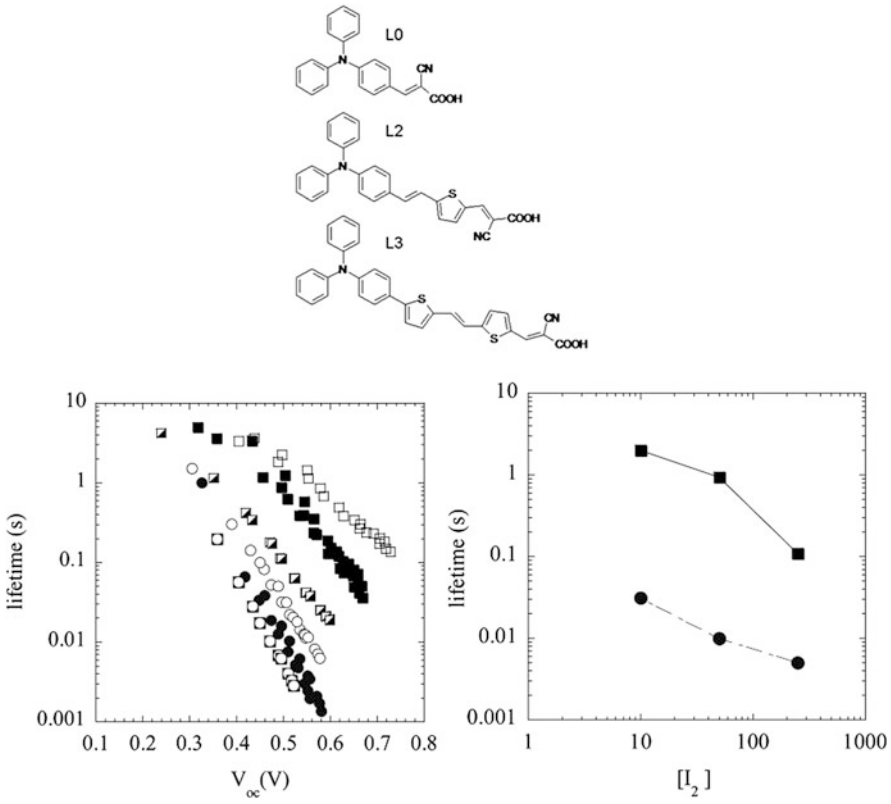

Fig. 14 (*Top*) Series of triphenylamine (TPA)-based dyes where the linker conjugation is systematically increased with vinylene and thiophene units. (*Left*) Electron lifetime as function of V_{oc} for DSCs based on L0 (*squares*) and L3 (*circles*) using three different I_2 concentrations: (*open symbols*) 10 mM, (*solid symbols*) 50 mM, and (*half-filled squares*, *gray circles in squares*) 250 mM in the redox electrolyte. Electrolyte: 0.6 M TBAI, 0.1 M LiI, and 0.5 M 4-*tert*-butylpyridine with different I_2 concentrations in acetonitrile. (*Right*) Electron lifetimes for DSCs based on L0 (*squares*) and L3 (*circles*) at $V_{oc} = 0.5$ V as a function of I_2 concentration. Reproduced with permission [155]

with the potential, as implied by (81), then the diffusion length varies with voltage, and it should increase according to [14]

$$L_n = \sqrt{D_0 \tau_f} \tag{84}$$

This feature, indicated in Fig. 13c, is often observed in experimental results; see Fig. 5d [152, 156]. The connection of the diffusion length with the trap dynamics has also been investigated by Monte Carlo simulation [13, 157, 158].

10 Chemical Diffusion Coefficient and Electron Conductivity

Details of Fermi level dependence of the diffusion coefficient, summarized in (77) can be obtained in the framework of a more general kinetic-thermodynamic formalism [13, 49, 154, 159].

First, the jump diffusion coefficient D_J is introduced, which is proportional to the tracer diffusion coefficient, D *, that reflects random walks of a particle:

$$D^* = \lim_{t \to \infty} \frac{1}{6Nt} \left\langle \sum_{i=1}^{N} (\Delta r_i)^2 \right\rangle \tag{85}$$

Consequently, D_J can be calculated by Monte Carlo simulation [13, 160, 161]. In the multiple trapping framework the jump diffusion coefficient is given by [49]

$$D_J = \frac{n_c}{n} D_0 \tag{86}$$

where $n \approx n_L$ is the total carrier density that coincides with trapped carriers in most conditions ($n_c << n_L$). The diffusion coefficient measured by small perturbation methods D_n is the *chemical diffusion coefficient* and differs from D_J by the quantity χ_n,

$$D_n = \chi_n D_J \tag{87}$$

that is called the *thermodynamic factor*, and is defined as follows:

$$\chi_n = \frac{n}{k_B T} \frac{\partial E_{Fn}}{\partial n} \tag{88}$$

Combining the general form of the chemical and jump diffusion coefficient, (86) and (87), we have, for the exponential distribution,

$$D_n = \frac{T_0}{T} \frac{n_{c0}}{{n_{L0}}^{1/\alpha}} {n_L}^{(1-\alpha)/\alpha} D_0 \tag{89}$$

This is exactly the same result as given above in (80). Another way to arrive at the same conclusion starts from the equation

$$D_n = \frac{k_B T}{q} \chi_n u_n \tag{90}$$

that is an statement of the generalized Einstein relation [49]. In (90) u_n is the mobility. From (87) we obtain

$$u_{\mathrm{n}} = \frac{qD_{\mathrm{J}}}{k_{\mathrm{B}}T} \tag{91}$$

u_{n} is related to the displacement of carriers in the total DOS, and is therefore proportional to the jump diffusion coefficient. Considering both free and trapped carriers, the thermodynamic factor can be written as

$$\chi_{\mathrm{n}} = \frac{n}{n_{\mathrm{c}}} \frac{1}{1 + \frac{\partial n_{\mathrm{L}}}{\partial n_{\mathrm{c}}}} \approx \frac{n}{n_{\mathrm{c}}} \frac{\partial n_{\mathrm{c}}}{\partial n_{\mathrm{L}}} \tag{92}$$

By combining (90), (91), and (92), one gets

$$D_{\mathrm{n}} = \left(1 + \frac{\partial n_{\mathrm{L}}}{\partial n_{\mathrm{c}}}\right)^{-1} D_0 \tag{93}$$

that coincides with (73).

In summary, there is a difference between the jump diffusion coefficient, which reflects the random walk of a particle in the available DOS and geometry, and the chemical diffusion coefficient measured by inducing a gradient by a small step method. The difference is expressed in (87) and consists of the thermodynamic factor that accounts for the difference between a gradient in concentration, and a gradient in electrochemical potential, thus generalizing Fick's law [12].

This connection is a fundamental one and it can be expected to operate more generally for other types of quantities. Indeed, the same type of relationship can be postulated for the electron lifetime, as shown recently by Ansari-Rad et al. [13, 56]. On the one hand, the small perturbation lifetime τ_{n} is related to the decay of the Fermi level after injection of excess carriers. On the other hand a "jump lifetime" τ_{J} can be calculated by Monte Carlo simulation by following the survival time of a specific carrier that undergoes the sequence of events indicated in Fig. 11b, i.e., random walk in the total DOS and charge transfer to acceptor species in the electrolyte. τ_{J} is different from the free carrier lifetime, τ_{f}, introduced above, in that the latter takes into account the survival time of a free carrier, just by the charge transfer mechanism, without counting the prior random walk. In fact τ_{f} corresponds to the free electrons diffusion coefficient in the diffusion formalism, D_0. The relationship between these two lifetime quantities is given by [13]

$$\tau_{\mathrm{n}} = \frac{\chi_{\mathrm{r}}}{\chi_{\mathrm{n}}} \tau_{\mathrm{J}} \tag{94}$$

where χ_{r} is a recombination factor that plays a role similar to thermodynamic factor χ_{n}.

It can be concluded that a general distinction exists between single particle quantities that can be monitored by random walk simulation methods, and collective

quantities that are measured by small perturbation, involving a modification of the chemical potential of the species. Both quantities are related by the classical thermodynamic factor [162] and its generalizations [13].

While the measurement of diffusion coefficient requires some type of small perturbation methods, the electron conductivity drives d.c. transport and can be measured in steady state conditions, for example by electrochemical gating [163, 164]. The electron conductivity can be given in terms of the total number of carriers and the mobility as [49]

$$\sigma_{\mathrm{n}} = n q u_{\mathrm{n}} \tag{95}$$

Using (91) we can write

$$\sigma_{\mathrm{n}} = \frac{q^2}{k_{\mathrm{B}} T} n D_{\mathrm{J}} \tag{96}$$

We can also express the conductivity in terms of the free carrier density as follows:

$$\sigma_{\mathrm{n}} = \frac{q^2 D_0}{k_{\mathrm{B}} T} n_{\mathrm{c}} \tag{97}$$

Additionally, we may provide a formulation of the generalized Einstein relation (90) that links the conductivity, the chemical diffusion coefficient, and the chemical capacitance [49, 165]:

$$\sigma_{\mathrm{n}} = D_{\mathrm{n}} c_{\mu} \tag{98}$$

It is important to note that (97) indicates that the conductivity is determined exclusively by the transport level and is *completely independent* of the presence and distribution of traps, in the context of the multiple trapping model that we have used herein. The steady-state conduction is not affected by the trapping process because the traps remain in equilibrium. Alternatively, one can view conduction as the result of the displacement of the whole electron density, n, with a smaller jump diffusion coefficient; see (96).

11 Delocalized Electrons in the Conduction Band

We have already commented that measurement of electron density by the chemical capacitance invariably reveals the exponential distribution associated with the trap states, or in general the shape of the dominant DOS at the Fermi level in the given material. The question arises whether the free carrier density, n_{c}, is really accessible

or is just a theoretical feature that conveniently describes the voltage V_F. We have seen that even if the free electron density is relatively low, the role of the free carrier density is crucial to provide long range transport. This feature is emphasized in Figs. 1c and 11b. Even though the general picture of Fig. 13, is very well supported by measurements of the time constants τ_n and D_n, it should be noticed that these parameters depend strongly on the traps in the system. It should be interesting to detect kinetic phenomena that depend exclusively on conduction band carriers.

Experimentally, such an observation is, however, far from straightforward. In principle, the method to access the free electrons density seems obvious. One has to apply the potential V_F large enough for increasing E_{Fn} close to E_c (see Fig. 11) in which case the large DOS at E_c will make the n_c population larger than n_L. However, this method encounters practical problems of large charging and band unpinning [166], so that increasing V_{app} does not really change V_F, as a result of which the conduction band capacitance of (32) has never been detected, as far as we know. (It can be observed, however, in defect-free silicon solar cells [79].) Connected with this question there is also a difficult problem, which is to determine the *exact position* of the conduction band, E_c, which has many implications for electron injection from the absorber and recombination models.

A direct method of detection of free electrons is provided by techniques such as spectroelectrochemistry and microwave conductivity. The first is based on the detection of the delocalized carrier by the specific absorption features, such as the Burstein shift, which is a spectral blueshift due to band filling, and additional intraband absorption in the infrared region of the spectrum [129, 151, 167, 168]. Recently Hamann et al. developed a detailed method based on temperature dependence of the free carrier density to locate the position of the conduction band [166]. The time-resolved microwave conductivity allows for a detection of electron carriers [169, 170] although the distinction between free and trapped electrons requires a detailed analysis [151]. A similar concern arises often in the interpretation of absorption data, since there are a number of possible absorption effects and these cannot be simply linked to the concentration [168].

A very important piece of evidence about the free carrier transport arises from the voltage dependence of the electron conductivity in (97). According to (40) the conductivity dependence on Fermi level voltage must satisfy the Boltzmann exponent q/k_BT,

$$\sigma_n = \frac{q^2 D_0 n_{c0}}{k_B T} e^{qV_F/k_BT} \tag{99}$$

This relationship is often observed to hold almost exactly [16, 34, 151, 171]. An example of the fit is shown in Fig. 5a [45], that displays the transport resistance, r_{tr}, that is the reciprocal to the electronic conductivity σ_n:

$$r_{tr} = \sigma_n{}^{-1} \tag{100}$$

as further discussed below. Some authors have introduced additional exponents in the carrier density related to d.c. conductivity [116], but the accurate measurement

of the transport resistance by IS [34, 151] shows that (99) based on the Boltzmann statistics of the free electrons is well satisfied in good quality cells. Indeed, for obtaining meaningful voltage dependence of transport and recombination resistances, a number of aspects of the experiment have to be carefully balanced, such as the possible bandshifts, or temperature changes of the redox potential [39].

The good behavior of electron conductivity according to the multiple transport model is, however, not conclusive about the dynamic effects of the carriers in extended states. One important consequence of the dominance of n_c is that the effect of traps on D_n should be removed, since $\Theta_L \rightarrow 1$. As a consequence, at high V_F, D_n must saturate to D_0 and exhibit a constant value [154]. Only a few results have been reported about these effects. Archana et al. [172] suggest that a band-edge type electron diffusion mechanism is observed in doped anatase mesoporous electrodes. Wang and Jennings reported recombination via the conduction band [173], which follows (49) by a recombination exponent $\beta = 1$, as further commented on below in the sections on recombination. This type of recombination mechanism has also been observed by Hamann et al. for the redox couple $[Co(Me_2bpy)_3]^{3+/2+}$ [148].

12 Diffusion-Recombination in Small Signal Methods

We have discussed above how the carrier density transport-kinetic equation is reduced to a linear form, with density dependent parameters, by the small perturbation method. Such an approach can also be applied for the measurement of a.c. current with respect to a.c. voltage analysis at variable frequency ω. The resulting impedance spectroscopy models for DSC have been presented in several works [29, 44, 150, 174, 175]. In brief, the conservation at (79) for the small perturbation of the carrier density can be translated to the general expression of the diffusion impedance in a film of thickness L:

$$Z(\omega) = [\zeta(\omega) r_{tr}]^{1/2} \coth\left\{L[\zeta(\omega) r_{tr}]^{1/2}\right\} \tag{101}$$

In (101) r_{tr} is the resistivity of the material (or *distributed* transport impedance, per unit length per area):

$$r_{tr} = A(1-p)R_{tr}/L \tag{102}$$

where R_{tr} is the macroscopic transport resistance of the film of geometric area A and p is porosity. r_{tr} is related to electron conductivity as indicated in (99). The diffusion impedance of (101) can be represented as a distributed equivalent circuit, the transmission line of Fig. 15a, that is closely connected to a class of transmission lines for porous electrodes as shown in Fig. 15b.

The case of interest for DSC and solar cells in general is the diffusion-recombination impedance with a reflecting boundary condition at the end of the

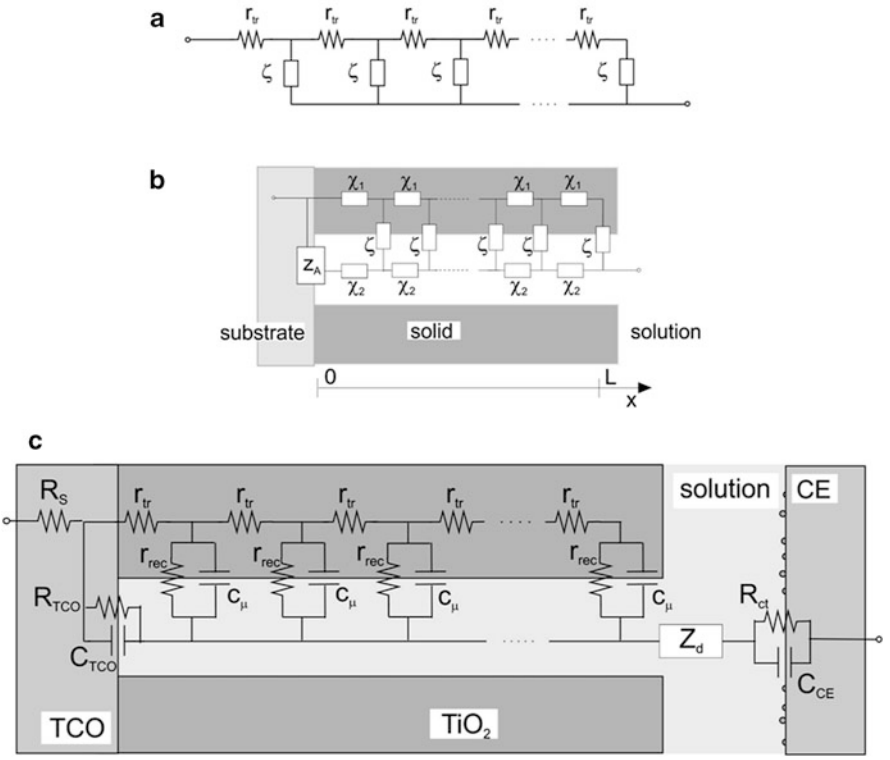

Fig. 15 (**a**) Transmission line model for the generalized diffusion impedance. (**b**) Transmission line model for a porous electrode. (**c**) Transmission line impedance model for diffusion-recombination in a mesoporous TiO_2 electrode, including also interfacial impedances and mass transport impedance in electrolyte

electron transport channel. The model is shown in Fig. 15c. The recombination process introduces a recombination resistance in parallel with the chemical capacitance in the transmission line [44]. The transverse ζ -impedance in (101) in this case is

$$\zeta = \frac{r_{\text{rec}}}{1 + i\omega/\omega_{\text{rec}}} \tag{103}$$

The characteristic frequency of recombination is related to electron lifetime τ_n by

$$\omega_{\text{rec}} = \tau_n^{-1} \tag{104}$$

The distributed recombination resistance is given by

$$r_{\mathrm{rec}} = LA(1-p)R_{\mathrm{rec}} = LA(1-p)\frac{\tau_{\mathrm{n}}}{C_{\mu}} \tag{105}$$

Here C_{μ} is the chemical capacitance. R_{rec} is the macroscopic recombination resistance of the layer that was introduced in (20) and will be the object of detailed analysis in the remaining sections of this chapter. The impedance model for diffusion-recombination adopts the form [44]

$$Z(\omega) = \left(\frac{R_{\mathrm{tr}}R_{\mathrm{rec}}}{1+i\omega/\omega_{\mathrm{rec}}}\right)^{1/2} \coth\left[(R_{\mathrm{tr}}/R_{\mathrm{rec}})^{1/2}(1+i\omega/\omega_{\mathrm{rec}})^{1/2}\right] \tag{106}$$

The transmission line circuit and impedance spectra of the model of (106) are shown in Fig. 16. By fitting the spectra to this model we can obtain:

1. The electron conductivity; see (99).
2. The chemical diffusion coefficient, D_{n}:

$$D_{\mathrm{n}} = \frac{1}{R_{\mathrm{tr}}C_{\mu}} = \frac{\omega_{\mathrm{d}}}{L^2} \tag{107}$$

This last equation corresponds to the generalized Einstein relation given in (90).

3. The electron lifetime, that is obtained as follows:

$$\tau_{\mathrm{n}} = \omega_{\mathrm{rec}}^{-1} = R_{\mathrm{rec}}C_{\mu} \tag{108}$$

The impedance model of (106) produces different types of spectra, as shown in Fig. 16. The shape of the impedance spectra is determined by the factor relating the characteristic frequencies, which can be expressed in several alternative ways [44]:

$$\frac{\omega_{\mathrm{d}}}{\omega_{\mathrm{rec}}} = \frac{R_{\mathrm{rec}}}{R_{\mathrm{tr}}} = \left(\frac{L_{\mathrm{n}}}{L}\right)^2 \tag{109}$$

Note that the diffusion length can be obtained from the measured resistances by the expression

$$L_{\mathrm{n}} = \left(\frac{R_{\mathrm{rec}}}{R_{\mathrm{tr}}}\right)^{1/2} L \tag{110}$$

The spectrum for $R_{\mathrm{tr}} < R_{\mathrm{rec}}$ is shown in Fig. 16b, c. It corresponds to a long diffusion length $L_{\mathrm{n}} > L$ and indicates efficient charge collection in a DSC at moderate forward bias [16]. The opposite case, for strong recombination, requires $R_{\mathrm{tr}} > R_{\mathrm{rec}}$, and is shown in Fig. 16e. The intermediate spectrum for $R_{\mathrm{tr}} \approx R_{\mathrm{rec}}$ is

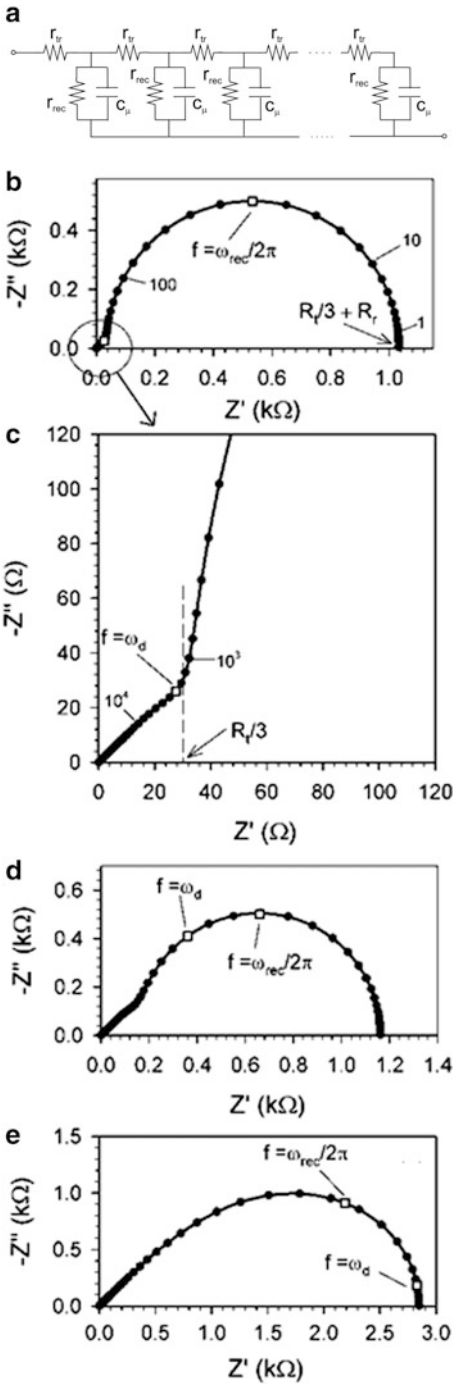

Fig. 16 Diffusion-recombination transmission line with reflecting boundary conditions. (**a**) Simulation of the impedance with parameters $R_{rec} = 10^3\ \Omega$, $C_\mu = 5 \times 10^{-6}$ F and increasing transport resistance, (**b**, **c**) $R_{tr} = 10^2\ \Omega$, (**d**) $R_{tr} = 10^3\ \Omega$, (**e**) $R_{tr} = 10^4\ \Omega$. Shown are the frequencies in Hertz at selected points, the characteristic frequency of the low frequency arc (*square point*), related to the angular frequency $\omega_{rec} = \tau_n^{-1} = 1/R_{rec}C_\mu$, and the low frequency resistance. The frequency (Hz) of the turnover from Warburg behavior to low frequency recombination arc (*square point*), related to the characteristic frequency $\omega_d = 1/R_{tr}C_\mu$ is also shown

shown in Fig. 16d. These impedance spectra have been widely described and utilized in experiments [16, 34, 37, 39, 43, 45, 151, 156].

13 General Picture of Recombination in a DSC

In the discussion of the fundamental diode model we have already emphasized the outstanding importance of recombination of photogenerated electrons for the energy conversion properties of the DSC device. In practice, the DSC progress has been very much based on the development of better dyes and coadsorbents. Indeed, current collection, as generated by dye injection, is not generally a major limitation, and charge collection efficiencies close to unity are routinely obtained in good quality devices. A major problem of the DSC is the loss of voltage, from the dye bandgap about 1.6 eV to the actual V_{oc} of less than 1 V [92]. Figure 7 shows the dramatic loss of voltage that occurs due to the deep position of the dye ground state with respect to the redox level of the electrolyte. Optimization of DSC requires one to govern the position of the TiO_2 conduction band, as high as possible, while not hindering injection from the dye, and most of all, controlling the recombination rate [11].

These features occurring at the semiconductor/dye/hole conductor system can be analyzed using a variety of techniques [60, 176]. We have already commented on how to measure recombination properties, via electrons lifetimes and recombination resistance, among a variety of available methods [126, 127, 155, 177–179]. In the final sections of this chapter we aim to provide deeper insight into the fundamental mechanisms of recombination in a DSC.

Starting from our general knowledge of electronic states, and fundamental properties of charge transfer at semiconductor-electrolyte interface, reviewed in the next section, a general model of recombination by electron transfer from TiO_2 to a redox electrolyte has been developed [16, 50, 180, 181], based on the scheme of Fig. 12; this model has been well validated by experimental results, as discussed later. We will focus here on the recombination towards a well defined redox species in a redox electrolyte, while other situations, such as the organic hole conductor or the solid absorbers, will not be specifically discussed and we refer the reader to the literature [40, 102, 176].

14 Fundamental Factors Determining Rates of Electron Transfer

When an electron is transferred from one reactant in a solution to another, for example, from a Ru $(NH_3)_6^{2+}$ ion in water to a Fe $(H_2O)_6^{3+}$ ion in the same solvent, the electron cannot simply jump from one ion to the other, because the

solvent environment, namely, the ensemble of orientations of the surrounding solvent molecules after the jump, would not be appropriate to the new ionic charges, and so just after the electron transfer the system would have a much higher total energy than before the jump. The atomic nuclei move so slowly that they do not have time to adapt their positions or velocities to the new charges during the electron jump (Franck–Condon principle), and so the transfer would violate the law of conservation of energy.

Instead, as discussed in a 1956 article on the theory of electron transfer reactions [182], before an electron can jump from one reactant to the other there first has to be a "reorganization" of the solvent molecules around the ions. Similarly, there also has to be a "reorganization" of relevant vibrational bond lengths in each reactant, and sometimes in the bond angles [183, 184]. After a suitable configurational reorganization of the relevant coordinates has been achieved such that the total energy of the entire system before and after the electron jump is unchanged, energy is conserved in the jump. This energy is the sum of all contributions to the potential energy and kinetic energy of the molecules and ions present. The reorganization involves suitable changes in the relevant orientations and in the bond lengths and sometimes in the bond angles of the species present prior to the electron transfer. There are, thus, fluctuations in all coordinates of the reactants and their surroundings, ~10^{24} coordinates for a mole of solvent.

If the system has N position and momentum coordinates, where $N \sim 10^{24}$, the transition state for an electron transfer reaction occupies an $N-1$ dimensional "hypersurface" in this N-dimensional space. Accordingly, in the reacting system when the reacting pair and its surroundings cross that $N-1$ dimensional hypersurface, they form the reaction products, according to transition state theory. We treated this reorganization for electron transfer between a pair of reactants in a solvent [182], and subsequently for an electron transfer at metal electrodes [184–188], electron transfer at semiconductor electrodes [187, 189, 190], and electron transfer across liquid–liquid interfaces [191]. In each case there is a reorganization of the orientations of the solvent molecules, of reactant bond lengths, and sometimes of their bond angles [183–188, 192–194].

The theoretical expressions for these different experimentally studied systems are given in the following, where k_{rate} denotes the reaction rate constant [185]:

$$k_{\text{rate}} = Ae^{-\Delta G^*/k_B T} \tag{111}$$

where

$$\Delta G^* = w^{\text{r}} + m^2\lambda \tag{112}$$

$$-(2m+1)\lambda = -\Delta G^0_{\text{R}} \tag{113}$$

$$\Delta G^0_{\text{R}} = \Delta G^0 + w^{\text{p}} - w^{\text{r}} \tag{114}$$

and

$$\lambda = \lambda_0 + \lambda_i \tag{115}$$

In the case where the electron transfer is to or from an electrode, (114) is replaced by [184, 185, 193]

$$\Delta G_R^0 = -z_q q\eta + w^p - w^r \tag{116}$$

In (114) w^r is the "work" (free energy change) required to bring the reactants from a large distance (sufficiently large that they do not interact at that distance), to a separation distance R, or in the case of an electron transfer with an electrode (see (115)), to a distance R from its electrostatic image in the electrode (twice the distance between the center of charge of the reactant and the electrode surface) and w^p is the corresponding quantity for the products. The ΔG^0 in (114) is the "standard" free energy of reaction in the existing solvent medium. The m in (112) can actually serve as a reaction coordinate, being 0 for the reactants and -1 for the products and given by (113) for the transition state.

In (116) z_q is $-$ |z| (+ |z|) for the transfer of |z| electrons (holes), q is the positive elementary charge, and η is the overpotential of the electrode, defined as $\eta = U - U^{0'}$. Here U is the electrode potential in the electrochemical convention (note that with respect to the voltage V defined in previous sections, $U = -V$) and $U^{0'}$ is the "standard" reduction potential of the electrode for the transfer of electron from the electrode to the reactant in the prevailing solvent. For example, if the metal electrode is biased negatively to promote a one electron transfer electrochemical reduction reaction, then $\eta < 0$, and $z = -1$. The "work" separating products from reactants is $-q\eta$, so that $\Delta G_R{}^0 < 0$.

The units of A in (111) depend on the geometry, for example in an electron transfer in solution, the units depend on whether or not the reactants are bound together and, in the electrode case, on whether the reactant is or is not bound to the electrode. In the unbound case, A could be written as a relevant "collision frequency" Z multiplied by κ, an electronic transition probability of electron transfer in the transition state, being about or near unity for an "adiabatic" or a "nearly adiabatic" electron transfer, and substantially less than unity for a highly "nonadiabatic" electron transfer. In a nonadiabatic electron transfer the electronic coupling of the reactant wave functions is small and so the probability of electron transfer when the system reaches the intersection of the reactant and the product potential energy surfaces is also small. In contrast, in an adiabatic electron transfer the electronic coupling element, coupling the reactant and the product wave functions near or at the intersection, is substantial and essentially every system reaching that intersection region undergoes an electron transfer. An approximate expression for the transition probability is given by the famous 1932 Landau–Zener expression [195, 196]. A recent survey and analysis of these adiabatic-nonadiabatic effects is given in [197]. An example of a nonadiabatic electron transfer to or from an

electrode is an electron transfer across a layer of parallel long chain of CH_2's bridging groups in thioalkanes, each bound via its sulfide atom to a gold electrode and at the other end of the chain bound, in a classic experiment, to a ferrocene [198]. We will return to the nonadiabatic case later.

The reorganization effects relate the thermodynamic free energy difference ΔG^0 between reactants and products to the transition state activation free energy ΔG^* that actually determines the rate constant in (111). Combining (112)–(114) we obtain the form of the rate constant for electron transfer:

$$k_{\text{rate}} = A\exp\left[-\frac{w^{\text{r}}}{k_{\text{B}}T} - \frac{1}{4\lambda k_{\text{B}}T}\left(\lambda + \Delta G^0_{\text{R}}\right)^2\right] \tag{117}$$

The rate constants for both the nonadiabatic and adiabatic electron transfers critically depend on the reorganization energy λ and on a prefactor A whose value depends on the "nonadiabaticity" of the electron transfer. We describe the properties of both parameters in turn.

The λ_0 in (115) describes the reorganization energy of the dielectric medium (the solvent and, in the semiconductor electrode case, also the solid). The λ_i in (115) arises from the change in equilibrium values of vibrational coordinates of the reactants, including, in the semiconductor case, any of its relevant vibrational coordinates. For example, if the reactant(s) undergoes a change Δq_i in the equilibrium value of some collective coordinate, a "normal coordinate" of a reactant, and if k_j^r and k_j^p are the "force constants" of that normal mode for the reactant and for the product, respectively, then classically [184]

$$\lambda_i = \sum_j \left[k_j^r k_j^p / \left(k_j^r + k_j^p\right)\right]\left(\Delta q_j\right)^2 \tag{118}$$

where Δq_j is the change in the jth normal mode coordinate, normal mode because there are no cross-terms between the different js in (118). Some ions, such as $Ru(NH_3)_6^{2+}$ + $Ru(NH_3)_6^{3+}$ undergoing electron transfer have a small Δq_j while some others, such as the $Fe(H_2O)_6^{2+}$ + $Fe(H_2O)_6^{3+}$ have a larger Δq_j and hence a larger λ_i. The magnitude of these quantities is explained by electronic structure arguments. In the ions cited above the largest contributor to Δq_j comes from the symmetric stretching ("breathing") coordinate of the coordination shell of a reactant.

For an electron transfer reaction between two reactants in solution a dielectric continuum treatment for the reorganization energy λ_0 gave [182]

$$\lambda_0 = (\Delta e)^2\left(\frac{1}{2a_1} + \frac{1}{2a_2} - \frac{1}{R}\right)\left(\frac{1}{\varepsilon_{\text{op}}} - \frac{1}{\varepsilon_{\text{s}}}\right) \tag{119}$$

where Δe is the charged transferred, the two a_is are the radii of the two reactants, ε_{op} is the optical dielectric constant (square of the refractive index) of the solvent, and ε_{s} is the static dielectric constant.

For electron transfer at a metal electrode, λ_0 is given instead by [184, 185]

$$\lambda_0 = (\Delta e)^2 \left(\frac{1}{2a} - \frac{1}{R}\right)\left(\frac{1}{\varepsilon_{\text{op}}} - \frac{1}{\varepsilon_{\text{s}}}\right) \tag{120}$$

where R is the distance between the center of charge of the ion and its electrostatic image in the electrode.

For a semiconductor electrode, the expression for λ_0 is a little more complex, since now there is also a reorganization in the semiconductor electrode itself. The λ_0 is given by [189, 190, 199]

$$\lambda_0 = \frac{(\Delta e)^2}{2a}\left(\frac{1}{\varepsilon_1^{\text{op}}} - \frac{1}{\varepsilon_1^{\text{s}}}\right) - \frac{(\Delta e)^2}{2R}\left(\frac{\varepsilon_2^{\text{op}} - \varepsilon_1^{\text{op}}}{\varepsilon_2^{\text{op}} + \varepsilon_1^{\text{op}}}\frac{1}{\varepsilon_1^{\text{op}}} - \frac{\varepsilon_2^{\text{s}} - \varepsilon_1^{\text{s}}}{\varepsilon_2^{\text{s}} + \varepsilon_1^{\text{s}}}\frac{1}{\varepsilon_1^{\text{s}}}\right) \tag{121}$$

The λ_0 for electron transfer across the interface of two liquids is more complex, since there are now two media and two reactants. The λ_0 for this case is given in [191], omitted here since the present main focus is not on electron transfer across a liquid–liquid interface.

The simplest type of electron transfer reaction is the self-exchange reaction, for example, the transfer of an electron from an $Fe(H_2O)_6^{2+}$ to an $Fe(H_2O)_6^{3+}$. The ΔG^0 in (114) is now zero, w^{r} and w^{p} are equal, and $a_1 = a_2$. This class of reactions (known in the literature as "self exchange" or "isotopic exchange" reactions) is the simplest class of reactions in all of chemistry. In a simple electron transfer, no chemical bonds are broken or are formed. The m in (112) and (113) is now $-1/2$. Apart from w^{r} and w^{p} in (114) and (116), the free energy barrier to reaction ΔG^* is $\lambda/4$.

It can be seen from (119) that the smaller the radii a_i of the reactants the larger is λ_0. Small ions like Fe^2 have a larger λ_0 than large ions such as $Ru(bpy)_3^{2+}$. A physical interpretation is clear: the smaller the radii a_i the larger the orientating force of the ionic charges on the nearby solvent molecules, and so the greater the difference between the ion-polar solvent interaction before and after electron transfer, and so the larger the reorganization energy λ_0. The role of the separation distance R that appears in (119)–(121) is also clear. When the two ions in solution are close to each other (see (119)), or when an ion approaches a metal electrode (see (120)) or a semiconductor electrode (see (121)), that is, when R in each case is smaller, the reorganization energy λ_0 is smaller. This effect is readily understood in physical terms: when R is smaller, solvent molecules at every point in the system see less of a change in the electric field acting on them, comparing before and after the electron transfer. These two different fields are the field created by the reactant charges and the field created by product charges. Indeed, when the separation distance R of the reactants is small, distant solvent molecules hardly see a change of electric field accompanying the electron transfer. In the case of a charge near an electrode, there is only one ion experiencing that change of electric field, and in that case the image charge tends to nullify the field of the ionic charge, and the nullifying effect is larger the smaller the R.

One also sees that when the solvent is nonpolar, that is when $\varepsilon_s = \varepsilon_{op}$, the solvent contribution to λ_0 arising from the orientational and vibrational part of its dielectric polarization disappears. So λ_0 is smaller the less polar the medium. There may also be specific solvent effects, absent in a dielectric continuum treatment but present in a molecular treatment of the solvent.

There are various estimates one can make for A in (111). For example, if the reaction is between two reactants in solution, and if they are linked together or in a precursor complex, then A has units of a first-order rate constant (sec^{-1}). For a nonadiabatic reaction (weak electronic coupling element) it can be written as (see [194] and references cited therein)

$$A = \frac{2\pi}{\hbar} \frac{|H|^2}{(4\pi\lambda k_B T)^{1/2}} \tag{122}$$

where H is the electronic matrix element coupling the two reactants. One approximation for the latter for a coupling bridge of length R is (see [194] and references cited therein)

$$|H|^2 \approx 10^{13} e^{-\alpha_b R}/s \tag{123}$$

where α_b depends on the nature of the bridge between the reactants. It is about $0.1\ nm^{-1}$ for a chain of CH_2 groups and much smaller for a link of conjugated units. Estimates have been made for various systems and are available from interpretations of experimental data.

For a nonadiabatic electron transfer to or from an electrode, denoting by ε an energy state of the electrode, the first-order rate constant k_{rate} is given by [186, 187]

$$k_{rate} = \frac{2\pi \int d\varepsilon\, e^{-\Delta G^*(\varepsilon)/k_B T} |H(\varepsilon)|^2 f(\varepsilon) d\varepsilon}{\hbar (4\pi\lambda k_B T)^{1/2}} \tag{124}$$

where $\Delta G^*(\varepsilon)$ (apart from the work terms – if the reactant is brought from infinity) [184] for the case of transfer from the metal electrode is given by

$$\Delta G^*(\varepsilon) = \frac{[\lambda - z_q q\eta - \varepsilon]^2}{4\lambda} \tag{125}$$

In (124) $f(\varepsilon)$ is the Fermi–Dirac distribution function for the probability that a state $\mathbf{k}$ in the electrode with an energy $\varepsilon(\mathbf{k})$ is occupied, and $|H(\varepsilon)|^2$ is an electron wave number $\mathbf{k}$-weighted interaction coupling element [186, 187],

$$|H(\varepsilon)|^2 \equiv \int d^3k |H_{kA}|^2 \delta[\varepsilon(\mathbf{k}) - \varepsilon] \tag{126}$$

where H_{kA} is the electronic matrix element coupling the reactant A and a state $\mathbf{k}$ of the electrode, and δ is the Dirac delta function.

To depict the energetics of chemical reactions one often plots some quantity such as the potential energy or free energy along a reaction coordinate. When a reaction involves breaking one bond and forming another a commonly used reaction coordinate is some linear combination of the two bond lengths. In the present case we have an overwhelmingly large number of relevant coordinates and, even in a dielectric continuum model, an infinite number of relevant coordinates. So in this case a quite different type of reaction coordinate is needed. One possibility is to introduce a linear combination of the equilibrium values for the reactants and for the products and to plot various quantities as a function of that coordinate. For example, for a vibrational coordinate q_j one could introduce a reaction coordinate x, via $q_j(x) = q_j^{\mathrm{r}} + x(q^{\mathrm{p}} - q_j^{\mathrm{r}})$ and for a vectorial quantity $\mathbf{P}_{\mathrm{u}}(\mathbf{r})$ related to the orientation-vibrational dielectric polarization of the solvent at each point $\mathbf{r}$ of the system and introduced in the 1956 article [182], one would write $\mathbf{P}_{\mathrm{u}}(\mathbf{r},\mathbf{n}) = \mathbf{P}_{\mathrm{u}}^{\mathrm{r}}(\mathbf{r}) + x[\mathbf{P}_{\mathrm{u}}^{\mathrm{p}}(\mathbf{r}) - \mathbf{P}_{\mathrm{u}}^{\mathrm{r}}(\mathbf{r})]$, where the $\mathbf{P}_{\mathrm{u}}(\mathbf{r})$s denote the equilibrium value of that quantity when the charges are those of the reactants (superscript r) and when they are those of the products (superscript p).

In terms of this reaction coordinate x, and the free energy of the reactants and surroundings, relative to their initial value, $\Delta G^*(x)$ is a function of a reaction coordinate x, given by

$$\Delta G^{*\mathrm{r}}(x) = w^{\mathrm{r}} + x^2\lambda \tag{127}$$

Along this curve for the reactant free energy vs x, $x = 0$ corresponds to the reactants but in surroundings appropriate to the reactant charges, $x = 1$ corresponds to the products but in surroundings appropriate to the product charges, and $x = -m$ where m is given by (113) corresponds to the transition state. The free energy for the products relative to their initial configuration is given by

$$\Delta G^{*\mathrm{p}}(x) = w^{\mathrm{p}} + (1-x)^2\lambda \tag{128}$$

A plot of the free energy changes is given in Fig. 17. R denotes the free energy curve given by (127) and P denotes the curve given by (128). The difference in vertical heights of the bottoms of the two wells is $\Delta G_{\mathrm{R}}^{0'}$, the "standard" free energy of reaction in the prevailing medium at the separation distance R, and contains all three terms in (114). Reaction proceeds via fluctuations of all the coordinates, starting from $x = 0$ on the R curve, transitioning to the P curve at the intersection, and proceeding on the P curve to the region at $x = 1$.

When instead one uses a purely statistical mechanical approach, and also perhaps with a view to do computer simulations of the free energy curves, a reaction coordinate grounded in statistical mechanics is needed. One introduced in [183], and later elaborated in [184] is an energy difference coordinate. The potential energy of all particles in the reacting system U^{r} is a function of all the coordinates, whose totality is denoted by $\mathbf{Q}$ and written as $\mathrm{U}^{\mathrm{r}}(\mathbf{Q})$. Similarly, the reaction products and their environment have a potential energy function $\mathrm{U}^{\mathrm{P}}(\mathbf{Q})$.

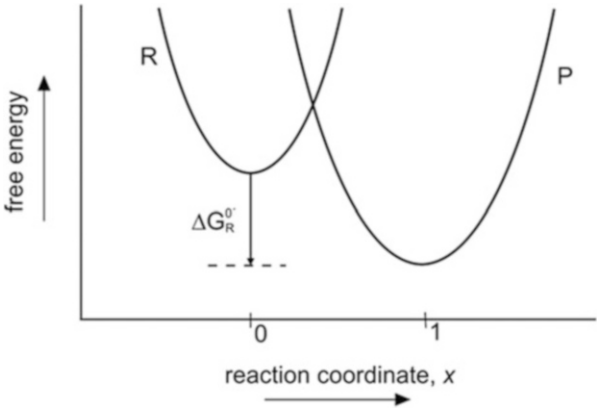

Fig. 17 Free energy curves as a function of the reaction coordinate. $\Delta G_R^{0'}$ indicates the "standard" change of free energy from reactants (R) to products (P) and is negative in the illustrated case in the figure

The potential energy difference $U^{\mathrm{r}}(\mathbf{Q}) - U^{\mathrm{r}}(\mathbf{Q})$, a function of the N coordinates, has a fixed value on an $N = 1$ dimensional surface in N-dimensional space and so can be used as a reaction coordinate in a statistical mechanical treatment of the electron transfer, as in [183, 184]. One can calculate a free energy of the system with the reactant charges and a free energy of a system with the product charges, as a function of that coordinate. The free energy plots for the reactant and for the products would look as in Fig. 17.

Some of the factors discussed earlier in this section can be seen in Fig. 17. When the bond length change from reactants to products is less, it corresponds to shifting the two parabolas in Fig. 17 closer horizontally, so reducing the height of the intersection. Similarly, when the radii of the reactants are larger the difference in ion–solvent interaction before and after the electron transfer is less and again corresponds to shifting the curves horizontally closer together and so reduces the height of the intersection. When, because of a more favorable standard free energy of reaction, i.e., more negative or more favorable standard potential, the P curve in Fig. 17 is shifted vertically downward relative to the R curve, and the free energy barrier is smaller for the system depicted by Fig. 17.

15 Carrier Transfer at Semiconductor/Electrolyte Interface

The mechanism of charge transfer that constitutes recombination in a DSC can be formulated as a product of three quantities: the electron density, the concentration of the acceptor (the oxidized half of the redox electrolyte), c_{ox}, and the probability of single transfer event ν_{el}, that is described by the electron transfer model of the previous section, as shown in Fig. 12a. Due to the disorder in the energy axis of the metal oxide, we have a variety of possible electronic channels that constitute parallel recombination mechanisms, as indicated in Fig. 12b.

For the direct charge transfer of conduction band electrons, we have the recombination rate given by

$$U_{\mathrm{cb}} = \nu_{\mathrm{el}}^{\mathrm{cb}}(E_{\mathrm{c}}) c_{\mathrm{ox}} [n_{\mathrm{c}} - n_{\mathrm{c0}}] \tag{129}$$

This formula is also expressed as

$$U_{\mathrm{cb}} = [n_{\mathrm{c}} - n_{\mathrm{c0}}] e_{\mathrm{ox}}^{\mathrm{cb}} \tag{130}$$

where

$$e_{\mathrm{ox}}^{\mathrm{cb}} = c_{\mathrm{ox}} \nu_{\mathrm{el}}^{\mathrm{cb}}(E_{\mathrm{c}}) \tag{131}$$

The model of (129) leads to a linear recombination rate, as stated in (51). In addition, the charge transfer from the metal oxide may occur via a distribution of surface states, as shown in Fig. 12b, and the recombination rate has the form

$$\mathrm{d}U_{\mathrm{ss}}(E) = g_{\mathrm{ss}}(E) f_{\mathrm{ss}}(E)\, e_{\mathrm{ox}}^{\mathrm{ss}}(E)\, \mathrm{d}E \tag{132}$$

where $g_{\mathrm{ss}}(E)$ is the density of surface states, $f_{\mathrm{ss}}(E)$ is the fractional occupancy, and

$$e_{\mathrm{ox}}^{\mathrm{ss}}(E) = c_{\mathrm{ox}} \nu_{\mathrm{el}}^{\mathrm{ss}}(E) \tag{133}$$

The total rate of recombination via surface states is

$$U_{\mathrm{ss}} = c_{\mathrm{ox}} \int_{E_{\mathrm{redox}}}^{E_{\mathrm{c}}} g_{\mathrm{ss}}(E) f_{\mathrm{ss}}(E) \nu_{\mathrm{el}}^{\mathrm{ss}}(E)\, \mathrm{d}E \tag{134}$$

In the situation of Fig. 12a, the starting state of the electron in the semiconductor surface has energy E, while the free energy of electrons in the electrolyte is E_{redox}. The probability of an elementary electron transfer event is given in [186]. For a planar interface

$$\nu_{\mathrm{el}}(E) = \frac{2\pi}{\hbar} |H|^2 \frac{l_{\mathrm{sc}}}{\alpha_{\mathrm{sc}}\, \delta_{\mathrm{np}}\, {d_{\mathrm{sc}}}^{2/3} (6/\pi)^{1/3}} \mathrm{FC} \tag{135}$$

where

$$\mathrm{FC} = \frac{1}{\sqrt{4\pi k_{\mathrm{B}} T \lambda}} \exp\left[-\frac{(\lambda + \Delta G)^2}{4\lambda k_{\mathrm{B}} T} \right] \tag{136}$$

$$\Delta G = E_{\mathrm{redox}} - E \tag{137}$$

In (135) l_{sc} (cm^{-1}) is the effective coupling length between the oxidized redox ion and the electrode, α_{sc} (cm^{-1}) is the coupling attenuation factor as in (123), and

d_{sc} (cm^{-3}) is the density of the atoms that contribute to the density of states of either the surface states or the band of concern [200, 201]. δ_{np} (cm) is a volume to area ratio in the nanoparticulate semiconductor electrode.

The electron transfer rate is therefore given by the following formula:

$$\nu_{el}(E) = k_0 \exp\left[-\frac{(E_{redox} - E + \lambda)^2}{4\lambda k_B T}\right] \tag{138}$$

where $k_0 = A\, l_{sc}/[\alpha_{sc}\, \delta_{np}\, {d_{sc}}^{2/3}(6/\pi)^{1/3}]$, A being as in (122), so that k_0 is measured in units $cm^3\ s^{-1}$. $E_{redox} - E$ is negative in the situation of Fig. 12a. Equation (138) applies to each of the recombination channels indicated in Fig. 12b, according to the actual distribution of surface states that allow the electron transfer to the oxidized ion at the semiconductor surface.

It should be noted that when the energy difference $E - E_{redox}$ becomes larger than the reorganization energy λ, as for example for the transference from the conduction band states in Fig. 12b, the rate of charge transfer decreases (the "Marcus inverted region"). This reduction of the rate at high energy difference has an outstanding importance in biological systems for sunlight energy conversion in order to avoid recombination of spatially separated charges.

We have discussed in Sect. 7 that differences in the parameter j_{0k} could be attributed to changes of surface blocking, catalysis of charge transfer, etc. It should be desirable to pinpoint specific causes for the changes of recombination rates. As mentioned before, the usual shape of the recombination resistance dependence on voltage V_F is an exponential shape (see (21)) that relates to the phenomenological nonlinear recombination model of (13). Usually it is observed that $\beta = 0.6 - 0.75$, as mentioned before, but one report [173] has obtained the value $\beta = 1$ from the diode quality factor. This result corresponds to cells in which the conduction band edge was extremely low, so that conduction band transfer of (129) becomes the dominant mechanism. This is an exception, however, and one important task of the model is to explain the normal values $\beta = 0.6 - 0.75$, by a combination of charge transfer pathways, as indicated in (134). This result will be demonstrated in Sect. 16. The combined measurement of capacitance, recombination resistance, and application of the recombination model has allowed researchers to provide a very detailed picture of energetics and kinetics of recombination.

A number of studies have discussed the Marcus model in DSC [39, 179, 201–206]. In general, however, detailed insight to the basic charge transfer mechanisms has been prevented by the exceedingly complex reaction rate steps of the iodide/triiodide redox couple that shows very special characteristics, in which even the nature of the predominant electron acceptor is not clear yet, since it could be either via reduction of I_3^- or free iodine I_2 [207–211]. An example of the study of recombination is shown in Fig. 14, in which the electron lifetime is measured for a series of DSCs with triphenylamine (TPA) dyes in which the conjugation length is varied [155]. Larger dyes showed enhanced electron recombination while reducing

the dye size increases surface blocking of the dye layer and hence the electron lifetime. It was suggested that an interaction between the dye molecular structure and I_3^- and/or I_2 may be correlated to the increased polarizability of the larger TPA dyes. It is likely that dye-shuttle interaction [212] and a variety of reaction pathways associated with I_3^-/I^- prevent the successful application of outer sphere electron transfer in the Marcus model to this specific redox couple. Nonetheless it is also important to explain why this couple works so well in kinetic terms, i.e., why the injected electrons do not reduce I_3^- efficiently. Meyer et al. [213] have applied the Marcus model to one electron reduction of I_3^- and conclude that electrons trapped in TiO_2 react slowly with I_3^-. A different and very promising approach, which provides access to specific fundamental quantities governing charge transfer rates in a DSC, is the utilization of outer sphere redox couples, since these allow the observation of the lifetime features associated with the Marcus model [148, 179]. These last results are reviewed in the next section.

16 Recombination Resistance and Lifetime Models

In this section we aim to obtain the model calculation of the recombination flux, recombination resistance, and the electron lifetime in a DSC associated with the electron transfer by a combination of surface states that form an exponential distribution, with a DOS $g_{ss}(E)$, as shown in Fig. 12b, also considering the direct transfer from the conduction band [16, 50, 52, 180, 181, 206, 214].

The current per unit macroscopic area of an electrode of thickness L is

$$\begin{aligned} j_{rec} &= qLU_{ss} \\ &= qLc_{ox}\int_{E_{redox}}^{E_c} g_{ss}(E) f_{ss}(E)\nu_{el}^{ss}(E)\,dE \end{aligned} \tag{139}$$

The calculation of j_{rec} requires a stipulation of the surface states that are occupied. Since surface states exchange electrons both with the conduction band and the electrolyte, the statistics are more complex than in a bulk trap. The occupation of the surface states is determined by a demarcation level and in general it is not possible to define a Fermi level [180, 215]. For simplicity we assume here that the trapping–release rate is sufficiently fast, so that the surface state is in equilibrium with the transport states, and the occupancy of both is described by Fermi–Dirac distribution, with a single Fermi level.

The recombination resistance is

$$R_{rec}^{ss}(E_{Fn})^{-1} = A\frac{dj_{rec}(E_{Fn})}{dV} \tag{140}$$

Thus

$$R_{\mathrm{rec}}^{\mathrm{ss}}(E_{\mathrm{Fn}})^{-1} = q^2 L A c_{\mathrm{ox}} \int g_{\mathrm{ss}}(E)\, \nu_{\mathrm{el}}^{\mathrm{ss}}(E)\, \frac{\mathrm{d}f_{\mathrm{ss}}(E - E_{\mathrm{Fn}})}{\mathrm{d}E_{\mathrm{Fn}}} \mathrm{d}E \tag{141}$$

Applying the zero temperature limit of the Fermi–Dirac distribution, the following result is obtained [16]:

$$R_{\mathrm{rec}}^{\mathrm{ss}}(E_{\mathrm{Fn}})^{-1} = q^2 L A g_{\mathrm{ss}}(E_{\mathrm{Fn}}) e_{\mathrm{ox}}^{\mathrm{ss}}(E_{\mathrm{Fn}}) \tag{142}$$

Equation (142) states that the reciprocal charge-transfer resistance is proportional to the product of the density of surface states at the Fermi level, and the probability of electron transfer from such states. The calculation of the recombination resistance involves a small displacement of the Fermi level that fills the surface states precisely at the Fermi level, and hence the resistance detects only those states. In summary we have

$$R_{\mathrm{rec}}^{\mathrm{ss}}(E_{\mathrm{Fn}})^{-1} = C_{\mu}^{\mathrm{ss}}(E_{\mathrm{Fn}}) e_{\mathrm{ox}}^{\mathrm{ss}}(E_{\mathrm{Fn}}) \tag{143}$$

The free carrier lifetime can now be calculated from (108) by selecting the capacitance of just those electron states that participate in charge transfer [50, 52]. Therefore

$$\tau_{\mathrm{f}} = R_{\mathrm{rec}} C_{\mu}^{\mathrm{ss}} \tag{144}$$

where

$$C_{\mu}^{\mathrm{ss}} = L A q^2 g_{\mathrm{ss}}(E_{\mathrm{Fn}}) \tag{145}$$

is the chemical capacitance of the surface states. Using (143) we get

$$\tau_{\mathrm{f}}(E_{\mathrm{Fn}}) = \frac{1}{e_{\mathrm{ox}}^{\mathrm{ss}}(E_{\mathrm{Fn}})} = \frac{1}{c_{\mathrm{ox}} \nu_{\mathrm{el}}^{\mathrm{ss}}(E_{\mathrm{Fn}})} \tag{146}$$

The free carrier lifetime is inversely proportional to the fundamental charge transfer rate at the Fermi level. If we also consider bulk traps, described by the DOS $g_{\mathrm{b}}(E)$, and a chemical capacitance

$$C_{\mu}^{\mathrm{b}} = L A q^2 g_{\mathrm{b}}(E_{\mathrm{Fn}}) \tag{147}$$

then the measured lifetime contains a trapping factor as shown in (71), and we obtain the expression

$$\tau_{\mathrm{n}}(E_{\mathrm{Fn}}) = \frac{C_{\mu}^{\mathrm{b}} + C_{\mu}^{\mathrm{ss}}}{C_{\mu}^{\mathrm{ss}} e_{\mathrm{ox}}^{\mathrm{ss}}(E_{\mathrm{Fn}})} \tag{148}$$

If both bulk traps and surface states consist of an exponential distribution with a similar T_0, and number density N_{s} for surface states and N_{L} for total number of traps, the trapping factor is just a numerical constant that does not influence the voltage dependence of the lifetime. Equation (148) can therefore be stated as function of voltage as follows:

$$\tau_{\mathrm{n}}(V) = \tau_{\mathrm{n0}} \exp\left[\frac{(qV - \lambda)^2}{4\lambda k_{\mathrm{B}} T}\right] \tag{149}$$

where

$$\tau_{\mathrm{n0}} = \frac{N_{\mathrm{L}}}{N_{\mathrm{s}}} \sqrt{\frac{\pi\lambda}{k_{\mathrm{B}} T}} \frac{1}{c_{\mathrm{ox}} k_0^{\mathrm{ss}}} \tag{150}$$

There is no functional difference between τ_{n} and τ_{f}. The significance of this result must be emphasized. In a DSC we measure recombination resistance, chemical capacitance, and electron lifetime. However, when we wish to study fundamental charge transfer questions we really want to determine ν_{el}. Equation (146) states that we have access to the electron transfer probability.

The model of (149) is illustrated in Fig. 18 [50]. First Fig. 18a shows the electron transfer probability according to Marcus model as stated in (138). Here $V = \lambda/q$ is the point of maximum charge transfer rate, where activationless charge transfer occurs, and the Marcus inverted region occurs when $V > \lambda/q$. In Fig. 18b we observe the reciprocal product of chemical capacitance and transfer rate, which is the recombination resistance of (142) that is further discussed below. The lifetime is plotted in Fig. 18c. Note that the carrier transference at the interface through the exponential distribution of surface states corresponds to the curved region at low voltage. The lifetime has a parabolic shape (semilogarithmic) as it follows exactly the Marcus rate ν_{el} dependence on the Fermi level [50].

The expression (148) can be generalized very easily to include additional parallel recombination pathways. For example we can incorporate the direct transference from the conduction band that has a recombination resistance

$$R_{\mathrm{rec}}^{\mathrm{cb}}(E_{\mathrm{Fn}})^{-1} = C_{\mu}^{\mathrm{cb}}(E_{\mathrm{Fn}}) \mathrm{e}_{\mathrm{ox}}^{\mathrm{cb}} \tag{151}$$

We observe that the denominator of (148) is the reciprocal of the total recombination resistance, (151), and the numerator is the total chemical capacitance. Since the reciprocal parallel resistances are added to obtain a total resistance, we have more generally [50]

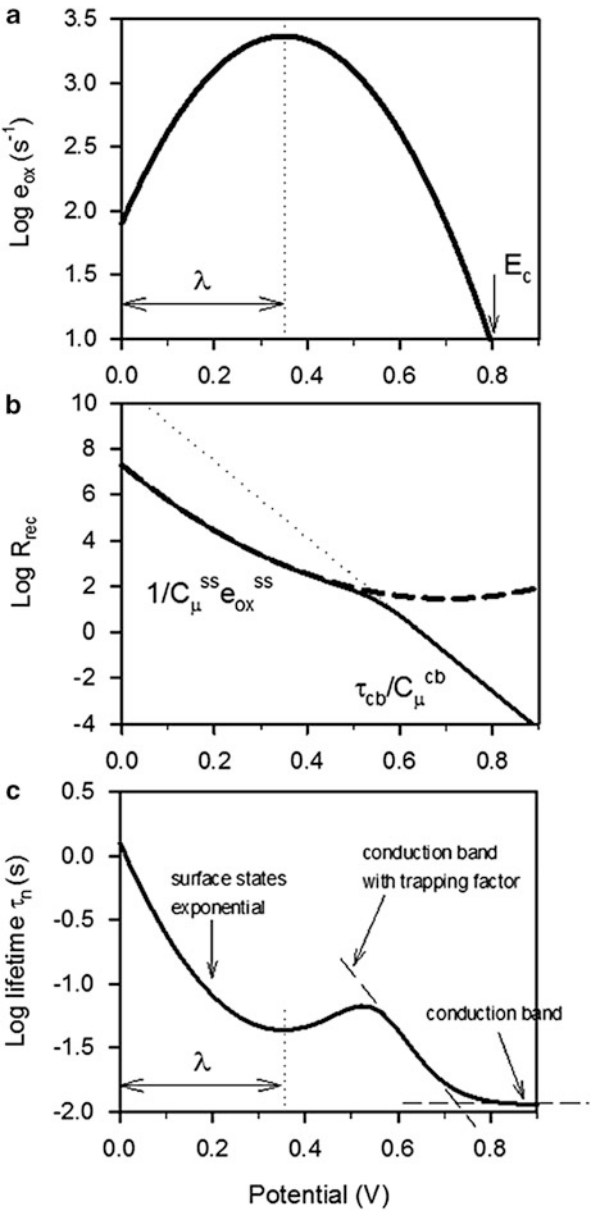

Fig. 18 Recombination in a DSC according to the Marcus model of charge transfer in an exponential distribution of surface states. *Horizontal axis* is the voltage or equivalently the electron Fermi level. (**a**) Probability electron transfer to the electronic levels of oxidized species in solution. (**b**) The inverse of charge transfer rates, both for conduction band and surface trap transfer mechanisms, and total recombination resistance in *thick line*. (**c**) The lifetime, indicating the charge transfer mechanism that corresponds to each domain. Simulation parameters are:

$$\tau_n(E_{Fn}) = \frac{C_\mu^b + C_\mu^{ss} + C_\mu^{cb}}{C_\mu^{ss} e_{ox}^{ss}(E_{Fn}) + C_\mu^{cb} e_{ox}^{cb}(E_{Fn})} \tag{152}$$

Now according to (152) there are three regions in the lifetime plot of Fig. 18c. The curved region at low voltage corresponds to the combination of the exponential surface state distribution, and the curvature of the Marcus transfer model indicated in Fig. 18a. It should be noted that the minimum of the lifetime occurs at the same point of the maximum charge transference. A second region is due to charge transfer via the conduction band, in which τ_f is independent of voltage, and the lifetime decreases at increasing voltage due to the trapping factors indicated in (71). Finally, conduction band electrons become dominant when the Fermi level approaches the conduction band, and here $\Theta_L \to 1$ in (71) so that $\tau_n \approx \tau_f$ is a constant.

Alternatively we may analyze the recombination resistance dependence on voltage. The resistance in (142) takes the form [16]

$$R_{rec}(E_{Fn}) = R_{0\lambda} \exp\left[\frac{(E_{Fn} - E_{redox} - \lambda)^2}{4\lambda k_B T} - \frac{E_{Fn} - E_c}{k_B T_0}\right] \tag{153}$$

where

$$R_{0\lambda} = \frac{\sqrt{\pi \lambda k_B T}}{q^2 L A k_0^{ss} c_{ox} N_s \alpha} \tag{154}$$

Equation (153) can also be expressed as

$$R_{rec}(E_{Fn}) = R_{0\lambda} \exp\left[\frac{q^2 (V - V_\mu)^2}{4\lambda k_B T} + \frac{E_c - E_{redox} - \lambda(1+\alpha)}{k_B T_0}\right] \tag{155}$$

where the following constant has been introduced:

$$V_\mu = \left(1 + 2\frac{T}{T_0}\right)\frac{\lambda}{q} \tag{156}$$

Figure 19a shows the characteristic probability of electron transfer according to the Marcus model, for different values of the reorganization energy. According to (155) the resistance dependence on voltage, shown in Fig. 19b, consists in a

Fig. 18 (continued) $\lambda = 0.35$ eV, $T = 300$ K, $L = 10$ μm, $E_c = 0.8$ eV vs E_{redox}, $N_c = 6.8 \times 10^{20}$ cm^{-3}, $N_b = 1 \times 10^{20}$ cm^{-3}, $N_s = 1 \times 10^{18}$ cm^{-3}, $T_{0s} = T_{0b} = 600$ K, $c_{ox} = 3 \times 10^{19}$ cm^{-3}, $k_0^{(cb)} = 5 \times 10^{-15}$ cm^{3}s^{-1}, $k_0^{(ss)} = 5 \times 10^{-16}$ cm^{3}s^{-1}. Reproduced with permission [50]

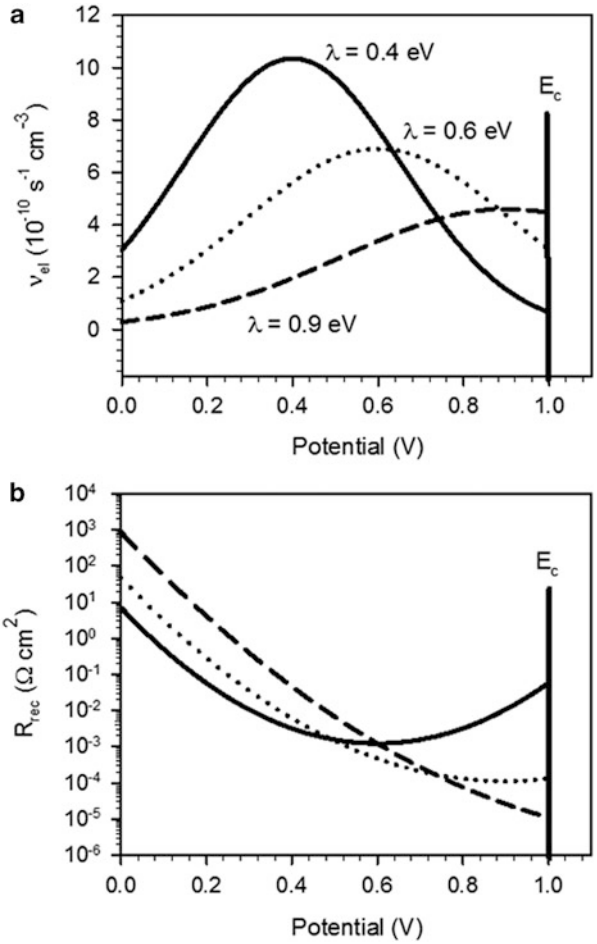

Fig. 19 Recombination in a DSC according to the Marcus model of charge transfer in an exponential distribution of surface states. *Horizontal axis* is the voltage or equivalently the electron Fermi level. The position of the conduction band, E_C, is indicated. Plots at different values of reorganization energy as indicated. (**a**) Electron transfer probability. (**b**) Electron recombination resistance. Simulation parameters are: $T = 300$ K, $T_0 = 1{,}200$ K, $\alpha = 0.25$, $\beta = 0.75$, $E_c = 1$ eV vs E_{redox}, $k_0^{ss} = 1 \times 10^{-7}$ cm^{-3}s^{-1}, $R_{0\lambda} = 10^{-5}$ Ω cm^2

Gaussian function, an inverted parabola (semilogarithmic), centered at the energy V_μ indicated in (156). The minimum of the parabola of R_{rec} is shifted positive in the scale of the Fermi level, with respect to the point of maximum charge transfer, at the voltage λ/q, by an amount $2\lambda\alpha = 2\lambda T/T_0$. The displacement of the minimum of the resistance with respect to that of ν_{el} is due to the product of the chemical capacitance of the exponential distribution.

In previous sections we have remarked that R_{rec} usually shows in DSC an exponential dependence on voltage, as stated in (21). While the result in (155)

produces a parabolic shape, we can observe in Fig. 19b that, for a large λ, the shape observed at $V << \lambda$ is a straight line. Thus the model of (21) can be obtained as a limit case of (155). Let us write the recombination resistance in the form

$$R_{\rm rec}(V) = R_0 \exp\left[-\frac{q\beta V}{k_{\rm B}T} + \frac{q^2V^2}{4\lambda k_{\rm B}T}\right] \tag{157}$$

where

$$R_0 = R_{0\lambda} \exp\left[\frac{E_{\rm c} - E_{\rm redox}}{k_{\rm B}T_0} + \frac{\lambda}{4k_{\rm B}T}\right] \tag{158}$$

$$\beta = \frac{1}{2} + \frac{T}{T_0} \tag{159}$$

The main feature is that the parabola in the exponential of the Marcus model electron, corresponding to transfer rate between the semiconductor surface and redox acceptor in the electrolyte, translates in curvatures. When $V << \lambda$, (155) reduces to the exponential dependence that was suggested above as a phenomenological approach. Furthermore, based on the microscopic model, the parameter β accepts the form (159) [16].

Summarizing the model results, we find that despite many simplifications the model of Fig. 12b provides a detailed description of the lifetime and recombination resistance, quantities that can be measured as a function of the voltage in a DSC. The main feature is that the parabola in the exponential of the Marcus model electron transfer rate between the semiconductor surface and redox acceptor in the electrolyte translates in curvatures of $\tau_{\rm n}$ and $R_{\rm rec}$. These quantities have been reported in hundreds of publications, but usually a linear behavior in semilogarithmic plot is observed, as reported in representative measurements of Figs. 4, 5, and 14. The absence of curvature could be evidence of a large reorganization energy in the DSC with I_3^-/I^- redox couples, and the value $\lambda = 1$eV is often used [213]. A simpler explanation is that the outer sphere transfer model is not satisfied because this couple causes a complex reaction scheme [207–209]. It is nonetheless deceptive that all the microscopic complexity of charge transference between TiO_2 and the redox couple, as described in Fig. 12b, ends up in just two parameters for recombination, $j_{0\rm k}$ and β. It is really highly desirable to obtain and explain with theory more structured data sets. Some early results [50] showed a curvature for the lifetime in I_3^-/I^- redox; however, it was suggested that the recombination from the substrate would produce such results [216]. This problem has, however, been controlled by employing suitable TiO_2 blocking layers on top of the conducting substrate. Recently, very promising results have been obtained for the understanding of recombination in a DSC by Hamann et al. [148]. They used outer-sphere redox shuttles $[Co(Me_2bpy)_3]^{3+/2+}$ and $[Ru(bpy)_2(MeIm)_2]^{3+/2+}$ that should follow the Marcus model well and they obtained the results in Fig. 20. These results can be explained by a combination of charge transfer mechanisms. The remarkable point is

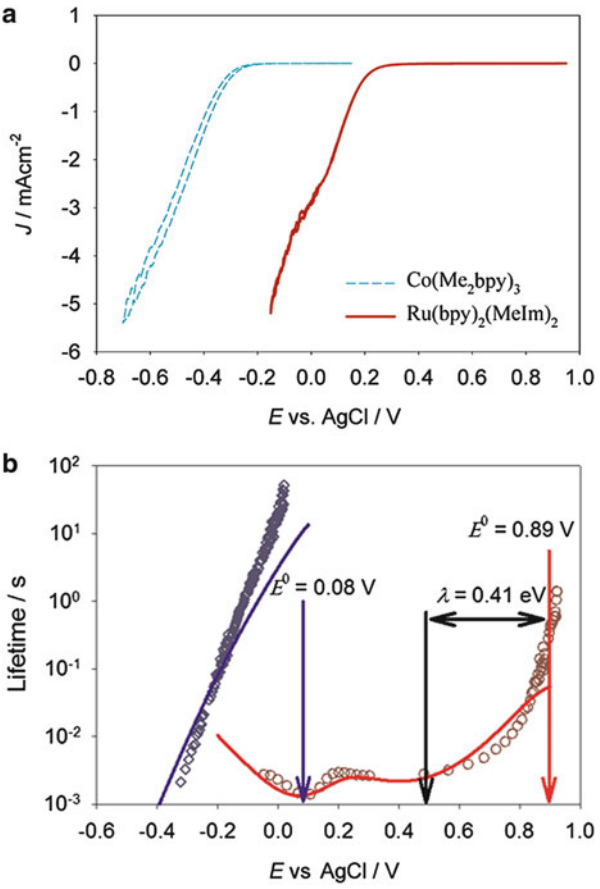

Fig. 20 (**a**) Current density vs applied potential curves and (**b**) electron lifetimes in DSCs. The two data sets correspond to different redox carriers $[Co(Me_2bpy)_3]^{3+/2+}$ (*open diamonds*) and $[Ru(bpy)_2(MeIm)_2]^{3+/2+}$ (*open circles*) with redox potential indicated in (**b**). The reorganization energy λ has been determined for the Co-based redox carrier and it is indicated in (**b**). Note that the potential V is more negative when the Fermi level of electrons raises (electrochemical convention). Courtesy of Tom Hamann, adapted from [148], reproduced with permission

that the curved lifetime, devoid of any substrate effects, is well observed in the case of $[Ru(bpy)_2(MeIm)_2]^{3+/2+}$, while $[Co(Me_2bpy)_3]^{3+/2+}$ has a much more negative redox potential and provides the usual exponential dependence. This observation allows one to obtain detailed information about the physical characteristics of charge transfer [179], such as the reorganization energy that has been indicated in Fig. 20b.

Further investigation of this type is required to confirm the validity of the model at (155), getting closer to a microscopic picture of the events occurring at the semiconductor/electrolyte interface in a DSC, which may finally also serve for the characterization of more complex mechanisms such as the redox couple I_3^-/I^- or the recombination in solid absorbers and organic hole conductors [40, 41, 102].

17 Conclusion

Modeling of the dye solar cell has been very much developed in the last decade, until establishing very detailed models that allow the extraction of significant information about the device and materials properties and on the operation mechanisms. Modeling the device is quite challenging because of the need to deal with a large number of features: a combination of phases, energy disorder in low temperature processed semiconductor networks, and a multiplicity of interfaces. A variety of experimental techniques have been developed that are up to this task, and the convergence of independent techniques speaks about the reality of the concepts that have been proposed. Especially important are those techniques that employ small perturbation methods, since they allow linearization of quantities that depend on local Fermi level, and therefore that are well defined in the framework of a highly nonlinear system. This is why we have emphasized quantities such as electron lifetime in their different meanings. Any quantity that is well defined physically can be checked by different experimental and computational methods and can also be related to other quantities, if necessary. In contrast, a quantity that is linked to one particular measurement may be practical in some respects but cannot enter the larger conceptual pool that broadens the knowledge about these systems.

The confirmation that jump and chemical diffusion coefficient concepts can be also realized for the lifetimes has closed a general interpretation of transport that implements the basic multiple trapping model to a broad set of measurements and stochastic simulation. This theory can be considered very advanced now. The main challenge is to obtain a more detailed theoretical and experimental understanding of the details of interfacial carrier transfer. So far most of the work has preferred to study a comparison of several samples that usually show too similar behavior. The use of model systems that allow isolation of specific experimental behavior concerning charge transfer should be highly recommended, and can bring new light to the implementation of charge transfer in nanostructured systems, and a better control of recombination in these solar cells.

Acknowledgments We thank the following agencies for support of this research. Juan Bisquert's research is supported by Ministerio de Educacion y Ciencia under project HOPE CSD2007-00007, Generalitat Valenciana (ISIC/2012/008). Rudolph A. Marcus's research is supported by ARO, ONR and NSF agencies. Rudolph A. Marcus contributed in Sects. 14 and 15 of this chapter.

References

1. O'Regan B, Grätzel M (1991) A low-cost high-efficiency solar cell based on dye-sensitized colloidal TiO_2 films. Nature 353:737–740
2. Yella A, Lee H-W, Tsao HN, Yi C, Chandiran AK, Nazeeruddin MK, Diau EW-G, Yeh C-Y, Zakeeruddin SM, Grätzel M (2011) Porphyrin-sensitized solar cells with cobalt (II/III) based redox electrolyte exceed 12 percent efficiency. Science 334:629–634

3. Chang JA, Rhee JH, Im SH, Lee YH, Kim H-J, Seok SI, Nazeeruddin MK, Grätzel M (2010) High-performance nanostructured inorganic–organic heterojunction solar cells. Nano Lett 10:2609–2612
4. Kim H-S, Lee C-R, Im J-H, Lee K-B, Moehl T, Marchioro A, Moon S-J, Humphry-Baker R, Yum J-H, Moser JE, Grätzel M, Park N-G (2012) Lead iodide perovskite sensitized all-solid-state submicron thin film mesoscopic solar cell with efficiency exceeding 9%. Sci Rep 2:591
5. Lee MM, Teuscher J, Miyasaka T, Murakami TN, Snaith HJ (2012) Efficient hybrid solar cells based on meso-superstructured organometal halide perovskites. Science 338:643–647
6. Bignozzi CA, Argazzi R, Boaretto R, Busatto E, Carli S, Ronconi F, Caramori S (2013) The role of transition metal complexes in dye sensitized solar devices. Coord Chem Rev 257:1472–1492
7. Mora-Seró I, Bisquert J (2010) Breakthroughs in the development of semiconductor-sensitized solar cells. J Phys Chem Lett 1:3046–3052
8. Hodes G (2008) Comparison of dye- and semiconductor-sensitized porous nanocrystalline liquid junction solar cells. J Phys Chem C 112:17778–17787
9. Dittrich T, Belaidi A, Ennaoui A (2011) Concepts of inorganic solid-state nanostructured solar cells. Sol Energ Mat Sol Cells 95(6):1527–1536
10. Fabregat-Santiago F, Bisquert J, Palomares E, Otero L, Kuang D, Zakeeruddin SM, Grätzel M (2007) Correlation between photovoltaic performance and impedance spectroscopy of dye-sensitized solar cells based on ionic liquids. J Phys Chem C 111:6550–6560
11. Barea EM, Ortiz J, Payá FJ, Fernández-Lázaro F, Fabregat-Santiago F, Sastre-Santos A, Bisquert J (2010) Energetic factors governing injection, regeneration and recombination in dye solar cells with phthalocyanine sensitizers. Energ Environ Sci 3:1985–1994
12. Bisquert J (2008) Physical electrochemistry of nanostructured devices. Phys Chem Chem Phys 10:49–72
13. Ansari-Rad M, Anta JA, Bisquert J (2013) Interpretation of diffusion and recombination in nanostructured and energy disordered materials by stochastic quasiequilibrium simulation. J Phys Chem C. doi:10.1021/jp403232b
14. Bisquert J, Mora-Seró I (2010) Simulation of steady-state characteristics of dye-sensitized solar cells and the interpretation of the diffusion length. J Phys Chem Lett 1:450–456
15. Södergren S, Hagfeldt A, Olsson J, Lindquist SE (1994) Theoretical models for the action spectrum and the current–voltage characteristics of microporous semiconductor films in photoelectrochemical cells. J Phys Chem 98:5552–5556
16. Wang Q, Ito S, Grätzel M, Fabregat-Santiago F, Mora-Seró I, Bisquert J, Bessho T, Imai H (2006) Characteristics of high efficiency dye-sensitized solar cells. J Phys Chem B 110:19406–19411
17. Nayak PK, Garcia-Belmonte G, Kahn A, Bisquert J, Cahen D (2012) Photovoltaic efficiency limits and material disorder. Energ Environ Sci 5:6022–6039
18. Halme J, Boschloo G, Hagfeldt A, Lund P (2008) Spectral characteristics of light harvesting, electron injection, and steady-state charge collection in pressed TiO_2 dye solar cells. J Phys Chem C 112:5623–5637
19. Li L-L, Diau EW-G (2012) Porphyrin-sensitized solar cells. Chem Soc Rev 42:291–304
20. Bertoluzzi L, Ma S (2013) On the methods of calculation of the charge collection efficiency of dye sensitized solar cells. Phys Chem Chem Phys 15:4283–4285
21. Usami A (1999) Rigorous solutions of light scattering of neighboring TiO_2 particles in nanocrystalline films. Sol Energ Mat Sol Cells 59:163–166
22. Usami A (2000) A theoretical simulation of light scattering of nanocrystalline films in photoelectrochemical solar cells. Sol Energ Mat Sol Cells 62:239–246
23. Usami A (2000) Theoretical simulations of optical confinement in dye-sensitized nanocrystalline solar cells. Sol Energ Mat Sol Cells 64:73–83
24. Tachibana Y, Hara K, Sayama K, Arakawa H (2002) Quantitative analysis of light-harvesting efficiency and electron-transfer yield in ruthenium-dye-sensitized nanocrystalline TiO_2 solar cells. Chem Mater 14:2527–2535

25. Galvez FE, Kemppainen E, Miguez H, Halme J (2012) Effect of diffuse light scattering designs on the efficiency of dye solar cells: an integral optical and electrical description. J Phys Chem C 116:11426–11433
26. Lin Y, Ma YT, Yang L, Xiao XR, Zhou XW, Li XP (2006) Computer simulations of light scattering and mass transport of dye-sensitized nanocrystalline solar cells. J Electroanal Chem 588:51–58
27. Raga SR, Barea EM, Fabregat-Santiago F (2012) Analysis of the origin of open circuit voltage in dye solar cells. J Phys Chem Lett 3:1629–1634
28. Fabregat-Santiago F, Garcia-Belmonte G, Mora-Seró I, Bisquert J (2011) Characterization of nanostructured hybrid and organic solar cells by impedance spectroscopy. Phys Chem Chem Phys 13:9083–9118
29. Bisquert J, Fabregat-Santiago F (2010) Impedance spectroscopy: a general introduction and application to dye-sensitized solar cells. In: Kalyanasundaram K (ed) Dye-sensitized solar cells. CRC, Boca Raton
30. Barea EM, Zafer C, Gultein B, Aydin B, Koyuncu S, Icli S, Fabregat-Santiago F, Bisquert J (2010) Quantification of the effects of recombination and injection in the performance of dye-sensitized solar cells based on N-substituted carbazole dyes. J Phys Chem C 114:19840–19848
31. Barea EM, Gonzalez-Pedro V, Ripolles-Sanchis T, Wu H-P, Li L-L, Yeh C-Y, Diau EW-G, Bisquert J (2011) Porphyrin dyes with high injection and low recombination for highly efficient mesoscopic dye-sensitized solar cells. J Phys Chem C 115:10898–10902
32. Zhou D, Bai Y, Zhang J, Cai N, Su M, Wang Y, Zhang M, Wang P (2010) Anion effects in organic dye-sensitized mesoscopic solar cells with ionic liquid electrolytes: tetracyanoborate vs dicyanamide. J Phys Chem C 115:816–822
33. Xu X, Cao K, Huang D, Shen Y, Wang M (2012) Disulfide/thiolate based redox shuttle for dye-sensitized solar cells: an impedance spectroscopy study. J Phys Chem C 116:25233–25241
34. Yu Q, Zhou D, Shi Y, Si X, Wang Y, Wang P (2010) Stable and efficient dye-sensitized solar cells: photophysical and electrical characterizations. Energe Environ Sci 3:1722–1725
35. Bai Y, Yu Q, Cai N, Wang Y, Zhang M, Wang P (2011) High-efficiency organic dye-sensitized mesoscopic solar cells with a copper redox shuttle. Chem Commun 47:4376–4378
36. Zhang M, Liu J, Wang Y, Zhou D, Wang P (2011) Redox couple related influences of pi-conjugation extension in organic dye-sensitized mesoscopic solar cells. Chem Sci 2:1401–1406
37. Zhou D, Yu Q, Cai N, Bai Y, Wang Y, Wang P (2011) Efficient organic dye-sensitized thin-film solar cells based on the tris(1,10-phenanthroline)cobalt(II/III) redox shuttle. Energ Environ Sci 4:2030–2034
38. Bai Y, Zhang J, Zhou D, Wang Y, Zhang M, Wang P (2011) Engineering organic sensitizers for iodine-free dye-sensitized solar cells: red-shifted current response concomitant with attenuated charge recombination. J Am Chem Soc 133:11442–11445
39. Liu Y, Jennings JR, Zakeeruddin SM, Grätzel M, Wang Q (2013) Heterogeneous electron transfer from dye-sensitized nanocrystalline TiO_2 to [Co(bpy)3]3+: insights gained from impedance spectroscopy. J Am Chem Soc 135:3939–3952
40. Mora-Seró I, Giménez S, Fabregat-Santiago F, Gomez R, Shen Q, Toyoda T, Bisquert J (2009) Recombination in quantum dot sensitized solar cells. Acc Chem Res 42:1848–1857
41. Gónzalez-Pedro V, Xu X, Mora-Seró I, Bisquert J (2010) Modeling high-efficiency quantum dot sensitized solar cells. ACS Nano 4:5783–5790
42. Boix PP, Guerrero A, Marchesi LF, Garcia-Belmonte G, Bisquert J (2011) Current–voltage characteristics of bulk heterojunction organic solar cells: connection between light and dark curves. Adv Energ Mater 1:1073–1078
43. Wang H, Peter LM (2009) A comparison of different methods to determine the electron diffusion length in dye-sensitized solar cells. J Phys Chem C 113:18125–18133

44. Bisquert J (2002) Theory of the impedance of electron diffusion and recombination in a thin layer. J Phys Chem B 106:325–333
45. Jennings JR, Liu Y, Safari-Alamuti F, Wang Q (2012) Dependence of dye-sensitized solar cell impedance on photoelectrode thickness. J Phys Chem C 116:1556–1562
46. Jaegermann W (1996) The semiconductor/electrolyte interface: a surface science approach. Mod Asp Electrochem 30:1–185
47. Bisquert J, Cahen D, Rühle S, Hodes G, Zaban A (2004) Physical chemical principles of photovoltaic conversion with nanoparticulate, mesoporous dye-sensitized solar cells. J Phys Chem B 108:8106–8118
48. Bisquert J (2007) Hopping transport of electrons in dye-sensitized solar cells. J Phys Chem C 111:17163–17168
49. Bisquert J (2008) Interpretation of electron diffusion coefficient in organic and inorganic semiconductors with broad distributions of states. Phys Chem Chem Phys 10:3175–3194
50. Bisquert J, Zaban A, Greenshtein M, Mora-Seró I (2004) Determination of rate constants for charge transfer and the distribution of semiconductor and electrolyte electronic energy levels in dye-sensitized solar cells by open-circuit photovoltage decay method. J Am Chem Soc 126:13550
51. Bisquert J, Vikhrenko VS (2004) Interpretation of the time constants measured by kinetic techniques in nanostructured semiconductor electrodes and dye-sensitized solar cells. J Phys Chem B 108:2313–2322
52. Bisquert J, Fabregat-Santiago F, Mora-Seró I, Garcia-Belmonte G, Giménez S (2009) Electron lifetime in dye-sensitized solar cells: theory and interpretation of measurements. J Phys Chem C 113:17278–17290
53. van de Lagemaat J, Frank AJ (2001) Nonthermalized electron transport in dye-sensitized nanocrystalline TiO_2 films: transient photocurrent and random-walk modeling studies. J Phys Chem B 105:11194–11205
54. Benkstein KD, Kopidakis N, Van de Lagemaat J, Frank AJ (2003) Influence of the percolation network geometry on the electron transport in dye-sensitized titanium dioxide solar cells. J Phys Chem B 107:7759–7767
55. Anta JA (2009) Random walk numerical simulation for solar cell applications. Energ Environ Sci 2:387–392
56. Ansari-Rad M, Abdi Y, Arzi E (2012) Simulation of non-linear recombination of charge carriers in sensitized nanocrystalline solar cells. J Appl Phys 112:074319
57. Mendels D, Tessler N (2013) Drift and diffusion in disordered organic semiconductors: the role of charge density and charge energy transport. J Phys Chem C 117:3287–3293
58. Rego LGC, Batista VS (2003) Quantum dynamics simulations of interfacial electron transfer in sensitized TiO_2 semiconductors. J Am Chem Soc 125:7989–7997
59. Ronca E, Pastore M, Belpassi L, Tarantelli F, De Angelis F (2012) Influence of the dye molecular structure on the TiO_2 conduction band in dye-sensitized solar cells: disentangling charge transfer and electrostatic effects. Energ Environ Sci 6:183–193
60. Pastore M, de Angelis F (2013) Intermolecular interactions in dye-sensitized solar cells: a computational modeling perspective. J Phys Chem Lett 4:956–974
61. Baumeier B, May F, Lennartz C, Andrienko D (2012) Challenges for in silico design of organic semiconductors. J Mater Chem 22:10971–10976
62. Ruhle V, Lukyanov A, May F, Schrader M, Vehoff T, Kirkpatrick J, Baumeier B, Andrienko D (2011) Microscopic simulations of charge transport in disordered organic semiconductors. J Chem Theory Comput 7:3335–3345
63. Coehoorn R, Bobbert PA (2012) Effects of Gaussian disorder on charge carrier transport and recombination in organic semiconductors. Physica Status Solidi A 209:2354–2377
64. Cao F, Oskam G, Meyer GJ, Searson PC (1996) Electron transport in porous nanocrystalline TiO_2 photoelectrochemical cells. J Phys Chem 100:17021–17027
65. Villanueva J, Anta JA, Guillen E, Oskam G (2009) Numerical simulation of the current–voltage curve in dye-sensitized solar cells. J Phys Chem C 113:19722–19731

66. Cai JH, Chen H, Han LY (2012) Models of electron injection, diffusion and recombination in dye-sensitized solar cells. Int J Mod Phys B 26:19
67. Cass MJ, Qiu FL, Walker AB, Fisher AC, Peter LM (2003) Influence of grain morphology on electron transport in dye sensitized nanocrystalline solar cells. J Phys Chem B 107:113–119
68. Kambili A, Walker AB, Qiu FL, Fisher AC, Savin AD, Peter LM (2002) Electron transport in the dye sensitized nanocrystalline cell. Physica E 14:203–209
69. Duffy NW, Peter LM, Rajapakse RMG, Wijayantha KGU (2000) Investigation of the kinetics of the back reaction of electrons with tri-iodide in dye-sansitized nanocrystalline photovoltaic cells. J Phys Chem B 104:8916–8919
70. Duffy NW, Peter LM, Rajapakse RMG, Wijayantha KGU (2000) A novel charge extraction method for the study of electron transport and interfacial transfer in dye sensitized nanocrystalline solar cells. Electrochem Commun 2:658–662
71. Jennings JR, Peter LM (2007) A reappraisal of the electron diffusion length in solid-state dye-sensitized solar cells. J Phys Chem C 111:16100–16104
72. Lobato K, Peter LM, Wurfel U (2006) Direct measurement of the internal electron quasi-Fermi level in dye sensitized solar cells using a titanium secondary electrode. J Phys Chem B 110:16201–16204
73. Paasch G, Micka K, Gersdorf P (1993) Theory of the electrochemical impedance of macrohomogeneous porous electrodes. Electrochim Acta 38:2653–2662
74. Stangl R, Ferber J, Luther J (1998) On the modeling of the dye-sensitized solar cell. Sol Energ Mat Sol Cells 54:255–264
75. Ferber J, Stangl R, Luther J (1998) An electrical model of the dye-sensitized solar cell. Sol Energ Mat Sol Cells 53:29–54
76. Burgelman M, Grasso C (2004) Network of flatband solar cells as a model for solid-state nanostructured solar cells. J Appl Phys 95:2020–2024
77. Newman JS (1973) Electrochemical systems. Prentice-Hall, Englewoods Cliffs
78. Sze SM (1981) Physics of semiconductor devices, 2nd edn. Wiley, New York
79. Mora-Seró I, Garcia-Belmonte G, Boix PP, Vázquez MA, Bisquert J (2009) Impedance characterisation of highly efficient silicon solar cell under different light illumination intensities. Energe Environ Sci 2:678–686
80. Rickert H (1982) Electrochemistry of solids. Springer, Berlin
81. Riess I (1997) What does a voltmeter measure? Solid State Ion 95:327–328
82. Schwarzburg K, Willig F (1999) Origin of photovoltage and photocurrent in the nanoporous dye-sensitized electrochemical solar cell. J Phys Chem B 28:5743–5746
83. Pichot F, Gregg BA (2000) The photovoltage-determining mechanism in dye-sensitized solar cells. J Phys Chem B 104:6–10
84. Cahen D, Hodes G, Grätzel M, Guillemoles JF, Riess I (2000) Nature of photovoltaic action in dye-sensitized solar cells. J Phys Chem B 104:2053–2059
85. Levy B, Liu W, Gilbert SE (1997) Directed photocurrents in nanostructured TiO_2/SnO_2 heterojunction diodes. J Phys Chem B 101:1810–1816
86. Turrión M, Bisquert J, Salvador P (2003) Flatband potential of $F:SnO_2$ in a TiO_2 dye-sensitized solar cell: an interference reflection study. J Phys Chem B 107:9397–9403
87. Fabregat-Santiago F, Garcia-Belmonte G, Bisquert J, Bogdanoff P, Zaban A (2003) Mott-Schottky analysis of nanoporous semiconductor electrodes in the dielectric state deposited on SnO2(F) conducting substrates. J Electrochem Soc 150:E293–E298
88. Rühle S, Dittrich T (2005) Investigation of the electric field in TiO_2/FTO junctions used in dye-sensitized solar cells by photocurrent transients. J Phys Chem B 109:9522–9526
89. Ruhle S, Cahen D (2004) Electron tunneling at the TiO_2/substrate interface can determine dye-sensitized solar cell performance. J Phys Chem B 108:17946–17951
90. Liu WQ, Kou DX, Hu LH, Dai SY (2011) The kinetics of electron transfer across the multi-point contact interface through simplifying the complex structure in dye-sensitized solar cell. Chem Phys Lett 513:145–148

91. van de Lagemaat J, Park N-G, Frank AJ (2000) Influence of electrical potential distribution, charge transport, and recombination on the photopotential and photocurrent conversion efficiency of dye-sensitized nanocrystalline TiO_2 solar cells: a study by electrical impedance and optical modulation techniques. J Phys Chem B 104:2044–2052
92. Bisquert J (2011) Dilemmas of dye-sensitized solar cells. ChemPhysChem 12:1633–1636
93. Zhang Z, Zakeeruddin SM, O'Regan BC, Humphry-Baker R, Grätzel M (2005) Influence of 4-guanidinobutyric acid as coadsorbent in reducing recombination in dye-sensitized solar cells. J Phys Chem B 109:21818–21824
94. Guerrero A, Marchesi LF, Boix PP, Ruiz-Raga S, Ripolles-Sanchis T, Garcia-Belmonte G, Bisquert J (2012) How the charge-neutrality level of interface states controls energy level alignment in cathode contacts of organic bulk-heterojunction solar cells. ACS Nano 6:3453–3460
95. Mora-Seró I, Fabregat-Santiago F, Denier B, Bisquert J, Tena-Zaera R, Elias J, Lévy-Clement C (2006) Determination of carrier density of ZnO nanowires by electrochemical techniques. Appl Phys Lett 89:203117
96. Tena-Zaera R, Elias J, Lévy-Clément C, Bekeny C, Voss T, Mora-Seró I, Bisquert J (2008) Influence of the potassium chloride concentration on the physical properties of electrodeposited ZnO nanowire arrays. J Phys Chem C 112:16318–16323
97. Foley JM, Price MJ, Feldblyum JI, Maldonado S (2012) Analysis of the operation of thin nanowire photoelectrodes for solar energy conversion. Energe Environ Sci 5:5203–5220
98. Kambe S, Nakade S, Kitamura T, Wada Y, Yanagida S (2002) Influence of the electrolytes on electron transport in mesoporous TiO_2-electrolyte systems. J Phys Chem B 106:2967–2972
99. Feldt SM, Gibson EA, Gabrielsson E, Sun L, Boschloo G, Hagfeldt A (2010) Design of organic dyes and cobalt polypyridine redox mediators for high-efficiency dye-sensitized solar cells. J Am Chem Soc 132:16714–16724
100. Bignozzi CA, Argazzi R, Boaretto R, Busatto E, Carli S, Ronconi F, Caramori S (2013) The role of transition metal complexes in dye sensitized solar devices. Coord Chem Rev 257(9–10):1472–1492
101. Snaith HJ, Grätzel M (2007) Light-enhanced charge mobility in a molecular hole transporter. Phys Rev Lett 98:177402
102. Fabregat-Santiago F, Bisquert J, Cevey L, Chen P, Wang M, Zakeeruddin SM, Grätzel M (2009) Electron transport and recombination in solid state dye solar cell with spiro-OMeTAD as hole conductor. J Am Chem Soc 131:558–562
103. Wang M, Chen P, Humphry-Baker R, Zakeeruddin SM, Grätzel M (2009) The influence of charge transport and recombination on the performance of dye-sensitized solar cells. ChemPhysChem 10:290–299
104. Boix PP, Larramona G, Jacob A, Delatouche B, Mora-Sero I, Bisquert J (2011) Hole transport and recombination in all-solid Sb2S3-sensitized TiO_2 solar cells using CuSCN as hole transporter. J Phys Chem C 116:1579–1587
105. Boix PP, Lee YH, Fabregat-Santiago F, Im SH, Mora-Sero I, Bisquert J, Seok SI (2012) From flat to nanostructured photovoltaics: balance between thickness of the absorber and charge screening in sensitized solar cells. ACS Nano 6:873–880
106. Dualeh A, Moehl T, Nazeeruddin MK, Grätzel M (2013) Temperature dependence of transport properties of Spiro-MeOTAD as a hole transport material in solid-state dye-sensitized solar cells. ACS Nano 7:2292–2301
107. Noh JH, Im SH, Heo JH, Mandal TN, Seok SI (2013) Chemical management for colorful, efficient, and stable inorganic–organic hybrid nanostructured solar cells. Nano Lett 13: 1764–1769
108. Kopidakis N, Schiff EA, Park NG, van de Lagemaat J, Frank AJ (2000) Ambipolar diffusion of photocarriers in electrolyte-filled, nanoporous TiO_2. J Phys Chem B 104:3930–3936
109. Champlain JG (2011) On the use of the term "ambipolar". Appl Phys Lett 99:123502

110. Ritter D, Zeldov E, Weiser K (1988) Ambipolar transport in amorphous semiconductors in the lifetime and relaxation-time regimes investigated by the steady-state photocarrier grating technique. Phys Rev B 38:8296
111. Papageorgiou N, Grätzel M, Infelta PP (1996) On the relevance of mass transport in thin layer nanocrystalline photoelectrochemical solar cells. Sol Energ Mat Sol Cells 44:405–438
112. Kalaignan GP, Kang YS (2006) A review on mass transport in dye-sensitized nanocrystalline solar cells. J Photochem Photobiol C-Photochem Rev 7:17–22
113. Usami A, Ozaki H (2001) Computer simulations of charge transport in dye-sensitized nanocrystalline photovoltaic cells. J Phys Chem B 105:4577–4583
114. Usami A (1998) Theoretical study of charge trasportation in dye-sensitized nanocrystalline TiO_2 electrodes. Chem Phys Lett 292:223–228
115. Hyk W, Augustynski J (2006) Steady-state operation of porous photoelectrochemical cells under the conditions of mixed diffusional and migrational mass transport. J Electrochem Soc 153:A2326
116. Barnes PRF, Anderson AY, Durrant JR, O'Regan BC (2011) Simulation and measurement of complete dye sensitised solar cells: including the influence of trapping, electrolyte, oxidised dyes and light intensity on steady state and transient device behaviour. Phys Chem Chem Phys 13:5798–5816
117. Andrade L, Sousa J, Aguilar Ribeiro H, Mendes A (2012) Phenomenological modeling of dye-sensitized solar cells under transient conditions. Sol Energ 85:781–793
118. Gagliardi A, der Maur MA, Gentilini D, Di Carlo A (2011) Simulation of dye solar cells: through and beyond one dimension. J Comput Electron 10:424–436
119. Chua J, Mathews N, Jennings JR, Yang G, Wang Q, Mhaisalkar SG (2011) Patterned 3-dimensional metal grid electrodes as alternative electron collectors in dye-sensitized solar cells. Phys Chem Chem Phys 13:19314–19317
120. Miettunen K, Halme J, Visuri A-M, Lund P (2011) Two-dimensional time-dependent numerical modeling of edge effects in dye solar cells. J Phys Chem C 115:7019–7031
121. Mastroianni S, Lanuti A, Penna S, Reale A, Brown TM, Di Carlo A, Decker F (2012) Physical and electrochemical analysis of an indoor–outdoor ageing test of large-area dye solar cell devices. ChemPhysChem 13:2925–2936
122. Anta JA, Idigoras J, Guillen E, Villanueva-Cab J, Mandujano-Ramirez HJ, Oskam G, Pelleja L, Palomares E (2012) A continuity equation for the simulation of the current–voltage curve and the time-dependent properties of dye-sensitized solar cells. Phys Chem Chem Phys 14:10285–10299
123. Gagliardi A, Mastroianni S, Gentilini D, Giordano F, Reale A, Brown TM, Di Carlo A (2010) Multiscale modeling of dye solar cells and comparison with experimental data. IEEE J Select Top Quant Electron 16:1611–1618
124. Halme J, Vahermaa P, Miettunen K, Lund P (2010) Device physics of dye solar cells. Adv Mater 22:E210–E234
125. Peter LM (2007) Characterization and modeling of dye-sensitized solar cells. J Phys Chem C 111:6601–6612
126. Barnes PRF, Miettunen K, Li X, Anderson AY, Bessho T, Gratzel M, O'Regan BC (2013) Interpretation of optoelectronic transient and charge extraction measurements in dye-sensitized solar cells. Adv Mater 25:1881–1922
127. Li L-L, Chang Y-C, Wu H-P, Diau EW-G (2012) Characterisation of electron transport and charge recombination using temporally resolved and frequency-domain techniques for dye-sensitised solar cells. Int Rev Phys Chem 31:420–467
128. Schwarzburg K, Willig F (1991) Influence of trap filling on photocurrent transients in polycrystalline TiO_2. Appl Phys Lett 58:2520–2522
129. Franco G, Gehring J, Peter LM, Ponomarev EA, Uhlendorf I (1999) Frequency-resolved optical detection of photoinjected electrons in dye-sensitized nanocrystalline photovoltaic cells. J Phys Chem B 103:692–698

130. van de Lagemaat J, Frank AJ (2000) Effect of the surface state distribution on electron transport in dye sensitized TiO_2 solar cells: nonlinear electron-transport kinetics. J Phys Chem B 104:4292–4294
131. Vanmaekelbergh D, de Jongh PE (1999) Driving force for electron transport in porous nanostructured photoelectrodes. J Phys Chem B 103:747–750
132. Vanmaekelbergh D, de Jongh PE (2000) Electron transport in disordered semiconductors studied by a small harmonic modulation of the steady state. Phys Rev B 61:4699–4707
133. Nelson J (1999) Continuous-time random-walk model of electron transport in nanocrystalline TiO_2 electrodes. Phys Rev B 59:15374
134. Bisquert J (2003) Chemical capacitance of nanostructured semiconductors: its origin and significance for heterogeneous solar cells. Phys Chem Chem Phys 5:5360–5364
135. Jamnik J, Maier J (2001) Generalised equivalent circuits for mass and charge transport: chemical capacitance and its implications. Phys Chem Chem Phys 3:1668–1678
136. Shockley W (1958) Electrons, holes, and traps. Proc IRE 46:973–990
137. Garcia-Belmonte G, Guerrero A, Bisquert J (2013) Elucidating operating modes of bulk-heterojunction solar cells from impedance spectroscopy analysis. J Phys Chem Lett 4:877–886
138. Lee PA (1982) Density of states and screening near the mobility edge. Phys Rev B 26:5882–5885
139. Berger T, Monllor-Satoca D, Jankulovska M, Lana-Villarreal T, Gomez R (2012) The electrochemistry of nanostructured titanium dioxide electrodes. ChemPhysChem 13 (12):2824–2875
140. Zaban A, Greenshtein M, Bisquert J (2003) Determination of the electron lifetime in nanocrystalline dye solar cells by open-circuit voltage decay measurements. ChemPhysChem 4:859–864
141. van Roosbroeck W (1953) The transport of added current carriers in a homogeneous semiconductor. Phys Rev 91:282–289
142. Rose A (1963) Concepts in photoconductivity and allied problems. Interscience, New York
143. van Roosbroeck W, Shockley W (1954) Photon-radiative recombination of electrons and holes in germanium. Phys Rev 94:1558–1560
144. Schmidt J (1999) Measurement of differential and actual recombination parameters in crystalline silicon wafers. IEEE Trans Electron Devices 46:2018–2025
145. Tiedje T, Rose A (1981) A physical interpretation of dispersive transport in disordered semiconductors. Solid State Commun 37:49
146. Orenstein J, Kastner M (1981) Photocurrent transient spectroscopy: mesurament of the density of localized states in a–As2Se3. Phys Rev Lett 46:1421–1424
147. Hoesterey DC, Letson GM (1963) The trapping of photocarriers in anthracene. J Phys Chem Solids 24:1609
148. Ondersma JW, Hamann TW (2011) Measurements and modeling of recombination from nanoparticle TiO_2 electrodes. J Am Chem Soc 133:8264–8271
149. Ansari-Rad M, Abdi Y, Arzi E (2012) Reaction order and ideality factor in dye-sensitized nanocrystalline solar cells: a theoretical investigation. J Phys Chem C 116:10867–10872
150. Bisquert J (2008) Beyond the quasi-static approximation: impedance and capacitance of an exponential distribution of traps. Phys Rev B 77:235203
151. Dunn HK, Peter LM, Bingham SJ, Maluta E, Walker AB (2012) In situ detection of free and trapped electrons in dye-sensitized solar cells by photo-induced microwave reflectance measurements. J Phys Chem C 116:22063–22072
152. Chen J, Li B, Zheng J, Jia S, Zhao J, Jing H, Zhu Z (2011) Role of one-dimensional ribbonlike nanostructures in dye-sensitized TiO_2-based solar cells. J Phys Chem C 115:7104–7113
153. Ondersma JW, Hamann TW (2009) Impedance investigation of dye-sensitized solar cells employing outer-sphere redox shuttles. J Phys Chem C 114:638–645
154. Bisquert J (2004) Chemical diffusion coefficient in nanostructured semiconductor electrodes and dye-sensitized solar cells. J Phys Chem B 108:2323–2332

155. Marinado T, Nonomura K, Nissfolk J, Karlsson MK, Hagberg DP, Sun L, Mori S, Hagfeldt A (2009) How the nature of triphenylamine-polyene dyes in dye-sensitized solar cells affects the open-circuit voltage and electron lifetimes. Langmuir 26:2592–2598
156. Jennings JR, Li F, Wang Q (2010) Reliable determination of electron diffusion length and charge separation efficiency in dye-sensitized solar cells. J Phys Chem C 114:14665–14674
157. González-Vázquez JP, Anta JA, Bisquert J (2009) Random walk numerical simulation for hopping transport at finite carrier concentrations: diffusion coefficient and transport energy concept. Phys Chem Chem Phys 11:10359–10367
158. Gonzalez-Vazquez JP, Oskam G, Anta JA (2012) Origin of nonlinear recombination in dye-sensitized solar cells: interplay between charge transport and charge transfer. J Phys Chem C 116:22687–22697
159. van de Lagemaat J, Kopidakis N, Neale NR, Frank AJ (2005) Effect of nonideal statistics on electron diffusion in sensitized nanocrystalline TiO_2. Phys Rev B 71:035304
160. Anta JA, Mora-Seró I, Dittrich T, Bisquert J (2008) Interpretation of diffusion coefficients in nanostructured materials from random walk numerical simulation. Phys Chem Chem Phys 10:4478–4485
161. Gonzalez-Vazquez JP, Anta JA, Bisquert J (2010) Determination of the electron diffusion length in dye-sensitized solar cells by random walk simulation: compensation effects and voltage dependence. J Phys Chem C 114:8552–8558
162. Darken LS (1948) Trans Am Inst Min Eng 175:184
163. Paul EW, Ricco AJ, Wrighton MS (1985) Resistance of polyaniline films as a function of electrochemical potential and the fabrication of polyaniline based microelectronic devices. J Phys Chem 89:1441
164. Vanmaekelbergh D, Houtepen AJ, Kelly JJ (2007) Electrochemical gating: a method to tune and monitor the (opto)electronic properties of functional materials. Electrochim Acta 53:1140–1149
165. Pomerantz Z, Zaban A, Ghosh S, Lellouche J-P, Garcia-Belmonte G, Bisquert J (2008) Capacitance, spectroelectrochemistry and conductivity of polarons and bipolarons in a polydicarbazole based conducting polymer. J Electroanal Chem 614:49–60
166. Ondersma JW, Hamann TW (2012) Conduction band energy determination by variable temperature spectroelectrochemistry. Energ Environ Sci 5:9476–9480
167. Boschloo G, Fitzmaurice D (1999) Electron accumulation in nanostructured TiO_2 (anatase) electrodes. J Phys Chem B 103:7860–7868
168. Berger T, Anta JA, Morales-Florez V (2012) Electrons in the band gap: spectroscopic characterization of anatase TiO_2 nanocrystal electrodes under Fermi level control. J Phys Chem C 116:11444–11455
169. Kroeze JE, Savenije TJ, Warman JM (2003) Electrodeless determination of the trap density, decay kinetics and charge separation efficiency of dye-sensitized nanocrystalline TiO_2. J Am Chem Soc 126:7608
170. Friedrich D, Kunst M (2011) Analysis of charge carrier kinetics in nanoporous systems by time resolved photoconductance measurements. J Phys Chem C 115:16657–16663
171. Fabregat-Santiago F, Garcia-Belmonte G, Bisquert J, Zaban A, Salvador P (2002) Decoupling of transport, charge-storage and interfacial charge-transfer in the nanocrystalline TiO_2/electrolyte system by impedance methods. J Phys Chem B 106:334–339
172. Archana PS, Jose R, Yusoff MM, Ramakrishna S (2011) Near band-edge electron diffusion in electrospun Nb-doped anatase TiO[sub 2] nanofibers probed by electrochemical impedance spectroscopy. Appl Phys Lett 98:152106
173. Jennings JR, Wang Q (2010) Influence of lithium ion concentration on electron injection, transport, and recombination in dye-sensitized solar cells. J Phys Chem C 114:1715–1724
174. Bisquert J, Grätzel M, Wang Q, Fabregat-Santiago F (2006) Three-channel transmission line impedance model for mesoscopic oxide electrodes functionalized with a conductive coating. J Phys Chem B 110:11284–11290

175. Bisquert J (2000) Influence of the boundaries in the impedance of porous film electrodes. Phys Chem Chem Phys 2:4185–4192
176. Barea EM, Bisquert J (2013) Properties of chromophores determining recombination at TiO_2-dye-electrolyte interface. Langmuir 29:8773–8781
177. Clifford JN, Martinez-Ferrero E, Palomares E (2012) Dye mediated charge recombination dynamics in nanocrystalline TiO_2 dye sensitized solar cells. J Mater Chem 22:12415–12422
178. de Vries MJ, Pellin MJ, Hupp JT (2010) Dye-sensitized solar cells: driving-force effects on electron recombination dynamics with cobalt-based shuttles. Langmuir. doi:10.1021/la904643t
179. Ondersma JW, Hamann TW (2013) Recombination and redox couples in dye-sensitized solar cells. Coord Chem Rev 257:1533–1543
180. Bisquert J, Zaban A, Salvador P (2002) Analysis of the mechanism of electron recombination in nanoporous TiO_2 dye-sensitized solar cells. Nonequilibrium steady state statistics and transfer rate of electrons in surface states. J Phys Chem B 106:8774–8782
181. Salvador P, González-Hidalgo M, Zaban A, Bisquert J (2005) Illumination intensity dependence of the photovoltage in nanostructured TiO_2 dye-sensitized solar cells. J Phys Chem B 109:15915–15926
182. Marcus RA (1956) On the theory of oxidation-reduction reactions involving electron transfer. I. J Chem Phys 24:966
183. Marcus RA (1960) Exchange reactions and electron transfer reactions inclunding isotopic exchange. Theory of oxidation–reduction reactions involving electron transfer. Part 4. Faraday Discuss Chem Soc 29:21
184. Marcus RA (1965) On the theory of electron-transfer reactions. VI. Unified treatment for homogeneous and electrode reactions. J Chem Phys 43:679
185. Marcus RA (1959) On the theory of electrochemical and chemical electron transfer processes. Can J Chem 37:155–163
186. Gosavi S, Marcus RA (2000) Nonadiabatic electron transfer at metal surfaces. J Phys Chem B 104:2067–2072
187. Gosavi S, Qin Gao Y, Marcus RA (2001) Temperature dependence of the electronic factor in the nonadiabatic electron transfer at metal and semiconductor electrodes. J Electroanal Chem 500:71–77
188. Marcus RA (1968) Electron transfer at electrodes and in solution: comparison of theory and experiment. Electrochim Acta 13:995–1004
189. Marcus RA (1990) Reorganization free energy for electron transfers at liquid–liquid and dielectric semiconductor–liquid interfaces. J Phys Chem 94:1050–1055
190. Gao YQ, Georgievskii Y, Marcus RA (2000) On the theory of electron transfer reactions at semiconductor electrode/liquid interfaces. J Chem Phys 112:3358–3369
191. Marcus RA (1990) Theory of electron-transfer rates across liquid–liquid interfaces. J Phys Chem 94:4152–4155
192. Marcus RA (1963) On the theory of oxidation–reduction reactions involving electron transfer. V. Comparison and properties of electrochemical and chemical rate constants. J Phys Chem 67:853
193. Marcus RA (1964) Chemical and electrochemical electron-transfer theory. Annu Rev Phys Chem 15:155–196
194. Marcus RA, Sutin N (1985) Electron transfers in chemistry and biology. Biochim Biophys Acta 811:265–322
195. Landau LD (1932) Assotsiatsiya dvukhatomnykh molekul. Sovetskii Fizicheskii Zhurnal 2:46–52
196. Zener C (1933) Dissociation of excited diatomic molecules by external perturbations. Proc R Soc Lond A 140:660–668
197. Feldberg SW, Sutin N (2006) Distance dependence of heterogeneous electron transfer through the nonadiabatic and adiabatic regimes. Chem Phys 324:216–225

198. Chidsey CED (1991) Free energy and temperature dependence of electron transfer at the metal-electrolyte interface. Science 251:918–922
199. Hamann TW, Gstrein F, Brunschwig BS, Lewis NS (2005) Measurement of the dependence of interfacial charge-transfer rate constants on the reorganization energy of redox species at n-ZnO/H_2O interfaces. J Am Chem Soc 127:13949–13954
200. Royea WJ, Fajardo AM, Lewis NS (1997) Fermi golden rule approach to evaluating outer-sphere electron-transfer rate constants at semiconductor/liquid interfaces. J Phys Chem B 101:11152–11159
201. Kuciauskas D, Freund MS, Gray HB, Winkler JR, Lewis N (2001) Electron transfer dynamics in nanocrystaline titanium dioxide solar cells sensitized with ruthenium or osmium polypyridyl complexes. J Phys Chem B 105:392–403
202. Lyon LA, Hupp JT (1999) Energetics of the nanocrystalline titanium dioxide/aqueous solution interface: approximate conduction band edge variations. J Phys Chem B 103:4623–4628
203. Miyashita M, Sunahara K, Nishikawa T, Uemura Y, Koumura N, Hara K, Mori A, Abe T, Suzuki E, Mori S (2008) Interfacial electron-transfer kinetics in metal-free organic dye-sensitized solar cells: combined effects of molecular structure of dyes and electrolytes. J Am Chem Soc 130:17874–17881
204. Gaal DA, Hupp JT (2000) Thermally activated, inverted interfacial electron transfer kinetics: high driving force reactions between tin oxide nanoparticles and electrostatically-bound molecular reactants. J Am Chem Soc 122:10956–10963
205. Maggio E, Martsinovich N, Troisi A (2012) Theoretical study of charge recombination at the TiO_2-electrolyte interface in dye sensitised solar cells. J Chem Phys 137:22A508
206. Sun Z, Zhang R-K, Xie H-H, Wang H, Liang M, Xue S (2013) Non-ideal charge recombination and conduction band edge shifts in dye-sensitized solar cells based on adsorbent doped poly(ethylene oxide) electrolytes. J Phys Chem C 117:4364–4373
207. Boschloo G, Hagfeldt A (2009) Characteristics of the iodide/triiodide redox mediator in dye-sensitized solar cells. Acc Chem Res 42:1819–1826
208. Ardo S, Meyer GJ (2009) Photodriven heterogeneous charge transfer with transition-metal compounds anchored to TiO_2 semiconductor surfaces. Chem Soc Rev 38:115–164
209. Richards CE, Anderson AY, Martiniani S, Law C, O'Regan BC (2012) The mechanism of iodine reduction by TiO_2 electrons and the kinetics of recombination in dye-sensitized solar cells. J Phys Chem Lett 3:1980–1984
210. Rowley JG, Farnum BH, Ardo S, Meyer GJ (2011) Iodide chemistry in dye-sensitized solar cells: making and breaking I–I bonds for solar energy conversion. J Phys Chem Lett 1:3132–3140
211. Rowley JG, Ardo S, Sun Y, Castellano FN, Meyer GJ (2011) Charge recombination to oxidized iodide in dye-sensitized solar cells. J Phys Chem C 115:20316–20325
212. O'Regan BC, Walley K, Juozapavicius M, Anderson A, Matar F, Ghaddar T, Zakeeruddin SM, Klein C, Durrant JR (2009) Structure/function relationships in dyes for solar energy conversion: a two-atom change in dye structure and the mechanism for its effect on cell voltage. J Am Chem Soc 131:3541–3548
213. Farnum BH, Gardner JM, Meyer GJ (2010) Flash-quench technique employed to study the one-electron reduction of triiodide in acetonitrile: evidence for a diiodide reaction product. Inorg Chem 49:10223–10225
214. Shi Y, Dong X (2013) Coupled analysis of steady-state and dynamic characteristics of dye-sensitized solar cells for determination of conduction band movement and recombination parameters. Phys Chem Chem Phys 15:299–306
215. Mora-Seró I, Bisquert J (2003) Fermi level of surface states in TiO_2 nanoparticles. Nano Lett 3:945–949
216. Cameron PJ, Peter LM (2005) How does back-reaction at the conducting glass substrate influence the dynamic photovoltage response of nanocrystalline dye-sensitized solar cells? J Phys Chem B 109:7392

Index